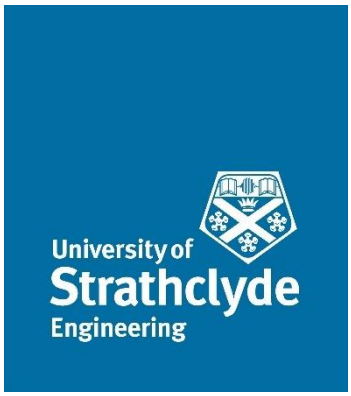

University of Strathclyde

Department of Naval Architecture, Ocean & Marine Engineering

PERIDYNAMICS FOR DAMAGE PREDICTION IN SHIPS AND OFFSHORE STRUCTURES

By

Cong Tien Nguyen

A thesis presented in fulfillment of the requirement for the degree of Doctor of Philosophy

Glasgow, UK

2020

AUTHOR STATEMENT

This thesis is the result of the author's original research. It has been composed by the author and has not been previously submitted for the examination which has led to the award of a degree.

Signed: Cong Tien Nguyen *Date*: 01 October 2020

DEDICATION

Dedicated to

My wife, Thu Thi Nguyen, and my daughter, Anh Thu Nguyen

ACKNOWLEDGEMENTS

I would like to thank to:

- My supervisor, Dr. Selda Oterkus for her help, great guidance, and strong support.
- Dr. Erkan Oterkus for his help, guidance, and strong support.
- Dr. Evangelos Boulougouris who is my second supervisor.
- Professor Atilla Incecik and Professor Peilin Zhou for giving me the initial idea of studying at the NAOME Department.
- Professor Osman Turan for inviting me to Glasgow and introducing me to Dr. Selda Oterkus and Dr. Evangelos Boulougouris.
- Administrative staff and technical staff of the NAOME Department for their great support.
- My sponsors, the Ministry of Education and Training in Vietnam, and the University of Strathclyde for their sponsorships.
- All of my friends in the NAOME Department for their friendship.
- Finally, my family for their support.

ABSTRACT

Ships and offshore structures can experience damages due to many reasons such as collisions, groundings, explosions, corrosion, fatigue, overloading, or extreme conditions, etc. To date, the prediction of progressive damages in these structures is a challenging research area. The classical continuum mechanics uses partial differential equations which become invalid in the presence of discontinuities. By contrast, the recently introduced nonlocal peridynamics (PD) theory uses integro-differential equations that are valid in both continuous and discontinuous models. Therefore, the peridynamics theory is highly suitable for predicting crack initiation and crack growth.

In this thesis, progressive damages in ship and offshore structures are predicted by using peridynamics. To do that, first, novel PD models for predicting linear elastic deformations of 3D beam structures and 3D shell structures are developed. The deformations of 3D beams and 3D shell structures predicted by using the developed PD beam and shell models agree very well with the FEA results with less than 3% relative errors. It is also found that the developed PD beam and shell models are suitable for predicting progressive brittle damages in ship and offshore structures. The PD shell model can also predict the ultimate bending moment of a ship with only 0.102% difference from the experimental result.

Second, novel nonlinear PD models for predicting damages in one-dimensional (1D), two-dimensional (2D), and three-dimensional (3D) structures, 3D beam structures, and plates subjected to large deformations are developed. The large deformations structures predicted by using the developed nonlinear PD models agree very well with the FEA results with maximum 5% relative errors. The developed nonlinear PD models show a capability to predict progressive damages for many complex problems. The damage patterns captured by the nonlinear PD models agree very well with the experimental results in the literature.

Third, a novel energy-based PD model for fatigue cracking is also developed. Instead of using the cyclic bond strain range for PD fatigue equations available in the literature, the energy-based PD fatigue model proposes a definition of the cyclic bond energy release rate range and use this term for PD fatigue equations. The fatigue life of the structure predicted by the energy-based PD fatigue model is 4.108% different from the experimental results while the predicted fatigue crack growth, $q - N$ curve agrees very well with experimental results. The energy-based PD fatigue model can be more suitable for beam and shell structures since in these structures, the bond energy release rate is unique although the bond strain consists of in-plane, shear, and bending components.

Finally, to reduce the computational cost for PD simulations, novel 1D and 2D peridynamic-based machine learning models for damage prediction are developed. The relations between displacements of a material point and the displacements of its family members as well as the externally applied forces are obtained by using linear regression. The machine learning models can easily be coupled with the PD models. Specifically, the PD model is used for the regions that are near crack surfaces or near boundary areas. Meanwhile, the ML model is used for the remaining regions to reduce the computational cost. Like the traditional PD model, it is found that the coupled PD-ML model is also suitable for damage prediction. The crack patterns predicted by using the coupled PD-ML model agree very well with experimental results in many complex problems. Therefore, the hybrid

approach of coupling ML with PD can be a potential approach for future research to reduce the computational cost for PD simulations while the capability of PD models in terms of damage prediction is maintained.

After All, it is expected that the results of the studies carried out in this thesis can make a significant contribution to the development of peridynamic theory and expand its application to ship and offshore structures. More importantly, the PD models developed in this thesis without any special treatment can be used for practical structural analysis to predict potential brittle damages in ship and offshore structures in complex phenomena. Therefore, the potential of structural damages can be minimized and the safety of the structures can be improved.

CONTENTS

LIST OF FIGURES

LIST OF TABLES

1. INTRODUCTION

This chapter aims to describe the background, motivation, objectives, and the novelty of the research contained in this Ph.D. thesis. First, the background and motivation of the research are presented in Section 1.1. Second, the aim and objectives of the research are presented in Sections 1.2 and 1.3, respectively. Next, the research approaches and thesis structure are presented in Sections 1.4 and 1.5, respectively. Finally, the assumptions adopted in this thesis are also presented.

1.1. Background and motivations

Damage prediction for ship and offshore structures: a big challenge

The safety of the ship and other marine structures is very important because their damages can cause many crucial issues. Therefore, these structures are often designed with high safety factors to minimize the potential of damages. However, according to the report in [1], there are still 1036 total losses for vessels over 100GT (GT: Gross Tonnage) over the past 10 years. The losses happened to various types of vessels as shown in Fig. 1.1 [1]. The cargo ship has the highest number of total losses with 429 cases, followed by fishery, bulk, passenger, and chemical product vessels with 149, 93, 67, and 56 cases, respectively. These ship losses can cause many serious effects such as environmental damages, human life, and economic losses. For example, the total number of losses for tanker, LPG, and chemical vessels are 78 which means that there were probably many thousands tons of environmentally harmful products left on or under the sea. This could destroy the sea environment as well as kill the sea and coastal creatures.

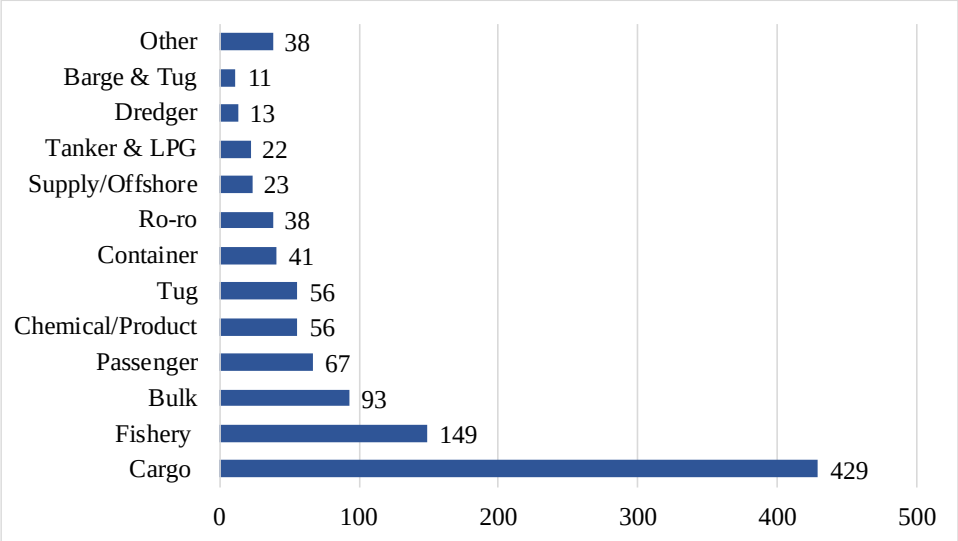

Fig. 1.1. Total losses by type of vessel over 100 GT from 2009 to 2018 [1]

For the reasons of ship losses, sinking and hull related damages are two main reasons as shown in Fig. 1.3 [1]. The high number of ship losses due to sinking and hull related damages shows that there are many uncertainties in the process of the ship structural design and assessment. One of these uncertainties is the limitation in terms of predicting possible progressive damages and fully understanding the behaviours of the ship structures during the damage progress.

Ship and offshore structures can experience either brittle or ductile fractures. Ductile fractures are common damages on ship structures. Beyond the elastic limit of the steel, the ship structures can experience plastic response before being collapsed. Brittle fractures can also occur on a ship structure due to high cycle fatigue loading or when the ship is subjected to the conditions of low-temperature, high-loading rate, multi-axial stress constraint, or low weldability of steel [2-6].

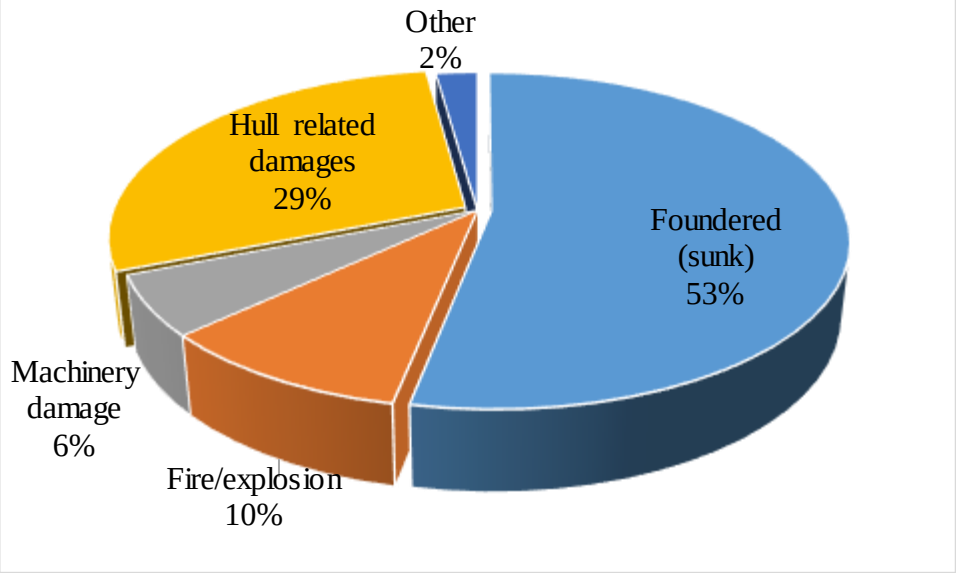

Fig. 1.2. Causes of losses from 2009 to 2018 for vessels over 100GT [1]

To date, analytical calculations based on regulations from classification society rules as well as finite element analysis (FEA) are common methods used in the ship structural design and assessment processes. However, in terms of damage prediction, the traditional finite element method (FEM) faces conceptual and mathematical difficulties to predict complex damages especially for multiple crack paths and crack branching problems since partial-differential equations used in CCM and FEM become invalid in presence of discontinuities.

To overcome this drawback for the traditional FEM, the simplest method is the use of remeshing techniques. However, for complex 3D structures and stiffened structures with multiple crack problems, the implementation of automatic remeshing techniques is very difficult.

To avoid the remeshing work, the extended finite element method (XFEM) was proposed [7-10]. This method allows cracks to pass through the elements leading to better approximations of crack paths without remeshing. However, XFEM uses additional criteria [7-10] to guide crack growth speed, direction, and coalescence or branching of cracks which are not easy to implement for multiple crack problems.

Besides, linear elastic fracture mechanics (LEFM) was also proposed for fracture problems. However, in LEFM, the size of the plastic zone ahead crack tips is assumed to be negligible. Therefore, LEFM applies to only brittle materials and the method also requires initial crack existing in the structures [11-13]. This means that bodies with blunt notches, but no cracks cannot be analysed using LEFM.

Unlike LEFM, the cohesive zone model (CZM) can adequately predict the behaviour of uncracked structures, including those with blunt notches [14-17]. Moreover, the size of the plastic zone need not be negligible in comparison with other dimensions of the cracked geometry in CZM. As the cohesive surfaces separate, traction first increases until a maximum is reached, and then subsequently reduces to zero which results in complete separation. In CZM, the cohesive constitutive relation must be selected with great caution since it decides the accuracy of the fracture predictions [18]. Therefore, a key issue for CZM is how to determine cohesive relations and parameters which often require experimentally studies [19]. Moreover, since the constitutive parameters in CZM may not have a clear physical meaning, that can be difficult to identify these parameters experimentally.

Peridynamics: a new paradigm for damage predictions

Peridynamic (PD) is a reformulation of classical continuum mechanics using integro-differential equations that are valid in both continuous and discontinuous models [20, 21]. Therefore, discontinuities can be naturally involved in the PD analysis without any special treatment. Peridynamics was first introduced by Silling [20] in 2000. After 20 years of development, the PD theory has been widely expanded to many applications. The PD theory can be used to analyze both elastic and inelastic material responses [22-26]. Moreover, it can also be either used to analyze composite and polycrystalline materials [27-31] or be applied for multiphysics [32-34] and multiscale modeling [35, 36]. Peridynamics can also be combined with finite element analysis [29, 37-39] as well as implemented in the FEA framework [40-42]. The extensive literature surveys on peridynamics can be found in [43-45].

In peridynamics, the motion of a material point is influenced by the collective deformations of surrounding material points within a distance, δ, which is called the horizon size. Material points within the horizon of a material point are called family members of that material point. As introduced by Silling [20], the motion of a particle in peridynamics is expressed by using integro-differential equations as

$$\rho(\mathbf{x})\ddot{\mathbf{u}}(\mathbf{x},t)=\int_{H_x}\left(\mathbf{t}(\mathbf{u}'-\mathbf{u},\mathbf{x}'-\mathbf{x},t)-\mathbf{t}'(\mathbf{u}-\mathbf{u}',\mathbf{x}-\mathbf{x}',t)\right)dV'+\mathbf{b}(\mathbf{x},t) \tag{1.1a}$$

which can also be represented in the discrete form as

$$\rho_{(k)}\ddot{\mathbf{u}}_{(k)}=\sum_{j=1}^{N}\begin{pmatrix}\mathbf{t}_{(k)(j)}(\mathbf{u}_{(j)}-\mathbf{u}_{(k)},\mathbf{x}_{(j)}-\mathbf{x}_{(k)},t)\\-\mathbf{t}_{(j)(k)}(\mathbf{u}_{(k)}-\mathbf{u}_{(j)},\mathbf{x}_{(k)}-\mathbf{x}_{(j)},t)\end{pmatrix}V_{(j)}+\mathbf{b}_{(k)} \tag{1.1b}$$

where ρ represents the mass density, $\mathbf{u}$ and $\mathbf{b}$ represent displacement and body force vectors, respectively. In Eq. (1.1b), N represents the number of family members of material point k, j represents the family member of material point k, $\mathbf{t}_{(k)(j)}$ represents the force density that material point j exerts on material point k, and $\mathbf{t}_{(j)(k)}$ represents the force density that material point k exerts on material point j.

Peridynamics theory includes bond-based, ordinary state-based, and non-ordinary state-based formulations. In the bond-based PD (BBPD) theory, the force densities $\mathbf{t}_{(k)(j)}$and $\mathbf{t}_{(j)(k)}$ are equal in magnitude but opposite in direction [21, 43, 44]. However, the volumetric and deviatoric parts of strain energy density are not

distinguished in the bond-based theory. Therefore, the bond-based PD theory is only applicable for elastic material with Poisson's ratio equal to 1/4 for 3D structures and 2D structures in the plane strain condition, or material with Poisson's ratio equal to 1/3 for 2D structure in the plane stress condition [43, 44].

In the ordinary state-based model (OSBPD), the force densities $\mathbf{t}_{(k)(j)}$and $\mathbf{t}_{(j)(k)}$ may have opposite direction but their magnitudes can be different [44, 46]. The PD strain energy density includes the volumetric and deviatoric parts. Therefore, the OSBPD can overcome the limitation of the BBPD in terms of Poisson's ratio. Note that, in both BBPD and OSBPD models, the force densities $\mathbf{t}_{(k)(j)}$ and $\mathbf{t}_{(j)(k)}$ are parallel to the line of interaction between material points k and j in the deformed configuration. On the other hand, in the non-ordinary state-based model (NOSBPD), the force densities $\mathbf{t}_{(k)(j)}$ and $\mathbf{t}_{(j)(k)}$ can have different directions and they may not be parallel to the line of interaction between material points k and j in the deformed configuration [44, 46].

The force densities in Eq. (1.1) can be calculated by using the relation between PD strain energy density, $W_{(k)}^{PD}$ and PD force densities developed by Madenci and Oterkus [44] as

$$\mathbf{t}_{(k)(j)} = -\frac{1}{V_{(j)}}\frac{\partial W_{(k)}^{PD}}{\partial \mathbf{u}_{(k)}},\ \mathbf{t}_{(j)(k)} = -\frac{1}{V_{(k)}}\frac{\partial W_{(j)}^{PD}}{\partial \mathbf{u}_{(j)}} \tag{1.2}$$

where $W_{(k)}^{PD}$ represents the PD strain energy density of material point k.

In peridynamics, progressive damage can be naturally involved by introducing the elimination of interactions between material points. When the interaction between two material points is broken, the force densities between these points are irreversibly removed, and it leads to crack growth. The state of the interaction between material points k and j can be represented by a function, $\psi_{(k)(j)}$ which is introduced by Silling and Askari [21] as

$$\psi_{(k)(j)}\left(\mathbf{x}_{(j)} - \mathbf{x}_{(k)}, t\right) = \begin{cases} 1 & \text{if interaction exists,} \\ 0 & \text{if interaction is broken} \end{cases} \tag{1.3}$$

Therefore, the PD equation of motion given in Eq. (1.1b) can be rewritten as

$$\rho_{(k)}\ddot{\mathbf{u}}_{(k)} = \sum_{j=1}^{N}\psi_{(k)(j)}\left(\mathbf{t}_{(k)(j)} - \mathbf{t}_{(j)(k)}\right)V_{(j)} + \mathbf{b}_{(k)} \tag{1.4}$$

In peridynamics, the local damage on the structures is represented by the damage index, $\phi\left(\mathbf{x}_{(k)}, t\right)$. This damage index is the ratio of eliminated interactions to the total number of interactions associated with a material point within its horizon, and it can be represented as [21]

$$\phi\left(\mathbf{x}_{(k)}, t\right) = 1 - \frac{\sum_{j=1}^{N}\mu_{(k)(j)}V_{(j)}}{\sum_{j=1}^{N}V_{(j)}} \tag{1.5}$$

The value of the damage index is between 0 and 1, in which $\phi = 0$ represents no damage at the material point, and $\phi = 1$ represents all interactions of that material point with its family members are eliminated.

The interaction state, $\psi_{(k)(j)}$, given in Eq. (1.3) can be decided by using two common damage criteria which are critical bond stretch [20, 21, 44] and critical energy release rate [25, 26, 47]. The damage criterion using critical bond stretch can be described as [21, 44]

$$\begin{aligned} &s_{(k)(j)} < s_c \rightarrow \text{interaction exists: } \psi_{(k)(j)} = 1 \\ &s_{(k)(j)} \geq s_c \rightarrow \text{interaction is broken: } \psi_{(k)(j)} = 0 \end{aligned} \tag{1.6}$$

where $s_{(k)(j)}$ represents the bond stretch between material points k and j. The term s_c represents the critical bond stretch which can be estimated as [44]

$$s_c = \sqrt{\frac{G_c}{\left(3\mu + \left(\frac{3}{4}\right)^4 \left(\kappa - \frac{5}{3}\mu\right)\right)\delta}} \quad \text{for 3D structures} \tag{1.7a}$$

$$s_c = \sqrt{\frac{G_c}{\left(\frac{6}{\pi}\mu + \frac{16}{9\pi^2}(\kappa - 2\mu)\right)\delta}} \quad \text{for 2D structures} \tag{1.7b}$$

where G_c represents the critical energy release rate of material, μ and κ are the shear modulus and Bulk modulus of the material, respectively.

The damage criterion using critical bond energy release rate can be described as [25, 26]

$$\begin{aligned} &\bar{g}_{(k)(j)} < g_c \rightarrow \text{interaction exists: } \psi_{(k)(j)} = 1 \\ &\bar{g}_{(k)(j)} \geq g_c \rightarrow \text{interaction is broken: } \psi_{(k)(j)} = 0 \end{aligned} \tag{1.8}$$

where $\bar{g}_{(k)(j)}$ represents the energy release rate for interaction between material points k and j which can be calculated as

$$\bar{g}_{(k)(j)} = \frac{1}{2}\left(g_{(k)(j)} + g_{(j)(k)}\right) \tag{1.9a}$$

with

$$g_{(k)(j)} = \frac{1}{A_{crack}} \Phi_{(k)(j)} V_{(k)} V_{(j)} \tag{1.9b}$$

$$g_{(j)(k)} = \frac{1}{A_{crack}} \Phi_{(j)(k)} V_{(j)} V_{(k)} \tag{1.9c}$$

where $\Phi_{(k)(j)}$ and $\Phi_{(j)(k)}$ represent micropotentials of the interaction between material points k and j. The term A_{crack} represents a unit crack surface in the PD model [25, 26] which can be defined as

$$A_{crack} = \begin{cases} A & \text{for 1D structures} \\ \Delta x\, h & \text{for 2D structures} \\ \Delta x^2 & \text{for 3D structures} \end{cases} \tag{1.10}$$

where Δx represents the mesh size for the PD model.

The term, g_c, in Eq. (1.8) represents the critical energy release rate for one interaction which can be approximated as [25, 26]

$$g_c = \frac{G_c}{N_c} \tag{1.11}$$

where N_c represents the total number of interactions passing through a unit crack

surface [25, 26].
For 1D structures, the unit crack surface can be considered as the beam cross-section. Therefore, as shown in Fig. 1.3, there are $N_c = 12$ interactions passing through the crack surface.

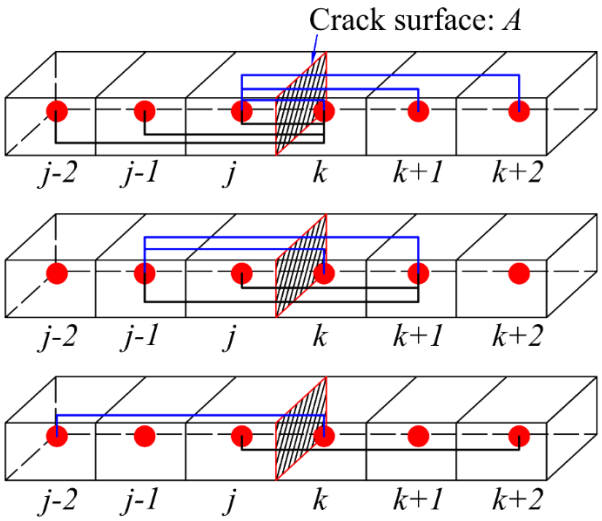

Fig. 1.3. Counting the number of interactions passing through the crack surface

For 2D structure, the line of interaction between two material points can pass either through the crack tips or through the crack surface as shown in Fig. 1.4. The interactions passing through the crack tips can be counted as $1/2$ interaction, meanwhile, the interaction passing through the crack surface can be counted as 1 interaction [25, 26]. As shown in Fig. 1.4, for 2D structures there are 24 interactions passing through the crack surface and 24 interactions passing through the crack tips. Therefore, the total number of interactions passing the unit crack surface can be counted as $N_c = 24 \times 1 + 24 \times 1/2 = 36$.

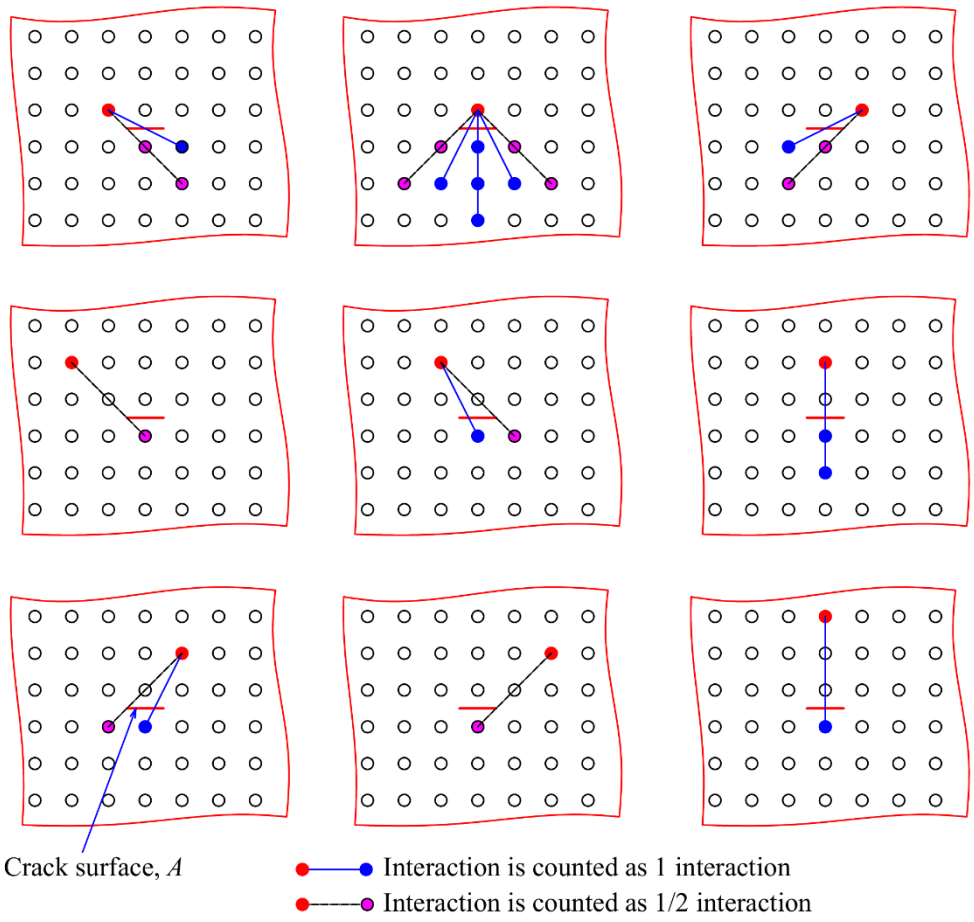

Fig. 1.4. Counting the number of interactions, N_c, passing unit crack surface on a 2D plate for $\delta = 3.015\Delta x$

For 3D structure, the line of interaction between two material points can pass through either crack edge, or crack corner, or crack surface, A_{crack} as shown in Fig. 1.5. The interaction passing through the crack surface can be counted as 1 interaction. The interaction passing through the crack edges can be counted as 1/2 interaction, meanwhile, the interaction passing through the crack corners can be counted as 1/4 interaction. For a PD model with a horizon size of $\delta = 3.015\Delta x$, there are 392 interactions passing through the unit crack surface, 320 interactions passing through the crack edges, and 32 interactions passing through the crack corners. Therefore, the total number of interactions passing the unit crack surface can be counted as $N_c = 392 \times 1 + 320 \times 1/2 + 32 \times 1/4 = 560$.

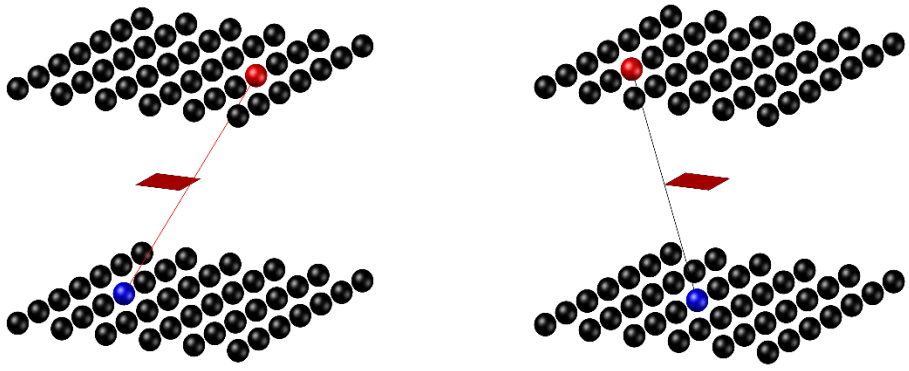

(a) (b)

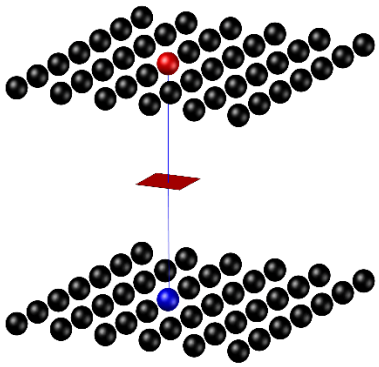

(c)

Fig. 1.5. Interaction passing (a) crack edges, (b) crack corners, (c) a point inside crack surface on 3D structures for $\delta = 3.015\Delta x$

Research gaps

Although the PD theory has many applications, developing a PD model for complex structures such as a ship and offshore structures is still challenging work. When analysing these complex structures, the existing three-dimensional PD model becomes computationally expensive. Therefore, simplified peridynamic structural models can be used to reduce the computational cost.

The first peridynamic model capturing the tension and compression for 1D bars is introduced by Silling, et al. [48]. Later, O'Grady and Foster [49] introduced a non-ordinary state-based PD model for the Euler-Bernoulli beam by including transverse displacements but disregarding the transverse shear deformations. To include transverse shear deformations, Diyaroglu, et al. [50] introduced a bond-based PD model based on the Timoshenko beam theory. The PD beam model provided by Diyaroglu, et al. [50] has two degrees of freedom (DOF), which are transverse displacement and rotation. Meanwhile, the PD beam model developed by O'Grady and Foster [49] has one degree of freedom, which is the transverse displacement. It is obvious that a 3D beam, based on the Timoshenko beam theory, has six degrees of freedom (DOFs) including three translational displacements and three rotations. Moreover, beam structures in the real world often include many beams joined together, and each beam can be straight or curved. Therefore, a PD model with 6 degrees of freedom, which can capture deformations for complex beam structures such as a jacket platform, needs to be developed.

Another common type of simplified structural model used in engineering is plates or shells. In peridynamics, the first simplified PD model for two-dimensional (2D) structures, which includes two in-plane DOFs, was introduced by Silling and Bobaru [51], and later by Madenci and Oterkus [44]. To account for bending deformations, O'Grady and Foster [52] introduced a non-ordinary state-based PD model based on Kirchhoff–Love plate theory. Later, Diyaroglu, et al. [50] developed a bond-based PD model for plates based on the Mindlin plate theory. The PD models developed by the authors can be applied for a single plate or flat shell. In practice, a shell structure can be constructed from many individual shells and plates. Therefore, a PD shell model with 6 DOFs that can capture the deformation and predict progressive damage for complex shell structures such as a ship needs to be developed.

Moreover, it is very common that large-scale bodies such as ship and offshore structures can experience large elastic or inelastic deformations during their operational process. In such cases, nonlinear analyses need to be used to capture the correct behaviours of the structures. A fundamental difference between elastic and inelastic analyses is that in the elastic solution the total stress can be directly evaluated from total strain, whereas in the inelastic analysis the stress and strain history is also included in the calculation of total stress. In peridynamics, the original PD model [20, 21] can capture large elastic deformations for 3D structures. Later, Foster, et al. [22], Mitchell [24], Madenci and Oterkus [25], Rahaman, et al. [53], Amani, et al. [54], Sun and Sundararaghavan [55], LADANYI and JENEI [56] developed PD models for inelastic deformations. However, within the elasticity, the current PD models for 1D and 2D structures [44, 57], for beams, plates, and shells [50, 58, 59] are only applicable for small deformations. Therefore, to make PD becomes applicable for analysing ship and offshore structures, nonlinear PD models for large deformations of 1D and 2D structures, as well as beam, plate, and shell structures need to be developed.

Besides, ships and offshore structures are often designed with the expectation of a long lifetime in the marine environment. Due to the repetition of the loading caused by wind, wave, current, and other harsh conditions, fatigue damages can occur on the structures, which may lead to major accidents. Therefore, fatigue design assessment (FDA) is one of the design drivers for ship and offshore structures. For fatigue crack prediction, the first PD fatigue model is proposed by Silling and Askari [60], in which, each interaction has its own remaining life. During the cyclic loading processes, the remaining life is updated by using the PD fatigue equations for the cyclic bond strain range. However, in some special cases, the bond strain can consist of different components. For instance, the bond strains in beams and shell structures consist of in-plane, shear, and bending components [61, 62]. Therefore, deciding which strain will be used for the PD fatigue equation can be a challenge. Therefore, to investigate fatigue damages in ship and offshore structures, a novel PD fatigue model which can be applicable for beam and shell structures is needed.

Moreover, solving PD equations of motion could be time-consuming, especially when real-time predictions on live data are required. By contrast, with the support of computer resources as well as the rapid growth of available data, data-driven models are providing an alternative, robust solution for physics-based models. Therefore, to speed up PD simulations for large complex ship and offshore structures, PD-based machine learning models for damage prediction is needed.

1.2. The aim of the research

This thesis aims to use peridynamics to predict accurately progressive damages in ship and offshore structures and clearly understand the behaviours of ship and offshore structures during their damage processes. Therefore, further actions can be made to prevent catastrophic failure and to enhance structural safety.

1.3. The objectives of the research

To obtain the research aim, the research in this thesis has five main objectives:

1. Development of a novel PD beam and shell models with 6DOFs for predicting progressive damages in the complex 3D beam and 3D shell structures.

2. Development of novel nonlinear PD models for geometrically nonlinear analyses of 1D, 2D, 3D structures, 3D beams, and plates.

3. Development of a novel energy-based PD fatigue model that is potentially applicable for predicting fatigue damage initiation and propagation in shell structures.

4. Development of a novel PD-based machine learning model for fracture prediction of structures as well as to speed up the traditional PD simulations.

5. Applying the developed PD models to predict progressive damages and residual strengths of ship and offshore structures subjected to different loading conditions.

1.4. The research approaches

To obtain the proposed objectives, the research in this thesis will be conducted using the following approaches:

1. To develop novel PD models for 3D beam and 3D shells, first, the existing PD models in the literature for beams and shells are critically reviewed to find out the needed further research. Second, the kinematics of the Timoshenko beam and Mindlin plate in classical continuum mechanics are studied. Third, the linear PD formulations for analysing 3D beams and shell structures are developed. Next, for verification purposes, the deformations of beam and shell structures predicted by using the developed PD models are compared against FEA results. Finally, the PD beam and shell models are used to predict damages in beams, shells, and stiffened structures. These goals are achieved in Nguyen and Oterkus [61-64] as parts of the research described in Chapter 2.

2. To develop novel nonlinear PD models for geometrically nonlinear analyses of 1D, 2D, 3D structures, 3D beams, and plates, first, the existing nonlinear PD models in the literature are critically reviewed to find out the needed further research. Second, the nonlinear kinematics of 1D, 2D, 3D structures, 3D beams, and plates in classical continuum mechanics are studied. Third, the nonlinear PD formulations for analysing large deformations of 1D, 2D, 3D structures, 3D beams, and plates are developed. Next, for verification purposes, the large deformations of the structures predicted by using the developed nonlinear PD models are compared against FEA results. Finally, the developed nonlinear PD models are used to predict damages in 2D, 3D

structures, 3D beams, and plates. These goals are achieved in Nguyen and Oterkus [65], [66, 67] as parts of the research described in Chapter 3.

3. To develop a novel energy-based PD fatigue model, first, the applicability of the existing PD fatigue model in the literature for shells and stiffened structures is critical reviewed. Second, a novel energy-based PD fatigue model is developed by proposing novel energy-based fatigue equations in PD. Finally, the capability of the developed energy-based PD fatigue model is verified by investigating mode I and mixed-mode fatigue crack growth problems. This goal is achieved in Nguyen and Oterkus [68] as part of the research described in Chapter 4.

4. To develop a novel PD-based machine learning model for fracture predictions, first, the potential applications of machine learning as well as physic-guided machine learning models for structural analysis and damage predictions are critically reviewed to determine the needed further development. Second, the PD-based machine learning model is developed by training data generated from modal analyses in ANSYS. Third, a hybrid approach to couple the developed PD-based machine learning model with the traditional PD model for damage predictions is developed. Finally, the accuracy and capability of the PD-based model and the coupled models for damage predictions are proven by investigating various fracture problems. This goal is achieved in Nguyen, et al. [69] as part of the research described in Chapter 5.

5. To apply the developed PD models for damage predictions of ship and offshore structures, the developed linear PD beam and shell models are used. Progressive damages on a jacket platform, a hull girder, and corroded stiffened structures subjected to different loading conditions are predicted. The residual strengths of the ship and stiffened structures during damage processes are also investigated. This goal is achieved in Nguyen and Oterkus [62], [63, 64] as part of the research described in Chapter 2.

1.5. Thesis Structure

This thesis is constituted by the following 6 chapters as follows:

Chapter 1. This chapter provides a review of ship losses and structural damages from 2009 to 2019. The critical challenges in terms of progressive damage prediction for ship structures are also addressed. Moreover, the suitability of peridynamics for damage prediction and the current research gaps are addressed. Finally, the research aim, objectives, and approaches as well as the thesis structure are described.

Chapter 2. This chapter provides detailed formulations for novel PD models for 3D beam and 3D shell structures. The bond-based PD model for three-dimensional complex beam structures with 6 degrees of freedom is developed based on the Timoshenko beam theory. The ordinary state-based PD model for 3D shell structures is developed based on Mindlin plate theory. The numerical techniques

for dealing with complex beam and shell structures are provided for the first time in the peridynamic literature. The energy-based damage criteria for 3D beam and 3D shell structures are also presented. The validity of peridynamic predictions for beams is established by considering various examples, including straight beams, curved beams, and offshore jacket platform. The validity of peridynamic predictions for shells is achieved by predicting mechanical and thermomechanical deformations for a flat shell, a curved shell, and a stiffened structure. Later, the developed PD beam model is used to predict damages for a pre-notched beam subjected to impact loading, for a jacket platform subjected to ship collisions. The developed PD shell model is used to predict progressive damages in different plates subjected to out-of-plane deformations, a ship structure subjected to different loading conditions, a stiffened structure with localized corrosion subjected to uniform pressure. The residual strength of the ship and stiffened structures during damage propagations are also numerically calculated.

Chapter 3. This chapter provides detailed formulations for novel peridynamic models for geometrically nonlinear analysis of 1D, 2D, 3D structures, 3D beams, and plates. The nonlinear PD models for 1D structures and 3D beams are bond-based PD formulations. Meanwhile, the nonlinear PD models for 2D, 3D structures and plates are ordinary state-based PD formulations. The nonlinear PD equations of motion are obtained based on the principle of virtual displacements using Total Lagrange formulation. The accuracy of the developed nonlinear PD model is verified by comparing it with nonlinear FEA. To further demonstrate the capabilities of the nonlinear PD models, damages on different 2D and 3D structures, a spaghetti subjected to bending and torsion, a plate with a single crack subjected to stretching and tearing, a plate with two parallel cracks subjected to tearing, and a plate subjected to torsional loading are predicted.

Chapter 4. This chapter provides detailed formulations for a novel energy-based peridynamic model for fatigue cracking. The definition of cyclic bond energy release rate and the energy-based peridynamic fatigue equations for both phases (crack initiation and crack growth) are introduced. For validation, first, a problem of mode-I fatigue crack growth is investigated. Next, different mixed-mode fatigue damages are also investigated and the peridynamic results are compared with the experimental results.

Chapter 5. This chapter provides detailed formulations for a novel peridynamic-based machine learning model for one and two-dimensional structures. The linear relationships between the displacement of a material point and displacements of its family members and applied forces are obtained by using linear regression. The numerical procedure for combining the peridynamic model and the machine learning model is also provided. The accuracy of the coupled model is verified by considering various examples of a one-dimensional bar and two-dimensional plate. To further demonstrate the capabilities of the coupled model, damage prediction for a plate with a pre-existing crack, a two-dimensional representation of a three-point bending test, and a plate subjected to dynamic load are simulated.

Chapter 6. This chapter highlights the novelty and contributions of this research. Moreover, the recommendations for the industry as well as the limitations of the current research are also presented. Finally, the recommended future work is also addressed.

Chapter 7. This chapter gives final remarks for the thesis as well as summarizes the major findings.

1.6. Assumptions used in this thesis

In this thesis, the following assumptions are adopted:

First, the linear and nonlinear PD beam models in Sections 2.2 and 3.3, the nonlinear PD model for 1D structure in Section 3.2, the PD-based machine learning model in Chapter 5 are based on bond-based PD formulations. Meanwhile, the PD models for the remaining sections and chapters are based on the ordinary state-based formulations.

Second, in Sections 2.2, 3.2, and 3.3, the numerical results were obtained for materials with zero Poisson's ratio, $\nu = 0$. Meanwhile, the Poisson's ratio in Chapter 5 is $\nu = 1/3$ for 2D plane stress and $\nu = 1/4$ for 2D plane strain and 3D models.

Third, the energy-based damage criteria given in Eq. (1.8) are used throughout the thesis except Chapter 5. In the PD models used in the thesis, every bond is assumed to have the same critical energy release rate, g_c. Therefore, the value of the critical energy release rate for a bond, g_c, is simply estimated by using Eq. (1.11).

Finally, material nonlinearity is not considered, and materials are assumed to have brittle damages.

2. PERIDYNAMICS FOR LINEAR ANALYSIS OF BEAM AND SHELL STRUCTURES

2.1. Introduction

Beam structures in the real world often include many beams joined together, and each beam can be straight or curved. Similarly, shell structures can be constructed from many individual shells and plates. In classical continuum mechanics, a 3D beam, based on the Timoshenko beam theory, has six local degrees of freedom (DOFs) including three translational displacements and three rotations. Meanwhile, a 3D beam, based on the Euler–Bernoulli beam theory, has only three translational displacements. In plate theories, a plate based on Mindlin plate theory can have five local degrees of freedom including three displacements and two rotations. Meanwhile, a plate based on the Kirchhoff–Love plate theory can have three local degrees of freedom which are three displacements. The formulations based on Mindlin plate theory are commonly used for shells and complex stiffened structures.

In FEA, to govern every parameter for complex beam and shell structures, the Cartesian coordinate system, which is fixed and unique, is often chosen as the reference coordinate system. In beam structures, each beam element has 6 global degrees of freedom. These 6 global DOFs can be obtained by multiplying the transformation matrix [70] with the vector of 6 local DOFs. In shell structures, each shell element also has 6 global degrees of freedom, meanwhile, based on Mindlin plate theory, it has only 5 local degrees of freedom. Therefore, if the drilling rotation is not considered as the sixth local DOF, all the resistance to the drilling rotation of each node comes directly from the coupling of other rotational DOFs of the non-planar surrounding nodes. When the model is discretized with very fine mesh, angles of the kinks between two elements, which are located next to each other, will become close to 2π and the coupling effect is much reduced [71]. As a result, the global stiffness matrix may become singular and it results in unrealistic solution results. Therefore, to avoid this problem, the drilling rotation can be considered as the 6^{th} local DOF and a small stiffness associated with drilling rotation can be added [71].

In peridynamics, the current studies in the literature only considered formulations for 2D plane beams and single plates and shells. Specifically, O'Grady and Foster [49] introduced a non-ordinary state-based PD model for a 2D plane beam based on Euler-Bernoulli beam theory. Later, Diyaroglu, et al. [58] also introduced an ordinary state-based PD model for a 2D plane beam based on this beam theory. For the Timoshenko beam, Diyaroglu, et al. [50] also introduced a bond-based PD model for 2D plane beams. The PD beam model [50] consists of two degrees of freedom (DOF), which are transverse displacement and rotation. For plates and flat shells, O'Grady and Foster [52] introduced a non-ordinary state-based PD model based on Kirchhoff–Love plate theory with 1 DOF which is the transverse displacement. Later, Diyaroglu, et al. [50] developed a bond-based PD model for plates based on the Mindlin plate theory. The model developed by Diyaroglu, et al. [50] can capture behaviours of a single plate with 3 local DOFS which are transverse displacement (w) and two rotations (θ_x, θ_y).

Therefore, in this chapter, novel PD models for 3D beam structures and 3D shell structures are developed. First, a bond-based PD beam model with 6 local degrees of freedom based on the Timoshenko beam theory is developed. The equations of motion for a beam element in the local coordinate system are obtained by using the Euler-Lagrange equation. Similar to FEA, six global equations of motion for a beam element are obtained by using the transformation matrix for a beam element [62]. Therefore, the developed PD beam model can capture deformations for a straight beam, curved beam, and complex beam structures. Second, a novel ordinary state-based PD model for a flat shell with 6 local DOFs based on Mindlin plate theory is developed. Similar to the PD beam model, equations of motion for 6 local DOFs are obtained by using the Euler-Lagrange equation. Next, equations of motion for 6 global DOFs are obtained by using the transformation matrix for a shell element [61, 64]. Therefore, the developed PD shell model can capture deformations for flat shells, curved shells, and complex stiffened structures.

2.2. Peridynamics for linear 3D beam structures

In this section, a novel bond-based peridynamic model is developed for three-dimensional complex beam structures with 6 degrees of freedom based on the Timoshenko beam theory. The energy-based damage criteria for beam structures with 6 degrees of freedom are also presented. The validity of peridynamic predictions is established by considering various examples. Initially, the proposed PD model is used to predict the structural behaviour of straight and curved beams. Next, the proposed PD model is used to investigate a jacket platform. The PD predictions are verified by comparing the predicted results with finite element solutions. Finally, the developed PD beam model is used to predict damage in a jacket platform subjected to ship-jacket platform collisions.

2.2.2. Beam kinematics in classical continuum mechanics

In this section, first, stress-strain relations for beam structures are obtained. Next, the strain energy density is established based on the small deformation assumption. According to the Timoshenko beam theory, it is assumed that plane cross-section remains plane after the deformation, but it does not have to remain normal to the neutral axis [70]. The Timoshenko beam has six degrees of freedom [72]; three displacements (u, v, w) and three cross-sectional rotations $(\theta_x, \theta_y, \theta_z)$ as shown in Fig. 2.1. The displacement components of a material point can be defined as [70]

$$u(x,y,z) = \hat{u}(x) + z\theta_y(x) - y\theta_z(x) \tag{2.1a}$$

$$v(x,y,z) = \hat{v}(x) - z\theta_x(x) \tag{2.1b}$$

$$w(x,y,z) = \hat{w}(x) + y\theta_x(x) \tag{2.1c}$$

where x represents the beam's longitudinal axis which is located at the centreline of the beam and $\hat{u}$, $\hat{v}$, $\hat{w}$ represent the displacement components at the centreline of the beam.

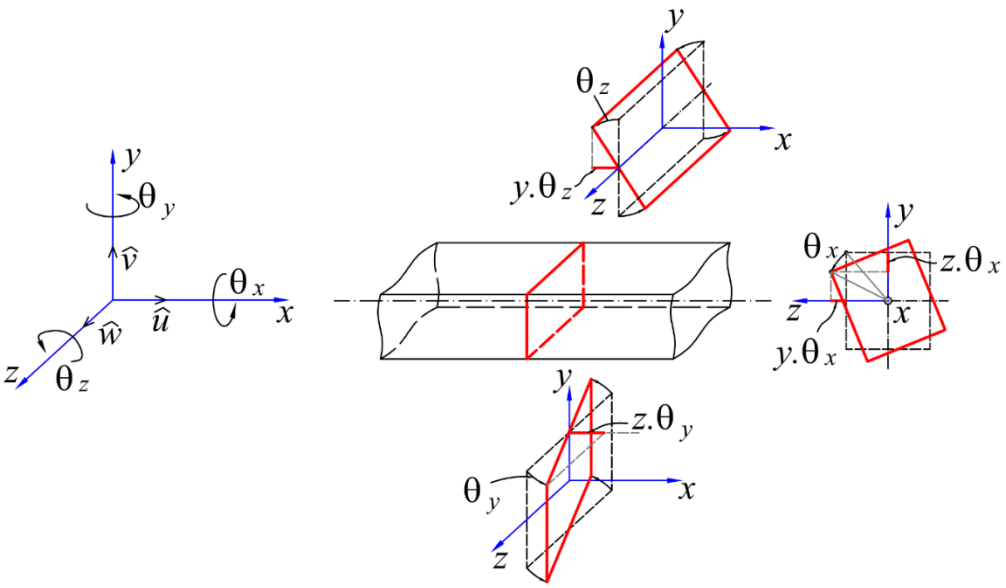

Fig. 2.1. Beam configuration with 6 DOFs

By using the displacement components defined in Eq. (2.1), the linear strain components of the beam can be calculated as

$$\varepsilon_{xx} = u_{,x} = \hat{u}_{,x} + z\theta_{y,x} - y\theta_{z,x} \tag{2.2a}$$

$$\gamma_{xy} = u_{,y} + v_{,x} = \hat{v}_{,x} - \theta_z - z\theta_{x,x} \tag{2.2b}$$

$$\gamma_{xz} = u_{,z} + w_{,x} = \hat{w}_{,x} + \theta_y + y\theta_{x,x} \tag{2.2c}$$

$$\varepsilon_{yy} = \varepsilon_{zz} = \gamma_{yz} = 0 \tag{2.2d}$$

Based on the small deformation assumptions in linear elasticity, Cauchy stress components can be directly calculated from linear strain components as [70]

$$\sigma_{xx} = E\varepsilon_{xx} = E\left(\hat{u}_{,x} + z\theta_{y,x} - y\theta_{z,x}\right) \tag{2.3a}$$

$$\sigma_{xy} = G\gamma_{xy} = G\left(\hat{v}_{,x} - \theta_z - z\theta_{x,x}\right) \tag{2.3b}$$

$$\sigma_{xz} = G\gamma_{xz} = G\left(\hat{w}_{,x} + \theta_y + y\theta_{x,x}\right) \tag{2.3c}$$

$$\sigma_{yy} = \sigma_{zz} = \sigma_{yz} = 0 \tag{2.3d}$$

where E represents the elastic modulus and G represents the shear modulus. The strain energy per unit length of the beam can be calculated as

$$U = \int_A \left[\frac{E}{2}\varepsilon_{xx}^{\ 2} + \frac{G}{2}\gamma_{xy}^{\ 2} + \frac{G}{2}\gamma_{xz}^{\ 2}\right] dA = U_1 + U_2 \tag{2.4a}$$

with

$$U_1 = \frac{E}{2}\int_A \varepsilon_{xx}^{\ 2} dA \tag{2.4b}$$

$$U_2 = \frac{G}{2}\int_A \left[\gamma_{xy}^{\ 2} + \gamma_{xz}^{\ 2}\right] dA \tag{2.4c}$$

where A represents the cross-sectional area of the beam.

Utilizing the strain definition given in Eq. (2.2), the strain energy per unit length of the beam given in Eq. (2.4) can be rewritten as

$$U_1 = \frac{E}{2}\int_A \left[\hat{u}_{,x}^{\ 2} + \left(z^2\theta_{y,x}^{\ 2} + y^2\theta_{z,x}^{\ 2} - 2yz\theta_{y,x}\theta_{z,x}\right) + 2\hat{u}_{,x}\left(z\theta_{y,x} - y\theta_{z,x}\right)\right] dA \tag{2.5a}$$

$$U_2 = \frac{G}{2}\int_A \begin{bmatrix} \left[\left(\hat{v}_{,x} - \theta_z\right)^2 + \left(\hat{w}_{,x} + \theta_y\right)^2\right] + \left(z^2 + y^2\right)\theta_{x,x}{}^2 \\ + \left(2y\left(\hat{w}_{,x} + \theta_y\right) - 2z\left(\hat{v}_{,x} - \theta_z\right)\right)\theta_{x,x} \end{bmatrix} dA \tag{2.5b}$$

By considering a beam with symmetric cross-section, the area moment of inertia and the first moment of area are obtained as

$$I_{yy} = \int_A z^2 dA;\ I_{zz} = \int_A y^2 dA;\ I_{yz} = \int_A yz dA = 0 \tag{2.6a}$$

$$S_y = \int_A z dA = 0;\ S_z = \int_A y dA = 0 \tag{2.6b}$$

By utilizing relations given in Eq. (2.6), strain energy per unit length can be written as

$$U_1 = \frac{EA}{2}\hat{u}_{,x}{}^2 + \frac{E}{2}\left(I_{yy}.\theta_{y,x}{}^2 + I_{zz}.\theta_{z,x}{}^2\right) \tag{2.7a}$$

$$U_2 = \frac{GA}{2}\left[\left(\hat{v}_{,x} - \theta_z\right)^2 + \left(\hat{w}_{,x} + \theta_y\right)^2\right] + \frac{G}{2}\left[\int_A \left(z^2 + y^2\right) dA\right]\theta_{x,x}{}^2 \tag{2.7b}$$

By adding the shear correction factor, k_s [73], and replacing $\int_A (z^2 + y^2) dA$ by torsional constant, k_t [74], Eq. (2.7b) becomes

$$U_2 = \frac{k_s GA}{2}\left[\left(\hat{v}_{,x} - \theta_z\right)^2 + \left(\hat{w}_{,x} + \theta_y\right)^2\right] + \frac{k_t G}{2}\theta_{x,x}{}^2 \tag{2.8}$$

By substituting Eq. (2.7a), (2.8) into Eq. (2.4a) the strain energy per unit length of the beam can be written as

$$\begin{aligned} U = {} & \frac{EA}{2}\hat{u}_{,x}{}^2 + \frac{E}{2}\left(I_{yy}.\theta_{y,x}{}^2 + I_{zz}.\theta_{z,x}{}^2\right) \\ & + \frac{k_s GA}{2}\left[\left(\hat{v}_{,x} - \theta_z\right)^2 + \left(\hat{w}_{,x} + \theta_y\right)^2\right] + \frac{k_t G}{2}\theta_{x,x}{}^2 \end{aligned} \tag{2.9}$$

The strain energy density can be defined as

$$\begin{aligned} W = \frac{U}{A} = {} & \frac{E}{2}\hat{u}_{,x}{}^2 + \frac{E}{2A}\left(I_{yy}.\theta_{y,x}{}^2 + I_{zz}.\theta_{z,x}{}^2\right) \\ & + \frac{k_s G}{2}\left[\left(\hat{v}_{,x} - \theta_z\right)^2 + \left(\hat{w}_{,x} + \theta_y\right)^2\right] + \frac{k_t G}{2A}\theta_{x,x}{}^2 \end{aligned} \tag{2.10}$$

The strain energy density can also be decomposed into its axial, bending, shear and torsional components as

$$W = W_{axial} + W_{bending} + W_{shear} + W_{torsional} \tag{2.11a}$$

where

$$W_{axial} = \frac{E}{2}\hat{u}_{,x}{}^2 \tag{2.11b}$$

$$W_{bending} = \frac{E}{2A}\left(I_{yy}\theta_{y,x}{}^2 + I_{zz}\theta_{z,x}{}^2\right) \tag{2.11c}$$

$$W_{shear} = \frac{k_s G}{2}\left[\left(\hat{v}_{,x} - \theta_z\right)^2 + \left(\hat{w}_{,x} + \theta_y\right)^2\right] \tag{2.11d}$$

$$W_{torsional} = \frac{k_t G}{2A}\theta_{x,x}{}^2 \tag{2.11e}$$

2.2.3. Beam kinematics in peridynamics

In the PD, a beam is uniformly discretized into material points along the beam centre line as shown in Fig. 2.2. As explained by Madenci and Oterkus [44], the

equation of motion can also be derived based on the principle of virtual work by satisfying the Lagrange equation. Therefore, in Section 2.3.1, a PD form of strain energy is established, and the PD constants are obtained by comparing SED in PD and classical continuum mechanics. After obtaining the Lagrangian function from kinetic energy and total potential energy, the equation of motion for the beam is obtained by using the Euler-Lagrange equation in Section 2.3.2.

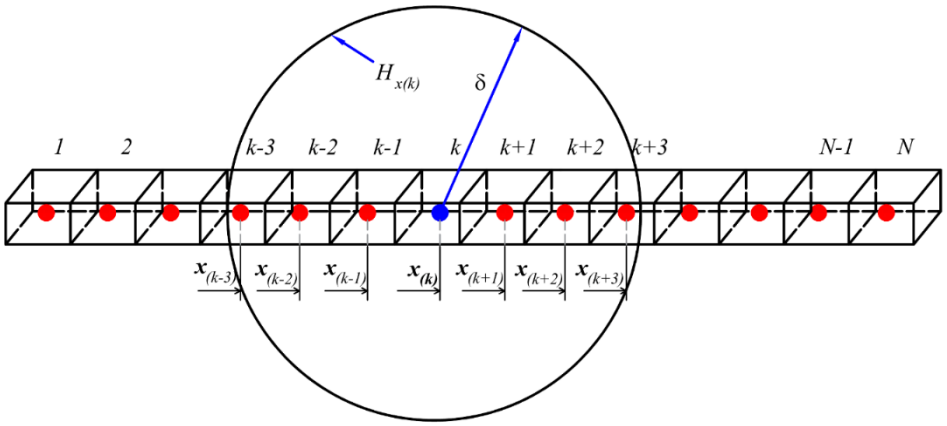

Fig. 2.2. PD material points and horizon size for a beam

2.2.3.1. Strain energy density

Similar to the SED in classical continuum mechanics provided in Eq. (2.11a), the SED for a beam in PD can also be represented as

$$W_{(k)}^{PD} = W_{axial(k)}^{PD} + W_{bending(k)}^{PD} + W_{shear(k)}^{PD} + W_{torsional(k)}^{PD} \tag{2.12}$$

Peridynamic form of the axial part of SED was introduced by Diyaroglu [75] as

$$W_{axial(k)}^{PD} = \frac{1}{2}\sum_{j=1}^{N}\frac{1}{2}C_{ax}\left(\frac{u_{(j)}-u_{(k)}}{\xi}\right)^2 \xi V_{(j)} \tag{2.13}$$

In which, the bond constant C_{ax} is defined as [75]

$$C_{ax} = \frac{2E}{A\delta^2} \tag{2.14}$$

In Eq. (2.13), N represents the number of family members of material point k, j represents the family member material point k. The terms $u_{(k)}$ and $u_{(j)}$ represent the axial displacement of material points k and j, respectively. The parameter ξ represents the distance between two material points k and j.

Peridynamic form of bending part of SED in Eq. (2.12) can be expressed as

$$W_{bending(k)}^{PD} = \frac{1}{2}\sum_{j=1}^{N}\frac{1}{2}\left[C_{by}\left(\frac{\theta_{y(j)}-\theta_{y(k)}}{\xi}\right)^2 + C_{bz}\left(\frac{\theta_{z(j)}-\theta_{z(k)}}{\xi}\right)^2\right]\xi V_{(j)} \tag{2.15}$$

where C_{by} and C_{bz} represent the bending bond constants which can be determined as follows.

First, the rotational angles of material point j are expressed by using the first two terms in Taylor's series expansion as

$$\theta_{y(j)} = \theta_{y(k)} + \theta_{y(k),x}(x_{(j)} - x_{(k)}) \tag{2.16a}$$

$$\theta_{z(j)} = \theta_{z(k)} + \theta_{z(k),x}(x_{(j)} - x_{(k)}) \tag{2.16b}$$

or

$$\frac{\theta_{y(j)}-\theta_{y(k)}}{\xi}=\theta_{y(k),x}\beta_{(k)(j)} \tag{2.16c}$$

$$\frac{\theta_{z(j)}-\theta_{z(k)}}{\xi}=\theta_{z(k),x}\beta_{(k)(j)} \tag{2.16d}$$

with

$$\beta_{(k)(j)}=\frac{x_{(j)}-x_{(k)}}{\xi} \tag{2.16e}$$

By using the relations in Eq. (2.16), the PD form of bending part of SED in Eq. (2.15) can be written as

$$W_{bending(k)}^{PD}=\frac{1}{2}\sum_{j=1}^{N}\frac{1}{2}\left[C_{by}\left(\theta_{y,x}\beta_{(k)(j)}\right)^2+C_{bz}\left(\theta_{y,x}\beta_{(k)(j)}\right)^2\right]\xi V_{(j)} \tag{2.17a}$$

or

$$W_{bending(k)}^{PD}=\frac{1}{2}\sum_{j=1}^{N}\frac{1}{2}\left[C_{by}\left(\theta_{y,x}\right)^2+C_{bz}\left(\theta_{y,x}\right)^2\right]\xi V_{(j)} \tag{2.17b}$$

Next, bending strain energy density given in Eq. (2.17b) can be rewritten in the integral form by disregarding the peridynamic interactions beyond the horizon as

$$W_{bending}^{PD}\left(x\right)=2A\int_0^{\delta}\frac{1}{4}\left[C_{by}\left(\theta_{y,x}\right)^2+C_{bz}\left(\theta_{y,x}\right)^2\right]\xi d\xi \tag{2.18}$$

After performing the integrations in Eq. (2.18), the strain energy density for the bending part becomes

$$W_{bending}^{PD}\left(x\right)=\frac{1}{4}A\delta^2\left[C_{by}{\theta_{y,x}}^2+C_{bz}{\theta_{z,x}}^2\right] \tag{2.19}$$

By comparing SED in Eq. (2.19) and Eq. (2.11c), the PD constants for bending can be determined as

$$C_{by}=\frac{2EI_{yy}}{A^2\delta^2} \tag{2.20a}$$

$$C_{bz}=\frac{2EI_{zz}}{A^2\delta^2} \tag{2.20b}$$

Peridynamic form of the shear part of SED in Eq. (2.12) can be expressed as

$$W_{shear(k)}^{PD}=\frac{1}{2}\sum_{j=1}^{N}\frac{1}{2}C_s\left[\begin{array}{l}\left(\frac{v_{(j)}-v_{(k)}}{\xi}\beta_{(k)(j)}-\frac{\theta_{z(j)}+\theta_{z(k)}}{2}\right)^2\\+\left(\frac{w_{(j)}-w_{(k)}}{\xi}\beta_{(k)(j)}+\frac{\theta_{y(j)}+\theta_{y(k)}}{2}\right)^2\end{array}\right]\xi V_{(j)} \tag{2.21}$$

where C_s represents the shear bond constant which can be determined as follows. First, similar to the bending part, the explicit expression of shear SED in Eq. (2.21) can be written in integral form as

$$W_{shear(k)}^{PD}=2AC_s\frac{1}{4}\int_0^{\delta}\left[\left(v_{,x}-\theta_z\right)^2+\left(w_{,x}+\theta_y\right)^2\right]\xi d\xi \tag{2.22}$$

Next, by performing integrations in Eq. (2.22), the peridynamic form of the shear part of SED can be rewritten as

$$W_s^{PD}=\frac{1}{4}A\delta^2C_s\left[\left(v_{,x}-\theta_z\right)^2+\left(w_{,x}+\theta_y\right)^2\right] \tag{2.23}$$

By comparing Eq. (2.23) and Eq. (2.11d), the PD constant for the shear part of SED can be defined as

$$C_s = \frac{2k_s G}{A\delta^2} \tag{2.24}$$

Peridynamic form of the torsional part of SED in Eq. (2.12) can be explicitly expressed according to Diyaroglu [75] as

$$W^{PD}_{torsional\,(k)} = \frac{1}{2}\sum_{j=1} C_t \frac{1}{2}\left(\frac{\theta_{x(j)} - \theta_{x(k)}}{\xi}\right)^2 \xi V_{(j)} \tag{2.25a}$$

In which, the torsional bond constant C_t can be defined as [75]

$$C_t = \frac{2k_t G}{A^2\delta^2} \tag{2.25b}$$

2.2.3.2. Equations of motion

The equations of motion for a beam can be achieved by using the Euler-Lagrange equation [44]. The Euler-Lagrange equation can be written as

$$\frac{d}{dt}\left(\frac{\partial L}{\partial \dot{q}_i}\right) - \frac{\partial L}{\partial q_i} = 0 \tag{2.26}$$

where L represents the Lagrangian, q_i represents the degree of freedom with $\boldsymbol{q} = \{u \quad v \quad w \quad \theta_x \quad \theta_y \quad \theta_z\}$ and $\dot{q}_i$ represents the time derivative of q_i.

The Lagrangian function for a beam can be expressed as

$$L = T - U \tag{2.27a}$$

with

$$T = \frac{\rho}{2}\sum_{k=1}^{N}\left(\dot{u}^2_{(k)} + \dot{v}^2_{(k)} + \dot{w}^2_{(k)} + \frac{I_{xx}}{A}\dot{\theta}^2_{x(k)} + \frac{I_{yy}}{A}\dot{\theta}^2_{y(k)} + \frac{I_{zz}}{A}\dot{\theta}^2_{z(k)}\right)V_{(k)} \tag{2.27b}$$

$$U = \sum_{k=1}^{N}\begin{pmatrix} W^{PD}_{(k)} - b_{x(k)}u_{(k)} - b_{y(k)}v_{(k)} - b_{z(k)}w_{(k)} \\ -m_{x(k)}\theta_{x(k)} - m_{y(k)}\theta_{y(k)} - m_{z(k)}\theta_{z(k)} \end{pmatrix} V_{(k)} \tag{2.27c}$$

where T represents the total kinetic energy, U represents the total potential energy, $b_{x(k)}$, $b_{y(k)}$, $b_{z(k)}$ represent the applied body forces, $m_{x(k)}$, $m_{y(k)}$, $m_{z(k)}$ represent the moment per unit volume at material point k. Substituting Lagrangian provided in Eq. (2.27) into Eq. (2.26), the peridynamic form of the equation of motion for a beam can be obtained as

$$\rho\ddot{u}_{(k)} = C_{ax}\sum_{j=1}^{N}\left(\frac{u_{(j)} - u_{(k)}}{\xi}\right)V_{(j)} + b_{x(k)} \tag{2.28a}$$

$$\rho\ddot{v}_{(k)} = C_s\sum_{j=1}^{N}\left(\frac{v_{(j)} - v_{(k)}}{\xi} - \frac{\theta_{z(j)} + \theta_{z(k)}}{2}\beta_{(k)(j)}\right)V_{(j)} + b_{y(k)} \tag{2.28b}$$

$$\rho\ddot{w}_{(k)} = C_s\sum_{j=1}^{N}\left(\frac{w_{(j)} - w_{(k)}}{\xi} + \frac{\theta_{y(j)} + \theta_{y(k)}}{2}\beta_{(k)(j)}\right)V_{(j)} + b_{z(k)} \tag{2.28c}$$

$$\frac{\rho I_{xx}}{A}\ddot{\theta}_{x(k)} = C_t\sum_{j=1}^{N}\left(\frac{\theta_{x(j)} - \theta_{x(k)}}{\xi}\right)V_{(j)} + m_{x(k)} \tag{2.28d}$$

$$\frac{\rho I_{yy}}{A}\ddot{\theta}_{y(k)} = C_{by}\sum_{j=1}^{N}\left(\frac{\theta_{y(j)}-\theta_{y(k)}}{\xi}\right)V_{(j)} - \frac{1}{2}C_s\sum_{j=1}^{N}\left(\frac{w_{(j)}-w_{(k)}}{\xi}\beta_{(k)(j)} + \frac{\theta_{y(j)}+\theta_{y(k)}}{2}\right)\xi V_{(j)} + m_{y(k)} \tag{2.28e}$$

$$\frac{\rho I_{zz}}{A}\ddot{\theta}_{z(k)} = C_{bz}\sum_{j=1}^{N}\left(\frac{\theta_{z(j)}-\theta_{z(k)}}{\xi}\right)V_{(j)} + \frac{1}{2}C_s\sum_{j=1}^{N}\left(\frac{v_{(j)}-v_{(k)}}{\xi}\beta_{(k)(j)} - \frac{\theta_{z(j)}+\theta_{z(k)}}{2}\right)\xi V_{(j)} + m_{z(k)} \tag{2.28f}$$

The PD form of the equation of motion given in Eq. (2.28) can also be written in the vector form as

$$\mathbf{m}^L_{(k)}\ddot{\mathbf{u}}^L_{(k)} = \sum_{j=1}^{N}\mathbf{f}^L_{(k)(j)}V_{(j)} + \mathbf{b}^L_{(k)} \tag{2.29a}$$

where

$$\mathbf{m}^L_{(k)} = \begin{bmatrix} \rho & 0 & 0 & 0 & 0 & 0 \\ 0 & \rho & 0 & 0 & 0 & 0 \\ 0 & 0 & \rho & 0 & 0 & 0 \\ 0 & 0 & 0 & \dfrac{\rho I_{xx}}{A} & 0 & 0 \\ 0 & 0 & 0 & 0 & \dfrac{\rho I_{yy}}{A} & 0 \\ 0 & 0 & 0 & 0 & 0 & \dfrac{\rho I_{zz}}{A} \end{bmatrix};\ \ddot{\mathbf{u}}^L_{(k)} = \begin{bmatrix} \ddot{u}_{(k)} \\ \ddot{v}_{(k)} \\ \ddot{w}_{(k)} \\ \ddot{\theta}_{x(k)} \\ \ddot{\theta}_{y(k)} \\ \ddot{\theta}_{z(k)} \end{bmatrix};\ \mathbf{b}^L_{(k)} = \begin{bmatrix} b_{x(k)} \\ b_{y(k)} \\ b_{z(k)} \\ m_{x(k)} \\ m_{y(k)} \\ m_{z(k)} \end{bmatrix} \tag{2.29b}$$

and

$$\mathbf{f}^L_{(k)(j)} = \begin{bmatrix} f^u_{(k)(j)} & f^v_{(k)(j)} & f^w_{(k)(j)} & f^{\theta_x}_{(k)(j)} & f^{\theta_y}_{(k)(j)} & f^{\theta_z}_{(k)(j)} \end{bmatrix}^T \tag{2.29c}$$

with

$$f^u_{(k)(j)} = C_{ax}\left(\frac{u_{(j)}-u_{(k)}}{\xi}\right) \tag{2.29d}$$

$$f^v_{(k)(j)} = C_s\left(\frac{v_{(j)}-v_{(k)}}{\xi} - \frac{\theta_{z(j)}+\theta_{z(k)}}{2}\beta_{(k)(j)}\right) \tag{2.29e}$$

$$f^w_{(k)(j)} = C_s\left(\frac{w_{(j)}-w_{(k)}}{\xi} + \frac{\theta_{y(j)}+\theta_{y(k)}}{2}\beta_{(k)(j)}\right) \tag{2.29f}$$

$$f^{\theta_x}_{(k)(j)} = C_t\left(\frac{\theta_{x(j)}-\theta_{x(k)}}{\xi}\right) \tag{2.29g}$$

$$f^{\theta_y}_{(k)(j)} = C_{by}\left(\frac{\theta_{y(j)}-\theta_{y(k)}}{\xi}\right) - \frac{1}{2}C_s\left(\frac{w_{(j)}-w_{(k)}}{\xi}\beta_{(k)(j)} + \frac{\theta_{y(j)}+\theta_{y(k)}}{2}\right)\xi \tag{2.29h}$$

$$f^{\theta_z}_{(k)(j)} = C_{bz}\left(\frac{\theta_{z(j)}-\theta_{z(k)}}{\xi}\right) + \frac{1}{2}C_s\left(\frac{v_{(j)}-v_{(k)}}{\xi}\beta_{(k)(j)} - \frac{\theta_{z(j)}+\theta_{z(k)}}{2}\right)\xi \tag{2.29i}$$

2.2.4. Coordinate systems and transformation of equations of motion

The equations of motion provided in Eq. (2.28) are derived in the local coordinate system. However, the geometrical properties of complex structures are often governed with respect to the global coordinate system. Therefore, the equation of motion for each material point needs to be transformed from local to global coordinates. In this section, first, the relationship between local and global coordinates is provided in Section 2.4.1. Next, the transformation of the equation of motion for straight and curved beams are presented in Sections 2.4.2 and 2.4.3, respectively.

2.2.4.1. Local and global coordinate systems

In the global coordinate system, the orientation of each beam is governed by the unit vectors, $\vec{n}_x$, $\vec{n}_y$, $\vec{n}_z$ located at the centreline of the beam as shown in Fig. 2.3. If the beam is straight, every cross-section of the beam has the same unit vectors. On the other hand, if the beam is curved, the unit vectors for each section will be different as shown in Fig. 2.3. Assuming that the unit vectors of material point k are defined as

$$\vec{n}_{x(k)} = \begin{bmatrix} a_{1(k)} & a_{2(k)} & a_{3(k)} \end{bmatrix}^T \tag{2.30a}$$

$$\vec{n}_{y(k)} = \begin{bmatrix} b_{1(k)} & b_{2(k)} & b_{3(k)} \end{bmatrix}^T \tag{2.30b}$$

$$\vec{n}_{z(k)} = \begin{bmatrix} c_{1(k)} & c_{2(k)} & c_{3(k)} \end{bmatrix}^T \tag{2.30c}$$

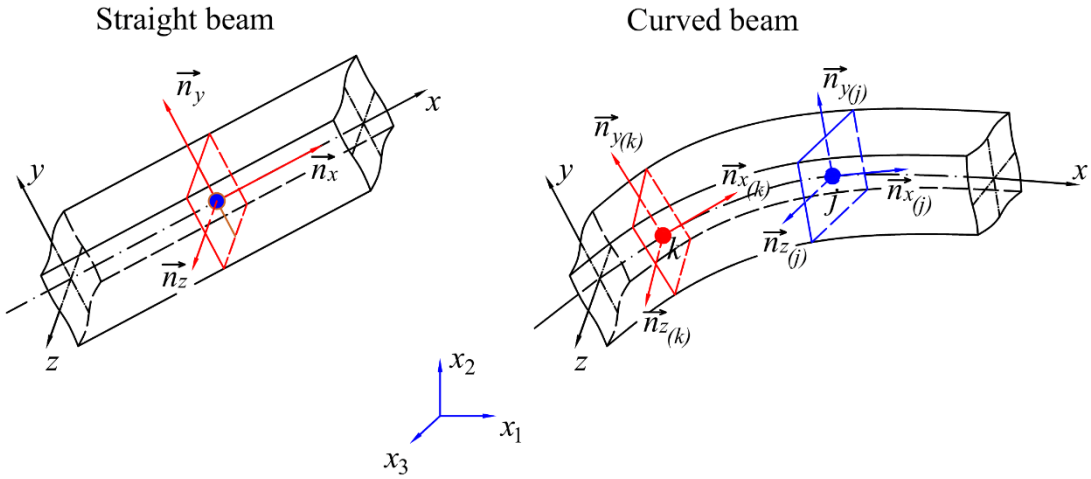

Fig. 2.3. Local and global coordinate systems

The relationship between global and local coordinates can be defined as

$$\begin{bmatrix} x_{(k)} \\ y_{(k)} \\ z_{(k)} \end{bmatrix} = \begin{bmatrix} a_{1(k)} & a_{2(k)} & a_{3(k)} \\ b_{1(k)} & b_{2(k)} & b_{3(k)} \\ c_{1(k)} & c_{2(k)} & b_{3(k)} \end{bmatrix} \begin{bmatrix} x_{1(k)} \\ x_{2(k)} \\ x_{3(k)} \end{bmatrix} = \mathbf{H}_{(k)} \begin{bmatrix} x_{1(k)} \\ x_{2(k)} \\ x_{3(k)} \end{bmatrix} \tag{2.31a}$$

with

$$\mathbf{H}_{(k)} = \begin{bmatrix} \vec{n}_{x(k)} & \vec{n}_{y(k)} & \vec{n}_{z(k)} \end{bmatrix}^T \tag{2.31b}$$

where $\mathbf{H}_{(k)}$ represents the coordinate transformation matrix of material point k. The

transformation of displacement vectors can be also defined as

$$\mathbf{u}_{(k)}^{L} = \mathbf{T}_{(k)}\mathbf{u}_{(k)}^{G} \tag{2.32a}$$

with

$$\mathbf{u}_{(k)}^{L} = \begin{bmatrix} u_{(k)} & v_{(k)} & w_{(k)} & \theta_{x(k)} & \theta_{y(k)} & \theta_{z(k)} \end{bmatrix}^{T} \tag{2.32b}$$

$$\mathbf{u}_{(k)}^{G} = \begin{bmatrix} u_{1(k)} & u_{2(k)} & u_{3(k)} & \theta_{1(k)} & \theta_{2(k)} & \theta_{3(k)} \end{bmatrix}^{T} \tag{2.32c}$$

where $\boldsymbol{u}_{(k)}^{L}$ and $\boldsymbol{u}_{(k)}^{G}$ are displacement vectors in the local and global coordinate systems, respectively. $\mathbf{T}_{(k)}$ represents the displacement transformation matrix of material point k. This matrix can be obtained from the coordinate transformation matrix, $\mathbf{H}_{(k)}$ as

$$\mathbf{T}_{(k)} = \begin{bmatrix} \mathbf{H}_{(k)} & \mathbf{0} \\ \mathbf{0} & \mathbf{H}_{(k)} \end{bmatrix} \tag{2.33}$$

2.2.4.2. Transformation of equations of motion from local to the global coordinate system

By using the relations given in Eq. (2.32a), the equations of motion for a beam given in Eq. (2.29a) can be written as

$$\mathbf{m}_{(k)}^{L}\mathbf{T}_{(k)}\ddot{\mathbf{u}}_{(k)}^{G} = \sum_{j=1}^{N}\mathbf{f}_{(k)(j)}^{L}V_{(j)} + \mathbf{b}_{(k)}^{L} \tag{2.34}$$

Multiplying both sides by $\boldsymbol{T}_{(k)}^{T}$ results in

$$\mathbf{m}_{(k)}^{G}\ddot{\mathbf{u}}_{(k)}^{G} = \mathbf{T}_{(k)}^{T}\left(\sum_{j=1}^{N}\mathbf{f}_{(k)(j)}^{L}V_{(j)} + \mathbf{b}_{(k)}^{L}\right) \tag{2.35}$$

As a result, the equation of motion in global coordinates becomes

$$\mathbf{m}_{(k)}^{G}\ddot{\mathbf{u}}_{(k)}^{G} = \sum_{j=1}^{N}\mathbf{f}_{(k)(j)}^{G}V_{(j)} + \mathbf{b}_{(k)}^{G} \tag{2.36}$$

where

$$\mathbf{f}_{(k)(j)}^{G} = \mathbf{T}_{(k)}^{T}\mathbf{f}_{(k)(j)}^{L} \tag{2.37}$$

$$\mathbf{b}_{(k)}^{G} = \mathbf{T}_{(k)}^{T}\mathbf{b}_{(k)}^{L} \tag{2.38}$$

$$\mathbf{m}_{(k)}^{G} = \mathbf{T}_{(k)}^{T}\mathbf{m}_{(k)}^{L}\mathbf{T}_{(k)} \tag{2.39}$$

Note that $\mathrm{sgn}\left(x_{(j)} - x_{(k)}\right)$ in Eq. (2.17c) can be calculated in global coordinates by using Eq. (2.31) as

$$\beta_{(k)(j)} = \frac{\left(a_{1(j)}x_{1(j)} + a_{2(j)}x_{2(j)} + a_{3(j)}x_{3(j)}\right) - \left(a_{1(k)}x_{1(k)} + a_{2(k)}x_{2(k)} + a_{3(k)}x_{3(k)}\right)}{\xi} \tag{2.40}$$

For curved beams, the transformation matrix $\boldsymbol{T}_{(k)}$ used in Eq. (2.34-2.39) can be replaced by $\boldsymbol{T}_{(k)(j)}$ which can be defined as

$$\mathbf{T}_{(k)(j)} = \begin{bmatrix} \mathbf{H}_{(k)(j)} & \mathbf{0} \\ \mathbf{0} & \mathbf{H}_{(k)(j)} \end{bmatrix} \tag{2.41c}$$

with

$$\mathbf{H}_{(k)(j)} = \begin{bmatrix} \vec{n}_{x(k)(j)} & \vec{n}_{y(k)(j)} & \vec{n}_{z(k)(j)} \end{bmatrix}^{T} \tag{2.41d}$$

where $\vec{n}_{x(k)(j)}$, $\vec{n}_{y(k)(j)}$, $\vec{n}_{z(k)(j)}$can be represented as

$$\vec{n}_{x(k)(j)} = \frac{\left(\vec{n}_{x(k)} + \vec{n}_{x(j)}\right)}{\left|\left(\vec{n}_{x(k)} + \vec{n}_{x(j)}\right)\right|} \tag{2.41e}$$

$$\vec{n}_{y(k)(j)} = \frac{\left(\vec{n}_{y(k)} + \vec{n}_{y(j)}\right)}{\left|\left(\vec{n}_{y(k)} + \vec{n}_{y(j)}\right)\right|} \tag{2.41f}$$

$$\vec{n}_{z(k)(j)} = \frac{\left(\vec{n}_{z(k)} + \vec{n}_{z(j)}\right)}{\left|\left(\vec{n}_{z(k)} + \vec{n}_{z(j)}\right)\right|} \tag{2.41g}$$

2.2.5. Damage prediction for PD beam model

For damage prediction, the PD equation of motion given in Eq. (2.36) can be written as

$$\mathbf{m}_{(k)}^{G}\ddot{\mathbf{u}}_{(k)}^{G} = \sum_{j=1}^{N} \psi_{(k)(j)} \mathbf{f}_{(k)(j)}^{G} V_{(j)} + \mathbf{b}_{(k)}^{G} \tag{2.42}$$

For beam structures, the damage criteria based on the critical energy release rate presented in Chapter 1 is used. By applying the same idea introduced by Madenci and Oterkus [25], [26], the micropotentials, $\Phi_{(k)(j)}$ and $\Phi_{(j)(k)}$ given in Eq. (1.9b-c) in Chapter 1, can be calculated as

$$\begin{aligned}\Phi_{(k)(j)} &= \Phi_{(k)(j)}^{u} + \Phi_{(k)(j)}^{v} + \Phi_{(k)(j)}^{w} + \Phi_{(k)(j)}^{\theta_x} + \Phi_{(k)(j)}^{\theta_y} + \Phi_{(k)(j)}^{\theta_z} \\ &= \int_0^{s_{(k)(j)}^{u}} t_{(k)(j)}^{u} \xi ds_{(k)(j)}^{u} + \int_0^{s_{(k)(j)}^{v}} t_{(k)(j)}^{v} \xi ds_{(k)(j)}^{v} + \int_0^{s_{(k)(j)}^{w}} t_{(k)(j)}^{w} \xi ds_{(k)(j)}^{w} \\ &+ \int_0^{s_{(k)(j)}^{\theta_x}} t_{(k)(j)}^{\theta_x} \xi ds_{(k)(j)}^{\theta_x} + \int_0^{s_{(k)(j)}^{\theta_y}} t_{(k)(j)}^{\theta_y} \xi ds_{(k)(j)}^{\theta_y} + \int_0^{s_{(k)(j)}^{\theta_z}} t_{(k)(j)}^{\theta_z} \xi ds_{(k)(j)}^{\theta_z}\end{aligned} \tag{2.43a}$$

$$\Phi_{(j)(k)} = \Phi_{(k)(j)} \tag{2.43b}$$

For linear elastic deformation problems, the micropotential $\Phi_{(k)(j)}$ given in Eq. (2.43) can be simplified as

$$\begin{aligned}\Phi_{(k)(j)} &= \frac{1}{2} t_{(k)(j)}^{u} \xi s_{(k)(j)}^{u} + \frac{1}{2} t_{(k)(j)}^{v} \xi s_{(k)(j)}^{v} + \frac{1}{2} t_{(k)(j)}^{w} \xi s_{(k)(j)}^{w} \\ &+ \frac{1}{2} t_{(k)(j)}^{\theta_x} \xi s_{(k)(j)}^{\theta_x} + \frac{1}{2} t_{(k)(j)}^{\theta_y} \xi s_{(k)(j)}^{\theta_y} + \frac{1}{2} t_{(k)(j)}^{\theta_z} \xi s_{(k)(j)}^{\theta_z}\end{aligned} \tag{2.44a}$$

where

$$s_{(k)(j)}^{u} = \frac{u_{(j)} - u_{(k)}}{\xi},\ t_{(k)(j)}^{u} = \frac{1}{2} f_{(k)(j)}^{u} \tag{2.44b}$$

$$s_{(k)(j)}^{v} = \frac{v_{(j)} - v_{(k)}}{\xi},\ t_{(k)(j)}^{v} = \frac{1}{2} f_{(k)(j)}^{v} \tag{2.44c}$$

$$s_{(k)(j)}^{w} = \frac{w_{(j)} - w_{(k)}}{\xi},\ t_{(k)(j)}^{w} = \frac{1}{2} f_{(k)(j)}^{w} \tag{2.44d}$$

$$s_{(k)(j)}^{\theta_x} = \frac{\theta_{x(j)} - \theta_{x(k)}}{\xi},\ t_{(k)(j)}^{\theta_x} = \frac{1}{2} f_{(k)(j)}^{\theta_x} \tag{2.44e}$$

$$s^{\theta_y}_{(k)(j)} = \frac{\theta_{y(j)} - \theta_{y(k)}}{\xi},\ t^{\theta_y}_{(k)(j)} = \frac{1}{2} f^{\theta_y}_{(k)(j)} \tag{2.44f}$$

$$s^{\theta_z}_{(k)(j)} = \frac{\theta_{z(j)} - \theta_{z(k)}}{\xi},\ t^{\theta_z}_{(k)(j)} = \frac{1}{2} f^{\theta_z}_{(k)(j)} \tag{2.44g}$$

with $f^{u}_{(k)(j)}$, $f^{v}_{(k)(j)}$, $f^{w}_{(k)(j)}$, $f^{\theta_x}_{(k)(j)}$, $f^{\theta_y}_{(k)(j)}$, $f^{\theta_z}_{(k)(j)}$ can be calculated by using Eq. (2.29).

2.2.6. Numerical implementations

In this section, the numerical implementations of the PD beam model are presented. First, the model discretization for a beam structure with three beams joined is presented in Section 2.6.1. Next, the determination for the geometrical and material properties of the joint points is presented in Section 2.6.2.

2.2.6.1. Model discretization

Fig. 2.4 demonstrates the model discretization for pin joined beam structures. As shown in Fig. 2.4, three beams A, B, and C are joined together at one point. To generate material points for this structure, each beam is firstly discretized into material points. After the discretization, for the points that share the same location such as points $i^{(A)}$, $k^{(B)}$, $j^{(C)}$as shown in Fig. 2.4, only one material point is kept, the other points are removed. The point $k^{(A,B,C)}$ in Fig. 2.4 represents the joint point for three beams.

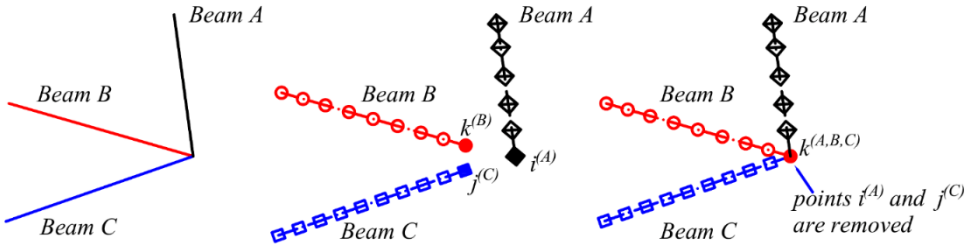

Fig. 2.4. The connection of beams at joint points

2.2.6.2. Geometrical and material properties at the joint points

It is considered that the family members for a joint point $k^{(A,B,C)}$ in Fig. 2.4 include the material points from all three beams. If material point $k^{(A,B,C)}$ interacts with material points in beam A, the material properties and geometrical parameters of material point $k^{(A,B,C)}$ are set the same as beam A. On the other hand, if material point $k^{(A,B,C)}$ interacts with material points in beam B, the material properties and geometrical parameters of material point $k^{(A,B,C)}$ are set the same as beam B.

2.2.7. Numerical results

In this section, first, for verification purposes, the results predicted by using the proposed PD beam model are compared with finite element solutions. The finite element analyses are conducted using ANSYS commercial software and the BEAM188 element is used. Next, in section 2.7.2, the progressive damage in the jacket platform subjected to ship collision is investigated.

The beams are made of steel material with Young's modulus $E = 2 \times 10^{11}$ N/m^2, shear modulus $G = 1 \times 10^{11}$ N/m^2, and mass density of $\rho = 7850$ kg/m^3. For static solutions, an explicit scheme is used by implementing the adaptive dynamic relaxation method [76, 77] (Appendix A2).

In this section, the PD predictions for a 2D frame with straight beams, a curved beam, and a jacket platform subjected to concentrated loads are presented. In all these examples, the weight of the structure is ignored.

2.2.7.1. 2D frame with straight beams subjected to a constant concentrated load

To verify the developed PD model for straight beams, a 2D frame subjected to point load is investigated. The steel frame consists of two beams as shown in Fig. 2.5. The frame is subjected to a concentrated force $F_3 = -3 \times 10^6$ N at $(L, L, 0)$ and it is clamped at both ends. Both beams have the same length $L = 1$ m and same square cross-section, $A = 0.1 \times 0.1$ m^2.

In the peridynamic model, both beams are discretized with uniform 200 integration points. To implement the fixed ends of the frame, three fictitious points [26, 33] are added at both ends and all the displacement and rotation components of these fictitious points are set equal to zero. In Fig. 2.5(b), red points represent the material points in the real region. On the other hand, black points represent the material points in the fictitious region. In the FEA model, each beam is meshed with 200 elements.

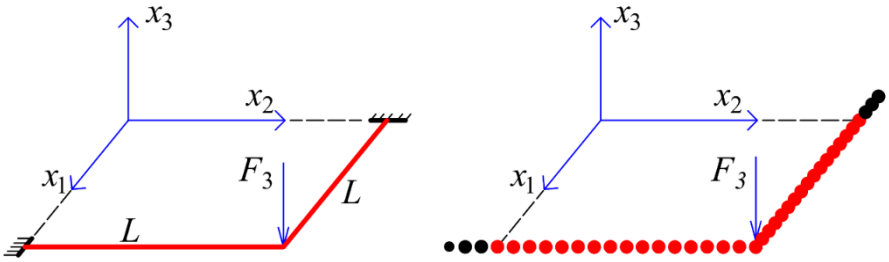

(a) (b)

Fig. 2.5. 2D frame subjected to concentrated load (a) geometry, (b) PD discretization

Due to the small deformation assumption, the beams have three nonzero DOFs. These are transverse displacement u_3, rotation θ_1 , and θ_2. Fig. 2.6-Fig. 2.8 represent the displacement variations along each beam in the deformed configuration. As can be seen in the figures, PD results agree very well with the FEA results which shows the accuracy of the developed PD model for straight beams.

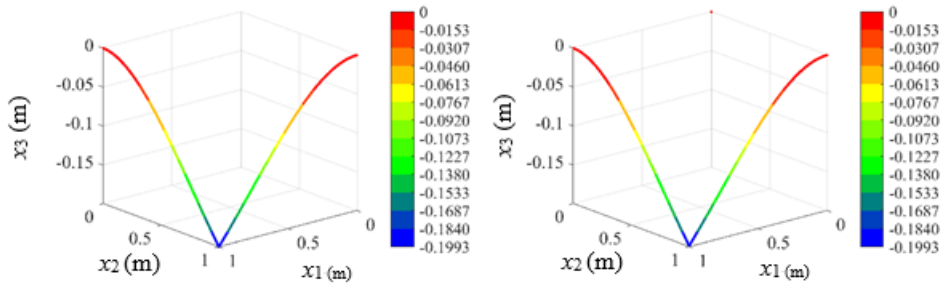

(a) (b)

Fig. 2.6. Variation of displacement u_3(m) in deformed configuration (a) PD, (b) FEA

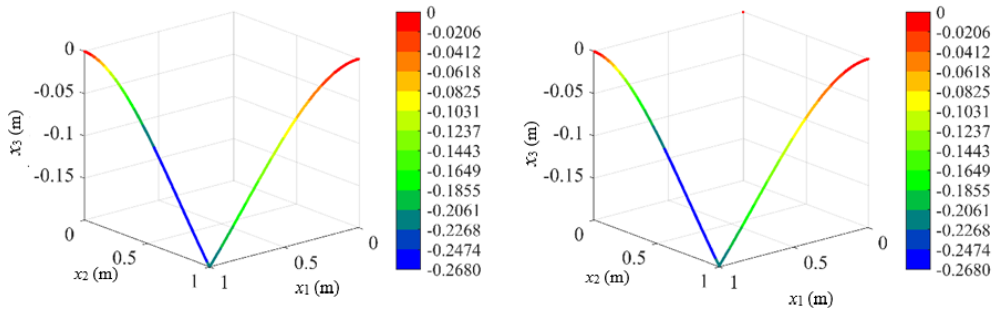

(a) (b)

Fig. 2.7. Variation of θ_1 (rad) in deformed configuration (a) PD, (b) FEA

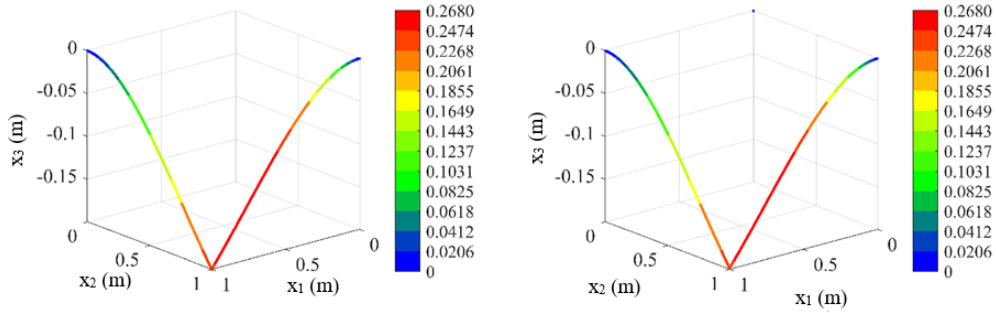

(a) (b)

Fig. 2.8. Variation of θ_2 (rad) in deformed configuration (a) PD, (b) FEA

2.2.7.2. Curved beam subjected to a constant concentrated load

To verify the developed PD model for curved beams, a semi-circular beam of radius R subjected to point load is investigated as shown in Fig. 2.9. The semi-circular beam is clamped at both ends and it is subjected to static loading $F_2 = -1 \times 10^8$ N and $F_3 = -2 \times 10^6$ N. The semi-circular beam has a radius of $R = 0.5$ m and square cross-section as $b = h = 0.1$ m.

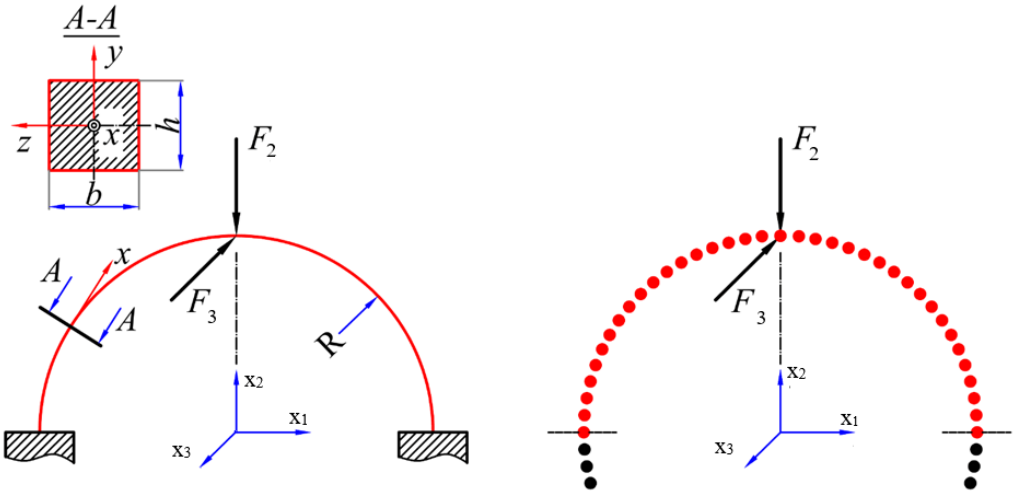

Fig. 2.9. Semi-circular beam subjects to concentrated load (a) geometry, (b) PD discretization

In the peridynamic model, the beam is discretized with uniform 500 integration points. In the FEA model, the beam is meshed with 500 elements. To implement the fixed ends of the frame, three fictitious points are added at both ends and all the displacement and rotation components of these fictitious points are set equal to zero. As shown in Fig. 2.9(b), red points represent the material points in the real region, and black points represent the material points in the fictitious region.

Fig. 2.10-Fig. 2.11 represent the deformed shape of the beam and displacement and rotation variations along the semi-circular beam, respectively. It can be seen from Fig. 2.10 that the deformed shape of the beam predicted by PD agrees very well with the FEA solutions. It is also observed that all 6 DOFs of the beam predicted by PD and FEA have a very good agreement as shown in Fig. 2.11.

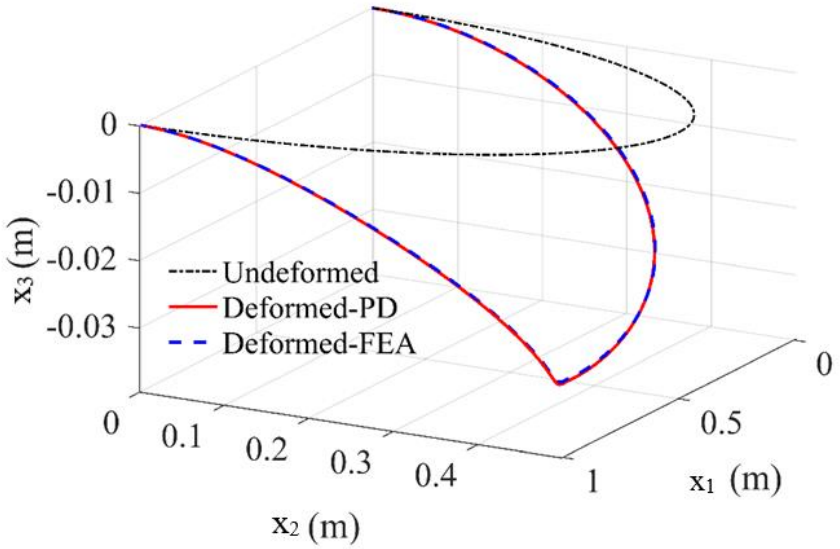

Fig. 2.10. The deformed and undeformed shape of the beam

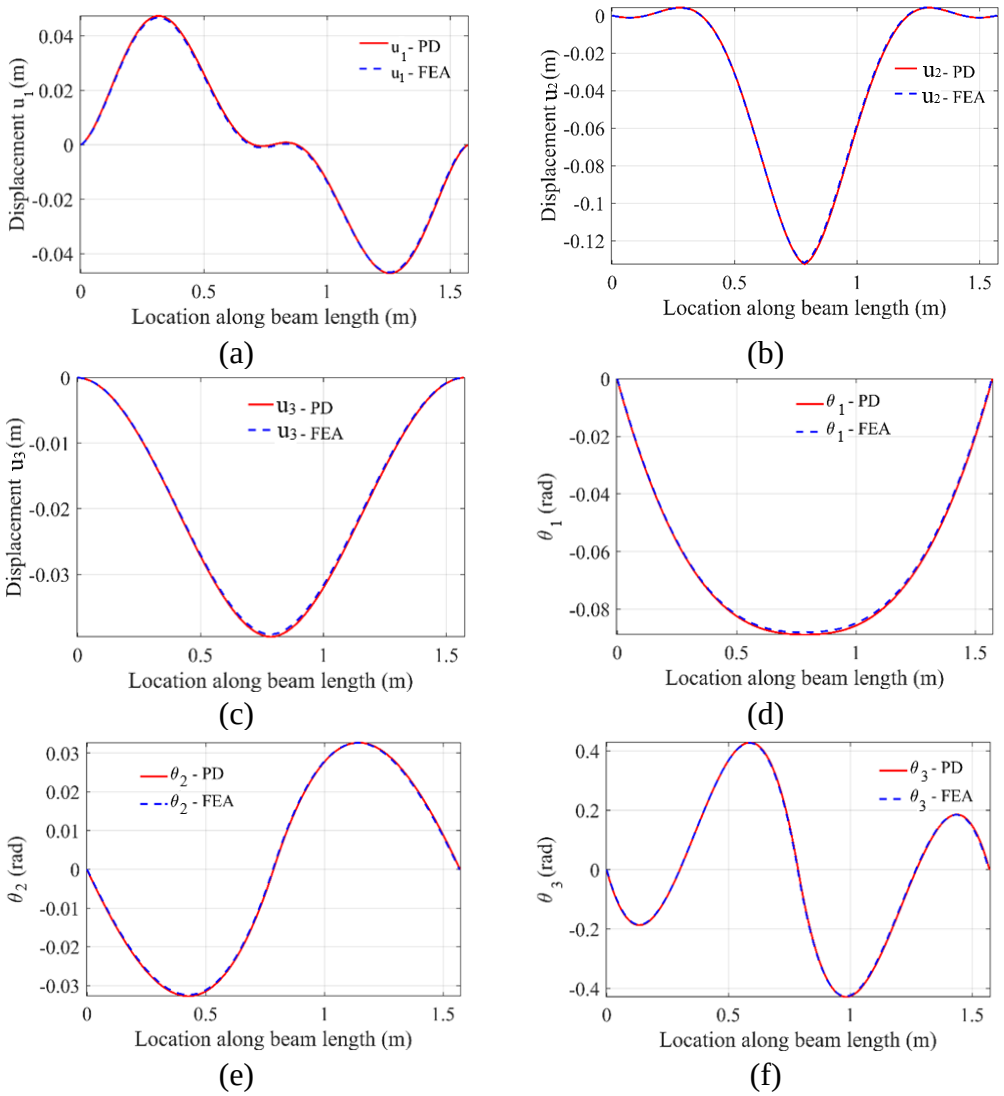

Fig. 2.11. Variation of (a) u_1, (b) u_2, (c) u_3, (d) θ_1, (e) θ_2, (f) θ_3 along the beam length

2.2.7.3. Jacket platform subjected to a constant concentrated load

After verifying the developed PD model for the simple frame and curved beam, the accuracy of the PD model is tested for a jacket platform which consists of 28 beams and 16 joints. For this purpose, a 27 m high jacket platform is modeled as shown in Fig. 2.12. The jacket platform has the following dimensions: $H_1 = 9$ m, $H_2 = 18$ m, $H_3 = 27$ m, $L_1 = L_2 = 12$ m, $L_3 = L_4 = 4$ m. The jacket platform is fixed on 4 legs at the location of $x_3 = 0$ and subjected to concentrated loading $F_2 = 2 \times 10^7$ N at $(L_3/2, -L_4/2, H_3)$ and $(-L_3/2, -L_4/2, H_3)$. Each beam component of the jacket platform has a hollow circular cross-section. Four main legs, shown in red, have an outer diameter of 0.6 m and inner diameter 0.576 m, the other beams, shown in blue, have an outer diameter of 0.4 m, and an inner diameter of 0.384 m.

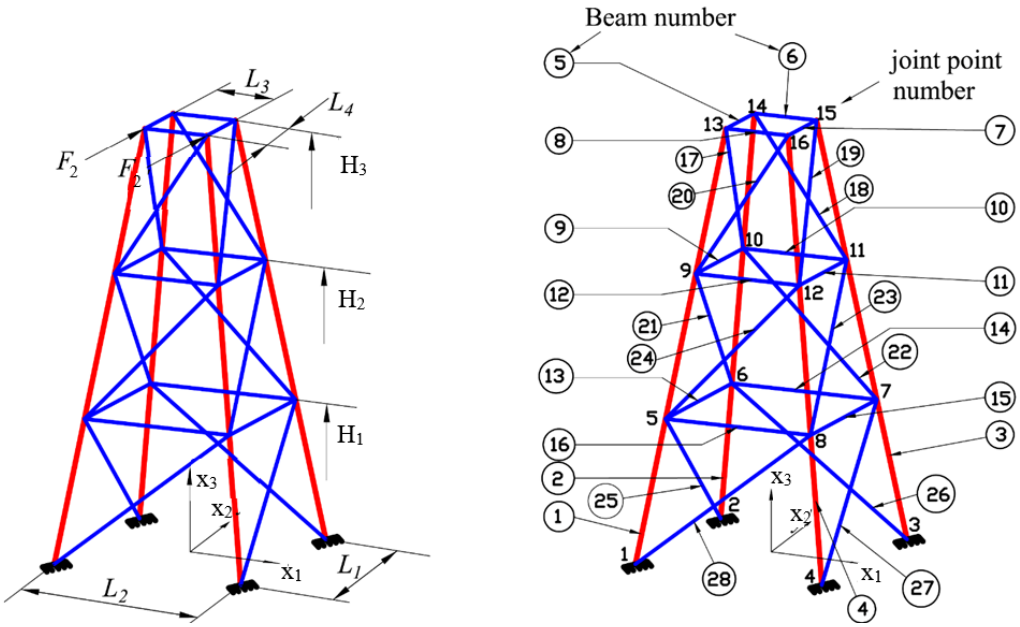

(a) (b)

Fig. 2.12. Jacket platform (a) geometry, (b) beam numbers and joint points

In the PD model, beams 1, 2, 3, 4 (shown in red) are discretized into 300 material points, and other beams (shown in blue) are discretized into 100 material points. Similarly, for the ANSYS model, beams 1, 2, 3, 4 are meshed with 300 elements, and other beams are meshed with 100 elements.

Similar to the previous examples, to apply boundary conditions, three fictitious material points are added for beam 1, 2, 3, 4, 25, 26, 27, and 28 on the centreline of each beam, a long negative x_3 direction and all DOF of these fictitious points are set equal to zero.

Shown in Fig. 2.13-Fig. 2.18 are the variations of 6 DOFs of the jacket platform in the deformed shape in the global coordinates. The results obtained from the PD analysis match very well with those in FEA.

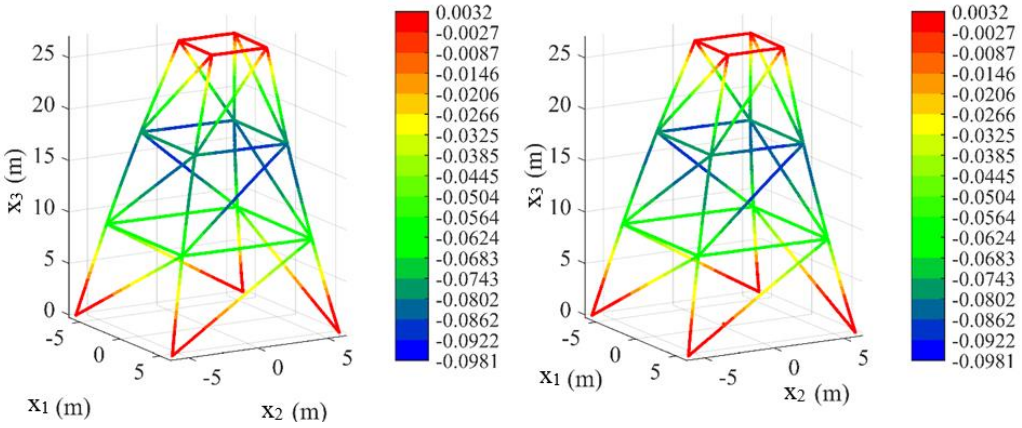

(a) (b)

Fig. 2.13. Displacement u_1 (m) in deformed configuration (a): PD analysis, (b): FEA

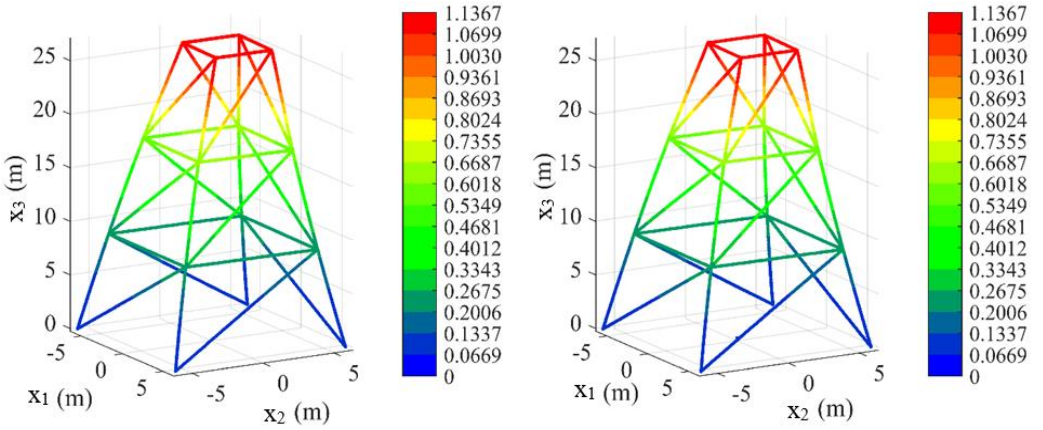

(a) (b)

Fig. 2.14. Displacement u_2(m) in deformed configuration (a): PD analysis, (b): FEA

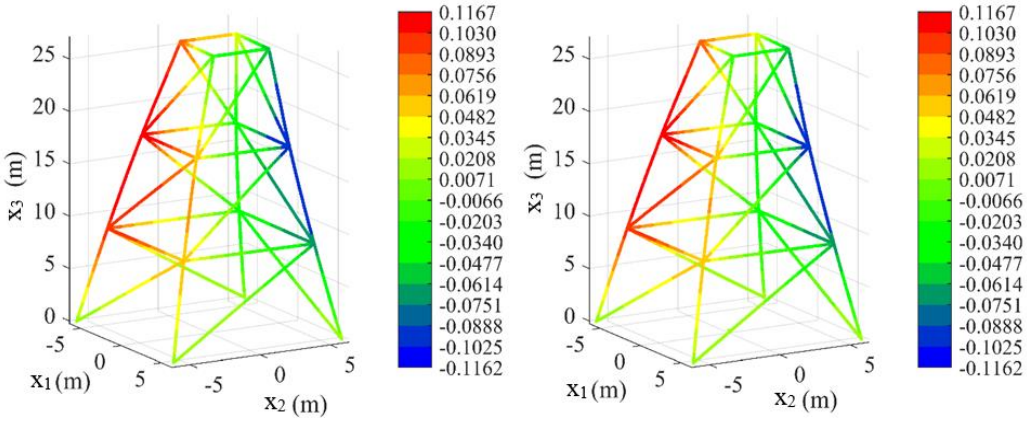

(a) (b)

Fig. 2.15. Displacement u_3 (m) in deformed configuration (a): PD analysis, (b): FEA

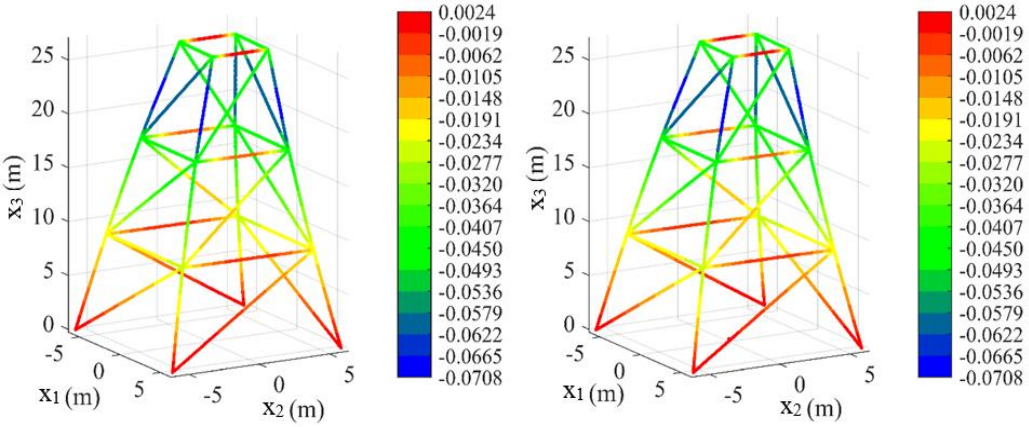

(a) (b)

Fig. 2.16. Rotational angle θ_1 (rad) in deformed configuration (a): PD analysis, (b): FEA

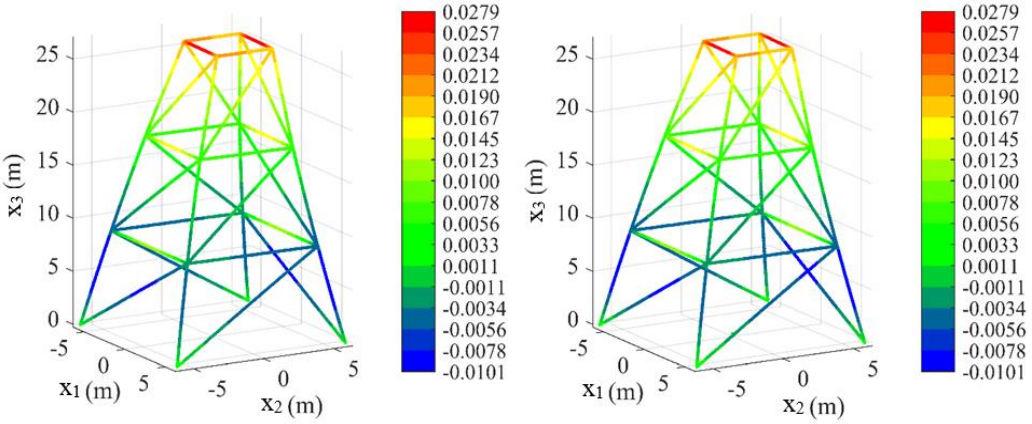

(a) (b)

Fig. 2.17. Rotational angle θ_2 (rad) in deformed configuration (a): PD analysis, (b): FEA

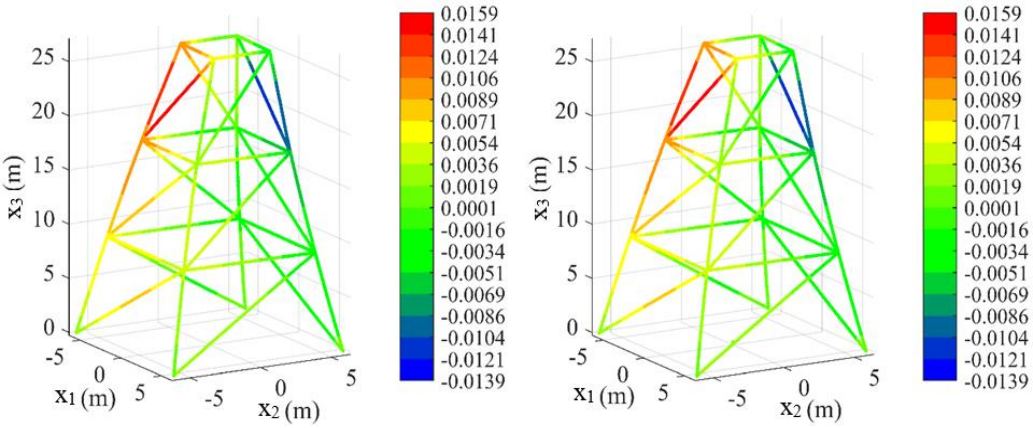

(a) (b)

Fig. 2.18. Rotational angle θ_3 (rad) in deformed configuration (a): PD analysis, (b): FEA

2.2.7.4. Damage prediction for jacket platform subjected to ship collision

In this example, the jacket platform subjected to ship collision is investigated. The ship is considered as a rigid body, moving with a constant velocity of $v_0 = 30$ m/s in x_1 direction. It is assumed that the collision is between the front part of the ship and the jacket platform. Therefore, only the front part of the ship is modeled as shown in Fig. 2.19. The geometrical and material properties of the jacket platform are the same as in Section 2.7.2. The structure does not have any initial damage, but it is hit by the ship at $t = 0$. For simplification, the critical energy release rate of the material is chosen as $G_c = G_{Ic} = 720$ J/m^2.

Fig. 2.19 presents the extent of damage due to contact between the ship and the jacket platform. As the ship moves to the left, the ship growingly collides with the jacket platform causing the increase of damage region on the jacket platform. As shown in Fig. 2.19, the deformed shape of the contact region on the jacket platform is also associated with the shape of the contact region on the ship's body. After 0.15 seconds, the ship with the velocity of $v_0 = 30$ m/s moves 0.45 m and breaks the jacket platform on contact regions.

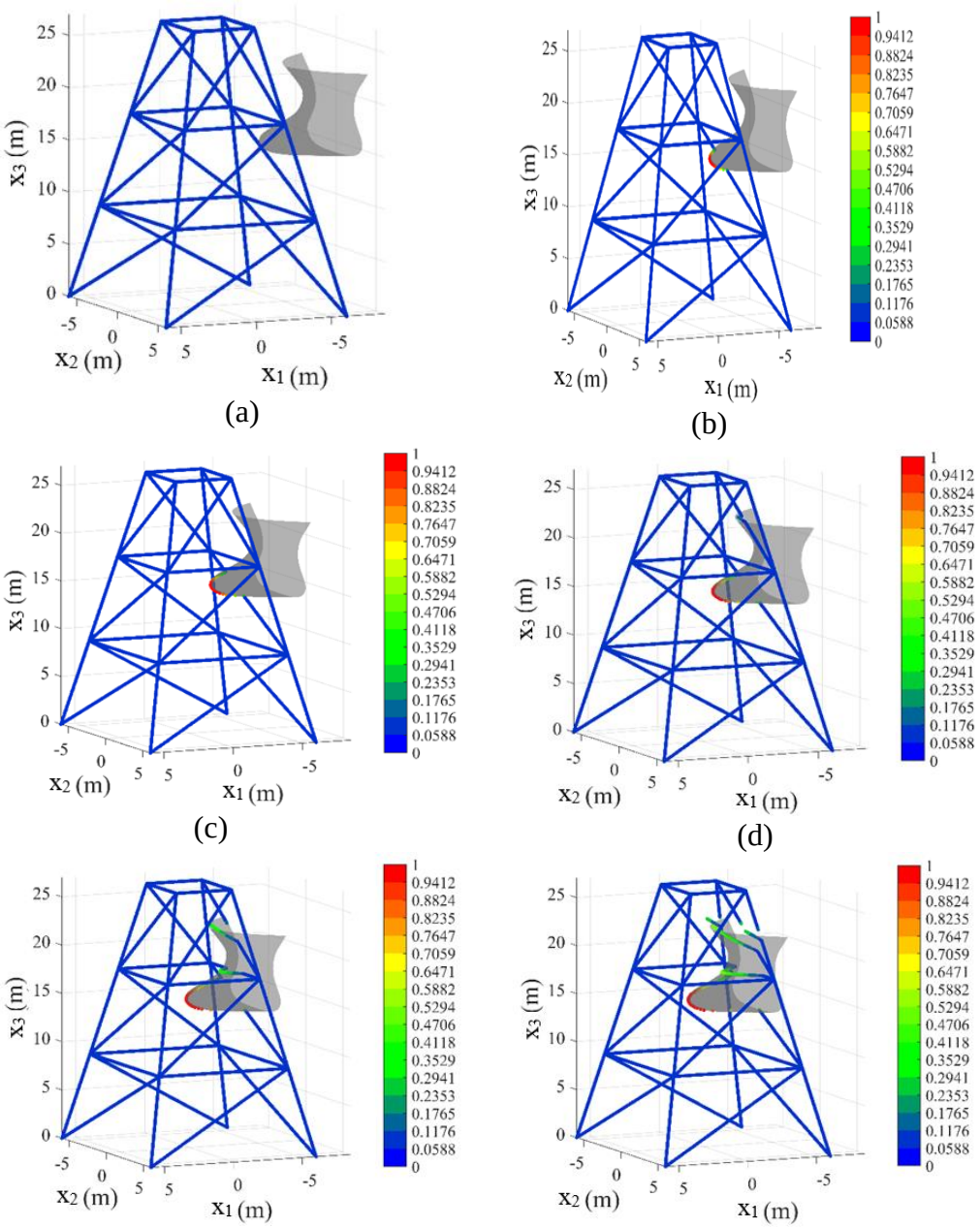

Fig. 2.19. Damage coefficient φ in deformed configuration at (a) $t = 0$, (b) $t = 0.03$ s, (c) $t = 0.06$ s, (d) $t = 0.09$ s, (e) $t = 0.12$ s, (f) $t = 0.15$ s

2.3. Peridynamics for linear 3D shell structures

This section focuses on developing a novel ordinary state-based peridynamic model to predict the thermomechanical behaviour of three-dimensional shell structures with 6 degrees of freedom. The numerical techniques to deal with complex shell structures are also provided. For verification purposes, static analyses of a flat shell, a curved shell, and a stiffened structure are presented. After verifying the accuracy of the PD model, damages on a flat shell in a double torsion problem, a flat shell with a rectangular cut-out subjected to bending, a hull girder subjected to bending and torsion, and a corroded stiffened structure subjected to uniform pressure are predicted.

2.3.2. Kinematics of Flat Shells in Classical Continuum Mechanics

In this section, first, the descriptions of degrees of freedom for a material point on a shell structure are provided. Next, the formulations for linear strain and stress are obtained. Finally, the strain energy density formulation in classical continuum mechanics for shell structures is presented.

2.3.2.1. Degrees of Freedom

The kinematics of a flat shell is initially based on the theory of plates by including transverse shear deformations [78-80]. According to assumptions in Mindlin [78], Reissner [79], [80], the deformation of each material point in a plate is represented by five degrees of freedom. As presented by Wisniewski [81], the drilling rotation, which is the rotation with respect to the normal axis of the plate's plane, can be added.

Fig. 2.20 presents a material point in a flat shell with 6 degrees of freedom; u_1, u_2, u_3, θ_1, θ_2, θ_3 in the global and u, v, w, θ_x, θ_y, θ_z in the local coordinate systems with respect to undeformed configuration. The components u and v represent the in-plane displacements of the mid-surface in x and y directions, respectively. Meanwhile, w represents the transverse displacement of the middle surface in z direction. The rotations θ_x, θ_y, θ_z represent the rotations of the plate around x, y and z, respectively. The drilling rotation, θ_z can be found from the rotational constraint equation as [81]

$$skew(\boldsymbol{Q}^T\boldsymbol{F}) = 0 \tag{2.45a}$$

where

$$\mathbf{Q} = \begin{bmatrix} \cos\theta_z & -\sin\theta_z \\ \sin\theta_z & \cos\theta_z \end{bmatrix} \tag{2.45b}$$

$$\mathbf{F} = \begin{bmatrix} 1+u_{,x} & u_{,y} \\ v_{,x} & 1+v_{,y} \end{bmatrix} \tag{2.45c}$$

The rotational constraint in Eq. (2.45a) can also be written as

$$-\left(v_{,y}+u_{,x}+2\right)\sin\theta_z + \left(v_{,x}-u_{,y}\right)\cos\theta_z = 0 \tag{2.46}$$

If $\theta_z \neq \pi/2$, Eq. (2.46) becomes [81]

$$\theta_z = \arctan\left(\frac{v_{,x}-u_{,y}}{v_{,y}+u_{,x}+2}\right) \tag{2.47}$$

For small rotation and small strain conditions, Eq. (2.47) becomes

$$\theta_z = \frac{1}{2}\left(v_{,x} - u_{,y}\right) \tag{2.48}$$

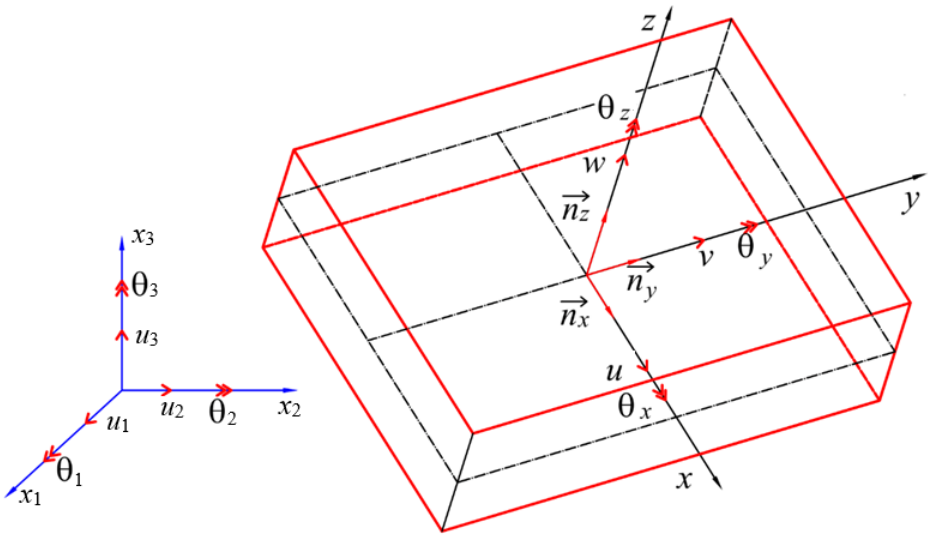

Fig. 2.20. A material point in a flat shell with 6 degrees of freedom

2.2.2.2. Linear Strain Components

For small deformations, the displacement components of a point located at (x, y, z) with respect to mid-surface can be expressed as [70, 78-80]

$$\hat{u}\left(x, y, z\right) = u\left(x, y\right) + z\theta_y \tag{2.49a}$$

$$\hat{v}\left(x, y, z\right) = v\left(x, y\right) - z\theta_x \tag{2.49b}$$

$$\hat{w}\left(x, y, z\right) = w\left(x, y\right) \tag{2.49c}$$

where u, v, w represent the displacement components of a point located at the mid-surface and $\hat{u}, \hat{v}, \hat{w}$ represent the displacement components at any point.

By using the displacement components given in Eq. (2.49), the linear strain components can be determined as

$$\boldsymbol{\varepsilon} = \begin{bmatrix} \varepsilon_{xx} & \varepsilon_{yy} & \gamma_{xy} & \gamma_{xz} & \gamma_{yz} \end{bmatrix}^T \tag{2.50a}$$

where

$$\varepsilon_{xx} = \partial\hat{u}/\partial x = u_{,x} + z\theta_{y,x} \tag{2.50b}$$

$$\varepsilon_{yy} = \partial\hat{v}/\partial y = v_{,y} - z\theta_{x,y} \tag{2.50c}$$

$$\gamma_{xy} = \partial\hat{u}/\partial y + \partial\hat{v}/\partial x = u_{,y} + v_{,x} + z\left(\theta_{y,y} - \theta_{x,x}\right) \tag{2.50d}$$

$$\gamma_{xz} = \partial\hat{u}/\partial z + \partial\hat{w}/\partial x = w_{,x} + \theta_y \tag{2.50e}$$

$$\gamma_{yz} = \partial\hat{v}/\partial z + \partial\hat{w}/\partial y = w_{,y} - \theta_x \tag{2.50f}$$

Note that based on the small deformation assumptions in linear elasticity, the strain component in the thickness direction of the shell can be neglected, $\varepsilon_{zz} = 0$ [70].

If the temperature effect is considered, total strain components in Eq. (2.50) can be determined as a summation of mechanical strain, $\boldsymbol{\varepsilon}^m$ and thermal strain, $\boldsymbol{\varepsilon}^T$ as [82]

$$\boldsymbol{\varepsilon} = \boldsymbol{\varepsilon}^m + \boldsymbol{\varepsilon}^T \tag{2.51a}$$

with

$$\boldsymbol{\varepsilon}^T = \begin{bmatrix} \alpha \Delta T & \alpha \Delta T & 0 & 0 & 0 \end{bmatrix}^T \tag{2.51b}$$

where α represents the coefficient of linear thermal expansion and ΔT represents the temperature change. Therefore, the mechanical strain components can be defined as

$$\boldsymbol{\varepsilon}^m = \boldsymbol{\varepsilon} - \boldsymbol{\varepsilon}^T = \begin{bmatrix} \varepsilon_{xx}^m & \varepsilon_{yy}^m & \gamma_{xy}^m & \gamma_{xz}^m & \gamma_{yz}^m \end{bmatrix}^T \tag{2.52a}$$

where

$$\varepsilon_{xx}^m = u_{,x} + z\theta_{y,x} - \alpha \Delta T \tag{2.52b}$$

$$\varepsilon_{yy}^m = v_{,y} - z\theta_{x,y} - \alpha \Delta T \tag{2.52c}$$

$$\gamma_{xy}^m = \gamma_{xy} = u_{,y} + v_{,x} + z\left(\theta_{y,y} - \theta_{x,x}\right) \tag{2.52d}$$

$$\gamma_{xz}^m = \gamma_{xz} = w_{,x} + \theta_y \tag{2.52e}$$

$$\gamma_{yz}^m = \gamma_{yz} = w_{,y} - \theta_x \tag{2.52f}$$

2.2.2.3. Stress Components

For a linear elastic isotropic, homogeneous material with $\sigma_{zz} = 0$, the stress components can be expressed as [82]

$$\boldsymbol{\sigma} = \mathbf{D}\boldsymbol{\varepsilon} - \mathbf{D}\boldsymbol{\alpha}\Delta T \tag{2.53a}$$

with

$$\mathbf{D} = \frac{E}{1-\nu^2}\begin{bmatrix} 1 & \nu & 0 & 0 & 0 \\ \nu & 1 & 0 & 0 & 0 \\ 0 & 0 & \dfrac{1-\nu}{2} & 0 & 0 \\ 0 & 0 & 0 & \dfrac{1-\nu}{2} & 0 \\ 0 & 0 & 0 & 0 & \dfrac{1-\nu}{2} \end{bmatrix} \tag{2.53b}$$

$$\boldsymbol{\alpha} = \begin{bmatrix} \alpha & \alpha & 0 & 0 & 0 \end{bmatrix}^T \tag{2.53c}$$

where $\boldsymbol{D}$ represents the constitutive relations and $\boldsymbol{\alpha}$ represents the vector of linear thermal expansion coefficients.

By substituting Eq. (2.50) into Eq. (2.53), the stress components can be expressed as

$$\sigma_{xx} = \frac{E}{1-\nu^2}\left[u_{,x} + z\theta_{y,x} + \nu\left(v_{,y} - z\theta_{x,y}\right) - \left(1+\nu\right)\alpha \Delta T\right] \tag{2.54a}$$

$$\sigma_{yy} = \frac{E}{1-\nu^2}\left[v_{,y} - z\theta_{x,y} + \nu\left(u_{,x} + z\theta_{y,x}\right) - \left(1+\nu\right)\alpha \Delta T\right] \tag{2.54b}$$

$$\sigma_{xy} = \frac{E}{2\left(1+\nu\right)}\left[u_{,y} + v_{,x} + z\left(\theta_{y,y} - \theta_{x,x}\right)\right] \tag{2.54c}$$

$$\sigma_{xz} = \frac{E}{2\left(1+\nu\right)}\left[w_{,x} + \theta_y\right] \tag{2.54d}$$

$$\sigma_{yz} = \frac{E}{2\left(1+\nu\right)}\left[w_{,y} - \theta_x\right] \tag{2.54e}$$

2.2.2.4. Strain Energy Density

In linear elasticity, the strain energy density (SED) can be expressed as [83]

$$W = \frac{1}{2}\left[\sigma_{xx}\varepsilon_{xx}^{m} + \sigma_{yy}\varepsilon_{yy}^{m} + \sigma_{zz}\varepsilon_{zz}^{m} + \sigma_{xy}\gamma_{xy}^{m} + \sigma_{xz}\gamma_{xz}^{m} + \sigma_{yz}\gamma_{yz}^{m}\right] \tag{2.55}$$

By substituting the stress and mechanical strain components given in Eq. (2.54) and Eq. (2.52) into Eq. (2.55), the strain energy density can be obtained as

$$\begin{aligned} W = \frac{1}{2}\Bigg\{ & \frac{E}{1-\nu^2}\left[u_{,x} + z\theta_{y,x} + \nu\left(v_{,y} - z\theta_{x,y}\right) - \left(1+\nu\right)\alpha.\Delta T\right]\left(u_{,x} + z\theta_{y,x} - \alpha\,\Delta T\right) \\ & + \frac{E}{1-\nu^2}\left[v_{,y} - z\theta_{x,y} + \nu\left(u_{,x} + z\theta_{y,x}\right) - \left(1+\nu\right)\alpha.\Delta T\right]\left(v_{,y} - z\theta_{x,y} - \alpha\,\Delta T\right) \\ & + \frac{E}{2\left(1+\nu\right)}\left[u_{,y} + v_{,x} + z\left(\theta_{y,y} - \theta_{x,x}\right)\right]^2 \\ & + \frac{E}{2\left(1+\nu\right)}\left[w_{,x} + \theta_y\right]^2 + \frac{E}{2\left(1+\nu\right)}\left[w_{,y} - \theta_x\right]^2\Bigg\} \end{aligned} \tag{2.56}$$

By integrating the SED given in Eq. (2.56) through the thickness of the shell, the strain energy per unit area, $\bar{W}$, can be obtained as

$$\begin{aligned} \bar{W} = \int_{-h/2}^{h/2} W dz = & \frac{Eh}{2\left(1-\nu^2\right)}\left(u_{,x} + v_{,y}\right)^2 + \frac{Eh}{4\left(1+\nu\right)}\left[\left(u_{,y} + v_{,x}\right)^2 - 4u_{,x}v_{,y}\right] \\ & + \frac{Eh}{1-\nu}\left[\left(\alpha\,\Delta T\right)^2 - \alpha\,\Delta T\left(u_{,x} + v_{,y}\right)\right] \\ & + \frac{Eh^3}{24(1-\nu^2)}\left[\left(\theta_{x,y} - \theta_{y,x}\right)^2 + \frac{1-\nu}{2}\left(\left(\theta_{x,x} - \theta_{y,y}\right)^2 + 4\theta_{y,x}\theta_{x,y}\right)\right] \\ & + \frac{k_s Eh}{4\left(1+\nu\right)}\left[\left(w_{,x} + \theta_y\right)^2 + \left(w_{,y} - \theta_x\right)^2\right] \end{aligned} \tag{2.57}$$

where h represents the thickness of the flat shell, ν represents the Poisson's ratio, E represents Young's modulus, $k_s = 5/6$ represents the shear correction factor to account for the non-uniformity of the shear stresses [70]

The strain energy per unit area given in Eq. (2.57) can be represented as

$$\bar{W} = \bar{W}_{inplane} + \bar{W}_{bending} + \bar{W}_{shear} \tag{2.58a}$$

with

$$\begin{aligned} \bar{W}_{inplane} = & \frac{Eh}{2\left(1-\nu^2\right)}\left(u_{,x} + v_{,y}\right)^2 + \frac{Eh}{4\left(1+\nu\right)}\left[\left(u_{,y} + v_{,x}\right)^2 - 4u_{,x}v_{,y}\right] \\ & + \frac{Eh}{1-\nu}\left[\left(\alpha\,\Delta T\right)^2 - \alpha\,\Delta T\left(u_{,x} + v_{,y}\right)\right] \end{aligned} \tag{2.58b}$$

$$\bar{W}_{bending} = \frac{Eh^3}{24(1-\nu^2)}\left[\left(\theta_{y,x} - \theta_{x,y}\right)^2 + \frac{1-\nu}{2}\left(\left(\theta_{x,x} - \theta_{y,y}\right)^2 + 4\theta_{y,x}\theta_{x,y}\right)\right] \tag{2.58c}$$

$$\bar{W}_{shear} = \frac{k_s Eh}{4\left(1+\nu\right)}\left[\left(w_{,x} + \theta_y\right)^2 + \left(w_{,y} - \theta_x\right)^2\right] \tag{2.58d}$$

where $\bar{W}_{inplane}$, $\bar{W}_{bending}$, $\bar{W}_{shear}$ represent the strain energy per unit area for in-plane, bending, and shear deformations, respectively.

According to the Mindlin–Reissner plate theory, plate element is developed with 5 degrees of freedom (DOF) as provided in Eq. (2.58). However, to simulate curved and stiffened structures 6 DOF shell elements are required. If the drilling rotation is not considered, all the resistance to the drilling rotation of each node comes directly from the coupling of other rotational DOFs of the non-planar surrounding nodes. When the model is discretized with very fine mesh, angles of the kinks between two elements, which are located next to each other, will become close to 2π and the coupling effect is much reduced [71]. As a result, the global stiffness matrix may become singular and it results in unrealistic solution results. Therefore, to produce a small stiffness associated with drilling rotation, an additional fictitious torsional strain energy per unit area corresponding to the drilling rotation can be added as [71]

$$\bar{W} = \bar{W}_{inplane} + \bar{W}_{bending} + \bar{W}_{shear} + \bar{W}_{torsional} \tag{2.59a}$$

where

$$\bar{W}_{torsional} = k_T \frac{Eh}{2(1+\nu)}\left[\theta_z - \frac{1}{2}\left(v_{,x} - u_{,y}\right)\right]^2 \tag{2.59b}$$

in which k_T represents torsional constant [71].
Note that, the value of the fictitious stiffness needs to be small enough to ensure that this stiffness will not distort the global solution results [71].

2.3.3. Kinematics of Flat Shells in Peridynamics

In this section, first, the peridynamic form of strain energy density is established. Next, the kinetic energy, total potential energy, Lagrangian function are obtained by using Eq. (2.27). Finally, the equations of motion for shells are obtained by using the Euler-Lagrange equation given in Eq. (2.26).

2.3.3.1. PD Strain Energy Density

Similar to the strain energy per unit area in classical continuum mechanics provided in Eq. (2.59a), the peridynamic form of strain energy per unit area for a flat shell can be presented as

$$\bar{W}^{PD}_{(k)} = \bar{W}^{PD}_{inplane(k)} + \bar{W}^{PD}_{bending(k)} + \bar{W}^{PD}_{shear(k)} + \bar{W}^{PD}_{torsional(k)} \tag{2.60}$$

where $\bar{W}^{PD}_{inplane(k)}$, $\bar{W}^{PD}_{bending(k)}$, $\bar{W}^{PD}_{shear(k)}$ represent the components of strain energy per unit area for in-plane, bending, shear deformations, respectively. The term $\bar{W}^{PD}_{torsional(k)}$ represents the additional strain energy per unit area that corresponds to drilling rotation.

Similar to strain energy density definition by Madenci and Oterkus [44], the PD form of strain energy per unit area for in-plane deformations can be defined as

$$\bar{W}^{PD}_{inplane(k)} = a_{ip1}\vartheta^2_{(k)} - a_{ip2}\vartheta_{(k)}\Delta T_{(k)} + a_{ip3}\Delta T^2_{(k)} + b_{ip}\sum_{j=1}^{N}\left(s_{ip(k)(j)} - \alpha\,\Delta T_{(k)}\right)^2 \xi V_{(j)} \tag{2.61}$$

where $\vartheta_{(k)}$ represents the dilatation of material point k, $s_{ip(k)(j)}$ represents the relative bond stretch of in-plane displacement components between material point k and material point j.

In Eq. (2.61), the terms a_{ip1}, a_{ip2} , a_{ip3}, and b_{ip} represent in-plane PD constants which can be determined as (Appendix B1)

$$a_{ip1} = \frac{Eh(3\nu - 1)}{4(1-\nu^2)} \tag{2.62a}$$

$$a_{ip2} = \frac{Eh\alpha}{1-\nu^2}(3\nu - 1) = 4\alpha a_{ip1} \tag{2.62b}$$

$$a_{ip3} = \frac{Eh}{1-\nu^2}(3\nu - 1)\alpha^2 = 4\alpha^2 a_{ip1} \tag{2.62c}$$

$$b_{ip} = \frac{3}{\pi\delta^3}\frac{E}{1+\nu} \tag{2.62d}$$

The effect of temperature change on dilatation term can be included as [26, 44]

$$\vartheta_{(k)} = d_{ip}\sum_{j=1}^{N}\left(s_{ip(k)(j)} - \alpha\,\Delta T_{(k)}\right)V_{(j)} + 2\alpha\,\Delta T_{(k)} \tag{2.63}$$

where d_{ip} represents the in-plane PD constant for dilatation as (Appendix B1)

$$d_{ip} = \frac{2}{\pi h\delta^2} \tag{2.64}$$

The relative bond stretch for in-plane displacement components between two material points can be defined as [75]

$$s_{ip(k)(j)} = \frac{\left(u_{(j)} - u_{(k)}\right)\cos\varphi + \left(v_{(j)} - v_{(k)}\right)\sin\varphi}{\xi} \tag{2.65}$$

where $u_{(k)}$, $v_{(k)}$ and $u_{(j)}$, $v_{(j)}$ represent two in-plane degrees of freedom of material points k and j, respectively. The parameter φ represents the angle of interaction between material points k and j with respect to the local axis, x in the undeformed configuration as shown in Fig. 2.21.

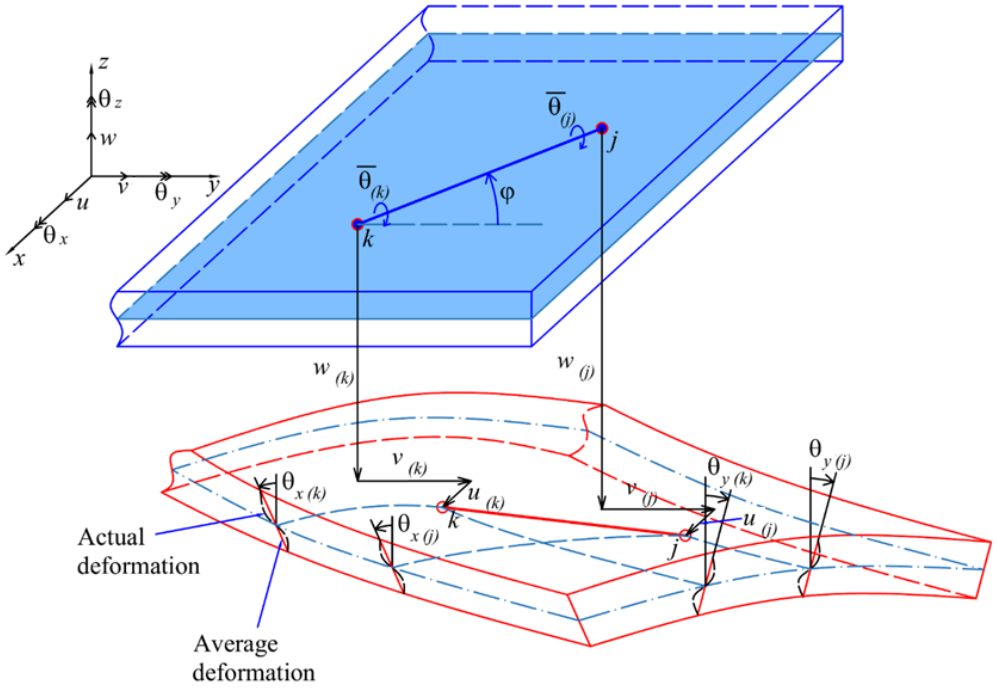

Fig. 2.21. Deformed and initial configuration of a flat shell in PD

The PD form of strain energy per unit area for bending deformations can be defined as

$$\bar{W}^{PD}_{bending(k)} = a_b \vartheta^2_{b(k)} + b_b \sum_{j=1}^{N} s^2_{b(k)(j)} \xi V_{(j)} \tag{2.66}$$

where a_b and b_b represent PD constants for bending which can be defined as (Appendix B2)

$$a_b = \frac{Eh^3}{48} \frac{3\nu - 1}{1 - \nu^2} \tag{2.67a}$$

$$b_b = \frac{Eh^2}{4(1+\nu)\pi\delta^3} \tag{2.67b}$$

The terms $\vartheta_{b(k)}$ and $s_{b(k)(j)}$ in Eq. (2.66) can be defined as

$$\vartheta_{b(k)} = d_b \sum_{j=1}^{N} s_{b(k)(j)} V_{(j)} \tag{2.68a}$$

$$s_{b(k)(j)} = \frac{-\left(\theta_{y(j)} - \theta_{y(k)}\right)\cos\varphi + \left(\theta_{x(j)} - \theta_{x(k)}\right)\sin\varphi}{\xi} \tag{2.68b}$$

with

$$d_b = \frac{2}{\pi h \delta^2} \tag{2.68c}$$

Here, θ_x and θ_y represent rotational degrees of freedom with respect to x and y axes as shown in Fig. 2.20.

The PD form of strain energy per unit area for shear deformations can be defined as

$$\bar{W}^{PD}_{shear(k)} = \frac{1}{4} C_s \sum_{j=1}^{N} \left(\frac{w_{(j)} - w_{(k)}}{\xi} - \frac{\bar{\theta}_{(k)} + \bar{\theta}_{(j)}}{2} \right)^2 \xi V_{(j)} \tag{2.69}$$

where C_s represents PD constant for the shear deformations as (Appendix B3)

$$C_s = \frac{3k_s}{\pi\delta^3} \frac{E}{(1+\nu)} \tag{2.70}$$

In Eq. (2.69) the terms $\bar{\theta}_{(k)}$ and $\bar{\theta}_{(j)}$ represent the rotations with respect to the line of action between the material points k and j as shown in Fig. 2.21. These rotations can be calculated as [50]

$$\bar{\theta}_{(k)} = -\theta_{y(k)} \cos\varphi + \theta_{x(k)} \sin\varphi \tag{2.71a}$$

$$\bar{\theta}_{(j)} = -\theta_{y(j)} \cos\varphi + \theta_{x(j)} \sin\varphi \tag{2.71b}$$

The torsional strain energy per unit area in PD can be defined as

$$\bar{W}^{PD}_{torsional(k)} = \frac{1}{2} \sum_{j=1}^{N} C_t \left[\frac{\theta_{z(k)} + \theta_{z(j)}}{2} - \left(\frac{v_{(j)} - v_{(k)}}{\xi} \cos\varphi - \frac{u_{(j)} - u_{(k)}}{\xi} \sin\varphi \right) \right]^2 \xi V_{(j)} \tag{2.72}$$

where $\theta_{z(k)}$ and $\theta_{z(j)}$ represent drilling rotations, which are with respect to z-axis, of material points k and j, respectively.

In Eq. (2.72), C_t represents PD constant for torsional deformations as (Appendix B4)

$$C_t = k_T \frac{3}{2\pi\delta^3} \frac{E}{1+\nu} \tag{2.73}$$

As explained in Section.2.4, the value of the fictitious stiffness corresponding to the drilling rotation needs to be small enough to ensure that this stiffness will not distort the global solution results. As suggested by Kanok-nukulchai [71], the value of the

torsional constant, k_T, can be chosen to make the torsional strain energy per unit area has the same order as the bending strain energy per unit area. Therefore, by equating Eq. (2.67b) and Eq. (2.73), the value of k_T can be chosen as

$$k_T = k_0 \frac{h^2}{6} \tag{2.74}$$

where k_0 constant is added for convergence in PD solution, which is inherited from the suggestion by Kanok-nukulchai [71] for convergence in FEA simulations, and it is chosen as $k_0 \geq 1$.

Note that ordinary state-based formulations for in-plane and bending strain energy as provided in Eq. (2.63) and (2.66) removed the limitation on Poisson's ratio.

2.3.3.2. PD Equations of Motion in the Local Coordinate System

By using Eq. (2.27), the PD form of kinetic energy, total potential energy, and the Lagrangian function can be defined as

$$T = \frac{1}{2}\sum_{k=1}^{N_p}\left(\rho h \dot{u}_{(k)}^2 + \rho h \dot{v}_{(k)}^2 + \rho h \dot{w}_{(k)}^2 + \frac{\rho h^3}{12}\left(\dot{\theta}_{x(k)}^2 + \dot{\theta}_{y(k)}^2 \right) + \frac{\rho h I_{zz(k)}}{A_{(k)}} \dot{\theta}_{z(k)}^2 \right) A_{(k)} \tag{2.75a}$$

$$U = \sum_{k=1}^{N_p}\left(\bar{W}_{(k)}^{PD} - \bar{b}_{x(k)} u_{(k)} - \bar{b}_{y(k)} v_{(k)} - \bar{b}_{z(k)} w_{(k)} - \bar{m}_{x(k)} \theta_{x(k)} - \bar{m}_{y(k)} \theta_{y(k)} \right) A_{(k)} \tag{2.75b}$$

$$L = T - U \tag{2.75c}$$

where N_p represents the total number of material points of the PD model, $\bar{b}_{x(k)}$, $\bar{b}_{y(k)}$ and $\bar{b}_{z(k)}$ represent the applied forces per unit area at material point k in x, y, and z directions, respectively. The parameters $\bar{m}_{x(k)}$ and $\bar{m}_{y(k)}$ represent applied moments per unit area with respect to local coordinate x and y, respectively. The parameter $I_{zz(k)}$ represents the moment of inertia with respect to z-axis. If the shell is uniformly discretized with a grid size Δx, the moment of inertia, $I_{zz(k)}$ for each material point can be calculated as [61]

$$I_{zz(k)} = \frac{(\Delta x)^4}{6} \tag{2.76}$$

Therefore, by substituting the Lagrangian function obtained from Eq. (2.75) into Eq. (2.26) in Chapter 2, the equations of motion for flat shells can be obtained as

$$\rho h \ddot{u}_{(k)} = \sum_{j=1}^{N}\left[\begin{array}{l} 2a_{ip1} d_{ip} \frac{1}{\xi}\left(\vartheta_{(k)} + \vartheta_{(j)} \right) - a_{ip2} d_{ip} \frac{1}{\xi}\left(\Delta T_{(k)} + \Delta T_{(j)} \right) \\ +4b_{ip}\left(s_{ip(k)(j)} - \alpha \Delta T_{(k)} \right) \end{array} \right] \cos\varphi V_{(j)} + \bar{b}_{x(k)} \tag{2.77a}$$

$$\rho h \ddot{v}_{(k)} = \sum_{j=1}^{N}\left[\begin{array}{l} 2a_{ip1} d_{ip} \frac{1}{\xi}\left(\vartheta_{(k)} + \vartheta_{(j)} \right) - a_{ip2} d_{ip} \frac{1}{\xi}\left(\Delta T_{(k)} + \Delta T_{(j)} \right) \\ +4b_{ip}\left(s_{ip(k)(j)} - \alpha \Delta T_{(k)} \right) \end{array} \right] \sin\varphi V_{(j)} + \bar{b}_{y(k)} \tag{2.77b}$$

$$\rho h \ddot{w}_{(k)} = C_s \sum_{j=1}^{N}\left\{ \frac{w_{(j)} - w_{(k)}}{\xi} - \frac{1}{2}\left[\begin{array}{l} -\left(\theta_{y(k)} + \theta_{y(j)} \right)\cos\varphi \\ +\left(\theta_{x(k)} + \theta_{x(j)} \right)\sin\varphi \end{array} \right] \right\} V_{(j)} + \bar{b}_{z(k)} \tag{2.77c}$$

$$\frac{\rho h^3}{12}\ddot{\theta}_{x(k)} = \sum_{j=1}^{N}\left[\frac{2a_b d_b}{\xi}\left(\vartheta_{b(k)}+\vartheta_{b(j)}\right)+4b_b s_{b(k)(j)}\right]\sin\varphi V_{(j)}$$
$$+\frac{1}{2}C_s\sum_{j=1}^{N}\left\{\left(w_{(j)}-w_{(k)}\right)\sin\varphi-\frac{\xi}{2}\begin{bmatrix}-\left(\theta_{y(k)}+\theta_{y(j)}\right)\sin\varphi\cos\varphi\\+\left(\theta_{x(k)}+\theta_{x(j)}\right)\sin^2\varphi\end{bmatrix}\right\}V_{(j)} \qquad (2.77d)$$
$$+\bar{m}_{x(k)}$$

$$\frac{\rho h^3}{12}\ddot{\theta}_{y(k)} = -\sum_{j=1}^{N}\left[\frac{2a_b d_b}{\xi}\left(\vartheta_{b(k)}+\vartheta_{b(j)}\right)+4b_b s_{b(k)(j)}\right]\cos\varphi V_{(j)}$$
$$-\frac{1}{2}C_s\sum_{j=1}^{N}\left\{\left(w_{(j)}-w_{(k)}\right)\cos\varphi-\frac{\xi}{2}\begin{bmatrix}-\left(\theta_{y(k)}+\theta_{y(j)}\right)\cos^2\varphi\\+\left(\theta_{x(k)}+\theta_{x(j)}\right)\sin\varphi\cos\varphi\end{bmatrix}\right\}V_{(j)} \qquad (2.77e)$$
$$+\bar{m}_{y(k)}$$

$$\frac{\rho h I_{zz(k)}}{A_{(k)}}\ddot{\theta}_{z(k)} = C_t\sum_{j=1}^{N}\left[\frac{\theta_{z(k)}+\theta_{z(j)}}{2}-\left(\frac{v_{(j)}-v_{(k)}}{\xi}\cos\varphi-\frac{u_{(j)}-u_{(k)}}{\xi}\sin\varphi\right)\right]\xi V_{(j)} \qquad (2.77f)$$

The equations of motion in the local coordinate system given in Eq. (2.77) can be rewritten in vector form as

$$\bar{\mathbf{m}}^L_{(k)}\ddot{\mathbf{u}}^L_{(k)} = \sum_{j=1}^{N}\mathbf{f}^L_{(k)(j)}V_{(j)}+\bar{\mathbf{b}}^L_{(k)} \qquad (2.78a)$$

where

$$\bar{\mathbf{m}}^L_{(k)} = \begin{bmatrix}\rho h & 0 & 0 & 0 & 0 & 0\\ 0 & \rho h & 0 & 0 & 0 & 0\\ 0 & 0 & \rho h & 0 & 0 & 0\\ 0 & 0 & 0 & \frac{\rho h^3}{12} & 0 & 0\\ 0 & 0 & 0 & 0 & \frac{\rho h^3}{12} & 0\\ 0 & 0 & 0 & 0 & 0 & \frac{\rho h I_{zz}}{A_{(k)}}\end{bmatrix};\ \ddot{\mathbf{u}}^L_{(k)} = \begin{bmatrix}\ddot{u}_{(k)}\\ \ddot{v}_{(k)}\\ \ddot{w}_{(k)}\\ \ddot{\theta}_{x(k)}\\ \ddot{\theta}_{y(k)}\\ \ddot{\theta}_{z(k)}\end{bmatrix};\ \bar{\mathbf{b}}^L_{(k)} = \begin{bmatrix}\bar{b}_{x(k)}\\ \bar{b}_{y(k)}\\ \bar{b}_{z(k)}\\ \bar{m}_{x(k)}\\ \bar{m}_{y(k)}\\ 0\end{bmatrix} \qquad (2.78b)$$

and

$$\mathbf{f}^L_{(k)(j)} = \begin{bmatrix} f^u_{(k)(j)} & f^v_{(k)(j)} & f^w_{(k)(j)} & f^{\theta_x}_{(k)(j)} & f^{\theta_y}_{(k)(j)} & f^{\theta_z}_{(k)(j)}\end{bmatrix}^T \qquad (2.78c)$$

with

$$f^u_{(k)(j)} = \begin{bmatrix}2a_{ip1}d_{ip}\frac{1}{\xi}\left(\vartheta_{(k)}+\vartheta_{(j)}\right)-a_{ip2}d_{ip}\frac{1}{\xi}\left(\Delta T_{(k)}+\Delta T_{(j)}\right)\\ +4b_{ip}\left(s_{ip(k)(j)}-\alpha\Delta T_{(k)}\right)\end{bmatrix}\cos\varphi \qquad (2.78d)$$

$$f^v_{(k)(j)} = \begin{bmatrix}2a_{ip1}d_{ip}\frac{1}{\xi}\left(\vartheta_{(k)}+\vartheta_{(j)}\right)-a_{ip2}d_{ip}\frac{1}{\xi}\left(\Delta T_{(k)}+\Delta T_{(j)}\right)\\ +4b_{ip}\left(s_{ip(k)(j)}-\alpha\Delta T_{(k)}\right)\end{bmatrix}\sin\varphi \qquad (2.78e)$$

$$f_{(k)(j)}^{w} = C_s \left\{ \frac{w_{(j)} - w_{(k)}}{\xi} - \frac{1}{2}\left[-\left(\theta_{y(k)} + \theta_{y(j)}\right)\cos\varphi + \left(\theta_{x(k)} + \theta_{x(j)}\right)\sin\varphi \right] \right\} \tag{2.78f}$$

$$\begin{aligned} f_{(k)(j)}^{\theta_x} = & \left[\frac{2a_b d_b}{\xi}\left(\vartheta_{b(k)} + \vartheta_{b(j)}\right) + 4b_b s_{b(k)(j)} \right]\sin\varphi \\ & + \frac{1}{2}C_s \left\{ \left(w_{(j)} - w_{(k)}\right)\sin\varphi - \frac{\xi}{2}\left[\begin{array}{l} -\left(\theta_{y(k)} + \theta_{y(j)}\right)\sin\varphi\cos\varphi \\ +\left(\theta_{x(k)} + \theta_{x(j)}\right)\sin^2\varphi \end{array} \right] \right\} \end{aligned} \tag{2.78g}$$

$$\begin{aligned} f_{(k)(j)}^{\theta_y} = & -\left[\frac{2a_b d_b}{\xi}\left(\vartheta_{b(k)} + \vartheta_{b(j)}\right) + 4b_b s_{b(k)(j)} \right]\cos\varphi \\ & - \frac{1}{2}C_s \left\{ \left(w_{(j)} - w_{(k)}\right)\cos\varphi - \frac{\xi}{2}\left[\begin{array}{l} -\left(\theta_{y(k)} + \theta_{y(j)}\right)\cos^2\varphi \\ +\left(\theta_{x(k)} + \theta_{x(j)}\right)\sin\varphi\cos\varphi \end{array} \right] \right\} \end{aligned} \tag{2.78h}$$

$$f_{(k)(j)}^{\theta_z} = C_t \left[\frac{\theta_{z(k)} + \theta_{z(j)}}{2} - \left(\frac{v_{(j)} - v_{(k)}}{\xi}\cos\varphi - \frac{u_{(j)} - u_{(k)}}{\xi}\sin\varphi \right) \right]\xi \tag{2.78i}$$

Note that the torsional strain energy per unit area is fictitious and it creates a small stiffness corresponding to drilling DOF. Therefore, the contribution of drilling rotation to in-plane displacements can be neglected in the equations of motion [71]. Note that the PD constants provided in Appendices B1-B4 are obtained based on the small deformation assumption. Therefore, the developed PD model is applicable for linear analysis of shell structures with small deformations.

2.3.4. PD Equations of Motion in the Global Coordinate System

The equations of motion provided in Eq. (2.78) are derived in local or body-attached coordinates. For a structure that includes plates and shells joined, the equations of motion for each material point needs to be transformed from local coordinates to global coordinates. Therefore, in this section, the transformation of equations of motion for flat and curved shells is presented.

2.3.4.1. Coordinate Transformation

As shown in Fig. 2.20, the local coordinates of a shell can be defined with respect to the global coordinates by unit vectors $\vec{n}_x$, $\vec{n}_y$, $\vec{n}_z$. The unit vectors for material point k can be defined from the geometry of the shell as

$$\vec{n}_{x(k)} = \begin{bmatrix} a_{1(k)} & a_{2(k)} & a_{3(k)} \end{bmatrix}^T \tag{2.79a}$$

$$\vec{n}_{y(k)} = \begin{bmatrix} b_{1(k)} & b_{2(k)} & b_{3(k)} \end{bmatrix}^T \tag{2.79b}$$

$$\vec{n}_{z(k)} = \begin{bmatrix} c_{1(k)} & c_{2(k)} & c_{3(k)} \end{bmatrix}^T \tag{2.79c}$$

Similar to the relations presented in Chapter 2, the relationship between global and local coordinates can be written as

$$\mathbf{x}_{(k)}^L = \mathbf{H}_{(k)}\mathbf{x}_{(k)}^G \tag{2.80a}$$

where

$$\mathbf{x}_{(k)}^L = \begin{bmatrix} x_{(k)} & y_{(k)} & z_{(k)} \end{bmatrix}^T \tag{2.80b}$$

$$\mathbf{x}^G_{(k)} = \begin{bmatrix} x_{1(k)} & x_{2(k)} & x_{3(k)} \end{bmatrix}^T \tag{2.80c}$$

$$\mathbf{H}_{(k)} = \begin{bmatrix} \vec{n}_{x(k)} & \vec{n}_{y(k)} & \vec{n}_{z(k)} \end{bmatrix}^T = \begin{bmatrix} a_{1(k)} & a_{2(k)} & a_{3(k)} \\ b_{1(k)} & b_{2(k)} & b_{3(k)} \\ c_{1(k)} & c_{2(k)} & b_{3(k)} \end{bmatrix} \tag{2.80d}$$

The transformation of the displacement vector can be defined as

$$\mathbf{u}^L_{(k)} = \mathbf{T}_{(k)} \mathbf{u}^G_{(k)} \tag{2.81a}$$

with

$$\mathbf{u}^L_{(k)} = \begin{bmatrix} u_{(k)} & v_{(k)} & w_{(k)} & \theta_{x(k)} & \theta_{y(k)} & \theta_{z(k)} \end{bmatrix}^T \tag{2.81b}$$

$$\mathbf{u}^G_{(k)} = \begin{bmatrix} u_{1(k)} & u_{2(k)} & u_{3(k)} & \theta_{1(k)} & \theta_{2(k)} & \theta_{3(k)} \end{bmatrix}^T \tag{2.81c}$$

where $\mathbf{u}^L_{(k)}$ and $\mathbf{u}^G_{(k)}$ represent displacement vectors in the local and global coordinate systems, respectively. The parameter $\mathbf{T}_{(k)}$ represents the displacement transformation matrix of material point k, which can be obtained from the coordinate transformation matrix, $\mathbf{H}_{(k)}$ as

$$\mathbf{T}_{(k)} = \begin{bmatrix} \mathbf{H}_{(k)} & \mathbf{0} \\ \mathbf{0} & \mathbf{H}_{(k)} \end{bmatrix} \tag{2.82}$$

2.3.4.2. Transformation of Equations of Motion for Flat Shells

By using the relations given in Eq. (2.81a), the equations of motion for shell given in Eq. (2.78a) can be written as

$$\bar{\mathbf{m}}^L_{(k)} \mathbf{T}_{(k)} \ddot{\mathbf{u}}^G_{(k)} = \sum_{j=1}^{N} \mathbf{f}^L_{(k)(j)} V_{(j)} + \bar{\mathbf{b}}^L_{(k)} \tag{2.83}$$

Multiplying both sides by $\boldsymbol{T}^T_{(k)}$ results in

$$\mathbf{T}^T_{(k)} \bar{\mathbf{m}}^L_{(k)} \mathbf{T}_{(k)} \ddot{\mathbf{u}}^G_{(k)} = \mathbf{T}^T_{(k)} \left(\sum_{j=1}^{N} \mathbf{f}^L_{(k)(j)} V_{(j)} + \bar{\mathbf{b}}^L_{(k)} \right) \tag{2.84}$$

As a result, the equation of motion in global coordinates becomes

$$\bar{\mathbf{m}}^G_{(k)} \ddot{\mathbf{u}}^G_{(k)} = \sum_{j=1}^{N} \mathbf{f}^G_{(k)(j)} V_{(j)} + \bar{\mathbf{b}}^G_{(k)} \tag{2.85a}$$

where

$$\mathbf{f}^G_{(k)(j)} = \mathbf{T}^T_{(k)} \mathbf{f}^L_{(k)(j)} \tag{2.85b}$$

$$\bar{\mathbf{b}}^G_{(k)} = \mathbf{T}^T_{(k)} \bar{\mathbf{b}}^L_{(k)} \tag{2.85c}$$

$$\bar{\mathbf{m}}^G_{(k)} = \mathbf{T}^T_{(k)} \bar{\mathbf{m}}^L_{(k)} \mathbf{T}_{(k)} \tag{2.85d}$$

2.3.4.3. Transformation of Equations of Motion for Curved Shells

In general, curved shells can be analysed by dividing them into a suitable number of flat shell elements [84]. Each flat shell element can be considered as a material point with kinematics described in Section 3 with the orientation represented by three unit vectors given in Eq. (2.79). Therefore, the equations of motions for each material point need to be transformed into the global coordinate system. Since each material point has a different displacement transformation matrix, the equations of motion for curved shells can be obtained by modifying Eq. (2.84) as

$$\mathbf{T}_{(k)(j)}^{T}\bar{\mathbf{m}}_{(k)}^{L}\mathbf{T}_{(k)(j)}\ddot{\mathbf{u}}_{(k)}^{G}=\mathbf{T}_{(k)(j)}^{T}\left(\sum_{j=1}^{N}\mathbf{f}_{(k)(j)}^{L}V_{(j)}+\bar{\mathbf{b}}_{(k)}^{L}\right) \tag{2.86a}$$

where $\boldsymbol{T}_{(k)(j)}$ represent the transformation matrix of interaction between material points k and j. This transformation matrix can be defined as [62, 84]

$$\mathbf{T}_{(k)(j)}=\begin{bmatrix}\mathbf{H}_{(k)(j)} & \mathbf{0}\\ \mathbf{0} & \mathbf{H}_{(k)(j)}\end{bmatrix} \tag{2.87a}$$

with

$$\mathbf{H}_{(k)(j)}=\begin{bmatrix}\vec{n}_{x(k)(j)} & \vec{n}_{y(k)(j)} & \vec{n}_{z(k)(j)}\end{bmatrix}^{T} \tag{2.87b}$$

where $\vec{n}_{x(k)(j)}$, $\vec{n}_{y(k)(j)}$, $\vec{n}_{z(k)(j)}$can be represented as [62, 84]

$$\vec{n}_{x(k)(j)}=\frac{\left(\vec{n}_{x(k)}+\vec{n}_{x(j)}\right)}{\left|\left(\vec{n}_{x(k)}+\vec{n}_{x(j)}\right)\right|} \tag{2.87c}$$

$$\vec{n}_{y(k)(j)}=\frac{\left(\vec{n}_{y(k)}+\vec{n}_{y(j)}\right)}{\left|\left(\vec{n}_{y(k)}+\vec{n}_{y(j)}\right)\right|} \tag{2.87d}$$

$$\vec{n}_{z(k)(j)}=\frac{\left(\vec{n}_{z(k)}+\vec{n}_{z(j)}\right)}{\left|\left(\vec{n}_{z(k)}+\vec{n}_{z(j)}\right)\right|} \tag{2.87e}$$

2.3.5. Damage prediction for the linear PD shell model

In this section, a PD damage criterion based on the critical energy release rate is introduced. The energy release rate for each interaction is calculated and compared with the critical value. By including function $\psi_{(k)(j)}$, the PD equations of motion given in Eq. (2.86a) can be written as

$$\left[\mathbf{T}_{(k)(j)}^{T}\bar{\mathbf{m}}_{(k)}^{L}\mathbf{T}_{(k)(j)}\right]\ddot{\mathbf{u}}_{(k)}^{G}=\sum_{j=1}^{N}\left[\mathbf{T}_{(k)(j)}^{T}\psi_{(k)(j)}\mathbf{f}_{(k)(j)}^{L}\right]V_{(j)}+\bar{\mathbf{b}}_{(k)}^{G} \tag{2.88}$$

Note that, by including the state of interaction represented by $\psi_{(k)(j)}$ [21], the dilatation, $\vartheta_{(k)}$, given in Eq. (2.63), and the term, $\vartheta_{b(k)}$, given in Eq. (2.68a) can be rewritten as

$$\vartheta_{(k)}=d_{ip}\sum_{j=1}^{N}\psi_{(k)(j)}\left(s_{ip(k)(j)}-\alpha\,\Delta T_{(k)}\right)V_{(j)}+2\alpha\,\Delta T_{(k)} \tag{2.89a}$$

$$\vartheta_{b(k)}=d_{b}\sum_{j=1}^{N}\psi_{(k)(j)}s_{b(k)(j)}V_{(j)} \tag{2.89b}$$

To decide the state of interaction which is represented by the function $\psi_{(k)(j)}$, the damage criteria based on the critical energy release rate as presented in Chapter 1 is used. The micropotentials, $\Phi_{(k)(j)}$ and $\Phi_{(j)(k)}$, of the interaction between material point k and j can be calculated as

$$\Phi_{(k)(j)}=\Phi_{inplane(k)(j)}+\Phi_{shear(k)(j)}+\Phi_{bending(k)(j)} \tag{2.90a}$$

$$\Phi_{(k)(j)}=\Phi_{inplane(k)(j)}+\Phi_{shear(k)(j)}+\Phi_{bending(k)(j)} \tag{2.90b}$$

where $\Phi_{inplane(k)(j)}$, $\Phi_{shear(k)(j)}$, $\Phi_{bending(k)(j)}$ represent micropotentials for in-plane, shear, and bending deformations, respectively. Note that the contribution of drilling rotation is not included in the calculation of total micropotential in Eq. (2.90) because the strain energy density caused by this DOF is fictitious.

In linear elasticity with small deformation, the relationship between relative bond stretch and force density is linear. Therefore, by applying the same idea introduced by [25], Madenci and Oterkus [26], the in-plane micropotential $\Phi_{inplane(k)(j)}$ can be calculated as

$$\Phi_{inplane(k)(j)} = \frac{1}{2h} t_{ip(k)(j)} \xi \left(s_{ip(k)(j)} - \alpha \Delta T_{(k)} \right) \tag{2.91a}$$

where

$$t_{ip(k)(j)} = \left[\frac{2a_{ip1} d_{ip}}{\xi} \vartheta_{(k)} - \frac{a_{ip2} d_{ip}}{\xi} \Delta T_{(k)} + 2b_{ip} \left(s_{ip(k)(j)} - \alpha \Delta T_{(k)} \right) \right] \tag{2.91b}$$

The bending micropotential $\Phi_{bending(k)(j)}$ can be calculated as

$$\Phi_{bending(k)(j)} = \frac{1}{2h} t_{b(k)(j)} \xi s_{b(k)(j)} \tag{2.92a}$$

where

$$\begin{aligned} t_{b(k)(j)} = & \left[\frac{2a_b d_b}{\xi} \vartheta_{b(k)} + 2b_b s_{b(k)(j)} \right] \\ & + \frac{1}{4} C_s \left\{ \left(w_{(j)} - w_{(k)} \right) - \frac{\xi}{2} \begin{bmatrix} -\left(\theta_{y(k)} + \theta_{y(j)} \right) \cos\varphi \\ +\left(\theta_{x(k)} + \theta_{x(j)} \right) \sin\varphi \end{bmatrix} \right\} \end{aligned} \tag{2.92b}$$

The shear micropotential $\Phi_{shear(k)(j)}$ can be calculated as

$$\Phi_{shear(k)(j)} = \frac{1}{2h} t_{shear(k)(j)} \xi s_{shear(k)(j)} \tag{2.93a}$$

where

$$t_{shear(k)(j)} = \frac{1}{2} f^{w}_{(k)(j)} = \frac{1}{2} C_s \left\{ \frac{w_{(j)} - w_{(k)}}{\xi} - \frac{1}{2} \begin{bmatrix} -\left(\theta_{y(k)} + \theta_{y(j)} \right) \cos\varphi \\ +\left(\theta_{x(k)} + \theta_{x(j)} \right) \sin\varphi \end{bmatrix} \right\} \tag{2.93b}$$

$$s_{shear(k)(j)} = \frac{w_{(j)} - w_{(k)}}{\xi} \tag{2.93c}$$

Note that the micropotentials given in Eq. (2.90) include in-plane, shear, and bending components. The in-plane micropotential can be caused by either in-plane tension or compression. The shear micropotential is caused by shear deformations. Meanwhile, the bending micropotential is caused by bending deformations. Therefore, the contribution of tensional, compressional, shear, and bending deformations are considered for the calculation of bond energy release rate for damage prediction which is given in Eq. (1.9) in Chapter 1. Hence, the energy-based damage criteria used in this Section are applicable for tensional, compressional, shear, and bending deformations for linear analysis.

It should be noted that to predict damages in shells and stiffened structures using the energy-based damage criteria given in Eq. (1.9), the critical energy release rate of material should be a value that is applicable for mixed-mode loading. However, to simplify the determination for the value of G_c in section 2.3.7, the critical energy release rate of the material is simply chosen as $G_c = G_{Ic}$.

2.3.6. Numerical implementation

For stiffened structures, the geometrical and material properties as well as family members for each material point need to be defined. Depending on the location of the material point, different procedures are used. As an example, the stiffened structure shown in Fig. 2.22(a) is considered. Fig. 2.22(b) demonstrates the model discretization for a stiffened structure with three shells S_A, S_B, S_C. In Fig. 2.22(a) lines L_1, L_2, L_3 represent the intersections between shells and point k represents the intersection of the three shells. The material points located at the intersection lines are identified such as (L_{1A}, L_{1B}), (L_{2A}, L_{2C}), (L_{3B}, L_{3C}) as shown in Fig. 2.22(b). During the discretization, material points along lines L_{1B}, L_{2C}, L_{3C} are removed, material points along lines L_{1A}, L_{2A}, L_{3B} are set as joint points and the material point k is set as the intersection point of three shells as shown in Fig. 2.22(b).

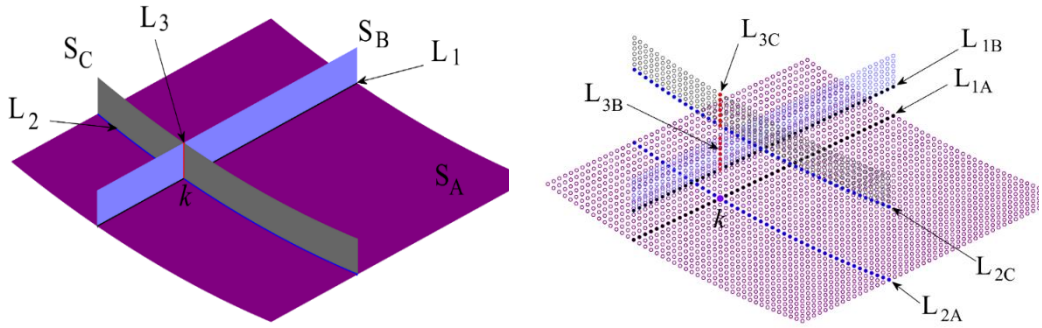

(a) (b)

Fig. 2.22. Stiffened structure (a) geometry, (b) model discretization

Fig. 2.23 represents the family members for material points at two different locations. As shown in Fig. 2.23(a), material point 8 is located on the shell S_B, therefore the family members of this material point belong to the shell S_B. On the other hand, material point 4 is located at the intersection of shell S_A and S_B as shown in Fig. 2.23(b), therefore its family members belong to both shells. As a demonstration, Fig. 2.24 shows the number of family members for a stiffened structure.

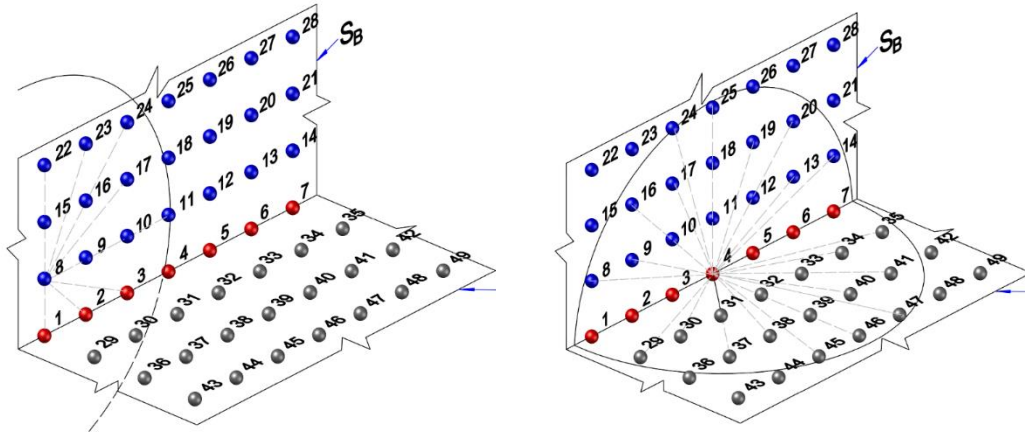

(a) (b)

Fig. 2.23. Identification of family members for a material point located (a) on the shell (b) at the intersection

For a stiffened structure, each shell may have different material and geometrical properties. The material and geometrical properties of each interaction are determined based on the family member of each material point. As shown in Fig. 2.23(a), since material point 8 and its family members are located on the shell S_B, the material and geometrical properties of material point 8 are obtained from the shell S_B. On the other hand, as shown in Fig. 2.23(b) material point 4 and its family members are located at both shells S_A and S_B. Therefore, material and geometrical properties are determined based on the interaction between material points. For the interaction between material points 4 and 10, since the neighbour material point 10 belongs to the shell S_B, the material and geometrical properties of the interaction are included for the shell S_B. Similarly, for the interaction between material points 4 and 31, since the neighbour material point 31 belongs to the shell S_A, the material and geometrical properties of the interaction are included for the shell S_A. Material points 4 and 5 are located at the interface. Therefore, the interaction forces between these points are calculated by summing two interaction forces. Each interaction force in the shell's local coordinate system is calculated by using Eq. (2.78) and transformed into the global coordinates by using Eq. (2.85) or Eq. (2.86a).

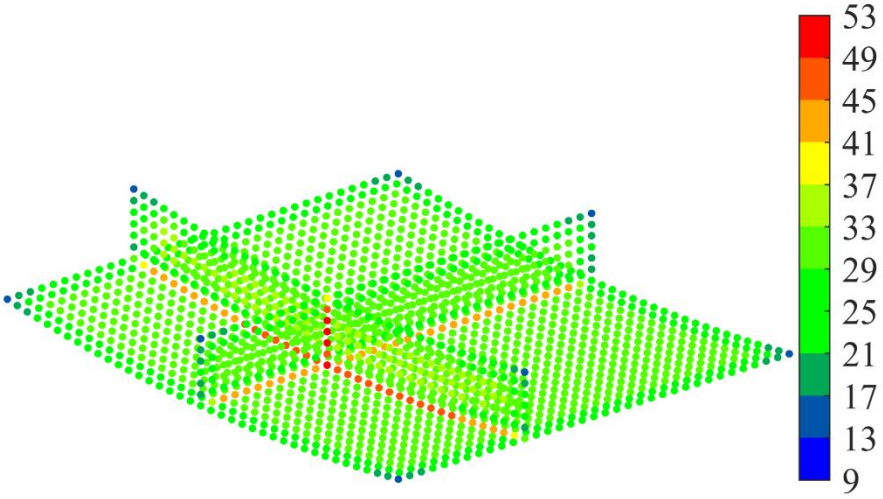

Fig. 2.24. Number of family members of material points on a stiffened structure

2.3.7. Numerical results

For verification purposes, the proposed PD model is compared to FEA solutions. For static or quasi-static problems, the adaptive dynamic relaxation method, which is described in Appendix A3, is used in PD. The FEA solutions are conducted by using ANSYS commercial software with the SHELL181 element. In PD theory, the boundary conditions can be implemented through fictitious layers as described by Macek and Silling [40]. Based on numerical experiments, to ensure that the imposed boundary condition is accurately reflected in the real domain, this layer needs to be at least at the size of the horizon, δ.

2.3.7.1. A flat shell subjected to constant static loading

To verify the developed PD model for flat shells, a square flat shell with dimensions $L = W = 1$ m, and thickness $h = 0.1$ m is investigated as shown in Fig. 2.25(a). The flat shell is fixed on the left end and subjected to uniformly distributed loading along the right edge in both x_1 and negative x_3 directions as $p_1 = 1 \times 10^7$ N/m, $p_3 = -1 \times 10^7$ N/m, respectively. The material has Young's modulus of $E = 2 \times 10^{11}$ N/m^2 and Poisson's ratio of $\nu = 0.45$.

In the PD model, the shell is discretized with uniform 150 integration points along each direction. As shown in Fig. 2.25(b), to apply boundary conditions along the left edge, fictitious layers of material points, shown in black, are added on the left edge. All DOFs of these fictitious points are set equal to zero. In the FEA model, the same mesh size is also used.

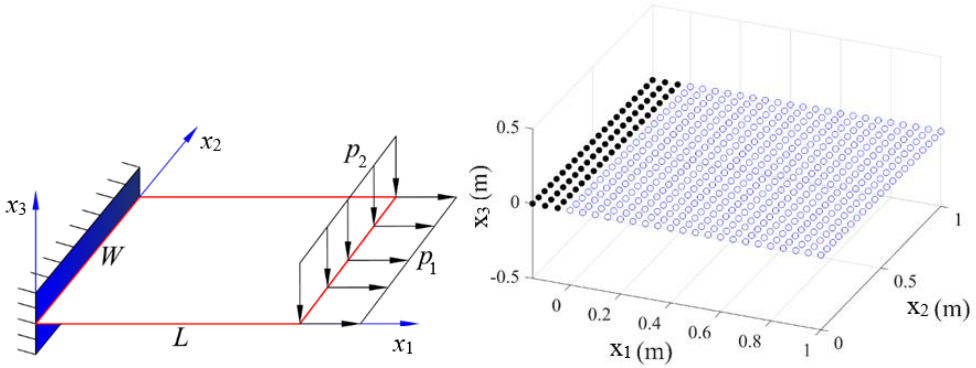

(a) (b)

Fig. 2.25. Flat shell subjected to static constant loading (a) geometry, (b) model discretization

As given in Eq. (3.29-30), the PD constant for torsional deformations depends on k_0 which is added for convergence in PD solutions. Therefore, the effect of k_0 to the PD solution is investigated as shown in Fig. 2.26 with the horizon size of $\delta = 3.015\Delta x$. As can be seen from the figure, the PD results for displacements and rotations of the flat shell is stable for various values of k_0. After checking the stability of the PD solutions, $k_0 = 1$ is chosen.

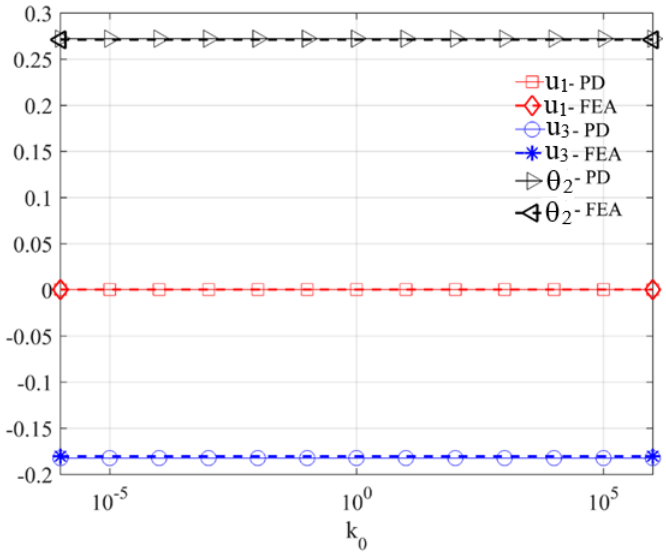

Fig. 2.26. Effect of the torsional coefficient k_0 on PD results at $(x_1 = L, x_2 = W/2)$, horizon size $\delta = 3.015\Delta x$.

The effect of horizon size on PD results is investigated by comparing with FEA solutions. Fig. 2.27 shows the variation of relative error between PD and ANSYS predictions. The relative error for each DOF is calculated as

$$\%\,\text{error}(q) = \frac{\left|q^{FEA} - q^{PD}\right|}{\left|q^{FEA}\right|} \times 100 \tag{2.94}$$

where q^{FEA} and q^{PD} represent the FEA and PD solution for a degree of freedom, q, respectively.

As can be seen from Fig. 2.27, the relative error between PD and ANSYS predictions reduces as the horizon size increases. When the horizon size is bigger than $\delta = 3\Delta x$, the relative error for all degrees of freedom is less than 3%. Therefore, to reduce the computational time $\delta = 3.015\Delta x$ is chosen. Note that, the extra value $0.015\Delta x$ is added into horizon size to ensure that all material points within a distance of $3\Delta x$ is included.

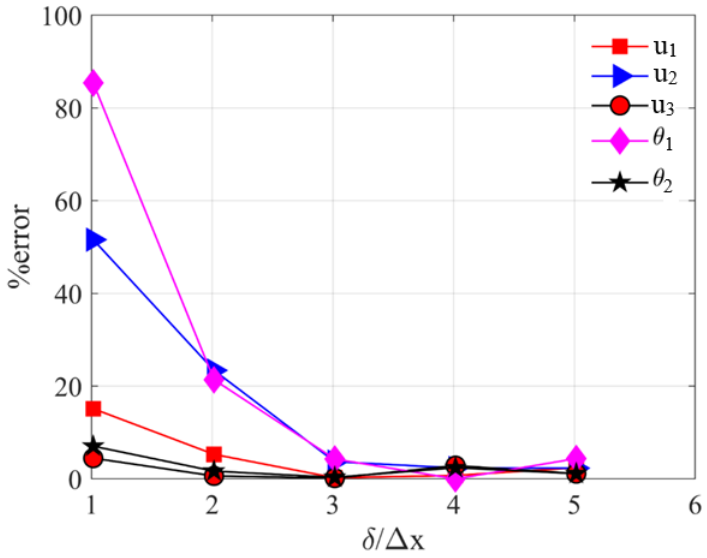

Fig. 2.27. Effect of horizon size on PD prediction results at $(x_2 = L, x_2 = 3W/4)$

Fig. 2.28-Fig. 2.33 present the comparison of PD and ANSYS predictions for 6 DOFs with $\delta = 3.015\Delta x$ and $k_0 = 1$. As can be seen from the figures, PD predictions agree very well with FEA results. Moreover, the good agreement of drilling rotation, θ_3 shows that the additional PD equation of motion for drilling rotation is acceptable.

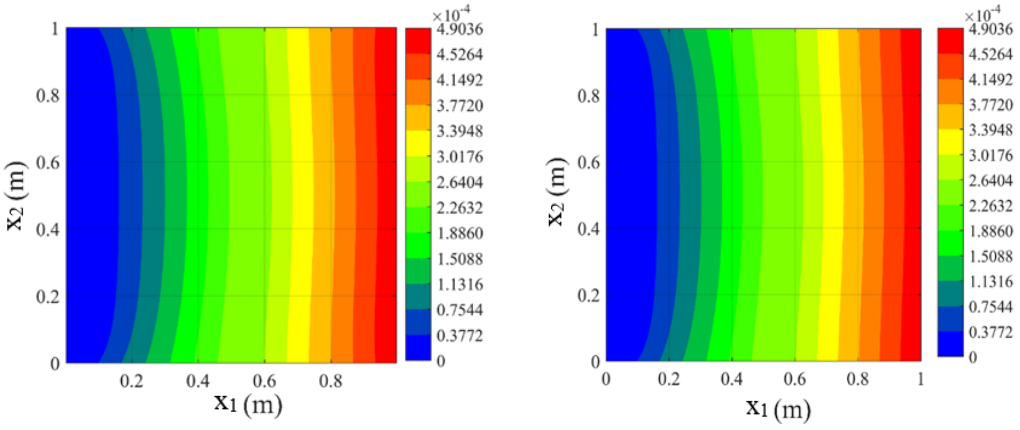

(a) (b)

Fig. 2.28. Variation of displacement $u_1(m)$ of shell with $L/h = 10$ (a) PD, (b) FEA results

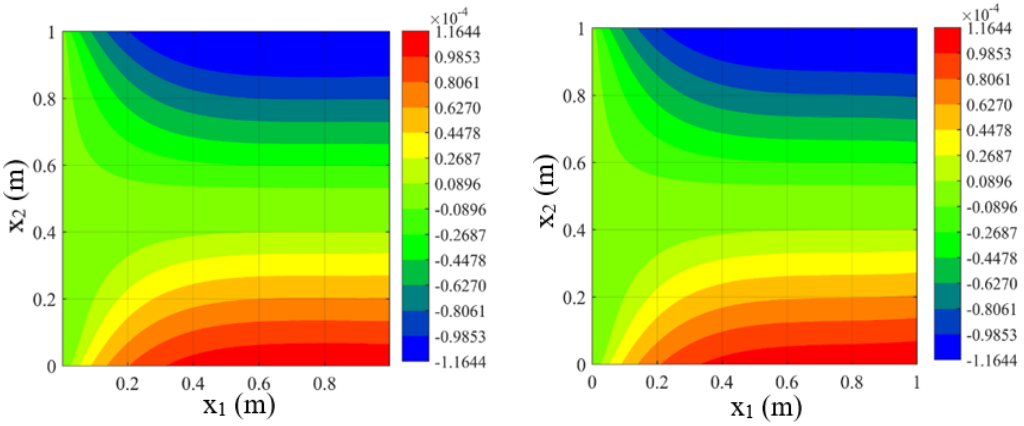

(a) (b)

Fig. 2.29. Variation of displacement $u_2\ (m)$ of shell with $L/h = 10$ (a) PD, (b) FEA results

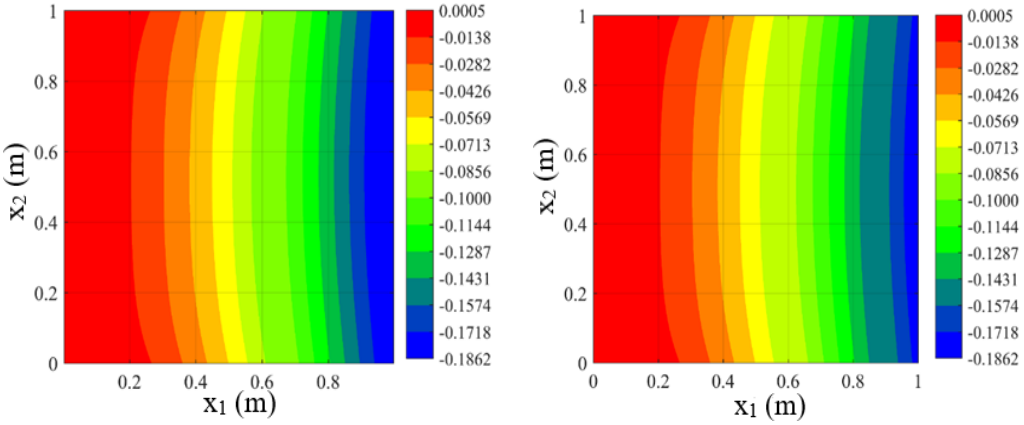

(a) (b)

Fig. 2.30. Variation of displacement $u_3\ (m)$ of shell with $L/h = 10$ (a) PD, (b) FEA results

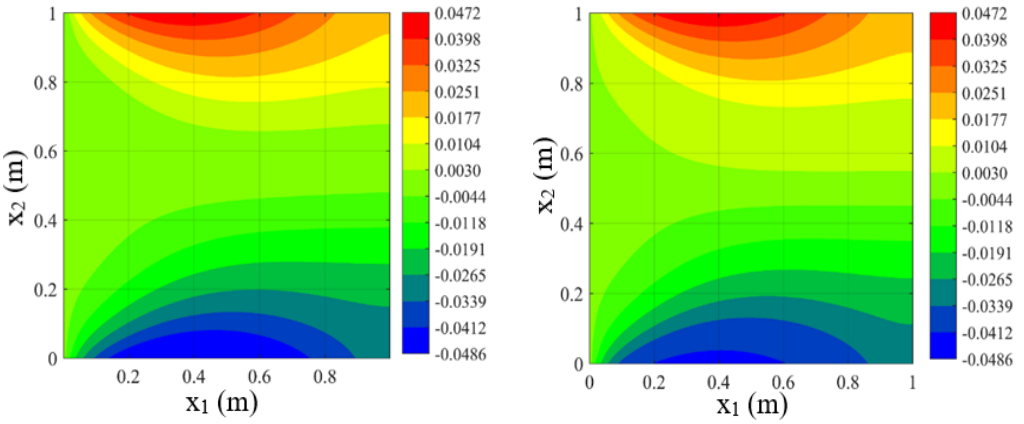

(a) (b)

Fig. 2.31. Variation of rotation θ_1 (rad) of shell with $L/h = 10$ (a) PD, (b) FEA results

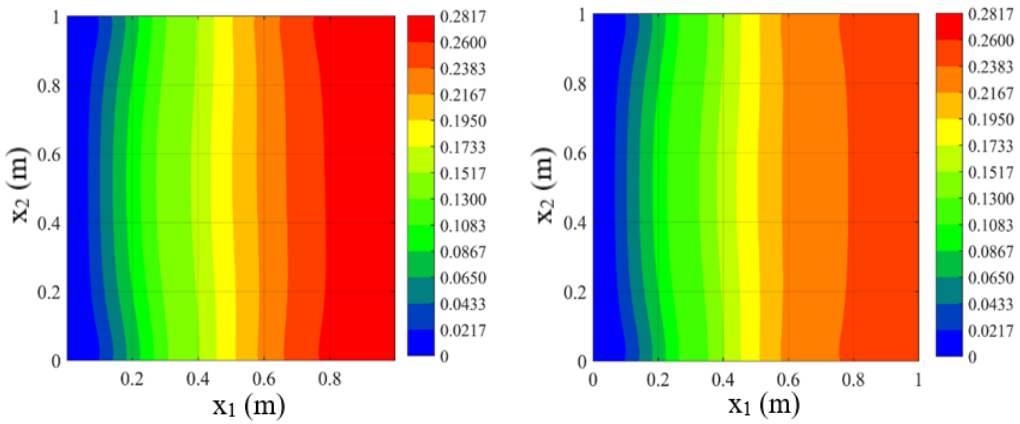

(a) (b)

Fig. 2.32. Variation of rotation θ_2(rad) of shell with $L/h = 10$ (a) PD, (b) FEA results

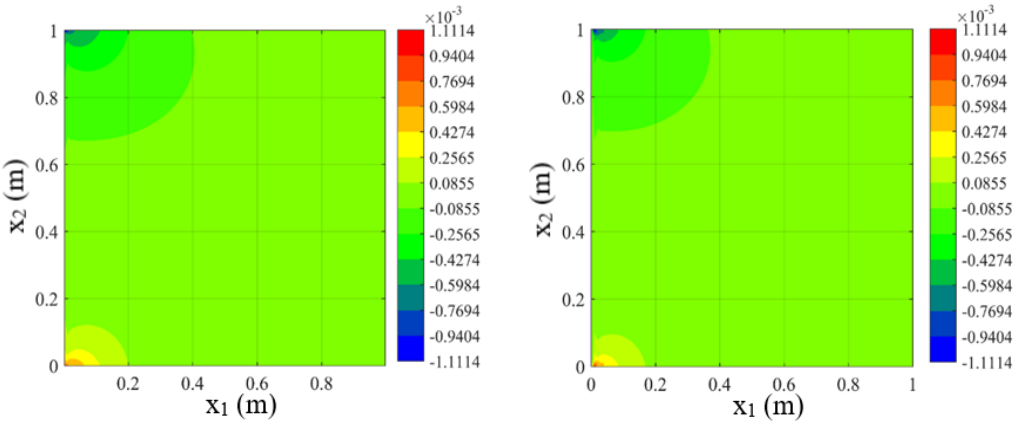

(a) (b)

Fig. 2.33. Variation of rotation θ_3(rad) of shell with $L/h = 10$ (a) PD, (b) FEA results

To have a better comparison, the PD and FEA solution results along $x_2 = W/2$ and $x_1 = L/2$ are compared as shown in Fig. 2.34 and Fig. 2.35, respectively. As can be seen from the figures, PD and FEA solution results agree very well for both in-plane and out-of-plane deformations. Therefore, the developed PD model for thick flat shells is verified.

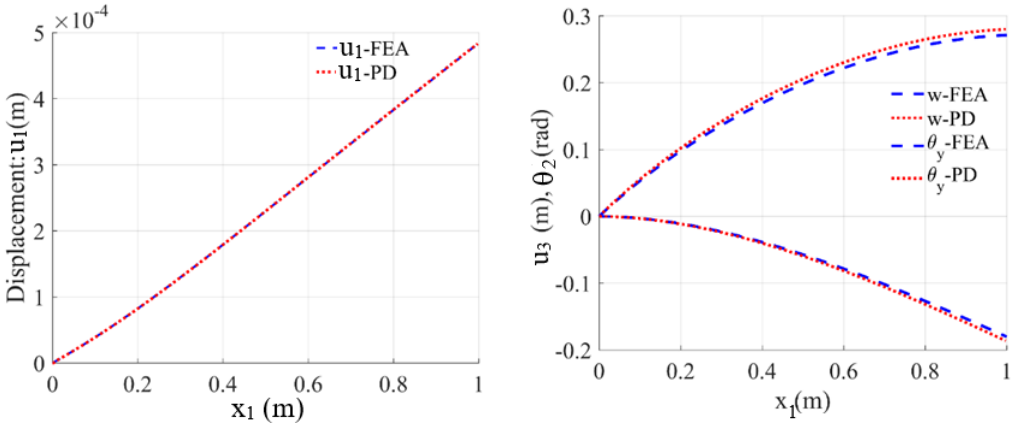

(a) (b)

Fig. 2.34. Variation of (a): $u_1\ (m)$, (b): $u_3\ (m)$ and θ_2 (rad) along $x_2 = W/2$

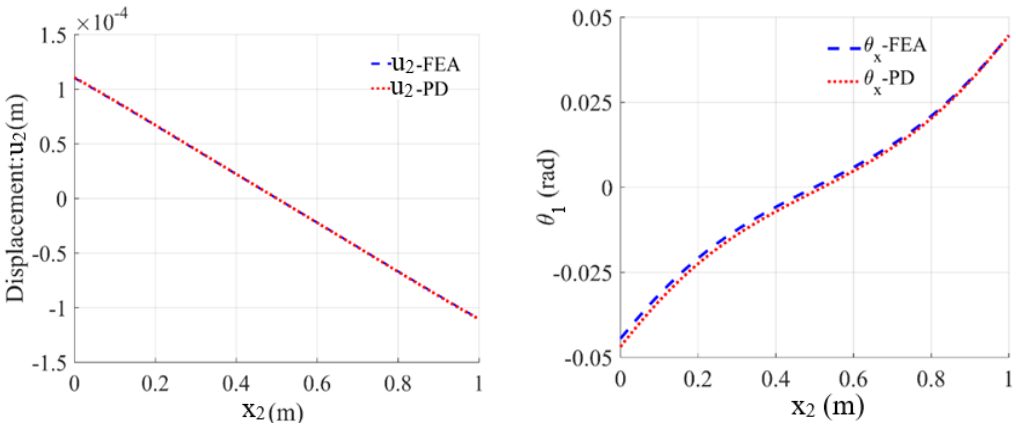

(a) (b)

Fig. 2.35. Variation of DOFs $u_2\ (m)$, θ_1 (rad) along $x_2 = L/2$

2.3.7.2. A curved shell subjected to constant static loading

To verify the developed PD model for curved shells, a shell with a radius of R is investigated as shown in Fig. 2.36(a). The shell is clamped at $\beta = 75°$ and it is subjected to a distributed load as $p_3 = -1 \times 10^7$ N/m at $\beta = 90°$. The shell has a thickness of $h = 0.1$ m and a length of $L = 0.7907$ m. It is made of steel with Young's modulus $E = 2 \times 10^{11}$ N/m^2 and Poisson's ratio $\nu = 0.27$.

The shell is discretized with uniform 150 integration points in each direction. To apply boundary conditions, fictitious layers of material points are added as shown in Fig. 2.36(b). All DOFs of these fictitious points are set equal to zero. In the FEA model, the same mesh size is used.

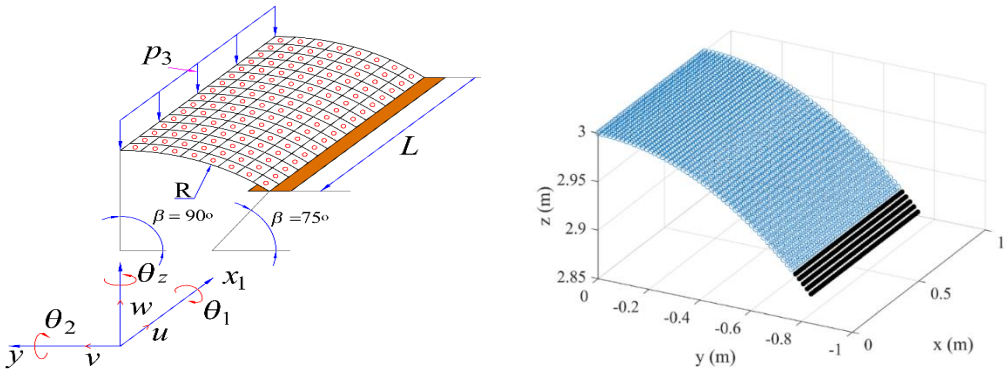

(a) (b)

Fig. 2.36. A curved shell subjected to static loading (a) geometry, (b) model discretization

Similar to the previous example, the effects of k_0 on PD predictions with horizon size $\delta = 3.015\Delta x$ are investigated as shown in Fig. 2.37. To check the effect of the curvature, the curved shell is studied with two different values of radius, $R = 1$m and $R = 3$m. As can be seen from the figure, the PD predictions for all degrees of freedom of the two curved shells have good agreement with the FEA solution when $k_0 \geq 1$. Therefore, it can be concluded that the value of k_0 given in Eq. (2.76) can be chosen as $k_0 \geq 1$ for both flat and curved shells. Therefore, in the following sections $k_0 = 1$ is chosen.

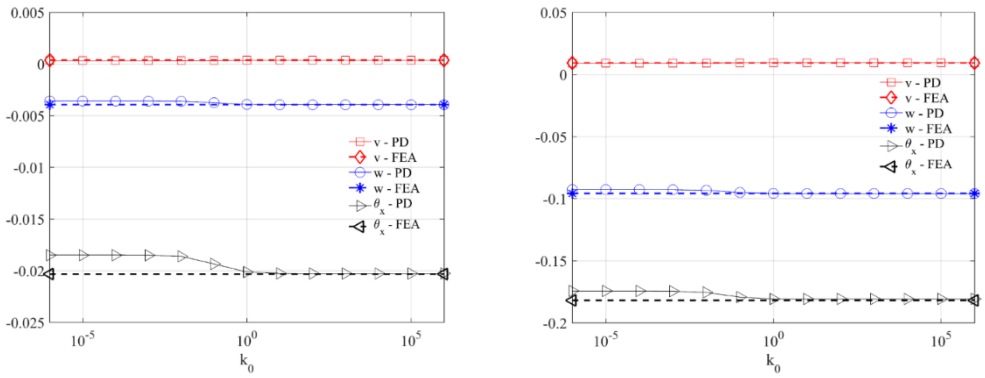

(a) (b)

Fig. 2.37. Effect of the torsional coefficient k_0 to solutions of curved shell radius of curvature (a) $R = 1m$ (b) $R = 3m$ at $(x_1 = L/2, x_2 = 0, x_3 = R)$

The effects of horizon size on PD results for curved shells are also investigated. Fig. 2.38 shows the relative errors between PD and FEA results for nonzero DOFs of the material point located at $(x_1 = L/2, x_2 = 0, x_3 = 3)$ on the curved shell with $R = 3m$. As can be seen from the figure, the PD results converge to the FEA solution when $\delta = 3.015\Delta x$ in which all the relative errors are smaller than 1.5%. Therefore, $\delta = 3.015\Delta x$ is chosen for the PD representation of curved shells.

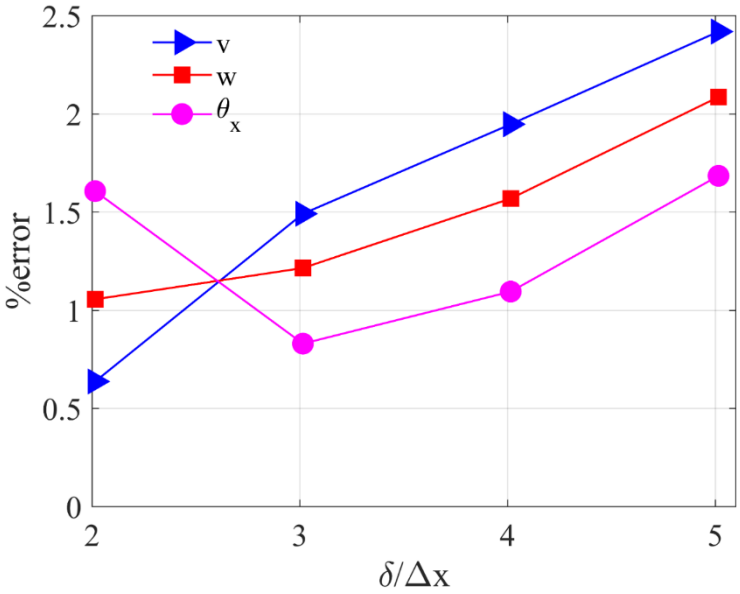

Fig. 2.38. Effect of horizon size on PD results at $(x_1 = L/2, x_2 = 0, x_3 = 3)$

After investigating the stability of the PD prediction, the PD predictions with $k_0 = 1$ and $\delta = 3.015\Delta x$ for the curved shell with radius $R = 3m$ are compared with the FEA solution. Fig. 2.39-Fig. 2.44 show the variations of 6 DOFs of the shell in the deformed configuration. The results obtained from PD analysis agree very well with those in FEA. Moreover, as shown in Fig. 2.45, the deformed shape along the line of $x_1 = L/2$ captured in PD and FEA solutions are on top of each other which shows the accuracy of the developed PD model for curved shells.

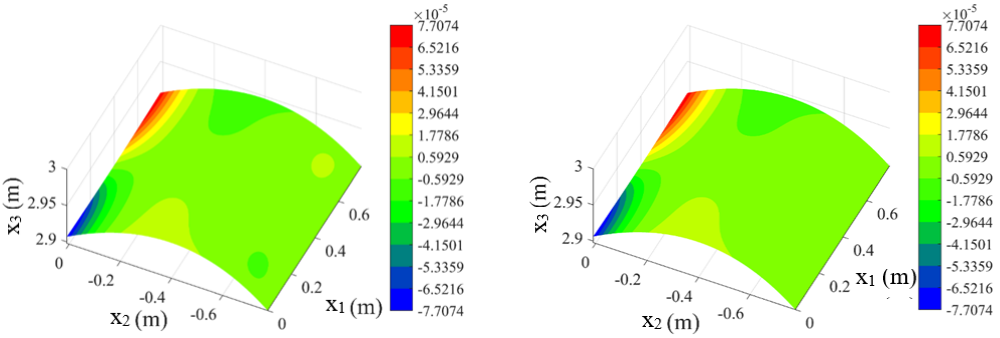

(a) (b)

Fig. 2.39. Variation of displacement $u_1(m)$ in the deformed configuration (a) PD, (b) FEA

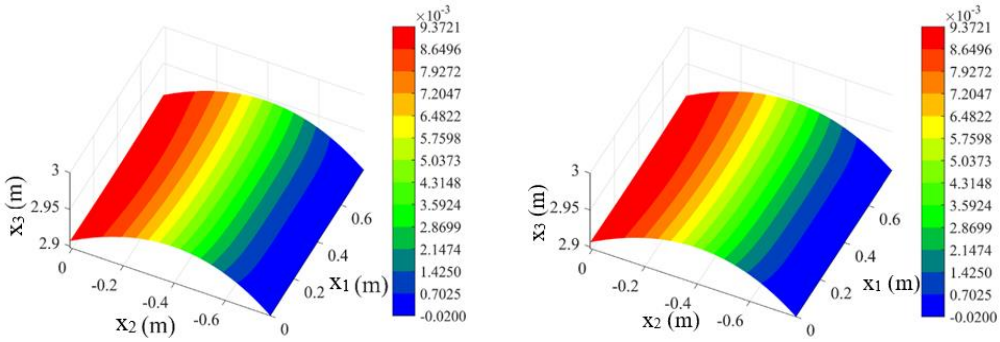

(a) (b)

Fig. 2.40. Variation of displacement $u_2\ (m)$ in the deformed configuration (a) PD, (b) FEA

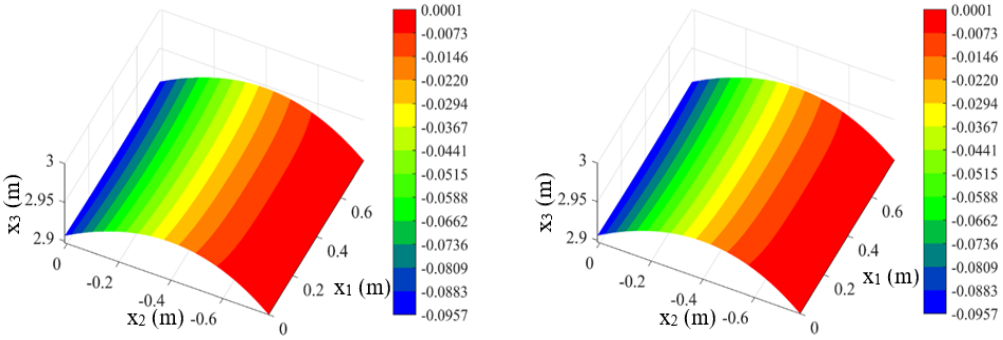

(a) (b)

Fig. 2.41. Variation of displacement $u_3\ (m)$ in the deformed configuration (a) PD, (b) FEA

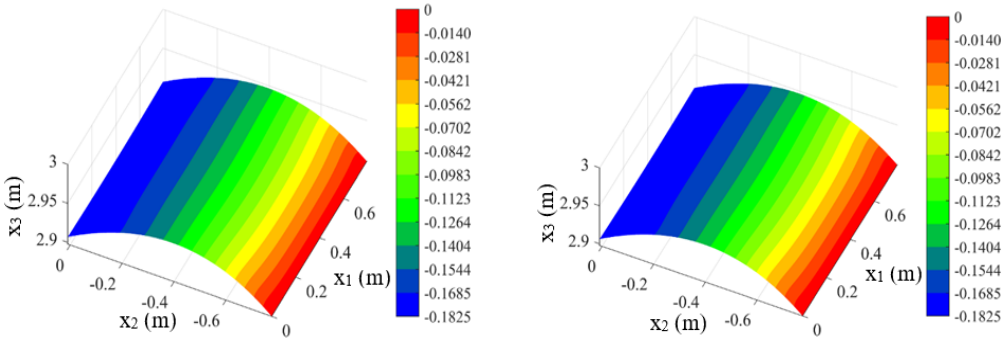

(a) (b)

Fig. 2.42. Variation of rotation θ_1(rad) in the deformed configuration (a) PD, (b) FEA

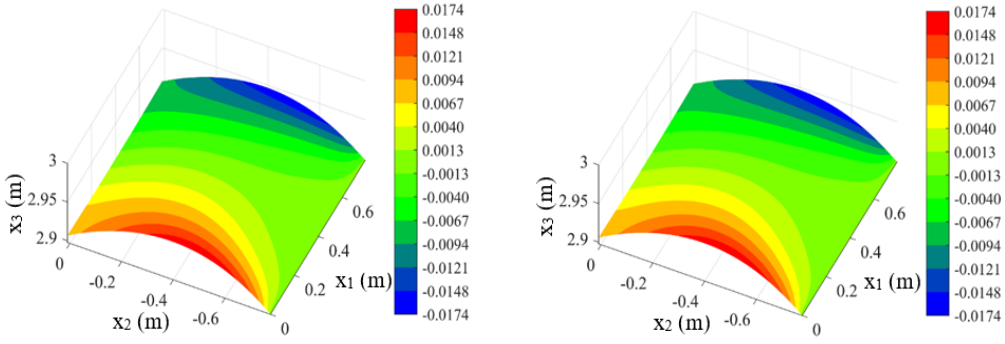

(a) (b)

Fig. 2.43. Variation of rotation θ_2(rad) in the deformed configuration (a) PD, (b) FEA

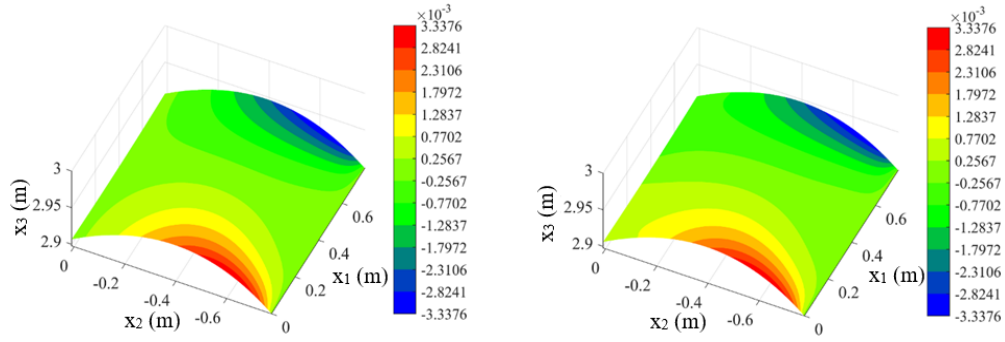

(a) (b)

Fig. 2.44. Variation of rotation θ_3(rad) in the deformed configuration (a) PD, (b) FEA

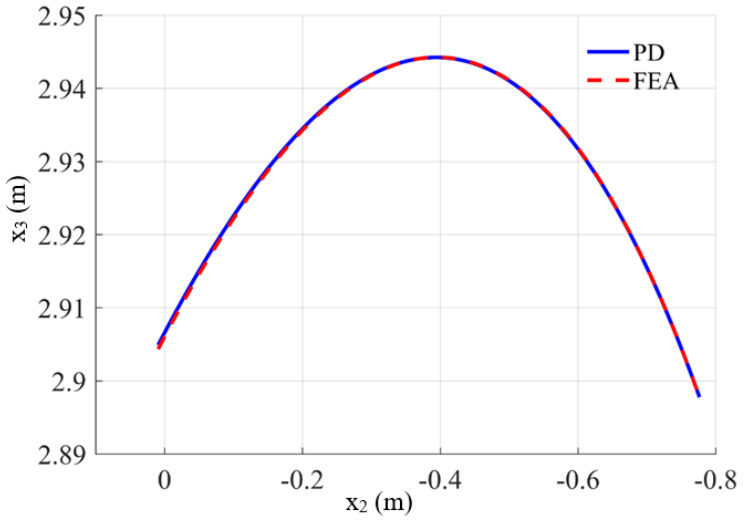

Fig. 2.45. Deformed configuration of the curved shell along $x_1 = L/2$

2.3.7.3. A stiffened structure subjected to constant static pressure

After verifying the developed PD model for flat and curved shells, this example is to verify the developed PD model for stiffened structures. As shown in Fig. 2.46(a), a stiffened structure constructed by a cylindrical shell and four stringers is investigated. The cylindrical shell has a radius of $R = 2$ m and total length of $L = L_1 + L_2 + L_3 = 1.0472$ m with $L_1 = L_3 = L/4$ m. The side view of the stiffened structure is shown in Fig. 2.46(b). The height of each stringer is $H = 0.1057$ m. All the shells have a thickness of $h = 0.1$ m and they are made of steel with Young's modulus $E = 2 \times 10^{11}$ N/m^2 and Poisson's ratio $\nu = 0.27$. The cylindrical shell is subjected to the constant pressure of $p_0 = 2 \times 10^9$ N/m^2. All four edges of the curved shell and two ends of each stringer, shown in black in Fig. 2.46(a), are clamped.

In the peridynamic model, the curved shell is discretized with 150×150 material points and each stringer is discretized with 150×20 material points. The horizon size is $\delta = 3.015\Delta x$. To apply boundary conditions, four fictitious layers of material points, shown in black, are added as shown in Fig. 2.47. All 6 DOFs of these fictitious material points are set equal to zero. In the FEA model, the same mesh size is used.

Fig. 2.48-Fig. 2.53 show the variation of 6 DOFs of the shell structure. As shown in Fig. 2.50, due to the applied pressure, the middle region of the curved shell has the highest deformation in the vertical direction. As a result, due to the connection between the curved shell and the stringers, all stringers are twisted towards the centre of the cylindrical shell as shown in Fig. 2.48 and Fig. 2.49. As can be seen from the figures, the PD results agree very well with the FEA results which shows the accuracy of the developed PD model for stiffened structures.

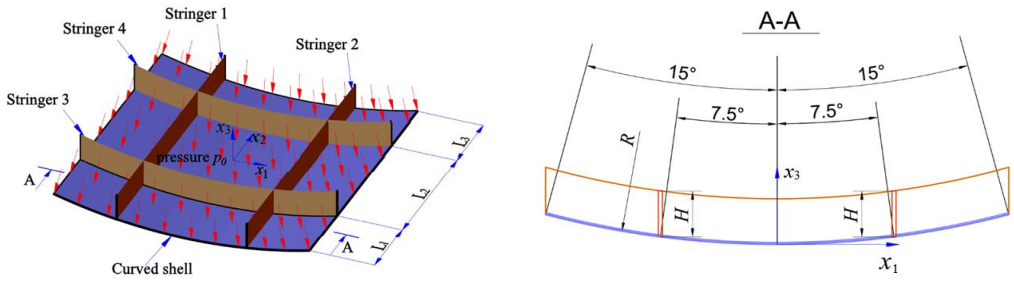

(a) (b)

Fig. 2.46. Stiffened structure subjected to constant pressure (a) 3D view, (b) side view

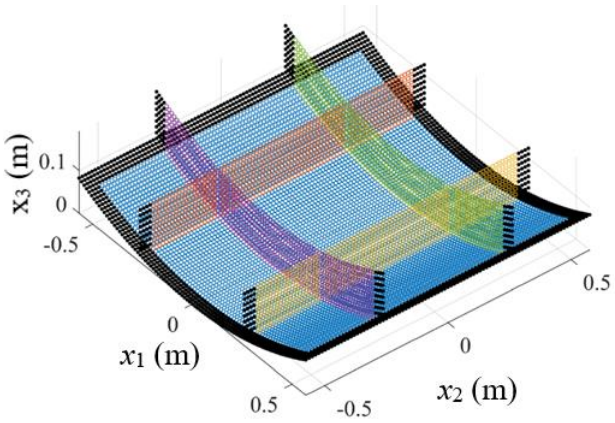

Fig. 2.47. Model discretization for stiffened structure

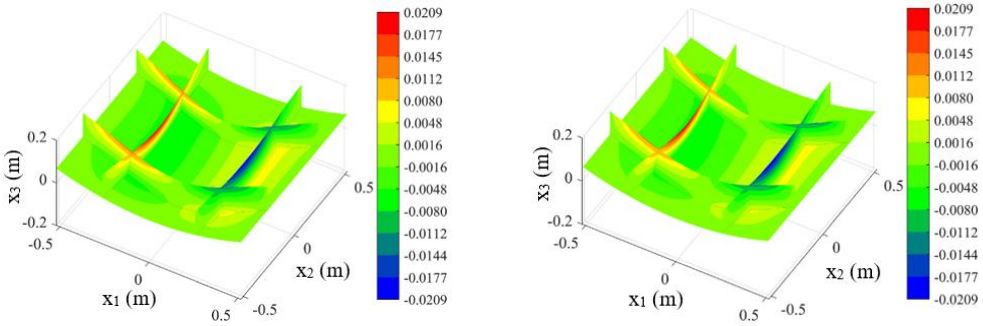

(a) (b)

Fig. 2.48. Variation of displacement u_1 (rad) (a) PD, (b) FEA results

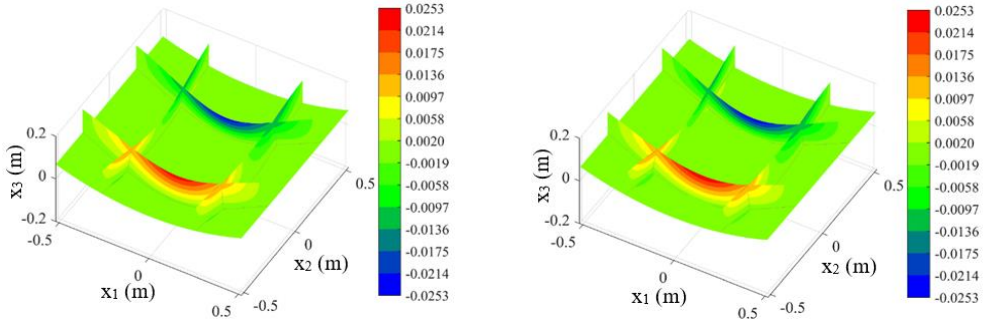

(a) (b)

Fig. 2.49. Variation of displacement u_2 (rad) (a) PD, (b) FEA results

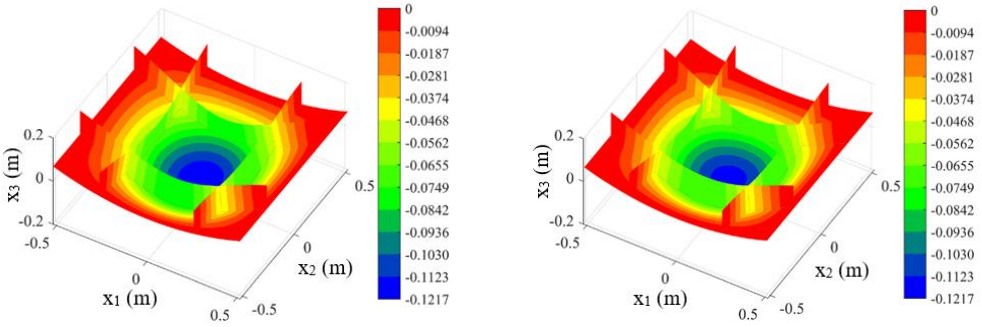

(a) (b)

Fig. 2.50. Variation of displacement u_3 (rad) (a) PD, (b) FEA results

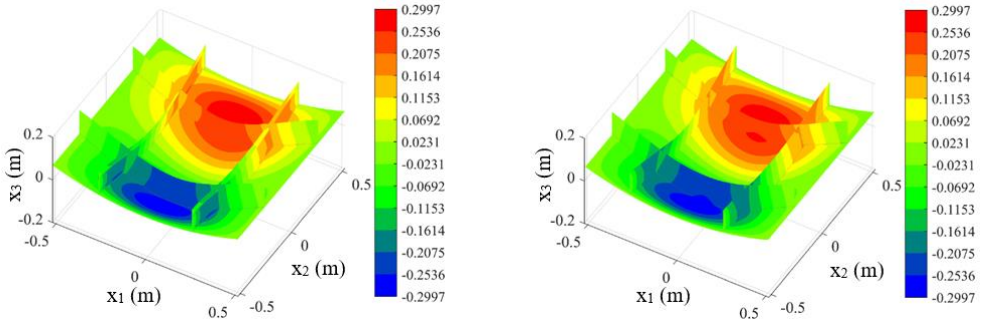

(a) (b)

Fig. 2.51. Variation of rotation θ_1 (rad) (a) PD, (b) FEA results

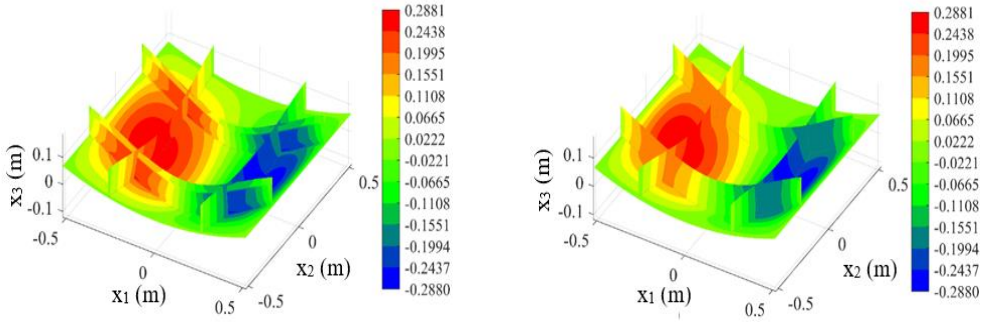

(a) (b)

Fig. 2.52. Variation of rotation θ_2 (rad) (a) PD, (b) FEA results

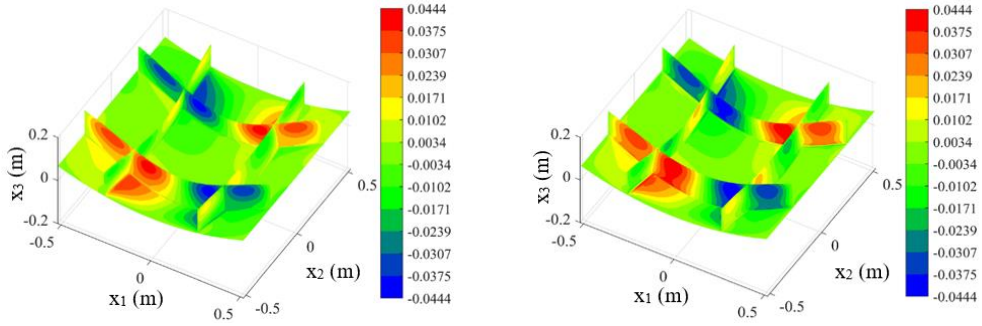

(a) (b)

Fig. 2.53. Variation of rotation θ_3 (rad) (a) PD, (b) FEA results

2.3.7.4. A glass cup subjected to a constant temperature change

To verify the developed PD model for the thermomechanical behaviour of shell structures, a glass cup subjected to uniform temperature change is considered as shown in Fig. 2.54. The shape of the cup is defined as

$$x = b\cos\theta\cos\phi \tag{2.95a}$$

$$y = b\cos\theta\sin\phi \tag{2.95b}$$

$$z = \left(a + e\sin\theta\right)\sin\theta \tag{2.95c}$$

where $a = 0.1$ m, $b = 0.06$ m, $e = 0.04$ m, $-\pi/2 \leq \theta \leq \pi/12$, $-\pi \leq \phi \leq \pi$

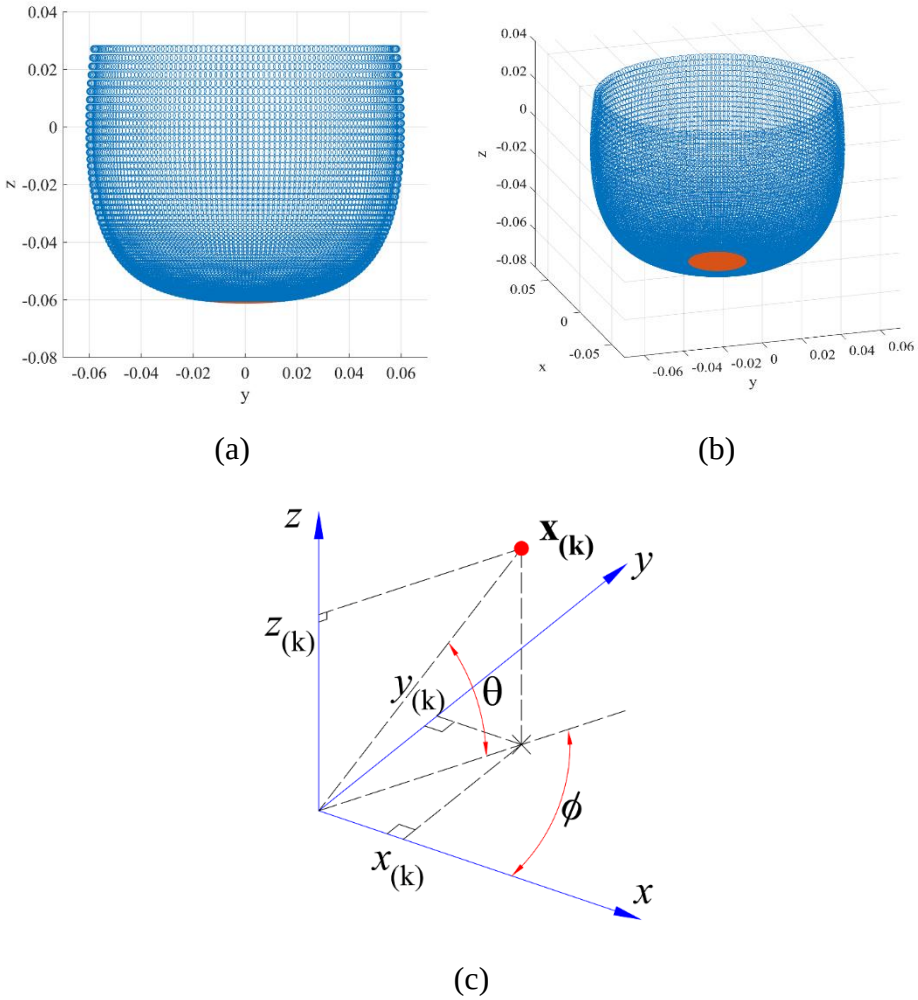

Fig. 2.54. Glass cup subjected to a uniform temperature change (a) side view, (b) 3D view, (c) coordinate system

The cup is made of glass with Young's modulus $E = 68 \times 10^9$ N/m^2, Poisson's ratio $\nu = 0.17$, mass density $\rho = 2710$ kg/m^3, and linear thermal expansion coefficient $\alpha = 8.5 \times 10^{-6}$ m/mK [34]. The thickness of the cup is $h = 1 \times 10^{-3}$ m. The cup is subjected to $\Delta T = 80$ °C uniform temperature change and it is fixed from the bottom part as shown with the red region in Fig. 2.54(b). The

PD model is discretized by setting incremental angles as $d\theta = \pi/120$ and $d\phi = \pi/90$.

Since the material is isotropic and the cup is subjected to uniform temperature change, the rotation θ_3 is almost zero. Fig. 2.55-Fig. 2.60 show the variations of displacements and rotations of the cup. Fig. 39 represents the deformed shape of the cup along the centreline at $x_1 = 0$. Since the cup is fixed from the bottom, the bending deformations are more visible in the bottom part of the cup as shown in Fig. 39. As can be seen from the results, the PD and FEA solutions have a very good agreement. Therefore, it can be concluded that the thermomechanical behaviour of shell structure in the developed PD model is verified.

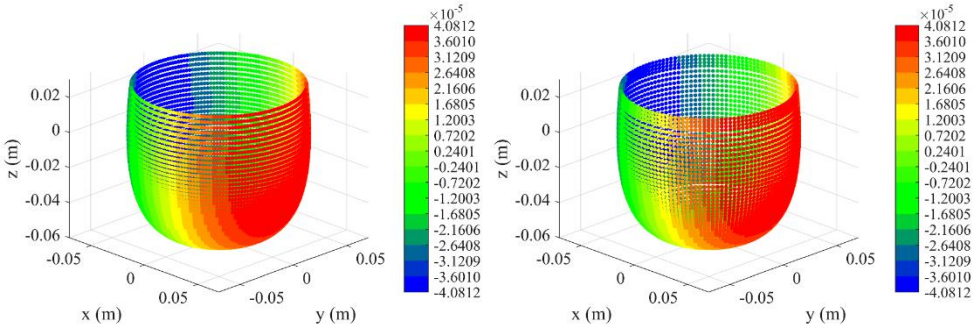

(a) (b)

Fig. 2.55. Variation of displacement $u_1(m)$ (a) PD, (b) FEA results

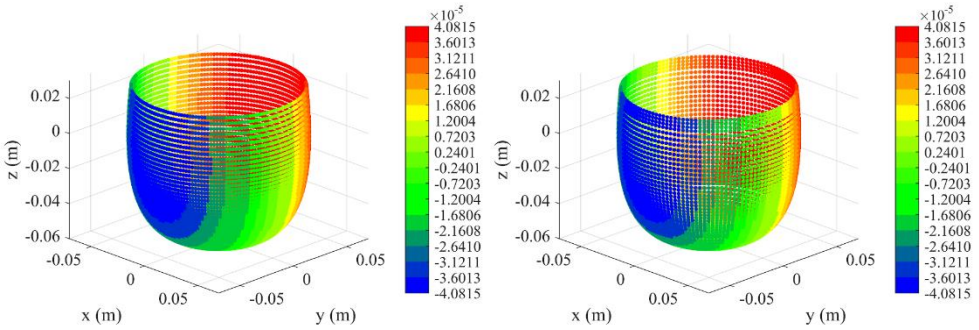

(a) (b)

Fig. 2.56. Variation of displacement $u_2(m)$ (a) PD, (b) FEA results

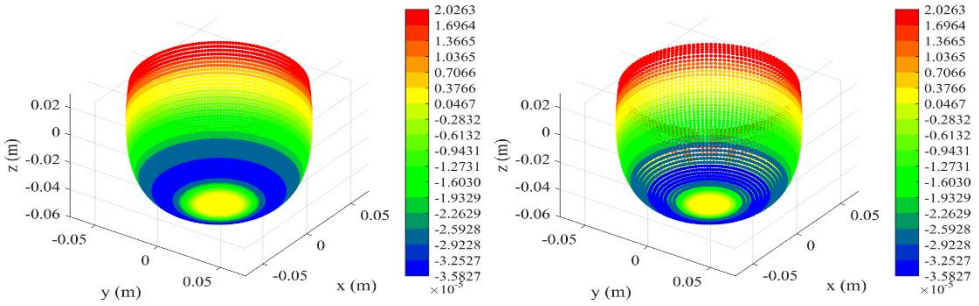

(a) (b)

Fig. 2.57. Variation of displacement $u_3(m)$ in (a) PD, (b) FEA results

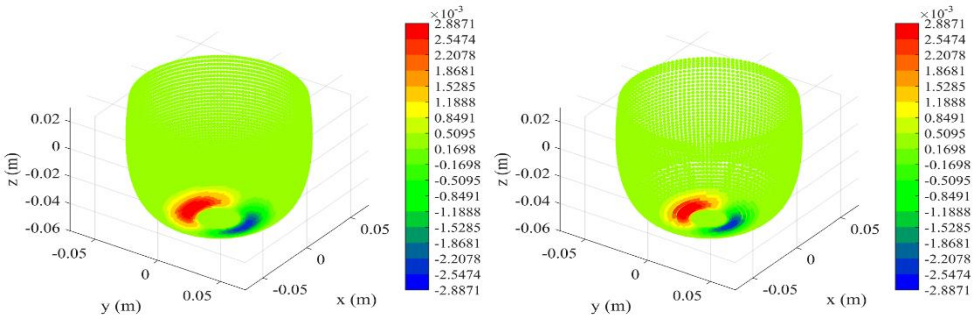

(a) (b)

Fig. 2.58. Variation of rotation $\theta_1(\text{rad})$ in (a) PD, (b) FEA results

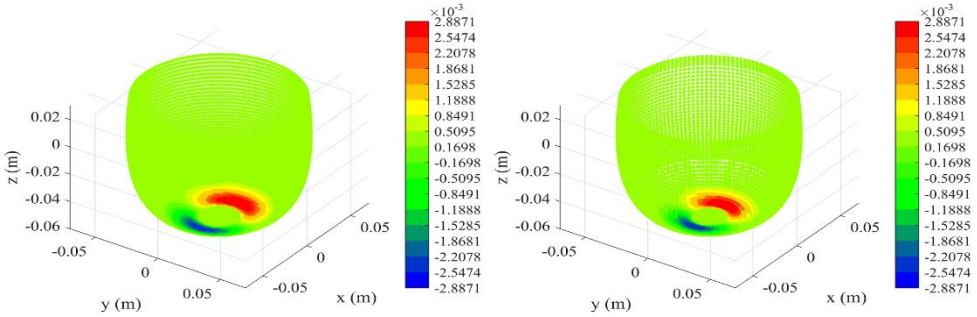

(a) (b)

Fig. 2.59. Variation of rotation $\theta_2(\text{rad})$ in (a) PD, (b) FEA results

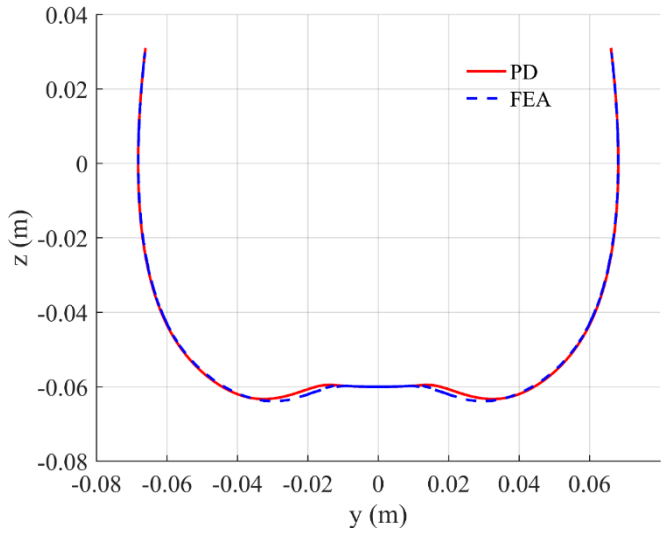

Fig. 2.60. Deformed configuration of the centreline at $x_1 = 0$ (displacements are magnified by 200 times)

2.3.7.5. Damage prediction for double torsion problem

After verifying the developed PD model for both mechanical and thermomechanical behaviour of shell structures, the damage process in a flat shell in a double torsion problem is investigated. As shown in Fig. 2.61, the dimensions of the flat shell are $L = 180$ mm, $W = 60$ mm, $W_n = 23.35$ mm, $h = 5$ mm [85]. The shell has an initial notch at $x_1 = W/2$ with initial notch length, $a = 3.6$ mm. Along the line $x_1 = W/2$, an initial channel is created with $b = 2.4$ mm and $h_n =$

2.48 mm [85]. The material is marble with Young's modulus $E = 26.68$ GPa, Poisson's ratio $\nu = 0.24$ [85], the fracture toughness $K_{Ic} = 0.644$ MPa$\sqrt{\text{m}}$ [86]. For simplification, the critical energy release rate of the material is calculated as $G_c = G_{\text{Ic}} = K_{Ic}^2/E = 15.545$ J/m^2.

The shell is placed on 4 steel balls located at four corners with distances $\Delta = 1.2$ mm from corners. The shell is applied quasi-static loading on two points located at $x_1 = W_n$ and $x = W - W_n$, respectively. The history of the total applied force, F, includes two stages as shown in Fig. 2.62 [85]. In the first stage, the load is increased to the peak value of $F = 158$ N at $t = 17.079$ s. Next, in the second stage, the load is slowly decreased to $F = 120$ N as shown in Fig. 2.62.

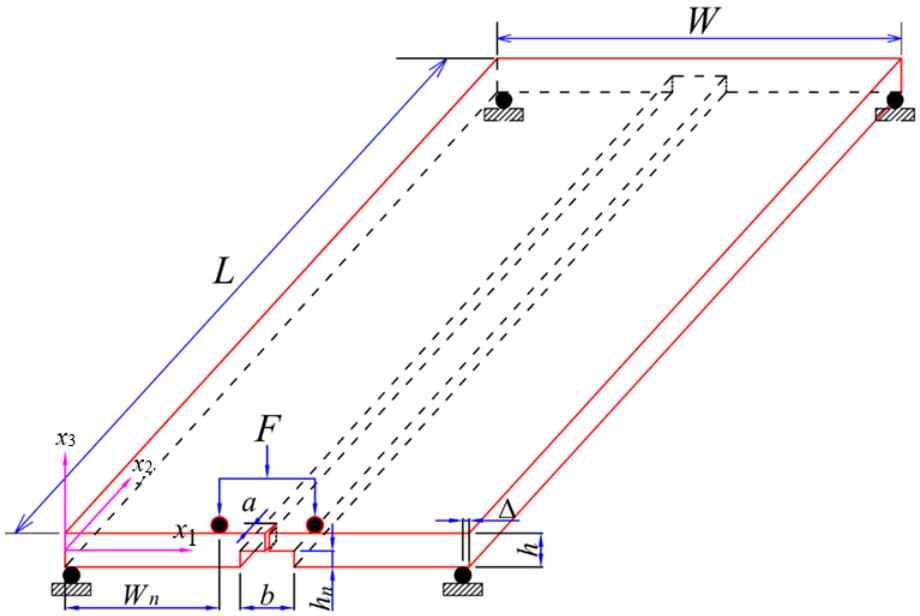

Fig. 2.61. Double torsion problem

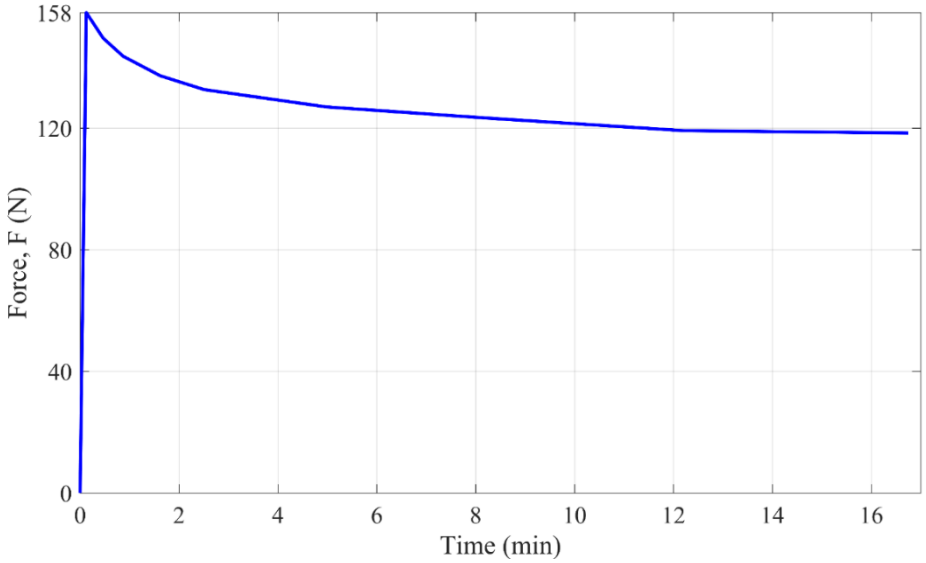

Fig. 2.62. Load–time curve [85]

In PD simulations, the model is discretized into 50×150 material points (50 layers of material points along $x_1$direction and 150 layers along x_2 direction). To represent the initial trough, the thickness of material points located along the trough is defined as $h - h_n$, meanwhile, other material points have a constant thickness h. To apply loading conditions, two material points located at the locations of loading are defined. During the simulation, these two material points are equally applied force per unit area $\bar{b}_3 = F/2(\Delta x^2)$ in which the value of F as a function of time is given in Fig. 2.62. The adaptive dynamic relaxation methodology [76, 77] is used in the PD solution for this quasi-static problem (Appendix A3). The problem is simulated in 40000 load steps, in which 15000 load steps are used for the first loading stage, and 25000 load steps are used for the second loading stage. Based on this information, the loading history in real-time given in Fig. 2.62 is converted to loading history for a quasi-static solution.

Fig. 2.63 shows the damage evolution on the flat shell predicted by using the developed PD model. The damage coefficient is presented in a range of $0 \leq \phi \leq 0.37$. Material points that have $\phi \geq 0.37$ are considered as completely damaged. As shown in Fig. 2.63(a), after $t = 17.079$ s when the load reaches the peak value, the structure is primarily damaged along the initial trough. The damage coefficients of material points along the trough are smaller than 0.1 which can be understood that the crack is not visibly propagated. At $t = 22.794$ s, the crack starts propagating and the structure is more damaged along the channel as shown in Fig. 2.63(b). As shown in Figs. 40(c, d, e), the crack propagates along the channel up to the locations at, $x_2 = 50$ mm, $x_2 = 85$ mm and $x_2 = 121$ mm when $t = 88.425$ s, $t = 247.989$ s and $t = 567.116$ s, respectively. Fig. 2.63(f) shows the completely damaged experimental specimens in [85]. As can be seen from the figures, the crack paths captured by PD simulation and experiment [85] agree very well.

Fig. 2.64 shows the variation of crack length and crack growth velocity captured by PD simulation and experiments in [85]. As can be seen from the figure, both the crack length and crack growth velocity captured by PD simulation agree with the experiment which shows the capacity of the developed PD model.

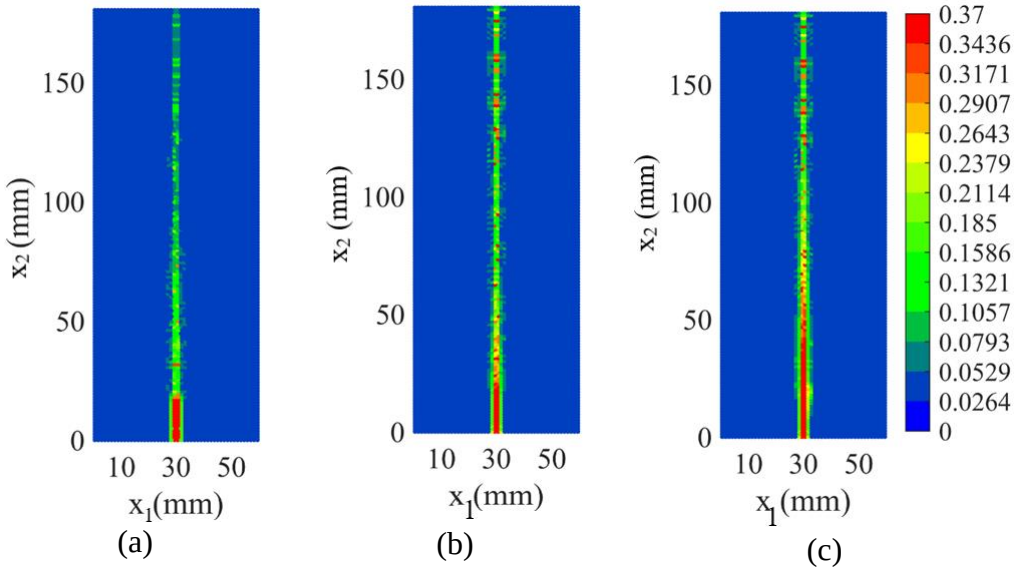

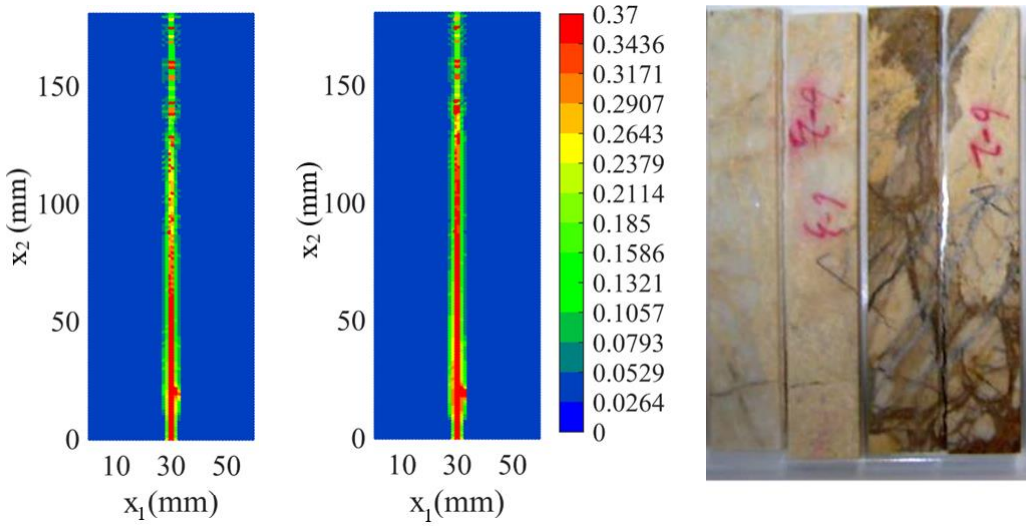

(d) (e) (f)

Fig. 2.63. Variation of damage coefficient, ϕ at (a) $t = 17.079$ s, (b) $t = 22.794$ s, (c) $t = 88.425$ s, (d) $t = 247.989$ s, (e) $t = 567.116$ s, (f) completely damaged specimens [85].

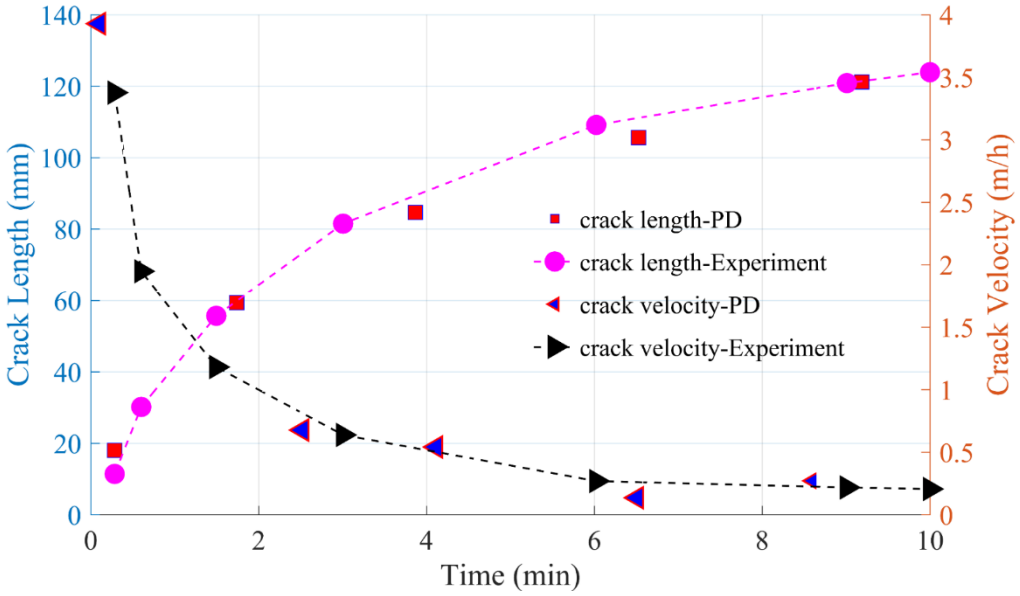

Fig. 2.64. Variation of crack length and crack growth velocity (experiment [85])

2.3.7.6. A flat shell with a rectangular cut-out

A square plate with dimensions of $L = B = 1$ m and thickness of $h = 0.01$ m is investigated as shown in Fig. 2.65. The plate has a rectangular cut-out in the middle. The cut-out has dimensions of $l = 0.4$ m, $b = 0.3$ m.

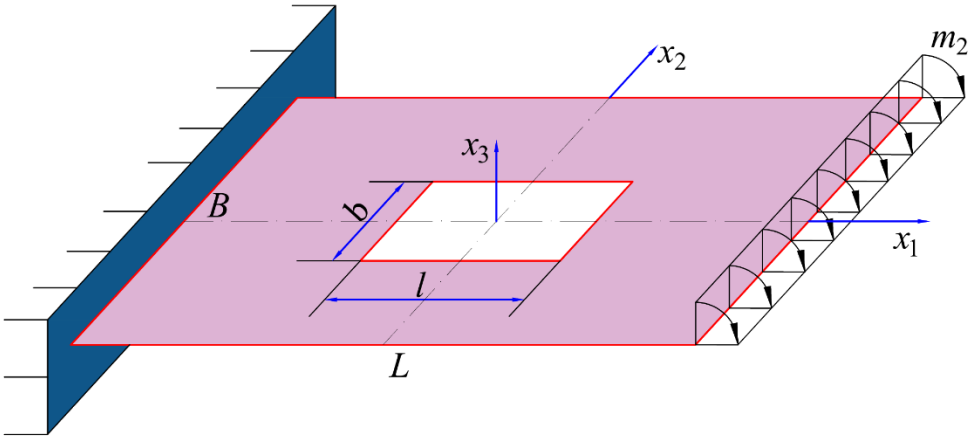

Fig. 2.65. Plate with a rectangular cut-out

The plate is made of steel with Young's modulus $E = 2 \times 10^{11}\ \mathrm{N/m^2}$, Poisson's ratio $\nu = 0.27$, the fracture toughness $K_{Ic} = 70 \times 10^6\ \mathrm{Nm^{-3/2}}$ [87]. For simplification, the critical energy release rate of the material is calculated as $G_c = G_{\mathrm{Ic}} = K_{Ic}^2/E = 2.2714\ \mathrm{J/m^2}$. The plate is fixed on the left edge and it is subjected to bending moments on the right edge as shown in Fig. 2.65.

In the PD model, the shell is uniformly discretized with a mesh size of $\Delta x = 0.0067\ \mathrm{m}$, and the horizon size $\delta = 3.015\Delta x$ is used. To apply boundary conditions, three fictitious layers of material points are added on the left side of the plate and all degrees of freedom of these fictitious points and material points located at $x = -L/2$ are set equal to zero [61].

The right end of the plate is subjected to the bending moment per unit length m_2 as shown in Fig. 2.65. Therefore, the loading for each material point on the right edge can be calculated as

$$\mathbf{B}^G = \begin{bmatrix} 0 & 0 & 0 & 0 & m_2 \Delta x & 0 \end{bmatrix}^T \tag{2.96}$$

At each load step, the value of the bending moment per unit length, m_2, is chosen to have at least one new broken interaction in the PD model. The value of m_2 is also not too large to avoid the breakages of too many bonds in a load step which may lead to numerical instabilities.

Fig. 2.66 shows the damage evolution on the plate predicted by using the PD shell model. As shown in Fig. 2.66(a), at 20^{th} load step when the applied bending moment per unit length is $m_2 = 1.606 \times 10^3\ \mathrm{Nm/m}$, the damage initiates at two corners of the cut-out, which are near the right edge of the plate where the bending moment is applied. To further investigate the behaviour of the plate when it is subjected to the bending moment per unit length $m_2 = 1.606 \times 10^3\ \mathrm{Nm/m}$ at 20^{th} load step, the variations of von Mises stresses captured by PD and FEA are compared as shown in Fig. 2.67. The FEA is conducted by using the ANSYS SHELL181 element. As shown in Fig. 2.67, von Mises stress distribution in ANSYS is similar to PD results. Moreover, the maximum stress locations agree with the locations of the damage initiation predicted by PD as shown in Fig. 2.66(a).

The damages predicted by PD propagate nearly parallel to the right edge of the plate as shown in Fig. 2.66(b-d). After 1120 load steps when the applied bending

moment is $m_2 = 1.066 \times 10^3$ Nm/m, the damage propagation reaches locations at $x_2 = \pm 0.31$ m as shown in Fig. 2.66(d).

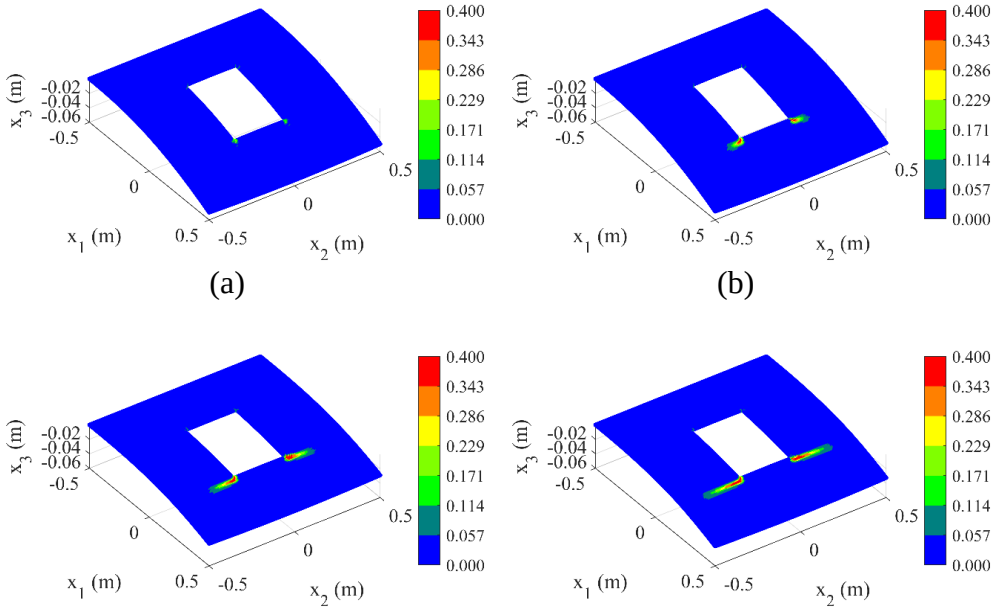

Fig. 2.66. Damage evolution on the plate at (a) 20^{th}, (b) 400^{th}, (c) 800^{th} (d) 1120^{th} load steps when applied bending moment $m_2 = 1.606 \times 10^3$, 1.537×10^3, 1.238×10^3, 1.066×10^3 Nm/m, respectively

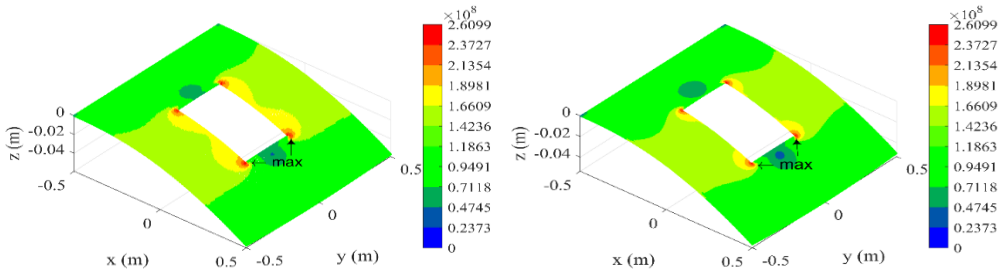

Fig. 2.67. Variation of von Mises stress (Pa) predicted by (a) PD, (b) FEA

Fig. 2.68 shows the loading history of applied bending moment per unit length, m_2 and corresponding crack paths, shown in black, on the plate at different load steps. Since the plate is symmetric with respect to the x_1 axis, only the crack path on the positive direction of the x_2 axis is presented. As can be seen from the figure, as the crack propagates during the first 200 load steps, the applied bending moment, m_2 reduces quickly from 1.606×10^3 Nm/m to 1.474×10^3 Nm/m. Initially, the cracks propagate with an angle of 10^o with respect to the x_1 axis. Later, the cracks change their directions and propagate parallel to the right edge of the plate. At 400^{th} load step, the applied bending moment increases slightly to 1.537×10^3 Nm/m. Afterward, the cracks propagate towards the location $(x_1 = 0.2133 \text{ m}, x_2 = \pm 0.31 \text{ m})$ at the 1120^{th} load step. The required bending moment is sharply reduced due to reduced strength caused by damage growth.

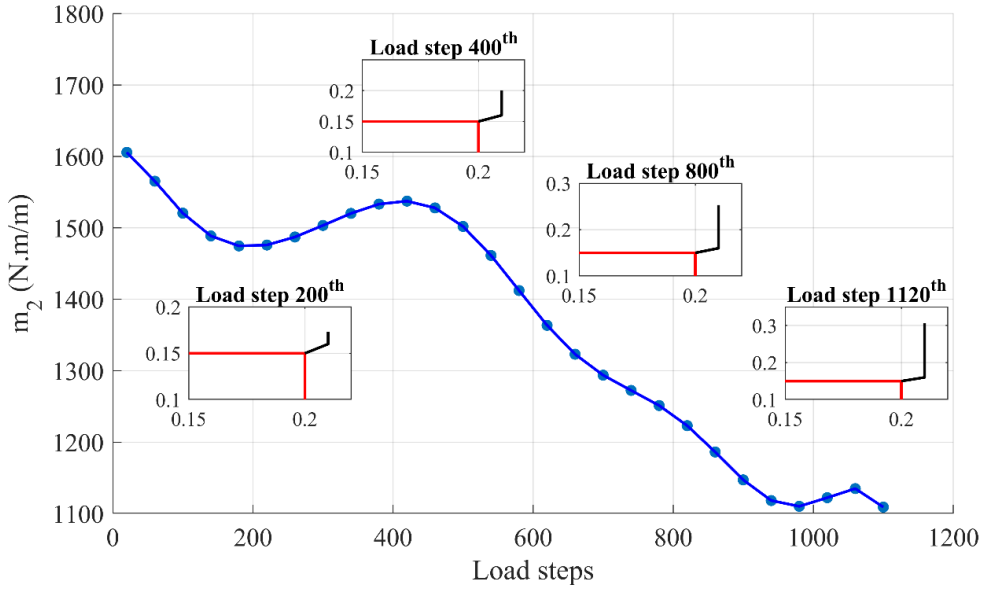

Fig. 2.68. Load history of applied bending moment per unit length, m_2

2.3.7.7. Damage prediction for a ship structure

An experimental MST4-ship model developed by Nishihara [88] with dimensions of $L \times B \times H = 0.9 \times 0.72 \times 0.72\ \mathrm{m}^3$ is investigated. The 3D model and the cross-section details of the ship are shown in Fig. 2.69. The ship is made of steel with Young's modulus $E = 2.08 \times 10^{11}\mathrm{N/m}^2$, Poisson's ratio $\nu = 0.281$ [88], fracture toughness, $K_{Ic} = 54 \times 10^6\ \mathrm{Nm}^{-3/2}$ [89]. For simplification, the critical energy release rate of the material is calculated as $G_c = G_{\mathrm{Ic}} = K_{Ic}^2/E = 1.2912\ \mathrm{J/m}^2$.

The ship is investigated for two basic loading conditions which are bending and torsion as shown in Fig. 2.70. In the PD model, the ship is discretized with a mesh size of $\Delta x = 0.02$ m. Similar to the previous examples, the horizon size $\delta = 3.015\Delta x$ is used. To apply loading conditions, two thick rigid plates are added at two ends of the model as shown in Fig. 2.71. The rigid plates are represented by Young's modulus $E_r = 20 \times E$, Poisson's ratio $\nu_r = \nu$, and thickness $h_r = 20 \times h$.

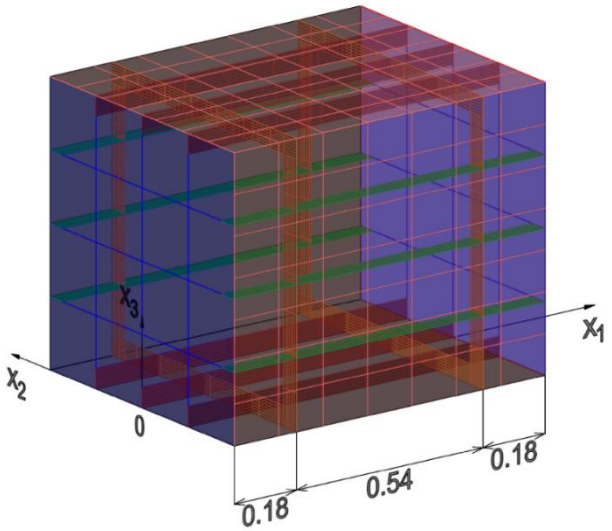

(a)

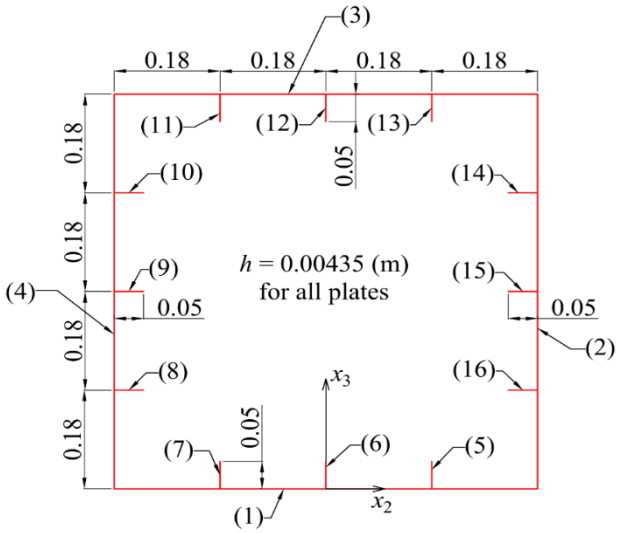

(b)

Fig. 2.69. MST4 ship model [88] (a): 3D model (b): ship cross-section at $x_1 = 0.45$ m

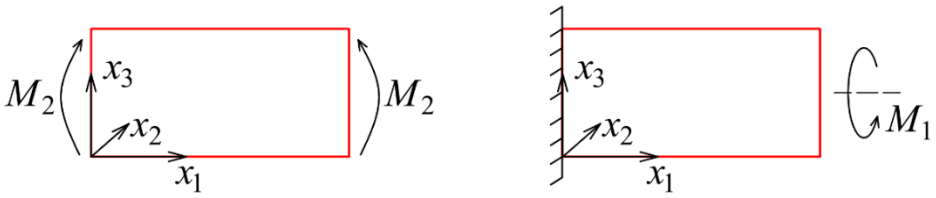

(a) (b)

Fig. 2.70. Two basic loading conditions (a): Sagging, (b): Torsion

In Fig. 2.71, the plates on the deck, the sides, and the bottom are discretized with 1794 material points. Each longitudinal frame includes 184 material points. Each transverse frame includes 560 material points. Moreover, each rigid plate is discretized into 1521 material points. Therefore, 12058 material points are corresponding to 72348 DOFs used for the intact ship model.

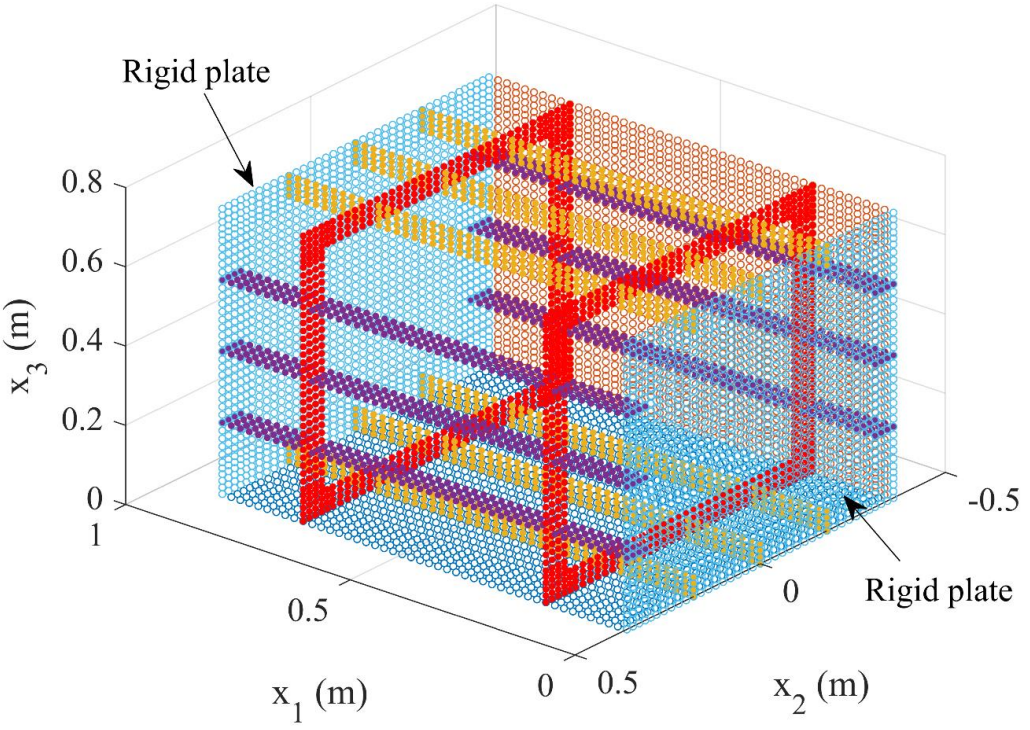

Fig. 2.71. PD discretized model for the ship model (the plates at $x_3 = H$ and $x_2 = B/2$ are hidden for visualization purposes)

Ship structure subjected to bending (sagging)

In this section, the ship is subjected to bending loading as shown in Fig. 2.70(a). The bending moments for the material points located at the left end of the model at $x_1 = 0$ are applied as

$$M_{2L} = M_2 / N_L \tag{2.97}$$

On the other hand, the bending moments for the material points located at the right end of the model at $x_1 = L$ are applied as

$$M_{2R} = -M_2 / N_R \tag{2.98}$$

where N_L and N_R represent total numbers of material points located at the left end and right end of the model, respectively. The parameter M_2 represents the total bending moment applied on the ship structure as shown in Fig. 2.70(a).

Similar to the previous example, the value of the bending moment, M_2, at each load step is chosen as the critical value to have at least one new broken interaction.

The boundary conditions for this loading condition can be described as

$$u_1 = 0 \text{ at } \left(x_1 = L/2, -B/2 \le x_2 \le B/2, 0 \le x_3 \le H\right) \tag{2.99a}$$

$$u_2 = 0 \text{ at } \left(x_1 = 0, x_2 = 0, 0 \le x_3 \le H\right) \tag{2.99b}$$

$$u_2 = 0 \text{ at } \left(x_1 = L, x_2 = 0, 0 \le x_3 \le H\right) \tag{2.99c}$$

$$u_3 = 0 \text{ at } \left(x_1 = 0, -B/2 \le x_2 \le B/2, x_3 = H\right) \tag{2.99d}$$

$$u_3 = 0 \text{ at } \left(x_1 = L, -B/2 \le x_2 \le B/2, x_3 = H\right) \tag{2.99e}$$

The ship structure is investigated for different scenarios. First, the intact ship subjected to bending loading is investigated. Next, the ship is assumed to have square cut-outs on the bottom with dimensions of 0.2×0.2 m^{2}or 0.4×0.4 m^2 as shown in Fig. 2.72.

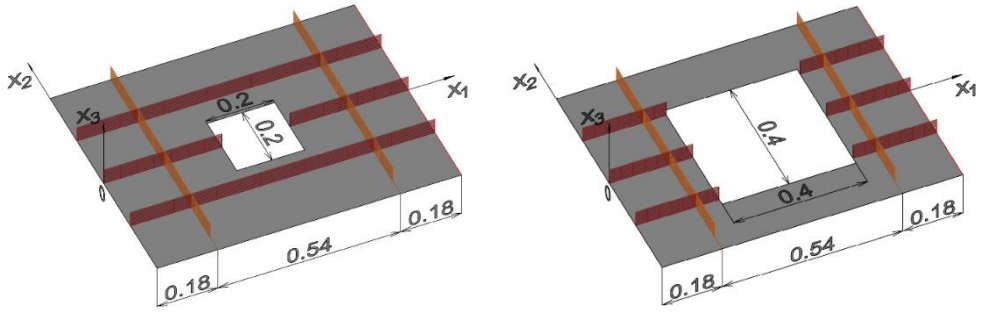

(a) (b)

Fig. 2.72. The bottom of the ship with a square cut-out with dimensions of (a) 0.2×0.2 m^2, (b) 0.4×0.4 m^2

Intact ship subjected to bending loading

By using the uniform mesh size of $\Delta x = 0.02$ m, 12058 material points are corresponding to 72348 degrees of freedom in the PD discretized model. Fig. 2.73-Fig. 2.75 present the damage evolution on the ship structure. As shown in Fig. 2.73, at 400^{th} load step when the applied bending moment is $M_2 = 4.73 \times 10^5$ N.m, there is significant damage in the middle of the deck. As the applied bending continues, the damage on the deck propagates toward two sides of the ship as shown in Fig. 2.74-Fig. 2.75. At 1200^{th} load step when the applied bending moment is $M_2 = 2.05 \times 10^5$ N.m, the damage develops beyond the ship deck and propagates towards the ship side as shown in Fig. 2.75.

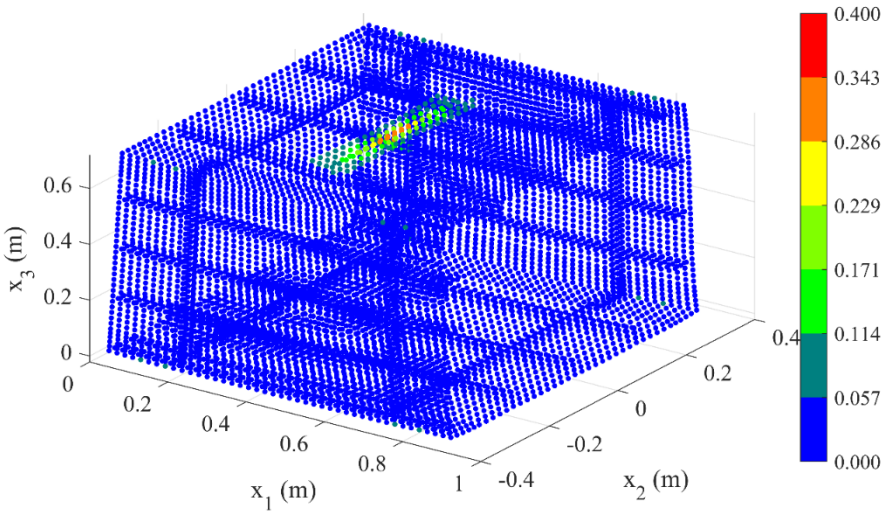

Fig. 2.73. Damage plot at 400^{th} load step when applied bending moment $M_2 = 4.73 \times 10^5$ N.m (displacements are magnified 100 times for deformed configuration. Rigid plates are removed for visualization.)

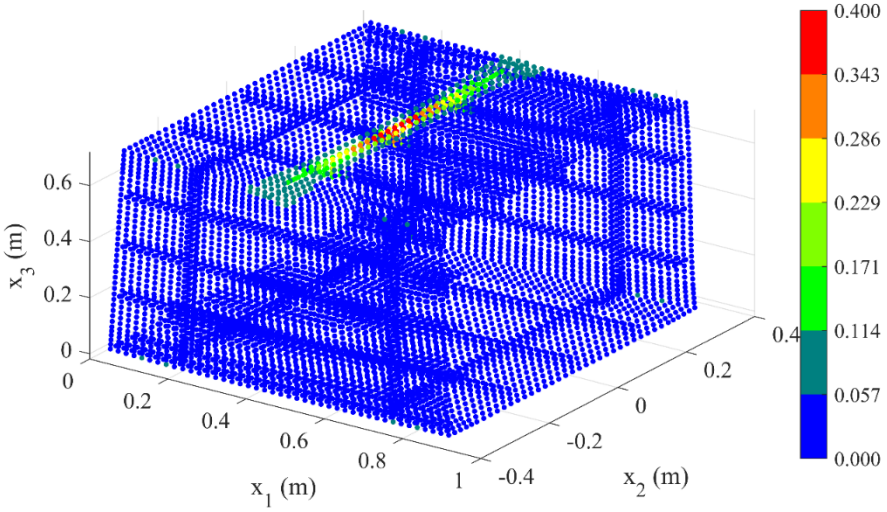

Fig. 2.74. Damage plot at 800^{th} load step when applied bending moment $M_2 = 3.19 \times 10^5$ N.m (displacements are magnified 100 times for deformed configuration. Rigid plates are removed for visualization.)

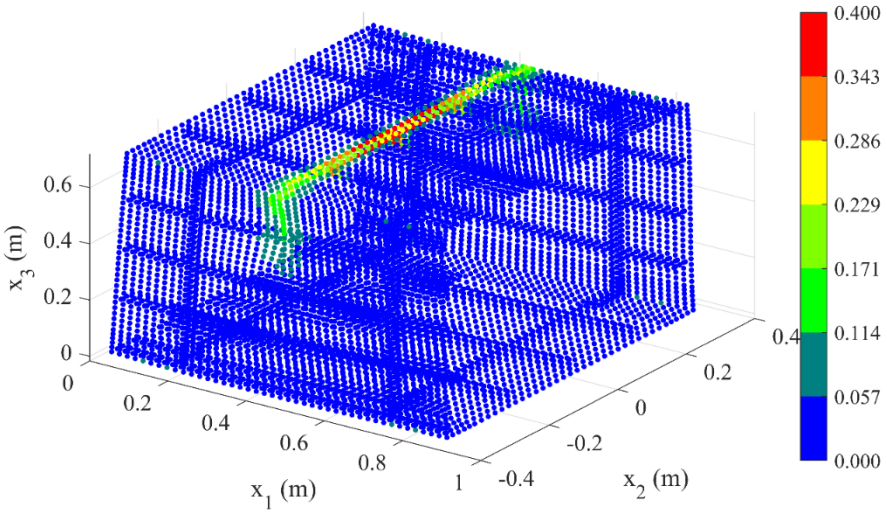

Fig. 2.75. Damage plot at 1200^{th} load step when applied bending moment $M_2 = 2.05 \times 10^5$ N.m (displacements are magnified 100 times for deformed configuration. Rigid plates are removed for visualization.)

Ship with square cut-out subjected to bending loading

Similar to the previous case, the mesh size of $\Delta x = 0.02$ m is used. Therefore, in the PD discretized model for the ship with the smaller cut-out, 11904 material points are corresponding to 71424 degrees of freedom. In the PD discretized model for the ship with the larger cut-out, there are 11428 material points and 68568 degrees of freedom. Fig. 2.76-Fig. 2.78 present damage evolution on the ship with 0.2×0.2 m^{2}cut-out. In this case, the damages initiate at four corners of the cut-out as shown in Fig. 2.76. As can be seen from the figures, the cracks propagate from four corners of the cut-out towards the two sides of the ship structure. As the load

is continuously applied, the cracks propagate vertically on two sides of the ship structure as shown in Fig. 2.77-Fig. 2.78.

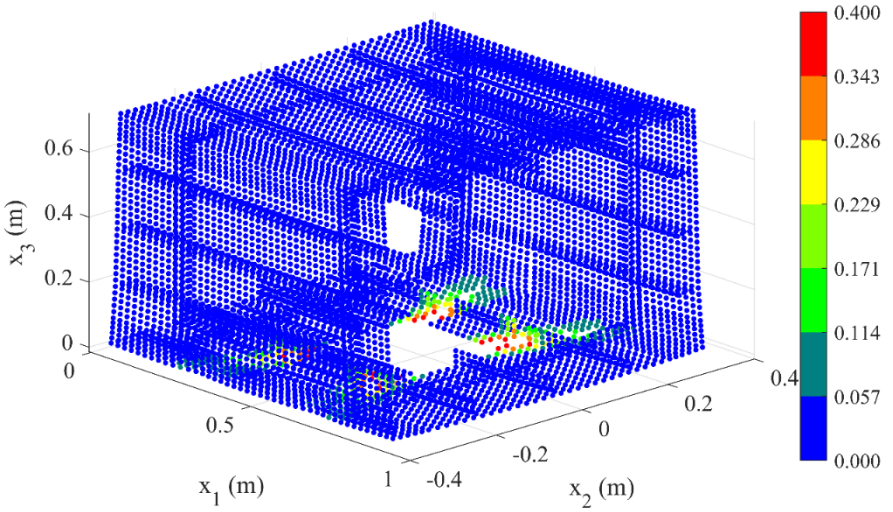

(a)

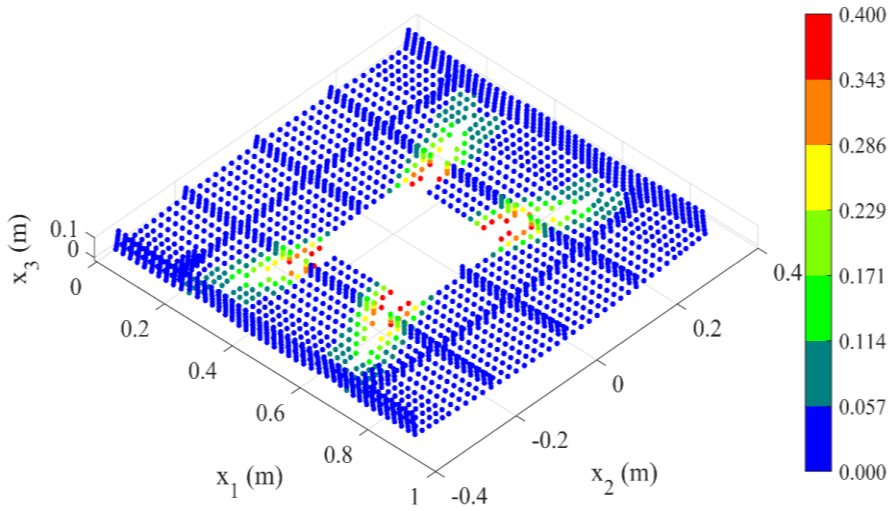

(b)

Fig. 2.76. Damage plot at load step 400^{th} when applied bending moment $M_2 = 2.22 \times 10^5$ N.m (a): 3D model (b): a view for material points with $x_3 \leq 0.1$ m (displacements are magnified 100 times for deformed configuration. Rigid plates are removed for visualization.)

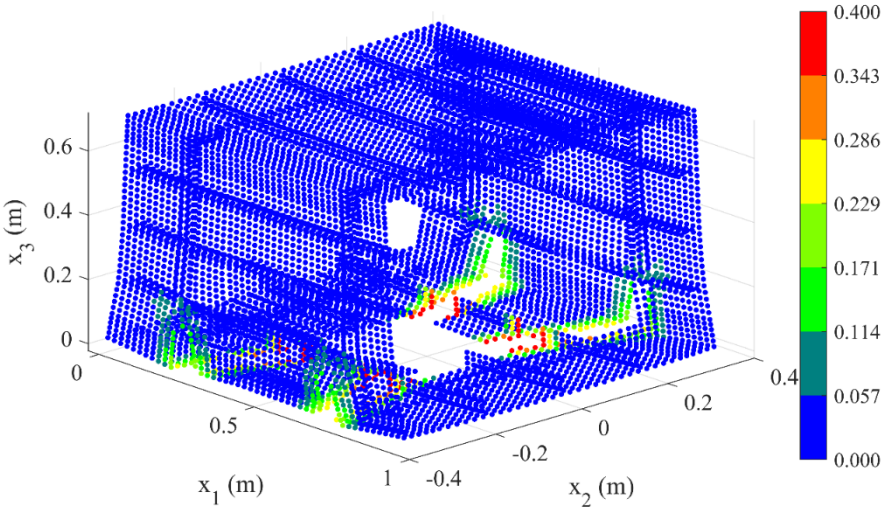

(a)

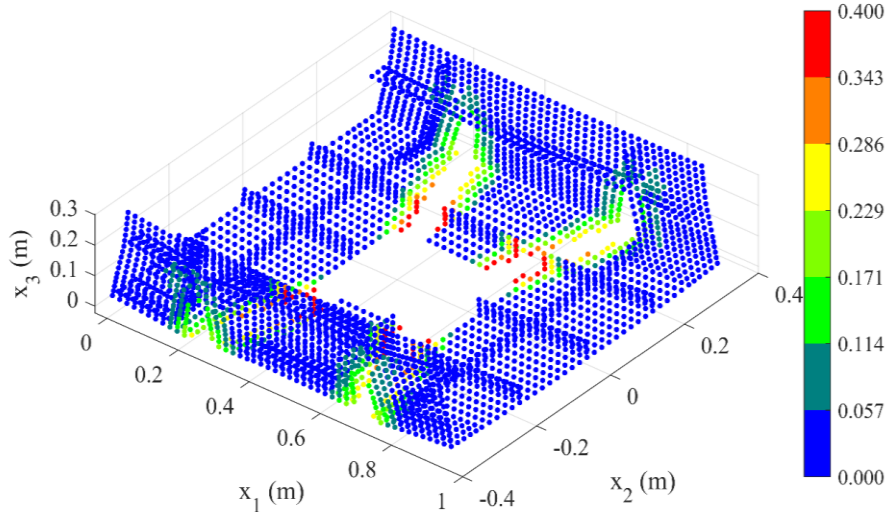

(b)

Fig. 2.77. Damage plot at 800^{th} load step when applied bending moment $M_2 = 1.58 \times 10^5$ N.m (a): 3D model (b): a view for material points with $x_3 \leq 0.3$ m (displacements are magnified 100 times for deformed configuration. Rigid plates are removed for visualization.)

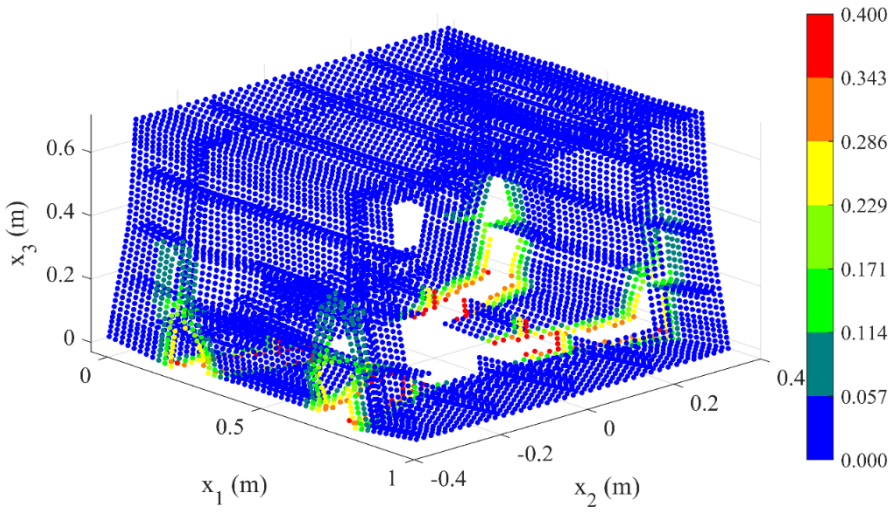

(a)

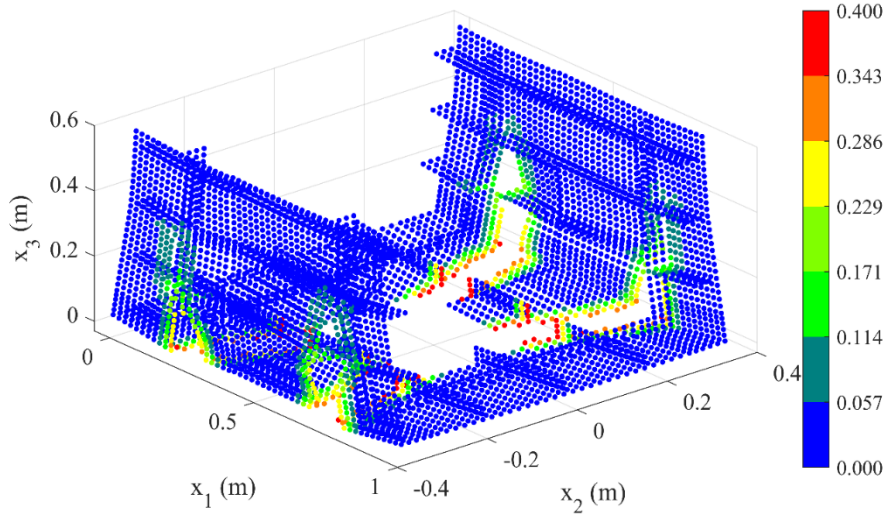

(b)

Fig. 2.78. Final damage plot on the ship at 1200^{th} load step when applied bending moment $M_2 = 8.53 \times 10^4$ N.m (a): 3D model (b): a view for material points with $x_3 \leq 0.6$ m (displacements are magnified 100 times for deformed configuration. Rigid plates are removed for visualization.)

Loading history

Fig. 2.79 shows the variations of bending moment, M_2 and change in the moment of inertia, ΔI_2, of the ship cross-section for three cases. The moment of inertia reduces with respect to the intact ship. The reduction of the moment of inertia, ΔI_2, can be defined as

$$\Delta I_2 = \frac{I_{2(\text{current})} - I_{2(\text{intact})}}{I_{2(\text{intact})}} \times 100\% \tag{2.100}$$

where $I_{2(\text{intact})}$ and $I_{2(\text{current})}$ represent the moment of inertia with respect to the neutral axis in x_2 direction for the intact ship and damaged ship, respectively. At each load step, material points with damage coefficients $\phi \geq 0.3$ are determined and they are defined as damaged parts of the ship structure. Therefore, neutral axis

locations and moment of inertia $I_{2(\text{current})}$ values are recalculated based on the remaining intact parts.

As shown in Fig. 2.79, the maximum bending moment for the intact ship captured by PD is $M_{2max} = 9.28 \times 10^5\ Nm$ which is 0.102% different from the experimental result of $M_{2\,max(\,exp\,eriemnt)} = 9.2705 \times 10^5$ Nm conducted by Nishihara [88]. As it can also be observed from the loading history curve for case 1, shown in blue, there is a stage that the bending moment drops suddenly from 4.65×10^5 Nm to 2.38×10^5 Nm while the moment of inertia is not much reduced. This is the stage that all the shells on the ship deck which are numbered 3, 11, 12, 13, are collapsed and the crack starts propagating along two sides of the ship structure. Therefore, at this stage, the ship structure is much weakened, and the required bending moment is much reduced. For case 2, shown in red, due to the initial cut-out, the moment of inertia of the ship cross-section is initially reduced by 12.6% compared to the intact ship. The maximum bending moment captured by PD is $M_{2max} = 3.85 \times 10^5\ Nm$ which is equal to 41.49% of the maximum bending moment for the intact case. For case 3, due to a bigger cut-out, the initial reduction of the moment of inertia is 27.4% and the maximum bending moment is $M_{2max} = 2.47 \times 10^5\ Nm$ which is equal to 26.62% of the maximum bending moment for the intact case. Moreover, the moment of inertia of the final damaged ship in both cases 2 and 3 decreases by more than 55% as shown in Fig. 2.79.

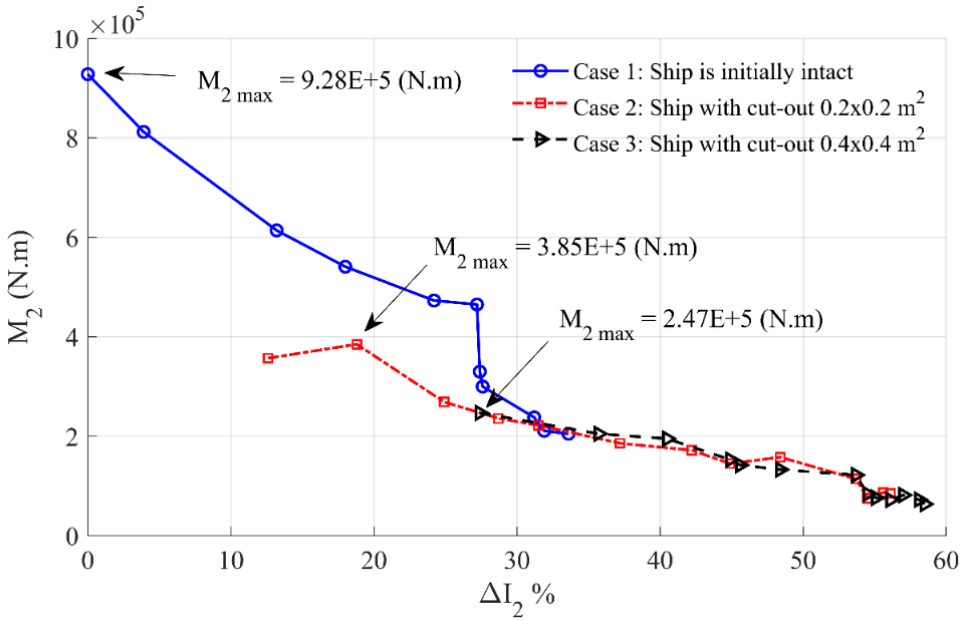

Fig. 2.79. Variations of the critical bending moment versus change in the moment of inertia for the ship structure

Ship structure subjected to torsional loading

After investigating the ship model in bending condition, the ship with the 0.2×0.2 m^2 cut-out is further investigated for the torsional loading condition as shown in Fig. 2.70(b). The left end of the ship is fixed, and the right end of the ship is subjected to torsional loading, M_1 with respect to the neutral axis of the ship in x_1 direction. Similar to the previous example, it is assumed that the right end of the ship structure is attached to a rigid plate. The torsional moment M_1 is applied by applying nodal forces as shown in Fig. 2.80 as

$$\mathbf{f}_{(k)} = f_{(k)}\mathbf{e}_{f(k)} \tag{2.101}$$

where $f_{(k)}$ represents the magnitude and $\boldsymbol{e}_{f_{(k)}}$ represents a unit vector of the nodal force $\boldsymbol{f}_{(k)}$. The magnitude of the nodal force is calculated as

$$f_{(k)} = \frac{M_1}{N_R}\frac{1}{d_{(k)}} \tag{2.102}$$

where M_1 represents the applied torque, N_R represents the total number of material points on the rigid plate at the right end, $d_{(k)}$ represents the distance between material point k and the centre of the rigid plate at $(x_1 = L, x_2 = 0, x_3 = H/2)$.

The unit vector, $\boldsymbol{e}_{f_{(k)}}$ in Eq. (2.101) can be defined as

$$\mathbf{e}_{f(k)} = \mathbf{i}_1 \times \mathbf{i}_{(k)} \tag{2.103a}$$

with

$$\mathbf{i}_1 = \begin{bmatrix} 1 & 0 & 0 \end{bmatrix}^T \tag{2.103b}$$

$$\mathbf{i}_{(k)} = \frac{\mathbf{i}_{0(k)}}{|\mathbf{i}_{0(k)}|} = \frac{\mathbf{i}_{0(k)}}{d_{(k)}} \tag{2.103c}$$

$$\mathbf{i}_{0(k)} = \begin{bmatrix} x_{1(k)} - L & x_{2(k)} - 0 & x_{3(k)} - H/2 \end{bmatrix}^T = \begin{bmatrix} 0 & x_{2(k)} & x_{3(k)} - H/2 \end{bmatrix}^T \tag{2.103d}$$

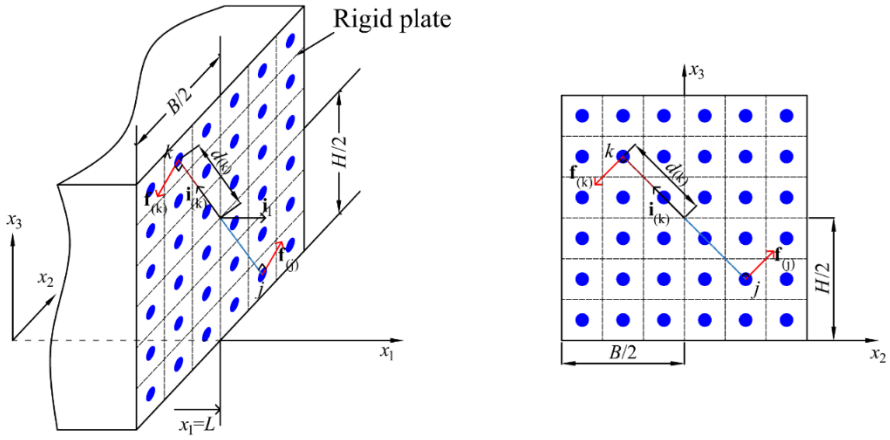

(a) (b)

Fig. 2.80. Applying torque on the rigid plate by using dual forces (a): 3D view, (b): 2D view

In the PD discretized model, the same mesh size $\Delta x = 0.02$ m is used. Fig. 2.81-Fig. 2.83 present damage evolution on the ship for torsional loading conditions. As can be seen from Fig. 2.81, damages initiate at four corners of the cut-out when applied torque is 2.365×10^5 Nm. At 600^{th} load step when applied torque is 1.699×10^5 Nm, the damages propagate from four corners of the cut-out as shown in Fig. 2.82. At 1200^{th} load step when applied torque is 1.6988×10^5 Nm, damages propagate along with the transverse frames as shown in Fig. 2.83.

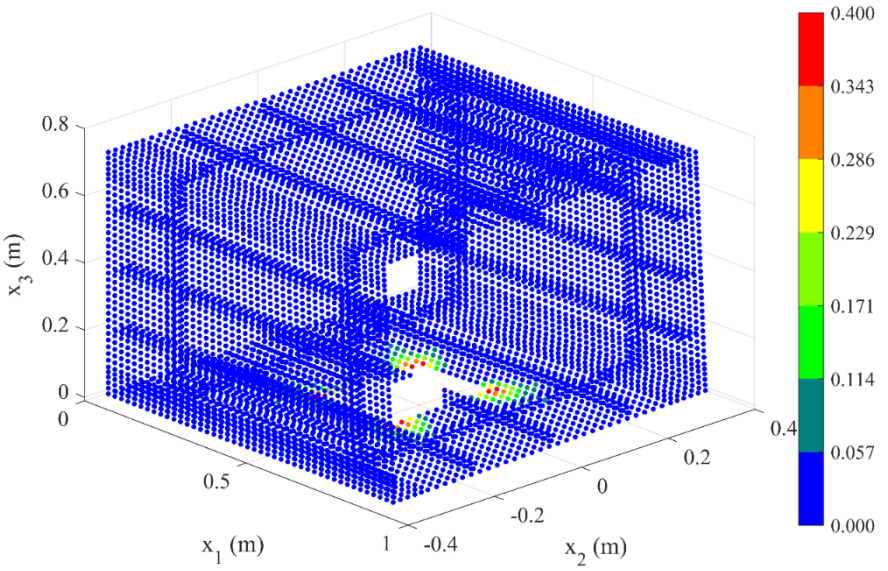

(a)

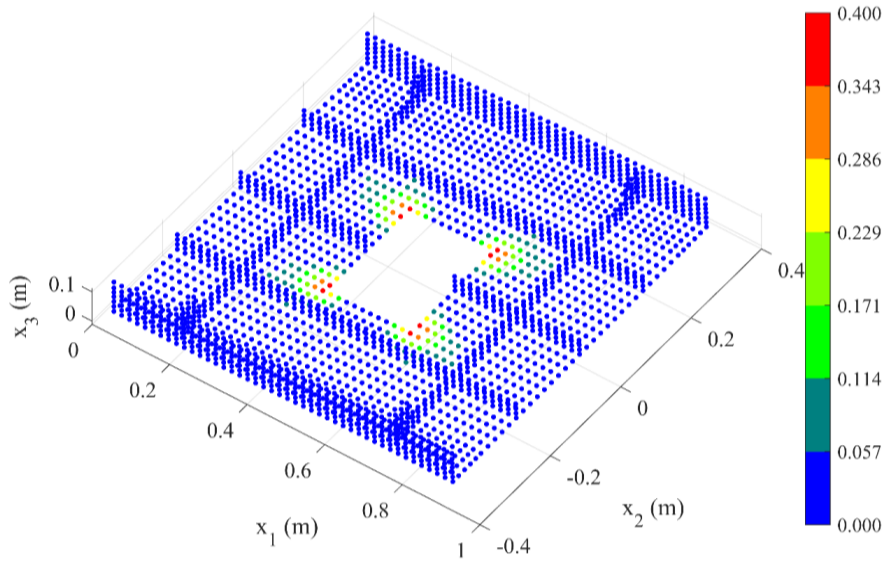

(b)

Fig. 2.81. Damage plot at load step 100^{th} when applied bending moment $M_1 = 2.365 \times 10^5$ Nm (a): 3D model (b): a view for material points with $x_3 \leq 0.1$ m (displacements are magnified 20 times for deformed configuration. Rigid plates are removed for visualization.)

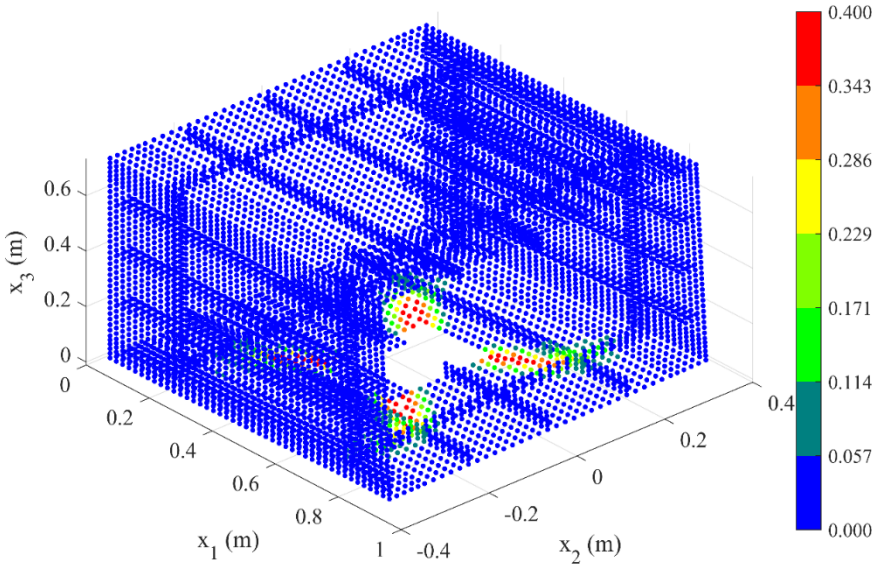

(a)

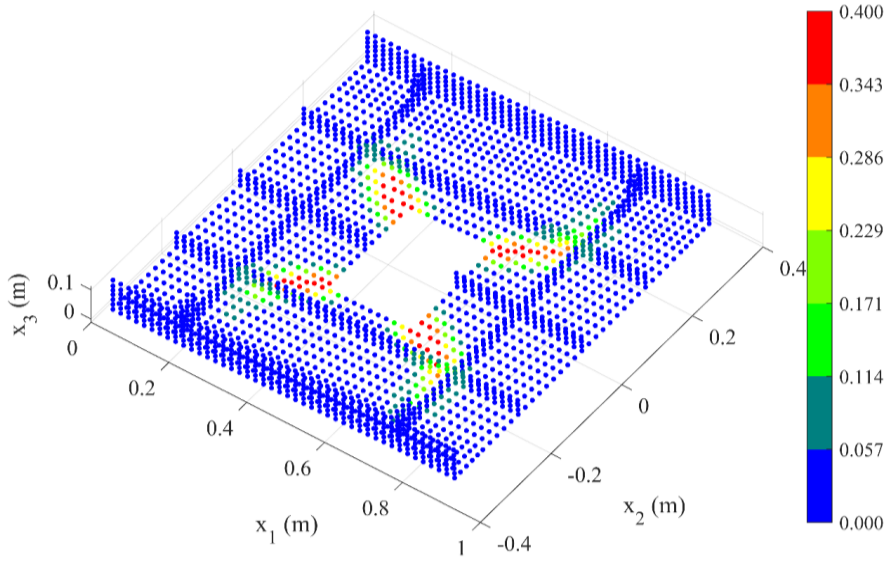

(b)

Fig. 2.82. Damage plot at load step 600^{th} when applied bending moment $M_1 = 1.699 \times 10^5$ Nm (a): 3D model (b): a view for material points with $x_3 \leq 0.1$ m (displacements are magnified 20 times for deformed configuration. Rigid plates are removed for visualization.)

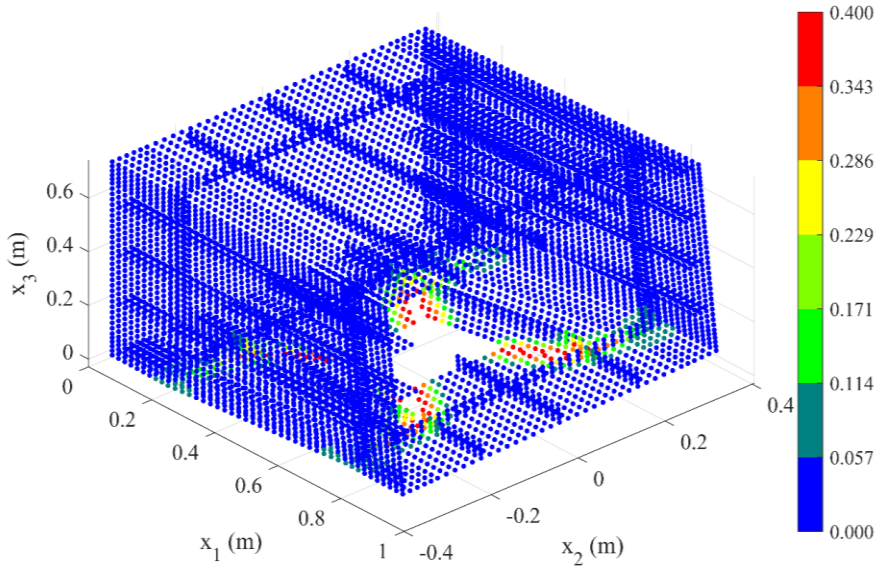

(a)

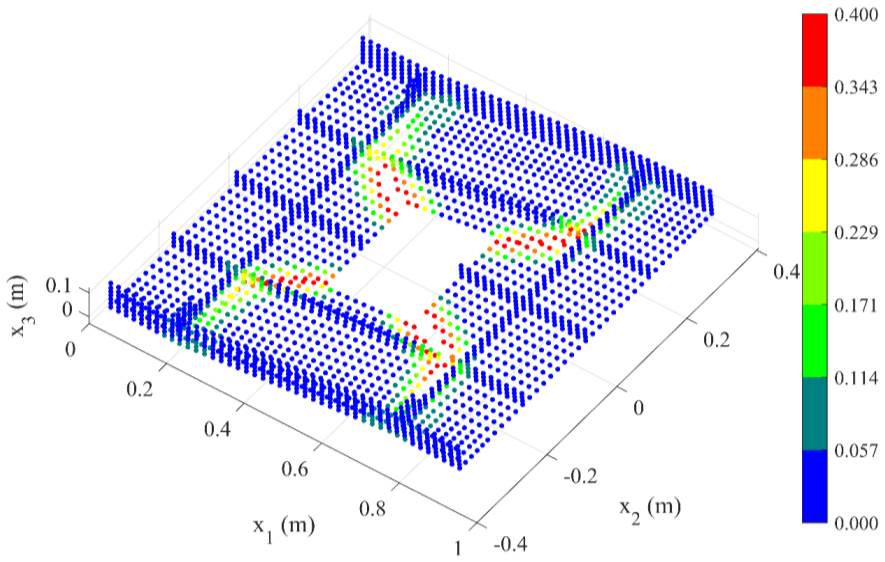

(b)

Fig. 2.83. Final damage plot at load step 1200^{th} when applied bending moment $M_2 = 1.6988 \times 10^5$ Nm (a): 3D model (b): a view for material points with $x_3 \leq 0.1$ m (displacements are magnified 20 times for deformed configuration. Rigid plates are removed for visualization)

Fig. 2.84 shows the loading history and the corresponding progressive damages on the bottom of the ship. In this figure, point (I) is associated with 600^{th} load step when applied torque equal to 1.699×10^5 N.m. Points (II) and (III) are associated with 800^{th} and 1200^{th} load steps when applied torques are 1.324×10^5 N.m and 1.6988×10^5 N.m, respectively. As can be seen from the figure, the applied torque is decreased from the initial value of 2.552×10^5 N.m to 1.699×10^5 N.m (point I) after 600 load steps. At 600^{th} load step (point I), cracks propagate on the shell (1), from 4 corners of the cut-out to two longitudinal shells, (5) and (7) (as shown in Fig. 2.69). Small vertical cracks also appeared on the longitudinal frames.

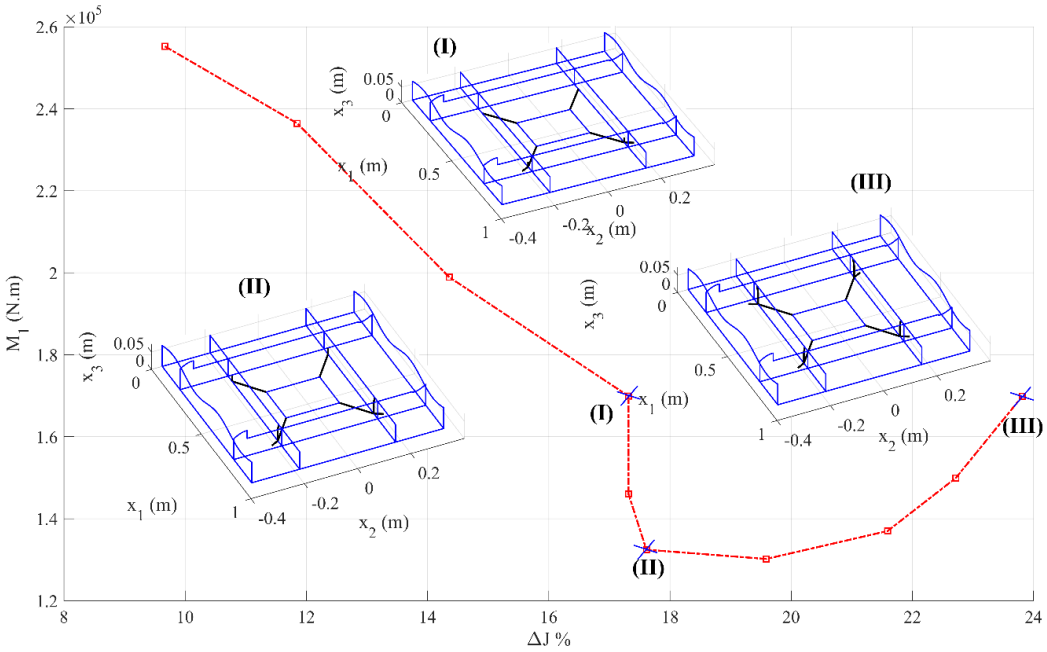

Fig. 2.84. Variations of the critical torsional moment, M_1 versus change in the polar moment of inertia for the ship structure with 0.2×0.2 m^2 cut-out

It is also observed from Fig. 2.84 that the applied torque is sharply reduced from 1.699×10^5 Nm at point (I) to 1.324×10^5 N.m at point (II). Later, the applied torque is increased to 1.6988×10^5 Nm at point (III). To analyse these interesting phenomena, details of the crack paths up to these points are shown in Fig. 2.85. In this figure, the blue lines represent the edges of the cut-out. The scatter data represents the material points that have the local damage index, ϕ exceeding 0.2. The black lines represent the possible crack paths on the ship structure. These crack paths are defined based on the local damage index, ϕ and the crack openings in the deformed configurations.

As shown in Fig. 2.85, the damage initiates at four corners A, B, C, D of the cut-out. By checking the damage plots every 20 load steps, it is observed that the damages start at the corners C and D first. Later, damages also appear at corners A and B. As shown in Fig. 2.85(a), after 600 load steps, the damages propagate from two corners C and D to the locations of $(x_1 = 0.7 \text{ m}, x_2 = 0.21 \text{ m}, x_3 = 0)$ and $(x_1 = 0.7 \text{ m}, x_2 = -0.21 \text{ m}, x_3 = 0)$, respectively. There are also two short vertical cracks on the longitudinal shells (shells 5 and 7 in Fig. 2.69) at the locations of $(x_1 = 0.68 \text{ m}, x_2 = \pm 0.18 \text{ m}, 0 \leq x_3 \leq 0.0167 \text{ m})$. Moreover, the damages also propagate from two corners A and B to the locations of $(x_1 = 0.24 \text{ m}, x_2 = 0.168 \text{ m}, x_3 = 0)$ and $(x_1 = 0.24 \text{ m}, x_2 = -0.168 \text{ m}, x_3 = 0)$, respectively.

From 600^{th} load step (point (I) in Fig. 2.84) to 800^{th} load step (point (II) in Fig. 2.84), the cracks propagate on the bottom and vertical shells by very short distances (approximately equal to Δx) as shown in Fig. 2.85(b). Since the vertical cracks are already created at 600^{th} load step, the required torques to continue propagating small amounts of cracks are much reduced from point (I) to point (II) as shown in Fig. 2.84.

At 1200^{th} load step (point (III) in Fig. 2.84), there are two new vertical cracks compared to the damages at 800^{th} load step (point (II) in Fig. 2.84) as shown in Fig. 2.85(c). The locations of these new vertical cracks are ($x_1 = 0.21$ m, $x_2 = \pm 0.18$ m, $0 \leq x_3 \leq 0.05$ m) on the longitudinal shells (shells 5 and 7 in Fig. 2.69). Moreover, the vertical cracks observed from 600^{th} and 800^{th} load steps also propagate to the locations of ($x_1 = 0.68$ m, $x_2 = \pm 0.18$ m, $0 \leq x_3 \leq 0.05$ m). Note that all vertical cracks reach the height of 0.05 m which means the longitudinal shells (shells 5 and 7 in Fig. 2.69) are completely damaged at 1200^{th} load step.

Also, it can be observed from Fig. 2.85 that the cracks initiating from corners C and D propagate toward the free end of the ship where the loading conditions are applied. On the other hand, the cracks initiating from two corners A and B propagate toward the fixed end of the ship where the boundary conditions are applied. The fixed end and the free end of the ship are shown in Fig. 2.70(b). Moreover, it can also be observed that the cracks initiating from corners C and D propagate quicker than the cracks initiating from corners A and B. In other words, breaking the structures near the fixed end is more difficult than breaking the structures near the free end. This observation can be the reason for the increase of the required torques from 1.324×10^5 Nm for the point (II) to 1.6988×10^5 Nm for the point (III) as shown in Fig. 2.84.

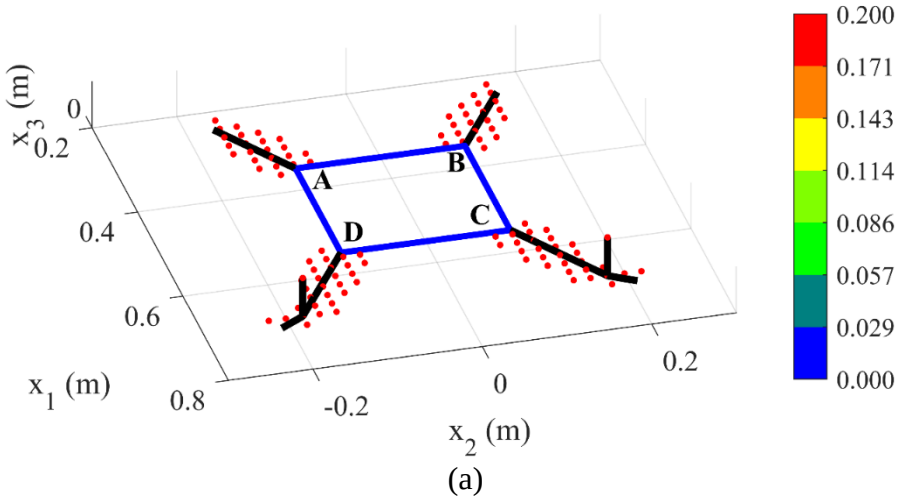

(a)

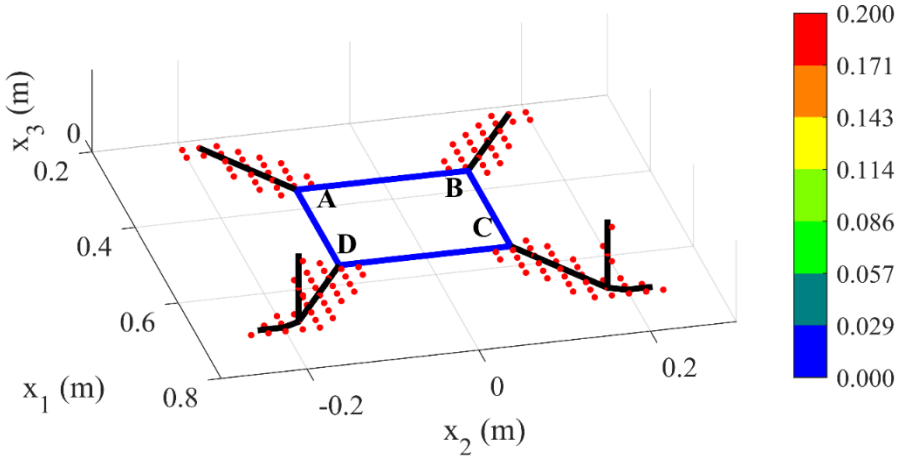

(b)

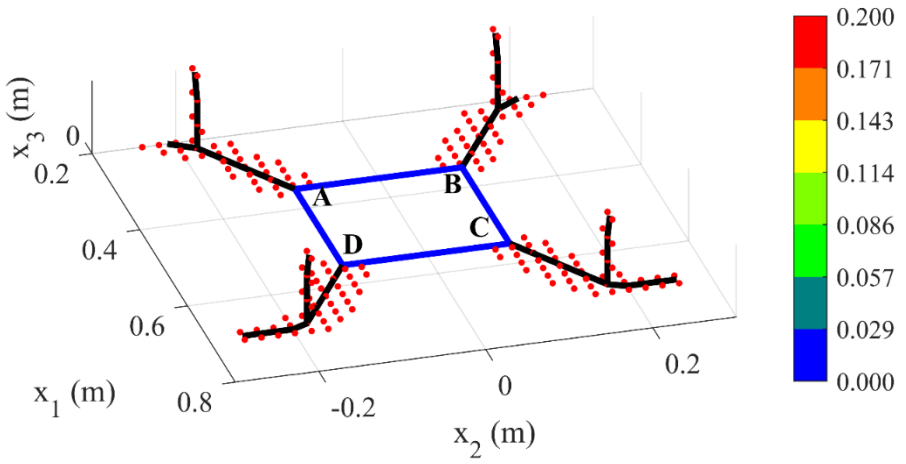

(c)

Fig. 2.85. Crack paths at (a) 600^{th} (point I), (b) 800^{th}(point II), (c) 1200^{th} (point III) load step

2.3.7.8. Damages on a corroded stiffened structure subjected to the uniform pressure

In this section, damage propagations on a stiffened structure subjected to uniform quasi-static pressure as shown in Fig. 2.86 are predicted. The stiffened structure is assumed to have localized corrosion located at $(x_1 = 0, x_2 = 0.145\ \text{m}, z = 0)$ on plate (1). The dimensions of the localized corrosion are represented by $a = 0.1\ \text{m}$, $b = 0.01\ \text{m}$ and the corrosion rate of 60% is assumed. The material has the elastic modulus of $E = 2.022 \times 10^{11}\ \text{N/m}^2$, the Poisson's ratio of $\nu = 0.3$, the fracture toughness of $K_{Ic} = 54 \times 10^6\ \text{Nm}^{-3/2}$ [89]. For simplification, the critical energy release rate of the material is calculated as $G_c = G_{\text{Ic}} = K_{Ic}^2/E = 13123\ \text{J/m}^2$.

The structure is fixed on the four boundaries as shown in black in Fig. 2.86. The plate (1) is subjected to uniform pressure, p_3 in a negative x_3 direction. Similar to previous examples, the critical value of pressure p_3 at each load step is chosen as the load required for crack growth by comparing the energy with the critical energy release rate value for each interaction [61, 64].

In the PD model, uniform mesh size $\Delta x = 0.005\ \text{m}$ and the horizon size $\delta = 3.015\Delta x$ are used. To represent the localized corrosion, material points located within the corroded regions are defined and the thickness of the plate (1) at these points is reduced by 60% as shown in Fig. 2.87.

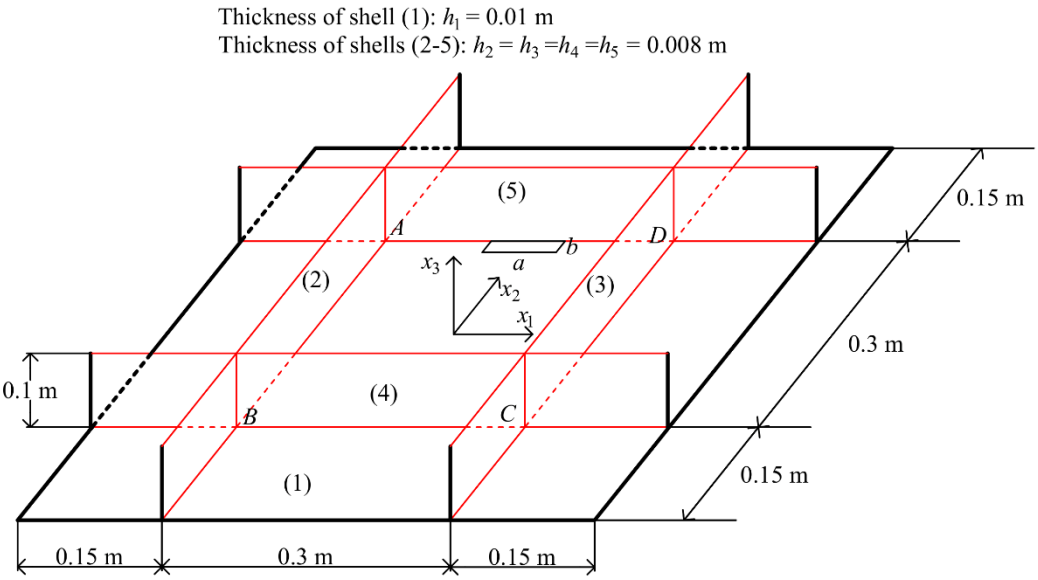

Fig. 2.86. The corroded stiffened structure

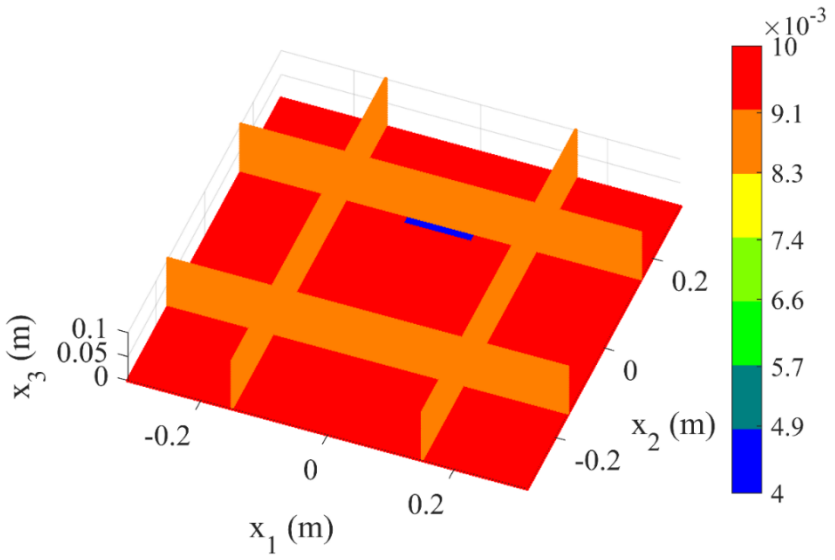

Fig. 2.87. Variation of thickness on the corroded stiffened structure

Fig. 2.88 shows the damage evolution on the stiffened structure. As shown in Fig. 2.88(a), after 100 load steps, the damage initiates at the location of the corroded region. As shown in Fig. 2.88(b), as the pressure is continuously applied, the damage grows along with the line AD (Fig. 2.86). It can be observed from Fig. 2.88(b) that after 1000 load steps, the crack changes its direction and then moves along line AB and DC as shown in Fig. 2.88(c). Later, the crack changes its direction again and moves along line BC as shown in Fig. 2.88(d). As can be observed from the figures, the crack changes its direction due to the presence of the stiffeners. Similar behaviour is also predicted for a pipe with a strap [90].

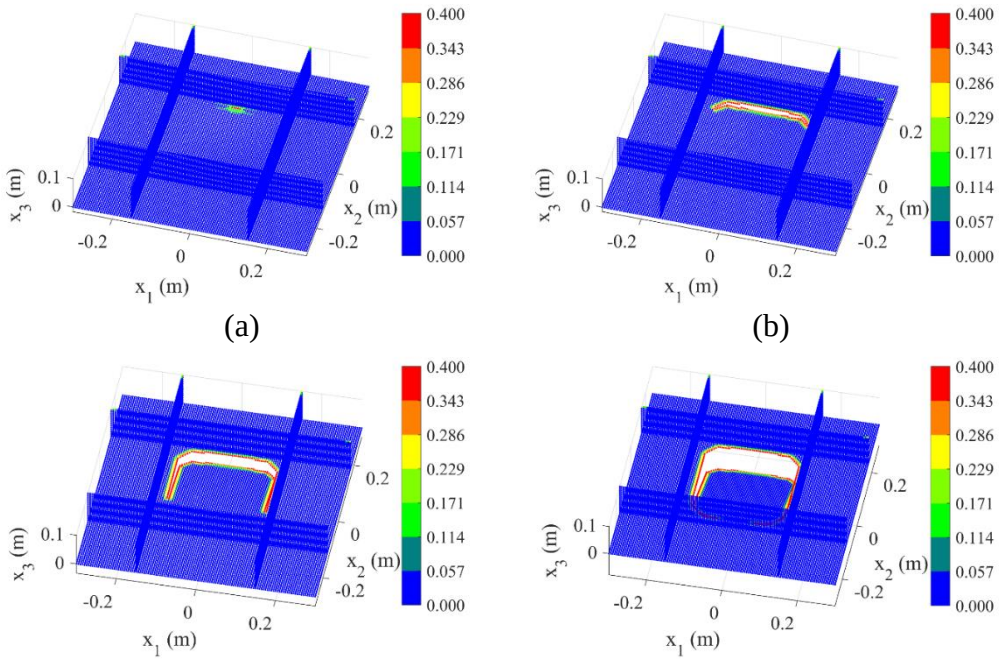

Fig. 2.88. Damage on the stiffened structure subjected to quasi-static pressure at (a): 100th, (b): 1000th, (c): 2000th, (d): 3000th load steps (Displacement is magnified by 10 for deformed configuration)

To visualize the damage patterns, the damage evolution on the plate (1) is shown in Fig. 2.89. As can be observed from Fig. 2.89, the damage propagates along the four intersection lines, AD, AB, DC, BC, between the plate (1) and the four stringers. After 3000 load steps, the damage nearly develops to a close region as shown in Fig. 2.89(d).

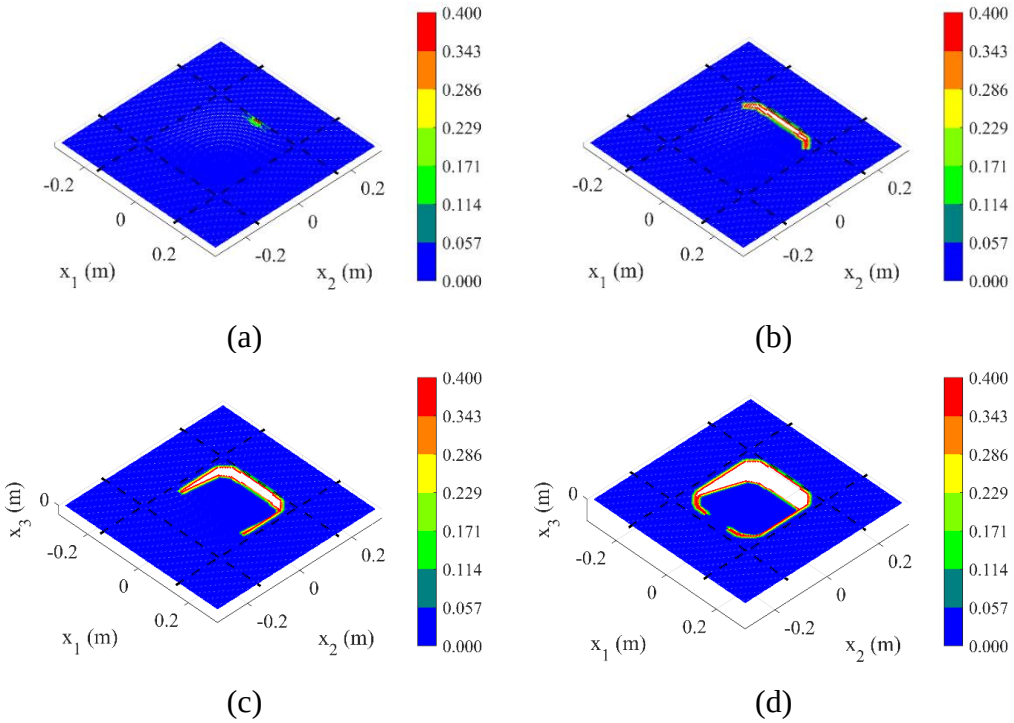

Fig. 2.89. Damage on the plate (1) at (a): 100^{th}, (b): 1000^{th}, (c): 2000^{th}, (d): 3000^{th} load steps (Displacement is magnified by 10 for deformed configurations. The black dash lines represent the locations of the stringers)

Fig. 2.90 shows the history of the required pressure for crack growth. As shown in Fig. 2.90, to initiate the first damage, the required pressure needs to reach the peak at 1.913×10^6 N/m^2. During the first 240 load steps afterward, the required pressure reduces quickly to 1.227×10^6 N/m^2 since the damage propagates within the corroded region. When the damage starts propagating beyond the corroded region, the required applied pressure increases significantly to 1.628×10^6 N/m^2 at 360^{th} load step. Afterward, the applied pressure continuously reduces due to the damage growth. After 3000 load steps, the required pressure reduces to 9.477×10^4 N/m^2.

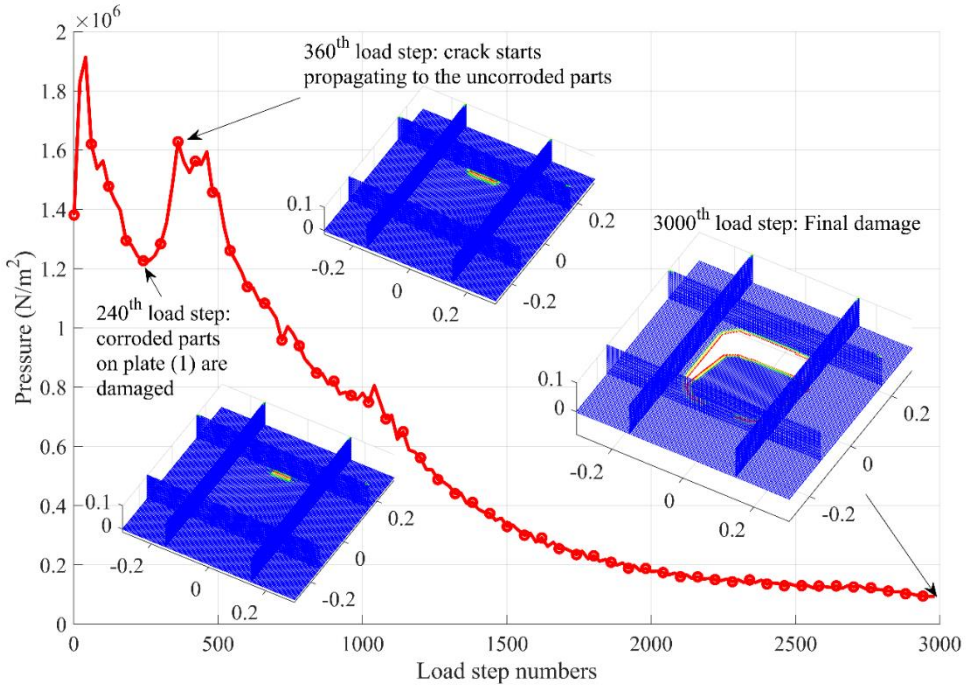

Fig. 2.90. History of required pressure for crack growth, p_3 for the stiffened structure

2.4. Concluding remarks

This chapter provides novel PD models for dealing with complex beam and shell structures. First, a bond-based PD beam model with 6 degrees of freedom is developed. The numerical implementations for investigating complex beam structures are also introduced for the first time in the PD literature. The results from PD analyses have good agreement with those in FEA solutions. Damage criteria for beam model based on critical energy release rate are provided for damage predictions. To demonstrate the capability of the PD beam model, the developed PD model is used to predict the damage for a 27 m high jacket platform subjected to collision. The developed PD beam model can be used for any type of beam structure such as jacket platforms with real dimensions to predict possible brittle damages that may occur during the operation process.

Second, a novel state-based PD model for the thermomechanical behaviour of shell structures in three-dimensional space with 6 degrees of freedom is developed. Initially, the PD model is developed for flat shells. Later, it is modified for curve shells and stiffened structures. The numerical implementations to deal with complex shell structures are also provided. The behaviours of shell structures captured by the developed PD model are verified by comparing with FEA solutions with very good agreements. The PD damage criteria for shell structures based on the critical energy release rate is provided for damage predictions. The developed PD shell model is used to predict damage on a flat shell in a double torsion problem, a flat shell with a rectangular cut-out subjected to bending, a hull girder subjected to bending and torsion, and a corroded stiffened structure subjected to uniform pressure. The developed PD model can be used for any type of shell structures such as ships and offshore structures to predict possible brittle damages that may occur during the operation process.

3. PERIDYNAMICS FOR NONLINEAR ANALYSIS

3.1. Introduction

This chapter focuses on developing novel nonlinear PD models for geometrically nonlinear analyses. The nonlinear PD formulations and equations of motion are obtained based on the principle of virtual displacements by using the Total Lagrange formulation.

First, as discussed by Madenci and Oterkus [44], Cauchy stress components can be expressed in terms of PD force densities. In classical continuum mechanics, Cauchy stress is calculated based on the deformed configuration which is affected by volume changes and rotations for large deformation problems. Therefore, rotations and volume changes can also affect the calculation of PD force densities. In current PD literature, the PD force densities, in bond-based and ordinary state-based PD models, are parallel to the line of interaction on the deformed configuration. However, the effect of volume change is excluded from the calculation of PD force densities. Therefore, for large deformation problems in which the effects of volume change are significant, a new formulation of PD force densities, which considers both effects of rotation and volume change, need to be used. Therefore, in this chapter, nonlinear PD models for 1D, 2D, and 3D structures that consider the effects of rotations and volume changes are developed.

Second, to investigate slender and thin-wall structures, the existing PD beam [48-50, 58] and shell [50, 52, 59] models in literature including the PD models [61-64] developed in Chapter 2 in this thesis can only apply for linear elastic material responses since they are based on small deformation assumptions. Therefore, in this chapter, novel nonlinear PD models for geometrically nonlinear analysis of beams and plates are developed. The nonlinear PD beam model is based on the Timoshenko beam theory. Meanwhile, the nonlinear PD plate model is based on the Mindlin–Reissner plate theory.

3.2. Peridynamics for nonlinear analysis of 1D, 2D, 3D structures

In this section, novel nonlinear PD models for 1D, 2D, and 3D structures are developed. The effects of rotations and volume changes are included in the calculation of PD force densities. The logarithmic bond stretch is defined and used for the first time in the PD literature. The PD formulation and equations of motion are obtained based on the principle of virtual displacements by using Total Lagrange formulation. The numerical procedure for PD nonlinear analysis is provided. The capabilities of the PD model are verified by considering 1D, 2D, and 3D structures subjected to large deformations. The developed nonlinear PD model is used to predict damages in 2D plates and 3D structures. The damage predictions are compared with experimental results conducted by Kalthoff [87], [91], Kalthoff and Winkler [92], Jenq and Shah [93].

3.2.1. Peridynamics equation of motion for large deformations

The PD equations of motion for nonlinear analyses can be written in a discrete form as

$$\rho_{(k)}\,{}^{t}\ddot{\mathbf{u}}_{(k)} = \sum_{j=1}^{N}\left({}^{t}_{0}\mathbf{t}_{(k)(j)} - {}^{t}_{0}\mathbf{t}_{(j)(k)}\right){}^{0}V_{(j)} + {}^{t}\mathbf{b}_{(k)} \tag{3.1a}$$

with

$$ {}^{t}_{0}\mathbf{t}_{(k)(j)} = \begin{bmatrix} {}^{t}_{0}t_{x(k)(j)} & {}^{t}_{0}t_{y(k)(j)} & {}^{t}_{0}t_{z(k)(j)} \end{bmatrix}^{T} \tag{3.1b} $$

$$ {}^{t}_{0}\mathbf{t}_{(j)(k)} = \begin{bmatrix} {}^{t}_{0}t_{x(j)(k)} & {}^{t}_{0}t_{y(j)(k)} & {}^{t}_{0}t_{z(j)(k)} \end{bmatrix}^{T} \tag{3.1c} $$

$$ {}^{t}\mathbf{b}_{(k)} = \begin{bmatrix} {}^{t}b_{x(k)} & {}^{t}b_{y(k)} & {}^{t}b_{z(k)} \end{bmatrix}^{T} \tag{3.1d} $$

where N represents the total number of family members of material point k.

Similar to the relation given in Eq. (1.2) in Chapter 1, the relationship between the PD force densities and the nonlinear PD strain energy density can be expressed as

$$ {}^{t}_{0}\mathbf{t}_{(k)(j)} = -\frac{1}{{}^{0}V_{(j)}}\frac{\partial W^{NLPD}_{(k)}}{\partial {}^{t}\mathbf{u}_{(k)}}, \; {}^{t}_{0}\mathbf{t}_{(j)(k)} = -\frac{1}{{}^{0}V_{(k)}}\frac{\partial W^{NLPD}_{(j)}}{\partial {}^{t}\mathbf{u}_{(j)}} \tag{3.2} $$

By using similar PD strain energy density expressions defined in [21, 44, 46], the PD strain energy density for large deformations can be described as

$$ W^{NLPD}_{(k)} = a\left({}^{t}_{0}\vartheta_{(k)}\right)^{2} + b\sum_{j=1}^{N}\left({}^{t}_{0}s_{H}\right)^{2} {}^{0}\xi \, {}^{0}V_{(j)} \quad \text{for 3D and 2D} \tag{3.3a} $$

$$ W^{NLPD}_{(k)} = b\sum_{j=1}^{N}\left({}^{t}_{0}s_{H}\right)^{2} {}^{0}\xi \, {}^{0}V_{(j)} \quad \text{for 1D} \tag{3.3b} $$

Here ${}^{t}_{0}\vartheta_{(k)}$ represents the PD volumetric strain, ${}^{t}_{0}s_{H}$ represents the logarithmic bond stretch and ${}^{0}V_{(j)}$ represents the volume of material point j in the undeformed configuration. The parameters a and b represent the peridynamic constants.

The logarithmic bond stretch, ${}^{t}_{0}s_{H}$, is defined similarly to Hencky strain definition [94] for large deformation problems as [70]

$$ {}^{t}_{0}s_{H} = \ln\left(1 + {}^{t}_{0}s\right) = \ln\left(\frac{{}^{t}\xi}{{}^{0}\xi}\right) \tag{3.4a} $$

with

$$ {}^{0}\xi = \sqrt{{}^{0}\xi_{x}{}^{2} + {}^{0}\xi_{y}{}^{2} + {}^{0}\xi_{z}{}^{2}} = \sqrt{\left({}^{0}x_{(j)} - {}^{0}x_{(k)}\right)^{2} + \left({}^{0}y_{(j)} - {}^{0}y_{(k)}\right)^{2} + \left({}^{0}z_{(j)} - {}^{0}z_{(k)}\right)^{2}} \tag{3.4b} $$

$$ {}^{t}\xi = \sqrt{{}^{t}\xi_{x}{}^{2} + {}^{t}\xi_{y}{}^{2} + {}^{t}\xi_{z}{}^{2}} = \sqrt{\left({}^{t}x_{(j)} - {}^{t}x_{(k)}\right)^{2} + \left({}^{t}y_{(j)} - {}^{t}y_{(k)}\right)^{2} + \left({}^{t}z_{(j)} - {}^{t}z_{(k)}\right)^{2}} \tag{3.4c} $$

where ${}^{t}\xi$ and ${}^{0}\xi$ represent the current length and initial length of the bond between two material points as shown in Fig. 3.1. Here $({}^{0}x, {}^{0}y, {}^{0}z)$ and $({}^{t}x, {}^{t}y, {}^{t}z)$ represent coordinates in the initial (undeformed) and current configurations, respectively. Whereas, $({}^{0}\xi_{x}, {}^{0}\xi_{y}, {}^{0}\xi_{z})$ and $({}^{t}\xi_{x}, {}^{t}\xi_{y}, {}^{t}\xi_{z})$ represent relative coordinates between two material points in the initial and current configurations, respectively.

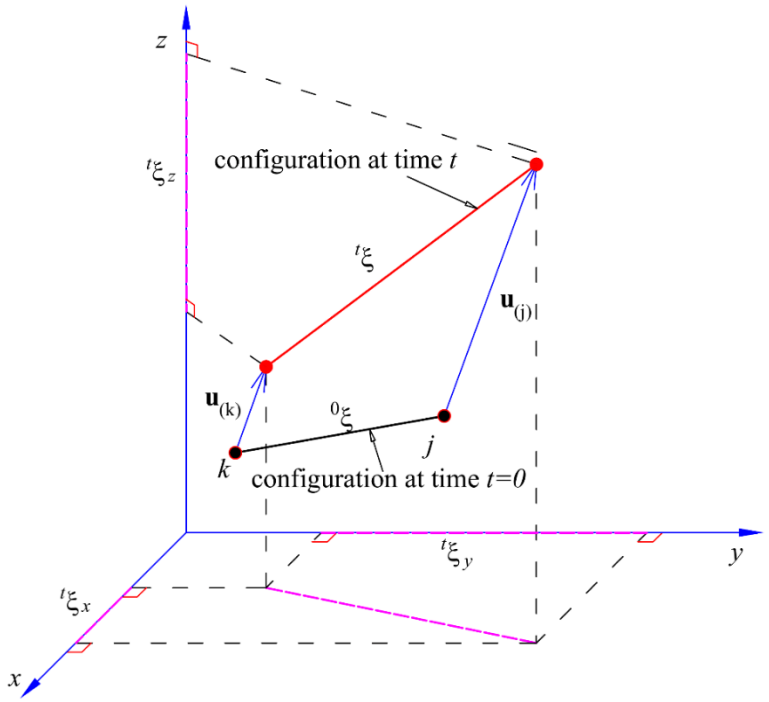

Fig. 3.1. Initial and deformed configuration of an interaction

In Eq. (3.4a), the linear form of stretch, ${}^t_0 s$, is defined according to [21] as

$$ {}^t_0 s = \frac{{}^t\xi - {}^0\xi}{{}^0\xi} \tag{3.5} $$

Similar to classical form, for small deformations, ${}^t_0 s \ll 1$, the logarithmic bond stretch reduces to its linear form as

$$ {}^t_0 s_H = \ln\left(1 + {}^t_0 s\right) \approx {}^t_0 s \tag{3.6} $$

The PD volumetric strain term in Eq. (3.3a) can be calculated as

$$ {}^t_0 \vartheta_{(k)} = d \sum_{j=1}^{N} {}^t_0 s_H \, {}^0 V_{(j)} \tag{3.7} $$

where d represents peridynamic constant.

By substituting strain energy density definitions provided in Eq. (3.3a) into Eq. (3.2), the force density components that material point j exerts on material point k can be represented as

$$ {}^t_0 \mathbf{t}_{(k)(j)} = \left(2ad \frac{1}{{}^0\xi} \left({}^t_0 \vartheta_{(k)} \right) + 2b \left({}^t_0 s_H \right) \right) \frac{{}^0\xi}{{}^t\xi} \frac{{}^t\boldsymbol{\xi}}{{}^t\xi} \tag{3.8} $$

Similarly, the force density components that material point k exerts on material point j can be represented as

$$ {}^t_0 \mathbf{t}_{(j)(k)} = -\left(2ad \frac{1}{{}^0\xi} \left({}^t_0 \vartheta_{(j)} \right) + 2b \left({}^t_0 s_H \right) \right) \frac{{}^0\xi}{{}^t\xi} \frac{{}^t\boldsymbol{\xi}}{{}^t\xi} \tag{3.9} $$

Note that the force densities given in Eqs. (3.8-3.9) are parallel to the deformed configuration and the term ${}^0\xi / {}^t\xi$ represents the ratio between initial and current bond lengths.

By substituting Eqs. (3.8-3.9) into Eq. (3.1), the nonlinear PD equation of motion can be obtained as

For 3D and 2D:

$$\rho\, {}^t\ddot{\mathbf{u}}_{(k)} = \sum_{j=1}^{N}\left(2ad\,\frac{1}{{}^0_{\xi}}\left({}^t_0\vartheta_{(k)} + {}^t_0\vartheta_{(j)} \right) + 4b\left({}^t_0 s_H \right) \right) \frac{{}^0\xi}{{}^t\xi}\frac{{}^t\boldsymbol{\xi}}{{}^t\xi}\, {}^0V_{(j)} + {}^t\mathbf{b}_{(k)} \tag{3.10}$$

For 1D:

$$\rho\, {}^t\ddot{u}_{(k)} = \sum_{j=1}^{N} 4b\left({}^t_0 s_H \right) \frac{{}^0\xi}{{}^t\xi}\frac{{}^t\xi_x}{{}^t\xi}\, {}^0V_{(j)} + {}^t b_{x(k)} \tag{3.11}$$

The PD constants, a and b, are determined by comparing the virtual values of strain energy density in PD and classical continuum mechanics based on the principle of virtual displacement provided in Eq. (C27) (Appendix C).

The peridynamic constants, a, b and d for 3D structures are obtained as (Appendix D1)

$$a = \frac{\lambda - \mu}{2};\ b = \frac{15}{2}\frac{\mu}{\pi\delta^4};\ d = \frac{9}{4\pi\delta^3} \tag{3.12}$$

where δ represents horizon size in the initial configuration, λ and μ represent Lame's constants

$$\lambda = \frac{E\nu}{(1+\nu)(1-2\nu)};\ \mu = \frac{E}{2(1+\nu)} \tag{3.13}$$

where E represents the elastic modulus and ν represents the Poisson's ratio.

The peridynamic constants, a, b and d for 2D structures are obtained as (Appendix D2)

$$a = \frac{\lambda\alpha - \mu}{2};\ b = \frac{6\mu}{\pi h\delta^3};\ d = \frac{2}{\pi h\delta^2} \tag{3.14}$$

where h represents the thickness of the plate in the initial configuration, α represents a constant which can be defined as

$$\alpha = \begin{cases} \dfrac{1-2\nu}{1-\nu} & \text{for plane stress} \\ 1 & \text{for plane strain} \end{cases} \tag{3.15}$$

As provided in Appendix D3, peridynamic constants for 1D structures can be obtained as

$$b = \frac{E}{2\left({}^0A \right)\delta^2} \tag{3.16}$$

where ${}^0A$ represents the cross-section area of the bar in the initial configuration.

Note that the PD constants provided in Eq. (3.12), Eq. (3.14), and Eq. (3.16) agree to those given in [44]. Therefore, it can be concluded that the key difference between PD formulations for small deformation problems and large deformation problems is the use of logarithmic bond stretch provided in Eq. (3.4). As a result, the change of bond length is included in the formulations of PD force densities as given in Eqs. (3.8-3.9).

3.2.2. Damage prediction

The nonlinear PD equations of motion given in Eqs. (3.10-3.11) can be rewritten as

$$\rho_{(k)}\,{}^t\ddot{\mathbf{u}}_{(k)} = \sum_{j=1}^{N} \psi_{(k)(j)}\,{}^t_0\mathbf{f}_{(k)(j)}\,{}^0V_{(j)} + {}^t\mathbf{b}_{(k)} \tag{3.17a}$$

with

$${}^t_0\mathbf{f}_{(k)(j)} = \begin{bmatrix} \left(2ad\,\frac{1}{{}^0\xi}\left({}^t_0\vartheta_{(k)} + {}^t_0\vartheta_{(j)}\right) + 4b\,{}^t_0s_H\right)\frac{{}^0\xi}{{}^t\xi}\frac{{}^t\xi_x}{{}^t\xi} \\ \left(2ad\,\frac{1}{{}^0\xi}\left({}^t_0\vartheta_{(k)} + {}^t_0\vartheta_{(j)}\right) + 4b\,{}^t_0s_H\right)\frac{{}^0\xi}{{}^t\xi}\frac{{}^t\xi_y}{{}^t\xi} \\ \left(2ad\,\frac{1}{{}^0\xi}\left({}^t_0\vartheta_{(k)} + {}^t_0\vartheta_{(j)}\right) + 4b\,{}^t_0s_H\right)\frac{{}^0\xi}{{}^t\xi}\frac{{}^t\xi_z}{{}^t\xi} \end{bmatrix} \text{ for 3D} \tag{3.17b}$$

$${}^t_0\mathbf{f}_{(k)(j)} = \begin{bmatrix} \left(2ad\,\frac{1}{{}^0\xi}\left({}^t_0\vartheta_{(k)} + {}^t_0\vartheta_{(j)}\right) + 4b\,{}^t_0s_H\right)\frac{{}^0\xi}{{}^t\xi}\frac{{}^t\xi_x}{{}^t\xi} \\ \left(2ad\,\frac{1}{{}^0\xi}\left({}^t_0\vartheta_{(k)} + {}^t_0\vartheta_{(j)}\right) + 4b\,{}^t_0s_H\right)\frac{{}^0\xi}{{}^t\xi}\frac{{}^t\xi_y}{{}^t\xi} \end{bmatrix} \text{ for 2D} \tag{3.17c}$$

$${}^t_0\mathbf{f}_{(k)(j)} = 4b\,{}^t_0s_H\,\frac{{}^0\xi}{{}^t\xi}\frac{{}^t\xi_x}{{}^t\xi} \text{ for 1D} \tag{3.17d}$$

where $\psi_{(k)(j)}$ is the damage parameter to represent the interaction state between material points k and j, which is given in Eq. (1.3) in Chapter 1.

Note that, the volumetric strain in PD for damage prediction can be updated by including the damage parameter, $\psi_{(k)(j)}$ as

$${}^t_0\vartheta_{(k)} = d\sum_{j=1}^{N} \psi_{(k)(j)}\,{}^t_0s_H\,{}^0V_{(j)} \tag{3.18}$$

Similar to the energy-based damage criteria used in Chapter 2 and 3, the state of interaction can be determined based on the critical energy rate as [25, 26]

$$\begin{aligned} &{}^t_0\bar{g}_{(k)(j)} < g^c \rightarrow \text{interaction exists: } \psi_{(k)(j)} = 1 \\ &{}^t_0\bar{g}_{(k)(j)} \geq g^c \rightarrow \text{interaction is broken: } \psi_{(k)(j)} = 0 \end{aligned} \tag{3.19}$$

where ${}_0^t\bar{g}_{(k)(j)}$ represents the average energy release rate for the interaction between material points k and j at time t. The parameter g_c represents the average critical energy release rate for one interaction which is presented in Chapter 1.

Similar to the formulation given in Chapter 1, the energy release rate for the interaction between material points k and j in Eq. (3.19) can be approximated as [25, 26]

$$ {}_0^t\bar{g}_{(k)(j)} = \frac{1}{A_{crack}}\left(\frac{1}{2}\left({}_0^t\Phi_{(k)(j)} + {}_0^t\Phi_{(j)(k)}\right)\right){}^0V_{(k)}\,{}^0V_{(j)} \tag{3.20} $$

where ${}_0^t\Phi_{(k)(j)}$ represents the micropotential at time t of the interaction between material points k and j in which material point j is a family member of material point k, ${}_0^t\Phi_{(j)(k)}$ represents the micropotential at time t of the interaction between material points j and k in which material point k is a family member of material point j. The term A_{crack} represents the unit crack surface which is described in Chapter 1.

As introduced by Madenci and Oterkus [25], [26] the micropotential ${}_0^t\Phi_{(k)(j)}$ can be calculated in the nonlinear analysis as

$$ {}_0^t\Phi_{(k)(j)} = \int_0^{{}_0^t s_{(k)(j)}} {}_0^t t_{(k)(j)}\,{}^0\xi\, ds = \int_{{}^0\xi}^{{}^t\xi} {}_0^t t_{(k)(j)}\, d\xi \tag{3.21a} $$

with

$$ {}_0^t t_{(k)(j)} = \begin{cases} 2b\,{}_0^t s_H \dfrac{{}^0\xi}{{}^t\xi} & \text{for 1D structures} \\ \left(ad\,\dfrac{1}{{}^0\xi}\left({}_0^t\vartheta_{(k)} + {}_0^t\vartheta_{(j)}\right) + 2b\,{}_0^t s_H\right)\dfrac{{}^0\xi}{{}^t\xi} & \text{for 2D and 3D structures} \end{cases} \tag{3.21b} $$

The integration in Eq. (3.21a) can be numerically calculated as

$$ {}_0^{t+\Delta t}\Phi_{(k)(j)} = {}_0^t\Phi_{(k)(j)} + \Delta\Phi_{(k)(j)} \tag{3.22} $$

where ${}_0^t\Phi_{(k)(j)}$ and ${}_0^{t+\Delta t}\Phi_{(k)(j)}$ represent micropotentials at the time step t and $t + \Delta t$, respectively. The term $\Delta\Phi_{(k)(j)}$ represents the incremental value of micropotential from time t to time $t + \Delta t$, which can be calculated as

$$ \Delta\Phi_{(k)(j)} = \frac{1}{2}\left({}_0^{t+\Delta t}t_{(k)(j)} - {}_0^t t_{(k)(j)}\right)\left({}^{t+\Delta t}\xi - {}^t\xi\right) \tag{3.23} $$

where the terms ${}_0^t t_{(k)(j)}$ and ${}_0^{t+\Delta t}t_{(k)(j)}$ represent the force densities, as given in Eq. (3.8), at time t and $t + \Delta t$, respectively.

3.2.3. Numerical results

In this section, first, the developed nonlinear PD model is verified by considering various examples of 1D, 2D, and 3D structures. For verification purposes, the proposed PD model is compared to FEA solutions. The explicit time integration is

used in the PD solution by using the ADR method as discussed in Appendix A [76, 77]. In the PD solution, the horizon size $\delta = 3.015\Delta x$ is used. The FEA solutions are conducted by using ANSYS commercial software with LINK180 element for the 1D bar, PLANE182 element for 2D plates, and SOLID185 element for 3D structures. Next, damage predictions on a steel plate subjected to dynamic loading, an L-shape plate subjected to large deformations, and on a concrete beam in three points bending test are presented.

3.2.3.1. Large deformations in a 1D structure

To verify the proposed PD model for one dimension, a bar with a cross-sectional area $A = 0.1 \times 0.1\ \mathrm{m}^2$ with a length of $L = 1\ \mathrm{m}$ subjected to axial loading is investigated as shown in Fig. 3.2. The bar is made of steel with Young's modulus $E = 2 \times 10^{11}\ \mathrm{N/m}^2$. The bar is subjected to two different loading conditions which are a tensile load of $F_x = 5 \times 10^8$ N and a compressive load of $F_x = -5 \times 10^8$ N.

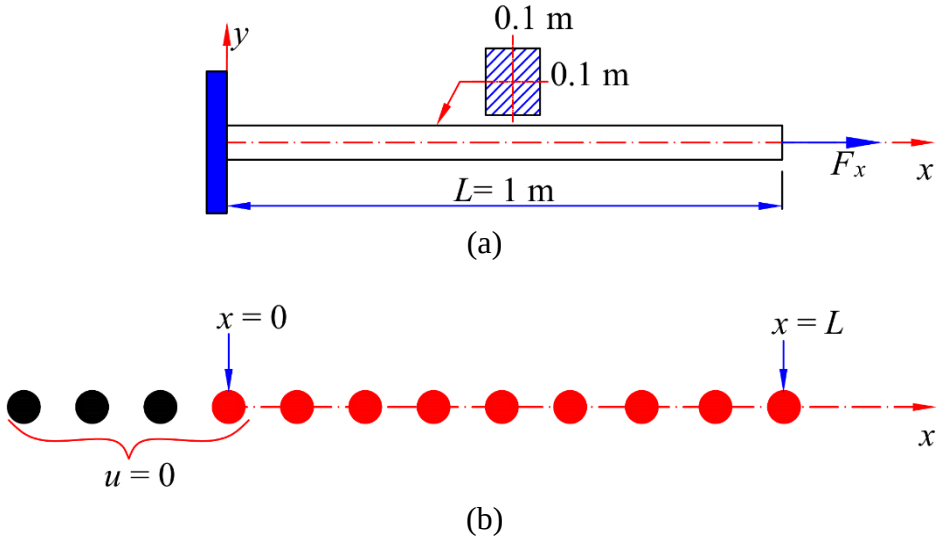

Fig. 3.2. Bar subjected to axial loading (a) geometry, (b) PD model discretization

In the peridynamic model, the bar is discretized with uniform 100 integration points. To implement the fixed end, three fictitious points [26, 95] are added as shown in Fig. 3.2(b) and displacements of these fictitious points and a material point located at $x = 0$ are set equal to zero. The red points represent the material points in the real region, on the other hand, black points represent the material points in the fictitious region as shown in Fig. 3.2(b). In the FEA model, the bar is discretized with 100 elements by using the link180 element. In both loading conditions, the constant body force ${}^{t}b_x = F_x / {}^{0}V$ is applied to the material point located at $x = L$.

Fig. 3.3 shows the displacement variations along the bar. As can be seen from Fig. 3.3(a), under tensile loading, the displacement of the bar in nonlinear cases is much larger than in the linear case. On the other hand, in the compressive loading condition, the nonlinear cases provide much smaller displacement values than those captured in the linear case as shown in Fig. 3.3(b). It can be observed that results captured in nonlinear PD analysis match very well with the results in nonlinear FEA.

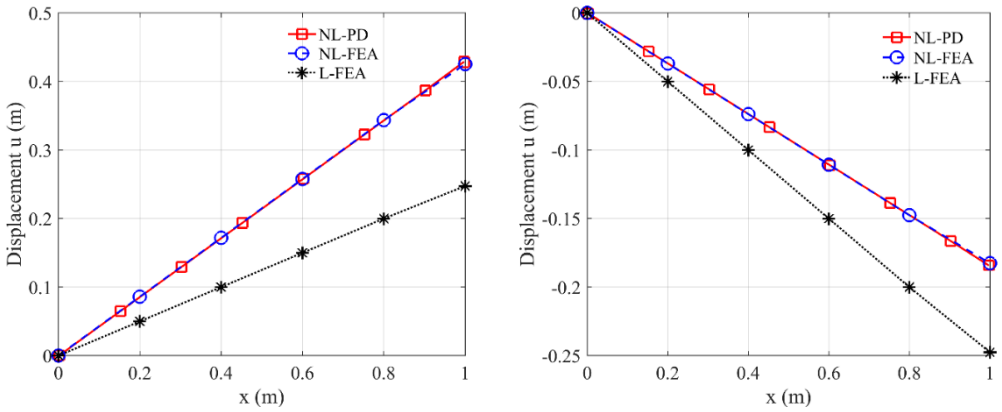

Fig. 3.3. Displacements of material points along the bar subjected to axial load: (a) $F_x = 5 \times 10^8 N$, (b) $F_x = -5 \times 10^8 N$ (L: linear, NL: nonlinear)

To further verify the developed 1D nonlinear PD model, the bar described in Fig. 3.2 is further investigated by applying various tensile forces. Fig. 3.4 shows the displacement variation of the material point located at $x = 1$ m. As can be seen from the figure, when the applied force is large, deformations observed in nonlinear and linear analyses have significant differences, and the results captured by the developed nonlinear PD model match very well with nonlinear FEA results.

Table 3.1 shows the comparison between nonlinear PD and nonlinear FEA displacement results at $x = 0.5$ m. The relative error between the two results is calculated as

$$Error\,(\%) = \left| \frac{u^{NL-PD} - u^{NL-FEA}}{u^{NL-FEA}} \right| \times 100 \tag{3.24}$$

As can be seen from Table 3.1, the relative errors between nonlinear PD and nonlinear FEA results are less than 0.5% for all loading cases. Therefore, it can be concluded that the developed PD model for large deformation analysis of one-dimensional structure is verified.

Table 3.1. Comparison between nonlinear PD and nonlinear FEA results

$F_x(N)$	$u^{NL-FEA}(m)$	$u^{NL-PD}(m)$	$Error\ (\%)$
1.0E+07	0.00252	0.00253	0.335%
4.0E+07	0.01299	0.01303	0.331%
1.0E+08	0.02706	0.02715	0.326%
2.0E+08	0.05916	0.05935	0.316%
3.0E+08	0.09829	0.09859	0.310%
4.0E+08	0.14785	0.14833	0.323%
4.0E+08	0.21442	0.21529	0.406%

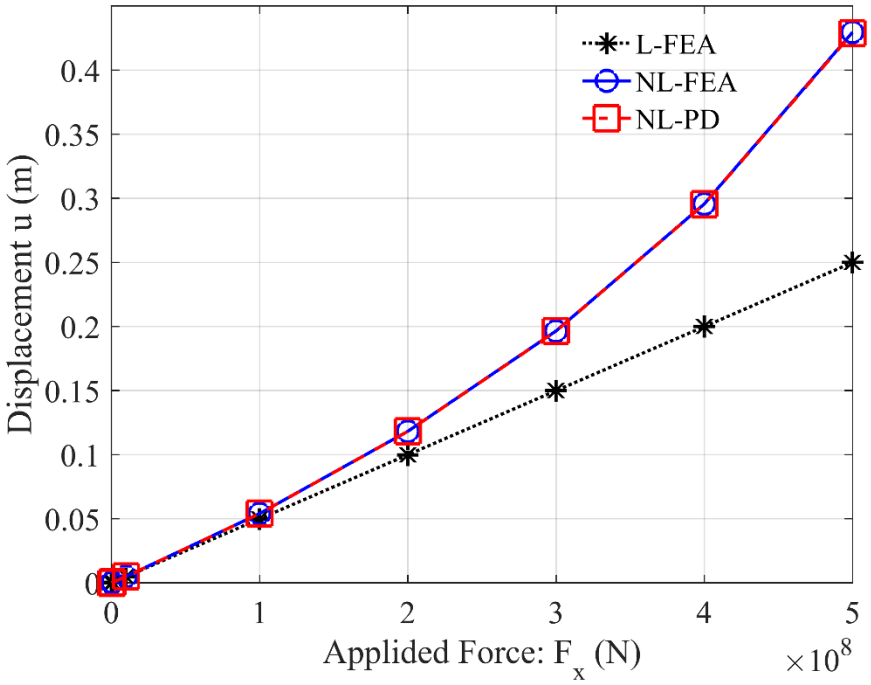

Fig. 3.4. Variation of displacement of the material point located at $x = 1$ m versus applied forces (L: linear, NL: nonlinear)

3.2.3.2. Large deformations in 2D structures

To verify the developed 2D nonlinear PD model, a square plate with $L = W = 1$ m and thickness of $h = 0.01$ m is investigated as shown in Fig. 3.5. The plate is made of steel with Young's modulus $E = 2 \times 10^{11}$ N/m^2 and Poisson's ratio $\nu = 0.27$. The plate is fixed on the left edge. The plate is investigated in two different loading conditions as shown in Fig. 3.5. In each loading condition, the plate is investigated for both plane strain and plane stress conditions.

To apply boundary conditions on the left edge, three fictitious layers of material points are added in the discretized model in PD as shown in Fig. 3.5(c) and all degrees of freedom of these fictitious points and material points located at $x = 0$ are set equal to zero. The plate is discretized with mesh size $\Delta x = L/100$ in both PD and FEA models.

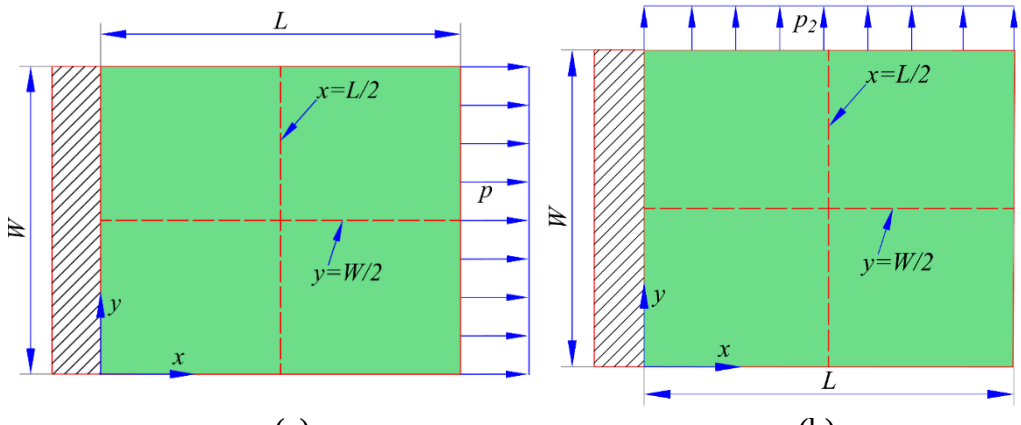

(a) (b)

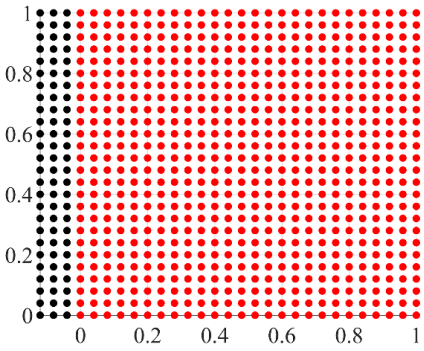

(c)

Fig. 3.5. Plate subjected to large deformations (a): tensional loading, (b): shear loading, (c): PD model discretization

Plate subjected to tensile loading

In this problem, the plate is subjected to the constant pressure, $p = 5 \times 10^{10}$ N/m^2 normal to the surface on the right edge of the plate as shown in Fig. 3.5(a). In the PD model, the loading condition is applied to the material points located at $x = L$ by converting the constant pressure to body forces. Details of the implementation of loading conditions are presented in Appendix D4.2.

Plane strain condition:

Fig. 3.6 and Fig. 3.7 present the variations of displacement components of the plate for the plane strain condition. As can be seen from the figures, the PD and nonlinear FEA prediction results match very well.

Fig. 3.8 shows the comparison between nonlinear PD and nonlinear FEA results for the variations of displacement components along two centrelines $x = L/2$ and $y = W/2$. Fig. 3.8(a) represents the horizontal displacements at $x = L/2$ and Fig. 3.8(b) represents the vertical displacements at $y = W/2$. As can be seen from the results, PD and nonlinear FEA solutions agree very well, and there is a big difference between linear FEA and nonlinear solutions.

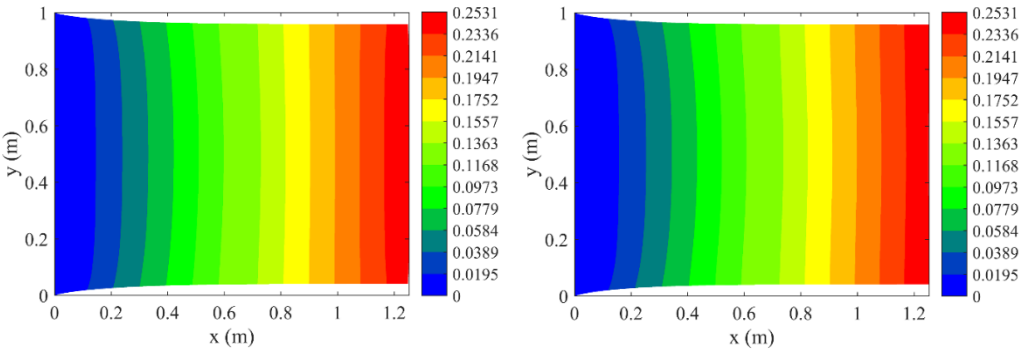

(a) (b)

Fig. 3.6. Variation of horizontal displacements, u in (a) nonlinear PD; (b) nonlinear FEA in the deformed configuration

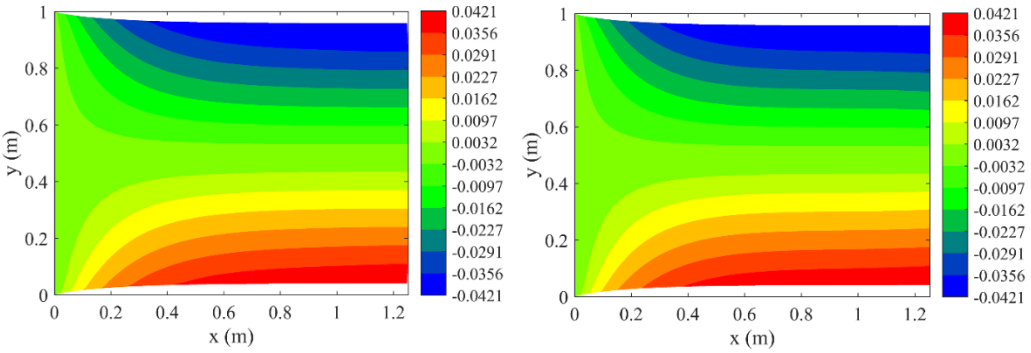

(a) (b)

Fig. 3.7. Variation of vertical displacements, v in (a) nonlinear PD; (b) nonlinear FEA in the deformed configuration

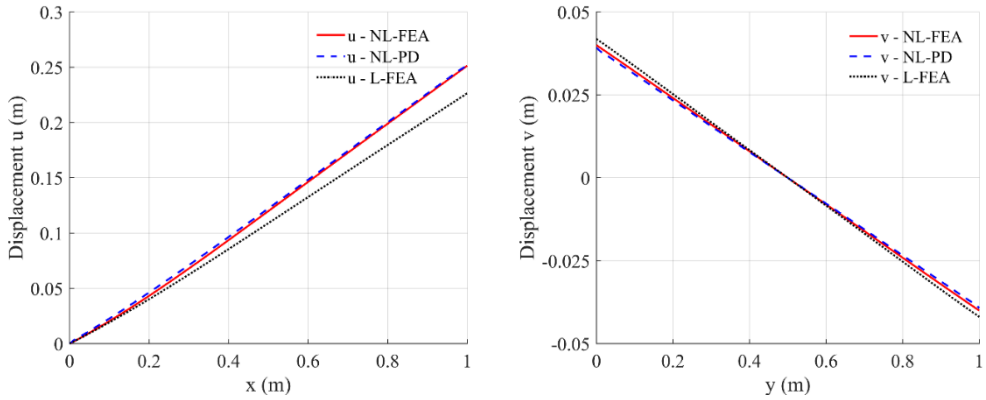

(a) (b)

Fig. 3.8. Variations of displacements (a) u along $y = W/2$; (b) v along $x = L/2$ (L: linear, NL: nonlinear)

Plane stress condition:

Fig. 3.9-Fig. 3.11 represent the variations of displacement components of the plate for plane stress conditions. Similar to the plane strain problem, the variations of displacement components along the centre lines are investigated. It is observed that the results provided by the developed PD model have good agreement with those captured in nonlinear FEA.

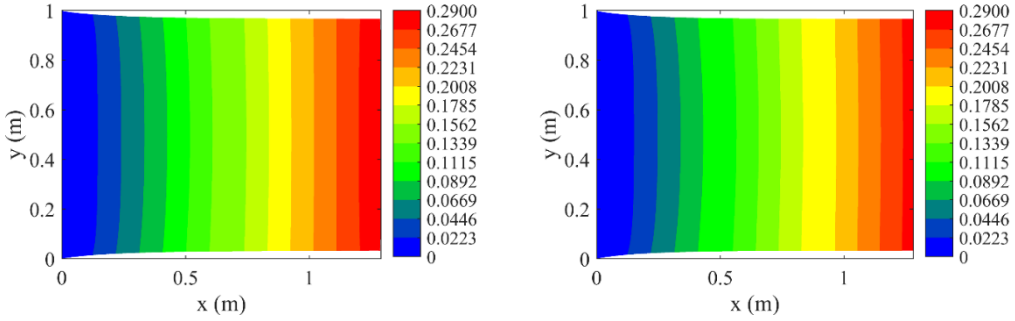

(a) (b)

Fig. 3.9. Variation of horizontal displacements, u in (a) nonlinear PD; (b) nonlinear FEA in the deformed configuration

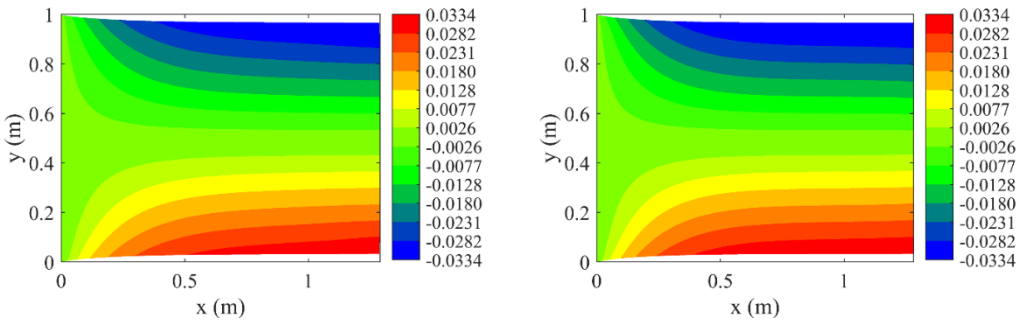

(a) (b)

Fig. 3.10. Variation of vertical displacements, v in (a) nonlinear PD; (b) nonlinear FEA in the deformed configuration

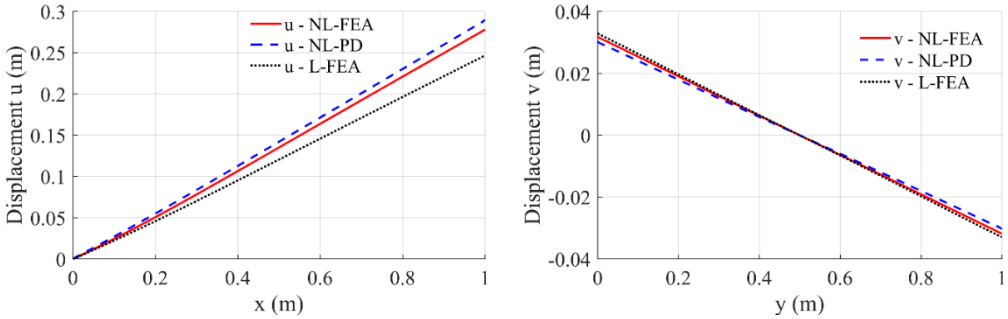

(a) (b)

Fig. 3.11. Variations of displacements (a) u along $y = W/2$; (b) v along $x = L/2$ (L: linear, NL: nonlinear)

Plate subjected to shear loading

In this problem, the plate is subjected to the uniform pressure $p_2 = 1.3 \times 10^{10}$ N/m^2 normal to the surface on the top edge as shown in Fig. 3.5(b). In the PD model, the loading condition is applied to the material points located at $y = W$ by converting the constant pressure to body forces. Details of the implementation of loading conditions are presented in Appendix D4.2.

Plane strain condition

Fig. 3.12-4.22 present the results for the plane strain condition. As can be seen from Fig. 3.12 and Fig. 3.13, the variations of displacements u and v captured in PD and FEA solutions have a very good agreement. Moreover, as presented in Fig. 3.14 and Fig. 3.15, the results captured by the developed PD model agree very well with those in nonlinear FEA whereas a significant difference between linear and nonlinear results is observed.

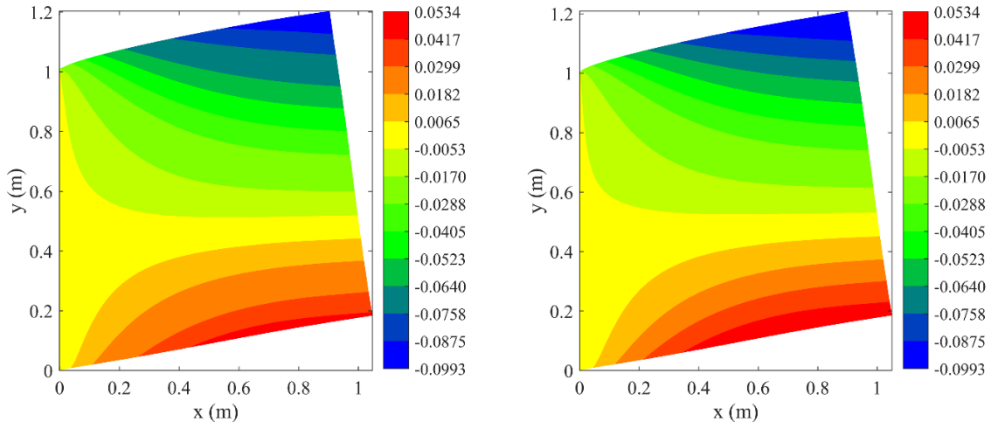

(a) (b)

Fig. 3.12. Variation of horizontal displacements, u in (a) nonlinear PD; (b) nonlinear FEA in the deformed configuration

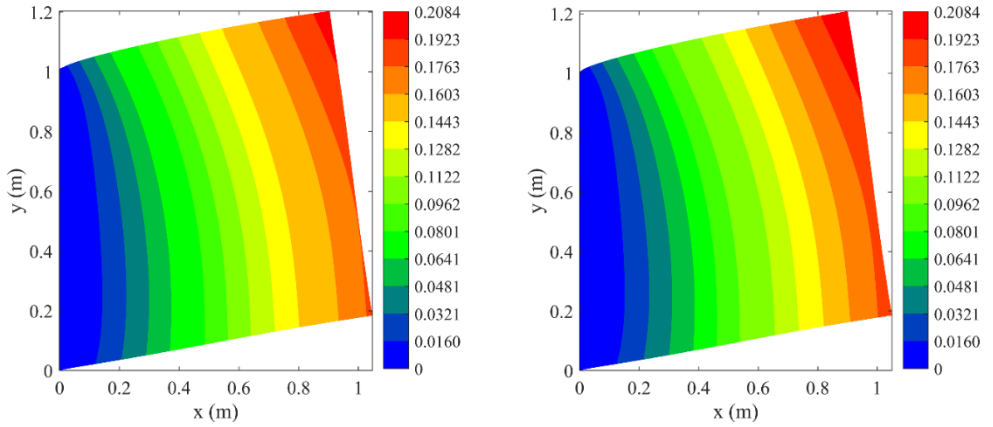

(a) (b)

Fig. 3.13. Variation of vertical displacements, v in (a) nonlinear PD; (b) nonlinear FEA in the deformed configuration

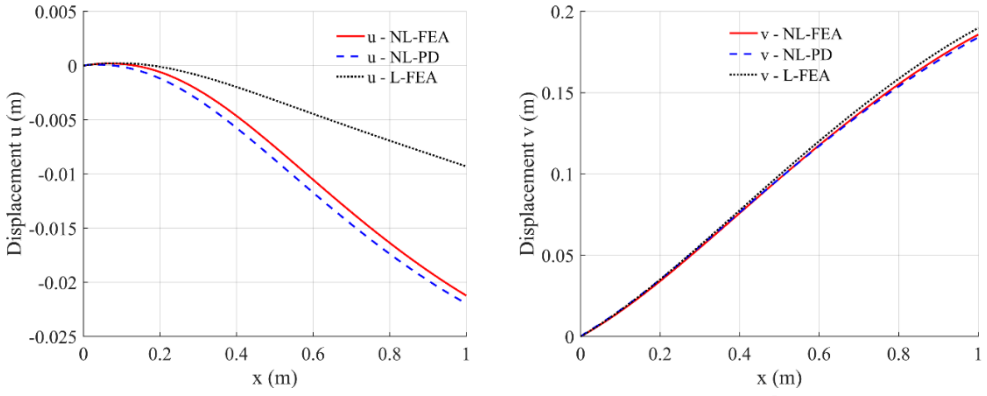

(a) (b)

Fig. 3.14. Variations of displacement components (a) u, (b) v at $y = W/2$ (L: linear, NL: nonlinear)

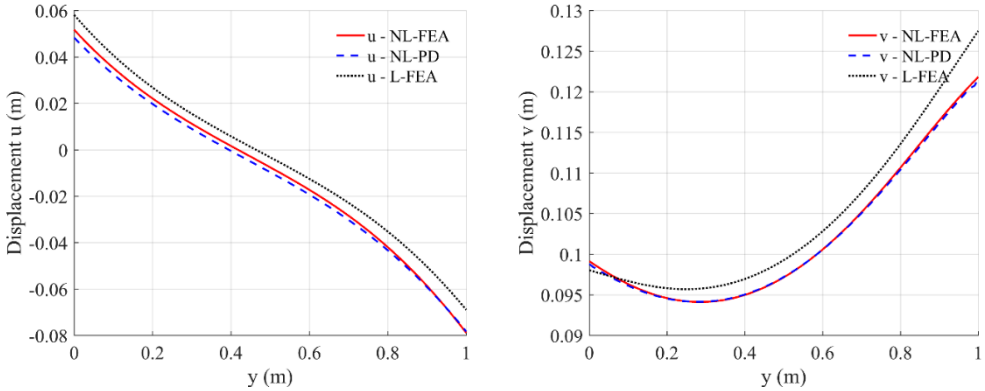

(a) (b)

Fig. 3.15. Variations of displacement components (a) u, (b) v along $x = L/2$

Plane stress condition

Fig. 3.16-Fig. 3.19 present the results for the plane stress condition. As can be seen from the figures, the results in nonlinear PD and nonlinear FEA solutions match very well. Therefore, it can be concluded that the accuracy of the developed 2D nonlinear PD model is verified.

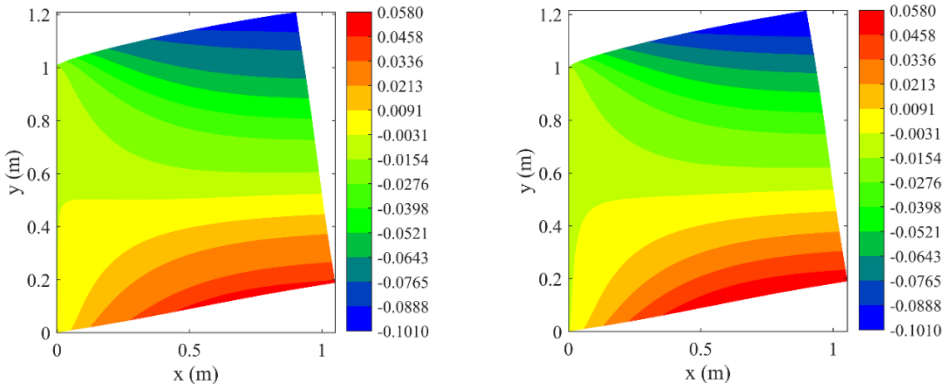

(a) (b)

Fig. 3.16. Variation of displacement, u in (a) nonlinear PD; (b) nonlinear FEA in the deformed configuration

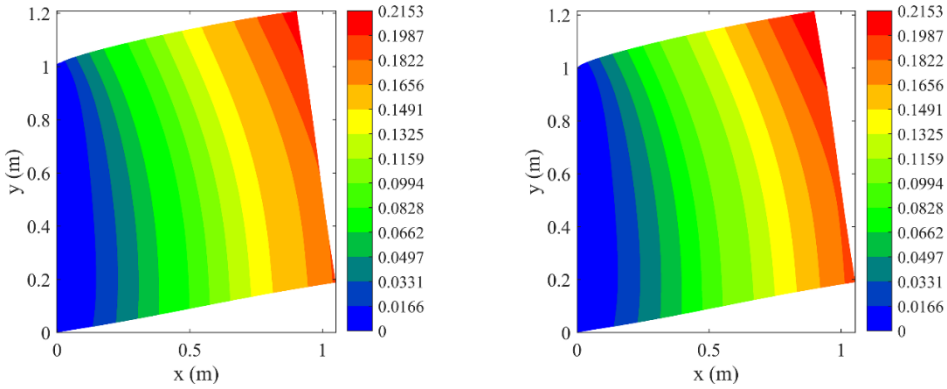

(a) (b)

Fig. 3.17. Variation of displacement, v in (a) nonlinear PD; (b) nonlinear FEA in the deformed configuration

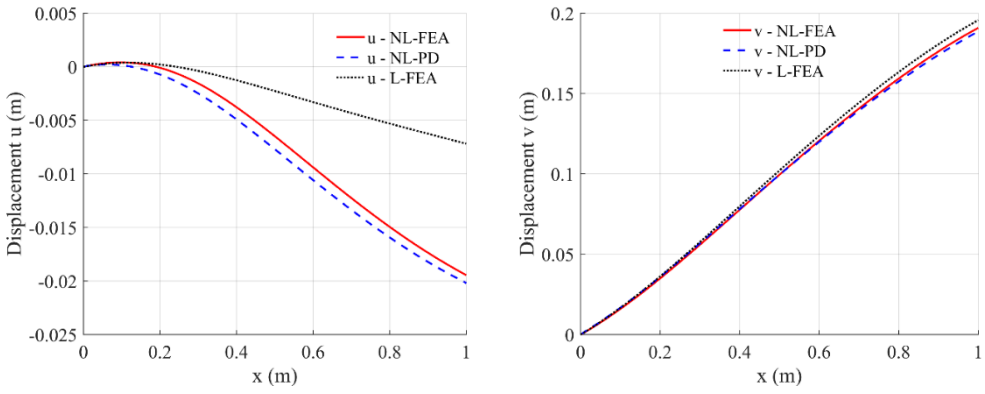

(a) (b)

Fig. 3.18. Variations of displacement components (a) u, (b) v along $y = L/2$ (L: linear, NL: nonlinear)

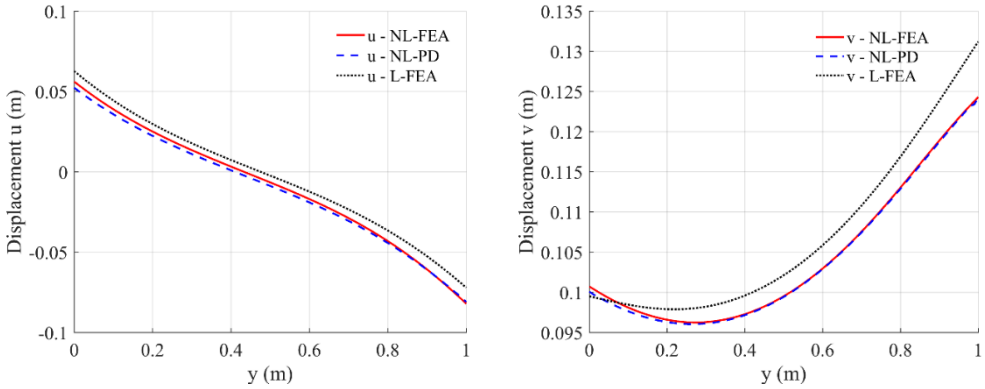

(a) (b)

Fig. 3.19. Variations of displacement components (a) u, (b) v along $x = L/2$ (L: linear, NL: nonlinear)

For further comparison, the displacements at $(x = 3L/4, y = 3W/4)$ obtained from nonlinear PD and nonlinear FEA are compared as shown in Table 3.2. As can be seen from the table, the relative errors between the results are less than 5% for all loading conditions. Therefore, the accuracy of the developed nonlinear PD model for 2D structures is verified for both plane stress and plane strain conditions.

Table 3.2. Comparison of displacements for a material point located at $(x = 3L/4, y = 3W/4)$

		u^{NLFEA} (m)	u^{NLPD} (m)	$Error$ (%)	v^{NLFEA} (m)	v^{NLPD} (m)	$Error$ (%)
Plate subjected to tensile loading	Plane strain	0.2531	0.2485	1.8%	-0.0421	-0.0416	1.2%
	Plane stress	0.2792	0.2862	2.5%	-0.0334	-0.0334	0.0%
Plate subjected to shear loading	Plane strain	-0.0993	-0.0959	3.4%	0.2084	0.2029	2.6%
	Plane stress	-0.101	-0.0969	4.0%	0.2153	0.209	2.9%

Table 3.3 shows the information in terms of computational time in nonlinear PD and nonlinear FEA simulations. The PD and FEA simulation time for the problem of the plate under tension in the plane strain condition with different mesh sizes is considered. As mentioned in the first paragraph of Section 3.2.3, the ADR method with the explicit time integration scheme is used for the nonlinear PD simulations. The PD codes are written using Matlab 2018b. On the other hand, nonlinear FEA simulations are conducted by using ANSYS with the implicit solver.

As can be observed from Table 3.3, the number of iterations required to obtain converged solutions, N_t, in the nonlinear PD simulations are much higher than those in the nonlinear FEA. In PD, the simulation with a finer mesh requires more iterations to obtain the converged solution. Specifically, for the PD model with 50×50 material points, the required number of iterations is 600. For the PD model with 150×150 material points, this number is 2000. In FEA, since the implicit solver is used, the FEA simulations converged after 100 iterations for all mesh sizes. As a result, the running time for nonlinear PD simulations is much higher than those of nonlinear FEA.

However, it is also observed that the time per iteration in nonlinear PD simulation is less than those in nonlinear FEA. The reason is that the nonlinear PD uses the explicit integration scheme meanwhile the nonlinear FEA uses the implicit solver which requires the solutions for large linear and nonlinear stiffness matrices.

Table 3.3. Computational time in NL-PD and NL-FEA for 2D plane strain problems

Number of material points (nodes)	50x50			100x100			150x150		
	N_t	Time: t (s)	Time per iteration: t/N_t (s)	N_t	Time: t (s)	Time per iteration: t/N_t (s)	N_t	Time: t (s)	Time per iteration: t/N_t (s)
NL PD explicit using ADR method	600	49.47	0.0825	1200	306.58	0.2555	2000	1134	0.5670
NL FEA implicit using ANSYS	100	15.77	0.1577	100	36.49	0.3649	100	78.96	0.7896
N_t: number of iterations to obtain converged solution.									

3.2.3.3. Large deformations in 3D structures

To verify the proposed PD model for 3D structures, a 3D beam subjected to constant shear force is investigated as shown in Fig. 3.20. The dimensions of the beam are $L \times B \times H = 1 \times 0.1 \times 0.1\ \mathrm{m}^3$ and it is made of steel with Young's modulus $E = 2.06 \times 10^{11}\ \mathrm{N/m}^2$ and Poisson's ratio $\nu = 0.3$. The structure is subjected to a distributed force $f_z = -1 \times 10^8\ \mathrm{N/m}$ at the right end as shown in Fig. 3.20.

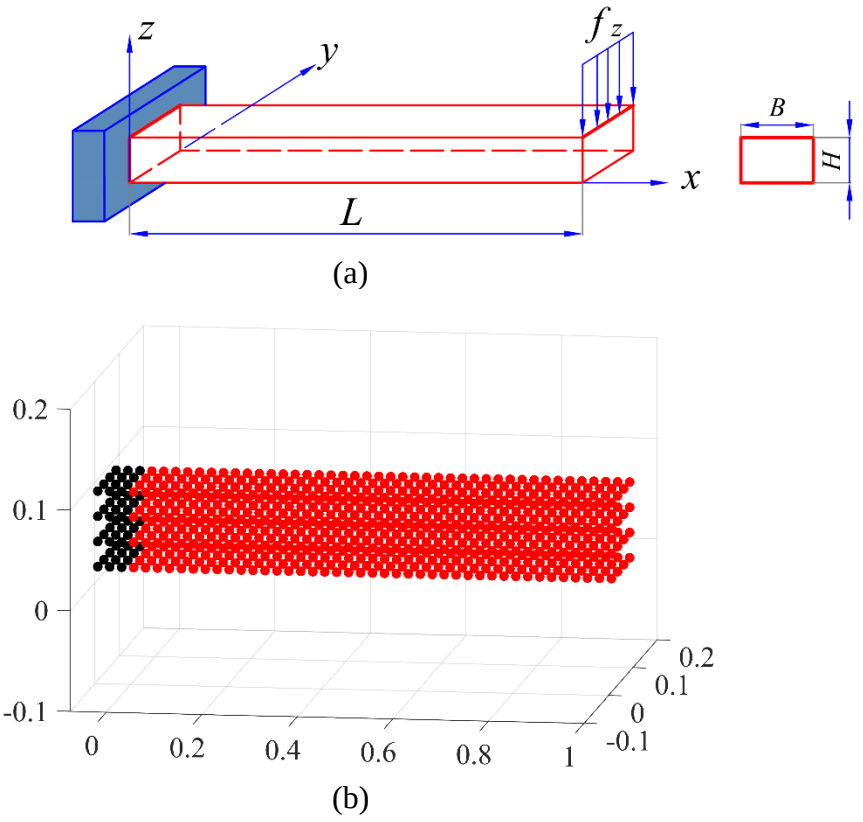

Fig. 3.20. 3D beam subjected to static loading (a) geometry, (b) PD model discretization

In the peridynamic model, the 3D beam is discretized with uniform $101 \times 10 \times 10$ material points. In the FEA model, the same mesh size is used. To apply boundary conditions, three fictitious layers of material points are added as shown in Fig. 3.20(b) and displacements of these fictitious points and material points located at $x = 0$ are set equal to zero. As shown in Fig. 3.20(b), red points represent the material points in the real region, on the other hand, black points represent the material points in the fictitious region. In the PD model, the loading condition is applied to the material points located at $x = L, 0 \leq y \leq B, z = H$ as body forces. The details of applying loading conditions in PD simulation are presented in Appendix D4.3.

Fig. 3.21-Fig. 3.23 show the displacement variations along the beam. The PD predictions are compared with nonlinear and linear FEA results. As shown in Fig. 3.21 for the variation of displacement u, both the nonlinear PD model and nonlinear FEA provide similar results, meanwhile, the linear FEA results are completely different. The maximum displacement captured by linear FEA is almost 8 times larger than nonlinear PD and FEA solutions. Moreover, the variation of displacement v along the beam captured by linear FEA is completely different from the nonlinear PD and FEA results as shown in Fig. 3.22. In Fig. 3.23, it is observed that the maximum displacement w of the beam captured by linear FEA solution is two times larger than the maximum deflection captured by nonlinear solutions. As can be seen from the results, the developed 3D nonlinear PD model and nonlinear FEA solution show very good agreement for all displacement components.

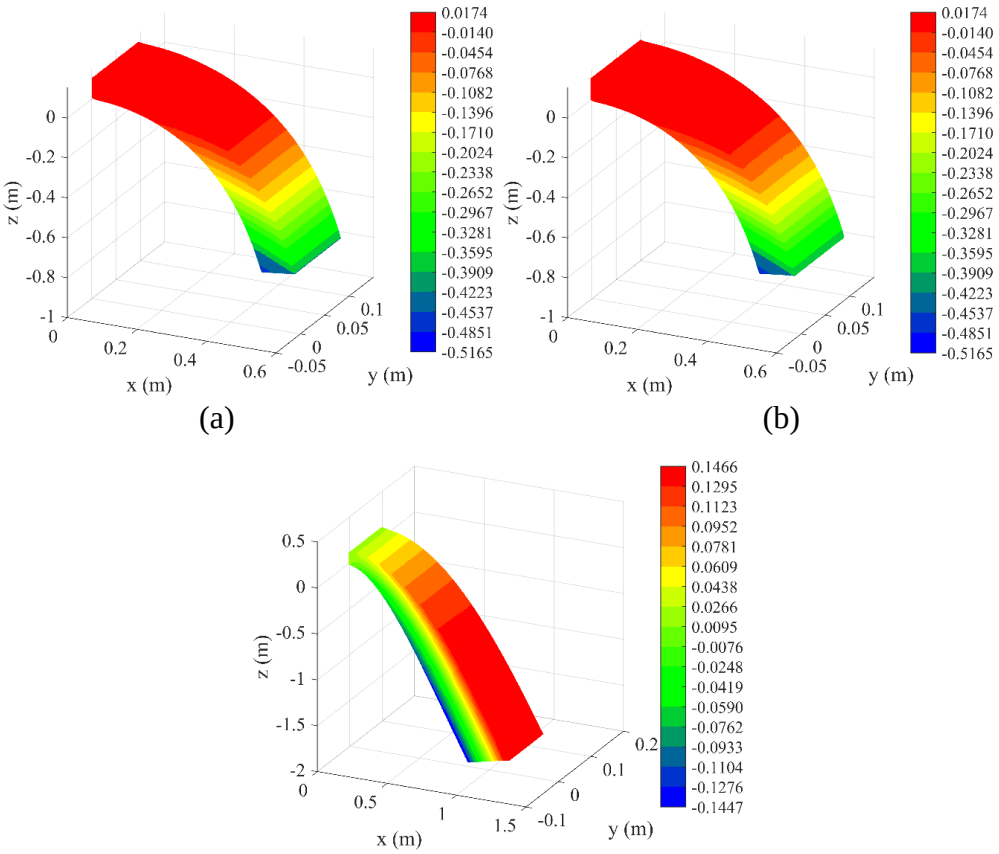

Fig. 3.21. Variations of displacement component u (m) in (a) nonlinear PD; (b) nonlinear FEA; (c) linear FEA results in the deformed configuration

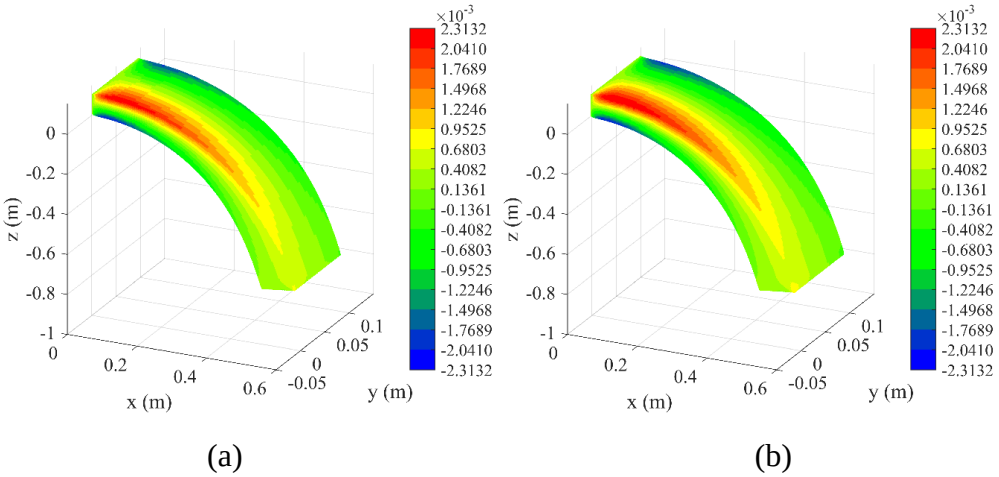

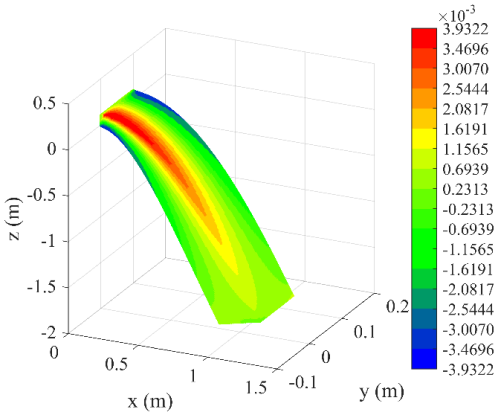

(c)

Fig. 3.22. Variations of displacement component v (m) in (a) nonlinear PD; (b) nonlinear FEA; (c) linear FEA results in the deformed configuration

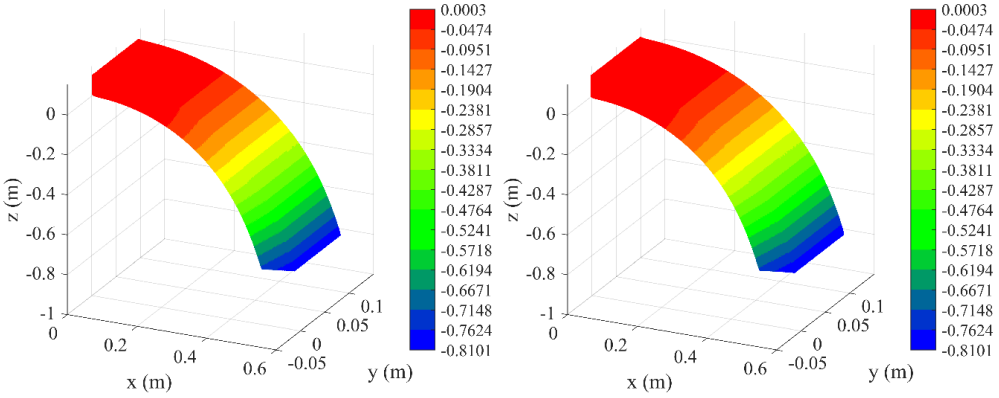

(a) (b)

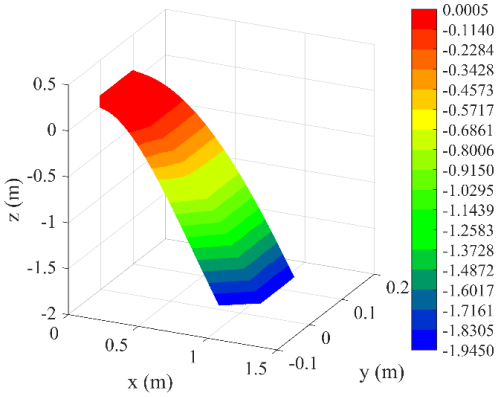

(c)

Fig. 3.23. Variations of displacement component w (m) in (a) nonlinear PD; (b) nonlinear FEA; (c) linear FEA results in the deformed configuration

Similar to previous examples, for further comparison, the nonlinear PD and nonlinear FEA displacements at $(x = 3L/4, y = 3B/4, z = 3H/4)$ are compared as shown in Table 3.4. It is found that the relative errors for all displacement

components are smaller than 1%. Therefore, it can be concluded that the accuracy of the developed 3D nonlinear PD model is verified.

Table 3.4. Comparison of displacements for a material point located at ($x = 3L/4, y = 3W/4$)

Displacement: u (m)	u^{NLFEA}	u^{NLPD}	*Error* (%)
	-0.248143	-0.248328	0.07%
Displacement: v (m)	v^{NLFEA}	v^{NLPD}	*Error* (%)
	-0.000131	-0.000130	0.70%
Displacement: w (m)	w^{NLFEA}	w^{NLPD}	*Error* (%)
	-0.534627	-0.539694	0.95%

3.2.3.4. Damage prediction in 2D plate

After verifying the accuracy of the developed nonlinear PD model for 2D structures, in this section, damage on a plate is predicted. The experiment presented by Kalthoff [87], [91], Kalthoff and Winkler [92] for a pre-notched plate subjected to dynamic load is simulated by using the developed PD model.

Since the problem is symmetric, only the upper haft plate is modelled as shown in Fig. 3.24. The plate with $L = W = 0.1$ m and thickness of $h = 0.009$ m is investigated [87]. The plate is made of steel with Young's modulus $E = 2 \times 10^{11}$ N/m^2, Poisson's ratio $\nu = 0.27$. The fracture toughness of steel is $K_{Ic} = 70 \times 10^6$ Nm$^{-3/2}$[87]. For simplification, the critical energy release rate of the material is calculated as $G_c = G_{\mathrm{I}c} = K_{Ic}^2/E = 22714$ J/m^2.

The left edge which is under the crack surface is subjected to velocity conditions as [96, 97]

$$|\mathbf{v}| = \begin{cases} \dfrac{t}{t_0} v_0 & \text{for } t \le t_0 \\ v_0 & \text{for } t > t_0 \end{cases} \tag{3.25}$$

with $v_0 = 16.5$ m/s, $t_0 = 1\ \mu s$.

The plate is considered in the plane stress condition and it is discretized into 200×200 material points. The horizon size is $\delta = 3.015\Delta x$. The problem is simulated using the dynamic explicit time integration scheme with the time step $0.01\ \mu s$ and the total simulation time of $80 \mu s$.

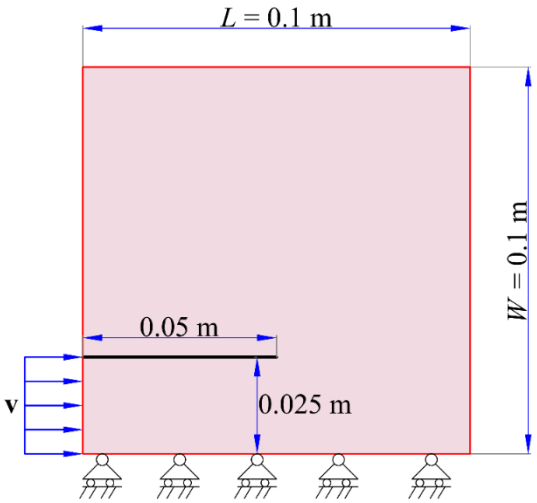

Fig. 3.24. The geometry and symmetrical boundary conditions for the Kalthoff experiment

Fig. 3.25 presents the crack evolution at different times captured by the nonlinear PD model with the horizon size of $\delta = 3.015\Delta x$. As shown in Fig. 3.25, the crack starts branching up 70.2^o with respect to the horizontal axis at $t = 30\ \mu s$. As time progresses, the crack continues propagating in the same direction and the crack reaches the top edge of the plate at $t = 80\ \mu s$.

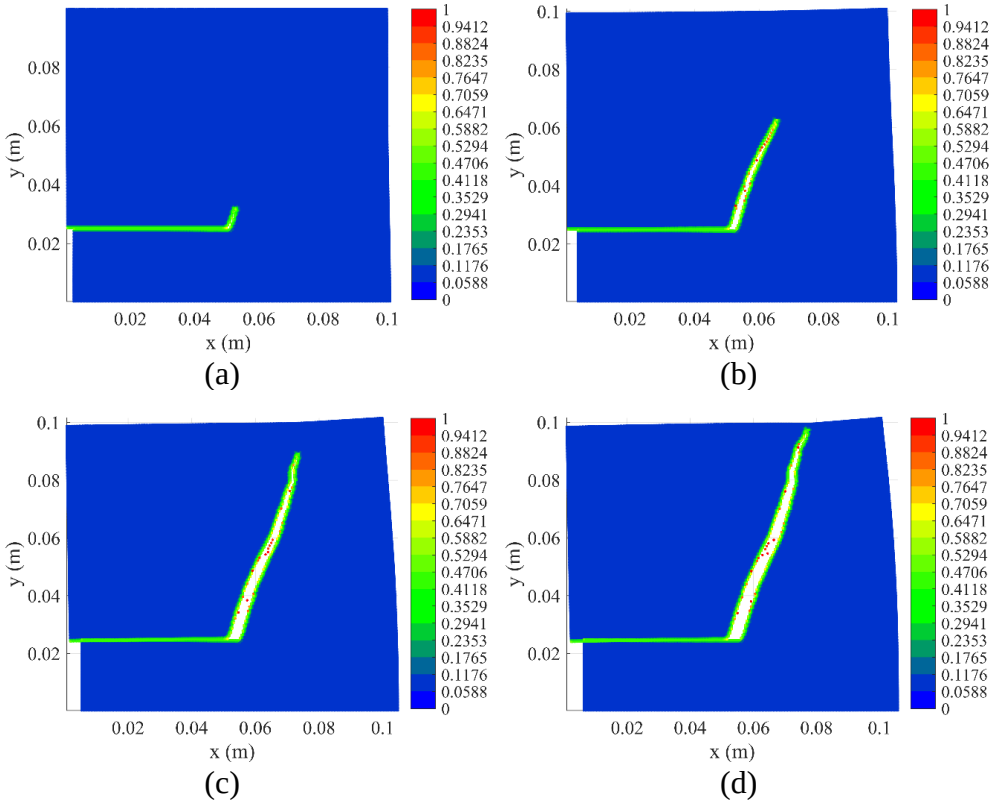

Fig. 3.25. Crack evolution at different times (a) $t = 30\ \mu s$, (b) $t = 50\ \mu s$, (c) $t = 70\ \mu s$, (d) $t = 80\ \mu s$ (displacements are magnified by 5 for the deformed configuration)

Fig. 3.26 shows the $\delta-$convergence study in terms of the crack path. In this convergence study, the nodal density is kept constant ($m = \delta/\Delta x = 3$) [98-100], meanwhile the horizon size is taken as smaller and smaller ($\delta \to 0$) [98-100]. As can be seen from Fig. 3.26(c-d), when the horizon size is small the predicted crack paths are 70.2^o with respect to the horizontal axis and it agrees very well with the experimental observations in [87, 91, 92], which is around 70^o.

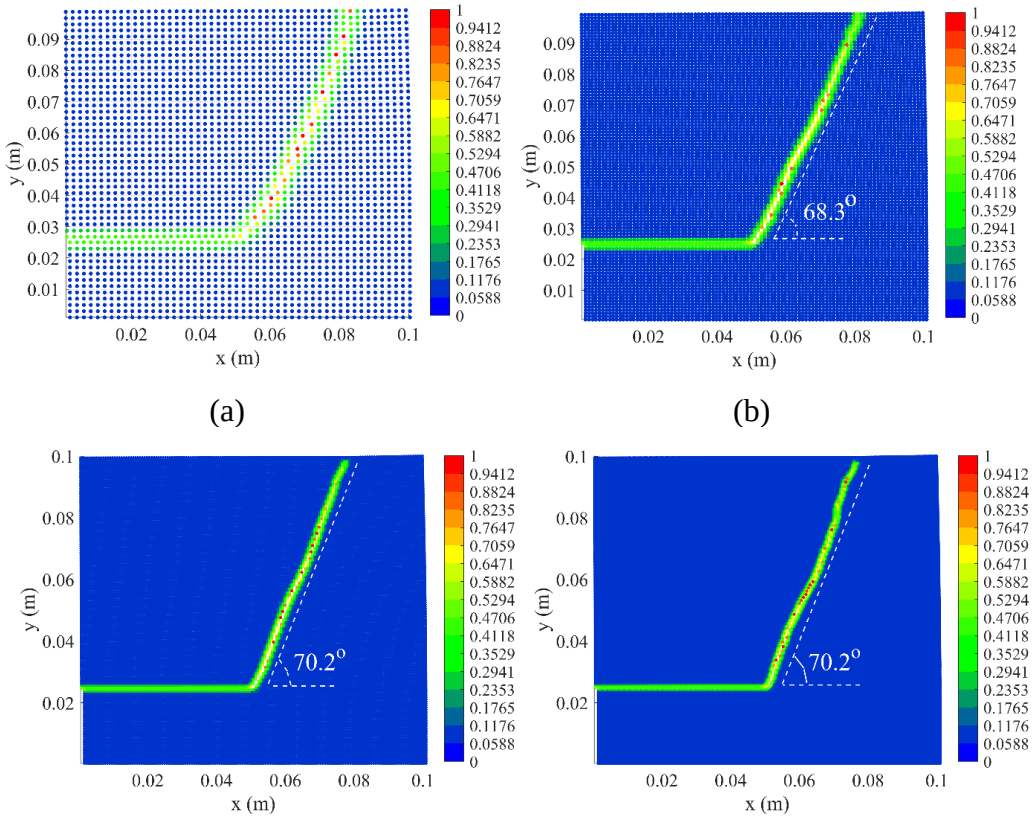

Fig. 3.26. $\delta-$convergence in terms of crack paths with $m = \delta/\Delta x = 3$ and horizon size (a): $\delta = 0.006$ m, (b): $\delta = 0.003$ m, (c): $\delta = 0.002$ m, (d): $\delta = 0.0015$ m

3.2.3.5. Damage prediction for an L-shape plate subjected to large deformation

In this section, damage in an L-shape plate subjected to large deformation, as shown in Fig. 3.27, is predicted. The L-shape plate has dimensions of $L = 10$ m, $W = 2$ mand thickness of $h = 0.1$ m. The material has Young's modulus of $E = 1.0667 \times 10^4$ N/m^2, Poisson's ratio of $\nu = 0.333$ and critical energy release rate of $G_c = 2.7 \times 10^3$ J/m^2 [101]. The bottom edge of the plate is fixed, and the right edge of the plate is attached to a stiff plate, shown in blue in Fig. 3.27.

In the PD model, plane stress condition is considered. Similar to Section 4.4.2, to apply boundary conditions, three fictitious layers of material are generated at the bottom, and all displacement components of the fictitious material points as well as material points located at the location at $y = 0$ are set equal to zero. To represent the stiff plate at the right edge, Young's modulus of the stiff plate is considered as $E = 1.0667 \times 10^5$ N/m^2.

The plate is subjected to incremental vertical displacement at $(x = L, y = L - W/2)$ as

$$v^{(n)} = v^{(n-1)} + \Delta v \text{ (m)} \tag{3.26}$$

with $v^{(0)} = 10.075$ m, $\Delta v = 0.001$ m
where $v^{(n)}$ represents applied displacement at n^{th} load step $(n = 1,2 \dots 2900)$, Δv represents the incremental value of applied displacement, $v^{(0)}$ represents the first value of vertical displacement applied for the plate.

In the PD model, the plate is discretized with the mesh size of $\Delta x = W/20$. The material point located at $(x = L, y = L - W/2)$ is subjected to the incremental displacement given in Eq. (3.38). The Adaptive Dynamic Relaxation (ADR) method [76, 77] is used to simulate this quasi-static problem (Appendix A1). To ensure the ADR solution is converged at each load step, the PD solution is run over 10000 time steps for each incremental displacement.

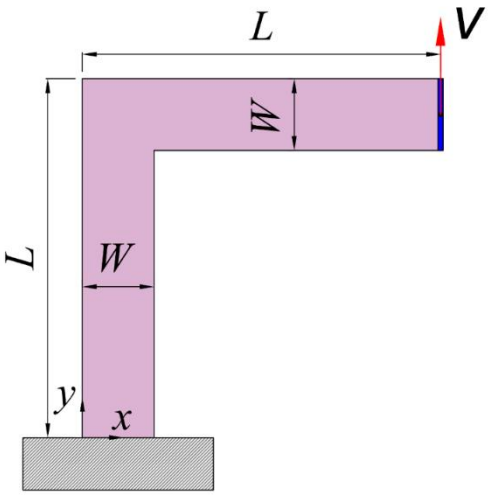

Fig. 3.27. L-shape plate subjected to large deformation

Fig. 3.28 shows the damage evolution on the plate subjected to large deformations. As shown in Fig. 3.28(a), when the applied displacement is $v = 10.175$ m, damage initiates around the inner corner of the plate, at $(x = W, y = L - W/2)$. As the applied displacement is increased, the crack propagates toward the outer corner of the L-shape plate as shown in Fig. 3.28(b-d). When the applied displacement is $v = 12.975$ m, the crack opens largely, and the L-shape plate is almost split into two parts as shown in Fig. 3.28(d). It is observed that the damage evolution captured by the nonlinear PD model agrees very well with the previous study [101].

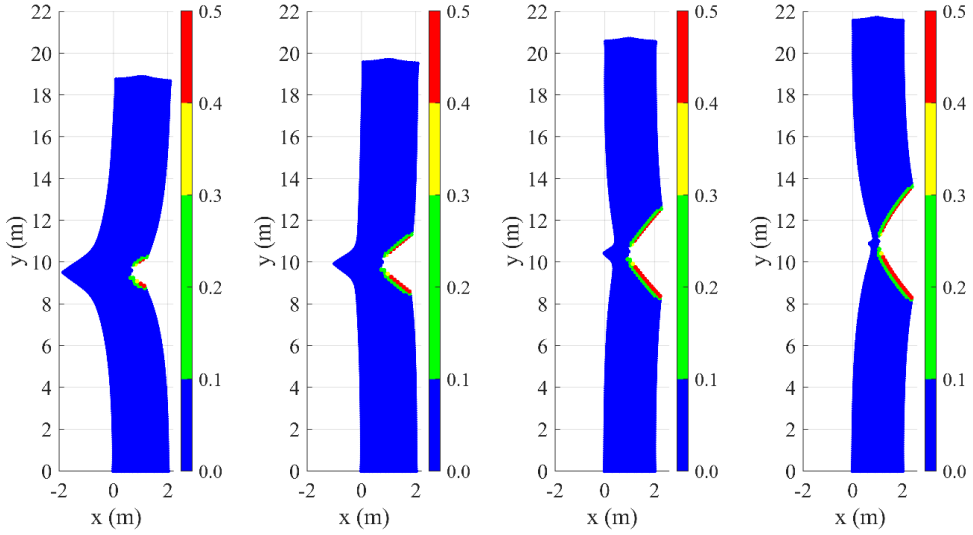

(a) (b) (c) (d)

Fig. 3.28. Crack evolution on the L-shape plate in the deformed configuration when the applied displacement is (a) $v = 10.175$ m, (b) $v = 10.975$ m, (c) $v = 11.975$ m, (d) $v = 12.975$ m

3.2.3.6. Damage prediction in 3D pre-notched concrete beam subjected to bending

After verifying the accuracy of the developed nonlinear PD model for 3D structures, damage on a 3D structure is predicted. The experiment presented by Jenq and Shah [93] for a pre-notched concrete beam is simulated by using the developed PD model. The concrete beam has dimensions of $L \times B \times H = 304.8 \times 28.6 \times 70.2$ mm^3 and the pre-notch has the height of $a = 35.1$ mm as shown in Fig. 3.29. The beam is placed on two rigid cylinders located at $x = 0.1L$ and $x = 0.9L$. The material has Young's modulus $E = 30 \times 10^9$ N/m^2, Poisson's ratio $\nu = 0.2$. For simplification, the critical energy release rate of the material is chosen as $G_c = G_{Ic} = 20.7368$ J/m^2.

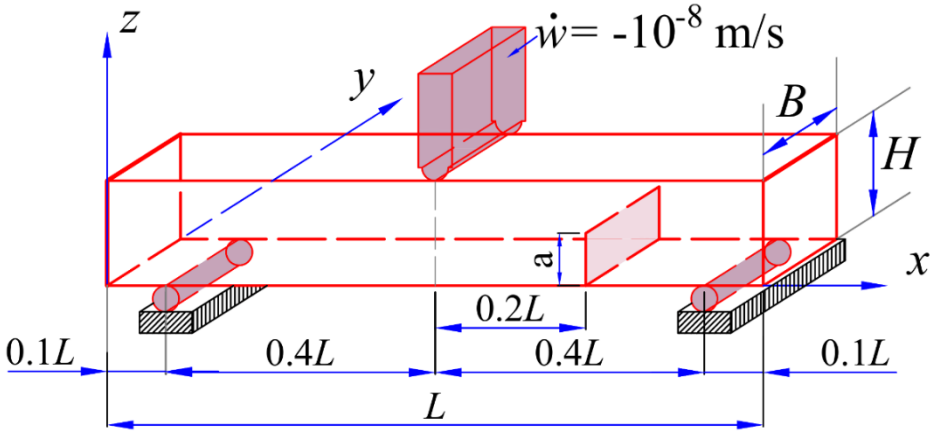

Fig. 3.29. 3D beam with pre-notched

In the PD model, the structure is discretized with uniform $101 \times 10 \times 24$ material points. To create the notch, the material points located at $x = 0.7L$, $0 \le y \le B$ and $z \le a$ are removed from the model.

The loading is applied by increasing the displacement by $\Delta w = -10^{-8}$ at $x = 0.5L$, $0 \le y \le B$, $z = H$ for each load step. Zero vertical displacements, $w = 0$ is applied at $x = 0.1L$, $0 \le y \le B$, $z = 0$ and $x = 0.9L$, $0 \le y \le B$, $z = 0$. The explicit time integration is used for this quasi-static problem by using the ADR method [76, 77].

Fig. 3.30-4.42 present the crack evolution for the concrete beam. In Fig. 3.30(b)-42(b), blue regions represent the initial notch and red regions represent the new crack surfaces. The new crack surfaces are represented by the material points with the damage coefficient $\phi \ge 0.3$. As shown in Fig. 3.30(a), when the applied displacement is $w(0.5L, y, H) = -2 \times 10^{-6}$ m, the crack propagates towards the middle section of the beam and reaches the location $(x = 0.206, y, z = 0.046)$. The peridynamic results show that the failure angle is $\beta = 34^o$ which is similar to the failure angle observed in experiments [93].

As time progresses, the crack continues propagating in the same direction and reaches the location $(x = 0.1962,\ y,\ z = 0.0582)$ when $w(0.5L, y, H) = -2.5 \times 10^{-6}$ m as shown in Fig. 3.31. The crack propagates to the location of $(x = 0.1928, y, z = 0.0625)$ when $w(0.5L, y, H) = -3 \times 10^{-6}$ m as shown in Fig. 3.32. The crack propagated to the location $(x = 0.1869, y, z = 0.0691)$ when $w(0.5L, y, H) = -4 \times 10^{-6}$ m as shown in Fig. 3.34, then propagated towards the top surface of the beam when $w(0.5L, y, H) = -4.5 \times 10^{-6}$ m as shown in Fig. 3.35.

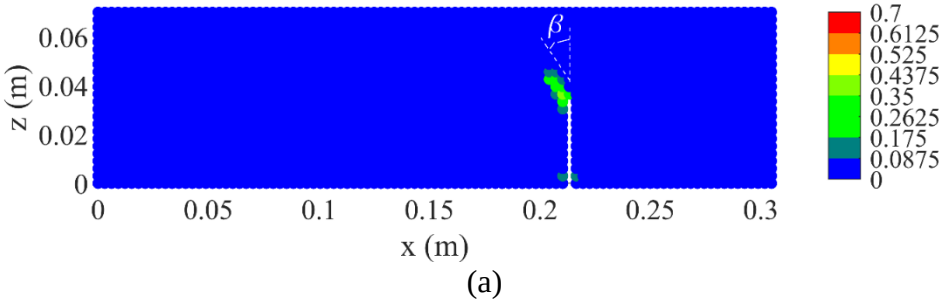

(a)

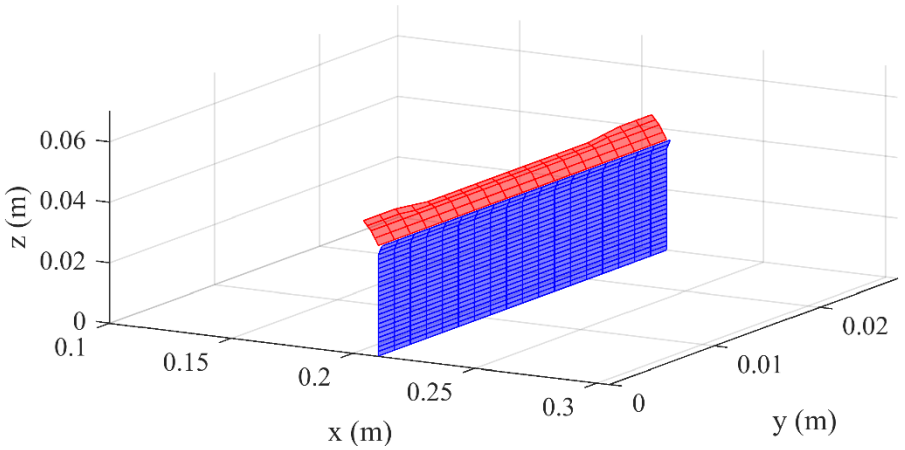

(b)

Fig. 3.30. Crack evolution when $w(0.5L, y, H) = -2 \times 10^{-6}$ m (a) front view for material points located at $y = B/2$ (b) 3D crack surface

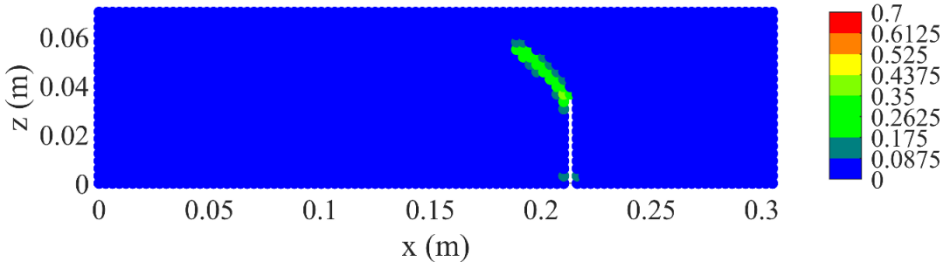

(a)

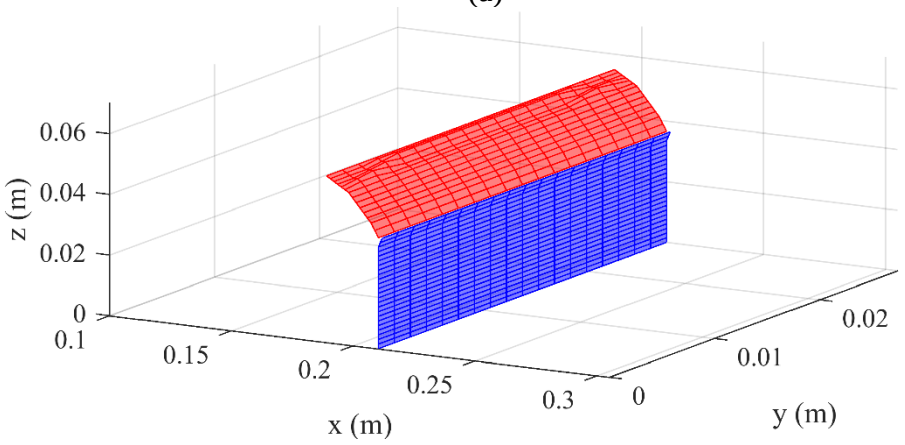

(b)

Fig. 3.31. Crack evolution when $w(0.5L, y, H) = -2.5 \times 10^{-6}$ m (a) front view for material points located at $y = B/2$ (b) 3D crack surface

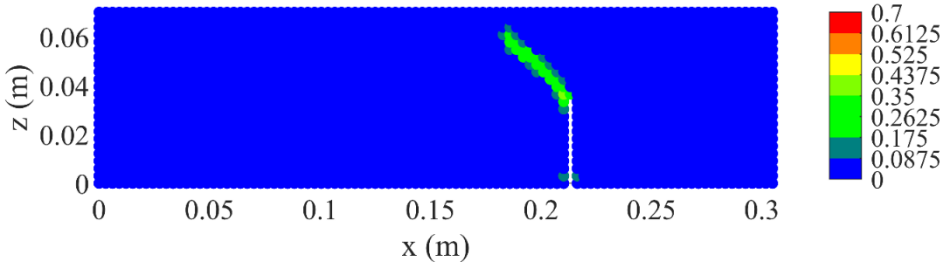

(a)

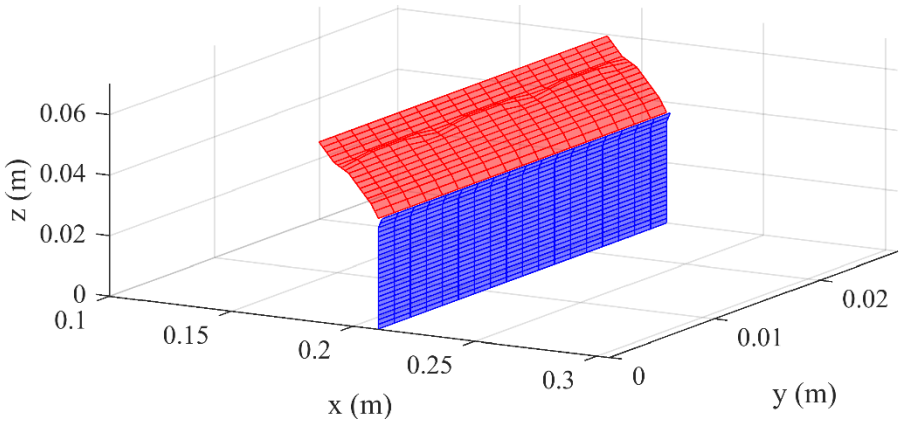

(b)

Fig. 3.32. Crack evolution when $w(0.5L, y, H) = -3 \times 10^{-6}$ m (a) front view for material points located at $y = B/2$ (b) 3D crack surface

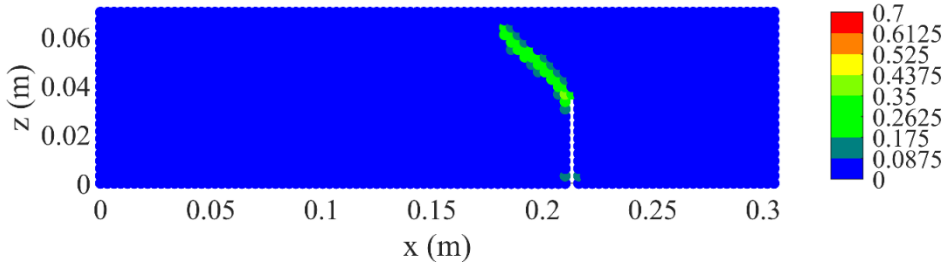

(a)

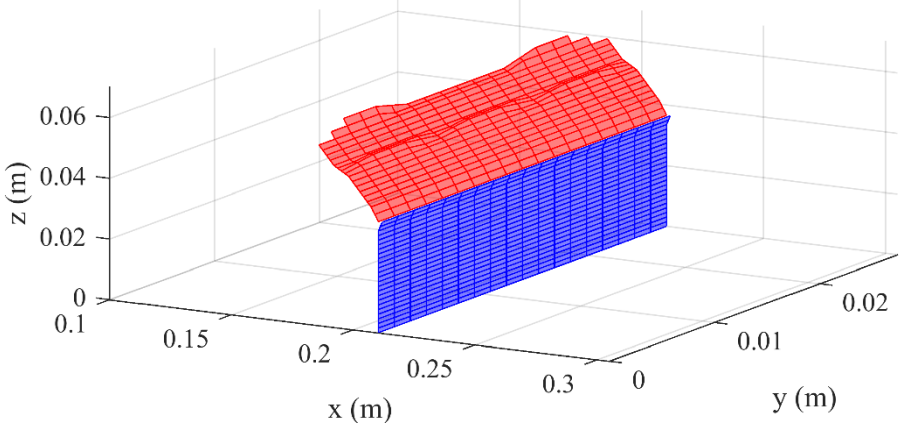

(b)

Fig. 3.33. Crack evolution when $w(0.5L, y, H) = -3.5 \times 10^{-6}$ m (a) front view for material points located at $y = B/2$ (b) 3D crack surface

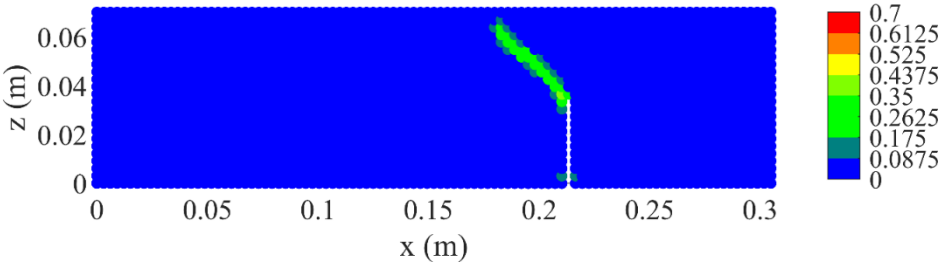

(a)

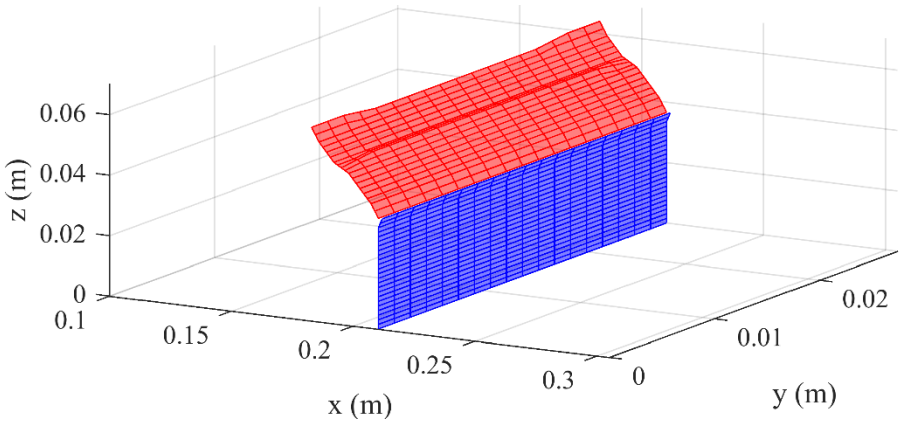

(b)

Fig. 3.34. Crack evolution when $w(0.5L, y, H) = -4 \times 10^{-6}$ m (a) front view for material points located at $y = B/2$ (b) 3D crack surface

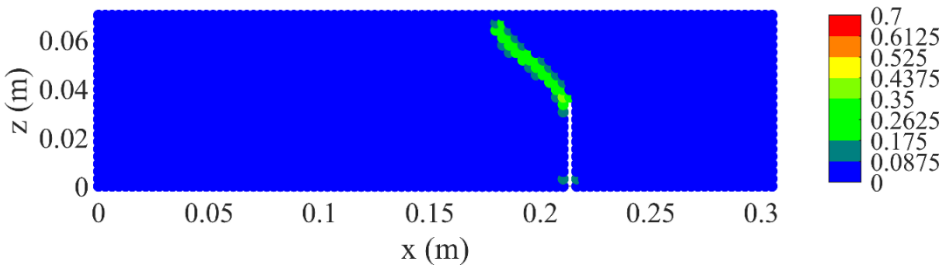

(a)

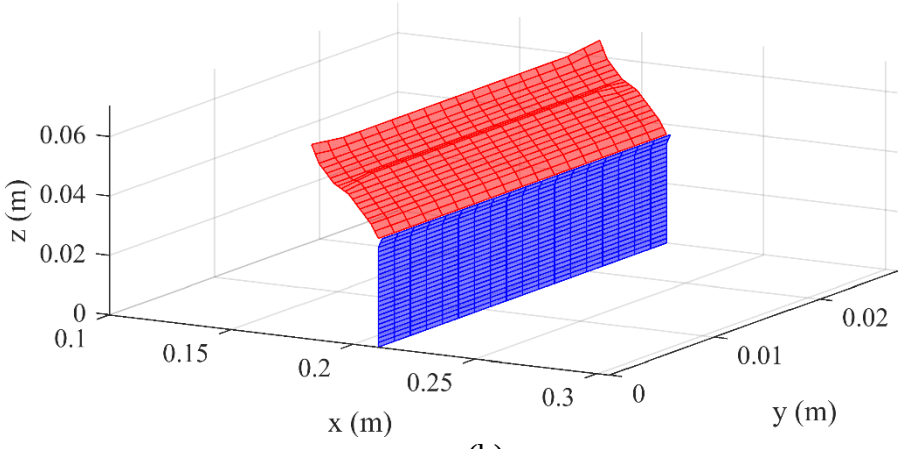

(b)

Fig. 3.35. Crack evolution when $w(0.5L, y, H) = -4.5 \times 10^{-6}$ m (a) front view for material points located at $y = B/2$ (b) 3D crack surface

3.3. Peridynamics for nonlinear analysis of 3d beam structures

In this section, a novel PD model for geometrically nonlinear analysis of beam structures with 6 DOFs is proposed. The nonlinear PD formulations and equations of motion are obtained based on the principle of virtual displacements by using the Total Lagrange formulation. The numerical procedure in PD nonlinear analysis for beams is provided. The capabilities of the nonlinear PD model are verified by considering various examples of straight beams and curved beams subjected to large deformations. The developed nonlinear PD model is used to predict damages on a straight beam, which is a representation of dry spaghetti, subjected to different loading conditions.

3.3.1. Nonlinear beam kinematics in classical continuum mechanics

In this section, a three-dimensional straight beam is considered as shown in Fig. 3.36. The beam kinematics are obtained with respect to the body-attached coordinate system of the beam, x, y, z, which is called the local coordinate system. The beam is assumed to have symmetric cross-sections. The nonlinear strain energy density for the beam is obtained through three main steps. First, the displacement components of a beam element are presented in Section 3.3.1.1. Next, the Green-Lagrange strain and Second Piola-Kirchhoff stress components are presented in Section 3.3.1.2 and 3.3.1.3, respectively. Finally, the nonlinear strain energy density for a beam structure is presented in Section 3.3.1.4.

3.3.1.1. Displacement components

Based on the Timoshenko theory [72], a beam has 6 local degrees of freedom, $u, v, w, \theta_x, \theta_y, \theta_z$ as shown in Fig. 3.36. The terms u, v, w represent the local displacements of the point located at the centre line of the beam and $\theta_x, \theta_y, \theta_z$ represent local rotations of beam cross-section.

Since in nonlinear analysis, three rotations $\theta_x, \theta_y, \theta_z$ are co-rotated, the rotations of the beam at time t are controlled by using director vectors, ${}^t\boldsymbol{V}_s$, ${}^t\boldsymbol{V}_t$ [70] as shown in Fig. 3.36.

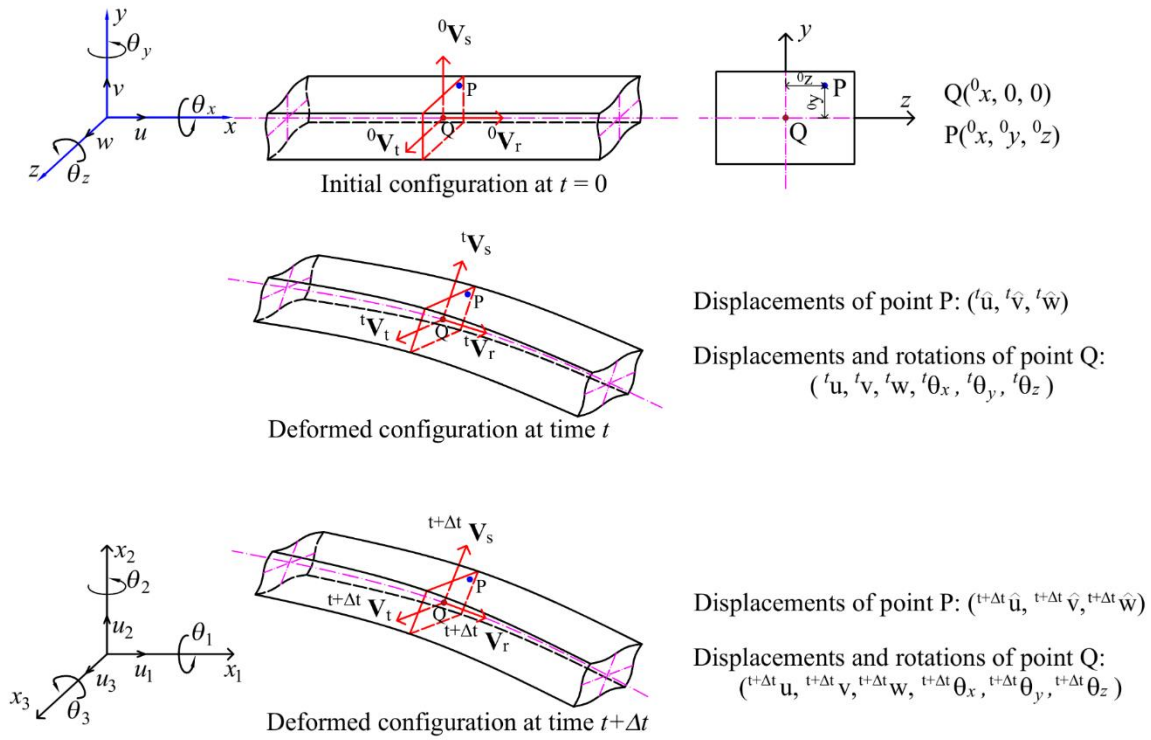

Fig. 3.36. Beam configurations with 6 local DOFs

As shown in Fig. 3.36, material point P is located at $\left({}^0x,\ {}^0y,\ {}^0z\right)$ and material point Q is located at $\left({}^0x, 0,0\right)$ which is on the centre line of the beam.

The degrees of freedom at time t and time $t+\Delta t$ for material points P and Q are represented as

$$\left({}^t\hat{u},\ {}^t\hat{v},\ {}^t\hat{w}\right),\left({}^{t+\Delta t}\hat{u},\ {}^{t+\Delta t}\hat{v},\ {}^{t+\Delta t}\hat{w}\right) \text{ for } P \tag{3.27a}$$

$$\left({}^t u,\ {}^t v,\ {}^t w,\ {}^t\theta_x,\ {}^t\theta_y,\ {}^t\theta_z\right),\quad \left({}^{t+\Delta t}u,\ {}^{t+\Delta t}v,\ {}^{t+\Delta t}w,\ {}^{t+\Delta t}\theta_x,\ {}^{t+\Delta t}\theta_y,\ {}^{t+\Delta t}\theta_z\right) \quad \text{for} \quad Q \tag{3.27b}$$

According to Bathe [70], the displacement components of material point P located at $\left({}^0x,\ {}^0y,\ {}^0z\right)$ at time t can be defined as

$${}^t\hat{u} = {}^t u + {}^0z\left({}^tV_{tx} - {}^0V_{tx}\right) + {}^0y\left({}^tV_{sx} - {}^0V_{sx}\right) \tag{3.28a}$$

$${}^t\hat{v} = {}^t v + {}^0z\left({}^tV_{ty} - {}^0V_{ty}\right) + {}^0y\left({}^tV_{sy} - {}^0V_{sy}\right) \tag{3.28b}$$

$${}^t\hat{w} = {}^t w + {}^0z\left({}^tV_{tz} - {}^0V_{tz}\right) + {}^0y\left({}^tV_{sz} - {}^0V_{sz}\right) \tag{3.28c}$$

where ${}^tV_{sx}$, ${}^tV_{sy}$, ${}^tV_{sz}$ represent components of the director vector ${}^t\boldsymbol{V}_s$ at time t with respect to local axes x, y, z, respectively. The terms ${}^0V_{sx}$, ${}^0V_{sy}$, ${}^0V_{sz}$ represent components of the director vector ${}^0\boldsymbol{V}_s$ at time $t = 0$ with respect to local axes x, y, z, respectively. Similarly, ${}^tV_{tx}$, ${}^tV_{ty}$, ${}^tV_{tz}$ represent components of the director vector ${}^t\boldsymbol{V}_t$ at time t with respect to local axes x, y, z, respectively. The

terms ${}^0V_{tx}$, ${}^0V_{ty}$, ${}^0V_{tz}$ represent components of the director vector ${}^0\boldsymbol{V}_t$ at time $t = 0$ with respect to local axes x, y, z, respectively.

Note that, in Eq. (3.28), the director vectors at time t, including (${}^tV_{sx}$, ${}^tV_{sy}$, ${}^tV_{sz}$) and (${}^tV_{tx}$, ${}^tV_{ty}$, ${}^tV_{tz}$) are unknown. These director vectors can be updated numerically by using the director vectors at the previous time step as given in Eq. (3.64d-f) in Section 4. Meanwhile, the director vectors at time $t = 0$ can be defined based on the initial configuration of the beam. In this section, for simplification, a straight beam is considered, and the beam's local coordinates are assumed to be aligned with the global coordinates as shown in Fig. 3.36. Therefore, the director vectors at time $t = 0$ for a straight beam can be defined as

$${}^0\mathbf{V}_s = \begin{bmatrix} 0 & 1 & 0 \end{bmatrix}^T \text{ with } {}^0V_{sx} = 0;\quad {}^0V_{sy} = 1;\quad {}^0V_{sz} = 0 \tag{3.29d}$$

$${}^0\mathbf{V}_t = \begin{bmatrix} 0 & 0 & 1 \end{bmatrix}^T \text{ with } {}^0V_{tx} = 0;\quad {}^0V_{ty} = 0;\quad {}^0V_{tz} = 1 \tag{3.29e}$$

$${}^0\mathbf{V}_r = \begin{bmatrix} 1 & 0 & 0 \end{bmatrix}^T \text{ with } {}^0V_{rx} = 1;\quad {}^0V_{ry} = 0;\quad {}^0V_{rz} = 0 \tag{3.29f}$$

By substituting Eq. (3.29) into Eq. (3.28), the displacement components of material point P located at (${}^0x$, ${}^0y$, ${}^0z$) at time t can be defined as [70]

$${}^t\hat{u} = {}^tu + {}^0z.{}^tV_{tx} + {}^0y.{}^tV_{sx} \tag{3.30a}$$

$${}^t\hat{v} = {}^tv + {}^0z.{}^tV_{ty} + {}^0y\left({}^tV_{sy} - 1\right) \tag{3.30b}$$

$${}^t\hat{w} = {}^tw + {}^0z\left({}^tV_{tz} - 1\right) + {}^0y.{}^tV_{sz} \tag{3.30c}$$

Similar to Eq. (3.30), the displacement components of material point P at time $t + \Delta t$ can be calculated as [70]

$${}^{t+\Delta t}\hat{u} = {}^{t+\Delta t}u + {}^0z.{}^{t+\Delta t}V_{tx} + {}^0y.{}^{t+\Delta t}V_{sx} \tag{3.31a}$$

$${}^{t+\Delta t}\hat{v} = {}^{t+\Delta t}v + {}^0z.{}^{t+\Delta t}V_{ty} + {}^0y\left({}^{t+\Delta t}V_{sy} - 1\right) \tag{3.31b}$$

$${}^{t+\Delta t}\hat{w} = {}^{t+\Delta t}w + {}^0z\left({}^{t+\Delta t}V_{tz} - 1\right) + {}^0y.{}^{t+\Delta t}V_{sz} \tag{3.31c}$$

By substituting Eq. (3.30) and Eq. (3.31) into Eq. (C2a), the incremental displacements from time t to time $t + \Delta t$ can be calculated as [70]

$$\underline{\hat{u}} = {}^{t+\Delta t}\hat{u} - {}^t\hat{u} = {}^{t+\Delta t}u - {}^tu + {}^0z\left({}^{t+\Delta t}V_{tx} - {}^tV_{tx}\right) + {}^0y\left({}^{t+\Delta t}V_{sx} - {}^tV_{sx}\right) \tag{3.32a}$$

$$\underline{\hat{v}} = {}^{t+\Delta t}\hat{v} - {}^t\hat{v} = {}^{t+\Delta t}v - {}^tv + {}^0z\left({}^{t+\Delta t}V_{ty} - {}^tV_{ty}\right) + {}^0y\left({}^{t+\Delta t}V_{sy} - {}^tV_{sy}\right) \tag{3.32b}$$

$$\underline{\hat{w}} = {}^{t+\Delta t}\hat{w} - {}^t\hat{w} = {}^{t+\Delta t}w - {}^tw + {}^0z\left({}^{t+\Delta t}V_{tz} - {}^tV_{tz}\right) + {}^0y\left({}^{t+\Delta t}V_{sz} - {}^tV_{sz}\right) \tag{3.32c}$$

The relations given in Eq. (3.32) can be rewritten as

$$\underline{\hat{u}} = \underline{u} + {}^0z\underline{V}_{tx} + {}^0y\underline{V}_{sx} \tag{3.33a}$$

$$\hat{\underline{v}} = \underline{v} + {}^{0}z\underline{V}_{ty} + {}^{0}y\underline{V}_{sy} \tag{3.33b}$$

$$\hat{\underline{w}} = \underline{w} + {}^{0}z\underline{V}_{tz} + {}^{0}y\underline{V}_{sz} \tag{3.33c}$$

with

$$\underline{u} = {}^{t+\Delta t}u - {}^{t}u \tag{3.33d}$$

$$\underline{v} = {}^{t+\Delta t}v - {}^{t}v \tag{3.33e}$$

$$\underline{w} = {}^{t+\Delta t}w - {}^{t}w \tag{3.33f}$$

and

$$\underline{V}_{sx} = {}^{t+\Delta t}V_{sx} - {}^{t}V_{sx}; \quad \underline{V}_{tx} = {}^{t+\Delta t}V_{tx} - {}^{t}V_{tx} \tag{3.33g}$$

$$\underline{V}_{sy} = {}^{t+\Delta t}V_{sy} - {}^{t}V_{sy}; \quad \underline{V}_{ty} = {}^{t+\Delta t}V_{ty} - {}^{t}V_{ty} \tag{3.33h}$$

$$\underline{V}_{sz} = {}^{t+\Delta t}V_{sz} - {}^{t}V_{sz}; \quad \underline{V}_{tz} = {}^{t+\Delta t}V_{tz} - {}^{t}V_{tz} \tag{3.33i}$$

In Eq. (3.33d-f), $\underline{u}$, $\underline{v}$, $\underline{w}$ represent the incremental displacements from time t to time $t + \Delta t$ of point Q located at $({}^{0}x, 0,0)$ on the centre line of the beam. The terms $\underline{V}_{sx}$, $\underline{V}_{sy}$, $\underline{V}_{sz}$ represent components of the incremental director vector, $\underline{\boldsymbol{V}}_{s}$, from time t to time $t + \Delta t$. Similarly, the terms $\underline{V}_{tx}$, $\underline{V}_{ty}$, $\underline{V}_{tz}$ represent components of the incremental director vector, $\underline{\boldsymbol{V}}_{t}$, from time t to time $t + \Delta t$.

The relations given in Eq. (3.33g-i) can be rewritten in the compact form as

$$\underline{\mathbf{V}}_{s} = {}^{t+\Delta t}\mathbf{V}_{s} - {}^{t}\mathbf{V}_{s} \tag{3.34a}$$

$$\underline{\mathbf{V}}_{t} = {}^{t+\Delta t}\mathbf{V}_{t} - {}^{t}\mathbf{V}_{t} \tag{3.34b}$$

with

$$\underline{\mathbf{V}}_{s} = \begin{bmatrix} \underline{V}_{sx} & \underline{V}_{sy} & \underline{V}_{sz} \end{bmatrix} \tag{3.34c}$$

$$\underline{\mathbf{V}}_{t} = \begin{bmatrix} \underline{V}_{tx} & \underline{V}_{ty} & \underline{V}_{tz} \end{bmatrix} \tag{3.34d}$$

According to Bathe [70], the incremental director vectors given in Eq. (3.34c-d) can be approximated by using the director vectors at time t as

$$\underline{\mathbf{V}}_{s} = \underline{\boldsymbol{\theta}} \times {}^{t}\mathbf{V}_{s} = \begin{bmatrix} \left(\underline{\theta}_{y}\,{}^{t}V_{sz} - \underline{\theta}_{z}\,{}^{t}V_{sy}\right) & \left(\underline{\theta}_{z}\,{}^{t}V_{sx} - \underline{\theta}_{x}\,{}^{t}V_{sz}\right) & \left(\underline{\theta}_{x}\,{}^{t}V_{sy} - \underline{\theta}_{y}\,{}^{t}V_{sx}\right) \end{bmatrix}^{T} \tag{3.35a}$$

$$\underline{\mathbf{V}}_{t} = \underline{\boldsymbol{\theta}} \times {}^{t}\mathbf{V}_{t} = \begin{bmatrix} \left(\underline{\theta}_{y}\,{}^{t}V_{tz} - \underline{\theta}_{z}\,{}^{t}V_{ty}\right) & \left(\underline{\theta}_{z}\,{}^{t}V_{tx} - \underline{\theta}_{x}\,{}^{t}V_{tz}\right) & \left(\underline{\theta}_{x}\,{}^{t}V_{ty} - \underline{\theta}_{y}\,{}^{t}V_{tx}\right) \end{bmatrix}^{T} \tag{3.35b}$$

with

$$\underline{\boldsymbol{\theta}} = {}^{t+\Delta t}\boldsymbol{\theta} - {}^{t}\boldsymbol{\theta} = \begin{bmatrix} \underline{\theta}_x & \underline{\theta}_y & \underline{\theta}_z \end{bmatrix}^T \tag{3.35c}$$

$$\underline{\theta}_x = {}^{t+\Delta t}\theta_x - {}^{t}\theta_x \tag{3.35d}$$

$$\underline{\theta}_y = {}^{t+\Delta t}\theta_y - {}^{t}\theta_y \tag{3.35e}$$

$$\underline{\theta}_z = {}^{t+\Delta t}\theta_z - {}^{t}\theta_z \tag{3.35f}$$

where $\underline{\theta}_x, \underline{\theta}_y, \underline{\theta}_z$ represent the incremental rotations of the beam cross-section from time t to time $t + \Delta t$ as

Therefore, by using the incremental director vectors given in Eq. (3.35a-b), the incremental displacements in Eq. (3.33a-c) can be calculated as

$$\underline{\hat{u}} = \underline{u} + {}^{0}z\left(\underline{\theta}_y\, {}^{t}V_{tz} - \underline{\theta}_z\, {}^{t}V_{ty}\right) + {}^{0}y\left(\underline{\theta}_y\, {}^{t}V_{sz} - \underline{\theta}_z\, {}^{t}V_{sy}\right) \tag{3.36a}$$

$$\underline{\hat{v}} = \underline{v} + {}^{0}z\left(\underline{\theta}_z\, {}^{t}V_{tx} - \underline{\theta}_x\, {}^{t}V_{tz}\right) + {}^{0}y\left(\underline{\theta}_z\, {}^{t}V_{sx} - \underline{\theta}_x\, {}^{t}V_{sz}\right) \tag{3.36b}$$

$$\underline{\hat{w}} = \underline{w} + {}^{0}z\left(\underline{\theta}_x\, {}^{t}V_{ty} - \underline{\theta}_y\, {}^{t}V_{tx}\right) + {}^{0}y\left(\underline{\theta}_x\, {}^{t}V_{sy} - \underline{\theta}_y\, {}^{t}V_{sx}\right) \tag{3.36c}$$

3.3.1.2. Strain components

By using displacements at time t given in Eq. (3.30), the Green-Lagrange strain components [70] in Eq. (C4) can be calculated as

$$\begin{aligned} {}^{t}_{0}\hat{\varepsilon}_{xx} = {}&{}^{t}_{0}u_{,x} + \frac{1}{2}\left\{\left({}^{t}_{0}u_{,x}\right)^2 + \left({}^{t}_{0}v_{,x}\right)^2 + \left({}^{t}_{0}w_{,x}\right)^2\right\} \\ &+ {}^{0}y\left\{{}^{t}_{0}V_{sx,x} + \left({}^{t}_{0}u_{,x}\right)\left({}^{t}_{0}V_{sx,x}\right) + \left({}^{t}_{0}v_{,x}\right)\left({}^{t}_{0}V_{sy,x}\right) + \left({}^{t}_{0}w_{,x}\right)\left({}^{t}_{0}V_{sz,x}\right)\right\} \\ &+ {}^{0}z\left\{{}^{t}_{0}V_{tx,x} + \left({}^{t}_{0}u_{,x}\right)\left({}^{t}_{0}V_{tx,x}\right) + \left({}^{t}_{0}v_{,x}\right)\left({}^{t}_{0}V_{ty,x}\right) + \left({}^{t}_{0}w_{,x}\right)\left({}^{t}_{0}V_{tz,x}\right)\right\} \end{aligned} \tag{3.37a}$$

$${}^{t}_{0}\hat{\varepsilon}_{xy} = \frac{1}{2}\left\{\begin{array}{l} {}^{t}V_{sy}\left({}^{t}_{0}v_{,x}\right) + {}^{t}V_{sx} + {}^{t}V_{sx}\left({}^{t}_{0}u_{,x}\right) + {}^{t}V_{sz}\left({}^{t}_{0}w_{,x}\right) \\ + {}^{0}y\left\{{}^{t}V_{sy}\left({}^{t}_{0}V_{sy,x}\right) + {}^{t}V_{sx}\left({}^{t}_{0}V_{sx,x}\right) + {}^{t}V_{sz}\left({}^{t}_{0}V_{sz,x}\right)\right\} \\ + {}^{0}z\left\{{}^{t}V_{sy}\left({}^{t}_{0}V_{ty,x}\right) + {}^{t}V_{sx}\left({}^{t}_{0}V_{tx,x}\right) + {}^{t}V_{sz}\left({}^{t}_{0}V_{tz,x}\right)\right\} \end{array}\right\} \tag{3.37b}$$

$${}^{t}_{0}\hat{\varepsilon}_{xz} = \frac{1}{2}\left\{\begin{array}{l} {}^{t}V_{tz}\left({}^{t}_{0}w_{,x}\right) + {}^{t}V_{tx} + {}^{t}V_{tx}\left({}^{t}_{0}u_{,x}\right) + {}^{t}V_{ty}\left({}^{t}_{0}v_{,x}\right) \\ + {}^{0}y\left\{{}^{t}V_{tz}\left({}^{t}_{0}V_{sz,x}\right) + {}^{t}V_{tx}\left({}^{t}_{0}V_{sx,x}\right) + {}^{t}V_{ty}\left({}^{t}_{0}V_{sy,x}\right)\right\} \\ + {}^{0}z\left\{{}^{t}V_{tz}\left({}^{t}_{0}V_{tz,x}\right) + {}^{t}V_{tx}\left({}^{t}_{0}V_{tx,x}\right) + {}^{t}V_{ty}\left({}^{t}_{0}V_{ty,x}\right)\right\} \end{array}\right\} \tag{3.37c}$$

$${}^{t}_{0}\hat{\varepsilon}_{yy} = {}^{t}_{0}\hat{\varepsilon}_{yz} = {}^{t}_{0}\hat{\varepsilon}_{zz} = 0 \tag{3.37d}$$

with

$$ {}_0^t u_{,x} = \frac{\partial^t u}{\partial^0 x}; \qquad {}_0^t v_{,x} = \frac{\partial^t v}{\partial^0 x}; \qquad {}_0^t w_{,x} = \frac{\partial^t w}{\partial^0 x} \tag{3.37e} $$

$$ {}_0^t V_{sx,x} = \frac{\partial^t V_{sx}}{\partial^0 x}; \qquad {}_0^t V_{sy,x} = \frac{\partial^t V_{sy}}{\partial^0 x}; \qquad {}_0^t V_{sz,x} = \frac{\partial^t V_{sz}}{\partial^0 x} \tag{3.37f} $$

$$ {}_0^t V_{tx,x} = \frac{\partial^t V_{tx}}{\partial^0 x}; \qquad {}_0^t V_{ty,x} = \frac{\partial^t V_{ty}}{\partial^0 x}; \qquad {}_0^t V_{tz,x} = \frac{\partial^t V_{tz}}{\partial^0 x} \tag{3.37g} $$

By using the displacements at time t given in Eq. (3.30) and the incremental displacements given in Eq. (3.36), the linear incremental strain components [70], ${}_0\underline{\hat{e}}_{ij}$, given in Eq. (C9) can be calculated as

$$ \begin{aligned} {}_0\underline{\hat{e}}_{xx} &= {}_0\underline{u}_{,x}\left(1+{}_0^t u_{,x}\right)+\left({}_0^t v_{,x}\right)\left({}_0\underline{v}_{,x}\right)+\left({}_0^t w_{,x}\right)\left({}_0\underline{w}_{,x}\right) \\ &+ {}^0y\left\{\begin{array}{l} \left(1+{}_0^t u_{,x}\right)\dfrac{\partial\left(\underline{\theta}_y\,{}^tV_{sz}-\underline{\theta}_z\,{}^tV_{sy}\right)}{\partial^0 x}+\left({}_0^t V_{sx,x}\right)\left({}_0\underline{u}_{,x}\right) \\ +\left({}_0^t V_{sy,x}\right)\left({}_0\underline{v}_{,x}\right)+{}_0^t v_{,x}\dfrac{\partial\left(\underline{\theta}_z\,{}^tV_{sx}-\underline{\theta}_x\,{}^tV_{sz}\right)}{\partial^0 x}+\left({}_0^t V_{sz,x}\right)\left({}_0\underline{w}_{,x}\right) \\ +{}_0^t w_{,x}\dfrac{\partial\left(\underline{\theta}_x\,{}^tV_{sy}-\underline{\theta}_y\,{}^tV_{sx}\right)}{\partial^0 x} \end{array}\right\} \\ &+ {}^0z\left\{\begin{array}{l} \left(1+{}_0^t u_{,x}\right)\dfrac{\partial\left(\underline{\theta}_y\,{}^tV_{tz}-\underline{\theta}_z\,{}^tV_{ty}\right)}{\partial^0 x}+\left({}_0^t V_{tx,x}\right)\left({}_0u_{,x}\right) \\ +\left({}_0^t V_{ty,x}\right)\left({}_0v_{,x}\right)+{}_0^t v_{,x}\dfrac{\partial\left(\underline{\theta}_z\,{}^tV_{tx}-\underline{\theta}_x\,{}^tV_{tz}\right)}{\partial^0 x}+\left({}_0^t V_{tz,x}\right)\left({}_0w_{,x}\right) \\ +{}_0^t w_{,x}\dfrac{\partial\left(\underline{\theta}_x\,{}^tV_{ty}-\underline{\theta}_y\,{}^tV_{tx}\right)}{\partial^0 x} \end{array}\right\} \end{aligned} \tag{3.38a} $$

$$ {}_0\underline{\hat{e}}_{xy} = \frac{1}{2}\left(\begin{array}{l} {}^tV_{sy}\left({}_0\underline{v}_{,x}\right)+{}^tV_{sx}\left({}_0\underline{u}_{,x}\right)+{}^tV_{sz}\left({}_0\underline{w}_{,x}\right) \\ +\left(1+{}_0^t u_{,x}\right)\left(\underline{\theta}_y\,{}^tV_{sz}-\underline{\theta}_z\,{}^tV_{sy}\right) \\ +\left(\underline{\theta}_z\,{}^tV_{sx}-\underline{\theta}_x\,{}^tV_{sz}\right){}_0^t v_{,x}+{}_0^t w_{,x}\left(\underline{\theta}_x\,{}^tV_{sy}-\underline{\theta}_y\,{}^tV_{sx}\right) \\ +{}^0z\left\{\begin{array}{l} {}_0\underline{\theta}_{x,x}\left({}^tV_{ty}\,{}^tV_{sz}-{}^tV_{tz}\,{}^tV_{sy}\right)+{}_0\underline{\theta}_{y,x}\left({}^tV_{tz}\,{}^tV_{sx}-{}^tV_{tx}\,{}^tV_{sz}\right) \\ +{}_0\underline{\theta}_{z,x}\left({}^tV_{tx}\,{}^tV_{sy}-{}^tV_{ty}\,{}^tV_{sx}\right) \end{array}\right\} \end{array}\right) \tag{3.38b} $$

$$
{}_0\underline{\hat{e}}_{xz} = \frac{1}{2}\begin{pmatrix}
{}^tV_{tz}\left({}_0\underline{w}_{,x}\right) + {}^tV_{tx}\left({}_0\underline{u}_{,x}\right) + {}^tV_{ty}\left({}_0\underline{v}_{,x}\right) \\
+\left(1+{}^t_0u_{,x}\right)\left(\underline{\theta}_y\,{}^tV_{tz} - \underline{\theta}_z\,{}^tV_{ty}\right) \\
+{}^t_0v_{,x}\left(\underline{\theta}_z\,{}^tV_{tx} - \underline{\theta}_x\,{}^tV_{tz}\right) + {}^t_0w_{,x}\left(\underline{\theta}_x\,{}^tV_{ty} - \underline{\theta}_y\,{}^tV_{tx}\right) \\
+{}^0y\begin{Bmatrix} {}_0\underline{\theta}_{x,x}\left({}^tV_{sy}\,{}^tV_{tz} - {}^tV_{sz}\,{}^tV_{ty}\right) + {}_0\underline{\theta}_{y,x}\left({}^tV_{sz}\,{}^tV_{tx} - {}^tV_{sx}\,{}^tV_{tz}\right) \\ +{}_0\underline{\theta}_{z,x}\left({}^tV_{sx}\,{}^tV_{ty} - {}^tV_{sy}\,{}^tV_{tx}\right) \end{Bmatrix}
\end{pmatrix} \tag{3.38c}
$$

$$
{}_0\underline{\hat{e}}_{yy} = {}_0\underline{\hat{e}}_{yz} = {}_0\underline{\hat{e}}_{zz} = 0 \tag{3.38d}
$$

with

$$
{}_0\underline{u}_{,x} = \frac{\partial \underline{u}}{\partial {}^0x}; \qquad {}_0\underline{v}_{,x} = \frac{\partial \underline{v}}{\partial {}^0x}; \qquad {}_0\underline{w}_{,x} = \frac{\partial \underline{w}}{\partial {}^0x} \tag{3.38e}
$$

3.3.1.3. Stress components

By using the Green-Lagrange strains given in Eq. (3.37a-d) and the stress-strain relations given in Eq. (C19) and Eq. (C21), the second Piola-Kirchhoff stress at time t can be calculated as [70]

$$
{}^t_0\hat{S}_{xx} = E\,{}^t_0\hat{\varepsilon}_{xx} = E\begin{bmatrix}
{}^t_0u_{,x} + \frac{1}{2}\left\{\left({}^t_0u_{,x}\right)^2 + \left({}^t_0v_{,x}\right)^2 + \left({}^t_0w_{,x}\right)^2\right\} \\
+{}^0y\begin{Bmatrix} {}^tV_{sx,x} + \left({}^t_0u_{,x}\right)\left({}^tV_{sx,x}\right) \\ +\left({}^t_0v_{,x}\right)\left({}^tV_{sy,x}\right) + \left({}^t_0w_{,x}\right)\left({}^tV_{sz,x}\right) \end{Bmatrix} \\
+{}^0z\begin{Bmatrix} {}^tV_{tx,x} + \left({}^t_0u_{,x}\right)\left({}^tV_{tx,x}\right) \\ +\left({}^t_0v_{,x}\right)\left({}^tV_{ty,x}\right) + \left({}^t_0w_{,x}\right)\left({}^tV_{tz,x}\right) \end{Bmatrix}
\end{bmatrix} \tag{3.39a}
$$

$$
{}^t_0\hat{S}_{xy} = 2k_sG\,{}^t_0\hat{\varepsilon}_{xy} = k_sG\begin{Bmatrix}
{}^tV_{sy}\left({}^t_0v_{,x}\right) + {}^tV_{sx} + {}^tV_{sx}\left({}^t_0u_{,x}\right) + {}^tV_{sz}\left({}^t_0w_{,x}\right) \\
+{}^0y\left\{{}^tV_{sy}\left({}^tV_{sy,x}\right) + {}^tV_{sx}\left({}^tV_{sx,x}\right) + {}^tV_{sz}\left({}^tV_{sz,x}\right)\right\} \\
+{}^0z\left\{{}^tV_{sy}\left({}^tV_{ty,x}\right) + {}^tV_{sx}\left({}^tV_{tx,x}\right) + {}^tV_{sz}\left({}^tV_{tz,x}\right)\right\}
\end{Bmatrix} \tag{3.39b}
$$

$$
{}^t_0\hat{S}_{xz} = 2k_sG\,{}^t_0\hat{\varepsilon}_{xz} = k_sG\begin{Bmatrix}
{}^tV_{tz}\left({}^t_0w_{,x}\right) + {}^tV_{tx} + {}^tV_{tx}\left({}^t_0u_{,x}\right) + {}^tV_{ty}\left({}^t_0v_{,x}\right) \\
+{}^0y\left\{{}^tV_{tz}\left({}^tV_{sz,x}\right) + {}^tV_{tx}\left({}^tV_{sx,x}\right) + {}^tV_{ty}\left({}^tV_{sy,x}\right)\right\} \\
+{}^0z\left\{{}^tV_{tz}\left({}^tV_{tz,x}\right) + {}^tV_{tx}\left({}^tV_{tx,x}\right) + {}^tV_{ty}\left({}^tV_{ty,x}\right)\right\}
\end{Bmatrix} \tag{3.39c}
$$

3.3.1.4. Strain energy density

By substituting the second Piola-Kirchhoff stress components given in Eq. (3.39)

and the incremental strain components given in Eq. (3.38) into Eq. (C32), the averaged strain energy density through the cross-section of the beam of a beam can be represented as [70]

$$
\begin{aligned}
\bar{W}^{NL} &= \frac{\int_{{}_0A}\left({}_0^tS_{xx}\,{}_0\underline{\hat{e}}_{xx}+2\,{}_0^tS_{xy}\,{}_0\underline{\hat{e}}_{xy}+2\,{}_0^tS_{xz}\,{}_0\underline{\hat{e}}_{xz}\right)d\left({}^0A\right)}{{}^0A}\\
&= E\left\{{}_0^tu_{,x}+\frac{1}{2}\left({}_0^tu_{,x}{}^2+{}_0^tv_{,x}{}^2+{}_0^tw_{,x}{}^2\right)\right\}\left\{{}_0\underline{u}_{,x}\left(1+{}_0^tu_{,x}\right)+\left({}_0^tv_{,x}\right)\left({}_0\underline{v}_{,x}\right)+\left({}_0^tw_{,x}\right)\left({}_0\underline{w}_{,x}\right)\right\}\\
&+\frac{EI_{yy}}{\left({}^0A\right)}\left\{\begin{matrix}{}_0^tV_{tx,x}+\left({}_0^tu_{,x}\right)\left({}_0^tV_{tx,x}\right)\\+\left({}_0^tv_{,x}\right)\left({}_0^tV_{ty,x}\right)\\+\left({}_0^tw_{,x}\right)\left({}_0^tV_{tz,x}\right)\end{matrix}\right\}\left\{\begin{matrix}\left({}_0^tV_{tx,x}\right)\left({}_0u_{,x}\right)+\left({}_0^tV_{ty,x}\right)\left({}_0v_{,x}\right)+\left({}_0^tV_{tz,x}\right)\left({}_0w_{,x}\right)\\+\left(1+{}_0^tu_{,x}\right)\dfrac{\partial\left(\underline{\theta}_y\,{}^tV_{tz}-\underline{\theta}_z\,{}^tV_{ty}\right)}{\partial\,{}^0x}+\\+{}_0^tv_{,x}\dfrac{\partial\left(\underline{\theta}_z\,{}^tV_{tx}-\underline{\theta}_x\,{}^tV_{tz}\right)}{\partial\,{}^0x}+{}_0^tw_{,x}\dfrac{\partial\left(\underline{\theta}_x\,{}^tV_{ty}-\underline{\theta}_y\,{}^tV_{tx}\right)}{\partial\,{}^0x}\end{matrix}\right\}\\
&+\frac{EI_{zz}}{\left({}^0A\right)}\left\{\begin{matrix}{}_0^tV_{sx,x}+\left({}_0^tu_{,x}\right)\left({}_0^tV_{sx,x}\right)\\+\left({}_0^tv_{,x}\right)\left({}_0^tV_{sy,x}\right)\\+\left({}_0^tw_{,x}\right)\left({}_0^tV_{sz,x}\right)\end{matrix}\right\}\left\{\begin{matrix}\left({}_0^tV_{sx,x}\right)\left({}_0\underline{u}_{,x}\right)+\left({}_0^tV_{sy,x}\right)\left({}_0\underline{v}_{,x}\right)+\left({}_0^tV_{sz,x}\right)\left({}_0\underline{w}_{,x}\right)\\+\left(1+{}_0^tu_{,x}\right)\dfrac{\partial\left(\underline{\theta}_y\,{}^tV_{sz}-\underline{\theta}_z\,{}^tV_{sy}\right)}{\partial\,{}^0x}+\\+{}_0^tv_{,x}\dfrac{\partial\left(\underline{\theta}_z\,{}^tV_{sx}-\underline{\theta}_x\,{}^tV_{sz}\right)}{\partial\,{}^0x}+{}_0^tw_{,x}\dfrac{\partial\left(\underline{\theta}_x\,{}^tV_{sy}-\underline{\theta}_y\,{}^tV_{sx}\right)}{\partial\,{}^0x}\end{matrix}\right\}\\
&+k_sG\left[\begin{matrix}\left\{\begin{matrix}{}^tV_{sx}\left(1+{}_0^tu_{,x}\right)+{}^tV_{sy}\,{}_0^tv_{,x}\\+{}^tV_{sz}\,{}_0^tw_{,x}\end{matrix}\right\}\left\{\begin{matrix}{}^tV_{sx}\left({}_0\underline{u}_{,x}\right)+{}^tV_{sy}\left({}_0\underline{v}_{,x}\right)+{}^tV_{sz}\left({}_0\underline{w}_{,x}\right)\\+\left(1+{}_0^tu_{,x}\right)\left(\underline{\theta}_y\,{}^tV_{sz}-\underline{\theta}_z\,{}^tV_{sy}\right)\\+\left(\underline{\theta}_z\,{}^tV_{sx}-\underline{\theta}_x\,{}^tV_{sz}\right){}_0^tv_{,x}+{}_0^tw_{,x}\left(\underline{\theta}_x\,{}^tV_{sy}-\underline{\theta}_y\,{}^tV_{sx}\right)\end{matrix}\right\}\\
+\left\{\begin{matrix}{}^tV_{tx}\left(1+{}_0^tu_{,x}\right)+{}^tV_{ty}\,{}_0^tv_{,x}\\+{}^tV_{tz}\,{}_0^tw_{,x}\end{matrix}\right\}\left\{\begin{matrix}{}^tV_{tz}\left({}_0\underline{w}_{,x}\right)+{}^tV_{tx}\left({}_0\underline{u}_{,x}\right)+{}^tV_{ty}\left({}_0\underline{v}_{,x}\right)\\+\left(1+{}_0^tu_{,x}\right)\left(\underline{\theta}_y\,{}^tV_{tz}-\underline{\theta}_z\,{}^tV_{ty}\right)\\+{}_0^tv_{,x}\left(\underline{\theta}_z\,{}^tV_{tx}-\underline{\theta}_x\,{}^tV_{tz}\right)+{}_0^tw_{,x}\left(\underline{\theta}_x\,{}^tV_{ty}-\underline{\theta}_y\,{}^tV_{tx}\right)\end{matrix}\right\}\end{matrix}\right]\\
&+\frac{k_tG}{\left({}^0A\right)}\left\{\begin{matrix}{}^tV_{sy}\left({}_0^tV_{ty,x}\right)\\+{}^tV_{sx}\left({}_0^tV_{tx,x}\right)+{}^tV_{sz}\left({}_0^tV_{tz,x}\right)\end{matrix}\right\}\left\{\begin{matrix}{}_0\underline{\theta}_{x,x}\left({}^tV_{ty}\,{}^tV_{sz}-{}^tV_{tz}\,{}^tV_{sy}\right)+{}_0\underline{\theta}_{y,x}\left({}^tV_{tz}\,{}^tV_{sx}-{}^tV_{tx}\,{}^tV_{sz}\right)\\+{}_0\underline{\theta}_{z,x}\left({}^tV_{tx}\,{}^tV_{sy}-{}^tV_{ty}\,{}^tV_{sx}\right)\end{matrix}\right\}
\end{aligned}
\tag{3.40}
$$

where k_s represents the shear correction factor for the beam cross-section [70], k_t represents torsional constant for beam cross-section. The terms I_{yy} and I_{zz} given in Eq. (3.40) represent the area moment of inertia of beam cross-section. The torsional constant, k_t, can be defined as [62, 74]

$$k_t=\int_A\left\{\left({}^0z\right)^2+\left({}^0y\right)^2\right\}d\left({}^0A\right) \tag{3.41}$$

The area moment of inertia of beam cross-section, I_{yy} and I_{zz}, can be defined as [70, 73]

$$I_{yy}=\int_A\left({}^0z\right)^2d\left({}^0A\right);\qquad I_{zz}=\int_A\left({}^0y\right)^2d\left({}^0A\right) \tag{3.42}$$

Similar to the study in [62], the strain energy density for a beam given in Eq. (3.40) can be decomposed into axial, bending, shear and torsional components as

$$\bar{W}^{NL} = \bar{W}^{NL}_{axial} + \bar{W}^{NL}_{bending} + \bar{W}^{NL}_{shear} + \bar{W}^{NL}_{torsion} \tag{3.43a}$$

with

$$\bar{W}^{NL}_{axial} = E\left\{ {}^{t}_{0}u_{,x} + \frac{1}{2}\left({}^{t}_{0}u_{,x}{}^{2} + {}^{t}_{0}v_{,x}{}^{2} + {}^{t}_{0}w_{,x}{}^{2} \right) \right\} \left\{ \begin{array}{l} {}_{0}\underline{u}_{,x}\left(1 + {}^{t}_{0}u_{,x}\right) + \left({}^{t}_{0}v_{,x} \right)\left({}_{0}\underline{v}_{,x} \right) \\ + \left({}^{t}_{0}w_{,x} \right)\left({}_{0}\underline{w}_{,x} \right) \end{array} \right\} \tag{3.43b}$$

$$\begin{aligned} \bar{W}^{NL}_{bending} = {} & \frac{EI_{yy}}{\left({}^{0}A \right)} \left\{ \begin{array}{l} {}^{t}_{0}V_{tx,x} + \left({}^{t}_{0}u_{,x} \right)\left({}^{t}_{0}V_{tx,x} \right) \\ + \left({}^{t}_{0}v_{,x} \right)\left({}^{t}_{0}V_{ty,x} \right) \\ + \left({}^{t}_{0}w_{,x} \right)\left({}^{t}_{0}V_{tz,x} \right) \end{array} \right\} \left\{ \begin{array}{l} \left({}^{t}_{0}V_{tx,x} \right)\left({}_{0}u_{,x} \right) + \left({}^{t}_{0}V_{ty,x} \right)\left({}_{0}v_{,x} \right) + \left({}^{t}_{0}V_{tz,x} \right)\left({}_{0}w_{,x} \right) \\ + \left(1 + {}^{t}_{0}u_{,x}\right) \dfrac{\partial\left(\underline{\theta}_{y}\,{}^{t}V_{tz} - \underline{\theta}_{z}\,{}^{t}V_{ty} \right)}{\partial\,{}^{0}x} + \\ + {}^{t}_{0}v_{,x}\, \dfrac{\partial\left(\underline{\theta}_{z}\,{}^{t}V_{tx} - \underline{\theta}_{x}\,{}^{t}V_{tz} \right)}{\partial\,{}^{0}x} \\ + {}^{t}_{0}w_{,x}\, \dfrac{\partial\left(\underline{\theta}_{x}\,{}^{t}V_{ty} - \underline{\theta}_{y}\,{}^{t}V_{tx} \right)}{\partial\,{}^{0}x} \end{array} \right\} \\ & + \frac{EI_{zz}}{\left({}^{0}A \right)} \left\{ \begin{array}{l} {}^{t}_{0}V_{sx,x} + \left({}^{t}_{0}u_{,x} \right)\left({}^{t}_{0}V_{sx,x} \right) \\ + \left({}^{t}_{0}v_{,x} \right)\left({}^{t}_{0}V_{sy,x} \right) \\ + \left({}^{t}_{0}w_{,x} \right)\left({}^{t}_{0}V_{sz,x} \right) \end{array} \right\} \left\{ \begin{array}{l} \left({}^{t}_{0}V_{sx,x} \right)\left({}_{0}\underline{u}_{,x} \right) + \left({}^{t}_{0}V_{sy,x} \right)\left({}_{0}\underline{v}_{,x} \right) + \left({}^{t}_{0}V_{sz,x} \right)\left({}_{0}\underline{w}_{,x} \right) \\ + \left(1 + {}^{t}_{0}u_{,x}\right) \dfrac{\partial\left(\underline{\theta}_{y}\,{}^{t}V_{sz} - \underline{\theta}_{z}\,{}^{t}V_{sy} \right)}{\partial\,{}^{0}x} + \\ + {}^{t}_{0}v_{,x}\, \dfrac{\partial\left(\underline{\theta}_{z}\,{}^{t}V_{sx} - \underline{\theta}_{x}\,{}^{t}V_{sz} \right)}{\partial\,{}^{0}x} \\ + {}^{t}_{0}w_{,x}\, \dfrac{\partial\left(\underline{\theta}_{x}\,{}^{t}V_{sy} - \underline{\theta}_{y}\,{}^{t}V_{sx} \right)}{\partial\,{}^{0}x} \end{array} \right\} \end{aligned} \tag{3.43c}$$

$$\begin{aligned} \bar{W}^{NL}_{shear} = k_{s}G \Bigg[& \left\{ \begin{array}{l} {}^{t}V_{sx}\left(1 + {}^{t}_{0}u_{,x}\right) + {}^{t}V_{sy}\,{}^{t}_{0}v_{,x} \\ + {}^{t}V_{sz}\,{}^{t}_{0}w_{,x} \end{array} \right\} \left\{ \begin{array}{l} {}^{t}V_{sx}\left({}_{0}\underline{u}_{,x} \right) + {}^{t}V_{sy}\left({}_{0}\underline{v}_{,x} \right) + {}^{t}V_{sz}\left({}_{0}\underline{w}_{,x} \right) \\ + \left(1 + {}^{t}_{0}u_{,x}\right)\left(\underline{\theta}_{y}\,{}^{t}V_{sz} - \underline{\theta}_{z}\,{}^{t}V_{sy} \right) \\ + \left(\underline{\theta}_{z}\,{}^{t}V_{sx} - \underline{\theta}_{x}\,{}^{t}V_{sz} \right){}^{t}_{0}v_{,x} + {}^{t}_{0}w_{,x}\left(\underline{\theta}_{x}\,{}^{t}V_{sy} - \underline{\theta}_{y}\,{}^{t}V_{sx} \right) \end{array} \right\} \\ & + \left\{ \begin{array}{l} {}^{t}V_{tx}\left(1 + {}^{t}_{0}u_{,x}\right) + {}^{t}V_{ty}\,{}^{t}_{0}v_{,x} \\ + {}^{t}V_{tz}\,{}^{t}_{0}w_{,x} \end{array} \right\} \left\{ \begin{array}{l} {}^{t}V_{tz}\left({}_{0}\underline{w}_{,x} \right) + {}^{t}V_{tx}\left({}_{0}\underline{u}_{,x} \right) + {}^{t}V_{ty}\left({}_{0}\underline{v}_{,x} \right) \\ + \left(1 + {}^{t}_{0}u_{,x}\right)\left(\underline{\theta}_{y}\,{}^{t}V_{tz} - \underline{\theta}_{z}\,{}^{t}V_{ty} \right) \\ + {}^{t}_{0}v_{,x}\left(\underline{\theta}_{z}\,{}^{t}V_{tx} - \underline{\theta}_{x}\,{}^{t}V_{tz} \right) + {}^{t}_{0}w_{,x}\left(\underline{\theta}_{x}\,{}^{t}V_{ty} - \underline{\theta}_{y}\,{}^{t}V_{tx} \right) \end{array} \right\} \Bigg] \end{aligned} \tag{3.43d}$$

$$\bar{W}^{NL}_{torsion} = \frac{k_{t}G}{\left({}^{0}A \right)} \left\{ \begin{array}{l} {}^{t}V_{sy}\left({}^{t}_{0}V_{ty,x} \right) \\ + {}^{t}V_{sx}\left({}^{t}_{0}V_{tx,x} \right) + {}^{t}V_{sz}\left({}^{t}_{0}V_{tz,x} \right) \end{array} \right\} \left\{ \begin{array}{l} {}_{0}\underline{\theta}_{x,x}\left({}^{t}V_{ty}\,{}^{t}V_{sz} - {}^{t}V_{tz}\,{}^{t}V_{sy} \right) \\ + {}_{0}\underline{\theta}_{y,x}\left({}^{t}V_{tz}\,{}^{t}V_{sx} - {}^{t}V_{tx}\,{}^{t}V_{sz} \right) \\ + {}_{0}\underline{\theta}_{z,x}\left({}^{t}V_{tx}\,{}^{t}V_{sy} - {}^{t}V_{ty}\,{}^{t}V_{sx} \right) \end{array} \right\} \tag{3.43e}$$

where $\bar{W}^{NL}_{axial}$, $\bar{W}^{NL}_{bending}$, $\bar{W}^{NL}_{shear}$ and $\bar{W}^{NL}_{torsion}$ represent strain energy density corresponding to axial, bending, shear, and torsional deformations, respectively.

For simplification, the SED components given in Eq. (3.43) can be rewritten as

$$\bar{W}^{NL}_{axial} = E\left({}^{t}_{0}a_{10} \right)\left({}_{0}\underline{a}_{10} \right) \tag{3.44a}$$

$$\bar{W}^{NL}_{bending} = \frac{EI_{yy}}{\left({}^{0}A \right)}\left({}^{t}_{0}a_{12} \right)\left({}_{0}\underline{a}_{12} \right) + \frac{EI_{zz}}{\left({}^{0}A \right)}\left({}^{t}_{0}a_{11} \right)\left({}_{0}\underline{a}_{11} \right) \tag{3.44b}$$

$$\bar{W}^{NL}_{shear} = k_{s}G\left[\left({}^{t}_{0}a_{13} \right)\left({}_{0}\underline{a}_{13} \right) + \left({}^{t}_{0}a_{14} \right)\left({}_{0}\underline{a}_{14} \right) \right] \tag{3.44c}$$

$$\bar{W}^{NL}_{torsion} = \frac{k_t G}{\left({}^0A\right)}\left({}^t_0a_{15}\right)\left({}_0\underline{a}_{15}\right) \tag{3.44d}$$

with

$${}^t_0a_1 = {}^t_0u_{,x}; \qquad {}^t_0a_2 = {}^t_0v_{,x}; \qquad {}^t_0a_3 = {}^t_0w_{,x} \tag{3.44e}$$

$${}^t_0a_4 = {}^t_0V_{sx,x}; \qquad {}^t_0a_5 = {}^t_0V_{sy,x}; \qquad {}^t_0a_6 = {}^t_0V_{sz,x} \tag{3.44f}$$

$${}^t_0a_7 = {}^t_0V_{tx,x}; \qquad {}^t_0a_8 = {}^t_0V_{ty,x}; \qquad {}^t_0a_9 = {}^t_0V_{tz,x} \tag{3.44g}$$

$${}^t_0a_{10} = {}^t_0u_{,x} + \frac{1}{2}\left({}^t_0u_{,x}{}^2 + {}^t_0v_{,x}{}^2 + {}^t_0w_{,x}{}^2\right) = {}^t_0a_1 + \frac{1}{2}\left({}^t_0a_1^2 + {}^t_0a_2^3 + {}^t_0a_3^2\right) \tag{3.44h}$$

$$\begin{aligned} {}^t_0a_{11} &= {}^t_0V_{sx,x} + {}^t_0u_{,x}\,{}^t_0V_{sx,x} + {}^t_0v_{,x}\,{}^t_0V_{sy,x} + {}^t_0w_{,x}\,{}^t_0V_{sz,x} \\ &= {}^t_0a_4 + \left({}^t_0a_1\right)\left({}^t_0a_4\right) + \left({}^t_0a_2\right)\left({}^t_0a_5\right) + \left({}^t_0a_3\right)\left({}^t_0a_6\right) \end{aligned} \tag{3.44i}$$

$$\begin{aligned} {}^t_0a_{12} &= {}^t_0V_{tx,x} + {}^t_0u_{,x}\,{}^t_0V_{tx,x} + {}^t_0v_{,x}\,{}^t_0V_{ty,x} + {}^t_0w_{,x}\,{}^t_0V_{tz,x} \\ &= {}^t_0a_7 + {}^t_0a_1\,{}^t_0a_7 + {}^t_0a_2\,{}^t_0a_8 + {}^t_0a_3\,{}^t_0a_9 \end{aligned} \tag{3.44j}$$

$$\begin{aligned} {}^t_0a_{13} &= {}^tV_{sy}\,{}^t_0v_{,x} + {}^tV_{sx} + {}^tV_{sx}\,{}^t_0u_{,x} + {}^tV_{sz}\,{}^t_0w_{,x} \\ &= {}^tV_{sy}\left({}^t_0a_2\right) + {}^tV_{sx} + {}^tV_{sx}\left({}^t_0a_1\right) + {}^tV_{sz}\left({}^t_0a_3\right) \end{aligned} \tag{3.44k}$$

$$\begin{aligned} {}^t_0a_{14} &= {}^tV_{tz}\,{}^t_0w_{,x} + {}^tV_{tx} + {}^tV_{tx}\,{}^t_0u_{,x} + {}^tV_{ty}\,{}^t_0v_{,x} \\ &= {}^tV_{tz}\left({}^t_0a_3\right) + {}^tV_{tx} + {}^tV_{tx}\left({}^t_0a_1\right) + {}^tV_{ty}\left({}^t_0a_2\right) \end{aligned} \tag{3.44l}$$

$${}^t_0a_{15} = {}^tV_{sy}\,{}^t_0V_{ty,x} + {}^tV_{sx}\,{}^t_0V_{tx,x} + {}^tV_{sz}\,{}^t_0V_{tz,x} = {}^tV_{sy}\left({}^t_0a_8\right) + {}^tV_{sx}\left({}^t_0a_7\right) + {}^tV_{sz}\left({}^t_0a_9\right) \tag{3.44m}$$

$${}_0\underline{a}_{10} = \left({}_0\underline{u}_{,x}\right)\left(1 + {}^t_0a_1\right) + {}^t_0a_2\left({}_0\underline{v}_{,x}\right) + {}^t_0a_3\left({}_0\underline{w}_{,x}\right) \tag{3.44n}$$

$$\begin{aligned} {}_0\underline{a}_{11} &= {}^t_0a_4\left({}_0\underline{u}_{,x}\right) + {}^t_0a_5\left({}_0\underline{v}_{,x}\right) + {}^t_0a_6\left({}_0\underline{w}_{,x}\right) + \left(1 + {}^t_0a_1\right)\frac{\partial\left(\underline{\theta}_y\,{}^tV_{sz} - \underline{\theta}_z\,{}^tV_{sy}\right)}{\partial\,{}^0x} + \\ &+ {}^t_0a_2\,\frac{\partial\left(\underline{\theta}_z\,{}^tV_{sx} - \underline{\theta}_x\,{}^tV_{sz}\right)}{\partial\,{}^0x} + {}^t_0a_3\,\frac{\partial\left(\underline{\theta}_x\,{}^tV_{sy} - \underline{\theta}_y\,{}^tV_{sx}\right)}{\partial\,{}^0x} \end{aligned} \tag{3.44o}$$

$$\begin{aligned} {}_0\underline{a}_{12} &= \left({}^t_0V_{tx,x}\right)\left({}_0u_{,x}\right) + {}^t_0a_8\left({}_0v_{,x}\right) + {}^t_0a_9\left({}_0w_{,x}\right) + \left(1 + {}^t_0a_1\right)\frac{\partial\left(\underline{\theta}_y\,{}^tV_{tz} - \underline{\theta}_z\,{}^tV_{ty}\right)}{\partial\,{}^0x} + \\ &+ {}^t_0a_2\,\frac{\partial\left(\underline{\theta}_z\,{}^tV_{tx} - \underline{\theta}_x\,{}^tV_{tz}\right)}{\partial\,{}^0x} + {}^t_0a_3\,\frac{\partial\left(\underline{\theta}_x\,{}^tV_{ty} - \underline{\theta}_y\,{}^tV_{tx}\right)}{\partial\,{}^0x} \end{aligned} \tag{3.44p}$$

$$\begin{aligned} {}_0\underline{a}_{13} &= {}^tV_{sx}\left({}_0\underline{u}_{,x}\right) + {}^tV_{sy}\left({}_0\underline{v}_{,x}\right) + {}^tV_{sz}\left({}_0\underline{w}_{,x}\right) + \left(1 + {}^t_0a_1\right)\left(\underline{\theta}_y\,{}^tV_{sz} - \underline{\theta}_z\,{}^tV_{sy}\right) \\ &+ {}^t_0a_2\left(\underline{\theta}_z\,{}^tV_{sx} - \underline{\theta}_x\,{}^tV_{sz}\right) + {}^t_0a_3\left(\underline{\theta}_x\,{}^tV_{sy} - \underline{\theta}_y\,{}^tV_{sx}\right) \end{aligned} \tag{3.44q}$$

$$
\begin{aligned}
{}_0\underline{a}_{14} = {}^tV_{tz}\left({}_0\underline{w}_{,x}\right) + {}^tV_{tx}\left({}_0\underline{u}_{,x}\right) + {}^tV_{ty}\left({}_0\underline{v}_{,x}\right) + \left(1 + {}_0^t a_1\right)\left(\underline{\theta}_y\,{}^tV_{tz} - \underline{\theta}_z\,{}^tV_{ty}\right) \\
+ {}_0^t a_2\left(\underline{\theta}_z\,{}^tV_{tx} - \underline{\theta}_x\,{}^tV_{tz}\right) + {}_0^t a_3\left(\underline{\theta}_x\,{}^tV_{ty} - \underline{\theta}_y\,{}^tV_{tx}\right)
\end{aligned} \tag{3.44r}
$$

$$
\begin{aligned}
{}_0\underline{a}_{15} = {}_0\underline{\theta}_{x,x}\left({}^tV_{ty}\,{}^tV_{sz} - {}^tV_{tz}\,{}^tV_{sy}\right) + {}_0\underline{\theta}_{y,x}\left({}^tV_{tz}\,{}^tV_{sx} - {}^tV_{tx}\,{}^tV_{sz}\right) \\
+ {}_0\underline{\theta}_{z,x}\left({}^tV_{tx}\,{}^tV_{sy} - {}^tV_{ty}\,{}^tV_{sx}\right)
\end{aligned} \tag{3.44s}
$$

3.3.2. Nonlinear beam kinematics in peridynamics

For nonlinear analysis of a beam, the PD equation of motion for material point k can be described in discrete form as

$$
\rho_{(k)}\left({}^t\ddot{\mathbf{u}}_{(k)}\right) = \sum_{j=1}^{N}\begin{pmatrix} {}_0^t\mathbf{t}_{(k)(j)}({}^t\mathbf{u}_{(j)} - {}^t\mathbf{u}_{(k)},\, {}^0\mathbf{x}_{(j)} - {}^0\mathbf{x}_{(k)}, t) \\ -{}_0^t\mathbf{t}_{(j)(k)}({}^t\mathbf{u}_{(k)} - {}^t\mathbf{u}_{(j)},\, {}^0\mathbf{x}_{(k)} - {}^0\mathbf{x}_{(j)}, t) \end{pmatrix}{}^0V_{(j)} + {}^t\mathbf{b}_{(k)} \tag{3.45}
$$

where ρ represents the mass density, ${}^t\ddot{\mathbf{u}}$ represents the vector of accelerations at time t. The term ${}^t\boldsymbol{u}$ represents the vector of displacements at time t, ${}^t\boldsymbol{b}_{(k)}$ represents the vector of external forces and moments per unit volume at time t. The term N represents the number of family members of material point k, and j represents a family member material point k. The term ${}_0^t\boldsymbol{t}_{(k)(j)}$ represents the force density at time t that material point j exerts on material point k, and ${}_0^t\boldsymbol{t}_{(j)(k)}$ represents the force density at time t that material point k exerts on point j. For a beam with six degrees of freedom, the parameters in Eq. (3.45) can be represented as

$$
{}_0^t\mathbf{t}_{(k)(j)} = \begin{bmatrix} {}_0^t t^{u}_{(k)(j)} & {}_0^t t^{v}_{(k)(j)} & {}_0^t t^{w}_{(k)(j)} & {}_0^t t^{\theta_x}_{(k)(j)} & {}_0^t t^{\theta_y}_{(k)(j)} & {}_0^t t^{\theta_z}_{(k)(j)} \end{bmatrix}^T \tag{3.46a}
$$

$$
{}_0^t\mathbf{t}_{(j)(k)} = \begin{bmatrix} {}_0^t t^{u}_{(k)(j)(k)} & {}_0^t t^{v}_{(j)(k)} & {}_0^t t^{w}_{(j)(k)} & {}_0^t t^{\theta_x}_{(j)(k)} & {}_0^t t^{\theta_y}_{(j)(k)} & {}_0^t t^{\theta_z}_{(j)(k)} \end{bmatrix}^T \tag{3.46b}
$$

$$
{}^t\ddot{\mathbf{u}}_{(k)} = \begin{bmatrix} {}^t\ddot{u}_{(k)} & {}^t\ddot{v}_{(k)} & {}^t\ddot{w}_{(k)} & {}^t\ddot{\theta}_{x(k)} & {}^t\ddot{\theta}_{y(k)} & {}^t\ddot{\theta}_{z(k)} \end{bmatrix}^T \tag{3.46c}
$$

$$
{}^t\mathbf{b}_{(k)} = \begin{bmatrix} {}^t b_{x(k)} & {}^t b_{y(k)} & {}^t b_{z(k)} & {}^t m_{x(k)} & {}^t m_{y(k)} & {}^t m_{z(k)} \end{bmatrix}^T \tag{3.46d}
$$

$$
{}^0\mathbf{x}_{(k)} = \begin{bmatrix} {}^0x_{(k)} & 0 & 0 \end{bmatrix} \tag{3.46e}
$$

$$
{}^t\mathbf{u}_{(k)} = \begin{bmatrix} {}^t u_{(k)} & {}^t v_{(k)} & {}^t w_{(k)} & {}^t\theta_{x(k)} & {}^t\theta_{y(k)} & {}^t\theta_{z(k)} \end{bmatrix}^T \tag{3.46f}
$$

where ${}_0^t t^{u}_{(k)(j)}$, ${}_0^t t^{v}_{(k)(j)}$, ${}_0^t t^{w}_{(k)(j)}$, ${}_0^t t^{\theta_x}_{(k)(j)}$, ${}_0^t t^{\theta_y}_{(k)(j)}$, and ${}_0^t t^{\theta_z}_{(k)(j)}$ represents force densities corresponding to six degrees of freedom, u, v, w, θ_x, θ_y, and θ_z, respectively.

Similar to the relation given in Eq. (1.2) in Chapter 1, the relationship between the components of force densities and strain energy density for nonlinear analysis of beam structures can be described as [44, 102]

$$ {}_0^t t_{(k)(j)}^{q_i} = -\frac{1}{{}^0V_{(j)}} \frac{\partial \bar{W}_{(k)}^{NLPD}}{\partial \underline{q}_{i\,(k)}} \tag{3.47a} $$

$$ {}_0^t t_{(j)(k)}^{q_i} = -\frac{1}{{}^0V_{(k)}} \frac{\partial \bar{W}_{(j)}^{NLPD}}{\partial \underline{q}_{i\,(j)}} \tag{3.47b} $$

with

$$ q_i = u,\ v,\ w,\ \theta_x,\ \theta_y,\ \theta_z \tag{3.47c} $$

$$ \underline{q}_i = \underline{u},\ \underline{v},\ \underline{w},\ \underline{\theta}_x,\ \underline{\theta}_y,\ \underline{\theta}_z \tag{3.47d} $$

where the parameter q_i represents the degree of freedom which can be u, v, w, θ_x, θ_y, or θ_z. The parameter $\underline{q}_i$ represents the incremental value of q_i which can be $\underline{u}$, $\underline{v}$, $\underline{w}$, $\underline{\theta}_x$, $\underline{\theta}_y$, or $\underline{\theta}_z$.

The terms ${}_0^t t_{(k)(j)}^{q_i}$ and ${}_0^t t_{(j)(k)}^{q_i}$ represent force densities corresponding to the degree of freedom q_i. The terms $\bar{W}_{(k)}^{NLPD}$ and $\bar{W}_{(j)}^{NLPD}$ represent PD nonlinear strain energy densities of material points k and j, respectively.

In the bond-based PD model, the force densities ${}_0^t\boldsymbol{t}_{(j)(k)}$ and ${}_0^t\boldsymbol{t}_{(k)(j)}$ have the same magnitude and they are in opposite directions (${}_0^t\boldsymbol{t}_{(k)(j)} = -{}_0^t\boldsymbol{t}_{(j)(k)}$) [21]. Therefore, the PD equations of motion given in Eq. (3.45) can be rewritten as

$$ \rho_{(k)} \left({}^t\ddot{\mathbf{u}}_{(k)} \right) = \sum_{j=1}^{N} {}_0^t\mathbf{f}_{(k)(j)}({}^t\mathbf{u}_{(j)} - {}^t\mathbf{u}_{(k)},\ {}^0\mathbf{x}_{(j)} - {}^0\mathbf{x}_{(k)}, t)\,{}^0V_{(j)} + {}^t\mathbf{b}_{(k)} \tag{3.48a} $$

with

$$ {}_0^t\mathbf{f}_{(k)(j)} = 2\,{}_0^t\mathbf{t}_{(k)(j)} \tag{3.48b} $$

In the following sections, first, the nonlinear PD strain energy densities and PD bond constants for a straight beam are presented in Section 3.3.2.1. Next, the PD equations of motion in the local coordinate system of a straight beam are obtained in Section 3.3.2.2. Finally, the transformation of equations of motion from the beam's local coordinate system to the global coordinate system is presented in Section 3.3.2.3.

3.3.2.1. Peridynamic strain energy density

Similar to the classical formulations given in Eq. (3.43a), the nonlinear SED in PD for a beam can be represented as

$$ \bar{W}^{NLPD} = \bar{W}_{axial}^{NLPD} + \bar{W}_{bending}^{NLPD} + \bar{W}_{shear}^{NLPD} + \bar{W}_{torsion}^{NLPD} \tag{3.49} $$

where $\bar{W}_{axial}^{NLPD}$, $\bar{W}_{bending}^{NLPD}$, $\bar{W}_{shear}^{NLPD}$, and $\bar{W}_{torsion}^{NLPD}$ represent the PD strain energy densities for axial, bending, shear, and torsional deformations, respectively. Similar to the classical formulation given in Eq. (3.44a), the PD strain energy density for axial deformations can be represented as

$$\bar{W}_{axial}^{NLPD} = \frac{1}{2}\sum_{j=1}^{N} C_{ax}\left({}_0^t a_{10}^{PD}\right)\left({}_0\underline{a}_{10}^{PD}\right)\left({}^0\xi_{(k)(j)}\right){}^0V_{(j)} \tag{3.50a}$$

with

$${}_0^t a_{10}^{PD} = {}_0^t a_1^{PD} + \frac{1}{2}\left(\left({}_0^t a_1^{PD}\right)^2 + \left({}_0^t a_2^{PD}\right)^2 + \left({}_0^t a_3^{PD}\right)^2\right) \tag{3.50b}$$

$${}_0\underline{a}_{10}^{PD} = \left(\frac{\underline{u}_{(j)} - \underline{u}_{(k)}}{{}^0\xi_{(k)(j)}}\left(1 + {}_0^t a_1^{PD}\right) + {}_0^t a_2^{PD}\,\frac{\underline{v}_{(j)} - \underline{v}_{(k)}}{{}^0\xi_{(k)(j)}} + {}_0^t a_3^{PD}\,\frac{\underline{w}_{(j)} - \underline{w}_{(k)}}{{}^0\xi_{(k)(j)}}\right)\left({}^0\beta_{(k)(j)}\right) \tag{3.50c}$$

$${}_0^t a_1^{PD} = \frac{{}^t u_{(j)} - {}^t u_{(k)}}{{}^0\xi_{(k)(j)}}\,{}^0\beta_{(k)(j)} \tag{3.50d}$$

$${}_0^t a_2^{PD} = \frac{{}^t v_{(j)} - {}^t v_{(k)}}{{}^0\xi_{(k)(j)}}\,{}^0\beta_{(k)(j)} \tag{3.50e}$$

$${}_0^t a_3^{PD} = \frac{{}^t w_{(j)} - {}^t w_{(k)}}{{}^0\xi_{(k)(j)}}\,{}^0\beta_{(k)(j)} \tag{3.50f}$$

$${}^0\xi_{(k)(j)} = \left|{}^0x_{(j)} - {}^0x_{(k)}\right| \tag{3.50g}$$

$${}^0\beta_{(k)(j)} = \frac{{}^0x_{(j)} - {}^0x_{(k)}}{{}^0\xi_{(k)(j)}} \tag{3.50h}$$

where C_{ax} in Eq. (3.50a) represents PD constant for axial deformations. This PD constant can be obtained by comparing nonlinear SED for axial deformations in CCM to PD as presented in Appendix E.1 as

$$C_{ax} = \frac{2E}{\left({}^0A\right)\delta^2} \tag{3.51}$$

Similar to the classical formulation given in Eq. (3.44b), the nonlinear PD strain energy density for bending deformations, $\bar{W}_{bending}^{NLPD}$, in Eq. (3.49) can be represented as

$$\begin{aligned}\bar{W}_{bending}^{NLPD} = {} & \frac{C_{bz}}{2}\sum_{j=1}^{N}\left({}_0^t a_{11}^{PD}\right)\left({}_0\underline{a}_{11}^{PD}\right)\left({}^0\xi_{(k)(j)}\right){}^0V_{(j)} \\ & + \frac{C_{by}}{2}\sum_{j=1}^{N}\left({}_0^t a_{12}^{PD}\right)\left({}_0\underline{a}_{12}^{PD}\right)\left({}^0\xi_{(k)(j)}\right){}^0V_{(j)}\end{aligned} \tag{3.52a}$$

with

$${}_0^t a_{11}^{PD} = {}_0^t a_4^{PD}\left(1 + {}_0^t a_1^{PD}\right) + \left({}_0^t a_2^{PD}\right)\left({}_0^t a_5^{PD}\right) + \left({}_0^t a_3^{PD}\right)\left({}_0^t a_6^{PD}\right) \tag{3.52b}$$

$${}_0^t a_{12}^{PD} = \left({}_0^t a_7^{PD}\right)\left(1 + {}_0^t a_1^{PD}\right) + \left({}_0^t a_2^{PD}\right)\left({}_0^t a_8^{PD}\right) + \left({}_0^t a_3^{PD}\right)\left({}_0^t a_9^{PD}\right) \tag{3.52c}$$

$$
{}_0\underline{a}_{11}^{PD} = \left(\begin{array}{l}
\left({}_0^t a_4^{PD}\right)\dfrac{\underline{u}_{(j)}-\underline{u}_{(k)}}{{}^0\xi_{(k)(j)}} + \left({}_0^t a_5^{PD}\right)\dfrac{\underline{v}_{(j)}-\underline{v}_{(k)}}{{}^0\xi_{(k)(j)}} + \left({}_0^t a_6^{PD}\right)\dfrac{\underline{w}_{(j)}-\underline{w}_{(k)}}{{}^0\xi_{(k)(j)}} \\
+\left(1+{}_0^t a_1^{PD}\right)\dfrac{\left(\underline{\theta}_{y(j)}\,{}^tV_{sz(j)}-\underline{\theta}_{z(j)}\,{}^tV_{sy(j)}\right)-\left(\underline{\theta}_{y(k)}\,{}^tV_{sz(k)}-\underline{\theta}_{z(k)}\,{}^tV_{sy(k)}\right)}{{}^0\xi_{(k)(j)}} \\
+\left({}_0^t a_2^{PD}\right)\dfrac{\left(\underline{\theta}_{z(j)}\,{}^tV_{sx(j)}-\underline{\theta}_{x(j)}\,{}^tV_{sz(j)}\right)-\left(\underline{\theta}_{z(k)}\,{}^tV_{sx(k)}-\underline{\theta}_{x(k)}\,{}^tV_{sz(k)}\right)}{{}^0\xi_{(k)(j)}} \\
+\left({}_0^t a_3^{PD}\right)\dfrac{\left(\underline{\theta}_{x(j)}\,{}^tV_{sy(j)}-\underline{\theta}_{y(j)}\,{}^tV_{sx(j)}\right)-\left(\underline{\theta}_{x(k)}\,{}^tV_{sy(k)}-\underline{\theta}_{y(k)}\,{}^tV_{sx(k)}\right)}{{}^0\xi_{(k)(j)}}
\end{array} \right)\left({}^0\beta_{(k)(j)}\right) \tag{3.52d}
$$

$$
{}_0\underline{a}_{12}^{PD} = \left(\begin{array}{l}
\left({}_0^t a_7^{PD}\right)\dfrac{\underline{u}_{(j)}-\underline{u}_{(k)}}{{}^0\xi_{(k)(j)}} + \left({}_0^t a_8^{PD}\right)\dfrac{\underline{v}_{(j)}-\underline{v}_{(k)}}{{}^0\xi_{(k)(j)}} + \left({}_0^t a_9^{PD}\right)\dfrac{\underline{w}_{(j)}-\underline{w}_{(k)}}{{}^0\xi_{(k)(j)}} \\
+\left(1+{}_0^t a_1^{PD}\right)\dfrac{\left(\underline{\theta}_{y(j)}\,{}^tV_{tz(j)}-\underline{\theta}_{z(j)}\,{}^tV_{ty(j)}\right)-\left(\underline{\theta}_{y(k)}\,{}^tV_{tz(k)}-\underline{\theta}_{z(k)}\,{}^tV_{ty(k)}\right)}{{}^0\xi_{(k)(j)}} \\
+\left({}_0^t a_2^{PD}\right)\dfrac{\left(\underline{\theta}_{z(j)}\,{}^tV_{tx(j)}-\underline{\theta}_{x(j)}\,{}^tV_{tz(j)}\right)-\left(\underline{\theta}_{z(k)}\,{}^tV_{tx(k)}-\underline{\theta}_{x(k)}\,{}^tV_{tz(k)}\right)}{{}^0\xi_{(k)(j)}} \\
+\left({}_0^t a_3^{PD}\right)\dfrac{\left(\underline{\theta}_{x(j)}\,{}^tV_{ty(j)}-\underline{\theta}_{y(j)}\,{}^tV_{tx(j)}\right)-\left(\underline{\theta}_{x(k)}\,{}^tV_{ty(k)}-\underline{\theta}_{y(k)}\,{}^tV_{tx(k)}\right)}{{}^0\xi_{(k)(j)}}
\end{array} \right)\left({}^0\beta_{(k)(j)}\right) \tag{3.52e}
$$

$$
{}_0^t a_4^{PD} = \frac{{}^tV_{sx(j)} - {}^tV_{sx(k)}}{{}^0\xi_{(k)(j)}}\,{}^0\beta_{(k)(j)} \tag{3.52f}
$$

$$
{}_0^t a_5^{PD} = \frac{{}^tV_{sy(j)} - {}^tV_{sy(k)}}{{}^0\xi_{(k)(j)}}\,{}^0\beta_{(k)(j)} \tag{3.52g}
$$

$$
{}_0^t a_6^{PD} = \frac{{}^tV_{sz(j)} - {}^tV_{sz(k)}}{{}^0\xi_{(k)(j)}}\,{}^0\beta_{(k)(j)} \tag{3.52h}
$$

$$
{}_0^t a_7^{PD} = \frac{{}^tV_{tx(j)} - {}^tV_{tx(k)}}{{}^0\xi_{(k)(j)}}\,{}^0\beta_{(k)(j)} \tag{3.52i}
$$

$$
{}_0^t a_8^{PD} = \frac{{}^tV_{ty(j)} - {}^tV_{ty(k)}}{{}^0\xi_{(k)(j)}}\,{}^0\beta_{(k)(j)} \tag{3.52j}
$$

$$
{}_0^t a_9^{PD} = \frac{{}^tV_{tz(j)} - {}^tV_{tz(k)}}{{}^0\xi_{(k)(j)}}\,{}^0\beta_{(k)(j)} \tag{3.52k}
$$

where the terms, C_{by}, C_{bz} in Eq. (3.52a) represent PD constants for bending deformations. As presented in Appendix E2, these PD constants can be obtained by comparing nonlinear SED for bending deformations in CCM to PD as

$$
C_{by} = \frac{2EI_{yy}}{\left({}^0A\right)^2\delta^2};\; C_{bz} = \frac{2EI_{zz}}{\left({}^0A\right)^2\delta^2} \tag{3.53}
$$

Similar to the classical formulation given in Eq. (3.44c), the PD strain energy density for shear deformations, $\bar{W}_{shear}^{NLPD}$, in Eq. (3.49) can be represented as

$$\bar{W}_{shear}^{NLPD} = \frac{1}{2}\sum_{j=1}^{N} C_s \left[\left({}_0^t a_{13}^{PD} \right) \left({}_0 \underline{a}_{13}^{PD} \right) + \left({}_0^t a_{14}^{PD} \right) \left({}_0 \underline{a}_{14}^{PD} \right) \right] \left({}^0\xi_{(k)(j)} \right) {}^0V_{(j)} \tag{3.54a}$$

with

$$\begin{aligned} {}_0^t a_{13}^{PD} = & \left(1 + {}_0^t a_1^{PD}\right) \frac{{}^tV_{sx(j)} + {}^tV_{sx(k)}}{2} + \left({}_0^t a_2^{PD} \right) \frac{{}^tV_{sy(j)} + {}^tV_{sy(k)}}{2} \\ & + \left({}_0^t a_3^{PD} \right) \frac{{}^tV_{sz(j)} + {}^tV_{sz(k)}}{2} \end{aligned} \tag{3.54b}$$

$$\begin{aligned} {}_0^t a_{14}^{PD} = & \left(1 + {}_0^t a_1^{PD}\right) \frac{{}^tV_{tx(j)} + {}^tV_{tx(k)}}{2} + \left({}_0^t a_2^{PD} \right) \frac{{}^tV_{ty(j)} + {}^tV_{ty(k)}}{2} \\ & + \left({}_0^t a_3^{PD} \right) \frac{{}^tV_{tz(j)} + {}^tV_{tz(k)}}{2} \end{aligned} \tag{3.54c}$$

$$\begin{aligned} {}_0 \underline{a}_{13}^{PD} = & \left(\begin{array}{l} \left(\dfrac{{}^tV_{sx(k)} + {}^tV_{sx(j)}}{2} \dfrac{\underline{u}_{(j)} - \underline{u}_{(k)}}{{}^0\xi_{(k)(j)}} + \dfrac{{}^tV_{sy(k)} + {}^tV_{sy(j)}}{2} \dfrac{\underline{v}_{(j)} - \underline{v}_{(k)}}{{}^0\xi_{(k)(j)}} \right) \\ + \dfrac{{}^tV_{sz(k)} + {}^tV_{sz(j)}}{2} \dfrac{\underline{w}_{(j)} - \underline{w}_{(k)}}{{}^0\xi_{(k)(j)}} \end{array} \right) {}^0\beta_{(k)(j)} \\ & + \left(1 + {}_0^t a_1^{PD}\right) \frac{\left(\underline{\theta}_{y(j)} {}^tV_{sz(j)} - \underline{\theta}_{z(j)} {}^tV_{sy(j)} \right) + \left(\underline{\theta}_{y(k)} {}^tV_{sz(k)} - \underline{\theta}_{z(k)} {}^tV_{sy(k)} \right)}{2} \\ & + \left({}_0^t a_2^{PD} \right) \frac{\left(\underline{\theta}_{z(j)} {}^tV_{sx(j)} - \underline{\theta}_{x(j)} {}^tV_{sz(j)} \right) + \left(\underline{\theta}_{z(k)} {}^tV_{sx(k)} - \underline{\theta}_{x(k)} {}^tV_{sz(k)} \right)}{2} \\ & + \left({}_0^t a_3^{PD} \right) \frac{\left(\underline{\theta}_{x(j)} {}^tV_{sy(j)} - \underline{\theta}_{y(j)} {}^tV_{sx(j)} \right) + \left(\underline{\theta}_{x(k)} {}^tV_{sy(k)} - \underline{\theta}_{y(k)} {}^tV_{sx(k)} \right)}{2} \end{aligned} \tag{3.54d}$$

$$\begin{aligned} {}_0 \underline{a}_{14}^{PD} = & \left(\begin{array}{l} \left(\dfrac{{}^tV_{tx(k)} + {}^tV_{tx(j)}}{2} \dfrac{\underline{u}_{(j)} - \underline{u}_{(k)}}{{}^0\xi_{(k)(j)}} + \dfrac{{}^tV_{ty(k)} + {}^tV_{ty(j)}}{2} \dfrac{\underline{v}_{(j)} - \underline{v}_{(k)}}{{}^0\xi_{(k)(j)}} \right) \\ + \dfrac{{}^tV_{tz(k)} + {}^tV_{tz(j)}}{2} \dfrac{\underline{w}_{(j)} - \underline{w}_{(k)}}{{}^0\xi_{(k)(j)}} \end{array} \right) {}^0\beta_{(k)(j)} \\ & + \left(1 + {}_0^t a_1^{PD}\right) \frac{\left(\underline{\theta}_{y(j)} {}^tV_{tz(j)} - \underline{\theta}_{z(j)} {}^tV_{ty(j)} \right) + \left(\underline{\theta}_{y(k)} {}^tV_{tz(k)} - \underline{\theta}_{z(k)} {}^tV_{ty(k)} \right)}{2} \\ & + \left({}_0^t a_2^{PD} \right) \frac{\left(\underline{\theta}_{z(j)} {}^tV_{tx(j)} - \underline{\theta}_{x(j)} {}^tV_{tz(j)} \right) + \left(\underline{\theta}_{z(k)} {}^tV_{tx(k)} - \underline{\theta}_{x(k)} {}^tV_{tz(k)} \right)}{2} \\ & + \left({}_0^t a_3^{PD} \right) \frac{\left(\underline{\theta}_{x(j)} {}^tV_{ty(j)} - \underline{\theta}_{y(j)} {}^tV_{tx(j)} \right) + \left(\underline{\theta}_{x(k)} {}^tV_{ty(k)} - \underline{\theta}_{y(k)} {}^tV_{tx(k)} \right)}{2} \end{aligned} \tag{3.54e}$$

where the term C_{sh} in Eq. (3.54a) represents the PD constant for shear deformations. As presented in Appendix E3, this PD constant can be obtained by comparing nonlinear SED for shear deformations in CCM to PD as

$$C_s = \frac{2k_s G}{\left({}^0A\right)\delta^2} \tag{3.55}$$

Similar to the classical formulation given in Eq. (3.44c), the PD strain energy density for torsional deformations, $\bar{W}_{torsion}^{NLPD}$, in Eq. (3.49) can be represented as

$$\bar{W}_{torsion}^{NLPD} = \frac{1}{2}\sum_{j=1}^{N} C_t \left({}_0^t a_{15}^{PD}\right)\left({}_0\underline{a}_{15}^{PD}\right)\left({}^0\xi_{(k)(j)}\right){}^0V_{(j)} \tag{3.56a}$$

with

$${}_0^t a_{15}^{PD} = \left({}_0^t a_8^{PD}\right)\frac{{}^tV_{sy(j)} + {}^tV_{sy(k)}}{2} + \left({}_0^t a_7^{PD}\right)\frac{{}^tV_{sx(j)} + {}^tV_{sx(k)}}{2} + \left({}_0^t a_9^{PD}\right)\frac{{}^tV_{sz(j)} + {}^tV_{sz(k)}}{2} \tag{3.56b}$$

$${}_0\underline{a}_{15}^{PD} = \left(\begin{array}{l} \left(\begin{array}{l} \dfrac{{}^tV_{ty(j)} + {}^tV_{ty(k)}}{2}\dfrac{{}^tV_{sz(j)} + {}^tV_{sz(k)}}{2} \\ -\dfrac{{}^tV_{tz(j)} + {}^tV_{tz(k)}}{2}\dfrac{{}^tV_{sy(k)} + {}^tV_{sy(j)}}{2} \end{array}\right)\dfrac{\underline{\theta}_{x(j)} - \underline{\theta}_{x(k)}}{{}^0\xi_{(k)(j)}} \\ + \left(\begin{array}{l} \dfrac{{}^tV_{tz(j)} + {}^tV_{tz(k)}}{2}\dfrac{{}^tV_{sx(j)} + {}^tV_{sx(k)}}{2} \\ -\dfrac{{}^tV_{tx(j)} + {}^tV_{tx(k)}}{2}\dfrac{{}^tV_{sz(j)} + {}^tV_{sz(k)}}{2} \end{array}\right)\dfrac{\underline{\theta}_{y(j)} - \underline{\theta}_{y(k)}}{{}^0\xi_{(k)(j)}} \\ + \left(\begin{array}{l} \dfrac{{}^tV_{tx(j)} + {}^tV_{tx(k)}}{2}\dfrac{{}^tV_{sy(k)} + {}^tV_{sy(j)}}{2} \\ -\dfrac{{}^tV_{ty(j)} + {}^tV_{ty(k)}}{2}\dfrac{{}^tV_{sx(j)} + {}^tV_{sx(k)}}{2} \end{array}\right)\dfrac{\underline{\theta}_{z(j)} - \underline{\theta}_{z(k)}}{{}^0\xi_{(k)(j)}} \end{array}\right)\left({}^0\beta_{(k)(j)}\right) \tag{3.56c}$$

where the term C_t in Eq. (3.56a) represents the PD constant for torsional deformations. As presented in Appendix E.4, this PD constant can be obtained by comparing nonlinear SED for torsional deformations in CCM to PD as

$$C_t = \frac{2k_t G}{\left({}^0A\right)^2\delta^2} \tag{3.57}$$

3.3.2.2. Nonlinear equation of motion in the local coordinate system for a beam

By substituting the nonlinear SED given in Eq. (3.49) into Eq. (3.47a), the PD force densities ${}_0^t t_{(k)(j)}^{q_i}$ can be represented as

$${}_0^t t_{(k)(j)}^{u} = \frac{1}{2}\left\{\begin{array}{l} C_{ax}\left({}_0^t a_{10}^{PD}\right)\left(1 + {}_0^t a_1^{PD}\right) \\ +C_{bz}\left({}_0^t a_{11}^{PD}\right)\left({}_0^t a_4^{PD}\right) + C_{by}\left({}_0^t a_{12}^{PD}\right)\left({}_0^t a_7^{PD}\right) \\ +C_{sh}\left(\left({}_0^t a_{13}^{PD}\right)\dfrac{{}^tV_{sx(k)} + {}^tV_{sx(i)}}{2} + \left({}_0^t a_{14}^{PD}\right)\dfrac{{}^tV_{tx(k)} + {}^tV_{tx(i)}}{2}\right) \end{array}\right\}\left({}^0\xi_{(k)(j)}\right) \tag{3.58a}$$

$$
{}_0^t t_{(k)(j)}^{v} = \frac{1}{2}\left\{\begin{array}{l} C_{ax}\left({}_0^t a_{10}^{PD}\right)\left({}_0^t a_{2}^{PD}\right) \\ +C_{bz}\left({}_0^t a_{11}^{PD}\right)\left({}_0^t a_{5}^{PD}\right)+C_{by}\left({}_0^t a_{12}^{PD}\right)\left({}_0^t a_{8}^{PD}\right) \\ +C_{sh}\left(\left({}_0^t a_{13}^{PD}\right)\dfrac{{}^tV_{sy(k)}+{}^tV_{sy(j)}}{2}+\left({}_0^t a_{14}^{PD}\right)\dfrac{{}^tV_{ty(k)}+{}^tV_{ty(j)}}{2}\right) \end{array}\right\}\left({}^0\xi_{(k)(j)}\right) \tag{3.58b}
$$

$$
{}_0^t t_{(k)(j)}^{w} = \frac{1}{2}\left\{\begin{array}{l} C_{ax}\left({}_0^t a_{10}^{PD}\right)\left({}_0^t a_{3}^{PD}\right) \\ +C_{bz}\left({}_0^t a_{11}^{PD}\right)\left({}_0^t a_{6}^{PD}\right)+C_{by}\left({}_0^t a_{12}^{PD}\right)\left({}_0^t a_{9}^{PD}\right) \\ C_{sh}\left(\left({}_0^t a_{13}^{PD}\right)\dfrac{{}^tV_{sz(k)}+{}^tV_{sz(j)}}{2}+\left({}_0^t a_{14}^{PD}\right)\dfrac{{}^tV_{tz(k)}+{}^tV_{tz(j)}}{2}\right) \end{array}\right\}\left({}^0\xi_{(k)(j)}\right) \tag{3.58c}
$$

$$
\begin{aligned}
{}_0^t t_{(k)(j)}^{\theta_x} &= \frac{1}{2}C_{bz}\left({}_0^t a_{11}^{PD}\right)\left\{-\left({}_0^t a_{2}^{PD}\right){}^tV_{sz(k)}+\left({}_0^t a_{3}^{PD}\right){}^tV_{sy(k)}\right\}\left({}^0\beta_{(k)(j)}\right) \\
&+\frac{1}{2}C_{by}\left({}_0^t a_{12}^{PD}\right)\left\{-\left({}_0^t a_{2}^{PD}\right){}^tV_{tz(k)}+\left({}_0^t a_{3}^{PD}\right){}^tV_{ty(k)}\right\}\left({}^0\beta_{(k)(j)}\right) \\
&+\frac{1}{4}C_{sh}\left({}^0\xi_{(k)(j)}\right)\left[\begin{array}{l}\left({}_0^t a_{13}^{PD}\right)\left\{\left({}_0^t a_{2}^{PD}\right){}^tV_{sz(k)}-\left({}_0^t a_{3}^{PD}\right){}^tV_{sy(k)}\right\} \\ +\left({}_0^t a_{14}^{PD}\right)\left\{\left({}_0^t a_{2}^{PD}\right){}^tV_{tz(k)}-\left({}_0^t a_{3}^{PD}\right){}^tV_{ty(k)}\right\}\end{array}\right] \\
&+\frac{1}{2}C_{t}\left({}_0^t a_{15}^{PD}\right)\left(\begin{array}{c}\dfrac{{}^tV_{ty(j)}+{}^tV_{ty(k)}}{2}\dfrac{{}^tV_{sz(j)}+{}^tV_{sz(k)}}{2} \\ -\dfrac{{}^tV_{tz(j)}+{}^tV_{tz(k)}}{2}\dfrac{{}^tV_{sy(k)}+{}^tV_{sy(j)}}{2}\end{array}\right)\left({}^0\beta_{(k)(j)}\right)
\end{aligned} \tag{3.58d}
$$

$$
\begin{aligned}
{}_0^t t_{(k)(j)}^{\theta_y} &= \frac{1}{2}C_{bz}\left({}_0^t a_{11}^{PD}\right)\left\{\left(1+{}_0^t a_{1}^{PD}\right){}^tV_{sz(k)}-\left({}_0^t a_{3}^{PD}\right){}^tV_{sx(k)}\right\}\left({}^0\beta_{(k)(j)}\right) \\
&+\frac{1}{2}C_{by}\left({}_0^t a_{12}^{PD}\right)\left\{\left(1+{}_0^t a_{1}^{PD}\right){}^tV_{tz(k)}-\left({}_0^t a_{3}^{PD}\right){}^tV_{tx(k)}\right\}\left({}^0\beta_{(k)(j)}\right) \\
&-\frac{1}{4}C_{sh}\left({}^0\xi_{(k)(j)}\right)\left[\begin{array}{l}\left({}_0^t a_{13}^{PD}\right)\left\{\left(1+{}_0^t a_{1}^{PD}\right){}^tV_{sz(k)}-\left({}_0^t a_{3}^{PD}\right){}^tV_{sx(k)}\right\} \\ +\left({}_0^t a_{14}^{PD}\right)\left\{\left(1+{}_0^t a_{1}^{PD}\right){}^tV_{tz(k)}-\left({}_0^t a_{3}^{PD}\right){}^tV_{tx(k)}\right\}\end{array}\right] \\
&+\frac{1}{2}C_{t}\left({}_0^t a_{15}^{PD}\right)\left(\begin{array}{c}\dfrac{{}^tV_{tz(j)}+{}^tV_{tz(k)}}{2}\dfrac{{}^tV_{sx(j)}+{}^tV_{sx(k)}}{2} \\ -\dfrac{{}^tV_{tx(j)}+{}^tV_{tx(k)}}{2}\dfrac{{}^tV_{sz(j)}+{}^tV_{sz(k)}}{2}\end{array}\right)\left({}^0\beta_{(k)(j)}\right)
\end{aligned} \tag{3.58e}
$$

$$
\begin{aligned}
{}_0^t t_{(k)(j)}^{\theta_z} &= \frac{1}{2} C_{bz} \left({}_0^t a_{11}^{PD} \right) \left\{ -\left(1 + {}_0^t a_1^{PD}\right) {}^t V_{sy(k)} + \left({}_0^t a_2^{PD} \right) {}^t V_{sx(k)} \right\} \left({}^0 \beta_{(k)(j)} \right) \\
&+ \frac{1}{2} C_{by} \left({}_0^t a_{12}^{PD} \right) \left\{ -\left(1 + {}_0^t a_1^{PD}\right) {}^t V_{ty(k)} + \left({}_0^t a_2^{PD} \right) {}^t V_{tx(k)} \right\} \left({}^0 \beta_{(k)(j)} \right) \\
&+ \frac{1}{4} C_{sh} \left({}^0 \xi_{(k)(j)} \right) \left[\begin{array}{l} \left({}_0^t a_{13}^{PD} \right) \left\{ \left(1 + {}_0^t a_1^{PD}\right) {}^t V_{sy(k)} - \left({}_0^t a_2^{PD} \right) {}^t V_{sx(k)} \right\} \\ + \left({}_0^t a_{14}^{PD} \right) \left\{ \left(1 + {}_0^t a_1^{PD}\right) {}^t V_{ty(k)} - \left({}_0^t a_2^{PD} \right) {}^t V_{tx(k)} \right\} \end{array} \right] \\
&+ \frac{1}{2} C_t \left({}_0^t a_{15}^{PD} \right) \begin{pmatrix} \dfrac{{}^t V_{tx(j)} + {}^t V_{tx(k)}}{2} \dfrac{{}^t V_{sy(k)} + {}^t V_{sy(j)}}{2} \\ -\dfrac{{}^t V_{ty(j)} + {}^t V_{ty(k)}}{2} \dfrac{{}^t V_{sx(j)} + {}^t V_{sx(k)}}{2} \end{pmatrix} \left({}^0 \beta_{(k)(j)} \right)
\end{aligned}
\tag{3.58f}
$$

Therefore, by substituting PD force densities given in Eq. (3.58) into Eq. (3.48), the nonlinear PD equations of motion for a straight beam can be obtained as

$$
\rho \left({}^t \ddot{u}_{(k)} \right) = \sum_{j=1}^{N} \left({}_0^t f_{(k)(j)}^{u} \right) {}^0 V_{(j)} + {}^t b_{x(k)} \tag{3.59a}
$$

$$
\rho \left({}^t \ddot{v}_{(k)} \right) = \sum_{j=1}^{N} \left({}_0^t f_{(k)(j)}^{v} \right) {}^0 V_{(j)} + {}^t b_{y(k)} \tag{3.59b}
$$

$$
\rho \left({}^t \ddot{w}_{(k)} \right) = \sum_{j=1}^{N} \left({}_0^t f_{(k)(j)}^{w} \right) {}^0 V_{(j)} + {}^t b_{w(k)} \tag{3.59c}
$$

$$
\frac{\rho I_{xx}}{A} \left({}^t \ddot{\theta}_{x(k)} \right) = \sum_{j=1}^{N} \left({}_0^t f_{(k)(j)}^{\theta_x} \right) {}^0 V_{(j)} + {}^t m_{x(k)} \tag{3.59d}
$$

$$
\frac{\rho I_{yy}}{A} \left({}^t \ddot{\theta}_{y(k)} \right) = \sum_{j=1}^{N} \left({}_0^t f_{(k)(j)}^{\theta_y} \right) {}^0 V_{(j)} + {}^t m_{y(k)} \tag{3.59e}
$$

$$
\frac{\rho I_{zz}}{A} \left({}^t \ddot{\theta}_{z(k)} \right) = \sum_{j=1}^{N} \left({}_0^t f_{(k)(j)}^{\theta_z} \right) {}^0 V_{(j)} + {}^t m_{z(k)} \tag{3.59f}
$$

with

$$
{}_0^t f_{(k)(j)}^{u} = 2 \left({}_0^t t_{(k)(j)}^{u} \right); \quad {}_0^t f_{(k)(j)}^{v} = 2 \left({}_0^t t_{(k)(j)}^{v} \right); \quad {}_0^t f_{(k)(j)}^{w} = 2 \left({}_0^t t_{(k)(j)}^{w} \right) \tag{3.59g}
$$

$$
{}_0^t f_{(k)(j)}^{\theta_x} = 2 \left({}_0^t t_{(k)(j)}^{\theta_x} \right); \quad {}_0^t f_{(k)(j)}^{\theta_y} = 2 \left({}_0^t t_{(k)(j)}^{\theta_y} \right); \quad {}_0^t f_{(k)(j)}^{\theta_z} = 2 \left({}_0^t t_{(k)(j)}^{\theta_z} \right) \tag{3.59h}
$$

The equations of motion given in Eq. (3.59) can be rewritten in matrix form as [61, 62]

$$
\mathbf{m}_{(k)}^{L} \left({}^t \ddot{\mathbf{u}}_{(k)}^{L} \right) = \sum_{j=1}^{N} \left({}_0^t \mathbf{f}_{(k)(j)}^{L} \right) {}^0 V_{(j)} + {}^t \mathbf{b}_{(k)}^{L} \tag{3.60}
$$

where $\mathbf{m}_{(k)}^{L}$, ${}^t \mathbf{b}_{(k)}^{L}$, ${}_0^t \mathbf{f}_{(k)(j)}^{L}$ and ${}^t \ddot{\mathbf{u}}_{(k)}^{L}$ represent mass matrix, body force vector, PD force density vector, and acceleration vector in the local coordinate system,

respectively. These terms can be defined as

$$\mathbf{m}_{(k)}^{L}=\begin{bmatrix}\rho & 0 & 0 & 0 & 0 & 0\\ 0 & \rho & 0 & 0 & 0 & 0\\ 0 & 0 & \rho & 0 & 0 & 0\\ 0 & 0 & 0 & \dfrac{\rho I_{xx}}{A} & 0 & 0\\ 0 & 0 & 0 & 0 & \dfrac{\rho I_{yy}}{A} & 0\\ 0 & 0 & 0 & 0 & 0 & \dfrac{\rho I_{zz}}{A}\end{bmatrix};\ {}^{t}\ddot{\mathbf{u}}_{(k)}^{L}=\begin{bmatrix}{}^{t}\ddot{u}_{(k)}\\ {}^{t}\ddot{v}_{(k)}\\ {}^{t}\ddot{w}_{(k)}\\ {}^{t}\ddot{\theta}_{x(k)}\\ {}^{t}\ddot{\theta}_{y(k)}\\ {}^{t}\ddot{\theta}_{z(k)}\end{bmatrix};\ {}^{t}\mathbf{b}_{(k)}^{L}=\begin{bmatrix}{}^{t}b_{x(k)}\\ {}^{t}b_{y(k)}\\ {}^{t}b_{z(k)}\\ {}^{t}m_{x(k)}\\ {}^{t}m_{y(k)}\\ {}^{t}m_{z(k)}\end{bmatrix} \tag{3.61a}$$

$${}^{t}_{0}\mathbf{f}_{(k)(j)}^{L}=\begin{bmatrix}{}^{t}_{0}f_{(k)(j)}^{u} & {}^{t}_{0}f_{(k)(j)}^{v} & {}^{t}_{0}f_{(k)(j)}^{w} & {}^{t}_{0}f_{(k)(j)}^{\theta_x} & {}^{t}_{0}f_{(k)(j)}^{\theta_y} & {}^{t}_{0}f_{(k)(j)}^{\theta_z}\end{bmatrix}^{T} \tag{3.61b}$$

3.3.2.3. Transformation of the equation of motion to the global coordinate system

As given in Eq. (3.60), the PD equations of motion for a beam are derived with respect to the beam's local coordinate system. Therefore, to investigate complex beam structures and curved beams, the equations of motion in the local coordinate system need to be transformed into the global coordinate system [62]. The global coordinate system is fixed and it is often chosen as the Cartesian coordinate system (x_1, x_2, x_3) as shown in Fig. 3.37. The beam has six global degrees of freedom denoted as $(u_1, u_2, u_3, \theta_1, \theta_2, \theta_3)$.

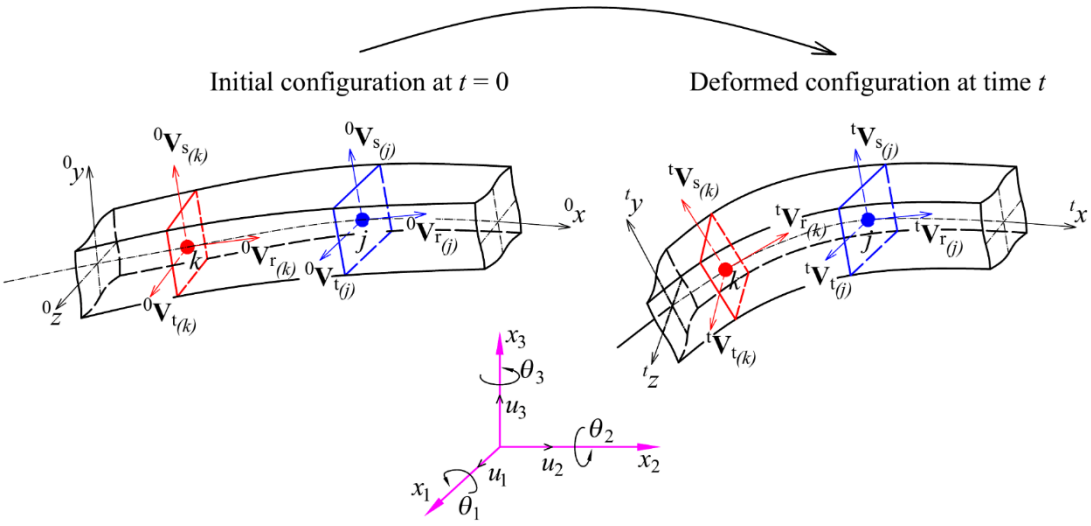

Fig. 3.37. Beam configurations in the global coordinate system

As presented in section 5.2, each material point has three director vectors $\left({}^{0}\boldsymbol{V}_r,\ {}^{0}\boldsymbol{V}_s,\ {}^{0}\boldsymbol{V}_t\right)$ or $\left({}^{t}\boldsymbol{V}_r,\ {}^{t}\boldsymbol{V}_s,\ {}^{t}\boldsymbol{V}_t\right)$ measured in the local coordinate system. These director vectors can be transformed to the global coordinate system by using the following relations as

$$\left[{}^{0}\mathbf{V}_{r(k)}^{G} \quad {}^{0}\mathbf{V}_{s(k)}^{G} \quad {}^{0}\mathbf{V}_{t(k)}^{G} \right] = {}^{0}\mathbf{H}_{(k)}^{T} \left[{}^{0}\mathbf{V}_{r(k)} \quad {}^{0}\mathbf{V}_{s(k)} \quad {}^{0}\mathbf{V}_{t(k)} \right] \tag{3.62a}$$

$$\left[{}^{t}\mathbf{V}_{r(k)}^{G} \quad {}^{t}\mathbf{V}_{s(k)}^{G} \quad {}^{t}\mathbf{V}_{t(k)}^{G} \right] = {}^{0}\mathbf{H}_{(k)}^{T} \left[{}^{t}\mathbf{V}_{r(k)} \quad {}^{t}\mathbf{V}_{s(k)} \quad {}^{t}\mathbf{V}_{t(k)} \right] \tag{3.62b}$$

with

$${}^{0}\mathbf{H}_{(k)} = \left[{}^{0}\mathbf{V}_{r(k)}^{G} \quad {}^{0}\mathbf{V}_{s(k)}^{G} \quad {}^{0}\mathbf{V}_{t(k)}^{G} \right]^{T} \tag{3.62c}$$

where ${}^{0}\mathbf{H}_{(k)}$ represents the coordinate transformation matrix for material point k [61, 62], ${}^{0}\mathbf{H}_{(k)}^{T}$ is transpose matrix of ${}^{0}\mathbf{H}_{(k)}$. The terms $\left({}^{0}\mathbf{V}_{r(k)}, {}^{0}\mathbf{V}_{s(k)}, {}^{0}\mathbf{V}_{t(k)} \right)$ and $\left({}^{t}\mathbf{V}_{r(k)}, {}^{t}\mathbf{V}_{s(k)}, {}^{t}\mathbf{V}_{t(k)} \right)$ are the director vectors in local coordinates at $t = 0$ and at time t, respectively. Meanwhile, $\left({}^{0}\mathbf{V}_{r(k)}^{G}, {}^{0}\mathbf{V}_{s(k)}^{G}, {}^{0}\mathbf{V}_{t(k)}^{G} \right)$ and $\left({}^{t}\mathbf{V}_{r(k)}^{G}, {}^{t}\mathbf{V}_{s(k)}^{G}, {}^{t}\mathbf{V}_{t(k)}^{G} \right)$ are the director vectors in the global coordinates at $t = 0$ and at time t, respectively. As given in Eq. (3.29), the director vectors in local coordinates at $t = 0$ are presented as

$${}^{0}\mathbf{V}_{r(k)} = [1 \quad 0 \quad 0]^{T} \tag{3.63a}$$

$${}^{0}\mathbf{V}_{s(k)} = [0 \quad 1 \quad 0]^{T} \tag{3.63b}$$

$${}^{0}\mathbf{V}_{t(k)} = [0 \quad 0 \quad 1]^{T} \tag{3.63c}$$

The global director vectors at time t given in Eq. (3.62b) can be estimated based on the director vectors in the previous configuration as [70]

$${}^{t}\bar{\mathbf{V}}_{s(k)}^{G} = {}^{t-\Delta t}\mathbf{V}_{s(k)}^{G} + \underline{\boldsymbol{\theta}}_{(k)}^{G} \times {}^{t-\Delta t}\mathbf{V}_{s(k)}^{G} \tag{3.64a}$$

$${}^{t}\bar{\mathbf{V}}_{t(k)}^{G} = {}^{t-\Delta t}\mathbf{V}_{t(k)}^{G} + \underline{\boldsymbol{\theta}}_{(k)}^{G} \times {}^{t-\Delta t}\mathbf{V}_{t(k)}^{G} \tag{3.64b}$$

and

$${}^{t}\mathbf{V}_{s(k)} = \frac{{}^{t}\bar{\mathbf{V}}_{s(k)}^{G}}{\left| {}^{t}\bar{\mathbf{V}}_{s(k)}^{G} \right|} \tag{3.64c}$$

$${}^{t}\mathbf{V}_{t(k)}^{G} = \frac{{}^{t}\bar{\mathbf{V}}_{t(k)}^{G}}{\left| {}^{t}\bar{\mathbf{V}}_{t(k)}^{G} \right|} \tag{3.64d}$$

$${}^{t}\mathbf{V}_{r(k)}^{G} = {}^{t}\mathbf{V}_{s(k)}^{G} \times {}^{t}\mathbf{V}_{t(k)}^{G} \tag{3.64e}$$

where ${}^{t}\bar{\mathbf{V}}_{s(k)}^{G}$ and ${}^{t}\bar{\mathbf{V}}_{t(k)}^{G}$ have the same directions with director vectors, ${}^{t}\mathbf{V}_{s(k)}^{G}$ and ${}^{t}\mathbf{V}_{t(k)}^{G}$. However, ${}^{t}\bar{\mathbf{V}}_{s(k)}^{G}$ and ${}^{t}\bar{\mathbf{V}}_{t(k)}^{G}$ may not be unit vectors. Therefore, to ensure the director vectors are unit vectors, the approximations in Eq. (3.64c-d) are used. The term $\underline{\boldsymbol{\theta}}_{(k)}^{G}$ represents the vector of the global incremental rotations from time $t - \Delta t$ to time t. This vector can be defined as

$$\underline{\boldsymbol{\theta}}_{(k)}^{G} = {}^{t}\underline{\boldsymbol{\theta}}_{(k)}^{G} - {}^{t-\Delta t}\underline{\boldsymbol{\theta}}_{(k)}^{G} = \left[\underline{\theta}_{1(k)} \quad \underline{\theta}_{2(k)} \quad \underline{\theta}_{3(k)} \right]^{T} \tag{3.65}$$

As given in Eq. (3.62c), ${}^0\boldsymbol{H}_{(k)}$ is the coordinate transformation matrix for material point k. Therefore, for the interaction between material points k and j, the coordinate transformation matrix can be approximated as [61, 62]

$$ {}^0\mathbf{H}_{(k)(j)} = \left[{}^0\mathbf{V}^G_{r(k)(j)} \quad {}^0\mathbf{V}^G_{s(k)(j)} \quad {}^0\mathbf{V}^G_{t(k)(j)} \right]^T \tag{3.66a} $$

with

$$ {}^0\mathbf{V}^G_{r(k)(j)} = \frac{\left({}^0\mathbf{V}^G_{r(k)} + {}^0\mathbf{V}^G_{r(j)} \right)}{\left| \left({}^0\mathbf{V}^G_{r(k)} + {}^0\mathbf{V}^G_{r(j)} \right) \right|} \tag{3.66b} $$

$$ {}^0\mathbf{V}^G_{s(k)(j)} = \frac{\left({}^0\mathbf{V}^G_{s(k)} + {}^0\mathbf{V}^G_{s(j)} \right)}{\left| \left({}^0\mathbf{V}^G_{s(k)} + {}^0\mathbf{V}^G_{s(j)} \right) \right|} \tag{3.66c} $$

$$ {}^0\mathbf{V}^G_{t(k)(j)} = \frac{\left({}^0\mathbf{V}^G_{t(k)} + {}^0\mathbf{V}^G_{t(j)} \right)}{\left| \left({}^0\mathbf{V}^G_{t(k)} + {}^0\mathbf{V}^G_{t(j)} \right) \right|} \tag{3.66d} $$

Therefore, the transformation matrix for six degrees of freedom of the beam, ${}^0\boldsymbol{T}_{(k)(j)}$, can be defined as

$$ {}^0\mathbf{T}_{(k)(j)} = \begin{bmatrix} {}^0\mathbf{H}_{(k)(j)} & \mathbf{0} \\ \mathbf{0} & {}^0\mathbf{H}_{(k)(j)} \end{bmatrix} \tag{3.67} $$

By using the transformation matrix ${}^0\boldsymbol{T}_{(k)(j)}$, the relationship between the local and global degrees of freedom can be presented as [61, 62]

$$ {}^t\mathbf{u}^L_{(k)} = {}^0\mathbf{T}_{(k)(j)} \, {}^t\mathbf{u}^G_{(k)} \tag{3.68a} $$

$$ {}^t\mathbf{u}^L_{(j)} = {}^0\mathbf{T}_{(k)(j)} \, {}^t\mathbf{u}^G_{(j)} \tag{3.68b} $$

with

$$ {}^t\mathbf{u}^L_{(k)} = \left[{}^tu_{(k)} \quad {}^tv_{(k)} \quad {}^tw_{(k)} \quad {}^t\theta_{x(k)} \quad {}^t\theta_{y(k)} \quad {}^t\theta_{z(k)} \right]^T \tag{3.68c} $$

$$ {}^t\mathbf{u}^G_{(k)} = \left[{}^tu_{1(k)} \quad {}^tu_{2(k)} \quad {}^tu_{3(k)} \quad {}^t\theta_{1(k)} \quad {}^t\theta_{2(k)} \quad {}^t\theta_{3(k)} \right]^T \tag{3.68d} $$

$$ {}^t\mathbf{u}^L_{(j)} = \left[{}^tu_{(j)} \quad {}^tv_{(j)} \quad {}^tw_{(j)} \quad {}^t\theta_{x(j)} \quad {}^t\theta_{y(j)} \quad {}^t\theta_{z(j)} \right]^T \tag{3.68e} $$

$$ {}^t\mathbf{u}^G_{(j)} = \left[{}^tu_{1(j)} \quad {}^tu_{2(j)} \quad {}^tu_{3(j)} \quad {}^t\theta_{1(j)} \quad {}^t\theta_{2(j)} \quad {}^t\theta_{3(j)} \right]^T \tag{3.68f} $$

where ${}^t\boldsymbol{u}^L_{(k)}$ and ${}^t\boldsymbol{u}^L_{(j)}$ represent vectors of DOFs in local coordinates for material points k and j, respectively. Meanwhile, ${}^t\boldsymbol{u}^G_{(k)}$ and ${}^t\boldsymbol{u}^G_{(j)}$ represent vectors of DOFs in global coordinates for material points k and j, respectively.

By multiplying both sides of Eq. (3.60) with the matrix ${}^0\boldsymbol{T}^T_{(k)(j)}$, the nonlinear equation of motion for a beam can be transformed to the global coordinate system as [61, 62]

$$ {}^{0}\mathbf{T}^{T}_{(k)(j)}\mathbf{m}^{L}_{(k)}\left({}^{0}\mathbf{T}_{(k)(j)}\,{}^{t}\ddot{\mathbf{u}}^{G}_{(k)}\right)=\sum_{j=1}^{N}{}^{0}\mathbf{T}^{T}_{(k)(j)}\left({}^{t}_{0}\mathbf{f}^{L}_{(k)(j)}\right){}^{0}V_{(j)}+{}^{0}\mathbf{T}^{T}_{(k)(j)}\,{}^{t}\mathbf{b}^{L}_{(k)} \tag{3.69a} $$

or

$$ \mathbf{m}^{G}_{(k)}\left({}^{t}\ddot{\mathbf{u}}^{G}_{(k)}\right)=\sum_{j=1}^{N}\left({}^{t}_{0}\mathbf{f}^{G}_{(k)(j)}\right){}^{0}V_{(j)}+{}^{t}\mathbf{b}^{G}_{(k)} \tag{3.69b} $$

with

$$ \mathbf{m}^{G}_{(k)}={}^{0}\mathbf{T}^{T}_{(k)(j)}\mathbf{m}^{L}_{(k)}\,{}^{0}\mathbf{T}_{(k)(j)} \tag{3.69c} $$

$$ \begin{aligned} {}^{t}_{0}\mathbf{f}^{G}_{(k)(j)} &= {}^{0}\mathbf{T}^{T}_{(k)(j)}\left({}^{t}_{0}\mathbf{f}^{L}_{(k)(j)}\right) \\ &=\begin{bmatrix} {}^{t}_{0}f^{u_1}_{(k)(j)} & {}^{t}_{0}f^{u_2}_{(k)(j)} & {}^{t}_{0}f^{u_3}_{(k)(j)} & {}^{t}_{0}f^{\theta_1}_{(k)(j)} & {}^{t}_{0}f^{\theta_2}_{(k)(j)} & {}^{t}_{0}f^{\theta_3}_{(k)(j)}\end{bmatrix}^{T} \end{aligned} \tag{3.69d} $$

$$ {}^{t}\mathbf{b}^{G}_{(k)}={}^{0}\mathbf{T}^{T}_{(k)(j)}\left({}^{t}\mathbf{b}^{L}_{(k)}\right)=\begin{bmatrix} {}^{t}b_{1(k)} & {}^{t}b_{2(k)} & {}^{t}b_{3(k)} & {}^{t}m_{1(k)} & {}^{t}m_{2(k)} & {}^{t}m_{3(k)}\end{bmatrix}^{T} \tag{3.69e} $$

where ${}^{0}\boldsymbol{T}^{T}_{(k)(j)}$ is the transpose matrix of ${}^{0}\boldsymbol{T}_{(k)(j)}$. The terms $\boldsymbol{m}^{G}_{(k)}$, ${}^{t}\ddot{\mathbf{u}}^{G}_{(k)}$, ${}^{t}\boldsymbol{f}^{G}_{(k)(j)}$ and ${}^{t}\boldsymbol{b}^{G}_{(k)}$ represent mass matrix, acceleration vector, PD force density vector and the applied body force vector in the global coordinate system, respectively.

Note that term ${}^{0}\beta_{(k)(j)}$ given in Eq. (3.50h) can be calculated in global coordinates as

$$ {}^{0}\beta_{(k)(j)}=\frac{{}^{0}\mathbf{V}^{G}_{r(k)(j)}\cdot\left({}^{0}\mathbf{x}^{G}_{(j)}-{}^{0}\mathbf{x}^{G}_{(k)}\right)}{\left|{}^{0}\mathbf{V}^{G}_{r(k)(j)}\cdot\left({}^{0}\mathbf{x}^{G}_{(j)}-{}^{0}\mathbf{x}^{G}_{(k)}\right)\right|}=\begin{cases}-1 \text{ if } {}^{0}\mathbf{V}^{G}_{r(k)(j)}\uparrow\downarrow\left({}^{0}\mathbf{x}^{G}_{(j)}-{}^{0}\mathbf{x}^{G}_{(k)}\right)\\ 1 \quad \text{if } {}^{0}\mathbf{V}^{G}_{r(k)(j)}\uparrow\uparrow\left({}^{0}\mathbf{x}^{G}_{(j)}-{}^{0}\mathbf{x}^{G}_{(k)}\right)\end{cases} \tag{3.70a} $$

with

$$ {}^{0}\mathbf{x}^{G}_{(k)}=\begin{bmatrix} {}^{0}x_{1(k)} & {}^{0}x_{2(k)} & {}^{0}x_{3(k)}\end{bmatrix}^{T} \tag{3.70b} $$

$$ {}^{0}\mathbf{x}^{G}_{(j)}=\begin{bmatrix} {}^{0}x_{1(j)} & {}^{0}x_{2(j)} & {}^{0}x_{3(j)}\end{bmatrix}^{T} \tag{3.70c} $$

where ${}^{0}\boldsymbol{x}^{G}_{(k)}$ and ${}^{0}\boldsymbol{x}^{G}_{(j)}$ represent the global coordinates in the initial configuration of material points k and j, respectively. Note that, the parameter ${}^{0}\beta_{(k)(j)}$ in Eq. (3.70a) equal to -1 if two vectors ${}^{0}\boldsymbol{V}^{G}_{r(k)(j)}$ and $\left({}^{0}\boldsymbol{x}^{G}_{(j)}-{}^{0}\boldsymbol{x}^{G}_{(k)}\right)$ have opposite directions. On the other hand, ${}^{0}\beta_{(k)(j)}$ equal to 1 if two vectors ${}^{0}\boldsymbol{V}^{G}_{r(k)(j)}$ and $\left({}^{0}\boldsymbol{x}^{G}_{(j)}-{}^{0}\boldsymbol{x}^{G}_{(k)}\right)$ have the same directions.

3.3.2.4. Damage prediction

By introducing the damage parameter $\psi_{(k)(j)}$ given in Eq. (1.3), the PD equations of motion in local and global coordinate systems given in Eq. (3.60) and Eq. (3.69b), respectively, can be rewritten as

$$\mathbf{m}_{(k)}^{L}\left({}^{t}\ddot{\mathbf{u}}_{(k)}^{L}\right)=\sum_{j=1}^{N}\psi_{(k)(j)}\left({}_{0}^{t}\mathbf{f}_{(k)(j)}^{L}\right){}^{0}V_{(j)}+{}^{t}\mathbf{b}_{(k)}^{L} \tag{3.71a}$$

$$\mathbf{m}_{(k)}^{G}\left({}^{t}\ddot{\mathbf{u}}_{(k)}^{G}\right)=\sum_{j=1}^{N}\psi_{(k)(j)}\left({}_{0}^{t}\mathbf{f}_{(k)(j)}^{G}\right){}^{0}V_{(j)}+{}^{t}\mathbf{b}_{(k)}^{G} \tag{3.71b}$$

As presented in the previous section, the deformations of the beam include axial, shear, bending, and torsional components. Therefore, to decide the state of interaction which is represented by the damage parameter $\psi_{(k)(j)}$ given in Eq. (1.3), the damage criterion based on the critical energy release rate is used. Similar to Eq. (1.8), the energy-based damage criterion for the nonlinear analysis of a beam can be described as [25, 26, 61, 62, 64, 102]

$$\begin{aligned}&{}_{0}^{t}\bar{g}_{(k)(j)}<g_c\rightarrow\text{interaction exists: }\psi_{(k)(j)}=1\\&{}_{0}^{t}\bar{g}_{(k)(j)}\geq g_c\rightarrow\text{interaction is broken: }\psi_{(k)(j)}=0\end{aligned} \tag{3.72}$$

where g_c represents the critical energy release rate for one interaction. As presented in Eq. (1.11) in Chapter 1, for beam structure $g_c = G_c/12$, in which G_c represents the critical energy release rate for the material.

Similar to Eq. (1.9) in Chapter 1, the energy release rate for interaction between material points k and j, ${}_{0}^{t}\bar{g}_{(k)(j)}$, can be calculated as

$${}_{0}^{t}\bar{g}_{(k)(j)}=\frac{1}{2}\left({}_{0}^{t}g_{(k)(j)}+{}_{0}^{t}g_{(j)(k)}\right) \tag{3.73a}$$

with

$${}_{0}^{t}g_{(k)(j)}=\frac{1}{{}_{0}A}\left({}_{0}^{t}\Phi_{(k)(j)}\right)\left({}^{0}V_{(k)}\right)\left({}^{0}V_{(j)}\right) \tag{3.73b}$$

$${}_{0}^{t}g_{(j)(k)}=\frac{1}{{}_{0}A}\left({}_{0}^{t}\Phi_{(j)(k)}\right)\left({}^{0}V_{(k)}\right)\left({}^{0}V_{(j)}\right) \tag{3.73c}$$

where ${}_{0}^{t}\Phi_{(k)(j)}$ and ${}_{0}^{t}\Phi_{(j)(k)}$ represent micropotentials at time t of the interaction between material points k and j. For the bond-based PD model, ${}_{0}^{t}\Phi_{(k)(j)}$ and ${}_{0}^{t}\Phi_{(j)(k)}$ are equal to each other. By applying the same idea introduced by Madenci and Oterkus [25], [26], the micropotentials ${}_{0}^{t}\Phi_{(k)(j)}$ and ${}_{0}^{t}\Phi_{(j)(k)}$ for one interaction can be calculated for the bond-based PD model as

$$
{}_0^t\Phi_{(j)(k)} = {}_0^t\Phi_{(k)(j)}
$$

$$
= \frac{1}{2}\left[\begin{array}{l}
\displaystyle\int_0^{{}^tu_{(j)}-{}^tu_{(k)}} {}_0^t f^u_{(k)(j)}\, d\left(u_{(j)}-u_{(k)}\right) + \int_0^{{}^tv_{(j)}-{}^tv_{(k)}} {}_0^t f^v_{(k)(j)}\, d\left(v_{(j)}-v_{(k)}\right) \\
+ \displaystyle\int_0^{{}^tw_{(j)}-{}^tw_{(k)}} {}_0^t f^w_{(k)(j)}\, d\left(w_{(j)}-w_{(k)}\right) + \int_0^{{}^t\theta_{x(j)}-{}^t\theta_{x(k)}} {}_0^t f^{\theta_x}_{(k)(j)}\, d\left(\theta_{x(j)}-\theta_{x(k)}\right) \\
+ \displaystyle\int_0^{{}^t\theta_{y(j)}-{}^t\theta_{y(k)}} {}_0^t f^{\theta_y}_{(k)(j)}\, d\left(\theta_{y(j)}-\theta_{y(k)}\right) + \int_0^{{}^t\theta_{z(j)}-{}^t\theta_{z(k)}} {}_0^t f^{\theta_z}_{(k)(j)}\, d\left(\theta_{z(j)}-\theta_{z(k)}\right)
\end{array}\right] \tag{3.74}
$$

where ${}_0^tf^u_{(k)(j)}$, ${}_0^tf^v_{(k)(j)}$, ${}_0^tf^w_{(k)(j)}$, ${}_0^tf^{\theta_x}_{(k)(j)}$, ${}_0^tf^{\theta_y}_{(k)(j)}$, ${}_0^tf^{\theta_z}_{(k)(j)}$ are given in Eq. (3.59g-h).

3.3.3. Numerical results

In this section, large deformations of beam structures are predicted. For verification purposes, the results predicted by the proposed nonlinear PD model are compared with nonlinear FEA results in Section 3.3.3.1. After verifying the accuracy of the nonlinear PD model, damages on a beam subjected to bending and torsional loading conditions are predicted in Section 3.3.3.2.

In nonlinear PD analyses, the horizon size of $\delta = 3.015\Delta x$, in which Δx represents the mesh size, is used. The adaptive dynamic relaxation (ADR) method [77] is used for these static loading conditions [76] as described in Appendix A2 The nonlinear FEA is conducted by using the BEAM188 element in ANSYS.

3.3.3.1. A cantilever beam subjected to static loading

In this section, a cantilever beam with a length of $L = 1$ m and a square cross-section of $b = h = 0.1$ m is investigated as shown in Fig. 3.38. The beam has an elastic modulus of $E = 2 \times 10^{11}$ N/m^2 and shear modulus of $G = 1 \times 10^{11}$ N/m^2. The shear correction factor for a square cross-section is $k_s = 5/6$ [70].

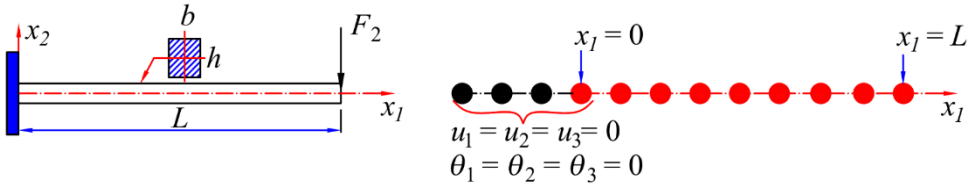

(a) (b)

Fig. 3.38. Cantilever beam: (a) geometry, (b) PD model discretization and boundary conditions

The beam is fixed on the left end and it is subjected to a transverse force $F_2 = -8 \times 10^6$ N in x_2 direction at the right end as shown in Fig. 3.38(a). In the PD model, the beam is discretized with a mesh size of $\Delta x = L/100$. In the FEA, the same mesh size is used.

To apply boundary conditions in PD, three fictitious material points, shown in black in Fig. 3.38(b), are added on the left end of the beam. All degrees of freedom of these fictitious material points and the material point located at $x_1 = 0$ are set equal to zero.

Fig. 3.39 shows a comparison between nonlinear PD results and FEA results. As shown in Fig. 3.39(a), the deformed configurations of the beam captured by using the nonlinear PD model and nonlinear FEA match very well, meanwhile the linear FEA gives a completely different deformed configuration. As can be seen from Fig. 3.39(b), the linear FEA results show that the beam does not have axial deformations when it is subjected to transverse force. On the contrary, both nonlinear PD and nonlinear FEA results show that the beam has nonzero axial deformations due to the coupling of the axial, shear, and bending deformations. As shown in Fig. 3.39(c-d), the nonlinear PD and nonlinear FEA solutions have a very good agreement on u_2 and θ_3, meanwhile, the linear FEA gives much larger values.

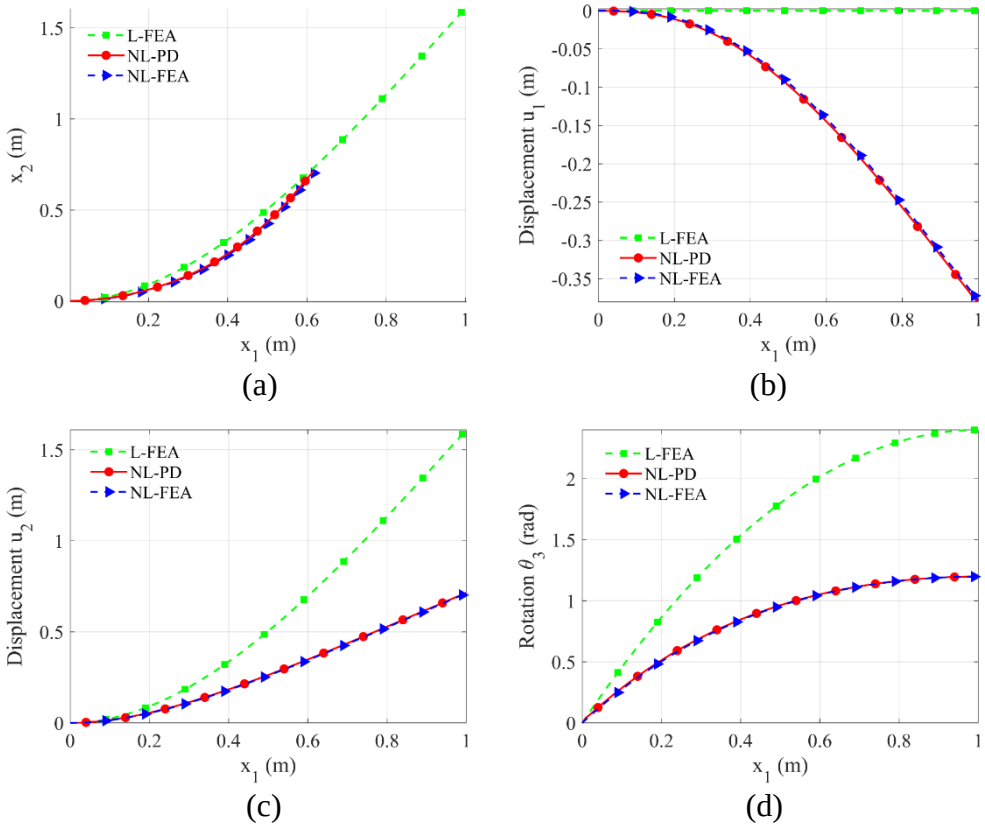

Fig. 3.39. The deformation of the beam subjected to a transverse end force $F_2 = -8 \times 10^6 N$ (a) deformed configurations, (b) displacements u_1, (c) displacement u_2, (d) rotation θ_3 (L represents linear; NL represents nonlinear)

Table 3.5 shows the information in terms of computational time in nonlinear PD and nonlinear FEA simulations for different mesh sizes. As mentioned in Section 3.3.3, the ADR method and the explicit time integration scheme are used for the nonlinear PD simulations. The PD codes are written using MATLAB 2018b. On the other hand, nonlinear FEA simulations are conducted by using ANSYS with the implicit solver.

As can be observed from Table 3.5, the number of iterations required to obtain converged solutions, N_t, in the nonlinear PD simulations are much higher than those in the nonlinear FEA. In PD, the simulation with a finer mesh requires more iterations to obtain the converged solution. Specifically, the nonlinear PD beam model with 50 material points requires 4000 iterations to obtain the converged

results. Meanwhile, the nonlinear PD beam model with 200 material points requires 15000 iterations to obtain the converged results. By contrast, the FEA simulations converged after 100 iterations for all mesh sizes since the implicit solver is used. As a result, the running time for nonlinear PD simulations is much higher than those of nonlinear FEA.

However, it is also observed that the time per iteration in nonlinear PD simulation is less than those in nonlinear FEA. The reason is that the nonlinear PD uses the explicit integration scheme meanwhile the nonlinear FEA uses the implicit solver which requires the solutions for large linear and nonlinear stiffness matrices.

Table 3.5. Computational time in NL-PD and NL-FEA models

Number of material points (nodes)	50			100			150			200		
	N_t	Time: t (s)	Time per iteration: t/N_t (s)	N_t	Time: t (s)	Time per iteration: t/N_t (s)	N_t	Time: t (s)	Time per iteration: t/N_t (s)	N_t	Time: t (s)	Time per iteration: t/N_t (s)
NL PD explicit using ADR method	4000	17.48	0.0044	8000	88.9	0.0111	12000	145.7	0.0121	15000	239	0.0159
NL FEA implicit using ANSYS	100	7.01	0.0701	100	7.06	0.0706	100	7.88	0.0788	100	8.12	0.0812
N_t: number of iterations to obtain converged solution.												

To further verify the nonlinear PD model for straight beams, a parametric study for the beam subjected to various transverse forces, $F_2 = -n \times 10^6$ N with $n = 2, 4, \ldots, 18, 20$, is investigated as shown in
Fig. **3.40**. As can be observed from
Fig. **3.40**(a), the deformed configurations of the beam captured by the nonlinear PD model match very well with those captured by nonlinear FEA.
Fig. **3.40**(b) shows the variations of nonzero degrees of freedom, u_1, u_2 and θ_3, on the right tip of the beam. As can be seen from the figure, the nonlinear PD and nonlinear FEA results agree very well which shows the accuracy of the nonlinear PD model for straight beams.

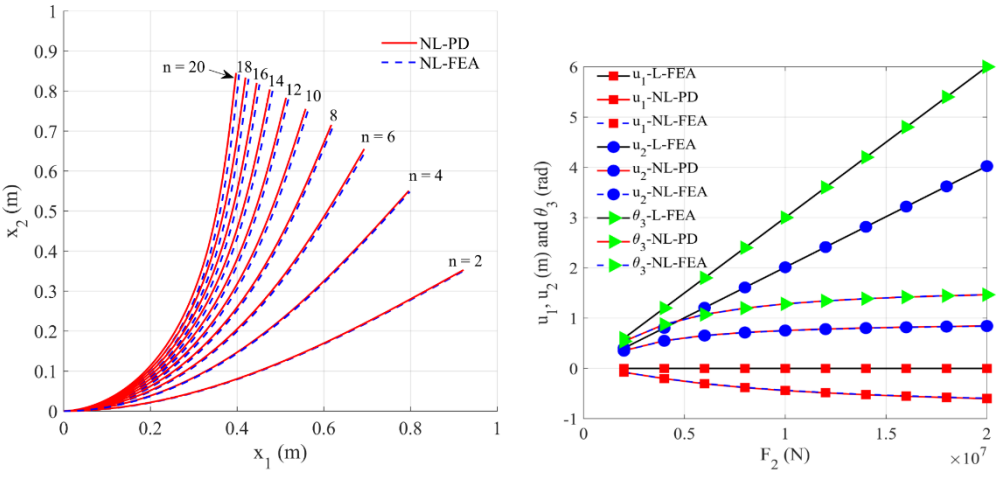

(a) (b)

Fig. 3.40. Deformations of the beam subjected to a transverse force $F_2 = -n \times 10^6$ N with $n = 2 \div 20$ (a) deformed configurations, (b) displacements and rotation of the right end (L represents linear; NL represents nonlinear)

To further verify the PD model, another parametric study for the beam subjected to various bending moments $M_2 = n \times 2\pi EI_{22}/L$ with $n = 1, 3/4, 1/2, 1/3, 1/4, 1/5, 1/10, 1/20$ on the right end is investigated as shown in Fig. 3.41. As can be observed from the figure, the deformed configurations of the beam captured by the nonlinear PD model agree very well with the nonlinear FEA results studied by Pai and Palazotto [103]. Therefore, the accuracy of the nonlinear PD for the straight beams is verified.

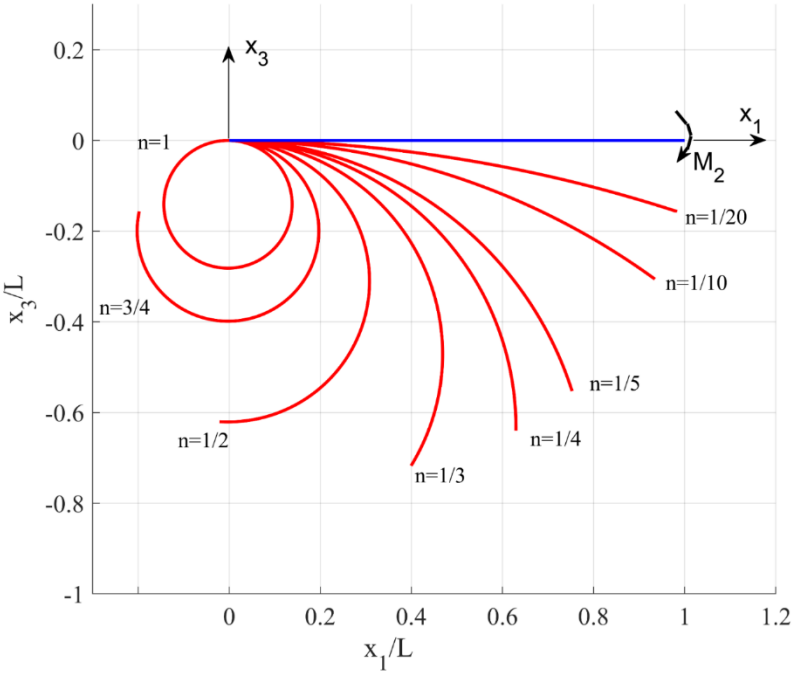

Fig. 3.41. Deformed configurations of the cantilever beam subjected to bending moment $M_2 = n \times 2\pi EI_{22}/L$

3.3.3.2. A half-circular beam subjected to tangential end load

In this section, a half-circular beam subjected to tangential end loads is investigated as shown in Fig. 3.42. The beam has a radius of $R = 0.127$ m and a rectangular cross-section with $b = 6.35 \times 10^{-3}$ m and $h = b/3$ [103]. The beam has an elastic modulus of $E = 6.895 \times 10^{10}$ N/m^2 and shear modulus of $G = 2.6518 \times 10^{10}$ N/m^2. For the rectangular cross-section, the shear correction factor is chosen as $k_s = 5/6$ [70] .

The beam is fixed at $(x_1 = 0, x_2 = 0, x_3 = 0)$ and subjected to a tangential force $F_1 = nEI_{22}/R^2$ with $n = 1, 0.8, 0.6, 0.5, 0.4, 0.3, 0.2, 0.1$ in x_1 direction at $(x_1 = 0, x_2 = 0, x_3 = -2R)$. In the PD model, the beam is discretized with a mesh size of $\Delta x = \pi R/300$. In FEA, the same mesh size is used. To apply the boundary conditions in PD, three fictitious material points are added on the fixed end, and all DOFs of these points, as well as DOFs of the material point located at $(x_1 = 0, x_2 = 0, x_3 = 0)$ are set equal to zero.

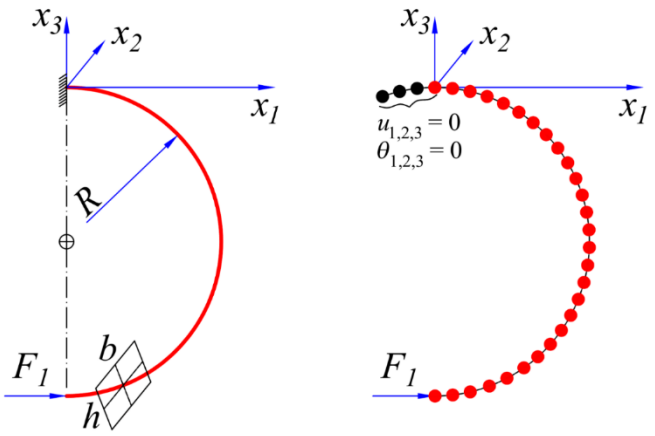

(a) (b)

Fig. 3.42. A half-circular beam subjected to tangential load: (a) geometry; (b) PD model discretization and boundary conditions

Fig. 3.43 shows the comparison between the nonlinear PD and nonlinear FEA results. Fig. 3.43(a) shows the deformed configurations for the beam in all loading conditions. Fig. 3.43(b) shows the deflection versus n curve of the right tip. It can be observed from the figures that the nonlinear PD and nonlinear FEA results have a very good agreement and both results agree very well with those captured by Pai and Palazotto [103].

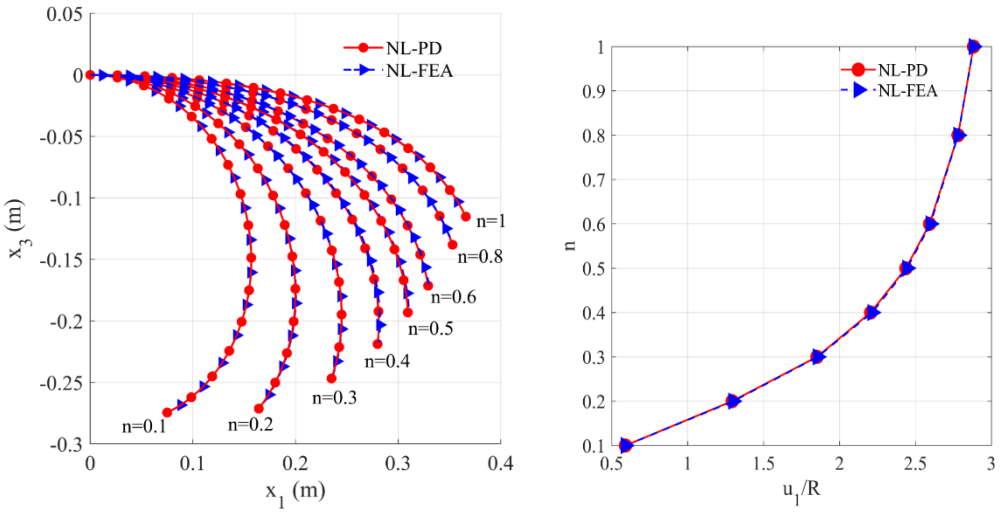

(a) (b)

Fig. 3.43. The deformations of a half-circular beam subjected to end force $F_1 = nEI_{22}/R^2$ (a) the deformed configurations, (b) the deflection versus n curve of the right tip (NL represents nonlinear)

3.3.3.3. Large displacements in the 3D analysis of a 45-degree curved beam

In this section, a 45-degree curved beam subjected to end load is investigated as shown in Fig. 3.44. The beam has a radius of $R = 2.54$ m and a square cross-section with $b = h = 0.0254$ m. The beam has the elastic modulus of $E = 6.895 \times 10^{10}$ N/m^2 and shear modulus of $G = 3.4474 \times 10^{10}$ N/m^2. The beam is investigated in two loading conditions with $F_3 = 1334.4665$ N and $F_3 =$

2668.933 N [104]. For the square cross-section, the shear correction factor is chosen as $k_s = 5/6$ [70], and the torsional constant can be chosen as $k_t = 0.1406 \times b^4$ [74]

In the PD model, the beam is discretized into 300 material points. Similar to previous analyses, three fictitious material points are added on the fixed end as shown in Fig. 3.44(b). All degrees of freedom of these fictitious points, as well as the material point located at $(x_1 = 0, x_2 = 0, x_3 = 0)$ are set equal to zero.

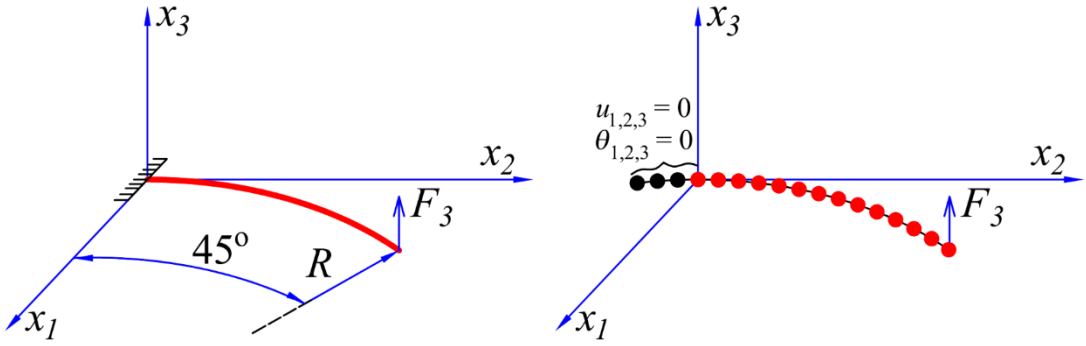

(a) (b)

Fig. 3.44. A 45-degree curved beam (a) geometry; (b) PD discretized model

Fig. 3.45 shows the deformed configurations of the beam. It can be observed from the figure that nonlinear PD and nonlinear FEA results have good agreement in both loading conditions. Table 3.6 shows the locations of the free end of the beam in two loading conditions. As can be seen from Table 3.6, the nonlinear PD results agree well with both nonlinear FEA results by using ANSYS and results studied by Bathe and Bolourchi [104]. Therefore, the accuracy of the nonlinear PD model is verified.

Table 3.6. Positions of the right tip with different applied force values

	Right tip location (x_1, x_2, x_3) in meters		
Applied force $F_3(N)$	Nonlinear PD (5.120 elements)	Nonlinear ANSYS (5.120 elements)	Bathe and Bolourchi [104] (8 elements)
1334.467	(0.565, 1.505, 1.008)	(0.563, 1.489, 1.025)	(0.5715, 1.504, 1.003)
2668.933	(0.388, 1.212, 1.355)	(0.397, 1.193, 1.360)	(0.404, 1.199, 1.356)

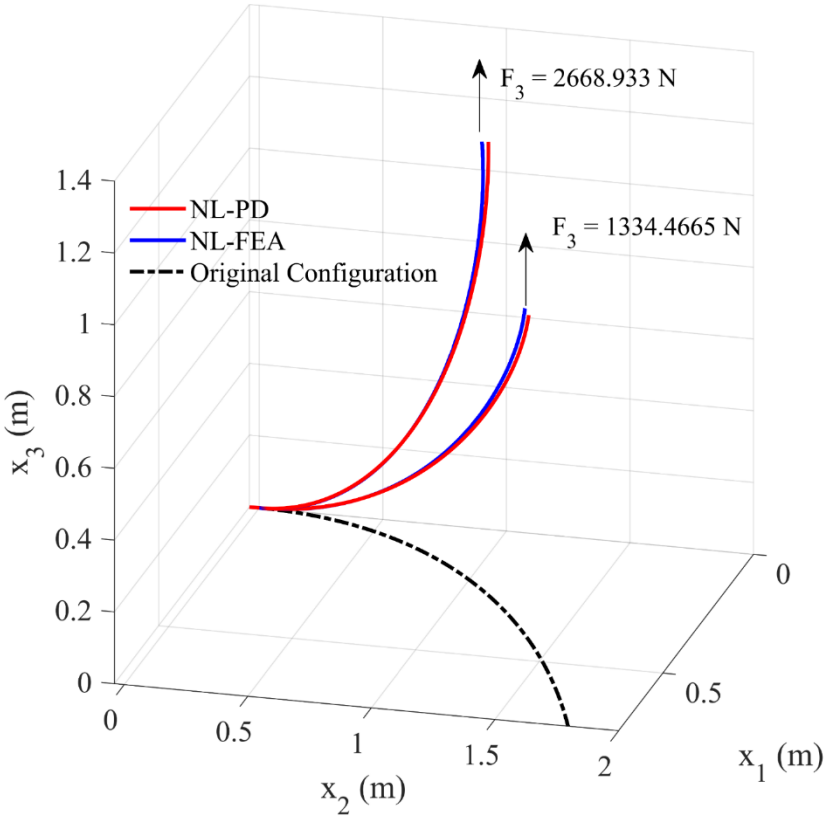

Fig. 3.45. Deformed configurations of the 45-degree curved beam

3.3.3.4. Damage prediction for a spaghetti

After verifying the accuracy of the proposed nonlinear PD model, in this section, damages on a dry spaghetti subjected to bending and torsion are predicted. The spaghetti is represented by a straight beam with a length of $L = 0.24$ m and it has a solid circular cross-section with an average radius of $r = 0.00085$ m as shown in Fig. 3.46 [105]. In the PD model, the beam is discretized with a mesh size of $\Delta x = L/6000$. To represent the imperfection of the spaghetti microstructure [106], the radius of the beam's cross-section is assumed to vary randomly in a range of $8.4832 \times 10^{-4} \leq r(x_1) \leq 8.5169 \times 10^{-4}$ m as shown in Fig. 3.46(b).

The material has a mass density of $\rho = 1500\ \text{kg/m}^3$, the elastic modulus of $E = 3.8 \times 10^9\ \text{N/m}^2$ [105], the fracture toughness of $K_{Ic} = 0.478\ \text{MPa}\sqrt{\text{m}}$ [106]. For simplification, the critical energy release rate of the material is calculated as $G_c = G_{\text{Ic}} = K_{Ic}^2/E = 60.1274\ \text{J/m}^2$. The spaghetti is investigated in two loading conditions: pure bending (case 1) and a combination of torsion and bending (case 2) [105].

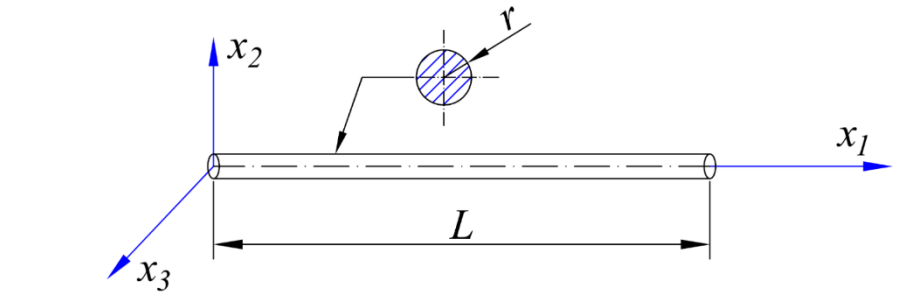

(a)

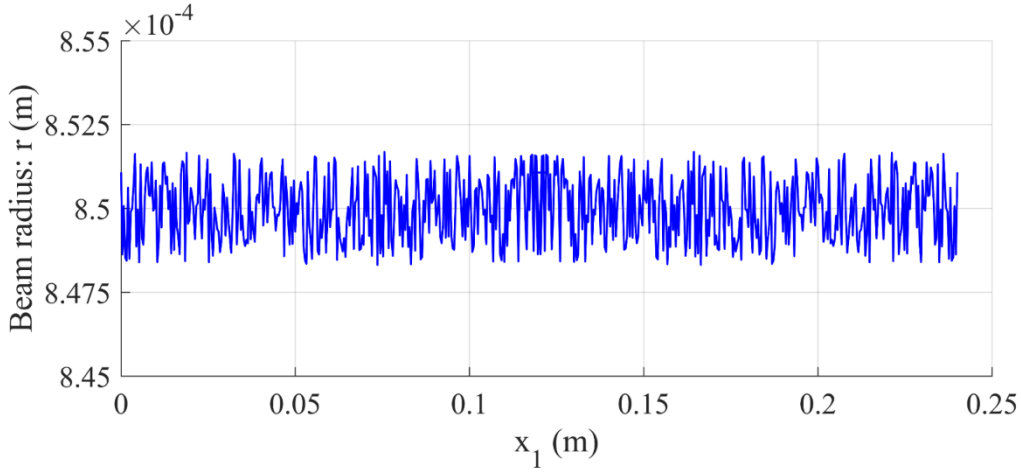

(b)

Fig. 3.46. A dry spaghetti (a): geometry, (b): randomly variation of cross-section radius along the beam length

Case 1: Spaghetti subjected to pure bending

In this case, the beam is subjected to bending moments at two ends as shown in Fig. 3.47. The boundary and loading conditions applied for the beam include two stages:

(1) Stage 1: the beam is subjected to incremental bending moments while fixing the node at the middle of the beam as shown in Fig. 3.47(a-b). The bending moments are kept increasing until the first damage occur as shown in Fig. 3.47(c).

(2) Stage 2: after the first damage occurs at the end of stage 1, the bending moments are released. Then, two ends of the beam are kept at the deformed configuration as shown in Fig. 3.48 until the final damages occur.

In stage 1, the beam is subjected to incremental bending moments per unit volume at two ends as

$$ {}^{t}m_{3(1)} = \frac{\left({}^{t-\Delta t}M + \Delta M\right)}{{}^{0}V_{(1)}} \tag{3.75a} $$

$$ {}^{t}m_{3(N)} = -\frac{\left({}^{t-\Delta t}M + \Delta M\right)}{{}^{0}V_{(N)}} \tag{3.75b} $$

with

$$ {}^{0}V_{(1)} = \pi r_{(1)}^{2}\Delta x, \quad {}^{0}V_{(N)} = \pi r_{(N)}^{2}\Delta x \tag{3.75c} $$

$${}^{0}M = 0, \quad \Delta M = 10^{-9} \text{ Nm} \tag{3.75d}$$

where ${}^{0}V_{(1)}$ and ${}^{0}V_{(N)}$ represent volumes of material points located at the left end and right end of the beam, respectively. The term ${}^{t-\Delta t}M$ represents the applied bending moment at the previous load step, ΔM represents the incremental value of the bending moment. In Eq. (3.75c), $r_{(1)}$ and $r_{(N)}$ represent the beam's radius of material points located at the left end and right end, respectively.

Besides, all material points along the beam are also subjected to the gravitational body forces as

$${}^{t}b_{2(k)} = -\rho g \tag{3.76}$$

where $g = 9.81 \text{ N/m}^2$ represents the gravitational acceleration.
The boundary conditions for the beam in this stage can be represented as

$$u_2(0,0,0) = u_2(L,0,0) = 0 \tag{3.77a}$$

$$u_3(0,0,0) = u_3(L,0,0) = 0 \tag{3.77b}$$

$$u_1(L/2,0,0) = u_3(L/2,0,0) = 0 \tag{3.77c}$$

In stage 2, when the first damage occurs, the gravitational forces given in Eq. (3.76) are maintained, meanwhile, the bending moments at the two ends given in Eq. (3.75) are released as

$${}^{t}m_{3(1)} = {}^{t}m_{3(N)} = 0 \tag{3.78}$$

To apply boundary conditions in the second stage, three material points on each end of the beam are maintained their configurations as the first damage occurs as shown in Fig. 3.48(b). The boundary conditions for the beam in stage 2 is represented as

$$\left({}^{t}u_1, {}^{t}u_2, {}^{t}u_3, {}^{t}\theta_1, {}^{t}\theta_2, {}^{t}\theta_3\right) = \left({}^{t_0}u_1, {}^{t_0}u_2, {}^{t_0}u_3, {}^{t_0}\theta_1, {}^{t_0}\theta_2, {}^{t_0}\theta_3\right) \quad \text{at } x_1 \le 3\Delta x \tag{3.79a}$$

$$\left({}^{t}u_1, {}^{t}u_2, {}^{t}u_3, {}^{t}\theta_1, {}^{t}\theta_2, {}^{t}\theta_3\right) = \left({}^{t_0}u_1, {}^{t_0}u_2, {}^{t_0}u_3, {}^{t_0}\theta_1, {}^{t_0}\theta_2, {}^{t_0}\theta_3\right) \quad \text{at } x_1 \ge L - 3\Delta x \tag{3.79b}$$

where t_0 is the moment that the first damage occurs and $\left({}^{t_0}u_1, {}^{t_0}u_2, {}^{t_0}u_3, {}^{t_0}\theta_1, {}^{t_0}\theta_2, {}^{t_0}\theta_3\right)$represent displacements and rotations at time t_0 when the first damage occurs.

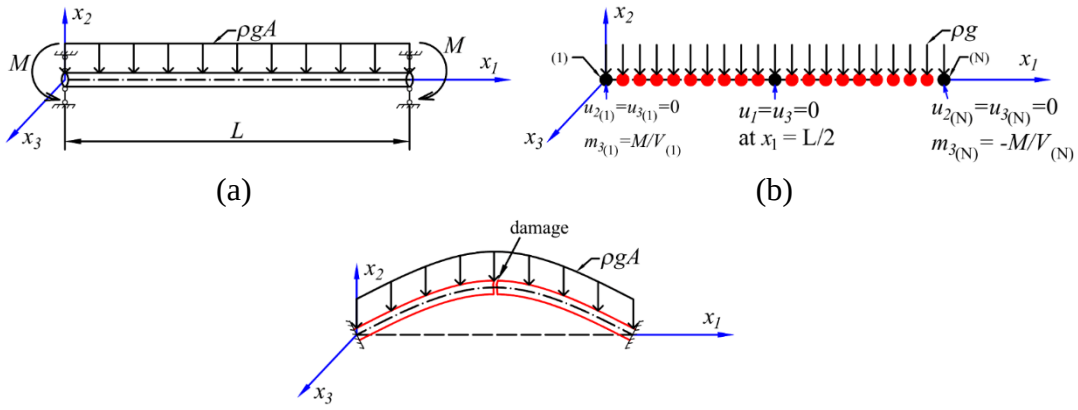

Fig. 3.47. Boundary and loading conditions for a spaghetti subjected to pure bending in stage 1 (a): geometry, (b): PD discretized model, (c): deformed configuration at the end of stage 1 when the first damage occurs

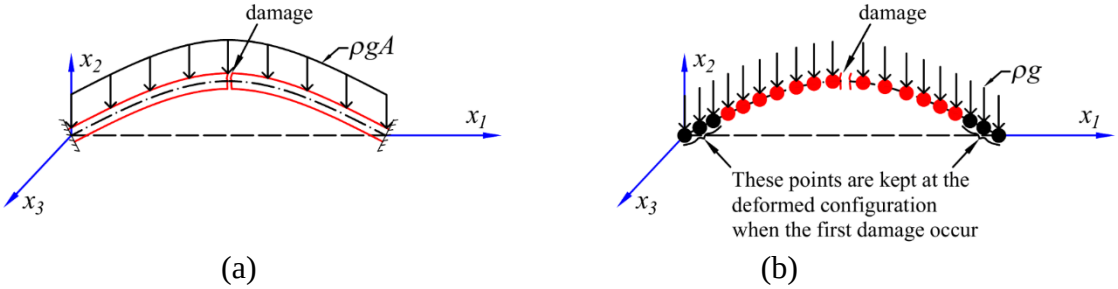

Fig. 3.48. Boundary and loading conditions for spaghetti in stage 2 (a): deformed configuration when the first damage occur and the bending moments are released, (b): PD discretized model

The beam is assumed to be in quasi-static loading conditions and the PD solution is obtained by using the ADR method [76, 77]. Fig. 3.49 shows the damage evolution on the beam in the pure bending condition after stage 1. As shown in Fig. 3.49(a), after 178×10^5 time steps, the first damage occurs at the middle section of the beam. After 178.26×10^5 time steps, in stage 2 the beam has two more damages located symmetrically with respect to the middle section of the beam as shown in Fig. 3.49(b). After 178.62×10^5 time steps, the beam is finally broken into 6 segments with 5 locations of damage located symmetrically with respect to the middle section of the beam as shown in Fig. 3.49(c). As it can be observed from the results, the damage evolution on the beam predicted by the nonlinear PD model has good agreement with the experimental results in [105].

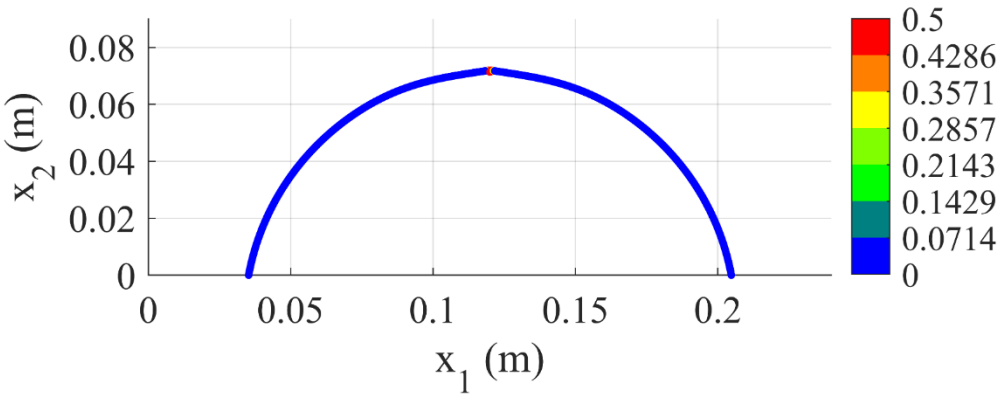

(a)

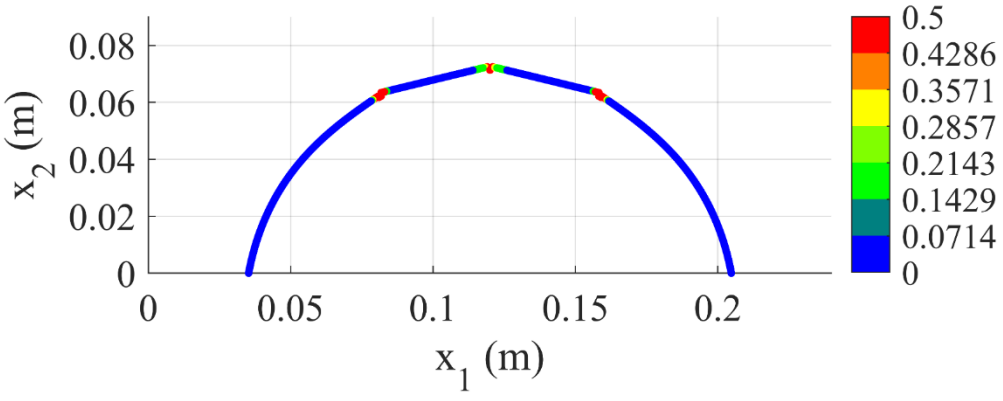

(b)

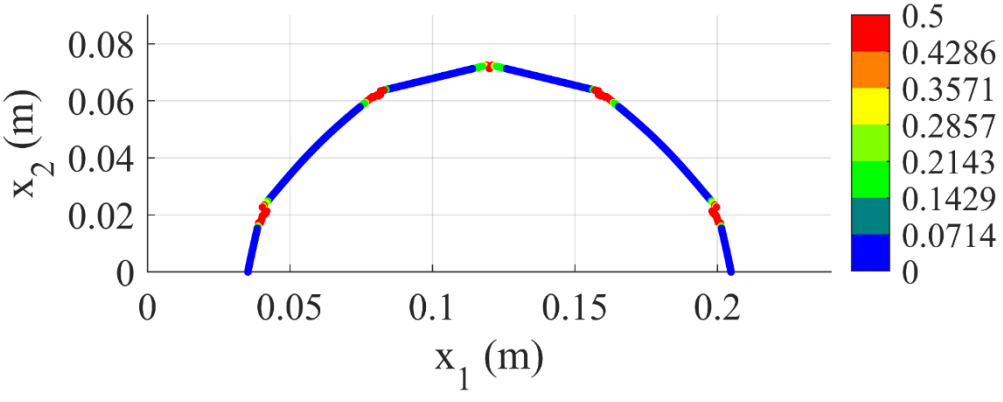

(c)

Fig. 3.49. Damage evolution on the dry spaghetti subjected to pure bending (a): first damage occurrence at (a) 178×10^5 (b): 178.26×10^5 , (c): 178.62×10^5 time steps

Case 2: spaghetti subjected to a combined loading: torsion and bending

In this case, the boundary and loading conditions applied for the beam include three stages as follows.

(1) Stage 1: the beam is twisted by $\theta* = 100^o$ $(\theta_1(0,0,0) = -\theta*/2, \theta_1(L,0,0) = \theta*/2)$ as shown in Fig. 3.50.

(2) Stage 2: In addition to torsional loading, the beam is subjected to incremental bending moments at two ends as shown in Fig. 3.51. The loading conditions in this stage are given in Eq. (3.75).

(3) Stage 3: when the first damage occurs, the bending moments are released. The beam is fixed at two ends and the remaining parts of the beam can be freely moved as shown in Fig. 3.52. In all stages, the beam is subjected to the gravitational forces as given in Eq. (3.76).

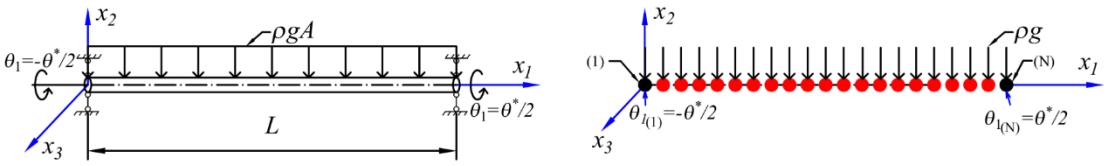

(a) (b)

Fig. 3.50. Spaghetti subjected to torsion in the stage 1 (a): geometry, (b): PD discretized model

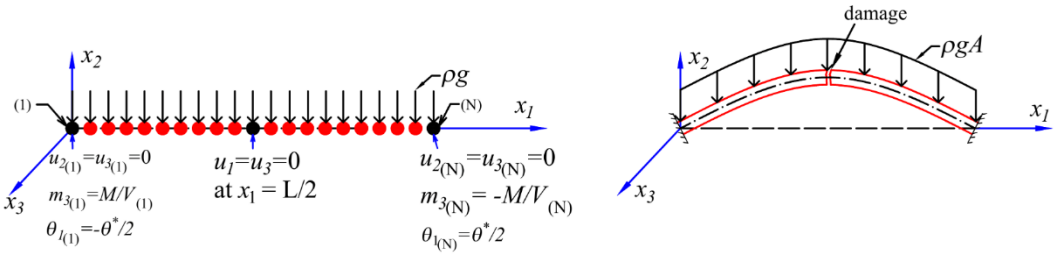

(a) (b)

Fig. 3.51. Spaghetti subjected to torsion and bending in stage 2 (a): PD discretized model, (b): deformed configuration at the end of stage 2 when the first damage occurs

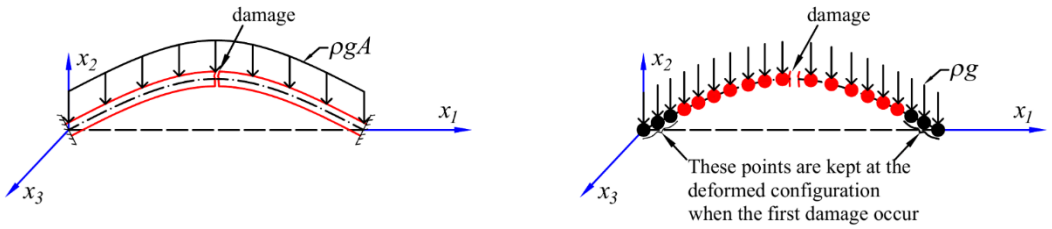

(a) (b)

Fig. 3.52. Boundary and loading conditions for the spaghetti in stage 3 (a): deformed configuration when the first damage occur and the bending moments and torsional loading are released, (b): PD discretized model

Similarly, the beam is considered in quasi-static loading conditions and the PD solution is obtained by using the ADR method. In stage 1 for the torsional loading, the converged solution is obtained after $N_0 = 2 \times 10^5$ time step. In the second stage, the torsional angles, θ_1 of the material points located at two ends of the beam are kept constant, meanwhile, the incremental bending moments are applied on two

ends of the beam as given in Eq. (3.75). Fig. 3.53 shows the damage evolution on the beam in the combined loading conditions. Similar to the previous loading condition in Section 5.5.2.1, the first damage occurs in the middle section of the beam at $N_0 + 175.6 \times 10^5$ load step as shown in Fig. 3.53(a). Later, two more new damage locations occur symmetrically with respect to the middle section of the beam as shown in Fig. 3.53(b). As can be observed from the figure, in this loading condition, the beam is only damaged into 4 pieces. This prediction also agrees with the experimental results in [105].

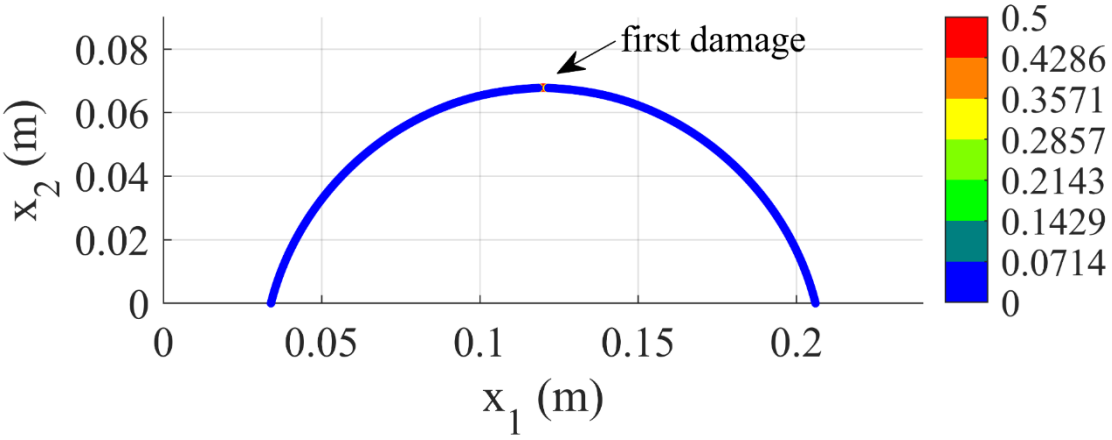

(a)

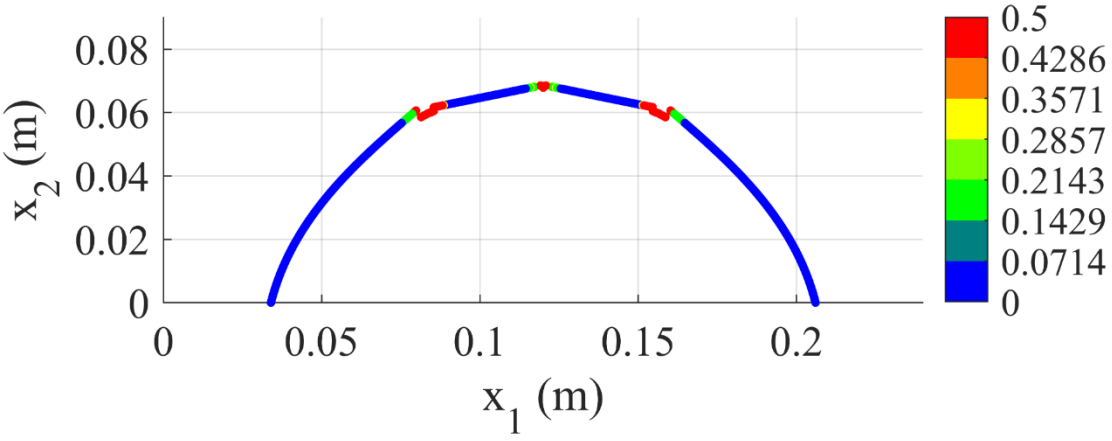

(b)

Fig. 3.53. Damage evolution on the dry spaghetti subjected to torsion and bending (a): first damage occurrence at (a) $N_0 + 175.6 \times 10^5$ time steps (when the first damage occurs), (b): $N_0 + 177.08 \times 10^5$ time steps. ($N_0 = 2 \times 10^5$ time steps for obtaining a converged solution for torsional loading in stage 1)

3.4. Peridynamics for nonlinear analysis of plates

In this section, a novel ordinary state-based PD model for geometrically nonlinear analysis of plates based on Mindlin–Reissner theory is developed. The nonlinear PD formulations and equations of motion are obtained based on the principle of virtual displacements by using the Total Lagrange formulation. The energy-based criterion for damage prediction is used. To verify the accuracy of the proposed nonlinear PD model, large deformations of a plate subjected to bending and a plate subjected to vertical shear force are investigated. For verification purposes, the predicted results by using the proposed nonlinear PD model are compared with the nonlinear FEA results. Furthermore, damages on a plate subjected to out-of-plane stretching and tearing, a plate subjected to tearing, and a plated subjected to torsional loading are also predicted by using the nonlinear PD model.

3.4.1. Nonlinear kinematics of plates in Classical Continuum Mechanics

In this section, the nonlinear kinematics of a plate are presented. According to Mindlin [78], Reissner [79], each material point on the mid-plane of the plate has five degrees of freedom, including three displacements (u, v, w) and two rotations (θ_x, θ_y) as shown in Fig. 3.54 and Fig. 3.55.

3.4.1.1. Displacement field

As shown in Fig. 3.54, material point *P* is located at $\left({}^0x,\ {}^0y,\ {}^0z\right)$ and material point *Q* is located at $\left({}^0x,\ {}^0y, 0\right)$ which is at the mid-plane of the undeformed plate. The degree of freedoms at time t and time $t + \Delta t$for material points *P* and *Q* are represented as

$$\left({}^t\hat{u},\ {}^t\hat{v},\ {}^t\hat{w}\right), \left({}^{t+\Delta t}\hat{u},\ {}^{t+\Delta t}\hat{v},\ {}^{t+\Delta t}\hat{w}\right) \text{ for } P \tag{3.80a}$$

$$\left({}^tu,\ {}^tv,\ {}^tw,\ {}^t\theta_x,\ {}^t\theta_y\right), \left({}^{t+\Delta t}u,\ {}^{t+\Delta t}v,\ {}^{t+\Delta t}w,\ {}^{t+\Delta t}\theta_x,\ {}^{t+\Delta t}\theta_y\right) \text{ for } Q \tag{3.80b}$$

According to Barut [107], the displacements of material point *P* located at $({}^0x,\ {}^0y,\ {}^0z)$ at time t and $t + \Delta t$ can be represented as [107]

$${}^t\hat{u} = {}^tu + {}^0z\sin\left({}^t\theta_y\right) \tag{3.81a}$$

$${}^t\hat{v} = {}^tv - {}^0z\sin\left({}^t\theta_x\right) \tag{3.81b}$$

$${}^t\hat{w} = {}^tw \tag{3.81c}$$

and

$${}^{t+\Delta t}\hat{u} = {}^{t+\Delta t}u + {}^0z\sin\left({}^{t+\Delta t}\theta_y\right) \tag{3.81d}$$

$${}^{t+\Delta t}\hat{v} = {}^{t+\Delta t}v - {}^0z\sin\left({}^{t+\Delta t}\theta_x\right) \tag{3.81e}$$

$${}^{t+\Delta t}\hat{w} = {}^{t+\Delta t}w \tag{3.81f}$$

with

$$-h/2 \le {}^0z \le h/2 \tag{3.81g}$$

where h represents the thickness of the plate.

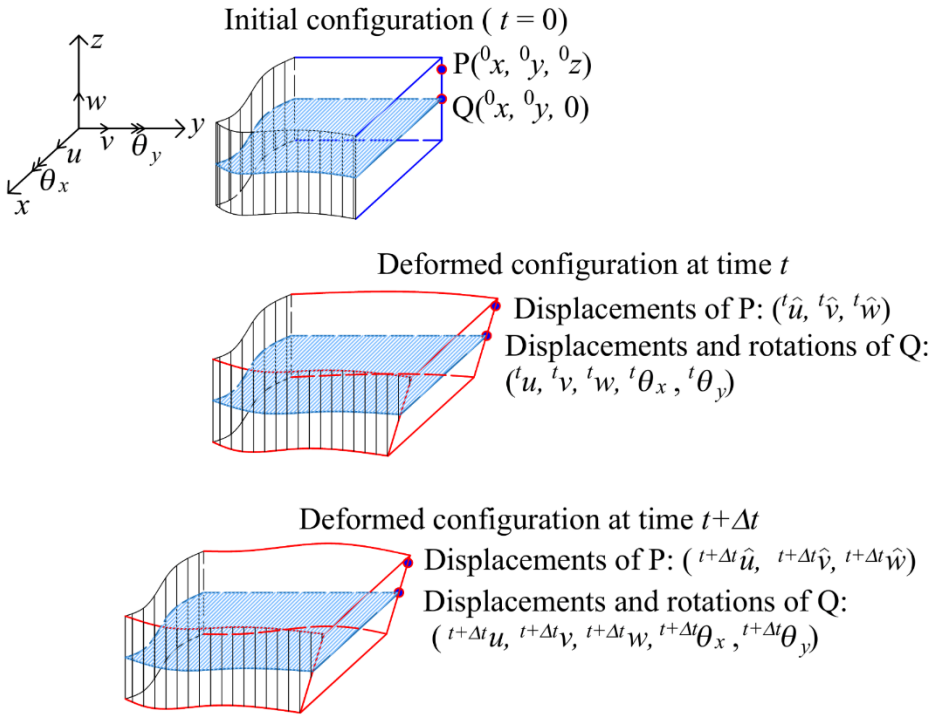

Fig. 3.54. Displacement vectors of a material point located on mid-plane and a material point located at any location in the initial and deformed configurations of a plate

On the other hand, the incremental displacements from time t to time $t+\Delta t$ of material point P located at (^0x, ^0y, ^0z) can be calculated by using Eq. (C2) in appendix C as

$$\underline{\hat{u}} = {}^{t+\Delta t}\hat{u} - {}^{t}\hat{u} \tag{3.82a}$$

$$\underline{\hat{v}} = {}^{t+\Delta t}\hat{v} - {}^{t}\hat{v} \tag{3.82b}$$

$$\underline{\hat{w}} = {}^{t+\Delta t}\hat{w} - {}^{t}\hat{w} \tag{3.82c}$$

By using Eq. (3.81), the incremental displacements in Eq. (3.82) can be represented as

$$\underline{\hat{u}} = \left({}^{t+\Delta t}u - {}^{t}u\right) + {}^{0}z\left[\sin\left({}^{t+\Delta t}\theta_y\right) - \sin\left({}^{t}\theta_y\right)\right] \tag{3.83a}$$

$$\underline{\hat{v}} = \left({}^{t+\Delta t}v - {}^{t}v\right) - {}^{0}z\left[\sin\left({}^{t+\Delta t}\theta_x\right) - \sin\left({}^{t}\theta_x\right)\right] \tag{3.83b}$$

$$\underline{\hat{w}} = {}^{t+\Delta t}w - {}^{t}w \tag{3.83c}$$

which can be rewritten as

$$\underline{\hat{u}} = \underline{u} + {}^{0}z\left[\sin\left({}^{t+\Delta t}\theta_y\right) - \sin\left({}^{t}\theta_y\right)\right] \tag{3.84a}$$

$$\underline{\hat{v}} = \underline{v} - {}^{0}z\left[\sin\left({}^{t+\Delta t}\theta_x\right) - \sin\left({}^{t}\theta_x\right)\right] \tag{3.84b}$$

$$\underline{\hat{w}} = \underline{w} \tag{3.84c}$$

with

$$\underline{u} = {}^{t+\Delta t}u - {}^{t}u \tag{3.84d}$$

$$\underline{v} = {}^{t+\Delta t}v - {}^{t}v \tag{3.84e}$$

$$\underline{w} = {}^{t+\Delta t}w - {}^{t}w \tag{3.84f}$$

where $\underline{u}$, $\underline{v}$, $\underline{w}$ represent the incremental displacements from time t to time $t + \Delta t$ of point Q located at $({}^{0}x,\ {}^{0}y, 0)$ at the mid-plane of the plate.

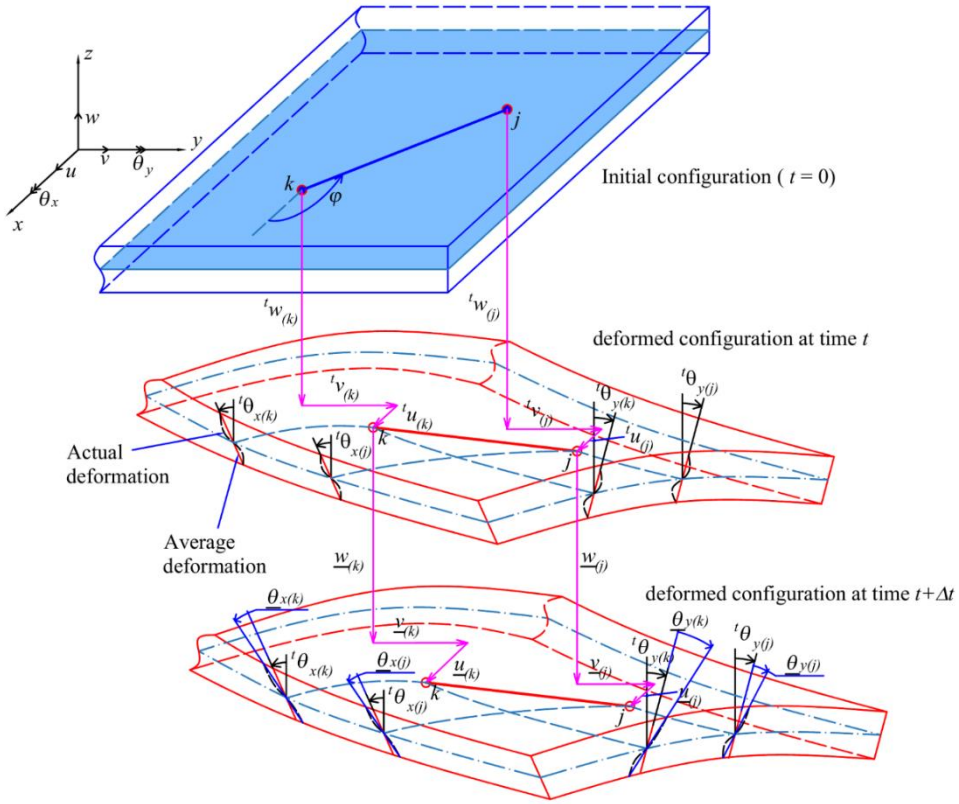

Fig. 3.55. Five degrees of freedom of material points located on the mid-plane in the initial and deformed configurations of a plate

By using the Eqs. (3.84a-c), the incremental displacements at any point P can be rewritten in terms of incremental displacements of point Q at the mid-plane by using trigonometric relations as

$$\underline{\hat{u}} = \underline{u} + 2\,{}^{0}z \sin\left(\frac{\underline{\theta}_y}{2}\right)\left[\cos\left({}^{t}\theta_y\right)\cos\left(\frac{\underline{\theta}_y}{2}\right) - \sin\left({}^{t}\theta_y\right)\sin\left(\frac{\underline{\theta}_y}{2}\right)\right] \tag{3.85a}$$

$$\underline{\hat{v}} = \underline{v} - 2\,{}^{0}z \sin\left(\frac{\underline{\theta}_x}{2}\right)\left[\cos\left({}^{t}\theta_x\right)\cos\left(\frac{\underline{\theta}_x}{2}\right) - \sin\left({}^{t}\theta_x\right)\sin\left(\frac{\underline{\theta}_x}{2}\right)\right] \tag{3.85b}$$

$$\underline{\hat{w}} = \underline{w} \tag{3.85c}$$

with

$$\underline{\theta}_x = {}^{t+\Delta t}\theta_x - {}^{t}\theta_x \tag{3.85d}$$

$$\underline{\theta}_y = {}^{t+\Delta t}\theta_y - {}^{t}\theta_y \tag{3.85e}$$

where $\underline{\theta}_x$ and $\underline{\theta}_y$ represent the incremental rotations from time t to time $t+\Delta t$ of a material point located on the mid-plane of the plate (see Fig. 3.55).

Similar to the approximation in nonlinear FEA [70], the incremental rotations $\underline{\theta}_x$ and $\underline{\theta}_y$ can be assumed very small as

$$\sin\left(\frac{\underline{\theta}_y}{2}\right) \approx \frac{\underline{\theta}_y}{2}, \quad \cos\left(\frac{\underline{\theta}_y}{2}\right) \approx 1, \quad \sin^2\left(\frac{\underline{\theta}_y}{2}\right) \approx 0 \tag{3.86}$$

Therefore, the incremental displacements at any point *P* located at $\left({}^{0}x,\ {}^{0}y,\ {}^{0}z\right)$ provided in Eqs. (3.85a-c) can be simplified as

$$\hat{\underline{u}} = \underline{u} + {}^{0}z\underline{\theta}_y \cos\left({}^{t}\theta_y\right) \tag{3.87a}$$

$$\hat{\underline{v}} = \underline{v} - {}^{0}z\underline{\theta}_x \cos\left({}^{t}\theta_x\right) \tag{3.87b}$$

$$\hat{\underline{w}} = \underline{w} \tag{3.87c}$$

3.4.1.2. Strain field

By using the displacements given in Eq. (3.81), the Green-Lagrange strain at time t given in Eq. (C4) in Appendix C2 for a material point located at $\left({}^{0}x,\ {}^{0}y,\ {}^{0}z\right)$ can be represented as [107]

$$\begin{aligned} {}^{t}_{0}\hat{\varepsilon}_{xx} &= {}^{t}_{0}u_{,x} + {}^{0}z\frac{\partial\left(\sin{}^{t}\theta_y\right)}{\partial\,{}^{0}x} + \frac{1}{2}\left[{}^{t}_{0}u_{,x}{}^{2} + {}^{t}_{0}v_{,x}{}^{2} + {}^{t}_{0}w_{,x}{}^{2}\right] \\ &+ \frac{1}{2}\left[{}^{0}z\frac{\partial\left(\sin{}^{t}\theta_y\right)}{\partial\,{}^{0}x}\left({}^{0}z\frac{\partial\left(\sin{}^{t}\theta_y\right)}{\partial\,{}^{0}x} + 2\,{}^{t}_{0}u_{,x}\right) + {}^{0}z\frac{\partial\left(\sin{}^{t}\theta_x\right)}{\partial\,{}^{0}x}\left({}^{0}z\frac{\partial\left(\sin{}^{t}\theta_x\right)}{\partial\,{}^{0}x} - 2\,{}^{t}_{0}v_{,x}\right)\right] \end{aligned} \tag{3.88a}$$

$$\begin{aligned} {}^{t}_{0}\hat{\varepsilon}_{yy} &= {}^{t}_{0}v_{,y} - {}^{0}z\frac{\partial\left(\sin{}^{t}\theta_x\right)}{\partial\,{}^{0}y} + \frac{1}{2}\left[{}^{t}_{0}u_{,y}{}^{2} + {}^{t}_{0}v_{,y}{}^{2} + {}^{t}_{0}w_{,y}{}^{2}\right] \\ &+ \frac{1}{2}\left[{}^{0}z\frac{\partial\left(\sin{}^{t}\theta_y\right)}{\partial\,{}^{0}y}\left(2\,{}^{t}_{0}u_{,y} + {}^{0}z\frac{\partial\left(\sin{}^{t}\theta_y\right)}{\partial\,{}^{0}y}\right) + {}^{0}z\frac{\partial\left(\sin{}^{t}\theta_x\right)}{\partial\,{}^{0}y}\left({}^{0}z\frac{\partial\left(\sin{}^{t}\theta_x\right)}{\partial\,{}^{0}y} - 2\,{}^{t}_{0}v_{,y}\right)\right] \end{aligned} \tag{3.88b}$$

$$
\begin{aligned}
{}_0^t\hat{\varepsilon}_{xy} = \frac{1}{2}\Bigg[& {}_0^t u_{,y} + {}^0z\frac{\partial\left(\sin{}^t\theta_y\right)}{\partial {}^0y} + {}_0^t v_{,x} - {}^0z\frac{\partial\left(\sin{}^t\theta_x\right)}{\partial {}^0x} + {}_0^t u_{,x}\,{}_0^t u_{,y} + {}_0^t v_{,x}\,{}_0^t v_{,y} + {}_0^t w_{,x}\,{}_0^t w_{,y} \Bigg] \\
& + \frac{1}{2}\begin{bmatrix} {}^0z\dfrac{\partial\left(\sin{}^t\theta_y\right)}{\partial {}^0x}\left({}_0^t u_{,y} + {}^0z\dfrac{\partial\left(\sin{}^t\theta_y\right)}{\partial {}^0y}\right) + \left({}_0^t u_{,x} + {}^0z\dfrac{\partial\left(\sin{}^t\theta_y\right)}{\partial {}^0x}\right){}^0z\dfrac{\partial\left(\sin{}^t\theta_y\right)}{\partial {}^0y} \\ -{}^0z\dfrac{\partial\left(\sin{}^t\theta_x\right)}{\partial {}^0x}\left({}_0^t v_{,y} - {}^0z\dfrac{\partial\left(\sin{}^t\theta_x\right)}{\partial {}^0y}\right) - \left({}_0^t v_{,x} - {}^0z\dfrac{\partial\left(\sin{}^t\theta_x\right)}{\partial {}^0x}\right){}^0z\dfrac{\partial\left(\sin{}^t\theta_x\right)}{\partial {}^0y} \end{bmatrix}
\end{aligned} \tag{3.88c}
$$

$$
\begin{aligned}
{}_0^t\hat{\varepsilon}_{xz} = & \frac{1}{2}\left[{}_0^t w_{,x} + \sin\left({}^t\theta_y\right) + {}_0^t u_{,x}\sin\left({}^t\theta_y\right) - {}_0^t v_{,x}\sin\left({}^t\theta_x\right)\right] \\
& + \frac{1}{2}\left[{}^0z\,{}_0^t\theta_{y,x}\sin\left({}^t\theta_y\right) + {}^0z\,{}_0^t\theta_{x,x}\sin\left({}^t\theta_x\right)\right]
\end{aligned} \tag{3.88d}
$$

$$
\begin{aligned}
{}_0^t\hat{\varepsilon}_{yz} = & \frac{1}{2}\left[{}_0^t w_{,y} - \sin\left({}^t\theta_x\right) + {}_0^t u_{,y}\sin\left({}^t\theta_y\right) - {}_0^t v_{,y}\sin\left({}^t\theta_x\right)\right] \\
& + \frac{1}{2}\left[{}^0z\,{}_0^t\theta_{y,y}\sin\left({}^t\theta_y\right) + {}^0z\,{}_0^t\theta_{x,y}\sin\left({}^t\theta_x\right)\right]
\end{aligned} \tag{3.88e}
$$

$$
{}_0^t\hat{\varepsilon}_{zz} \approx 0 \tag{3.88f}
$$

with

$$
{}_0^t\theta_{x,x} = \frac{\partial {}^t\theta_x}{\partial {}^0x};\ {}_0^t\theta_{x,y} = \frac{\partial {}^t\theta_x}{\partial {}^0y} \tag{3.88g}
$$

$$
{}_0^t\theta_{y,x} = \frac{\partial {}^t\theta_y}{\partial {}^0x};\ {}_0^t\theta_{y,y} = \frac{\partial {}^t\theta_y}{\partial {}^0y} \tag{3.88h}
$$

Note that, the relation given in Eq. (3.88f) is applicable for small strain problems. In the small strain conditions, the thickness of the plate is assumed as unchanged. Therefore, the strain in the thickness direction of the plate is ignored.

By assuming the plate is moderately thin, the following terms in Eq. (3.88) can be neglected as [107]

$$
\frac{1}{2}\left[{}^0z\frac{\partial\left(\sin{}^t\theta_y\right)}{\partial {}^0x}\left({}^0z\frac{\partial\left(\sin{}^t\theta_y\right)}{\partial {}^0x} + 2\,{}_0^t u_{,x}\right) + {}^0z\frac{\partial\left(\sin{}^t\theta_x\right)}{\partial {}^0x}\left({}^0z\frac{\partial\left(\sin{}^t\theta_x\right)}{\partial {}^0x} - 2\,{}_0^t v_{,x}\right)\right] \to 0 \tag{3.89a}
$$

$$
\frac{1}{2}\left[{}^0z\frac{\partial\left(\sin{}^t\theta_y\right)}{\partial {}^0y}\left(2\,{}_0^t u_{,y} + {}^0z\frac{\partial\left(\sin{}^t\theta_y\right)}{\partial {}^0y}\right) + {}^0z\frac{\partial\left(\sin{}^t\theta_x\right)}{\partial {}^0y}\left({}^0z\frac{\partial\left(\sin{}^t\theta_x\right)}{\partial {}^0y} - 2\,{}_0^t v_{,y}\right)\right] \to 0 \tag{3.89b}
$$

$$
\frac{1}{2}\begin{bmatrix} {}^0z\dfrac{\partial\left(\sin{}^t\theta_y\right)}{\partial {}^0x}\left({}_0^t u_{,y} + {}^0z\dfrac{\partial\left(\sin{}^t\theta_y\right)}{\partial {}^0y}\right) + \left({}_0^t u_{,x} + {}^0z\dfrac{\partial\left(\sin{}^t\theta_y\right)}{\partial {}^0x}\right){}^0z\dfrac{\partial\left(\sin{}^t\theta_y\right)}{\partial {}^0y} \\ -{}^0z\dfrac{\partial\left(\sin{}^t\theta_x\right)}{\partial {}^0x}\left({}_0^t v_{,y} - {}^0z\dfrac{\partial\left(\sin{}^t\theta_x\right)}{\partial {}^0y}\right) - \left({}_0^t v_{,x} - {}^0z\dfrac{\partial\left(\sin{}^t\theta_x\right)}{\partial {}^0x}\right){}^0z\dfrac{\partial\left(\sin{}^t\theta_x\right)}{\partial {}^0y} \end{bmatrix} \to 0 \tag{3.89c}
$$

$$\frac{1}{2}\left[{}^{0}z\,{}_{0}^{t}\theta_{y,x}\sin\left({}^{t}\theta_{y}\right)+{}^{0}z\,{}_{0}^{t}\theta_{x,x}\sin\left({}^{t}\theta_{x}\right)\right]\to 0 \tag{3.89d}$$

$$\frac{1}{2}\left[{}^{0}z\,{}_{0}^{t}\theta_{y,y}\sin\left({}^{t}\theta_{y}\right)+{}^{0}z\,{}_{0}^{t}\theta_{x,y}\sin\left({}^{t}\theta_{x}\right)\right]\to 0 \tag{3.89e}$$

Therefore, the Green-Lagrange strains in Eq. (3.88) can be simplified as [107]

$${}_{0}^{t}\hat{\varepsilon}_{xx}={}_{0}^{t}u_{,x}+{}^{0}z\frac{\partial\left(\sin{}^{t}\theta_{y}\right)}{\partial{}^{0}x}+\frac{1}{2}\left({}_{0}^{t}u_{,x}{}^{2}+{}_{0}^{t}v_{,x}{}^{2}+{}_{0}^{t}w_{,x}{}^{2}\right) \tag{3.90a}$$

$${}_{0}^{t}\hat{\varepsilon}_{yy}={}_{0}^{t}v_{,y}-{}^{0}z\frac{\partial\left(\sin{}^{t}\theta_{x}\right)}{\partial{}^{0}y}+\frac{1}{2}\left({}_{0}^{t}u_{,y}{}^{2}+{}_{0}^{t}v_{,y}{}^{2}+{}_{0}^{t}w_{,y}{}^{2}\right) \tag{3.90b}$$

$${}_{0}^{t}\hat{\varepsilon}_{xy}=\frac{1}{2}\left[{}_{0}^{t}u_{,y}+{}_{0}^{t}v_{,x}+{}^{0}z\left(\frac{\partial\left(\sin{}^{t}\theta_{y}\right)}{\partial{}^{0}y}-\frac{\partial\left(\sin{}^{t}\theta_{x}\right)}{\partial{}^{0}x}\right)+{}_{0}^{t}u_{,x}\,{}_{0}^{t}u_{,y}+{}_{0}^{t}v_{,x}\,{}_{0}^{t}v_{,y}+{}_{0}^{t}w_{,x}\,{}_{0}^{t}w_{,y}\right] \tag{3.90c}$$

$${}_{0}^{t}\hat{\varepsilon}_{xz}=\frac{1}{2}\left[{}_{0}^{t}w_{,x}+\sin\left({}^{t}\theta_{y}\right)+{}_{0}^{t}u_{,x}\sin\left({}^{t}\theta_{y}\right)-{}_{0}^{t}v_{,x}\sin\left({}^{t}\theta_{x}\right)\right] \tag{3.90d}$$

$${}_{0}^{t}\hat{\varepsilon}_{yz}=\frac{1}{2}\left[{}_{0}^{t}w_{,y}-\sin\left({}^{t}\theta_{x}\right)+{}_{0}^{t}u_{,y}\sin\left({}^{t}\theta_{y}\right)-{}_{0}^{t}v_{,y}\sin\left({}^{t}\theta_{x}\right)\right] \tag{3.90e}$$

$${}_{0}^{t}\hat{\varepsilon}_{zz}\approx 0 \tag{3.90f}$$

On the other hand, by substituting the displacement fields given in Eq. (3.81) and Eq. (3.87) into incremental Green-Lagrange strain, ${}_{0}\hat{\underline{e}}_{ij}$ in Eq. (C9) in appendix C2 and by neglecting higher-order terms, the linear components of the incremental Green-Lagrange strain, ${}_{0}\hat{\underline{e}}_{ij}$, can be represented as [107]

$${}_{0}\hat{\underline{e}}_{xx}={}_{0}\underline{u}_{,x}+{}^{0}z\frac{\partial\left(\underline{\theta}_{y}\cos{}^{t}\theta_{y}\right)}{\partial{}^{0}x}+{}_{0}\underline{u}_{,x}\,{}_{0}^{t}u_{,x}+{}_{0}\underline{v}_{,x}\,{}_{0}^{t}v_{,x}+{}_{0}\underline{w}_{,x}\,{}_{0}^{t}w_{,x} \tag{3.91a}$$

$${}_{0}\hat{\underline{e}}_{yy}={}_{0}\underline{v}_{,y}-{}^{0}z\frac{\partial\left(\underline{\theta}_{x}\cos{}^{t}\theta_{x}\right)}{\partial{}^{0}y}+{}_{0}\underline{u}_{,y}\,{}_{0}^{t}u_{,y}+{}_{0}\underline{v}_{,y}\,{}_{0}^{t}v_{,y}+{}_{0}\underline{w}_{,y}\,{}_{0}^{t}w_{,y} \tag{3.91b}$$

$${}_{0}\hat{\underline{e}}_{xy}=\frac{1}{2}\left[\begin{array}{l}{}_{0}\underline{u}_{,y}+{}_{0}\underline{v}_{,x}+{}^{0}z\dfrac{\partial\left(\underline{\theta}_{y}\cos{}^{t}\theta_{y}\right)}{\partial{}^{0}y}-{}^{0}z\dfrac{\partial\left(\underline{\theta}_{x}\cos{}^{t}\theta_{x}\right)}{\partial{}^{0}x}\\ +{}_{0}\underline{u}_{,x}\,{}_{0}^{t}u_{,y}+{}_{0}^{t}u_{,x}\,{}_{0}\underline{u}_{,y}+{}_{0}\underline{v}_{,x}\,{}_{0}^{t}v_{,y}+{}_{0}^{t}v_{,x}\,{}_{0}\underline{v}_{,y}+{}_{0}\underline{w}_{,x}\,{}_{0}^{t}w_{,y}+{}_{0}^{t}w_{,x}\,{}_{0}\underline{w}_{,y}\end{array}\right] \tag{3.91c}$$

$${}_{0}\hat{\underline{e}}_{xz}=\frac{1}{2}\left[{}_{0}\underline{w}_{,x}+\underline{\theta}_{y}\cos\left({}^{t}\theta_{y}\right)\right] \tag{3.91d}$$

$${}_{0}\hat{\underline{e}}_{yz}=\frac{1}{2}\left[{}_{0}\underline{w}_{,y}-\underline{\theta}_{x}\cos\left({}^{t}\theta_{x}\right)\right] \tag{3.91e}$$

with

$${}_{0}\underline{u}_{,x}=\frac{\partial\underline{u}}{\partial{}^{0}x};\ {}_{0}\underline{u}_{,y}=\frac{\partial\underline{u}}{\partial{}^{0}y} \tag{3.91f}$$

$$ {}_0\underline{v}_{,x} = \frac{\partial \underline{v}}{\partial {}^0x};\ {}_0\underline{v}_{,y} = \frac{\partial \underline{v}}{\partial {}^0y} \tag{3.91g} $$

$$ {}_0\underline{w}_{,x} = \frac{\partial \underline{w}}{\partial {}^0x};\ {}_0\underline{w}_{,y} = \frac{\partial \underline{w}}{\partial {}^0y} \tag{3.91h} $$

3.4.1.3. Second Piola-Kirchhoff stress

By substituting the Green-Lagrange strain at time t given in Eq. (3.90) into Eq. (C19) in Appendix C3, the second Piola-Kirchhoff stress components for a plate with large displacements, large rotations, but small elastic strains can be calculated as [107]

$$ {}_0^t\hat{S}_{xx} = \frac{E}{1-\nu^2}\left(\begin{array}{l} {}_0^tu_{,x} + \nu\, {}_0^tv_{,y} + {}^0z\left(\dfrac{\partial\left(\sin {}^t\theta_y\right)}{\partial {}^0x} - \nu\dfrac{\partial\left(\sin {}^t\theta_x\right)}{\partial {}^0y} \right) \\ + \dfrac{1}{2}\left[\left({}_0^tu_{,x}{}^2 + {}_0^tv_{,x}{}^2 + {}_0^tw_{,x}{}^2 \right) + \nu\left({}_0^tu_{,y}{}^2 + {}_0^tv_{,y}{}^2 + {}_0^tw_{,y}{}^2 \right) \right] \end{array} \right) \tag{3.92a} $$

$$ {}_0^t\hat{S}_{yy} = \frac{E}{1-\nu^2}\left(\begin{array}{l} {}_0^tv_{,y} + \nu\, {}_0^tu_{,x} - {}^0z\left(\dfrac{\partial\left(\sin {}^t\theta_x\right)}{\partial {}^0y} - \nu\dfrac{\partial\left(\sin {}^t\theta_y\right)}{\partial {}^0y} \right) \\ + \dfrac{1}{2}\left[\left({}_0^tu_{,y}{}^2 + {}_0^tv_{,y}{}^2 + {}_0^tw_{,y}{}^2 \right) + \nu\left({}_0^tu_{,x}{}^2 + {}_0^tv_{,x}{}^2 + {}_0^tw_{,x}{}^2 \right) \right] \end{array} \right) \tag{3.92b} $$

$$ {}_0^t\hat{S}_{xy} = \frac{E}{2(1+\nu)}\left[\begin{array}{l} {}_0^tu_{,y} + {}_0^tv_{,x} + {}^0z\left(\dfrac{\partial\left(\sin {}^t\theta_y\right)}{\partial {}^0y} - \dfrac{\partial\left(\sin {}^t\theta_x\right)}{\partial {}^0x} \right) \\ + {}_0^tu_{,x}\, {}_0^tu_{,y} + {}_0^tv_{,x}\, {}_0^tv_{,y} + {}_0^tw_{,x}\, {}_0^tw_{,y} \end{array} \right] \tag{3.92c} $$

$$ {}_0^t\hat{S}_{xz} = \frac{k_sE}{2(1+\nu)}\left[{}_0^tw_{,x} + \sin\left({}^t\theta_y \right) \right] \tag{3.92d} $$

$$ {}_0^t\hat{S}_{yz} = \frac{k_sE}{2(1+\nu)}\left[{}_0^tw_{,y} - \sin\left({}^t\theta_x \right) \right] \tag{3.92e} $$

$$ {}_0^t\hat{S}_{zz} \approx 0 \tag{3.92f} $$

3.4.1.4. The strain energy density

By substituting the second Piola-Kirchhoff stress components given in Eq. (3.92) and the incremental strains given in Eq. (3.91) into Eq. (C30) in Appendix C4, the SED of a plate can be represented as [107]

$$
\begin{aligned}
W^{NL} = {} & \frac{E}{1-\nu^2}\left\{ {}_0^t u_{,x} + \nu\, {}_0^t v_{,y} + \frac{1}{2}\left[\begin{matrix} \left({}_0^t u_{,x}{}^2 + {}_0^t v_{,x}{}^2 + {}_0^t w_{,x}{}^2 \right) \\ +\nu\left({}_0^t u_{,y}{}^2 + {}_0^t v_{,y}{}^2 + {}_0^t w_{,y}{}^2 \right) \end{matrix} \right] \right\} \left(\begin{matrix} {}_0\underline{u}_{,x} + {}_0\underline{u}_{,x}\, {}_0^t u_{,x} \\ +{}_0\underline{v}_{,x}\, {}_0^t v_{,x} + {}_0\underline{w}_{,x}\, {}_0^t w_{,x} \end{matrix} \right) \\
& + \frac{E}{1-\nu^2}\left\{ {}_0^t v_{,y} + \nu\, {}_0^t u_{,x} + \frac{1}{2}\left[\begin{matrix} \left({}_0^t u_{,y}{}^2 + {}_0^t v_{,y}{}^2 + {}_0^t w_{,y}{}^2 \right) \\ +\nu\left({}_0^t u_{,x}{}^2 + {}_0^t v_{,x}{}^2 + {}_0^t w_{,x}{}^2 \right) \end{matrix} \right] \right\} \left(\begin{matrix} {}_0\underline{v}_{,y} + {}_0\underline{u}_{,y}\, {}_0^t u_{,y} \\ +{}_0\underline{v}_{,y}\, {}_0^t v_{,y} + {}_0\underline{w}_{,y}\, {}_0^t w_{,y} \end{matrix} \right) \\
& + \frac{E}{2(1+\nu)}\left(\begin{matrix} {}_0^t u_{,y} + {}_0^t v_{,x} + {}_0^t u_{,x}\, {}_0^t u_{,y} \\ +{}_0^t v_{,x}\, {}_0^t v_{,y} + {}_0^t w_{,x}\, {}_0^t w_{,y} \end{matrix} \right) \left(\begin{matrix} {}_0\underline{u}_{,y} + {}_0\underline{v}_{,x} + {}_0\underline{u}_{,x}\, {}_0^t u_{,y} + {}_0^t u_{,x}\, {}_0\underline{u}_{,y} \\ +{}_0\underline{v}_{,x}\, {}_0^t v_{,y} + {}_0^t v_{,x}\, {}_0\underline{v}_{,y} + {}_0\underline{w}_{,x}\, {}_0^t w_{,y} + {}_0^t w_{,x}\, {}_0\underline{w}_{,y} \end{matrix} \right) \\
& + \frac{k_s E}{2(1+\nu)}\left[\begin{matrix} \left({}_0^t w_{,x} + \sin\left({}^t\theta_y \right) \right)\left({}_0\underline{w}_{,x} + \underline{\theta}_y \cos\left({}^t\theta_y \right) \right) \\ +\left({}_0^t w_{,y} - \sin\left({}^t\theta_x \right) \right)\left({}_0\underline{w}_{,y} - \underline{\theta}_x \cos\left({}^t\theta_x \right) \right) \end{matrix} \right] \\
& + \frac{E}{1-\nu^2}\left({}^0 z \right)^2 \left(\begin{matrix} \left(\frac{\partial\left(\sin {}^t\theta_y \right)}{\partial\, {}^0 x} - \nu \frac{\partial\left(\sin {}^t\theta_x \right)}{\partial\, {}^0 y} \right) \frac{\partial\left(\underline{\theta}_y \cos\left({}^t\theta_y \right) \right)}{\partial\, {}^0 x} \\ +\left(\frac{\partial\left(\sin {}^t\theta_x \right)}{\partial\, {}^0 y} - \nu \frac{\partial\left(\sin {}^t\theta_y \right)}{\partial\, {}^0 x} \right) \frac{\partial\left(\underline{\theta}_x \cos\left({}^t\theta_x \right) \right)}{\partial\, {}^0 y} \end{matrix} \right) \\
& + \frac{E}{2(1+\nu)}\left({}^0 z \right)^2 \left(\frac{\partial\left(\sin {}^t\theta_y \right)}{\partial\, {}^0 y} - \frac{\partial\left(\sin {}^t\theta_x \right)}{\partial\, {}^0 x} \right) \left(\frac{\partial\left(\underline{\theta}_y \cos\left({}^t\theta_y \right) \right)}{\partial\, {}^0 y} - \frac{\partial\left(\underline{\theta}_x \cos\left({}^t\theta_x \right) \right)}{\partial\, {}^0 x} \right)
\end{aligned} \tag{3.93}
$$

The strain energy per unit area, $\bar{W}^{NL}$, can be obtained by integrating the SED given in Eq. (3.93) through the thickness of the plate as [70, 108]

$$
\begin{aligned}
\bar{W}^{NL} = {} & \int_{-h/2}^{h/2} W^{NL}\, d\, {}^0 z \\
= {} & \frac{Eh}{1-\nu^2}\left[\begin{matrix} \left\{ {}_0^t u_{,x} + \nu\, {}_0^t v_{,y} + \frac{1}{2}\left[\begin{matrix} \left({}_0^t u_{,x}{}^2 + {}_0^t v_{,x}{}^2 + {}_0^t w_{,x}{}^2 \right) \\ +\nu\left({}_0^t u_{,y}{}^2 + {}_0^t v_{,y}{}^2 + {}_0^t w_{,y}{}^2 \right) \end{matrix} \right] \right\} \left(\begin{matrix} {}_0\underline{u}_{,x} + {}_0\underline{u}_{,x}\, {}_0^t u_{,x} \\ +{}_0\underline{v}_{,x}\, {}_0^t v_{,x} + {}_0\underline{w}_{,x}\, {}_0^t w_{,x} \end{matrix} \right) \\ +\left\{ {}_0^t v_{,y} + \nu\, {}_0^t u_{,x} + \frac{1}{2}\left[\begin{matrix} \left({}_0^t u_{,y}{}^2 + {}_0^t v_{,y}{}^2 + {}_0^t w_{,y}{}^2 \right) \\ +\nu\left({}_0^t u_{,x}{}^2 + {}_0^t v_{,x}{}^2 + {}_0^t w_{,x}{}^2 \right) \end{matrix} \right] \right\} \left(\begin{matrix} {}_0\underline{v}_{,y} + {}_0\underline{u}_{,y}\, {}_0^t u_{,y} \\ +{}_0\underline{v}_{,y}\, {}_0^t v_{,y} + {}_0\underline{w}_{,y}\, {}_0^t w_{,y} \end{matrix} \right) \end{matrix} \right] \\
& + \frac{Eh}{2(1+\nu)}\left(\begin{matrix} {}_0^t u_{,y} + {}_0^t v_{,x} + {}_0^t u_{,x}\, {}_0^t u_{,y} \\ +{}_0^t v_{,x}\, {}_0^t v_{,y} + {}_0^t w_{,x}\, {}_0^t w_{,y} \end{matrix} \right) \left(\begin{matrix} {}_0\underline{u}_{,y} + {}_0\underline{v}_{,x} + {}_0\underline{u}_{,x}\, {}_0^t u_{,y} + {}_0^t u_{,x}\, {}_0\underline{u}_{,y} \\ +{}_0\underline{v}_{,x}\, {}_0^t v_{,y} + {}_0^t v_{,x}\, {}_0\underline{v}_{,y} + {}_0\underline{w}_{,x}\, {}_0^t w_{,y} + {}_0^t w_{,x}\, {}_0\underline{w}_{,y} \end{matrix} \right) \\
& + \frac{k_s Eh}{2(1+\nu)}\left[\begin{matrix} \left({}_0^t w_{,x} + \sin\left({}^t\theta_y \right) \right)\left({}_0\underline{w}_{,x} + \underline{\theta}_y \cos\left({}^t\theta_y \right) \right) \\ +\left({}_0^t w_{,y} - \sin\left({}^t\theta_x \right) \right)\left({}_0\underline{w}_{,y} - \underline{\theta}_x \cos\left({}^t\theta_x \right) \right) \end{matrix} \right] \\
& + \frac{Eh^3}{12(1-\nu^2)}\left(\begin{matrix} \left(\frac{\partial\left(\sin {}^t\theta_y \right)}{\partial\, {}^0 x} - \nu \frac{\partial\left(\sin {}^t\theta_x \right)}{\partial\, {}^0 y} \right) \frac{\partial\left(\underline{\theta}_y \cos\left({}^t\theta_y \right) \right)}{\partial\, {}^0 x} \\ +\left(\frac{\partial\left(\sin {}^t\theta_x \right)}{\partial\, {}^0 y} - \nu \frac{\partial\left(\sin {}^t\theta_y \right)}{\partial\, {}^0 x} \right) \frac{\partial\left(\underline{\theta}_x \cos\left({}^t\theta_x \right) \right)}{\partial\, {}^0 y} \end{matrix} \right) \\
& + \frac{Eh^3}{24(1+\nu)}\left(\frac{\partial\left(\sin {}^t\theta_y \right)}{\partial\, {}^0 y} - \frac{\partial\left(\sin {}^t\theta_x \right)}{\partial\, {}^0 x} \right) \left(\frac{\partial\left(\underline{\theta}_y \cos\left({}^t\theta_y \right) \right)}{\partial\, {}^0 y} - \frac{\partial\left(\underline{\theta}_x \cos\left({}^t\theta_x \right) \right)}{\partial\, {}^0 x} \right)
\end{aligned} \tag{3.94}
$$

The strain energy per unit area given in Eq. (3.94) can be rewritten as

$$
\begin{aligned}
\bar{W}^{NL} &= \frac{Eh}{1-\nu^2}\left({}_0^t\vartheta\right)\left({}_0\underline{\vartheta}\right) \\
&+ \frac{Eh}{2(1+\nu)}\left[\begin{array}{l}
\left(\begin{array}{l} {}_0^tu_{,y} + {}_0^tv_{,x} + {}_0^tu_{,x}\,{}_0^tu_{,y} \\ +\,{}_0^tv_{,x}\,{}_0^tv_{,y} + {}_0^tw_{,x}\,{}_0^tw_{,y} \end{array}\right)\left(\begin{array}{l} {}_0\underline{u}_{,y} + {}_0\underline{v}_{,x} + {}_0\underline{u}_{,x}\,{}_0^tu_{,y} + {}_0^tu_{,x}\,{}_0\underline{u}_{,y} \\ +\,{}_0\underline{v}_{,x}\,{}_0^tv_{,y} + {}_0^tv_{,x}\,{}_0\underline{v}_{,y} + {}_0\underline{w}_{,x}\,{}_0^tw_{,y} + {}_0^tw_{,x}\,{}_0\underline{w}_{,y} \end{array}\right) \\
-2\left[{}_0^t\varepsilon_{yy}\left(\begin{array}{l} {}_0\underline{u}_{,x} + {}_0\underline{u}_{,x}\,{}_0^tu_{,x} \\ +\,{}_0\underline{v}_{,x}\,{}_0^tv_{,x} + {}_0\underline{w}_{,x}\,{}_0^tw_{,x} \end{array}\right) + {}_0^t\varepsilon_{xx}\left(\begin{array}{l} {}_0\underline{v}_{,y} + {}_0\underline{u}_{,y}\,{}_0^tu_{,y} \\ +\,{}_0\underline{v}_{,y}\,{}_0^tv_{,y} + {}_0\underline{w}_{,y}\,{}_0^tw_{,y} \end{array}\right)\right]
\end{array}\right] \\
&+ \frac{k_sEh}{2(1+\nu)}\left[\begin{array}{l}
\left({}_0^tw_{,x} + \sin\left({}^t\theta_y\right)\right)\left({}_0\underline{w}_{,x} + \underline{\theta}_y\cos\left({}^t\theta_y\right)\right) \\
+\left({}_0^tw_{,y} - \sin\left({}^t\theta_x\right)\right)\left({}_0\underline{w}_{,y} - \underline{\theta}_x\cos\left({}^t\theta_x\right)\right)
\end{array}\right] \\
&+ \frac{Eh^3}{12\left(1-\nu^2\right)}\left[\begin{array}{l}
\left(\dfrac{\partial\left(\sin{}^t\theta_y\right)}{\partial\,{}^0x} - \dfrac{\partial\left(\sin{}^t\theta_x\right)}{\partial\,{}^0y}\right)\left(\dfrac{\partial\left(\underline{\theta}_y\cos\left({}^t\theta_y\right)\right)}{\partial\,{}^0x} - \dfrac{\partial\left(\underline{\theta}_x\cos\left({}^t\theta_x\right)\right)}{\partial\,{}^0y}\right) \\
+\dfrac{1-\nu}{2}\left[\begin{array}{l}
\left(\dfrac{\partial\left(\sin{}^t\theta_y\right)}{\partial\,{}^0y} - \dfrac{\partial\left(\sin{}^t\theta_x\right)}{\partial\,{}^0x}\right)\left(\dfrac{\partial\left(\underline{\theta}_y\cos\left({}^t\theta_y\right)\right)}{\partial\,{}^0y} - \dfrac{\partial\left(\underline{\theta}_x\cos\left({}^t\theta_x\right)\right)}{\partial\,{}^0x}\right) \\
+2\dfrac{\partial\left(\sin{}^t\theta_x\right)}{\partial\,{}^0y}\dfrac{\partial\left(\underline{\theta}_y\cos\left({}^t\theta_y\right)\right)}{\partial\,{}^0x} + 2\dfrac{\partial\left(\sin{}^t\theta_y\right)}{\partial\,{}^0x}\dfrac{\partial\left(\underline{\theta}_x\cos\left({}^t\theta_x\right)\right)}{\partial\,{}^0y}
\end{array}\right]
\end{array}\right]
\end{aligned}
\tag{3.95a}
$$

with

$$
{}_0^t\varepsilon_{xx} = {}_0^tu_{,x} + \frac{1}{2}\left({}_0^tu_{,x}{}^2 + {}_0^tv_{,x}{}^2 + {}_0^tw_{,x}{}^2\right) \tag{3.95b}
$$

$$
{}_0^t\varepsilon_{yy} = {}_0^tv_{,y} + \frac{1}{2}\left({}_0^tu_{,y}{}^2 + {}_0^tv_{,y}{}^2 + {}_0^tw_{,y}{}^2\right) \tag{3.95c}
$$

$$
\begin{aligned}
{}_0^t\vartheta = {}_0^t\varepsilon_{xx} + {}_0^t\varepsilon_{yy} &= {}_0^tu_{,x} + {}_0^tv_{,y} + \frac{1}{2}\left({}_0^tu_{,x}{}^2 + {}_0^tv_{,x}{}^2 + {}_0^tw_{,x}{}^2\right) \\
&+ \frac{1}{2}\left({}_0^tu_{,y}{}^2 + {}_0^tv_{,y}{}^2 + {}_0^tw_{,y}{}^2\right)
\end{aligned}
\tag{3.95d}
$$

$$
\begin{aligned}
{}_0\underline{\vartheta} = {}& {}_0\underline{u}_{,x} + {}_0\underline{v}_{,y} + {}_0\underline{u}_{,x}\,{}_0^tu_{,x} + {}_0\underline{u}_{,y}\,{}_0^tu_{,y} \\
&+ {}_0\underline{v}_{,x}\,{}_0^tv_{,x} + {}_0\underline{v}_{,y}\,{}_0^tv_{,y} + {}_0\underline{w}_{,x}\,{}_0^tw_{,x} + {}_0\underline{w}_{,y}\,{}_0^tw_{,y}
\end{aligned}
\tag{3.95e}
$$

The strain energy per unit area given in Eq. (3.95a) can also be decomposed as [61]

$$
\bar{W}^{NL} = \bar{W}_{ip}^{NL} + \bar{W}_{sh}^{NL} + \bar{W}_{b}^{NL} \tag{3.96a}
$$

with

$$
\begin{aligned}
\bar{W}_{ip}^{NL} &= \frac{Eh}{1-\nu^2}\left({}_0^t\vartheta\right)\left({}_0\underline{\vartheta}\right) \\
&+ \frac{Eh}{2(1+\nu)}\left[\begin{array}{l}
\left(\begin{array}{l} {}_0^tu_{,y} + {}_0^tv_{,x} + {}_0^tu_{,x}\,{}_0^tu_{,y} \\ +\,{}_0^tv_{,x}\,{}_0^tv_{,y} + {}_0^tw_{,x}\,{}_0^tw_{,y} \end{array}\right)\left(\begin{array}{l} {}_0\underline{u}_{,y} + {}_0\underline{v}_{,x} + {}_0\underline{u}_{,x}\,{}_0^tu_{,y} + {}_0^tu_{,x}\,{}_0\underline{u}_{,y} \\ +\,{}_0\underline{v}_{,x}\,{}_0^tv_{,y} + {}_0^tv_{,x}\,{}_0\underline{v}_{,y} + {}_0\underline{w}_{,x}\,{}_0^tw_{,y} + {}_0^tw_{,x}\,{}_0\underline{w}_{,y} \end{array}\right) \\
-2\left[{}_0^t\varepsilon_{yy}\left(\begin{array}{l} {}_0\underline{u}_{,x} + {}_0\underline{u}_{,x}\,{}_0^tu_{,x} \\ +\,{}_0\underline{v}_{,x}\,{}_0^tv_{,x} + {}_0\underline{w}_{,x}\,{}_0^tw_{,x} \end{array}\right) + {}_0^t\varepsilon_{xx}\left(\begin{array}{l} {}_0\underline{v}_{,y} + {}_0\underline{u}_{,y}\,{}_0^tu_{,y} \\ +\,{}_0\underline{v}_{,y}\,{}_0^tv_{,y} + {}_0\underline{w}_{,y}\,{}_0^tw_{,y} \end{array}\right)\right]
\end{array}\right]
\end{aligned}
\tag{3.96b}
$$

$$\bar{W}_{sh}^{NL}=\frac{k_s Eh}{2(1+\nu)}\left[\begin{array}{l}\left({}_0^t w_{,x}+\sin\left({}^t\theta_y\right)\right)\left({}_0\underline{w}_{,x}+\underline{\theta}_y\cos\left({}^t\theta_y\right)\right)\\+\left({}_0^t w_{,y}-\sin\left({}^t\theta_x\right)\right)\left({}_0\underline{w}_{,y}-\underline{\theta}_x\cos\left({}^t\theta_x\right)\right)\end{array}\right] \tag{3.96c}$$

$$\bar{W}_{b}^{NL}=\frac{Eh^3}{12(1-\nu^2)}\left[\begin{array}{l}\left(\frac{\partial\left(\sin{}^t\theta_y\right)}{\partial^0 x}-\frac{\partial\left(\sin{}^t\theta_x\right)}{\partial^0 y}\right)\left(\frac{\partial\left(\underline{\theta}_y\cos\left({}^t\theta_y\right)\right)}{\partial^0 x}-\frac{\partial\left(\underline{\theta}_x\cos\left({}^t\theta_x\right)\right)}{\partial^0 y}\right)\\+\frac{1-\nu}{2}\left[\begin{array}{l}\left(\frac{\partial\left(\sin{}^t\theta_y\right)}{\partial^0 y}-\frac{\partial\left(\sin{}^t\theta_x\right)}{\partial^0 x}\right)\left(\frac{\partial\left(\underline{\theta}_y\cos\left({}^t\theta_y\right)\right)}{\partial^0 y}-\frac{\partial\left(\underline{\theta}_x\cos\left({}^t\theta_x\right)\right)}{\partial^0 x}\right)\\+2\frac{\partial\left(\sin{}^t\theta_x\right)}{\partial^0 y}\frac{\partial\left(\underline{\theta}_y\cos\left({}^t\theta_y\right)\right)}{\partial^0 x}+2\frac{\partial\left(\sin{}^t\theta_y\right)}{\partial^0 x}\frac{\partial\left(\underline{\theta}_x\cos\left({}^t\theta_x\right)\right)}{\partial^0 y}\end{array}\right]\end{array}\right] \tag{3.96d}$$

where $\bar{W}_{ip}^{NL}$, $\bar{W}_{sh}^{NL}$ and $\bar{W}_{b}^{NL}$ represent the strain energy per unit area for in-plane, shear, and bending deformations, respectively.

According to Barut [107], the strain energy per unit area for bending deformation given in Eq. (3.96d) can be further simplified as

$$\bar{W}_{b}^{NL}=\frac{Eh^3}{12(1-\nu^2)}\left[\begin{array}{l}\left(-{}_0^t\theta_{y,x}+{}_0^t\theta_{x,y}\right)\left(-{}_0\underline{\theta}_{y,x}+{}_0\underline{\theta}_{x,y}\right)\\+\frac{1-\nu}{2}\left[\begin{array}{l}\left({}_0^t\theta_{y,y}-{}_0^t\theta_{x,x}\right)\left({}_0\underline{\theta}_{y,y}-{}_0\underline{\theta}_{x,x}\right)\\+2\,{}_0^t\theta_{x,y}\left({}_0\underline{\theta}_{y,x}\right)+2\,{}_0^t\theta_{y,x}\left({}_0\underline{\theta}_{x,y}\right)\end{array}\right]\end{array}\right] \tag{3.97a}$$

which can be rewritten as

$$\bar{W}_{b}^{NL}=\frac{Eh^3}{12(1-\nu^2)}\left[\left({}_0^t\vartheta_b\right)\left({}_0\underline{\vartheta}_b\right)+\frac{1-\nu}{2}\left[\begin{array}{l}\left({}_0^t\theta_{y,y}-{}_0^t\theta_{x,x}\right)\left({}_0\underline{\theta}_{y,y}-{}_0\underline{\theta}_{x,x}\right)\\+2\,{}_0^t\theta_{x,y}\left({}_0\underline{\theta}_{y,x}\right)+2\,{}_0^t\theta_{y,x}\left({}_0\underline{\theta}_{x,y}\right)\end{array}\right]\right] \tag{3.97b}$$

with

$${}_0^t\vartheta_b=-{}_0^t\theta_{y,x}+{}_0^t\theta_{x,y} \tag{3.97c}$$

$${}_0\underline{\vartheta}_b=-{}_0\underline{\theta}_{y,x}+{}_0\underline{\theta}_{x,y} \tag{3.97d}$$

where

$${}_0\underline{\theta}_{x,x}=\frac{\partial\underline{\theta}_x}{\partial^0 x};\ {}_0\underline{\theta}_{x,y}=\frac{\partial\underline{\theta}_x}{\partial^0 y} \tag{3.97e}$$

$${}_0\underline{\theta}_{y,x}=\frac{\partial\underline{\theta}_y}{\partial^0 x};\ {}_0\underline{\theta}_{y,y}=\frac{\partial\underline{\theta}_y}{\partial^0 y} \tag{3.97f}$$

3.4.2. Nonlinear kinematics of plate in peridynamics

Similar to the equation of motion given in Eq. (3.1), the PD equation of motion for nonlinear analysis of a plate can be described in the discrete form as

$$\rho_{(k)}\left({}^{t}\ddot{\mathbf{u}}_{(k)}\right)=\sum_{j=1}^{N}\left({}_{0}^{t}\overline{\mathbf{t}}_{(k)(j)}-{}_{0}^{t}\overline{\mathbf{t}}_{(j)(k)}\right){}^{0}V_{(j)}+{}^{t}\overline{\mathbf{b}}_{(k)} \tag{3.98}$$

where ρ represents the mass density, ${}^{t}\ddot{\mathbf{u}}$ represents the vector of accelerations at time t. The term, ${}^{t}\boldsymbol{u}$ represents the vector of displacements at time t. Meanwhile, $\underline{\boldsymbol{u}}$ represents the vector of incremental displacement from time t to time $t+\Delta t$. The term ${}^{t}\overline{\mathbf{b}}_{(k)}$ represents the vector of external forces and moments per unit area at time t. The terms ${}_{0}^{t}\overline{\mathbf{t}}_{(k)(j)}$ and ${}_{0}^{t}\overline{\mathbf{t}}_{(j)(k)}$ represent the vectors of force densities at time t in which ${}_{0}^{t}\overline{\mathbf{t}}_{(k)(j)}$ is the force density that material point j exerts on material point k. On the other hand, ${}_{0}^{t}\overline{\mathbf{t}}_{(j)(k)}$ is the force density that material point k exerts on material point j. Both of these force densities are measured with respect to the initial configuration. For a plate with five degrees of freedom, these force densities can be represented as

$${}_{0}^{t}\overline{\mathbf{t}}_{(k)(j)}=\left[\begin{array}{ccccc}{}_{0}^{t}\overline{t}_{(k)(j)}^{u} & {}_{0}^{t}\overline{t}_{(k)(j)}^{v} & {}_{0}^{t}\overline{t}_{(k)(j)}^{w} & {}_{0}^{t}\overline{t}_{(k)(j)}^{\theta_x} & {}_{0}^{t}\overline{t}_{(k)(j)}^{\theta_y}\end{array}\right]^{T} \tag{3.99a}$$

$${}_{0}^{t}\overline{\mathbf{t}}_{(j)(k)}=\left[\begin{array}{ccccc}{}_{0}^{t}\overline{t}_{(j)(k)}^{u} & {}_{0}^{t}\overline{t}_{(j)(k)}^{v} & {}_{0}^{t}\overline{t}_{(j)(k)}^{w} & {}_{0}^{t}\overline{t}_{(j)(k)}^{\theta_x} & {}_{0}^{t}\overline{t}_{(j)(k)}^{\theta_y}\end{array}\right]^{T} \tag{3.99b}$$

where ${}_{0}^{t}\overline{t}_{(k)(j)}^{u}$, ${}_{0}^{t}\overline{t}_{(k)(j)}^{v}$, ${}_{0}^{t}\overline{t}_{(k)(j)}^{w}$, ${}_{0}^{t}\overline{t}_{(k)(j)}^{\theta_x}$, ${}_{0}^{t}\overline{t}_{(k)(j)}^{\theta_y}$ represents force densities corresponding to five degrees of freedom, u, v, w, θ_x, θ_y, respectively.

Similar to the relation given in Eq. (1.2) in chapter 1, the relationships between the PD force densities and the strain energy per unit area in nonlinear analysis of plates can be represented as

$${}_{0}^{t}\overline{t}_{(k)(j)}^{q_i}=-\frac{1}{{}^{0}V_{(j)}}\frac{\partial\overline{W}_{(k)}^{NLPD}}{\partial\underline{q}_{i\,(k)}} \tag{3.100a}$$

and

$${}_{0}^{t}\overline{t}_{(j)(k)}^{q_i}=-\frac{1}{{}^{0}V_{(k)}}\frac{\partial\overline{W}_{(j)}^{NLPD}}{\partial\underline{q}_{i\,(j)}} \tag{3.100b}$$

with

$$q_i=u,\ v,\ w,\ \theta_x,\ \theta_y \tag{3.100c}$$

$$\underline{q}_i=\underline{u},\ \underline{v},\ \underline{w},\ \underline{\theta}_x,\ \underline{\theta}_y \tag{3.100d}$$

where ${}_{0}^{t}\overline{t}_{(k)(j)}^{q_i}$ and ${}_{0}^{t}\overline{t}_{(j)(k)}^{q_i}$ represent the force density component that corresponds to the degree of freedom q_i as given in Eq. (3.99). The parameter q_i represents the degree of freedom which can be u, v, w, θ_x or θ_y. The parameter $\underline{q}_i$ represents the incremental value of q_i which can be $\underline{u}$, $\underline{v}$, $\underline{w}$, $\underline{\theta}_x$, or $\underline{\theta}_y$.

In the following sections, first, nonlinear strain energy per unit area for a plate in peridynamics is presented in Section 6.3.1. The PD constants are obtained by comparing the nonlinear strain energies per unit area in PD with those in classical

continuum mechanics. Later, the PD equations of motion for geometrically nonlinear analysis of a plate are presented in Section 6.3.2.

3.4.2.1. Peridynamic strain energy per unit area

Similar to the classical formulation of the nonlinear strain energy per unit area given in Eq. (3.96), the nonlinear strain energy per unit area in PD for a plate can be decomposed as

$$\bar{W}_{(k)}^{NLPD} = \bar{W}_{ip(k)}^{NLPD} + \bar{W}_{sh(k)}^{NLPD} + \bar{W}_{b(k)}^{NLPD} \tag{3.101}$$

where $\bar{W}_{ip(k)}^{NLPD}$, $\bar{W}_{sh(k)}^{NLPD}$, and $\bar{W}_{b(k)}^{NLPD}$ represent the nonlinear PD strain energies per unit area for the in-plane, shear, and bending deformations, respectively.

The nonlinear PD strain energy per unit area for the in-plane deformations can be represented as

$$\bar{W}_{ip(k)}^{NLPD} = 2a_{ip}\left({}_0^t\vartheta_{(k)}\right)\left({}_0\underline{\vartheta}_{(k)}\right) + 2b_{ip}\sum_{j=1}^{N}\left({}_0^t s_{ip(k)(j)}\right)\left({}_0\underline{s}_{ip(k)(j)}\right){}^0\xi\,{}^0V_{(j)} \tag{3.102a}$$

with

$$\begin{aligned} {}_0^t s_{ip(k)(j)} = {} & \frac{\left({}^t u_{(j)} - {}^t u_{(k)}\right)\cos\varphi + \left({}^t v_{(j)} - {}^t v_{(k)}\right)\sin\varphi}{{}^0\xi} \\ & + \frac{1}{2}\frac{\left({}^t u_{(j)} - {}^t u_{(k)}\right)^2 + \left({}^t v_{(j)} - {}^t v_{(k)}\right)^2 + \left({}^t w_{(j)} - {}^t w_{(k)}\right)^2}{{}^0\xi^2} \end{aligned} \tag{3.102b}$$

$$\begin{aligned} {}_0\underline{s}_{ip(k)(j)} = {} & \frac{\left(\underline{u}_{(j)} - \underline{u}_{(k)}\right)\cos\varphi + \left(\underline{v}_{(j)} - \underline{v}_{(k)}\right)\sin\varphi}{{}^0\xi} + \frac{\left({}^t u_{(j)} - {}^t u_{(k)}\right)\left(\underline{u}_{(j)} - \underline{u}_{(k)}\right)}{{}^0\xi^2} \\ & + \frac{\left({}^t v_{(j)} - {}^t v_{(k)}\right)\left(\underline{v}_{(j)} - \underline{v}_{(k)}\right)}{{}^0\xi^2} + \frac{\left({}^t w_{(j)} - {}^t w_{(k)}\right)\left(\underline{w}_{(j)} - \underline{w}_{(k)}\right)}{{}^0\xi^2} \end{aligned} \tag{3.102c}$$

$${}_0^t\vartheta_{(k)} = d_{ip}\sum_{j=1}^{N}{}_0^t s_{ip(k)(j)}\,{}^0V_{(j)} \tag{3.102d}$$

$${}_0\underline{\vartheta}_{(k)} = d_{ip}\sum_{j=1}^{N}\left({}_0\underline{s}_{ip(k)(j)}\right){}^0V_{(j)} \tag{3.102e}$$

$${}^0V_{(j)} = {}^0A_{(j)}h \tag{3.102h}$$

In Eq. (3.102), k is a material point in the PD discretized model and j is a family member of material point k. The parameter N represents the total number of family members of material point k. The term ${}_0^t s_{ip(k)(j)}$ in Eq. (3.102b) represents the nonlinear bond stretch at time t. Meanwhile, ${}_0\underline{s}_{ip(k)(j)}$ given in Eq. (3.102c) represents the incremental bond stretch from time t to time $t + \Delta t$. Both bond stretches are measured with respect to the initial configuration. The term ${}_0^t\vartheta_{(k)}$ in Eq. (3.102d) represents the dilatation at time t. The classical formulation of this dilatation is given in Eq. (3.95d). The term ${}_0\underline{\vartheta}_{(k)}$ in Eq. (3.102e) represents the

incremental dilatation from time t to time $t+\Delta t$. The classical formulation of this incremental dilatation is given in Eq. (3.95e).

In Eq. (3.102), the terms a_{ip}, b_{ip}, d_{ip} represent the PD constants for in-plane deformations. The terms ${}^{t}u_{(k)}$, ${}^{t}v_{(k)}$ and ${}^{t}w_{(k)}$ represent the displacements at time t of material point k. Meanwhile, $\underline{u}_{(k)}$, $\underline{v}_{(k)}$ and $\underline{w}_{(k)}$ represent the incremental displacements of material point k from time t to time $t+\Delta t$. Similarly, ${}^{t}u_{(j)}$, ${}^{t}v_{(j)}$ and ${}^{t}w_{(j)}$ represent the displacements at time t of material point j. Meanwhile, $\underline{u}_{(j)}$, $\underline{v}_{(j)}$ and $\underline{w}_{(j)}$ represent the incremental displacements of material point j from time t to time $t+\Delta t$. These displacements and incremental displacements are shown in Fig. 3.55. The term ${}^{0}V_{(j)}$ represents the volume of material point j in the undeformed configuration (at time $t=0$), ${}^{0}A_{(j)}$ represents the area of material point j in the undeformed configuration. The term ${}^{0}\xi$ represents the distance between material points k and j in the undeformed configuration which is defined as

$$ {}^{0}\xi=\sqrt{\left({}^{0}x_{(j)}-{}^{0}x_{(k)}\right)^{2}+\left({}^{0}y_{(j)}-{}^{0}y_{(k)}\right)^{2}} \tag{3.103}$$

In Eq. (3.102), φ represents the angle between the ${}^{0}x$ axis in the undeformed configuration and the line connecting material points k and j. The terms $sin\,\varphi$ and $cos\,\varphi$ in Eq. (3.102) can be calculated as

$$ \cos\varphi=\frac{{}^{0}x_{(j)}-{}^{0}x_{(k)}}{{}^{0}\xi};\quad \sin\varphi=\frac{{}^{0}y_{(j)}-{}^{0}y_{(k)}}{{}^{0}\xi} \tag{3.104}$$

The PD constants for the in-plane deformations, a_{ip}, b_{ip}, d_{ip} can be obtained by comparing the strain energy per unit area for in-plane deformations in PD to those in classical continuum mechanics as presented in Appendix F1. These PD constants can be represented as

$$ d_{ip}=\frac{2}{\pi h\delta^{2}} \tag{3.105a}$$

$$ a_{ip}=\frac{Eh\left(3\nu-1\right)}{4\left(1-\nu^{2}\right)} \tag{3.105b}$$

$$ b_{ip}=\frac{3E}{\left(1+\nu\right)\pi\delta^{3}} \tag{3.105c}$$

where δ represents the horizon size. The terms E and ν represent the elastic modulus and Poisson's ratio of the material, h represents the thickness of the plate.

Based on the classical formulation given in Eq. (3.96c), the nonlinear PD strain energy per unit area for the shear deformations given in Eq. (3.101) can be presented as

$$ \bar{W}_{sh(k)}^{NLPD}=\frac{1}{2}C_{s}\sum_{j=1}^{N}\left(\frac{{}^{t}w_{(j)}-{}^{t}w_{(k)}}{{}^{0}\xi}-\frac{{}^{t}\hat{\theta}_{(k)}+{}^{t}\hat{\theta}_{(j)}}{2}\right)\left(\frac{\underline{w}_{(j)}-\underline{w}_{(k)}}{{}^{0}\xi}-\frac{\hat{\underline{\theta}}_{(k)}+\hat{\underline{\theta}}_{(j)}}{2}\right){}^{0}\xi\,{}^{0}V_{(j)} \tag{3.106a}$$

with

$$ {}^{t}\hat{\theta}_{(k)} = -\left(\sin {}^{t}\theta_{y(k)}\right)\cos\varphi + \left(\sin {}^{t}\theta_{x(k)}\right)\sin\varphi \tag{3.106b} $$

$$ \underline{\hat{\theta}}_{(k)} = -\underline{\theta}_{y(k)}\cos\left({}^{t}\theta_{y(k)}\right)\cos\varphi + \underline{\theta}_{x(k)}\cos\left({}^{t}\theta_{x(k)}\right)\sin\varphi \tag{3.106c} $$

$$ {}^{t}\hat{\theta}_{(j)} = -\left(\sin {}^{t}\theta_{y(j)}\right)\cos\varphi + \left(\sin {}^{t}\theta_{x(j)}\right)\sin\varphi \tag{3.106d} $$

$$ \underline{\hat{\theta}}_{(j)} = -\underline{\theta}_{y(j)}\cos\left({}^{t}\theta_{y(j)}\right)\cos\varphi + \underline{\theta}_{x(j)}\cos\left({}^{t}\theta_{x(j)}\right)\sin\varphi \tag{3.106e} $$

where ${}^{t}\theta_{x(k)}$ and ${}^{t}\theta_{y(k)}$ represent the rotations of material point k at time t. The terms $\underline{\theta}_{x(k)}$ and $\underline{\theta}_{y(k)}$ represent the incremental rotations from time t to time $t+\Delta t$ of material point k (see Fig. 3.56). Similarly, ${}^{t}\theta_{x(j)}$ and ${}^{t}\theta_{y(j)}$ represent the rotations of material point j at time t. The terms $\underline{\theta}_{x(j)}$ and $\underline{\theta}_{y(j)}$ represent the incremental rotations from time t to time $t+\Delta t$ of material point j (see Fig. 3.56). The parameter C_{sh} represents the PD constant for shear deformations. As presented in Appendix F2, C_{sh} is determined by comparing the strain energy per unit area for shear deformations in PD to those in CCM as

$$ C_s = \frac{3k_s E}{(1+\nu)\pi\delta^3} \tag{3.107} $$

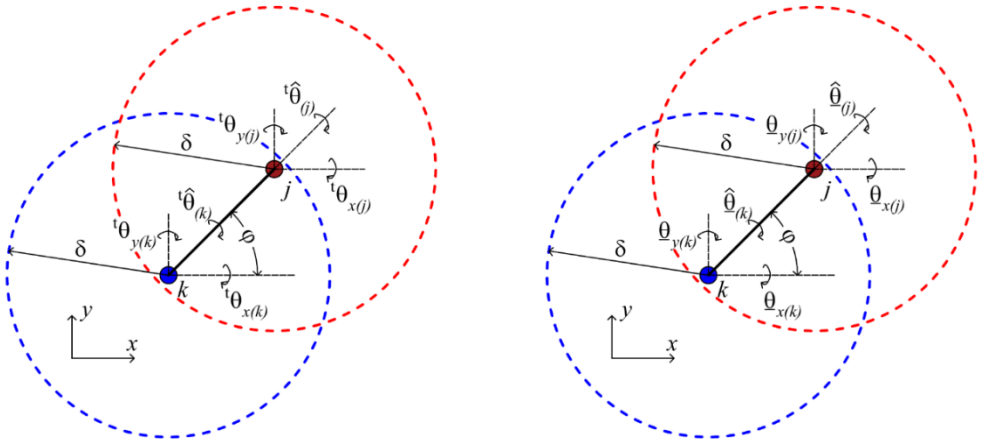

(a) (b)

Fig. 3.56. Rotations and incremental rotations of material points (a): rotations at time t, (b): incremental rotations from time t to time $t+\Delta t$

Based on the classical formulation given in Eq. (3.97b), the nonlinear PD strain energy per unit area for the bending deformations given in Eq. (3.101) can be presented as

$$ \bar{W}_{b(k)}^{NLPD} = 2a_b\left({}_0^{t}\vartheta_{b(k)}\right)\left({}_0\underline{\vartheta}_{b(k)}\right) + 2b_b\sum_{j=1}^{N}\left({}_0^{t}s_{b(k)(j)}\right)\left({}_0\underline{s}_{b(k)(j)}\right){}^{0}\xi\,{}^{0}V_{(j)} \tag{3.108a} $$

with

$$ {}_0^{t}\vartheta_{b(k)} = d_b\sum_{j=1}^{N}{}_0^{t}s_{b(k)(j)}\,{}^{0}V_{(j)} \tag{3.108b} $$

$$ {}_0\underline{\vartheta}_{b(k)} = d_b \sum_{j=1}^{N} \left({}_0\underline{s}_{b(k)(j)} \right) {}^0V_{(j)} \tag{3.108c} $$

$$ {}^t_0 s_{b(k)(j)} = \frac{-\left({}^t\theta_{y(j)} - {}^t\theta_{y(k)} \right)\cos\varphi + \left({}^t\theta_{x(j)} - {}^t\theta_{x(k)} \right)\sin\varphi}{{}^0\xi} \tag{3.108d} $$

$$ {}_0\underline{s}_{b(k)(j)} = \frac{-\left(\underline{\theta}_{y(j)} - \underline{\theta}_{y(k)} \right)\cos\varphi + \left(\underline{\theta}_{x(j)} - \underline{\theta}_{x(k)} \right)\sin\varphi}{{}^0\xi} \tag{3.108e} $$

where ${}^t_0 s_{b(k)(j)}$ represents the bond stretch for bending deformations at time t. Meanwhile, ${}_0\underline{s}_{b(k)(j)}$ represents the incremental bond stretch for bending deformation from time t to time $t + \Delta t$. The terms ${}^t\theta_{x(j)}$ and ${}^t\theta_{y(j)}$ represent the rotations at time t of material point j. Meanwhile, $\underline{\theta}_{x(j)}$ and $\underline{\theta}_{y(j)}$ represent the incremental rotations from time t to time $t + \Delta t$ of material point j. The term ${}^t_0\vartheta_{b(k)}$ and ${}_0\underline{\vartheta}_{b(k)}$ given in Eqs. (3.108b-c) corresponds to the term ${}^t_0\vartheta_b$ and ${}_0\underline{\vartheta}_b$ in classical continuum mechanics given in Eqs. (3.97c-d).

In Eq. (3.108), the terms a_b, b_b, d_b represent the PD constants for bending deformations. As presented in Appendix F3, these PD constants can be represented as

$$ d_b = \frac{2}{\pi h \delta^2} \tag{3.109a} $$

$$ a_b = \frac{Eh^3\left(3\nu - 1\right)}{48\left(1 - \nu^2\right)} \tag{3.109b} $$

$$ b_b = \frac{Eh^2}{4\left(1 + \nu\right)\pi\delta^3} \tag{3.109c} $$

3.4.2.2. Nonlinear peridynamic equations of motion for a plate

By substituting the strain energy per unit area components given in Eq. (3.102), Eq. (3.106), and Eq. (3.108) into Eq. (3.101), the strain energy per unit area for a material point k in the plate is calculated. Next, by substituting the strain energy per unit area given in Eq. (3.101) into Eq. (3.100a), the force density ${}^t_0\overline{t}^{q_i}_{(k)(j)}$ can be obtained as

$$ {}^t_0\overline{t}^{u}_{(k)(j)} = \left[\frac{2a_{ip}d_{ip}}{{}^0\xi}\, {}^t_0\vartheta_{(k)} + 2b_{ip}\, {}^t_0 s_{ip(k)(j)} \right]\left(\cos\varphi + \frac{{}^t u_{(j)} - {}^t u_{(k)}}{{}^0\xi} \right) \tag{3.110a} $$

$$ {}^t_0\overline{t}^{v}_{(k)(j)} = \left[\frac{2a_{ip}d_{ip}}{{}^0\xi}\, {}^t_0\vartheta_{(k)} + 2b_{ip}\, {}^t_0 s_{ip(k)(j)} \right]\left(\sin\varphi + \frac{{}^t v_{(j)} - {}^t v_{(k)}}{{}^0\xi} \right) \tag{3.110b} $$

$$
\begin{aligned}
{}_0^t\overline{t}^{w}_{(k)(j)} &= \left(\frac{2a_{ip}d_{ip}}{{}^0\xi}\,{}_0^t\vartheta_{(k)} + 2b_{ip}\,{}_0^t s_{ip(k)(j)} \right) \frac{{}^t w_{(j)} - {}^t w_{(k)}}{{}^0\xi} \\
&\quad + \frac{1}{2} C_s \left(\frac{{}^t w_{(j)} - {}^t w_{(k)}}{{}^0\xi} - \frac{{}^t\hat{\theta}_{(k)} + {}^t\hat{\theta}_{(j)}}{2} \right)
\end{aligned} \tag{3.110c}
$$

$$
{}_0^t\overline{t}^{\theta_x}_{(k)(j)} = \left[\begin{array}{l} \dfrac{2a_b d_b}{{}^0\xi}\,{}_0^t\vartheta_{b(k)} + 2b_b\,{}_0^t s_{b(k)(j)} \\ + \dfrac{C_s\,{}^0\xi}{2} \left(\dfrac{{}^t w_{(j)} - {}^t w_{(k)}}{{}^0\xi} - \dfrac{{}^t\hat{\theta}_{(k)} + {}^t\hat{\theta}_{(j)}}{2} \right) \dfrac{\cos\left({}^t\theta_{x(k)}\right)}{2} \end{array} \right] \sin\varphi \tag{3.110d}
$$

$$
{}_0^t\overline{t}^{\theta_y}_{(k)(j)} = -\left[\begin{array}{l} \dfrac{2a_b d_b}{{}^0\xi}\,{}_0^t\vartheta_{b(k)} + 2b_b\,{}_0^t s_{b(k)(j)} \\ + \dfrac{C_s\,{}^0\xi}{2} \left(\dfrac{{}^t w_{(j)} - {}^t w_{(k)}}{{}^0\xi} - \dfrac{{}^t\hat{\theta}_{(k)} + {}^t\hat{\theta}_{(j)}}{2} \right) \dfrac{\cos\left({}^t\theta_{y(k)}\right)}{2} \end{array} \right] \cos\varphi \tag{3.110e}
$$

Similarly, by considering material point j and its family members within its horizon size, the strain energy per unit area of material point j can be calculated using Eqs. (3.101-109). Therefore, the force density ${}_0^t\overline{t}^{q_i}_{(j)(k)}$ that material point k exerts on material point j can be obtained using Eq. (3.100b) as

$$
{}_0^t\overline{t}^{u}_{(j)(k)} = -\left[\frac{2a_{ip}d_{ip}}{{}^0\xi}\,{}_0^t\vartheta_{(j)} + 2b_{ip}\,{}_0^t s_{ip(k)(j)} \right] \left(\cos\varphi + \frac{{}^t u_{(j)} - {}^t u_{(k)}}{{}^0\xi} \right) \tag{3.111a}
$$

$$
{}_0^t\overline{t}^{v}_{(j)(k)} = -\left[\frac{2a_{ip}d_{ip}}{{}^0\xi}\,{}_0^t\vartheta_{(j)} + 2b_{ip}\,{}_0^t s_{ip(k)(j)} \right] \left(\sin\varphi + \frac{{}^t v_{(j)} - {}^t v_{(k)}}{{}^0\xi} \right) \tag{3.111b}
$$

$$
\begin{aligned}
{}_0^t\overline{t}^{w}_{(j)(k)} &= -\left(\frac{2a_{ip}d_{ip}}{{}^0\xi}\,{}_0^t\vartheta_{(j)} + 2b_{ip}\,{}_0^t s_{ip(k)(j)} \right) \frac{{}^t w_{(j)} - {}^t w_{(k)}}{{}^0\xi} \\
&\quad - \frac{1}{2} C_s \left(\frac{{}^t w_{(j)} - {}^t w_{(k)}}{{}^0\xi} - \frac{{}^t\hat{\theta}_{(k)} + {}^t\hat{\theta}_{(j)}}{2} \right)
\end{aligned} \tag{3.111c}
$$

$$
{}_0^t\overline{t}^{\theta_x}_{(j)(k)} = -\left[\begin{array}{l} \dfrac{2a_b d_b}{{}^0\xi}\,{}_0^t\vartheta_{b(j)} + 2b_b\,{}_0^t s_{b(k)(j)} \\ + \dfrac{C_s\,{}^0\xi}{2} \left(\dfrac{{}^t w_{(j)} - {}^t w_{(k)}}{{}^0\xi} - \dfrac{{}^t\hat{\theta}_{(k)} + {}^t\hat{\theta}_{(j)}}{2} \right) \dfrac{\cos\left({}^t\theta_{x(j)}\right)}{2} \end{array} \right] \sin\varphi \tag{3.111d}
$$

$$
{}_0^t\overline{t}^{\theta_y}_{(j)(k)} = \left[\begin{array}{l} \dfrac{2a_b d_b}{{}^0\xi}\,{}_0^t\vartheta_{b(j)} + 2b_b\,{}_0^t s_{b(k)(j)} \\ + \dfrac{C_s\,{}^0\xi}{2} \left(\dfrac{{}^t w_{(j)} - {}^t w_{(k)}}{{}^0\xi} - \dfrac{{}^t\hat{\theta}_{(k)} + {}^t\hat{\theta}_{(j)}}{2} \right) \dfrac{\cos\left({}^t\theta_{y(j)}\right)}{2} \end{array} \right] \cos\varphi \tag{3.111e}
$$

Therefore, by substituting the force densities given in Eqs. (3.110-3.111) into Eq. (3.98), the nonlinear PD equations of motion for a plate can be rewritten as

$$\rho h\left({}^{t}\ddot{u}_{(k)}\right)=\sum_{j=1}^{N}\left[\frac{2a_{ip}d_{ip}}{{}^{0}\xi}\left({}_{0}^{t}\vartheta_{(k)}+{}_{0}^{t}\vartheta_{(j)}\right)+4b_{ip}\,{}_{0}^{t}s_{ip(k)(j)}\right]\left(\cos\varphi+\frac{{}^{t}u_{(j)}-{}^{t}u_{(k)}}{{}^{0}\xi}\right){}^{0}V_{(j)}+{}^{t}\bar{b}_{x(k)} \tag{3.112a}$$

$$\rho h\left({}^{t}\ddot{v}_{(k)}\right)=\sum_{j=1}^{N}\left[\frac{2a_{ip}d_{ip}}{{}^{0}\xi}\left({}_{0}^{t}\vartheta_{(k)}+{}_{0}^{t}\vartheta_{(j)}\right)+4b_{ip}\,{}_{0}^{t}s_{ip(k)(j)}\right]\left(\sin\varphi+\frac{{}^{t}v_{(j)}-{}^{t}v_{(k)}}{{}^{0}\xi}\right){}^{0}V_{(j)}+{}^{t}\bar{b}_{y(k)} \tag{3.112b}$$

$$\rho h\left({}^{t}\ddot{w}_{(k)}\right)=\sum_{j=1}^{N}\left[\begin{array}{l}\left(\frac{2a_{ip}d_{ip}}{{}^{0}\xi}\left({}_{0}^{t}\vartheta_{(k)}+{}_{0}^{t}\vartheta_{(j)}\right)+4b_{ip}\,{}_{0}^{t}s_{ip(k)(j)}\right)\frac{{}^{t}w_{(j)}-{}^{t}w_{(k)}}{{}^{0}\xi}\\ +C_s\left(\frac{{}^{t}w_{(j)}-{}^{t}w_{(k)}}{{}^{0}\xi}-\frac{{}^{t}\hat{\theta}_{(k)}+{}^{t}\hat{\theta}_{(j)}}{2}\right)\end{array}\right]{}^{0}V_{(j)}+{}^{t}\bar{b}_{z(k)} \tag{3.112c}$$

$$\frac{\rho h^3}{12}\,{}^{t}\ddot{\theta}_{x(k)}=\sum_{j=1}^{N}\left[\begin{array}{l}\frac{2a_bd_b}{{}^{0}\xi}\left({}_{0}^{t}\vartheta_{b(k)}+{}_{0}^{t}\vartheta_{b(j)}\right)+4b_b\,{}_{0}^{t}s_{b(k)(j)}\\ +\frac{C_s\,{}^{0}\xi}{2}\left(\frac{{}^{t}w_{(j)}-{}^{t}w_{(k)}}{{}^{0}\xi}-\frac{{}^{t}\hat{\theta}_{(k)}+{}^{t}\hat{\theta}_{(j)}}{2}\right)\frac{\cos{}^{t}\theta_{x(k)}+\cos{}^{t}\theta_{x(j)}}{2}\end{array}\right]\sin\varphi\,{}^{0}V_{(j)}+{}^{t}\bar{m}_{x(k)} \tag{3.112d}$$

$$\frac{\rho h^3}{12}\,{}^{t}\ddot{\theta}_{y(k)}=-\sum_{j=1}^{N}\left[\begin{array}{l}\frac{2a_bd_b}{{}^{0}\xi}\left({}_{0}^{t}\vartheta_{b(k)}+{}_{0}^{t}\vartheta_{b(j)}\right)+4b_b\,{}_{0}^{t}s_{b(k)(j)}\\ +\frac{C_s\,{}^{0}\xi}{2}\left(\frac{{}^{t}w_{(j)}-{}^{t}w_{(k)}}{{}^{0}\xi}-\frac{{}^{t}\hat{\theta}_{(k)}+{}^{t}\hat{\theta}_{(j)}}{2}\right)\frac{\cos{}^{t}\theta_{y(k)}+\cos{}^{t}\theta_{y(j)}}{2}\end{array}\right]\cos\varphi\,{}^{0}V_{(j)}+{}^{t}\bar{m}_{y(k)} \tag{3.112e}$$

where ${}^{t}\bar{b}_{x(k)}$, ${}^{t}\bar{b}_{y(k)}$, ${}^{t}\bar{b}_{z(k)}$ represent external forces per unit area applied on material point k at time t, ${}^{t}\bar{m}_{x(k)}$ and ${}^{t}\bar{m}_{y(k)}$ represent external moments per unit area applied on material point k at time t. Note that, for small strain problems, the thickness of the plate and volume of material points are assumed to be unchanged. Therefore, the external loading at time t can be represented as

$${}^{t}\bar{b}_{x(k)}=\frac{{}^{t}F_{x(k)}}{{}^{0}A_{(k)}};\quad {}^{t}\bar{b}_{y(k)}=\frac{{}^{t}F_{y(k)}}{{}^{0}A_{(k)}};\quad {}^{t}\bar{b}_{z(k)}=\frac{{}^{t}F_{z(k)}}{{}^{0}A_{(k)}} \tag{3.113a}$$

$${}^{t}\bar{m}_{x(k)}=\frac{{}^{t}M_{x(k)}}{{}^{0}A_{(k)}};\quad {}^{t}\bar{m}_{y(k)}=\frac{{}^{t}M_{y(k)}}{{}^{0}A_{(k)}} \tag{3.113b}$$

with

$${}^{0}A_{(k)}=\frac{{}^{0}V_{(k)}}{h} \tag{3.113c}$$

where ${}^{0}A_{(k)}$ represents the area of material point k in the undeformed configuration. The terms ${}^{t}F_{x(k)}$, ${}^{t}F_{y(k)}$ and ${}^{t}F_{z(k)}$ represent the external forces

applied on material point k at time t. Meanwhile, ${}^{t}M_{x(k)}$ and ${}^{t}M_{y(k)}$ represent the external bending moments applied on material point k at time t.

3.4.3. Damage criteria

Similar to the equation of motion given in Eq. (3.17) in chapter 3, by introducing a damage parameter, $\psi_{(k)(j)}$, the PD equations of motion given in Eq. (3.112) can be rewritten as [21]

$$\bar{\mathbf{m}}_{(k)}\left({}^{t}\ddot{\mathbf{u}}_{(k)}\right)=\sum_{j=1}^{N}\psi_{(k)(j)}\,{}_{0}^{t}\bar{\mathbf{f}}_{(k)(j)}\,{}^{0}V_{(j)}+{}^{t}\bar{\mathbf{b}}_{(k)} \tag{3.114a}$$

or

$$\bar{\mathbf{m}}_{(k)}\left({}^{t}\ddot{\mathbf{u}}_{(k)}\right)={}_{0}^{t}\bar{\mathbf{F}}_{(k)}+{}^{t}\bar{\mathbf{b}}_{(k)} \tag{3.114b}$$

with

$$\bar{\mathbf{m}}_{(k)}=\begin{bmatrix}\rho h & 0 & 0 & 0 & 0\\ 0 & \rho h & 0 & 0 & 0\\ 0 & 0 & \rho h & 0 & 0\\ 0 & 0 & 0 & \dfrac{\rho h^{3}}{12} & 0\\ 0 & 0 & 0 & 0 & \dfrac{\rho h^{3}}{12}\end{bmatrix};\ {}^{t}\bar{\mathbf{b}}_{(k)}=\begin{bmatrix}{}^{t}\bar{b}_{x}\\ {}^{t}\bar{b}_{y}\\ {}^{t}\bar{b}_{z}\\ {}^{t}\bar{m}_{x}\\ {}^{t}\bar{m}_{y}\end{bmatrix};\ {}_{0}^{t}\bar{\mathbf{f}}_{(k)(j)}=\begin{bmatrix}{}_{0}^{t}\bar{f}_{(k)(j)}^{u}\\ {}_{0}^{t}\bar{f}_{(k)(j)}^{v}\\ {}_{0}^{t}\bar{f}_{(k)(j)}^{w}\\ {}_{0}^{t}\bar{f}_{(k)(j)}^{\theta_x}\\ {}_{0}^{t}\bar{f}_{(k)(j)}^{\theta_y}\end{bmatrix} \tag{3.114c}$$

$${}_{0}^{t}\bar{\mathbf{F}}_{(k)}=\sum_{j=1}^{N}\psi_{(k)(j)}\,{}_{0}^{t}\bar{\mathbf{f}}_{(k)(j)}\,{}^{0}V_{(j)} \tag{3.114d}$$

$${}_{0}^{t}\bar{\mathbf{f}}_{(k)(j)}={}_{0}^{t}\bar{\mathbf{t}}_{(k)(j)}-{}_{0}^{t}\bar{\mathbf{t}}_{(k)(j)} \tag{3.114e}$$

and

$$\begin{aligned}{}_{0}^{t}\bar{f}_{(k)(j)}^{u}&={}_{0}^{t}\bar{t}_{(k)(j)}^{u}-{}_{0}^{t}\bar{t}_{(j)(k)}^{u}\\&=\left[\frac{2a_{ip}d_{ip}}{{}^{0}\xi}\left({}_{0}^{t}\vartheta_{(k)}+{}_{0}^{t}\vartheta_{(j)}\right)+4b_{ip}\,{}_{0}^{t}s_{ip(k)(j)}\right]\left(\cos\varphi+\frac{{}^{t}u_{(j)}-{}^{t}u_{(k)}}{{}^{0}\xi}\right)\end{aligned} \tag{3.114f}$$

$$\begin{aligned}{}_{0}^{t}\bar{f}_{(k)(j)}^{v}&={}_{0}^{t}\bar{t}_{(k)(j)}^{v}-{}_{0}^{t}\bar{t}_{(j)(k)}^{v}\\&=\left[\frac{2a_{ip}d_{ip}}{{}^{0}\xi}\left({}_{0}^{t}\vartheta_{(k)}+{}_{0}^{t}\vartheta_{(j)}\right)+4b_{ip}\,{}_{0}^{t}s_{ip(k)(j)}\right]\left(\sin\varphi+\frac{{}^{t}v_{(j)}-{}^{t}v_{(k)}}{{}^{0}\xi}\right)\end{aligned} \tag{3.114g}$$

$$
\begin{aligned}
{}_0^t\bar{f}^{w}_{(k)(j)} = {}_0^t\bar{t}^{w}_{(k)(j)} - {}_0^t\bar{t}^{w}_{(j)(k)} &= \left(\frac{2a_{ip}d_{ip}}{{}^0\xi}\left({}_0^t\vartheta_{(k)} + {}_0^t\vartheta_{(j)} \right) + 4b_{ip}\,{}_0^t s_{ip(k)(j)} \right) \frac{{}^t w_{(j)} - {}^t w_{(k)}}{{}^0\xi} \\
&\quad + C_s \left(\frac{{}^t w_{(j)} - {}^t w_{(k)}}{{}^0\xi} - \frac{{}^t\hat{\theta}_{(k)} + {}^t\hat{\theta}_{(j)}}{2} \right)
\end{aligned}
\tag{3.114h}
$$

$$
\begin{aligned}
{}_0^t\bar{f}^{\theta_x}_{(k)(j)} &= {}_0^t\bar{t}^{\theta_x}_{(k)(j)} - {}_0^t\bar{t}^{\theta_x}_{(j)(k)} \\
&= \left[\begin{array}{l} \dfrac{2a_b d_b}{{}^0\xi}\left({}_0^t\vartheta_{b(k)} + {}_0^t\vartheta_{b(j)} \right) + 4b_b\,{}_0^t s_{b(k)(j)} \\ + \dfrac{C_s\,{}^0\xi}{2}\left(\dfrac{{}^t w_{(j)} - {}^t w_{(k)}}{{}^0\xi} - \dfrac{{}^t\hat{\theta}_{(k)} + {}^t\hat{\theta}_{(j)}}{2} \right) \dfrac{\cos\left({}^t\theta_{x(k)} \right) + \cos\left({}^t\theta_{x(j)} \right)}{2} \end{array} \right] \sin\varphi
\end{aligned}
\tag{3.114i}
$$

$$
\begin{aligned}
{}_0^t\bar{f}^{\theta_y}_{(k)(j)} &= {}_0^t\bar{t}^{\theta_y}_{(k)(j)} - {}_0^t\bar{t}^{\theta_y}_{(j)(k)} \\
&= -\left[\begin{array}{l} \dfrac{2a_b d_b}{{}^0\xi}\left({}_0^t\vartheta_{b(k)} + {}_0^t\vartheta_{b(j)} \right) + 4b_b\,{}_0^t s_{b(k)(j)} \\ + \dfrac{C_s\,{}^0\xi}{2}\left(\dfrac{{}^t w_{(j)} - {}^t w_{(k)}}{{}^0\xi} - \dfrac{{}^t\hat{\theta}_{(k)} + {}^t\hat{\theta}_{(j)}}{2} \right) \dfrac{\cos\left({}^t\theta_{y(k)} \right) + \cos\left({}^t\theta_{y(j)} \right)}{2} \end{array} \right] \cos\varphi
\end{aligned}
\tag{3.114j}
$$

To decide the interaction state, which is represented by the damage parameter, $\psi_{(k)(j)}$ given in Eq. (1.3), the energy-based damage criterion given in Eq. (1.8-1.11) in chapter 1 is used. Similar to the formulations given in Eq. (2.90) in Chapter 2 for the linear PD shell model, the micropotentials ${}_0^t\Phi_{(k)(j)}$ and ${}_0^t\Phi_{(j)(k)}$ can be calculated as [61, 64]

$$
{}_0^t\Phi_{(k)(j)} = {}_0^t\Phi^{u}_{(k)(j)} + {}_0^t\Phi^{v}_{(k)(j)} + {}_0^t\Phi^{w}_{(k)(j)} + {}_0^t\Phi^{\theta x}_{(k)(j)} + {}_0^t\Phi^{\theta y}_{(k)(j)} \tag{3.115a}
$$

$$
{}_0^t\Phi_{(j)(k)} = {}_0^t\Phi^{u}_{(j)(k)} + {}_0^t\Phi^{v}_{(j)(k)} + {}_0^t\Phi^{w}_{(j)(k)} + {}_0^t\Phi^{\theta x}_{(j)(k)} + {}_0^t\Phi^{\theta y}_{(j)(k)} \tag{3.115b}
$$

where ${}_0^t\Phi^{u}_{(k)(j)}$, ${}_0^t\Phi^{v}_{(k)(j)}$, ${}_0^t\Phi^{w}_{(k)(j)}$, ${}_0^t\Phi^{\theta x}_{(k)(j)}$, ${}_0^t\Phi^{\theta y}_{(k)(j)}$ represent the micropotentials at time t corresponding to the force densities ${}_0^t\bar{t}^{u}_{(k)(j)}$, ${}_0^t\bar{t}^{v}_{(k)(j)}$, ${}_0^t\bar{t}^{w}_{(k)(j)}$, ${}_0^t\bar{t}^{\theta_x}_{(k)(j)}$, ${}_0^t\bar{t}^{\theta_y}_{(k)(j)}$, respectively. Similarly, ${}_0^t\Phi^{u}_{(j)(k)}$, ${}_0^t\Phi^{v}_{(j)(k)}$, ${}_0^t\Phi^{w}_{(j)(k)}$, ${}_0^t\Phi^{\theta x}_{(j)(k)}$, ${}_0^t\Phi^{\theta y}_{(j)(k)}$ represent the micropotentials at time t corresponding to the force densities ${}_0^t\bar{t}^{u}_{(j)(k)}$, ${}_0^t\bar{t}^{v}_{(j)(k)}$, ${}_0^t\bar{t}^{w}_{(j)(k)}$, ${}_0^t\bar{t}^{\theta_x}_{(j)(k)}$, ${}_0^t\bar{t}^{\theta_y}_{(j)(k)}$, respectively. These micropotentials can be calculated as

$$
{}_0^t\Phi^{u}_{(k)(j)} = \frac{1}{h}\int_0^{({}^t u_{(j)} - {}^t u_{(k)})} {}_0^t\bar{t}^{u}_{(k)(j)}\, d(u_{(j)} - u_{(k)}) \tag{3.116a}
$$

$$
{}_0^t\Phi^{v}_{(k)(j)} = \frac{1}{h}\int_0^{({}^t v_{(j)} - {}^t v_{(k)})} {}_0^t\bar{t}^{v}_{(k)(j)}\, d(v_{(j)} - v_{(k)}) \tag{3.116b}
$$

$$
{}_0^t\Phi^{w}_{(k)(j)} = \frac{1}{h}\int_0^{({}^t w_{(j)} - {}^t w_{(k)})} {}_0^t\bar{t}^{w}_{(k)(j)}\, d(w_{(j)} - w_{(k)}) \tag{3.116c}
$$

$$ {}_0^t\Phi_{(k)(j)}^{\theta_x} = \frac{1}{h}\int_0^{({}^t\theta_{x(j)}-{}^t\theta_{x(k)})} {}_0^t\overline{t}_{(k)(j)}^{\theta_x} d(\theta_{x(j)}-\theta_{x(k)}) \tag{3.116d} $$

$$ {}_0^t\Phi_{(k)(j)}^{\theta_y} = \frac{1}{h}\int_0^{({}^t\theta_{y(j)}-{}^t\theta_{y(k)})} {}_0^t\overline{t}_{(k)(j)}^{\theta_y} d(\theta_{y(j)}-\theta_{y(k)}) \tag{3.116e} $$

and

$$ {}_0^t\Phi_{(j)(k)}^{u} = \frac{1}{h}\int_0^{({}^tu_{(k)}-{}^tu_{(j)})} {}_0^t\overline{t}_{(j)(k)}^{u} d(u_{(k)}-u_{(j)}) \tag{3.117a} $$

$$ {}_0^t\Phi_{(j)(k)}^{v} = \frac{1}{h}\int_0^{({}^tv_{(k)}-{}^tv_{(j)})} {}_0^t\overline{t}_{(j)(k)}^{v} d(v_{(k)}-v_{(j)}) \tag{3.117b} $$

$$ {}_0^t\Phi_{(j)(k)}^{w} = \frac{1}{h}\int_0^{({}^tw_{(k)}-{}^tw_{(j)})} {}_0^t\overline{t}_{(j)(k)}^{w} d(w_{(k)}-w_{(j)}) \tag{3.117c} $$

$$ {}_0^t\Phi_{(j)(k)}^{\theta_x} = \frac{1}{h}\int_0^{({}^t\theta_{x(k)}-{}^t\theta_{x(j)})} {}_0^t\overline{t}_{(j)(k)}^{\theta_x} d(\theta_{x(k)}-\theta_{x(j)}) \tag{3.117d} $$

$$ {}_0^t\Phi_{(j)(k)}^{\theta_y} = \frac{1}{h}\int_0^{({}^t\theta_{y(k)}-{}^t\theta_{y(j)})} {}_0^t\overline{t}_{(j)(k)}^{\theta_y} d(\theta_{y(k)}-\theta_{y(j)}) \tag{3.117e} $$

where the force densities ${}_0^t\overline{t}_{(k)(j)}^{u}$, ${}_0^t\overline{t}_{(k)(j)}^{v}$, ${}_0^t\overline{t}_{(k)(j)}^{w}$, ${}_0^t\overline{t}_{(k)(j)}^{\theta_x}$, ${}_0^t\overline{t}_{(k)(j)}^{\theta_y}$ and ${}_0^t\overline{t}_{(j)(k)}^{u}$, ${}_0^t\overline{t}_{(j)(k)}^{v}$, ${}_0^t\overline{t}_{(j)(k)}^{w}$, ${}_0^t\overline{t}_{(j)(k)}^{\theta_x}$, ${}_0^t\overline{t}_{(j)(k)}^{\theta_y}$ are given in Eq. (3.110) and Eq. (3.111), respectively.

Note that, the damage parameter $\psi_{(k)(j)}$ is also included in the calculation of the dilatations, ${}_0^t\vartheta_{(k)}$, ${}_0\underline{\vartheta}_{(k)}$ and the term, ${}_0^t\vartheta_{b(k)}$, ${}_0\underline{\vartheta}_{b(k)}$ by modifying Eqs. (3.102d-e) and Eqs. (3.108b-c) as

$$ {}_0^t\vartheta_{(k)} = d_{ip}\sum_{j=1}^{N}\psi_{(k)(j)}\left({}_0^t s_{ip(k)(j)}\right){}^0V_{(j)} \tag{3.118a} $$

$$ {}_0\underline{\vartheta}_{(k)} = d_{ip}\sum_{j=1}^{N}\psi_{(k)(j)}\left({}_0\underline{s}_{ip(k)(j)}\right){}^0V_{(j)} \tag{3.118b} $$

$$ {}_0^t\vartheta_{b(k)} = d_{b}\sum_{j=1}^{N}\psi_{(k)(j)}\left({}_0^t s_{b(k)(j)}\right){}^0V_{(j)} \tag{3.118c} $$

$$ {}_0\underline{\vartheta}_{b(k)} = d_{b}\sum_{j=1}^{N}\psi_{(k)(j)}\left({}_0\underline{s}_{b(k)(j)}\right){}^0V_{(j)} \tag{3.118d} $$

Note that, in the formulations of the micropotentials given in Eq. (3.115), the first two components, ${}_0^t\Phi_{(k)(j)}^{u}$, ${}_0^t\Phi_{(k)(j)}^{v}$, can be caused by in-plane tension or

compression. The micropotential ${}_0^t\Phi_{(k)(j)}^{w}$ can be caused by shear deformations. Meanwhile, the micropotential ${}_0^t\Phi_{(k)(j)}^{\theta_x}$ and ${}_0^t\Phi_{(k)(j)}^{\theta_y}$ can be caused by bending deformations. Therefore, the contribution of tensional, compressional, shear, and bending deformations are considered for the calculation of bond energy release rate for damage prediction which is given in Eq. (1.9) in Chapter 1. Hence, the energy-based damage criteria used in this section are applicable for tensional, compressional, shear, and bending deformations for non-linear analysis.

It should be noted that to predict damages in shells and stiffened structures using the energy-based damage criteria given in Eq. (1.9), the critical energy release rate of material should be a value that is applicable for mixed-mode loading. However, to simplify the determination for the value of G_c in section 3.4.4, the critical energy release rate of the material is simply chosen as $G_c = G_{Ic}$.

3.4.4. Numerical results

In this section, large deformations of plates are predicted by using the proposed nonlinear PD model. First, the verifications for the nonlinear model are presented in Sections 3.4.4.1 and 3.4.4.2. The nonlinear PD results are compared with the nonlinear FEA results. Next, in Sections 3.4.4.3-5, the nonlinear PD model is used to predict progressive damages on plates subjected to different loading conditions. For static and quasi-static loading conditions, the adaptive dynamic relaxation method [76, 77] is used. Details of the adaptive dynamic relaxation method for nonlinear PD analysis of plate are presented in Appendix A3.

3.4.4.1. A plate subjected to bending

In this section, a square plate subjected to bending as shown in Fig. 3.57 is investigated. The plate has dimensions of $L = W = 1$ m and the thickness of $h = L/10$. The plate is fixed on the left edge and it is subjected to bending, $m_y = 3 \times 10^7$ Nm/m on the right edge. The plate is made of steel with an elastic modulus of $E = 2 \times 10^{11}$ N/m^2 and Poisson's ratio of $\nu = 0.3$.

In the PD model, the plate is uniformly discretized with a mesh size of $\Delta x = L/100$. To apply boundary conditions, three fictitious layers of material points are added on the left side of the plate as shown in Fig. 3.57(b). All DOFs of the fictitious points as well as the DOFs of the material points located at $x = 0$ are set equal to zero. To apply the loading condition, the bending per unit area, $\bar{m}_y = m_y/\Delta x$, is applied to the material points located at $x = L$. In the FEA by using ANSYS, the SHELL181 element with the same mesh size $\Delta x = L/100$ is used.

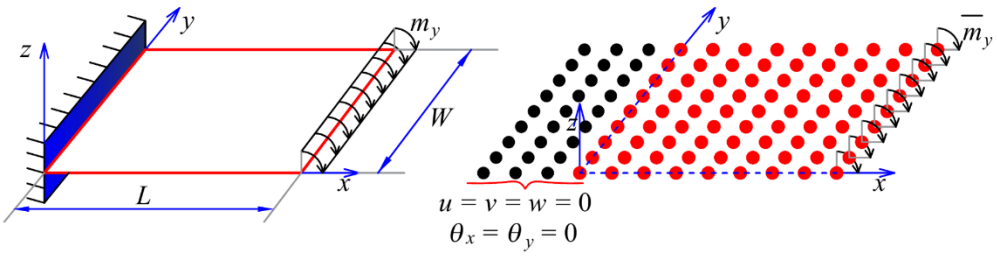

(a) (b)

Fig. 3.57. A square plate subjected to bending (a): geometry, (b): PD discretized model

To decide a suitable horizon size for the PD nonlinear model, the deformation of the plate is predicted by using the nonlinear PD model with different horizon sizes. The nonlinear PD results for significant DOFs, ($\boldsymbol{u, w,}$ and $\boldsymbol{\theta_y}$), of the material points located at $(x = L, y = W/2)$ and $(x = 3L/4, y = W/4)$ are compared with the nonlinear FEA results of the nodes located at the same locations as shown in Fig. 3.58. The relative errors between the nonlinear PD and nonlinear FEA results are calculated as

$$Error(q) = \frac{|q^{PD} - q^{FEA}|}{|q^{FEA}|} \times 100 \ \ (\%) \tag{3.119}$$

where q represents the degree of freedom, q^{PD} and q^{FEA} represent the nonlinear PD and nonlinear FEA results for the degree of freedom q, respectively.

As can be observed from Fig. 3.58, the nonlinear PD results start to converge to the nonlinear FEA results when the horizon size $\delta \geq 3\Delta x$. The relative errors between the nonlinear PD and nonlinear FEA results for the material point located at $(\boldsymbol{x = 3L/4, y = W/4})$ are smaller than $\mathbf{2}\%$. Meanwhile, these relative errors for the material point located at $(\boldsymbol{x = L, y = W/2})$ are smaller than $\mathbf{5}\%$. Therefore, to minimize the computational cost in the PD simulation, the horizon size $\delta \geq 3.015\Delta x$ is chosen.

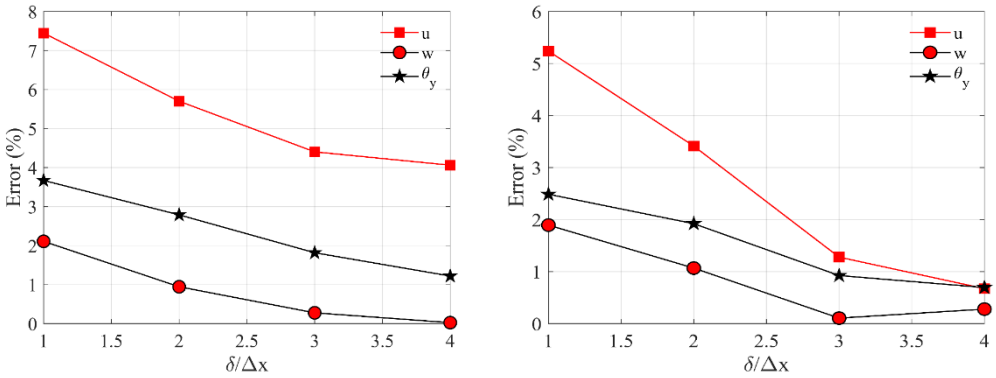

(a) (b)

Fig. 3.58. Relative errors between the nonlinear FEA and nonlinear PD results with different horizon sizes for significant DOFs: u, w, and θ_y of material points located at (a): $(x = L, y = W/2)$, (b): $(x = 3L/4, y = W/4)$

Fig. **3.59**-Fig. 3.63 show the comparison of nonlinear results for all DOFs in the deformed configuration of the plate. As can be seen from the figures, the nonlinear PD results and nonlinear FEA results have good agreements.

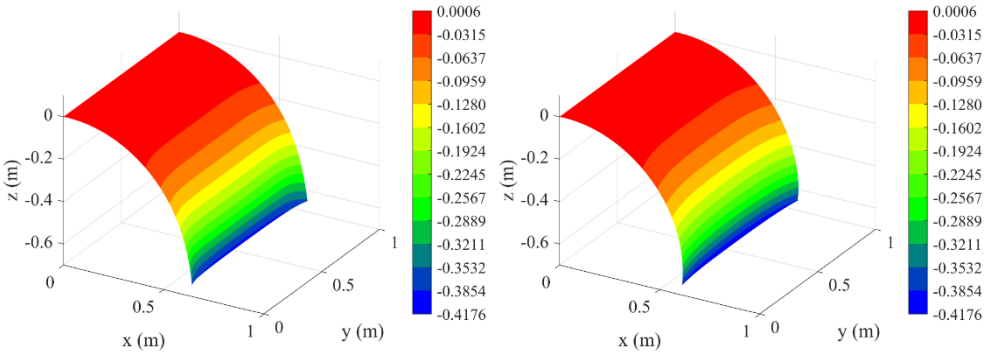

(a) (b)

Fig. 3.59. Variation of displacement $u\ (m)$ in (a): nonlinear PD, (b): nonlinear FEA

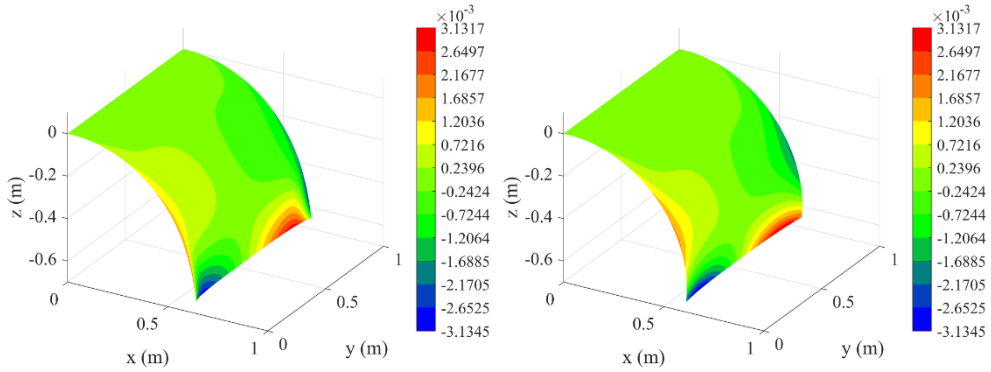

(a) (b)

Fig. 3.60. Variation of displacement $v\ (m)$ in (a): nonlinear PD, (b): nonlinear FEA

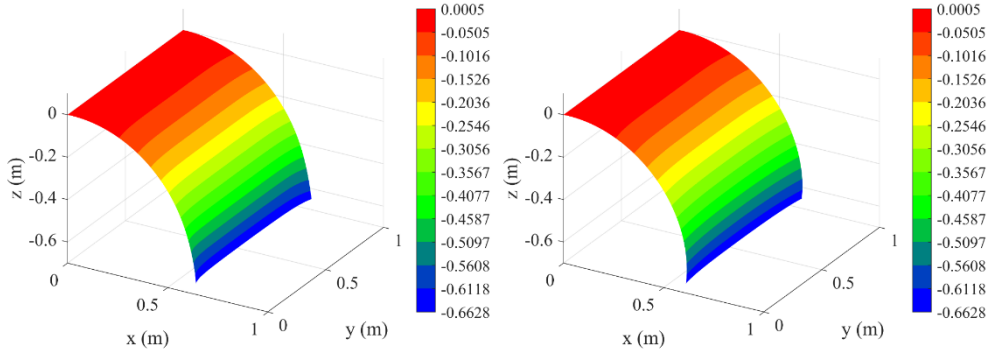

(a) (b)

Fig. 3.61. Variation of displacement $w\ (m)$ in (a): nonlinear PD, (b): nonlinear FEA

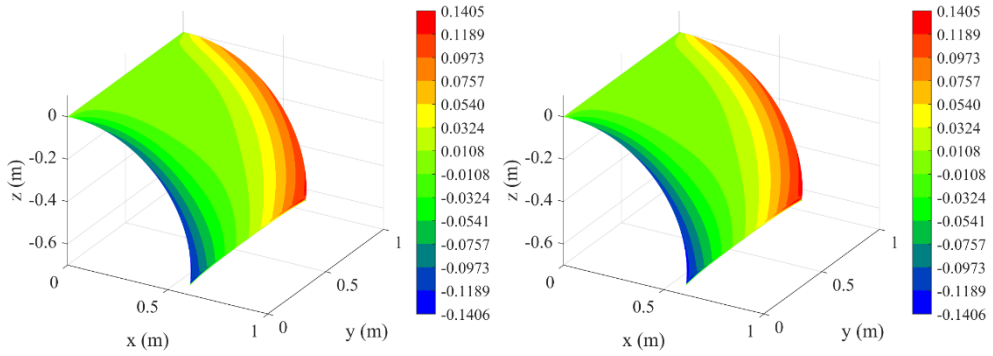

(a) (b)

Fig. 3.62. Variation of rotation $\theta_x\ (\mathrm{rad})$ in (a): nonlinear PD, (b): nonlinear FEA

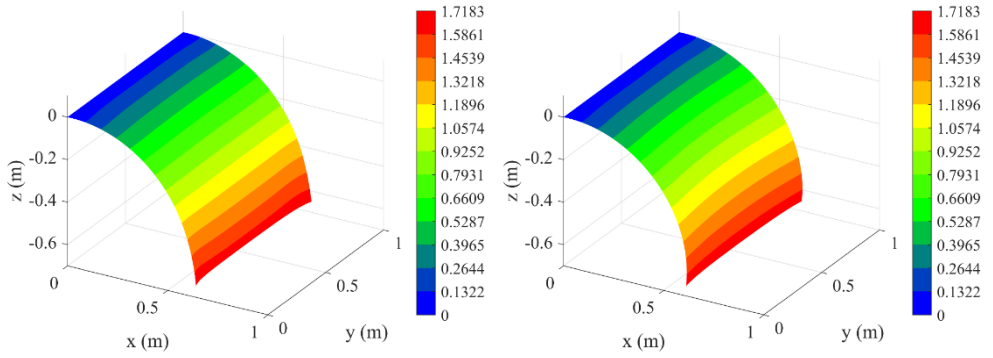

(a) (b)

Fig. 3.63. Variation of rotation $\theta_y\ (\mathrm{rad})$ in (a): nonlinear PD, (b): nonlinear FEA

Fig. 3.64 shows the comparison of the deformed configuration of the centreline at $y = W/2$ predicted by nonlinear PD analysis and nonlinear FEA. As it can be observed from the figure, the deformed configurations captured by both methods have a very good match except a small difference at the right end of the plate.

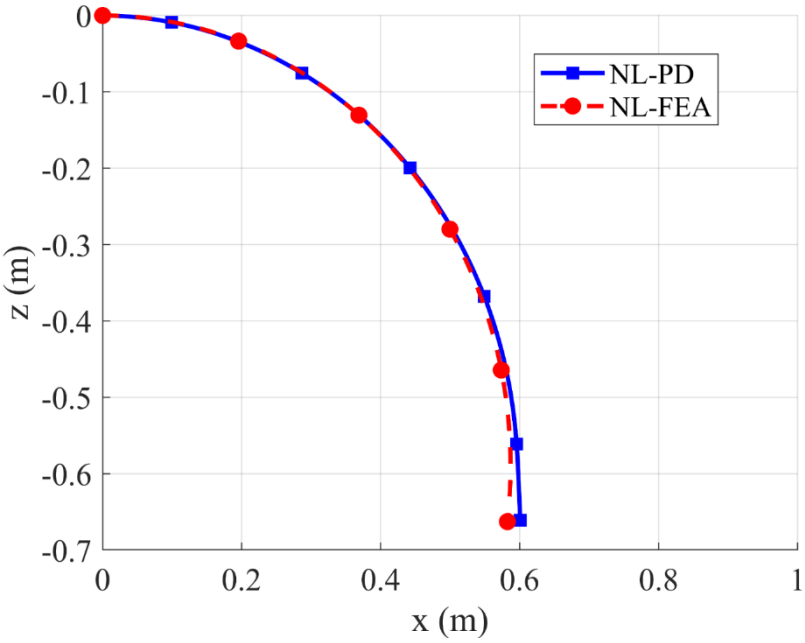

Fig. 3.64. Deformed configurations of the centreline $y = W/2$

3.4.4.2. A plate subjected to vertical shear forces

In this section, a rectangular plate with the dimensions of $L = 1$ m, $W = 0.2$ m, and thickness of $h = L/50$ is investigated as shown in Fig. 3.65. The plate is fixed on the left edge and it is subjected to vertical shear forces on the right edge. The values of the distributed forces are defined as $f_z = n \times 10^4$ N/m with $n = 5, 10, 50, 100$. The plate has the elastic modulus of $E = 2 \times 10^{11}$ N/m^2 and Poisson's ratio of $\nu = 0.4$.

In the PD model, the plate is uniformly discretized with a mesh size of $\Delta x = L/100$. The same method discussed in the previous section is used for applying boundary conditions. To apply the loading condition, the force per unit area $\bar{b}_z = f_z/\Delta x$ is applied to the material points located at $x = L$. In the nonlinear FEA, the SHELL181 element and the same mesh size are used.

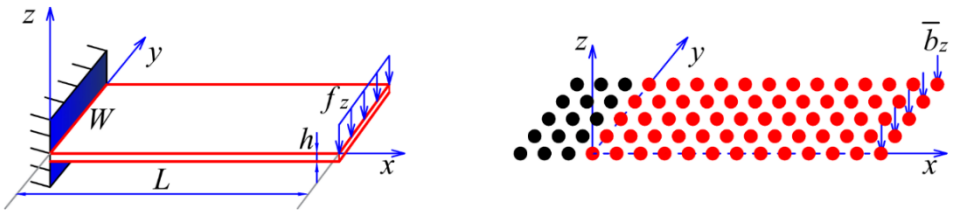

(a) (b)

Fig. 3.65. A plate subjected to vertical shear forces (a): geometry, (b): PD discretized model

Fig. 3.66 shows the deformed configurations of the plate in different loading conditions. Fig. 3.67 shows the deformed configurations of the plate along the centreline $y = W/2$. As can be seen from Fig. 3.67, the nonlinear PD and nonlinear FEA results show good agreements for all loading conditions. The difference

between the two results for the large loading condition with $n = 100$ is still small which can verify the accuracy of the nonlinear PD model.

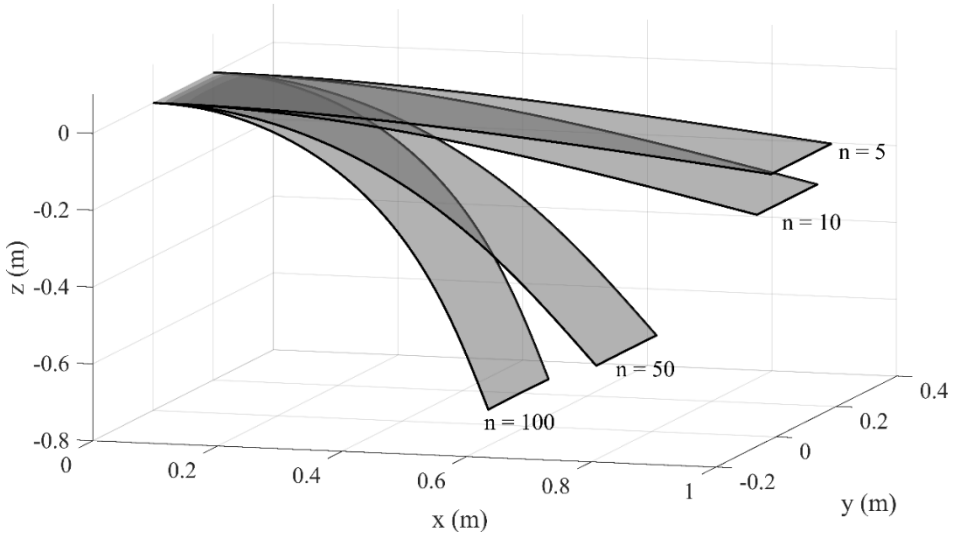

Fig. 3.66. Deformed configurations of the plate subjected to distributed force $f_z = n \times 10^4$ N/m with $n = 5, 10, 50, 100$

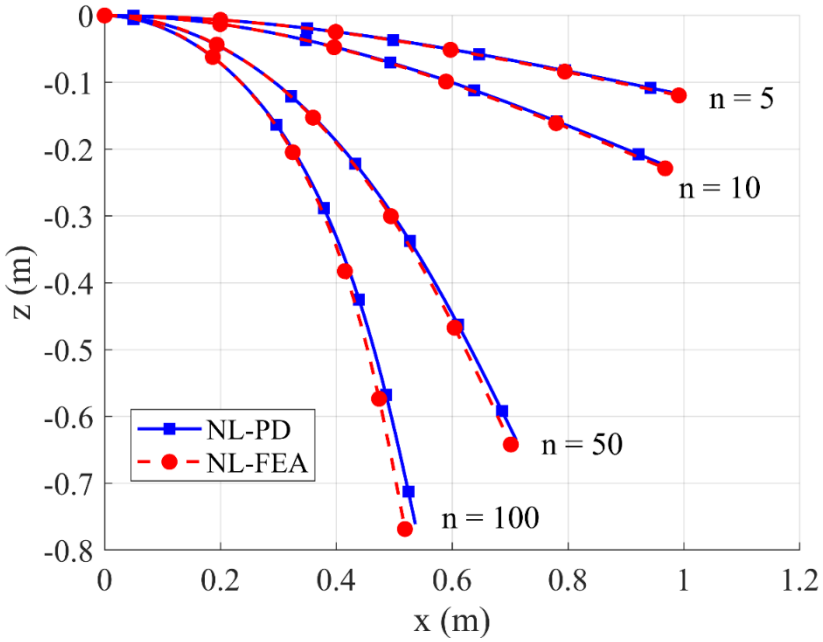

Fig. 3.67. Deformed configurations of the centreline at $y = W/2$ of the plate subjected to distributed force $f_z = n \times 10^4$ N/m with $n = 5, 10, 50, 100$

3.4.4.3. Out-of-plane stretching and tearing of a plate

After verifying the accuracy of the nonlinear PD model, in this section, progressive damage on a square plate with pre-existing crack subjected to out-of-plane stretching and tearing is investigated. The experimental details for this problem can be found in [109]. The square plate has dimensions of $L = W = 0.203$ m and

thickness of $h = 8 \times 10^{-4}$ m. The plate has an initial crack at $x = 0$ with the crack length of $a_0 = 60 \times 10^{-3}$ m. The plate has the elastic modulus of $E = 2 \times 10^{11}$ N/m^2, Poisson's ratio of $\nu = 0.3$. For simplification, the critical energy release rate of the material is chosen as $G_c = G_{Ic} = 255 \times 10^3$ J/m^2 [110]. The plate is fixed at two edges $x = -L/2$ and $x = L/2$, and it is subjected to incremental vertical displacements at two points located at ($x = \pm 3.3333 \times 10^{-4}$ m, $y = 6.6667 \times 10^{-4}$ m).

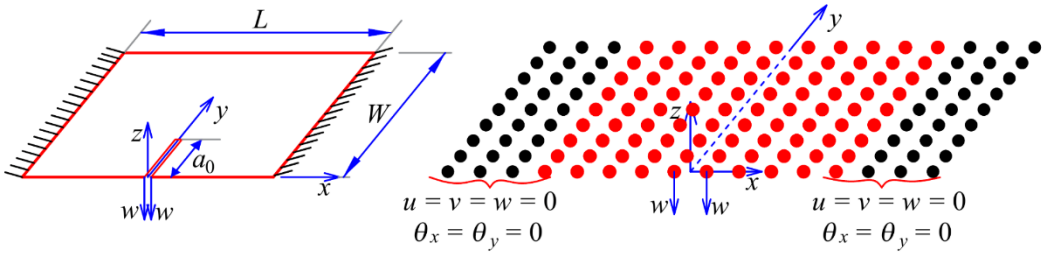

(a) (b)

Fig. 3.68. Plate subjected to stretching and tearing (a): geometry, (b): PD discretized model

In the PD model, the plate is uniformly discretized with the mesh size of $\Delta x = 6.6667 \times 10^{-4}$ m. To apply boundary conditions, three fictitious layers of material points are added on the left and the right sides of the plate. All DOFs of the fictitious material points as well as DOFs of the material points located at $x = -L/2$ and $x = L/2$ are set equal to zero. To apply the loading conditions, material points located at ($x = 3.3333 \times 10^{-4}$ m, $y = 6.6667 \times 10^{-4}$ m) and ($x = -3.3333 \times 10^{-4}$ m, $y = 6.6667 \times 10^{-4}$ m) are applied incremental displacements as $w = 0.002 \times i_l$, with $i_l = 1, \ldots, 42$ represents the load step number. At each load step, the quasi-static solution is obtained for 18000 iterations by using the ADR method [76, 77]. The numerical procedure for this problem is shown in Fig. 3.69.

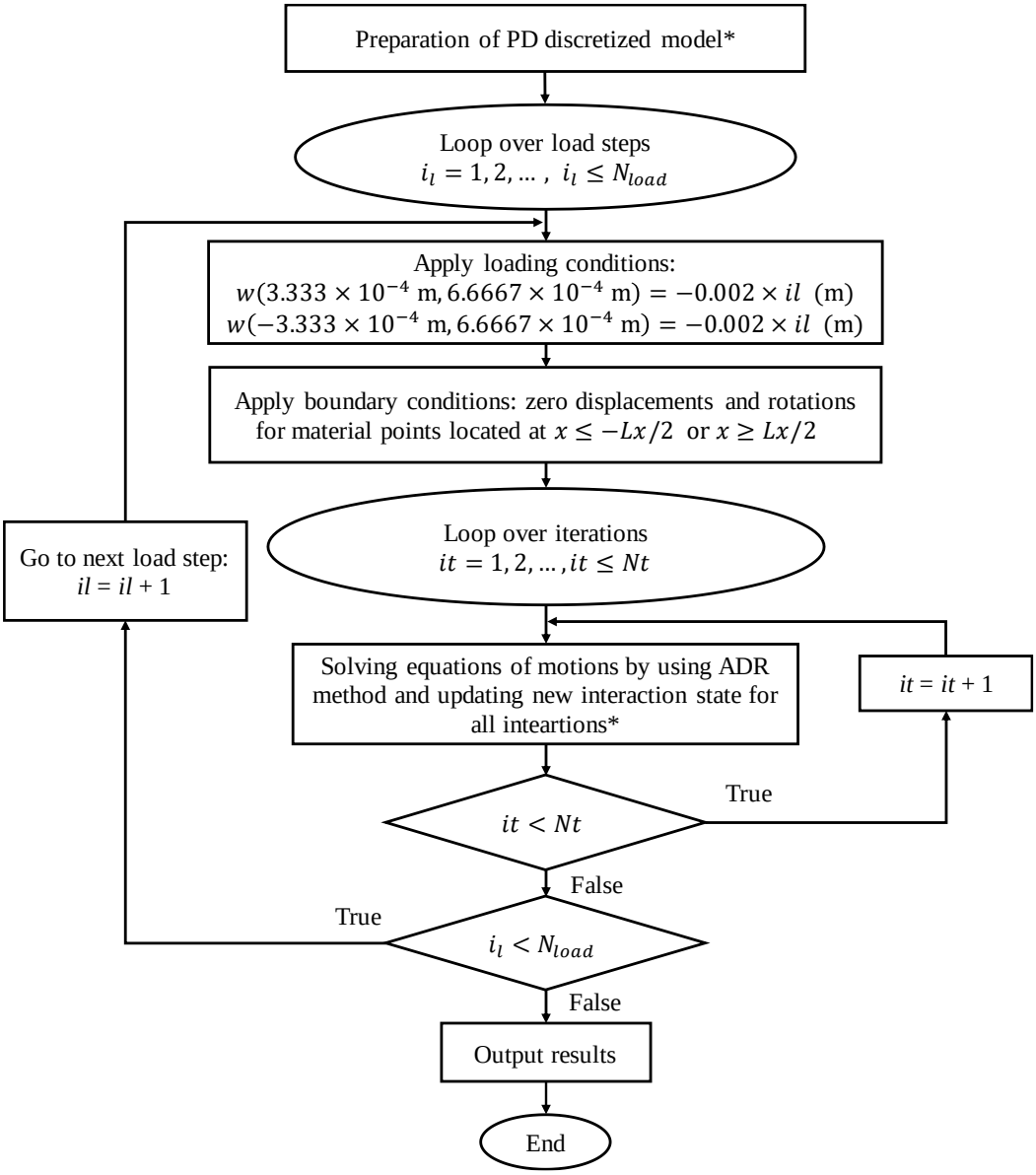

Fig. 3.69. Numerical procedure for the problem of a plate subjected to stretching and tearing

Fig. 3.70-Fig. 3.73 show the damage evolution on the plate. It can be observed from the figures that when the vertical displacements are continuously increased, the crack propagates along the positive *y*-direction. When the applied displacement is $w = 0.084$ m, the crack propagates to the location of nearly $(x = 0, y = 0.2\ \text{m}, z = 0)$ as shown in Fig. 3.73. Moreover, larger crack openings are observed due to the larger deformations. This observation agrees well with the experimental results in [109] and the numerical results in [110, 111].

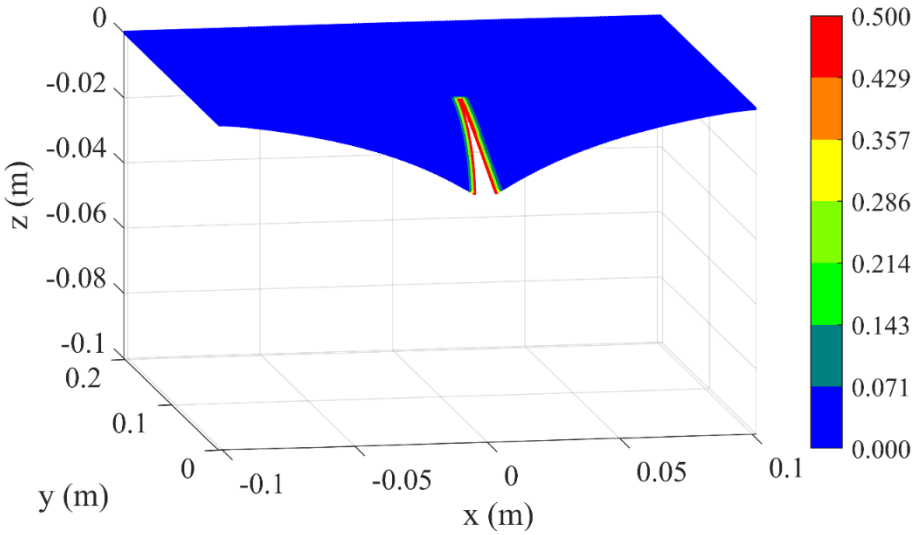

Fig. 3.70. Damage on the plate when the applied displacement $w = 0.024$ m

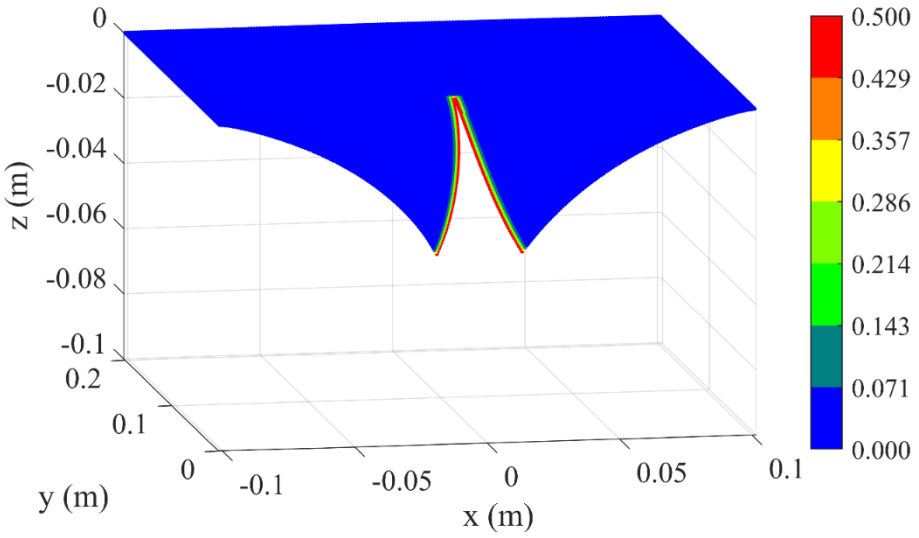

Fig. 3.71. Damage on the plate when the applied displacement $w = 0.044$ m

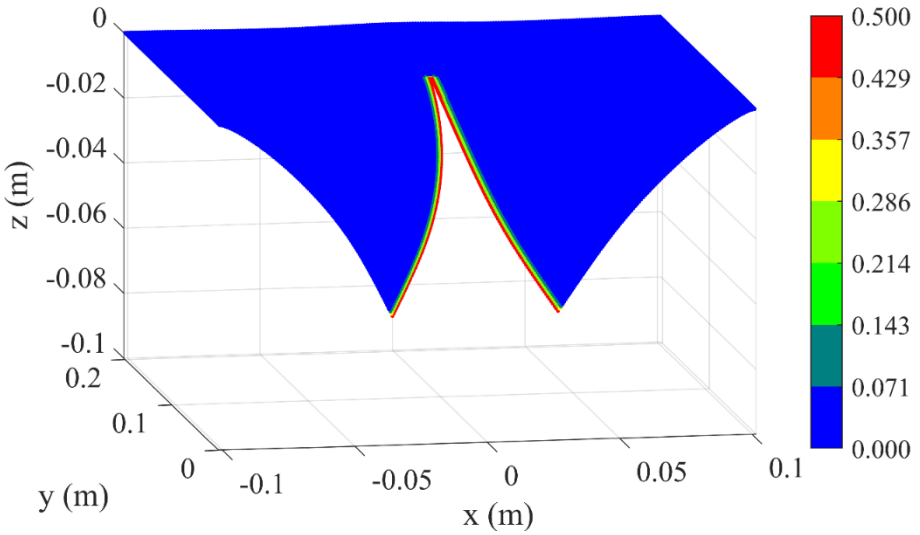

Fig. 3.72. Damage on the plate when the applied displacement $w = 0.064$ m

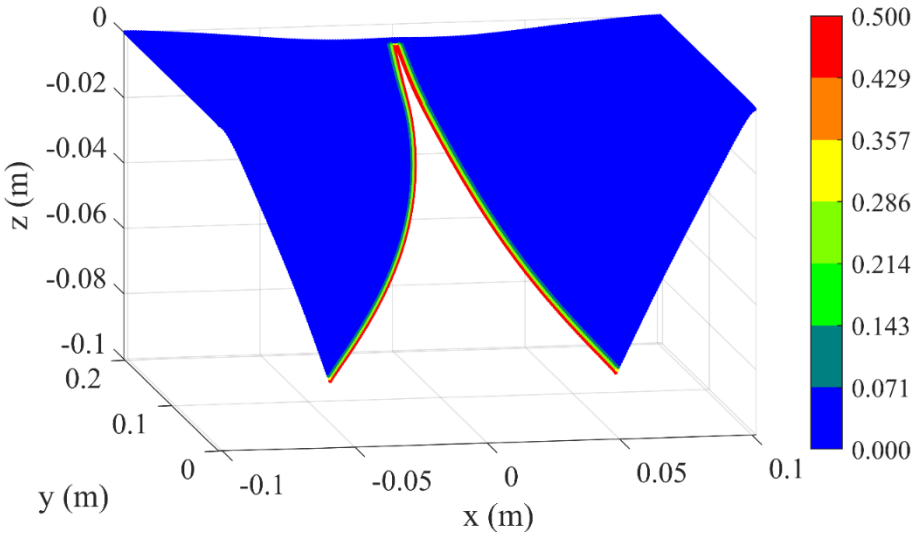

Fig. 3.73. Damage on the plate when the applied displacement $w = 0.084$ m

Fig. 3.74 shows the history of the equivalent applied forces versus the applied vertical displacements. At each load step, after 18000 iterations for the ADR solution, the equivalent applied forces on two material points located at ($x = 3.3333 \times 10^{-4}$ m, $y = 6.6667 \times 10^{-4}$ m) and ($x = -3.3333 \times 10^{-4}$ m, $y = 6.6667 \times 10^{-4}$ m) are calculated as

$$F_{z(i)} = \frac{{}^0V_{(i)}}{h} \sum_{j=1}^{N} \mu_{(i)(j)} \bar{\mathbf{f}}_{(i)(j)} {}^0V_{(j)} \tag{3.120a}$$

$$F_{z(l)} = \frac{{}^0V_{(l)}}{h} \sum_{j=1}^{N} \mu_{(l)(m)} \bar{\mathbf{f}}_{(l)(m)} {}^0V_{(m)} \tag{3.120b}$$

where i and l are the material points located at ($x = 3.3333 \times 10^{-4}$ m, $y = 6.6667 \times 10^{-4}$ m) and ($x = -3.3333 \times 10^{-4}$ m, $y = 6.6667 \times 10^{-4}$ m),

respectively. Material point j is one of the family members of material point i. Meanwhile, material point m is one of the family members of material point l. The equivalent applied forces shown in Fig. 3.74 are the average values of the forces calculated by using Eq. (3.120).

As can be observed from Fig. 3.74, the equivalent applied forces versus the applied displacements captured by the nonlinear PD model has a good agreement with the experimental results given in [109]. When the applied displacements are smaller than 0.06 m, the PD and the experimental results have a very good agreement. However, when the applied displacements are higher than 0.06 m, there are small differences between the calculated forces in PD and the experimental values. These differences can be caused by plastic deformation effects, which are not considered in the PD simulation.

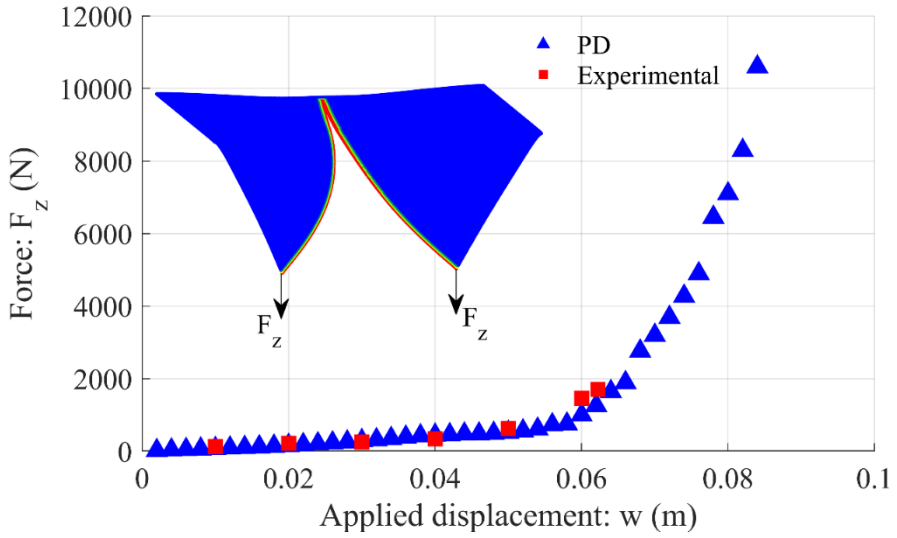

Fig. 3.74. Equivalent applied forces versus the applied displacements

3.4.4.4. Tearing a plate

In this section, another example of a plate subjected to tearing is investigated as shown in Fig. 3.75. The plate has the dimensions of $L = 0.06$ m, $W = 2L$, and thickness of $h = 5 \times 10^{-4}$ m. The plate has two initial cracks located at $x = 0.01$ m and $x = -0.01$ m. The initial crack lengths are $a = 0.03$ m. The material has an elastic modulus of $E = 5.96$ GPa, Poisson's ratio of $\nu = 0.2$. For simplification, the critical energy release rate of the material is chosen as $G_c = G_{Ic} = 8.8 \times 10^3$ J/m^2 [112].

Three edges of the plate are fixed and one edge is free as shown in Fig. 3.75. In PD, the model is uniformly discretized with the mesh size $\Delta x = L/200$. To apply the boundary conditions, three fictitious layers of material points are added on each fixed edge. All DOFs of the fictitious material points as well as material points located along the fixed edges of the plate at $x = \pm L/2$ and $y = W$ are set equal to zero.

The plate shown in Fig. 3.75 is subjected to incremental vertical displacements at the location of $(-0.01 \text{ m} \leq x \leq 0.01 \text{ m}, y = 0, z = 0)$. In the peridynamic model, the material points located at $(-0.01 \text{ m} \leq x \leq 0.01 \text{ m}, y = 0, z = 0)$ are subjected

to incremental displacements as $w = 0.001 \times i_l$, $i_l = 1, \ldots, 60$, where i_l represents the load step number. Similar to the previous example, at each load step, the quasi-static solution is obtained for 10000 iterations by using the ADR method. The same numerical procedure, except loading condition, shown in Fig. 3.69 is used for this problem for the given loading condition.

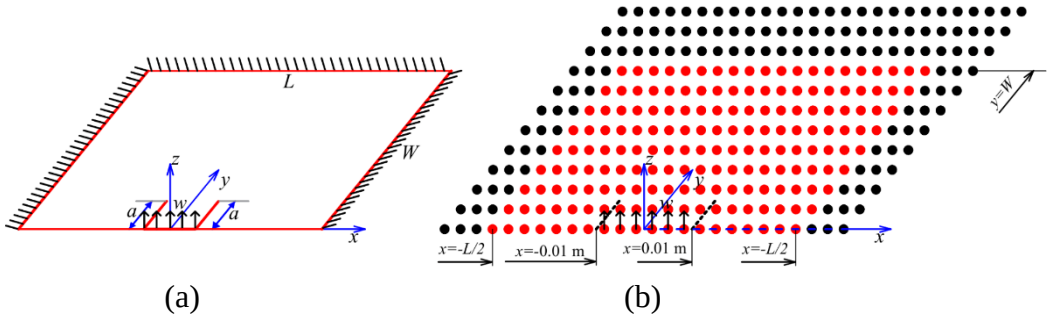

(a) (b)

Fig. 3.75. Tearing a plate (a): geometry, (b): PD discretized model

Fig. 3.76-Fig. 3.78 show the damage evolution on the plate. As shown in Fig. 3.76, the cracks start propagating when the applied displacement is $w = 0.025$ m. As the applied displacements are continuously increased, the cracks propagate diagonally as shown in Fig. 3.77. When the applied displacement is $w = 0.033$ m, two cracks meet each other at $(x = 0.039 \text{ m}, y = 0)$ as shown in Fig. 3.78. In Fig. 3.78, the final damage of the plate is shown in both deformed and undeformed configurations. It is observed that the damage pattern captured by the developed nonlinear PD model is similar to the results obtained by Silling and Bobaru [51].

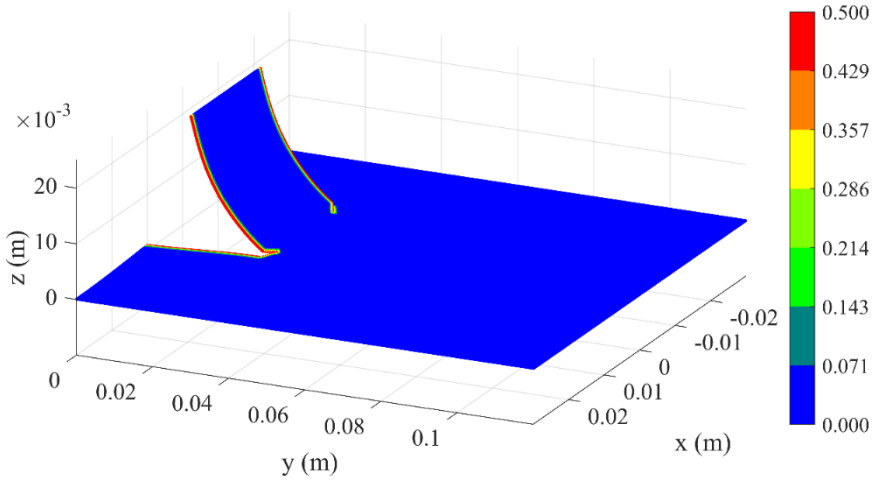

Fig. 3.76. Damage on the plate when the applied displacement $w = 0.025$ m

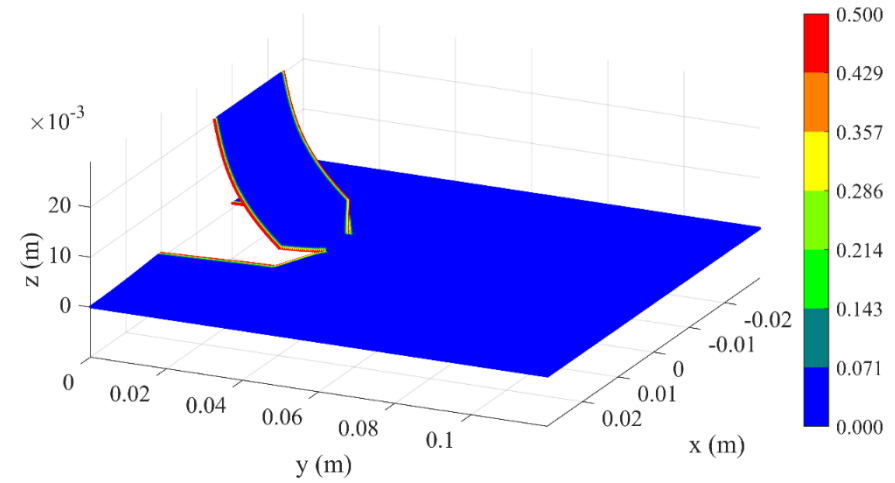

Fig. 3.77. Damage on the plate when the applied displacement $w = 0.029$ m

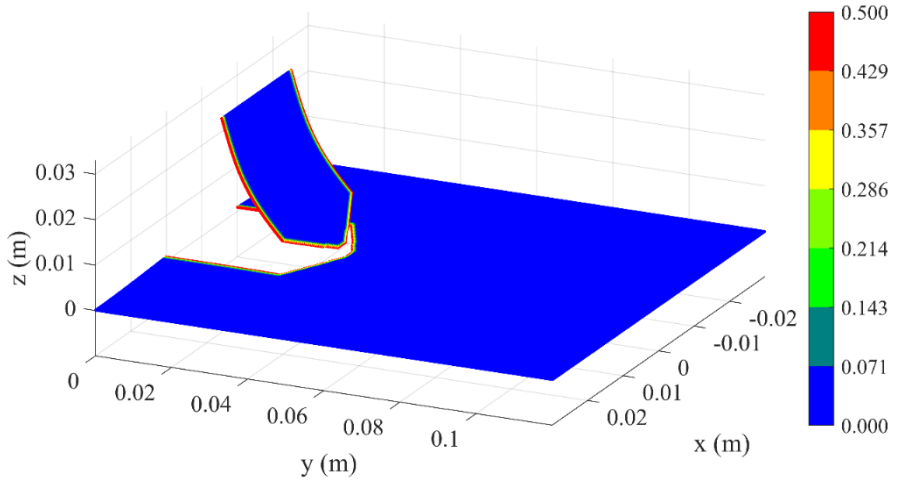

(a)

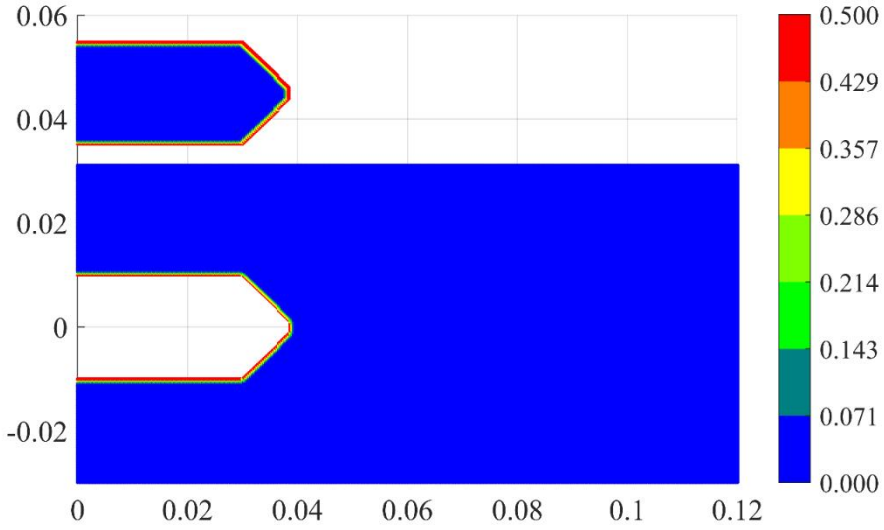

(b)

Fig. 3.78. Damage on the plate when the applied displacement $w = 0.033$ m, (a): 3D view in deformed configuration, (b): 2D view in the undeformed configuration

3.4.4.5. Plate subjected to torsion

In this section, damages on a plate subjected to torsional loading are investigated as shown in Fig. 3.79. The plate has dimensions of $L = 0.3$ m, $W = 0.127$ m, and thickness of $h = 6 \times 10^{-3}$ m. The plate has an initial crack with a length of $a_0 = 26 \times 10^{-3}$ m as shown in Fig. 3.79. The material has the elastic modulus of $E = 2 \times 10^{11}$ N/m^2 and Poisson's ratio of $\nu = 0.3$. For simplification, the critical energy release rate of the material is chosen as $G_c = G_{Ic} = 22295$ J/m^2 [113].

Two edges of the plate are attached with rigid parts, shown in black in Fig. 3.79(a), and they are applied incremental rotations as

$$\theta_{x(\text{left})} = -10^{-7} \times it \text{ (rad)}, \; it = 1,\ldots,10^7 \tag{3.121a}$$

$$\theta_{x(\text{right})} = 10^{-7} \times it \text{ (rad)}, \; it = 1,\ldots,10^7 \tag{3.121b}$$

In PD, the model is uniformly discretized with a mesh size of $\Delta x = L/100$, and the quasi-static solution is obtained by using the ADR method. To apply loading conditions, three fictitious layers of material points are added on the left and right sides of the plate as shown in Fig. 3.79(b). The rotation boundary conditions given in Eq. (68) are implemented by using displacement boundary conditions as

$$\begin{bmatrix} u & v & w \end{bmatrix}^T = \mathbf{R}\mathbf{x} - \mathbf{x} \tag{3.122}$$

where $\boldsymbol{R}$ is the rotation matrix. Therefore, the displacements of the fictitious material points on the left side are implemented as

$$\begin{bmatrix} u_{(k)} \\ v_{(k)} \\ w_{(k)} \end{bmatrix} = \begin{bmatrix} 1 & 0 & 0 \\ 0 & \cos\theta_{x(\text{left})} & -\sin\theta_{x(\text{left})} \\ 0 & \sin\theta_{x(\text{left})} & \cos\theta_{x(\text{left})} \end{bmatrix} \begin{bmatrix} x_{(k)} \\ y_{(k)} \\ z_{(k)} \end{bmatrix} - \begin{bmatrix} x_{(k)} \\ y_{(k)} \\ z_{(k)} \end{bmatrix} \tag{3.123}$$

Meanwhile, the displacements of the fictitious material points on the right side are implemented as

$$\begin{bmatrix} u_{(j)} \\ v_{(j)} \\ w_{(j)} \end{bmatrix} = \begin{bmatrix} 1 & 0 & 0 \\ 0 & \cos\theta_{x(\text{right})} & -\sin\theta_{x(\text{right})} \\ 0 & \sin\theta_{x(\text{right})} & \cos\theta_{x(\text{right})} \end{bmatrix} \begin{bmatrix} x_{(j)} \\ y_{(j)} \\ z_{(j)} \end{bmatrix} - \begin{bmatrix} x_{(j)} \\ y_{(j)} \\ z_{(j)} \end{bmatrix} \tag{3.124}$$

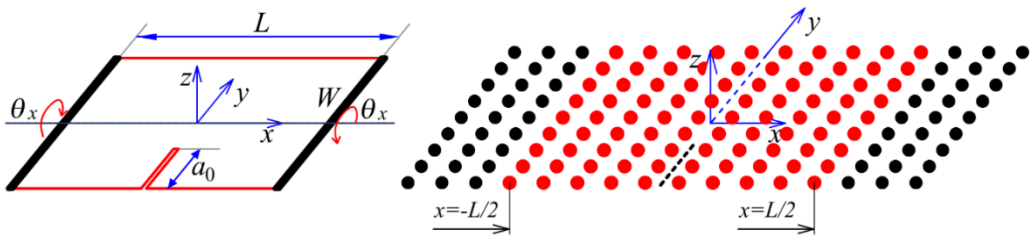

(a) (b)

Fig. 3.79. Plate subjected to torsion

Fig. 3.80-Fig. 3.82 show the damage evolution on the plate subjected to torsion. As shown in Fig. 3.80, the crack starts propagating when the applied rotational angle is $|\theta_x| = 0.082$ (rad). As the rotation $|\theta_x|$ is increased, the crack propagates along the positive y direction and reaches the final damage location at $(x = 0, y = 0.125$ m) when the applied rotational angle reaches $|\theta_x| = 0.094$ (rad) as shown in Fig. 3.82. It can also be observed that the damage pattern captured by the nonlinear PD agrees well with the results captured by Zavattieri [113].

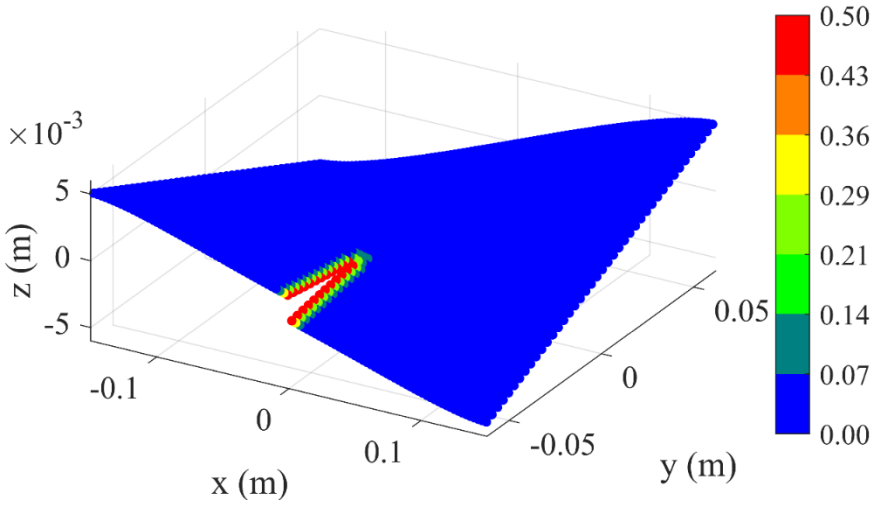

Fig. 3.80. Damage on the plate when $|\theta_x| = 0.082$ (rad)

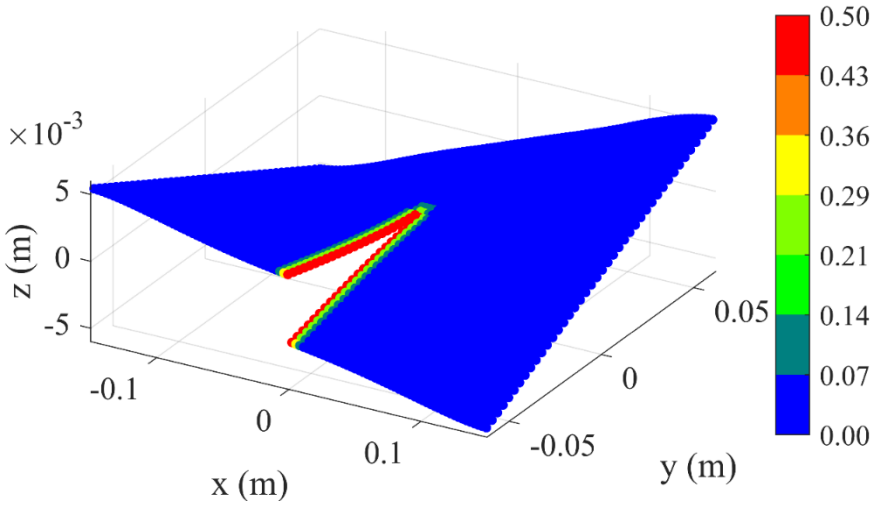

Fig. 3.81. Damage on the plate when $|\theta_x| = 0.088$ (rad)

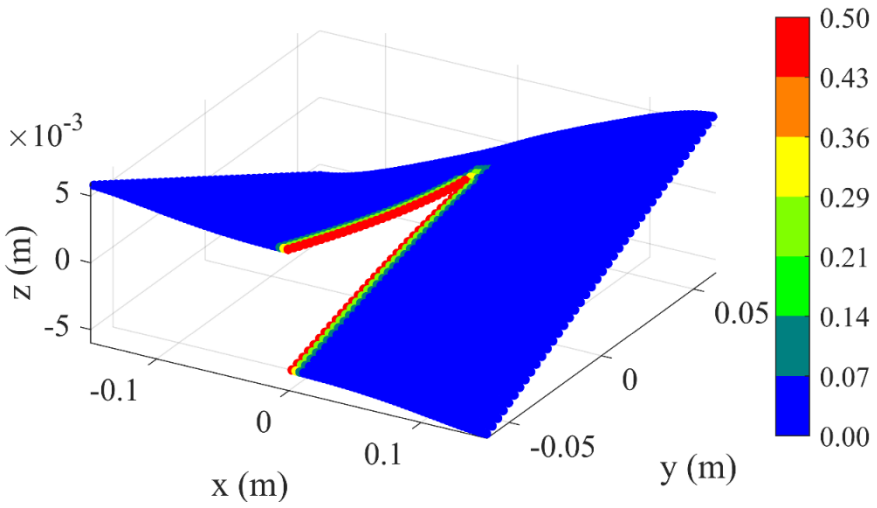

Fig. 3.82. Damage on the plate when $|\theta_x| = 0.094$ (rad)

Fig. 3.83 shows the variations of the crack length versus the rotational angles. As it can be observed from the figure, when the rotational angle is smaller than 0.08 (rad), the crack growth is quite slow. Beyond this limit, the crack starts growing much faster and reaches the final length of 0.125 m when the applied rotational angle is $|\theta_x| = 0.094$ (rad).

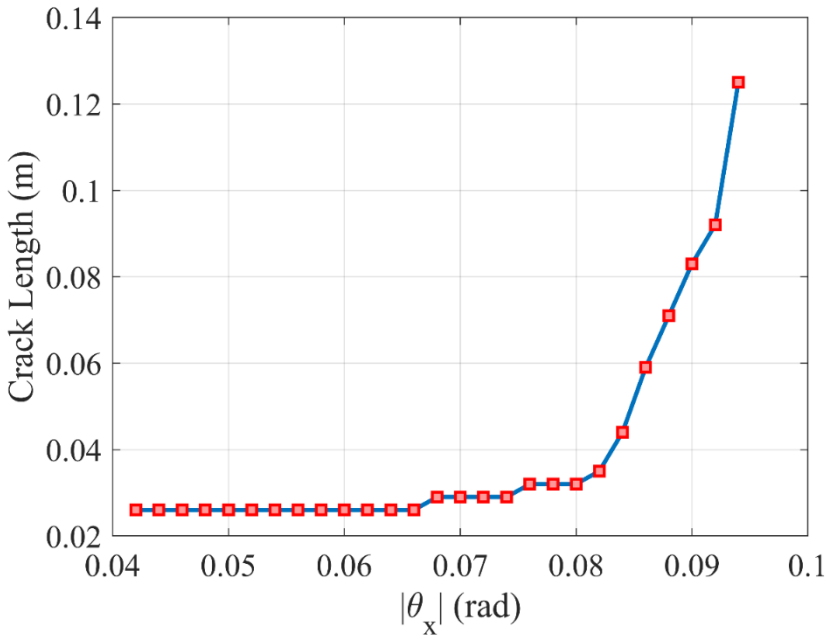

Fig. 3.83. Crack length (m) versus rotational angle (rad)

3.5. Concluding remarks

This chapter presents novel peridynamic models for geometrically nonlinear analysis based on Total Lagrange formulations. For nonlinear analysis of 1D, 2D, and 3D structures, a logarithmic bond stretch has been proposed for the first time in the PD literature. The effects of volume changes and rotations are considered in the calculation of PD force densities. The energy-based damage criterion is used for damage prediction. The accuracy of the developed nonlinear PD model is

verified by comparing it to nonlinear FEA solutions. For damage prediction, first, the developed nonlinear PD model is used to predict damages for a plate subjected to dynamic loading and an L-shape plate subjected to large deformation. Then, damage pattern in 3D pre-notched concrete beam subjected to quasi-static loading condition is predicted. All results show very good agreement with experimental results.

For nonlinear analysis of beam structures, a novel nonlinear bond-based PD beam model with 6 degrees of freedom is developed. The energy-based damage criterion is used for damage prediction. The accuracy of the nonlinear PD model is verified for both straight and curved beams. The results from nonlinear PD analyses have good agreement with those in nonlinear FEA solutions, as well as the results from previous studies in the literature. To show the capability of the developed PD model for damage prediction, damages on a spaghetti subjected to different loading conditions are predicted. The predicted PD results show a good agreement with the experimental results given in the literature. The developed PD model can be used for any type of beam structure to predict possible damages that may occur during the operation process.

For nonlinear analysis of shell structures, a novel nonlinear PD model for plates is developed. The energy-based damage criterion is used for damage prediction. The accuracy of the nonlinear PD model is verified by comparing the PD results with the nonlinear FEA results. After the verification, the nonlinear PD model is used to predict progressive damages on a plate subjected to out-of-plane stretching and tearing, a plate with two parallel cracks subjected to tearing, and a plate with a pre-existing crack subjected to torsional loading. The predicted results in terms of damage patterns agree very well with the observations from the experiments and previous numerical studies. The proposed nonlinear PD can be further applied to predict possible damages on plates and shell structures subjected to large deformations during their operation process.

4. PERIDYNAMICS FOR FATIGUE CRACKING

4.1. Introduction

Stochastic fatigue analyses are commonly used in the fatigue design assessment (FDA) for ship and offshore structures. First, the stress combination caused by hull girder loads, external wave pressure, and internal cargo pressure is obtained. Subsequently, by using a suitable wave energy spectrum, the short-term stress response in irregular waves and short-term accumulated fatigue damage for the structures are predicted by using the well-known Palmgren-Miner rule. Next, by using the service profile probability matrix, including wave heights, wave periods, ship headings, ship speeds, loading conditions, long-term accumulated fatigue damage, and deterministic fatigue life probability of failure are predicted. This approach is recommended by many classification societies [114-120], and it is also widely used in many practical ships and offshore structure analyses [121-125]. By using the stochastic approach, the total lifetime accumulated fatigue damage (in the long-term fatigue analysis) and the probability of failure (in the reliability fatigue damage analysis) are common outputs. Meanwhile, the details of damage initiation and propagation are still infrequently investigated.

To predict fatigue crack growth, the traditional finite element method (FEM) by using the remeshing techniques [126, 127], or various modified versions of the FEM such as the extended finite element method [128, 129], have been used. However, as mentioned in the previous Chapters, one conceptual problem for classical continuum mechanics (CCM) is that it uses the partial differential equations to represent structural behaviours. Therefore, additional criteria are needed to predict crack growth speed and direction or the branching of cracks [130-133].

In Peridynamics, the first PD model for fatigue cracking is proposed by Silling and Askari [60]. Further validations for the PD model were studied by Zhang, et al. [134], Jung and Seok [135]. As proposed by Silling and Askari [60], during the cyclic loading processes, the reduction of the remaining life of each interaction is updated by using the cyclic bond strain range. However, in some special cases, the bond strain can consist of different components. For instance, in beam and shell structures, the bond strain consists of in-plane, shear, and bending components [61, 62]. Therefore, deciding which strain will be used for the PD fatigue equation can be a challenge. By contrast, as presented in previous Chapters, the energy release rate for a bond is unique and it can be calculated by summing all components of the energy release rate. Therefore, this chapter proposes a novel energy-based PD model for fatigue cracking. The definition of the cyclic bond energy release rate range is introduced for the first time in the PD literature. The PD fatigue equations based on the cyclic bond energy release rate range are proposed. For simplification, this chapter focuses on the formulations for 2D structures. The proposed PD model is verified by considering both mode-I and mixed-mode fatigue crack growth problems.

4.2. Peridynamics for fatigue cracking based on cyclic bond strain range

In this section, a brief review of the existing PD model for fatigue cracking developed by Silling and Askari [60] is presented. In the model developed by

Silling and Askari [60], a bond can be defined in either the crack nucleation phase (phase I) or the crack growth phase (phase II). Rapid crack growth (Phase III) can also be incorporated with the PD fatigue model when some interactions in the PD model have stretches exceeding the critical value [134]. The fatigue life of each bond is represented by its remaining life, $\lambda(\boldsymbol{x},\boldsymbol{\xi},N)$ that is defined as [60]

$$\lambda_{(k)(j)}^{(N=0)}=1,\quad \frac{d\lambda_{(k)(j)}^{(N)}}{dN}=-A_1\left(\varepsilon_{(k)(j)}^{(N)}\right)^{m_1}\quad \text{with } A_1>0,\ m_1>0 \text{ for phase (I)} \tag{4.1a}$$

$$\lambda_{(k)(j)}^{(N=0)}=1,\quad \frac{d\lambda_{(k)(j)}^{(N)}}{dN}=-A_2\left(\varepsilon_{(k)(j)}^{(N)}\right)^{m_2}\quad \text{with } A_2>0,\ m_2>0 \text{ for phase (II)} \tag{4.1b}$$

where (A_1, m_1) and (A_2, m_2) represent the positive fatigue parameters for phase (I) and phase (II), respectively. The parameter $\lambda_{(k)(j)}^{(N)}$ represents the remaining life of the interaction between material points k and j at the N^{th} cycle of loading. The parameter $\varepsilon_{(k)(j)}^{(N)}$ represents the cyclic bond strain range between material points k and j at N^{th} cycle of loading which can be defined as [60]

$$\varepsilon_{(k)(j)}^{(N)}=\left|s_{(k)(j)}^{+}-s_{(k)(j)}^{-}\right|=\left|s_{(k)(j)}^{+}\left(1-R\right)\right| \tag{4.2}$$

where $s_{(k)(j)}^{+}$ represents the bond stretch corresponding to the maximum load P_{max}, $s_{(k)(j)}^{-}$ represents the bond stretch corresponding to the minimum load P_{min}. The term R represents the load ratio that can be defined as

$$R=P_{\min}/P_{\max}\approx s_{(k)(j)}^{-}/s_{(k)(j)}^{+} \tag{4.3}$$

If the fatigue limit is considered, Eq. (4.1a) can be rewritten for phase (I) as [60]

$$\lambda_{(k)(j)}^{(N=0)}=1,\quad \frac{d\lambda_{(k)(j)}^{(N)}}{dN}=\begin{cases}-A_1\left(\varepsilon_{(k)(j)}^{(N)}-\varepsilon_{\infty}\right)^{m_1}, & \text{if } \varepsilon_{(k)(j)}^{(N)}>\varepsilon_{\infty}\\ 0 & \text{otherwise}\end{cases} \tag{4.4}$$

where $\varepsilon_{\infty}\geq 0$ represents the fatigue limit which is the lowest cyclic bond strain range that still results in fatigue damages. The fatigue limit, ε_{∞} can be determined from the experiment. Note that ε_{∞} can be set equal to zero if the fatigue limit is not considered [60].

By using the relations given in Eq. (4.4), the remaining life of a bond in phase (I) can be calculated as

$$\lambda_{(k)(j)}^{(N=0)}=1,\quad \lambda_{(k)(j)}^{(N)}=\begin{cases}\lambda_{(k)(j)}^{(N-1)}-A_1\left(\varepsilon_{(k)(j)}^{(N)}-\varepsilon_{\infty}\right)^{m_1}, & \text{if } \varepsilon_{(k)(j)}^{(N)}>\varepsilon_{\infty}\\ \lambda_{(k)(j)}^{(N-1)} & \text{otherwise}\end{cases} \tag{4.5}$$

By using the relations given in Eq. (4.1b), the remaining life of a bond in phase (II) can be calculated as

$$\lambda_{(k)(j)}^{(N=0)}=1,\quad \lambda_{(k)(j)}^{(N)}=\lambda_{(k)(j)}^{(N-1)}-A_2\left(\varepsilon_{(k)(j)}^{(N)}\right)^{m_2} \tag{4.6}$$

Beyond the crack growth phase (phase II), the structures can experience rapid crack growth (phase III). In this case, the traditional PD model [21, 43, 44, 46] for damage prediction can be used. Therefore, the interaction state of a bond can be defined as

$$\begin{cases}\lambda_{(k)(j)}^{(N)}\leq 0 \quad \text{or} \quad s_{(k)(j)}\geq s_c \ \rightarrow\ \psi_{(k)(j)}=0\\ \lambda_{(k)(j)}^{(N)}>0 \quad \text{and} \quad s_{(k)(j)}<s_c \ \rightarrow\ \psi_{(k)(j)}=1\end{cases} \tag{4.7}$$

4.2.1. Fatigue parameters for phase (I)

Assuming that $\boldsymbol{\xi}_1$ is the bond that has the largest cyclic bond strain in the structure, according to Silling and Askari [60], crack nucleation occurs when

$$N_1 = \frac{1}{A_1 \varepsilon_1^{m_1}} \tag{4.8}$$

where ε_1 represents the largest cyclic bond strain in the PD model.
If the fatigue limit, ε_∞ is considered, Eq. (4.8) can be rewritten as

$$N_1 = \frac{1}{A_1 \left(\varepsilon_1 - \varepsilon_\infty\right)^{m_1}} \tag{4.9}$$

The relations in Eqs. (4.8-7.9) can be rewritten as

$$\log\left(\varepsilon_1\right) = -\frac{1}{m_1}\log\left(N_1\right) - \frac{\log\left(A_1\right)}{m_1} \tag{4.10a}$$

and

$$\log\left(\varepsilon_1 - \varepsilon_\infty\right) = -\frac{1}{m_1}\log\left(N_1\right) - \frac{\log\left(A_1\right)}{m_1} \tag{4.10b}$$

By using the relations in Eq. (4.10), the parameters A_1 and m_1 can be obtained from $\varepsilon - N$ test data for material as shown in Fig. 4.1.

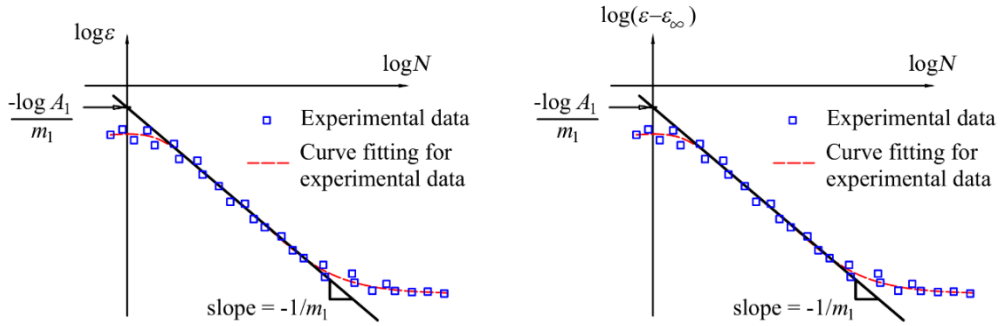

(a) (b)

Fig. 4.1. Calibration phase (I) parameters A_1 and m_1 (a) without fatigue limit, (b) with fatigue limit

As shown in Fig. 4.1, the experimental results for $log\,\varepsilon$ versus $log\,N$ or $log(\varepsilon - \varepsilon_\infty)$ versus $log\,N$ are often represented with scatter data, shown in blue. Based on these scatter data, the fitted curves, shown in red, can be obtained. The slopes of the fitted curves are equal to $-1/m_1$. Meanwhile, the intersections of the slopes with the $log\,\varepsilon$ or $log(\varepsilon - \varepsilon_\infty)$ axis (the vertical axis) are equal to $-\,log(A_1)\,/m_1$. Therefore, the fatigue parameters, (A_1, m_1), for phase (I) can be obtained from the fitted curve.

4.2.2. Fatigue parameters for phase (II)

In phase (II), the fatigue crack growth follows the well-known Paris law that can be represented as

$$\frac{dq}{dN} = c\Delta K^M \tag{4.11}$$

where q represents the crack length and N represents the number of loading cycles, c and $M$are material constants, ΔK represents the stress intensity factor range.
According to Silling and Askari [60], the parameter m_2 in Eq. (4.6) can be obtained directly from the material constant M as

$$m_2 = M \tag{4.12}$$

Meanwhile, the parameter A_2 in Eq. (4.6) needs to be calibrated by conducting a trial PD fatigue simulation. Details of the calibration for the parameter A_2 is presented in the appendix G1 which can be described as follows;

Step 1: Assume an arbitrary value for A_2 A_2 as: $A_2 = A_{2(\text{trial})}$

Step 2: Conduct a PD fatigue simulation with the trial value $A_2 = A_{2(\text{trial})}$ and calculate the crack growth rate and stress intensity (SIF) range for this trial case: $(dq/dN)_{(\text{trial})}$ and $\Delta K_{(\text{trial})}$.

Step 3: Plot the scatter data of $(\Delta K - dq/dN)_{(\text{trial})}$ in the logarithmic scale and find the best-fit equation: $(dq/dN)_{(\text{trial})} = C_{(\text{trial})}\Delta K^M$

Step 4: Calibrate the value for A_2 as [60]

$$A_2 = A_{2(\text{trial})} \frac{\left(dq/dN\right)_{(\text{experiment})}}{\left(dq/dN\right)_{(\text{trial})}} \tag{4.13a}$$

or

$$A_2 = A_{2(\text{trial})} \frac{C_{(\text{experiment})}\Delta K^M}{C_{(\text{trial})}\Delta K^M} = A_{2(\text{trial})} \frac{C_{(\text{experiment})}}{C_{(\text{trial})}} \tag{4.13b}$$

where

$$\left(dq/dN\right)_{(\text{experiment})} = C_{(\text{experiment})}\Delta K^M \tag{4.13c}$$

Here Eq. (4.13c) is the Paris law equation obtained from the experimental data.

Note that m_1, A_1 and m_2 are material constants which are independent of the horizon size. However, the parameter A_2 is dependent on the horizon size [60]. According to Silling and Askari [60], the relationship between the parameter A_2 and the horizon size δ can be presented as

$$A_2\left(\delta\right) = \hat{A}_2\delta^{(m_2-2)/2} \tag{4.14}$$

where $\hat{A}_2$ is a constant and it is independent of δ.
Therefore, the value of the parameter A_2 can be scaled due to the change of horizon size as follows:
Assuming that $A_2^{(1)}$ is the calibrated value for the parameter A_2 obtained from a trial PD simulation (see Appendix G1 for the calibration procedure) by using the horizon size of $\delta^{(1)}$, for example $\delta^{(1)} = 3\Delta x_1$ in which Δx_1 represents the mesh size used in the trial PD simulation.
By substituting $A_2^{(1)}$ and $\delta^{(1)}$ into Eq. (4.14), the value for the parameter $\hat{A}_2$ can be calculated as

$$\hat{A}_2 = \frac{A_2^{(1)}}{\left(\delta^{(1)}\right)^{(m_2-2)/2}} \tag{4.15}$$

Now, assuming that a PD fatigue simulation with a different mesh size $\Delta x_2 \neq \Delta x_1$ and a horizon size of $\delta^{(2)} = 3\Delta x_2$ is needed. Therefore, by substituting Eq. (4.15)

into Eq. (4.14) and by putting $\delta = \delta^{(2)}$, a new value of the parameter A_2 for the PD fatigue simulation with a mesh size of $\Delta x_2 \neq \Delta x_1$ and a horizon size of $\delta^{(2)} = 3\Delta x_2$ can be obtained as

$$A_2^{(2)} = \hat{A}_2 \left(\delta^{(2)}\right)^{(m_2-2)/2} = \frac{A_2^{(1)}}{\left(\delta^{(1)}\right)^{(m_2-2)/2}} \left(\delta^{(2)}\right)^{(m_2-2)/2} \tag{4.16}$$

4.3. An energy-based PD model for fatigue cracking

In this section, a novel PD model for fatigue damage prediction based on the cyclic bond energy release rate range for 2D structures is proposed. The fatigue equation in Eq. (4.1) is rewritten in the energy-based form. New fatigue parameters for the proposed model are also presented.

By considering only in-plane deformations in the PD shell model given in Chapter 2, the PD equations of motion for 2D structures can be found in Eq. (2.77a, b) in Chapter 2 as

$$\rho h \ddot{u}_{(k)} = \sum_{j=1}^{N} \psi_{(k)(j)} \left[2ad \frac{1}{\xi} \left(\vartheta_{(k)} + \vartheta_{(j)} \right) + 4bs_{(k)(j)} \right] \cos\varphi V_{(j)} + \bar{b}_{x(k)} \tag{4.17a}$$

$$\rho h \ddot{v}_{(k)} = \sum_{j=1}^{N} \psi_{(k)(j)} \left[2ad \frac{1}{\xi} \left(\vartheta_{(k)} + \vartheta_{(j)} \right) + 4bs_{(k)(j)} \right] \sin\varphi V_{(j)} + \bar{b}_{y(k)} \tag{4.17b}$$

where $\vartheta_{(k)}$ and $\vartheta_{(j)}$ represent the dilatations at material points k and j, respectively. The terms, a, b, d are the PD constants for in-plane deformations, $s_{(k)(j)}$ represents the linear bond stretch for in-plane deformations which is given in Eq. (2.65) in chapter 2. The terms, $\bar{b}_{x(k)}$ and $\bar{b}_{y(k)}$ represent the external forces per unit area. Details of these parameters can be found in Chapter 2.

Similarly, by substituting the micro-potentials of in-plane deformations given in Eq. (2.91) in Chapter 2 into Eq. (1.9) in Chapter 1, the energy release rate for interaction between material points k and j in 2D structures can be represented as

$$\bar{g}_{(k)(j)} = \frac{1}{2} \left(\frac{2ad}{\xi} \left(\vartheta_{(k)} + \vartheta_{(j)} \right) + 4bs_{(k)(j)} \right) \xi s_{(k)(j)} \frac{V_{(k)} V_{(j)}}{2(\Delta x) h^2} \tag{4.18}$$

The energy release rate in Eq. (4.18) can be rewritten as

$$\bar{g}_{(k)(j)} = \left(\frac{ad}{\xi} \left(\frac{\vartheta_{(k)}}{s_{(k)(j)}} + \frac{\vartheta_{(j)}}{s_{(k)(j)}} \right) + 2b \right) \frac{V_{(k)} V_{(j)}}{2(\Delta x) h^2} \xi s_{(k)(j)}^2 \tag{4.19a}$$

or

$$\bar{g}_{(k)(j)} = C_{0(k)(j)} s_{(k)(j)}^2 \tag{4.19b}$$

with

$$C_{0(k)(j)} = \left(\frac{ad}{\xi} \left(\frac{\vartheta_{(k)}}{s_{(k)(j)}} + \frac{\vartheta_{(j)}}{s_{(k)(j)}} \right) + 2b \right) \frac{V_{(k)} V_{(j)}}{2(\Delta x) h^2} \xi \tag{4.19c}$$

For the bond-based PD model, the term $a = 0$ in Eq. (4.19) [44]. Therefore, Eq. (4.19c) can be simplified as

$$C_{0(k)(j)} = b \frac{V_{(k)} V_{(j)}}{(\Delta x) h^2} \xi \tag{4.20}$$

As can be observed from Eq. (4.20) for the bond-based PD model, the parameter $C_{0(k)(j)}$ is independent of loading conditions. However, for the ordinary state-based PD model, the dilatation terms exist. Therefore, as given in Eq. (4.19c), $C_{0(k)(j)}$ is loading dependent and it can be updated during the PD fatigue prediction.

4.3.1. The cyclic bond energy release rate range

Similar to the definition of the cyclic bond strain range proposed by Silling and Askari [60], the cyclic bond energy release rate range at N^{th} cycle of loading can be defined as

$$g_{(k)(j)}^{(N)} = \left| \bar{g}_{(k)(j)}^{+} - \frac{R}{|R|} \bar{g}_{(k)(j)}^{-} \right| \tag{4.21}$$

where $\bar{g}_{(k)(j)}^{+}$ and $\bar{g}_{(k)(j)}^{-}$ represent the energy release rates for interaction between material points k and j in maximum and minimum loading conditions, respectively. These energy release rates can be calculated by using Eq. (4.19). The loading ratio R is defined in Eq. (4.3).

By using the relationship given in Eq. (4.19b), the cyclic bond energy release rate range in Eq. (4.21) can be rewritten as

$$g_{(k)(j)}^{(N)} = \left| C_{0(k)(j)} \right| \left| \left(s_{(k)(j)}^{+} \right)^2 - \frac{R}{|R|} \left(s_{(k)(j)}^{-} \right)^2 \right| \tag{4.22a}$$

or

$$g_{(k)(j)}^{(N)} = \left| C_{0(k)(j)} \right| \left| \left(1 - \frac{R}{|R|} R^2 \right) \right| \left(s_{(k)(j)}^{+} \right)^2 \tag{4.22b}$$

By using the relation given in Eq. (4.2), the cyclic bond energy release rate range in Eq. (4.22b) can be rewritten as

$$g_{(k)(j)}^{(N)} = \left| C_{0(k)(j)} \right| \left| \left(1 - \frac{R}{|R|} R^2 \right) \right| \left(\frac{\varepsilon_{(k)(j)}^{(N)}}{(1-R)} \right)^2 \tag{4.23a}$$

or

$$g_{(k)(j)}^{(N)} = C_{1(k)(j)} \left(\varepsilon_{(k)(j)}^{(N)} \right)^2 \tag{4.23b}$$

with

$$C_{1(k)(j)} = \left| C_{0(k)(j)} \right| \left| \left(1 - \frac{R}{|R|} R^2 \right) \right| \frac{1}{(1-R)^2} \tag{4.23c}$$

4.3.2. The energy-based PD fatigue model

Similar to the original PD fatigue model [60], in this energy-based model, the remaining life of the interaction between material points k and j can be represented in terms of the cyclic bond energy release rate range as

For phase (I):

$$\lambda_{(k)(j)}^{(N=0)}=1,\quad \frac{d\lambda_{(k)(j)}^{(N)}}{dN}=-B_{1(k)(j)}\left(g_{(k)(j)}^{(N)}\right)^{n_1}\ \text{with}\ B_{1(k)(j)}>0,\ n_1>0 \tag{4.24a}$$

For phase (II):

$$\lambda_{(k)(j)}^{(N=0)}=1,\quad \frac{d\lambda_{(k)(j)}^{(N)}}{dN}=-B_{2(k)(j)}\left(g_{(k)(j)}^{(N)}\right)^{n_2}\ \text{with}\ B_{2(k)(j)}>0,\ n_2>0 \tag{4.24b}$$

where $(B_{1(k)(j)}, n_1)$ and $(B_{2(k)(j)}, n_2)$ represent the fatigue parameters used in the energy-based PD fatigue model for phase (I) and phase (II), respectively. The parameter $g_{(k)(j)}^{(N)}$ represents the cyclic bond energy release rate range of the interaction between material points k and j at the N^{th} loading cycle.

If a fatigue limit is considered, the fatigue equation in Eq. (4.24a) for phase (I) can be rewritten as

$$\frac{d\lambda_{(k)(j)}^{(N)}}{dN}=\begin{cases}-B_{1(k)(j)}\left(g_{(k)(j)}^{(N)}-g_{\infty}\right)^{n_1}, & \text{if}\quad g_{(k)(j)}^{(N)}>g_{\infty}\\ 0 & \text{otherwise}\end{cases} \tag{4.25a}$$

with

$$g_{\infty}=C_{1(k)(j)}\varepsilon_{\infty}^{2} \tag{4.25b}$$

where g_∞ represents the cyclic bond energy release rate range corresponding to the fatigue limit ε_∞.

By integrating Eq. (4.25a), the remaining life of a bond in phase (I) can be calculated as

$$\lambda_{(k)(j)}^{(N=0)}=1,\quad \lambda_{(k)(j)}^{(N)}=\begin{cases}\lambda_{(k)(j)}^{(N-1)}-B_{1(k)(j)}\left(g_{(k)(j)}^{(N)}-g_{\infty}\right)^{n_1}, & \text{if}\quad g_{(k)(j)}^{(N)}>g_{\infty}\\ \lambda_{(k)(j)}^{(N-1)} & \text{otherwise}\end{cases} \tag{4.26}$$

By integrating Eq. (4.24b), the remaining life of a bond in phase (II) can be calculated as

$$\lambda_{(k)(j)}^{(N=0)}=1,\quad \lambda_{(k)(j)}^{(N)}=\lambda_{(k)(j)}^{(N-1)}-B_{2(k)(j)}\left(g_{(k)(j)}^{(N)}\right)^{n_2} \tag{4.27}$$

Similar to the damage criteria given in Eq. (4.7), the state of interaction in the energy-based model can be defined as

$$\begin{cases}\lambda_{(k)(j)}^{(N)}\le 0 \quad \text{or} \quad \bar{g}_{(k)(j)}\ge g_c \ \rightarrow\ \psi_{(k)(j)}=0\\ \lambda_{(k)(j)}^{(N)}>0 \quad \text{and} \quad \bar{g}_{(k)(j)}<g_c \ \rightarrow\ \psi_{(k)(j)}=1\end{cases} \tag{4.28}$$

4.3.3. Fatigue parameters ($B_{1(k)(j)}$, n_1), ($B_{2(k)(j)}$, n_2)

In this section, the relationships between the fatigue parameters in the proposed energy-based PD model, ($B_{i(k)(j)}$, n_i) and the fatigue parameters in the cyclic bond strain model, (A_i, m_i) are presented. The values of ($B_{i(k)(j)}$, n_i) can be obtained indirectly from the experimental data through the calibrations for (A_i, m_i). Note that, in this section, $i = 1$ denotes phase (I) and $i = 2$ denotes phase (II).

By comparing Eq. (4.24) with Eq. (4.1), the relationships between fatigue parameters in the energy-based model, ($B_{i(k)(j)}$, n_i) and the cyclic bond strain model, (A_i, m_i) can be obtained as

$$A_i \varepsilon_{(k)(j)}^{m_i} = B_{i(k)(j)} g_{(k)(j)}^{n_i} \tag{4.29a}$$

or

$$\log\left(A_i\right) + m_i \log\left(\varepsilon_{(k)(j)}\right) = \log\left(B_{i(k)(j)}\right) + n_i \log\left(g_{(k)(j)}\right) \tag{4.29b}$$

On the other hand, the relation given in Eq. (4.23b) can be rewritten as

$$\log\left(g_{(k)(j)}\right) = \log\left(C_{1(k)(j)}\right) + 2\log\left(\varepsilon_{(k)(j)}\right) \tag{4.30}$$

Therefore, by using the relation given in Eq. (4.30), the relations in Eq. (4.29b) can be rewritten as

$$\log\left(A_i\right) + m_i \log\left(\varepsilon_{(k)(j)}\right) = \log\left(B_{i(k)(j)}\right) + n_i \log\left(C_{1(k)(j)}\right) + 2n_i \log\left(\varepsilon_{(k)(j)}\right) \tag{4.31a}$$

or

$$\log\left(\frac{A_i}{\left(C_{1(k)(j)}\right)^{n_i}}\right) + m_i \log\left(\varepsilon_{(k)(j)}\right) = \log\left(B_{i(k)(j)}\right) + 2n_i \log\left(\varepsilon_{(k)(j)}\right) \tag{4.31b}$$

To ensure Eq. (4.31b) is correct for every interaction, the following relations between fatigue parameters in the energy-based PD model, ($B_{i(k)(j)}$, n_i) and the cyclic bond strain PD model, (A_i, m_i) can be obtained as

$$n_i = m_i / 2 \tag{4.32a}$$

$$B_{i(k)(j)} = \frac{A_i}{\left(C_{1(k)(j)}\right)^{m_i/2}} \tag{4.32b}$$

which can be written for phase (I) and (II) as

$$n_1 = m_1 / 2 \tag{4.33a}$$

$$B_{1(k)(j)} = \frac{A_1}{\left(C_{1(k)(j)}\right)^{m_1/2}} \tag{4.33b}$$

and

$$n_2 = m_2 / 2 \tag{4.34a}$$

$$B_{2(k)(j)} = \frac{A_2}{\left(C_{1(k)(j)}\right)^{m_2/2}} \tag{4.34b}$$

4.3.4. Phase transition

According to Silling and Askari [60], the PD bond strains in the nucleation phase can agree with the measured strain data. However, in the growth phase, the actual process zone at a crack tip is usually smaller than the PD continuum-level model. Therefore, bond strains in phase (II) could be fictitious. As a result, the transition between phase (I) and phase (II) might not be smooth.

To have a smooth transition between two phases for a material point, Silling and Askari [60] proposed a method for phase transition, which is based on the information of the damage index ϕ (given in Chapter 1) at that material point and its family members. Specifically, phase (I) fatigue equation given in Eq. (4.5) or Eq. (4.26) for a given material point k is valid, if all material points within its

horizon (including itself) has the damage index $\phi < \phi_0$. By contrast, the phase (II) fatigue equation given in Eq. (4.6) or Eq. (4.27) is valid when material point k or at least one of its family members have $\phi \geq \phi_0$. According to Silling and Askari [60], ϕ_0 can be chosen as $\phi_0 = 0.5$. In this study, the same approach is used. However, $\phi_0 = 0.398$ is used for two-dimensional models for considering damage at each material point.

If some interactions have energy release rates exceeding the critical value, $\bar{g}_{(k)(j)} \geq g_c$, the fatigue simulation is stopped and the conventional PD model for damage prediction (phase III) [21, 43, 44, 46] can be used.

4.4. Numerical results

In this section, mode-I and mixed-mode fatigue damages on 2D structures are predicted by using the proposed energy-based PD fatigue model as shown in Fig. 4.3 and Fig. 4.6. The structures are made of aluminum 6061-T6 with an elastic modulus of $E = 68 \times 10^9$ N/m^2, Poisson's ratio of $\nu = 0.33$ [136], and fracture toughness of $K_{IC} = 48.7 \times 10^6$ MPa$\sqrt{\text{m}}$[137]. For simplification, the critical energy release rate of the material is calculated as $G_c = G_{\text{Ic}} = K_{Ic}^2/E = 34878$ J/m^2.

The fatigue parameters for phase (I) can be calibrated by using the experimental results ($\varepsilon - N$ curve) provided in [138]. In this study, the $\varepsilon - N$ data provided in [138] is reconstructed and plotted on a log-log scale as shown in Fig. 4.2. Based on the calibration shown in Fig. 4.2, the fatigue parameters for phase (I) (without the consideration of fatigue limit) are obtained as

$$m_1 = 2.29153 \tag{4.35a}$$

$$-\frac{\log A_1}{m_1} = -0.87975 \tag{4.35b}$$

or

$$A_1 = 103.7465 \tag{4.35c}$$

Therefore, the fatigue parameters for phase (I) in the energy-based PD model can be obtained by using Eq. (4.33) as

$$n_1 = \frac{m_1}{2} = 1.145765 \tag{4.36a}$$

$$B_{1(k)(j)} = \frac{A_1}{\left(C_{1(k)(j)}\right)^{m_1/2}} \tag{4.36b}$$

where $C_{1(k)(j)}$ is obtained by using Eq. (4.23c).

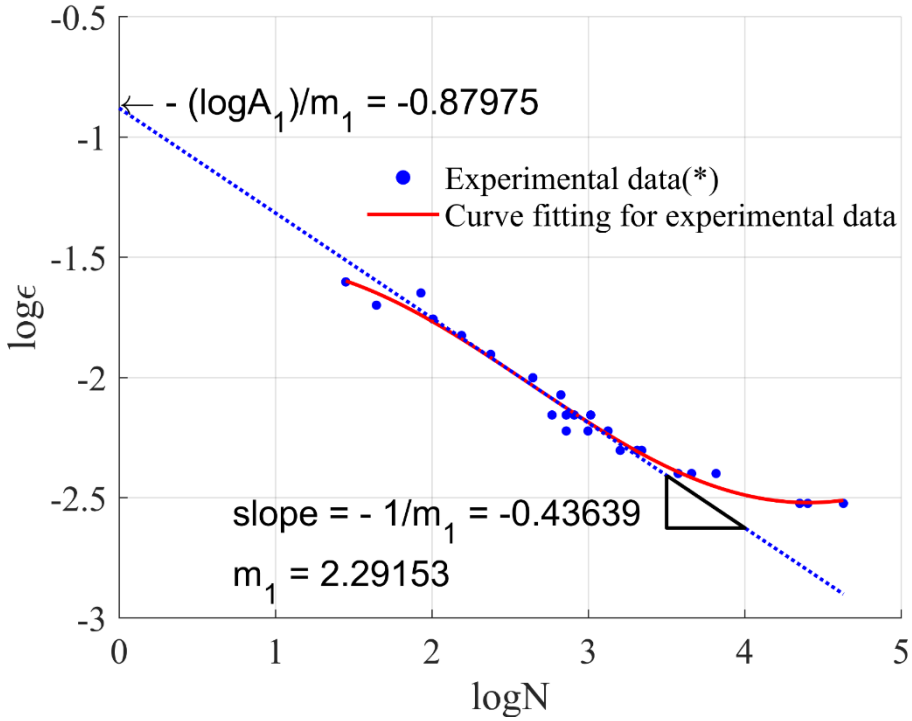

Fig. 4.2. Calibration for phase (I) parameters for aluminum 6061-T6 ((*): the experimental data is reproduced from [138])

4.4.1. Mode I fatigue crack propagation

In this section, the mode-I fatigue problem is investigated as shown in Fig. 4.3(a). The dimensions of the plate are shown in Fig. 4.3(a) and the PD discretized model is shown in Fig. 4.3(b). The plate is subjected to cyclic loading with the maximum loading $P_{max} = 14$ kN, load ratio $R = 0.1$, and loading frequency of 10 Hz [136].

In PD, the model is uniformly discretized with mesh size $\Delta x = 6 \times 10^{-4}$ mm, and the horizon size $\delta = 3.015\Delta x$ is used. Since the problem is symmetric, the fixed boundary conditions at two material points located at $(1.25W, \Delta x/2)$ and $(1.25W, -\Delta x/2)$, shown in black in Fig. 4.3(b), are assumed.

To apply loading conditions, first, material points located inside the cut-outs, shown in red in Fig. 4.3(b), are assumed as rigid with the elastic modulus of $E_{rigid} = 200E$. Next, the extreme load $P = 14 \times 10^3$ N is applied to the material points located at the centres of the cut-outs as shown in Fig. 4.3(b).

The fatigue parameter $m_2 = 2.6183$ is obtained from the experimental results given by Sajith, et al. [136]. Therefore, the phase (II) fatigue parameter for the energy-based PD model $n_2 = 1.3092$ is used.

To obtain values for parameters A_2 and $B_{2(k)(j)}$, a trial value $A_{2(\text{trial})} = 1174$ is assumed and the corresponding value $B_{2(k)(j)}^{(\text{trial})}$ is obtained for each interaction by using Eq. (4.34b). Next, A trial fatigue simulation using $\left(B_{1(k)(j)}, n_1\right)$ obtained from Eq. (4.37) for phase (I) and $\left(B_{2(k)(j)}^{(\text{trial})}, n_2 = 1.3092\right)$ for phase (II) is conducted

to calculate the fatigue crack growth rate $(dq/dN)_{(\text{trial})}$ and the SIF range $\Delta K_{(\text{trial})}$ (see appendix G1). The best-fit equation with the form of $(dq/dN)_{(\text{trial})} = C_{(\text{trial})}\Delta K^M$ is obtained by using $(dq/dN)_{(\text{trial})}$ and $\Delta K_{(\text{trial})}$ values. Finally, by comparing $(dq/dN)_{(\text{trial})}$ with the experimental values $(dq/dN)_{(\text{experiment})}$, the calibrated value of the parameter $A_2 = 1055$ is obtained by using Eq. (4.13b) and the parameter $B_{2(k)(j)}$ is obtained for each interaction by using Eq. (4.34b).

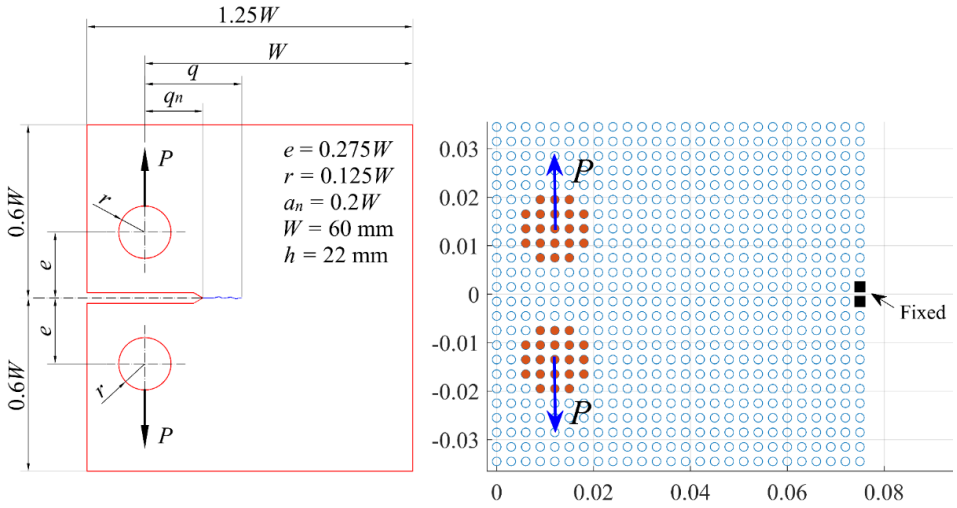

(a) (b)

Fig. 4.3. Mode I fatigue problem (a) geometry (b) PD discretized model

Fig. 4.4 shows the fatigue damage evolution on the plate under the mode-I loading condition. After 2000 loading cycles, the crack starts propagating as shown in Fig. 4.4(a). As expected, the crack propagates along its initial direction toward the right edge of the plate as shown in Fig. 4.4(b-d). After 40850 loading cycles, the crack reaches the location at $x = 0.0522$ mas shown in Fig. 4.4(d). Fig. 4.5 shows crack length, q versus load cycle, N for fatigue crack growth of the plate. As can be observed from the figure, the PD prediction results have good agreement with the experimental results [136]. The crack length, q versus load cycle, N predicted by the PD model agrees very well with the experimental curve for the first 30000 cycles. Later, the predicted crack growth is slightly quicker than the experimental results. The final predicted fatigue life is $N_f^{PD} = 40850$ (cycles), meanwhile, the experimental value is $N_f^{\text{experimental}} = 42600$ (cycles). Therefore, the relative error in terms of the final fatigue life can be estimated as

$$error(\%) = \frac{N_f^{PD} - N_f^{\text{ex perimental}}}{N_f^{\text{ex perimental}}} \times 100 = -4.108\% \tag{4.37}$$

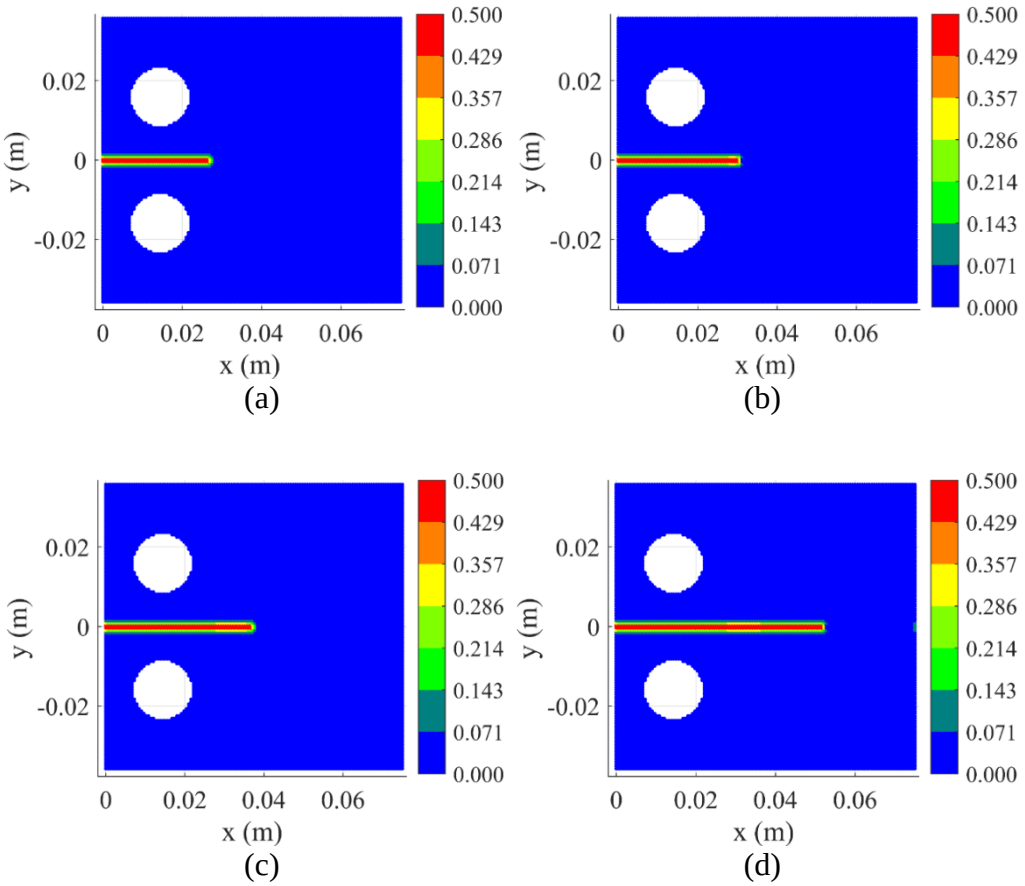

Fig. 4.4. Fatigue damage evolution at (a) 2000 cycles, (b) 15000 cycles, (c) 30000 cycles, (d) 40850 cycles

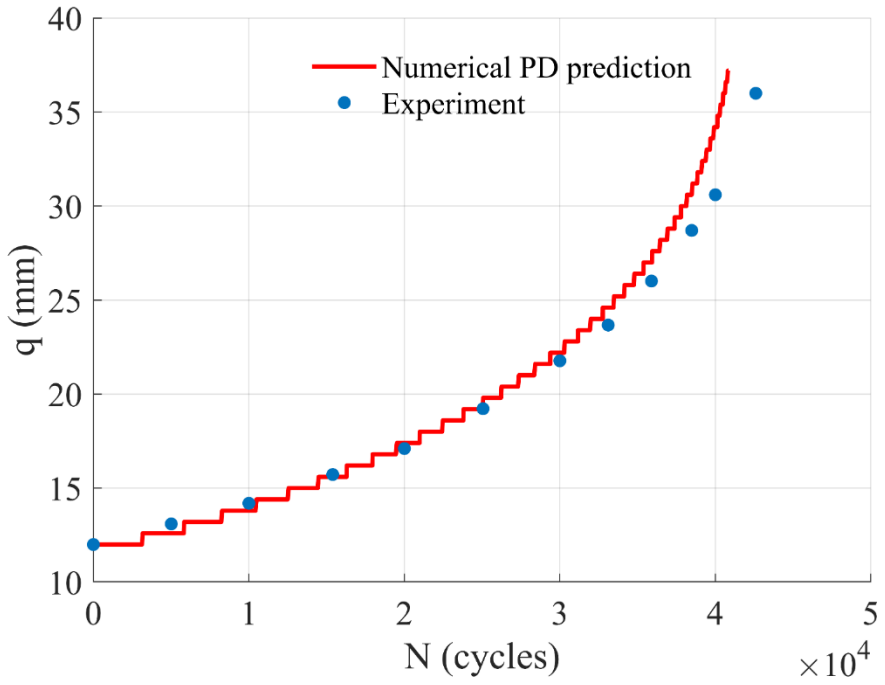

Fig. 4.5. Fatigue crack length, q versus load cycle, N (the experimental data is obtained from [136])

4.4.2. Mixed-mode fatigue crack propagation

After verifying the energy-based PD fatigue model for mode-I fatigue crack evolution, the proposed PD model is further used to predict fatigue damages in the mixed-mode loading conditions as shown in Fig. 4.6. The dimensions for the specimen are in mm as shown in Fig. 4.6(b). The plate has an initial notch with a length of 40 mm and a 5 mm initial fatigue crack is created [136]. The material properties are the same as in Section 7.5.1. The loading is defined by the extreme load $P = 16$ kN, load ratio $R = 0.1$, and the loading angle α as shown in Fig. 4.6(a) and Fig. 4.7(a).

The boundary and loading conditions for the numerical models suggested by Sajith, et al. [136] are shown in Fig. 4.7(a). In PD, the model is uniformly discretized with a mesh size of $\Delta x = 6 \times 10^{-4}$ mm. As shown in Fig. 4.7(b), material points, shown in blue, green, black, and red, which are associated with 6 cut-outs, are defined as rigid with the elastic modulus of $E_{rigid} = 200E$. Material points, shown in black in Fig. 4.7(b), located at the centres of the lower cut-outs are fixed. Meanwhile, material points, shown in red in Fig. 4.7(b), located at the centres of the upper cut-outs are subjected to applied forces as [136]

$$F_1 = P\left(0.5\cos\alpha + \left(e/f\right)\sin\alpha\right) \tag{4.38a}$$

$$F_2 = -P\sin\alpha \tag{4.38b}$$

$$F_3 = P\left(0.5\cos\alpha - \left(e/f\right)\sin\alpha\right) \tag{4.38c}$$

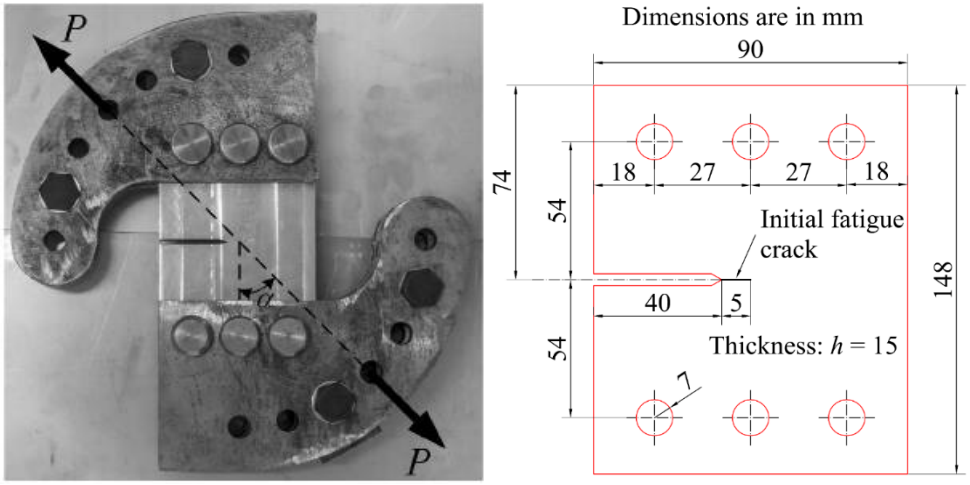

(a) (b)

Fig. 4.6. Mixed-mode fatigue problem (a) experimental configuration in [136], (b) specimen's dimensions

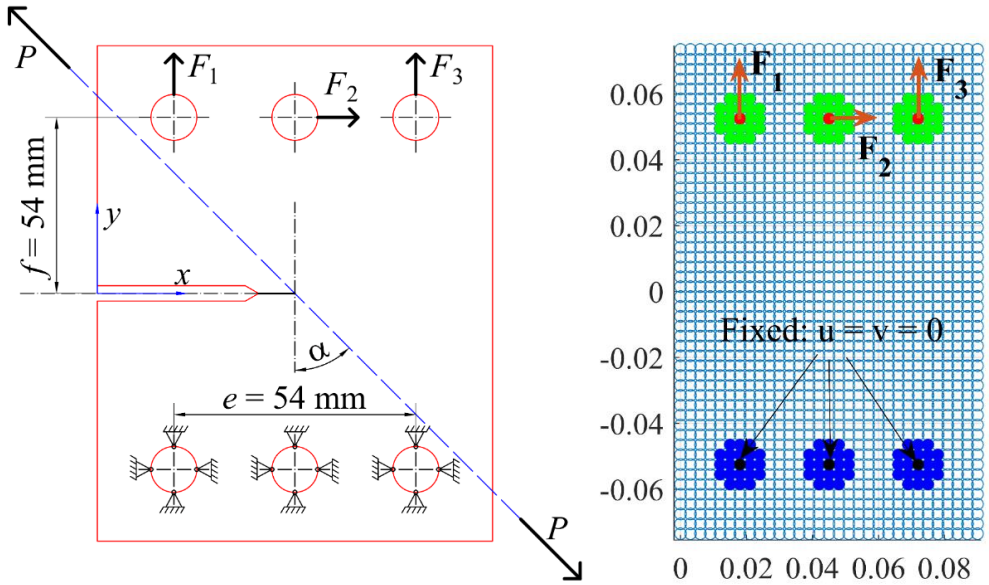

(a) (b)

Fig. 4.7. Loading and boundary conditions (a) suggested by Sajith, et al. [136], (b) used in the PD model

7.5.2.1. Crack path prediction

Fig. 4.8 shows the fatigue crack propagation in the mixed-mode loading in the case of $\alpha = 45^o$. As shown in Fig. 4.8(a), the crack starts propagating upward at 10000 loading cycles. The angle of crack propagation with respect to the horizontal axis is measured numerically as $\beta_{PD} = 38.66^o$ at 30000 loading cycles as shown in Fig. 4.8(c). This observation has good agreement with the experimental results which is $\beta_{experiment} = 40.263^o$. Later, the crack propagates with a slightly smaller angle and reaches the final fatigue crack growth state (before phase III) at 42768 loading cycles as shown in Fig. 4.8(d). The slight reduction of crack propagation angles is also observed in the experiment by Sajith, et al. [136], Chung and Yang [139], Borrego, et al. [140].

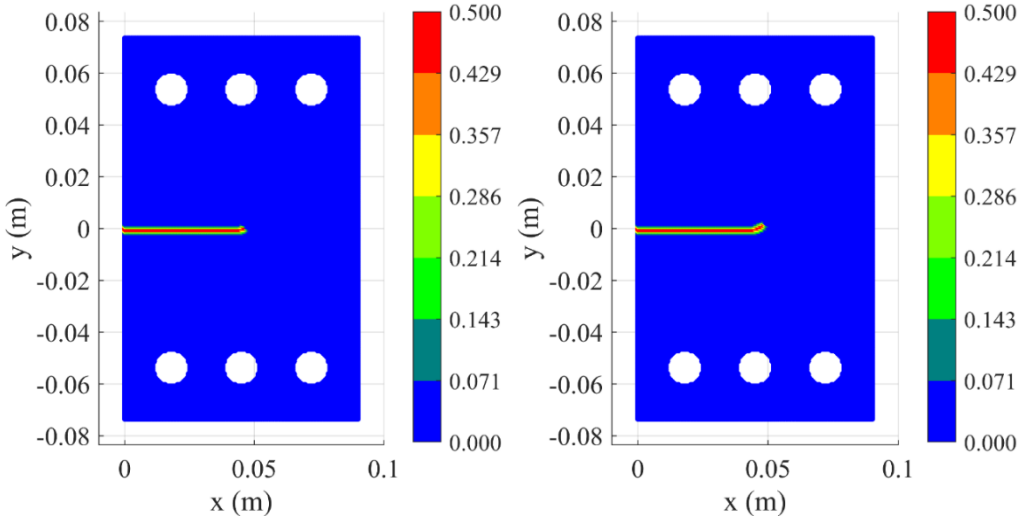

(a) (b)

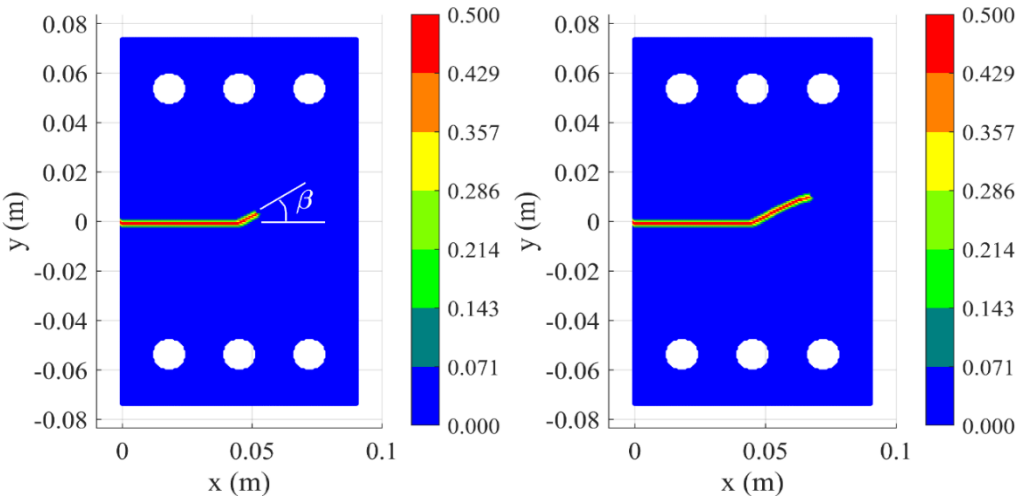

Fig. 4.8. Fatigue crack evolution in mixed-mode loading with $\alpha = 45^o$ at (a) 10000 (b) 20000, (c) 30000, (d) 42768 cycles

Fig. 4.9 shows the prediction results for the mixed-mode fatigue crack propagation in the case of $\alpha = 60^o$. Fig. 4.9(a-c) shows the crack evolution at 20000, 35000 and 44500 loading cycles, respectively. Similar to the previous loading condition, the fatigue crack also propagates upward but with a larger angle $\beta_{PD} = 50.19^o$. This observation has very good agreement with the experimental results $\beta_{ex\,periment} = 51.33^o$[136]. Similar to the previous loading condition, after 44500 loading cycles, the crack starts propagating with a slightly smaller angle and reaches the final fatigue crack growth state (before phase III) at 53727 loading cycles as shown in Fig. 4.9(d). This observation has good agreement with the experimental results studied by Sajith, et al. [136], Chung and Yang [139], Borrego, et al. [140].

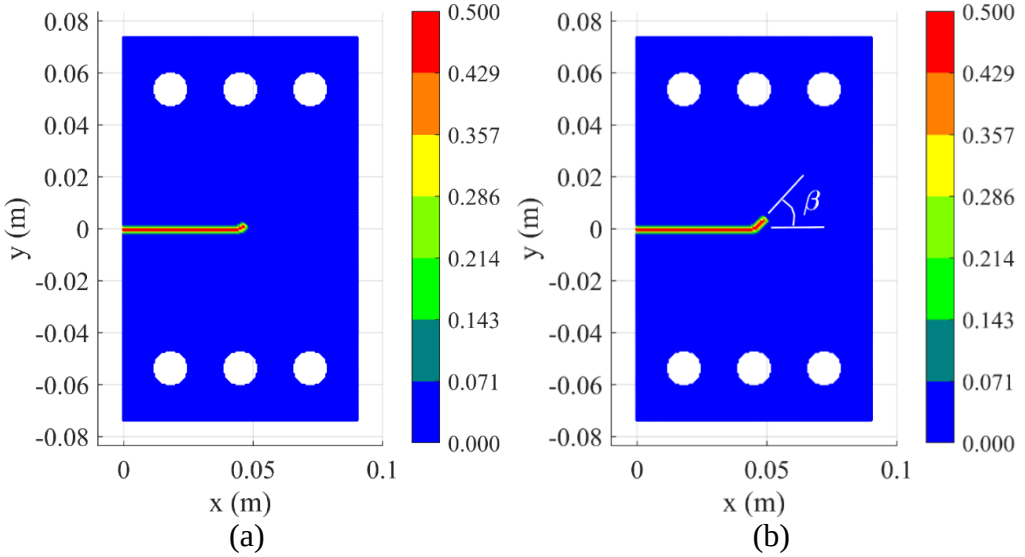

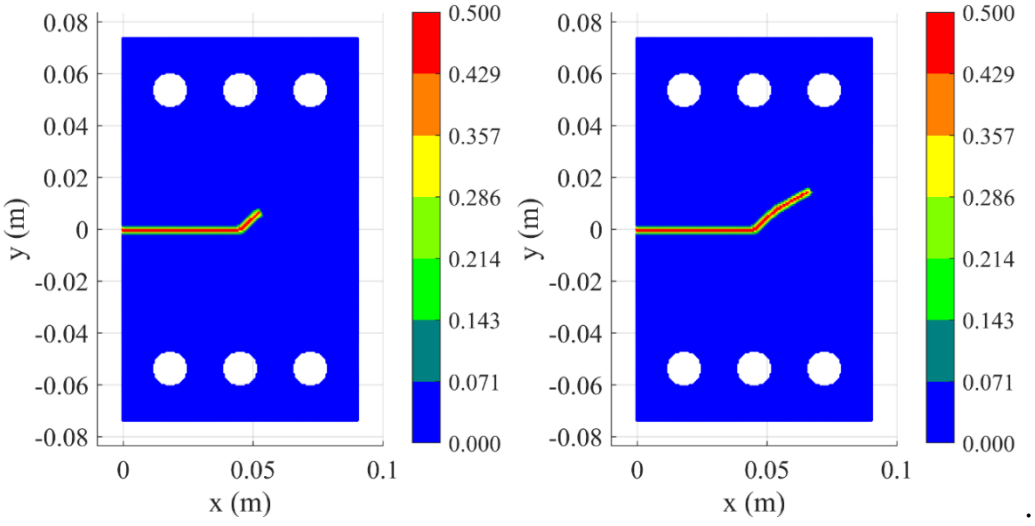

(c) (d)

Fig. 4.9. Fatigue crack evolution in mixed-mode loading with $\alpha = 60^o$ at (a) 20000 (b) 35000, (c) 44500, (d) 53727 cycles

Fig. 4.10 shows the crack tip positions in the two loading conditions predicted by the proposed energy-based PD fatigue model. As can be seen from the figure, the PD results have good agreement with the experimental results studied by Sajith, et al. [136] which shows the accuracy of the proposed PD model in terms of crack path prediction.

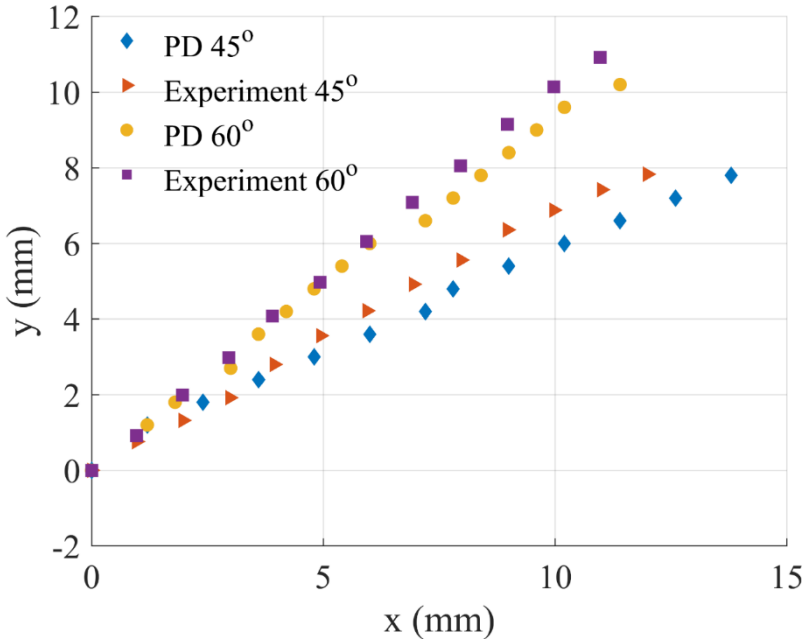

Fig. 4.10. Crack tip locations (the experimental data is obtained from [136])

7.5.2.2. Fatigue life prediction

Fig. 4.11 shows the fatigue crack length, q versus load cycle, N in two loading conditions. As can be seen from Fig. 4.11(a) for the loading condition with $\alpha = 45^o$, the predicted results have very good agreement with experimental results in the first 28000 loading cycles. Later, there is a small difference between the two results. The predicted results show a slightly slower crack growth compared to the

observation from the experiment [136]. As can be seen from Fig. 4.11(b), the predicted crack growth in case of $\alpha = 60^o$ has very good agreement with the experimental results which shows the accuracy of the proposed PD fatigue model in terms of fatigue life prediction.

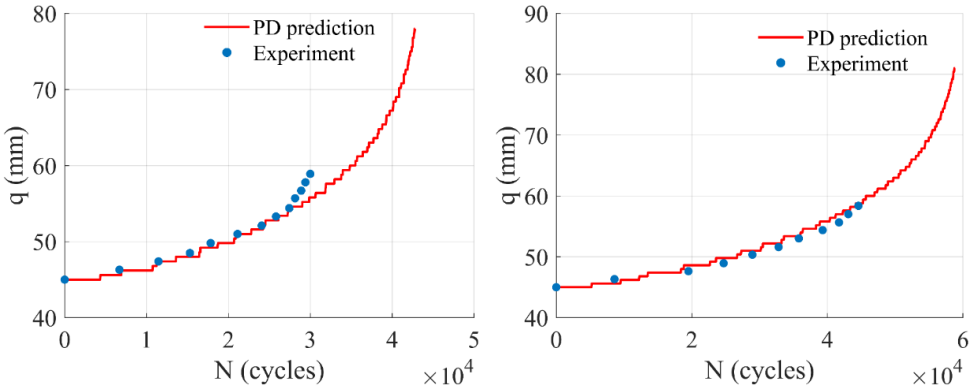

(a) (b)

Fig. 4.11. Crack length, q versus load cycle, N for mixed-mode fatigue crack growth with load angle (a) $\alpha = 45^o$, (b) $\alpha = 60^o$ (the experimental data is obtained from [136])

4.5. Concluding remarks

In this Chapter, a novel energy-based PD model for fatigue damage prediction is proposed. The definition of cyclic bond energy release rate range is proposed and used for fatigue equations for the first time in the PD literature. The numerical procedure to predict fatigue cracking by using the proposed PD model is presented. The capability of the proposed PD model is verified by considering mode-I and mixed-mode fatigue crack propagations. The results predicted by the proposed PD model show a good agreement with the experimental results in terms of the crack paths as well as the crack growth rates. The developed PD model can be further extended to the 3D formulation and it can also be used to predict fatigue damage for structures during the operation process.

5. COUPLING PERIDYNAMICS WITH MACHINE LEARNING

5.1. Introduction

In peridynamics, due to nonlocal interactions, solving equations of motion could be time-consuming. By contrast, with the support of computer resources as well as the rapid growth of available data, artificial intelligence (AI), machine learning (ML), and data analytics are providing an alternative solution for physics-based models. These data-driven models can be applicable for many scientific disciplines such as image recognition [141], natural language processing [142], cognitive science [143], and genomics [144]. In engineering, machine learning and artificial intelligence also show potential applications in many areas, including material science [145], fluid dynamics [146, 147], structural health monitoring [148], additive manufacturing [149], fracture mechanics, and failure analysis [150-152].

As proposed in [150, 152] for failure analysis, the neural networks are trained by using the crack propagation data that is generated in trial numerical predictions, which can be very computationally expensive and limited. On the other hand, when available data are limited, the vast majority of recent machine learning techniques are lacking robustness and accuracy [153]. Therefore, a hybrid approach of combining machine learning and physics-based modeling becomes highly beneficial. Therefore, in this chapter, a PD-based machine learning model or fracture prediction is developed. Moreover, a hybrid approach of coupling machine learning and peridynamic models for fracture prediction of structures is presented. Specifically, the PD model is applied for special regions in structures such as near crack surfaces or near boundary areas. Meanwhile, the ML model is used for the remaining regions to reduce the computational cost.

The machine learning models to find displacements of a material point based on displacements of its family members and its external body forces in one-dimensional (1D) and two-dimensional (2D) structures are presented. The capability of the hybrid approach is verified by considering various examples for 1D and 2D structures. The results predicted by the coupled models are compared with FEA and conventional PD results. For further verifying the capability of the coupling model, progressive damages in a plate with a pre-existing crack subjected to tension, on a 2D representation of a three-point bending test, on a plate subjected to dynamic loads are presented.

5.2. Multiple linear regression

In this section, the basic concept of multiple linear regression is presented. According to Montgomery et al. [154] and Alpaydin [155], in the multiple linear regression, the numeric output y is assumed to be written as a function of several input variables, $x_1, x_2, \dots, x_N$ and noise as

$$y = w_0 + w_1 x_1 + w_2 x_2 + \cdots + w_N x_N + \varepsilon \tag{5.1}$$

where $x_1, x_2, \dots, x_N$ represent the input variables that can be called the regressors. The parameters $w_0, w_1, \dots, w_N$ represent regression coefficients that need to be determined. The parameter ε represents the noise of the model.

The coefficients in Eq. (5.1) can be determined based on the least square criterion [154, 155]. The sum of the squares of the differences between the predicted values and the correct outputs are minimized. The minimization of the squared errors can be expressed as follows;

Let's assume that we have training data as $\left(x_{1(i)}, x_{2(i)}, \ldots, x_{N(i)}, y_{(i)}\right),\ i = 1, \ldots, M$. Therefore, Eq. (5.1) can be rewritten for every single data as

$$y_i = w_0 + w_1 x_{1(i)} + w_2 x_{2(i)} + \cdots + w_N x_{N(i)} + \varepsilon_{(i)}, \quad i = 1, 2, \ldots, M \tag{5.2}$$

The sum of squared errors can be calculated as

$$S(w_0, w_1, \cdots, w_N) = \sum_{i=1}^{M} \left(y_i - \left(w_0 + w_1 x_{1(i)} + w_2 x_{2(i)} + \cdots + w_N x_{N(i)} \right) \right)^2 \tag{5.3}$$

To minimize the squared errors given in Eq. (5.3), the coefficients w_j, $j = 1, 2, \ldots, N$ must satisfy the following conditions

$$\frac{\partial S}{\partial w_j} = 0, \quad j = 0, 1, 2, \ldots, N \tag{5.4}$$

By substituting Eq. (5.3) into Eq. (5.4), the following relations are obtained

$$\begin{aligned}
&\sum_{i=1}^{M} y_i = M w_0 + w_1 \sum_{i=1}^{M} x_{1(i)} + w_2 \sum_{i=1}^{M} x_{2(i)} + \cdots + w_N \sum_{i=1}^{M} x_{N(i)} \\
&\sum_{i=1}^{M} x_{1(i)} y_i = w_0 \sum_{i=1}^{M} x_{1(i)} + w_1 \sum_{i=1}^{M} \left(x_{1(i)} \right)^2 + w_2 \sum_{i=1}^{M} x_{1(i)} x_{2(i)} + \cdots + w_N \sum_{i=1}^{M} x_{1(i)} x_{N(i)} \\
&\quad \vdots \\
&\sum_{i=1}^{M} x_{N(i)} y_i = w_0 \sum_{i=1}^{M} x_{N(i)} + w_1 \sum_{i=1}^{M} x_{N(i)} x_{1(i)} + w_2 \sum_{i=1}^{M} x_{N(i)} x_{2(i)} + \cdots + w_N \sum_{i=1}^{M} \left(x_{N(i)} \right)^2
\end{aligned} \tag{5.5}$$

The relations in Eq. (5.5) can be rewritten in a matrix form as

$$\mathbf{X}^T \mathbf{X} \mathbf{w} = \mathbf{X}^T \mathbf{y} \tag{5.6a}$$

with

$$\mathbf{X} = \begin{bmatrix} 1 & x_{1(1)} & x_{2(1)} & \cdots & x_{N(1)} \\ 1 & x_{1(2)} & x_{2(2)} & \cdots & x_{N(2)} \\ \vdots & & & & \\ 1 & x_{1(M)} & x_{2(M)} & \cdots & x_{N(M)} \end{bmatrix}, \ \mathbf{w} = \begin{bmatrix} w_0 \\ w_1 \\ \vdots \\ w_N \end{bmatrix}, \ \mathbf{y} = \begin{bmatrix} y_{(1)} \\ y_{(2)} \\ \vdots \\ y_{(M)} \end{bmatrix} \tag{5.6b}$$

Therefore, the vector of coefficients, ***w***, can be obtained as

$$\mathbf{w} = \left(\mathbf{X}^T \mathbf{X} \right)^{-1} \mathbf{X}^T \mathbf{y} \tag{5.7}$$

5.3. Peridynamic models for 1D and 2D structures

In this section, the PD models for 1D and 2D structures are summarized. The PD equation of motion for 1D structures can be found in Eq. (2.28a) in Chapter 2 as [20, 43, 62, 75]

$$\rho \ddot{u}_{(k)} = C_{ax} \sum_{j=1}^{N} \frac{u_{(j)} - u_{(k)}}{\xi} V_{(j)} + b_{x(k)} \tag{5.9a}$$

with

$$b_{x(k)} = \frac{F_{x(k)}}{A\Delta x} \tag{5.9b}$$

and

$$C_{ax} = \frac{2E}{A\delta^2} \tag{5.9c}$$

where $b_{x(k)}$ represents the axial body force applied on the material point k, ξ represents the distance between material points k and j. The term C_{ax} represents the PD bond constant for axial deformations.

For a static state with $\ddot{u}_{(k)} = 0$, Eq. (5.9a) can be rewritten as

$$b_{x(k)} = -C_{ax} \sum_{j=1}^{N} \left(\frac{u_{(j)} - u_{(k)}}{\xi} \right) V_{(j)} \tag{5.10}$$

The bond-based PD equations of motion for 2D structures can be found in Eq. (4.17) by ignoring dilatation terms as [20, 43, 61, 75]

$$\rho h \ddot{u}_{(k)} = \sum_{j=1}^{N} C \mu_{(k)(j)} s_{(k)(j)} \cos\varphi V_{(j)} + \bar{b}_{x(k)} \tag{5.11a}$$

$$\rho h \ddot{v}_{(k)} = \sum_{j=1}^{N} C \mu_{(k)(j)} s_{(k)(j)} \sin\varphi V_{(j)} + \bar{b}_{y(k)} \tag{5.11b}$$

with

$$\bar{b}_{x(k)} = \frac{F_{x(k)}}{\Delta x^2} \tag{5.11c}$$

$$\bar{b}_{y(k)} = \frac{F_{y(k)}}{\Delta x^2} \tag{5.11d}$$

$$C = \frac{12E}{(1+\nu)\pi\delta^3} \tag{5.11e}$$

where $\bar{b}_{x(k)}$ and $\bar{b}_{y(k)}$ represent applied force per unit area as given in Chapter 2 [61], Δx represents uniform mesh size in the PD discretized model. The term $s_{(k)(j)}$ represents linearized bond stretch for in-plane deformations as given in Eq. (2.65), h represents the thickness of the plate, C represents bond constant for in-plane deformation. Note that, $C = 4b_{ip}$, where b_{ip} is given in Eq. (2.62d) in chapter 2.

If a static condition with $\ddot{u}_{(k)} = \ddot{v}_{(k)} = 0$ is considered, Eqs. (5.11a-b) can be rewritten as

$$\bar{b}_{x(k)} = -\left(\sum_{j=1}^{N} C \mu_{(k)(j)} s_{(k)(j)} \cos\varphi V_{(j)} \right) \tag{5.12a}$$

$$\bar{b}_{y(k)} = -\left(\sum_{j=1}^{N} C \mu_{(k)(j)} s_{(k)(j)} \sin\varphi V_{(j)} \right) \tag{5.12b}$$

5.4. PD-based machine learning model

In this section, the PD-based machine learning models for 1D and 2D structures are presented. The displacement of one material point is expressed as a linear function of displacements of its family members in the horizon size of $\delta = 3.015\Delta x$ and the external forces applied to it. The training data are generated by using modal analysis in ANSYS. The PD-based machine learning model is obtained from the data set by using linear regression.

5.4.1. PD based machine learning model for one-dimensional structures

As presented in Eq. (5.10), within the linear elasticity, the relation between applied body force and displacements of material points is linear. Moreover, the relationship between the displacement of a material point and its family members can also be linear. Therefore, the displacement value for a material point can be expressed as a linear function of displacements of its family members and the external force applied to it as

$$\begin{aligned} u_{(k)} = {} & m_1 u_{(k-3)} + m_2 u_{(k-2)} + m_3 u_{(k-1)} + m_4 u_{(k+1)} \\ & + m_5 u_{(k+2)} + m_6 u_{(k+3)} + m_7 \left(\frac{F_{x(k)} \Delta x}{AE} \right) \end{aligned} \tag{5.13a}$$

or

$$u_{(k)} = \mathbf{m}_{(j)} \cdot \mathbf{u}_{(j)} + m_7 \left(\frac{F_{x(k)} \Delta x}{AE} \right) \tag{5.13b}$$

with

$$\mathbf{m}_{(j)} = \begin{bmatrix} m_1 & m_2 & m_3 & m_4 & m_5 & m_6 \end{bmatrix} \tag{5.13c}$$

$$\mathbf{u}_{(j)} = \begin{bmatrix} u_{(k-3)} & u_{(k-2)} & u_{(k-1)} & u_{(k+1)} & u_{(k+2)} & u_{(k+3)} \end{bmatrix} \tag{5.13d}$$

where $m_i, i = 1, \ldots, 7$ represent coefficients that need to be determined for the ML model. The term $F_{x(k)}$ represents the axial force applied on the material point k, Δx represents mesh size in the discretized model, A represents the cross-sectional area of the 1D bar, and E represents material elastic modulus. In Eq. (5.13), $(k-3), \ldots, (k+3)$ represent family members of the material point k as shown in Fig. 5.1.

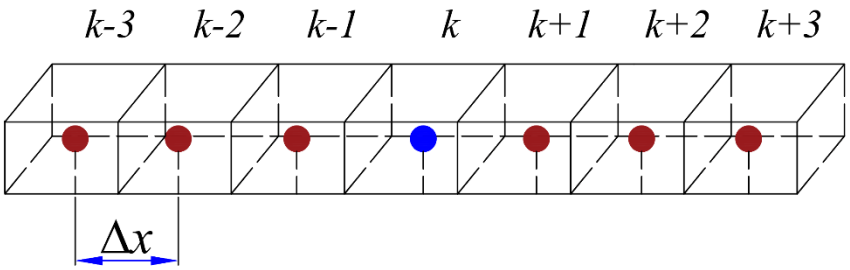

Fig. 5.1. A material point with its family members, $\delta = 3\Delta x$

Note that with the mesh size, elastic modulus, and cross-sectional area presented in the last term of Eq. (5.13a), the coefficient m_7 is expected to be independent of these geometrical and material properties. As a result, the expected ML model can be applied for any cross-sectional area, mesh size, and elastic modulus.

Generating the training and testing data set

In this section, the training and testing data for Eq. (5.13a) is obtained from the modal analysis. The data set includes seven input variables $(u_{(k-3)}, u_{(k-2)}, u_{(k-1)}, u_{(k+1)}, u_{(k+2)}, u_{(k+3)}, F_{x(k)}\Delta x/AE)$ and one output variable $u_{(k)}$.

By using Eq. (5.9c), the last input variable in Eq. (5.13a) can be represented as

$$\frac{F_{x(k)}\Delta x}{AE} = \frac{b_{x(k)}\left(\Delta x\right)^2}{E} \tag{5.14}$$

By utilizing the PD relation given in Eq. (5.10), the input variable in Eq. (5.14) can be calculated as

$$\frac{F_{x(k)}\Delta x}{AE} = \frac{\left(-C_{ax}\sum_{j=1}^{N}\frac{u_{(j)}-u_{(k)}}{\xi}V_{(j)}\right)\left(\Delta x\right)^2}{E} \tag{5.15}$$

To generate the data set for 1D structures, a bar with a length of $L = 6$ m, a cross-sectional area of $A = 0.01$ m^2 and the elastic modulus of $E = 2 \times 10^{11}$ N/m^2 is chosen. The bar is discretized with 6 elements (7 material points) with a uniform mesh size of $\Delta x = 1$ m and the link180 element is used by allowing only axial deformations. The bar is considered for 10 basic boundary conditions as shown in Fig. 5.2.

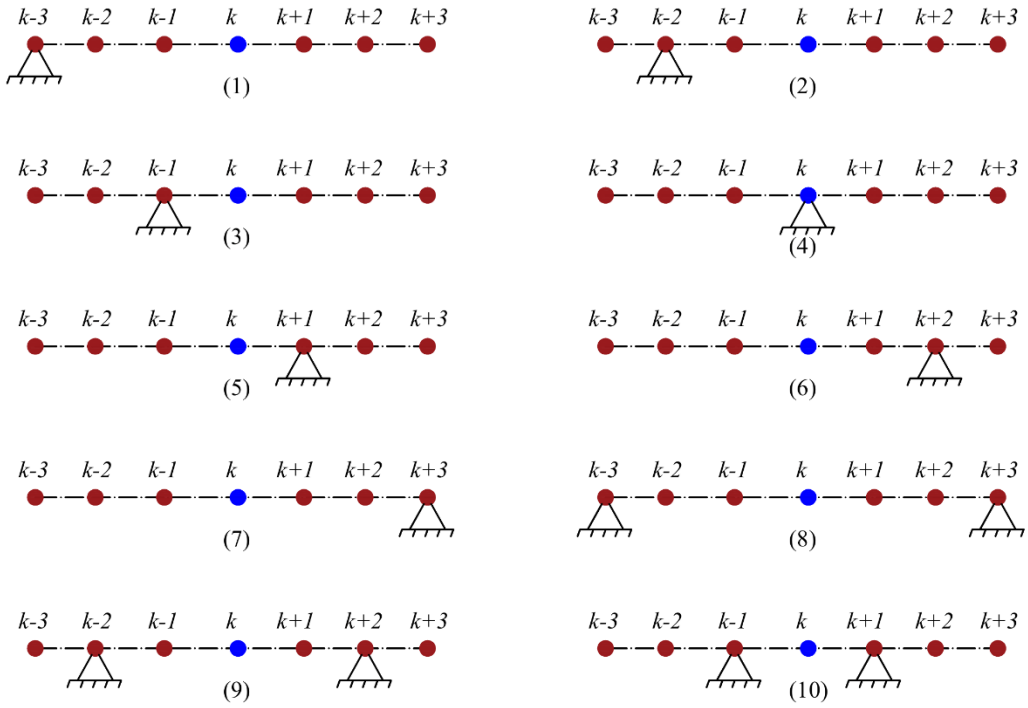

Fig. 5.2. Boundary conditions in modal analyses for 1D structure

By considering all possible vibration modes of the bar for 10 boundary conditions as shown in Fig. 5.2, 50 data sets are obtained. The data sets are arranged as shown in Table 5.1. Specifically, for each vibration mode of the bar, the displacements of all nodes are obtained. The displacement of node k is added into the output variable column in Table 5.1. The displacements of the remaining nodes ($u_{(k-3)}$, $u_{(k-2)}$, $u_{(k-1)}$, $u_{(k+1)}$, $u_{(k+2)}$, $u_{(k+3)}$) are added into the first 6 columns in Table 5.1. The input variable in 7^{th} column is calculated by using Eq. (5.15).

Table 5.1. Arrangement for the dataset for 1D machine learning model

dataset	Input variables							Output variable
	$u_{(k-3)}$	$u_{(k-2)}$	$u_{(k-1)}$	$u_{(k+1)}$	$u_{(k+2)}$	$u_{(k+3)}$	$\frac{F_{x(k)}\Delta x}{AE}$	$u_{(k)}$
1	0	0.0817	0.1414	0.1414	0.0817	0	0.0399	0.16331
2	0	-0.1514	-0.1514	0.1514	0.1514	0	0	0
.	.	.	.	.	.	.	.	.
.	.	.	.	.	.	.	.	.
49	0.2957	-0.2812	0.2392	0.0914	0	0	-0.1808	-0.1738
50	0.2719	-0.2626	0.2355	0.1359	-0.0704	0	-0.1968	-0.1922

Finding the coefficients for the ML model

The data are split into two parts for training and testing purposes. The first 45 data sets are used for training and the remainders are used for testing the accuracy of the ML model. By using linear regression, the coefficients for the relation given in Eq. (5.13a) are obtained as

$$m_1 = m_6 = 0.05134596 \tag{5.16a}$$

$$m_2 = m_5 = 0.14955135 \tag{5.16b}$$

$$m_3 = m_4 = 0.29910269 \tag{5.16c}$$

$$m_7 = 1.35942174 \tag{5.16d}$$

To evaluate the accuracy of the regression model, the obtained regression model is used to predict output for the test data. By using Eq. (5.3), the mean squared error between the predicted values and the original output values in the testing data is calculated as 9.09×10^{-20}.

Extending the PD based ML model for dynamic problems

The machine learning model provided in Eq. (5.13a) can be used for static problems. The model can also be further developed by adding the inertia term for dynamic problems.

The relationship provided in Eq. (5.13a) can be rewritten as

$$\frac{E}{\Delta x^2}\frac{1}{m_7}\begin{pmatrix} m_1 u_{(k-3)} + m_2 u_{(k-2)} + m_3 u_{(k-1)} \\ + m_4 u_{(k+1)} + m_5 u_{(k+2)} + m_6 u_{(k+3)} - u_{(k)} \end{pmatrix} + b_{x(k)} = 0 \tag{5.17}$$

Next, by adding the inertia term, Eq. (5.17) can be extended for dynamic problems as

$$\rho \ddot{u}_{(k)} = \frac{E}{\Delta x^2}\frac{1}{m_7}\begin{pmatrix} m_1 u_{(k-3)} + m_2 u_{(k-2)} + m_3 u_{(k-1)} \\ + m_4 u_{(k+1)} + m_5 u_{(k+2)} + m_6 u_{(k+3)} - u_{(k)} \end{pmatrix} + b_{x(k)} \tag{5.18a}$$

or

$$\rho \ddot{u}_{(k)} = \frac{E}{\Delta x^2}\frac{1}{m_7}\left(\mathbf{m}_j \cdot \mathbf{u}_{(j)} - u_{(k)}\right) + b_{x(k)} \tag{5.18b}$$

where the linear regression coefficients are presented in Eq. (5.16).

5.4.2. PD based machine learning model for two-dimensional structures

In this section, first, the machine learning model for 2D is presented. Next, training and testing data set are obtained from modal analyses by using ANSYS. The data set is then used for linear regression analysis to obtain the regression coefficients for the machine learning model.

The displacement of the material point k can be determined based on the displacements of its family members and the applied forces. In the discretized model, the material point k with a horizon size of $\delta = 3.015\Delta x$ has 28 family members that can be numbered in the order as shown in Fig. 5.3.

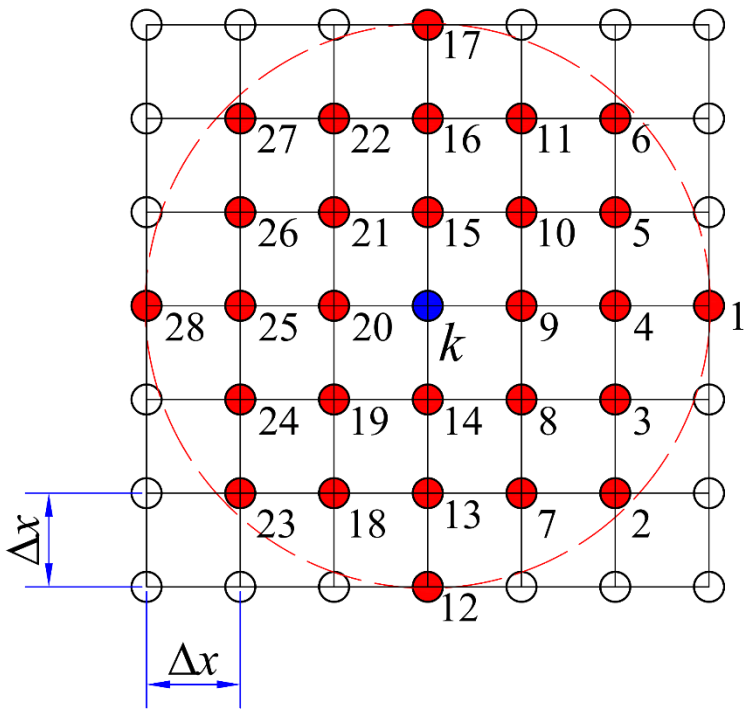

Fig. 5.3. PD horizon in the 2D model

Similar to the 1D structure, the displacement of a material point k can be assumed as a linear function of the displacements of its family members and the applied forces as

$$u_{(k)} = \sum_{j=1}^{28}\left(a_j u_j + b_j v_j\right) + c\left(\frac{2(1+\nu)}{Eh}F_{x(k)}\right) + d\left(\frac{2(1+\nu)}{Eh}F_{y(k)}\right) \tag{5.19a}$$

$$v_{(k)} = \sum_{j=1}^{28}\left(m_j u_j + n_j v_j\right) + p\left(\frac{2(1+\nu)}{Eh}F_{x(k)}\right) + q\left(\frac{2(1+\nu)}{Eh}F_{y(k)}\right) \tag{5.19b}$$

or

$$u_{(k)} = \mathbf{a}_j \cdot \mathbf{u}_j + \mathbf{b}_j \cdot \mathbf{v}_j + c\left(\frac{2(1+\nu)}{Eh}F_{x(k)}\right) + d\left(\frac{2(1+\nu)}{Eh}F_{y(k)}\right) \tag{5.19c}$$

$$v_{(k)} = \mathbf{m}_j \cdot \mathbf{u}_j + \mathbf{n}_j \cdot \mathbf{v}_j + p\left(\frac{2(1+\nu)}{Eh}F_{x(k)}\right) + q\left(\frac{2(1+\nu)}{Eh}F_{y(k)}\right) \tag{5.19d}$$

with

$$\mathbf{a}_j = \left[a_1, a_2, \cdots, a_{28}\right] \tag{5.19e}$$

$$\mathbf{b}_j = \left[b_1, b_2, \cdots, b_{28}\right] \tag{5.19f}$$

$$\mathbf{m}_j = \left[m_1, m_2, \cdots, m_{28}\right] \tag{5.19g}$$

$$\mathbf{n}_j = \left[n_1, n_2, \cdots, n_{28}\right] \tag{5.19h}$$

$$\mathbf{u}_j = \left[u_1, u_2, \cdots, u_{28}\right] \tag{5.19g}$$

$$\mathbf{v}_j = \left[v_1, v_2, \cdots, v_{28}\right] \tag{5.19h}$$

where a_j, b_j, m_j, n_j, c, d, p, q are coefficients that need to be determined for the ML model. The terms $F_{x(k)}$, $F_{y(k)}$ represent external forces in x, y directions that are applied to the material point k.

Note that the vectors $\boldsymbol{a}_j$, $\boldsymbol{b}_j$, $\boldsymbol{m}_j$, $\boldsymbol{n}_j$ store the coefficients a_j, b_j, m_j, n_j which are

associated with $1^{st}, \ldots, 28^{th}$ family members of the material point k. Similarly, vectors $\boldsymbol{u}_j$ and $\boldsymbol{v}_j$ store displacement components of $1^{st}, \ldots, 28^{th}$ family members of the material point k as shown in Fig. 5.3.

Generating the training and testing data set

In this section, the training and testing data for Eq. (5.19) is obtained from the modal analysis. The data set includes 58 input variables and two output variables $(u_{(k)}, v_{(k)})$.

By using Eq. (5.11c, d, g) the last two terms on the right-hand side of Eq. (5.19c-d) can be represented as

$$\frac{2(1+\nu)}{Eh} F_{x(k)} = \frac{\bar{b}_{x(k)}}{Ch\Delta x} \frac{24}{\pi(3^3)} \tag{5.20a}$$

$$\frac{2(1+\nu)}{Eh} F_{y(k)} = \frac{\bar{b}_{y(k)}}{Ch\Delta x} \frac{24}{\pi(3^3)} \tag{5.20b}$$

where C represent the bond constant given in Eq. (5.11g).
By using the PD relationships given in Eq. (5.12), the input variables in Eq. (5.20) can be calculated as

$$\frac{2(1+\nu)}{Eh} F_{x(k)} = \frac{-\left(\sum_{j=1}^{N} C\mu_{(k)(j)} s_{(k)(j)} \cos\varphi V_{(j)}\right)}{Ch\Delta x} \frac{24}{\pi(3^3)} \tag{5.21a}$$

$$\frac{2(1+\nu)}{Eh} F_{y(k)} = \frac{-\left(\sum_{j=1}^{N} C\mu_{(k)(j)} s_{(k)(j)} \sin\varphi V_{(j)}\right)}{Ch\Delta x} \frac{24}{\pi(3^3)} \tag{5.21b}$$

To generate data set for 2D structures, a 6×6 m^2 square plate is chosen as shown in Fig. 5.3. The plate has a thickness of 0.1 m, the elastic modulus of $E = 2 \times 10^{11}$ N/m^2 and Poisson's ratio of $\nu = 1/3$. The plate is discretized with a mesh size of $\Delta x = 1$ m. The material point k located at $(x = 3\text{ m}, y = 3\text{ m})$, shown in blue, and its 28 family members, shown in red, are considered for the data set.

Note that, the dimensions of the plate, as well as the elastic modulus, are chosen arbitrarily for obtaining the data set. The ML model is expected to be applicable for any geometry and linear elastic material.

The data set is obtained from modal analyses for the plate by using the PLANE182 element in ANSYS. The plate is considered in 16 basic boundary conditions as shown in Fig. 5.4. In each boundary condition, the 20 possible vibration modes of the plate are considered. The displacements of the material point k and its 28 family members are obtained and added into the data set. Therefore, the data set includes 320 deformation states and it is arranged as shown in Table 5.2. Specifically, in each vibration mode of the plate, the displacements of all nodes are obtained. The displacements of node k (see Fig. 5.3), $(u_{(k)}, v_{(k)})$, are added into the two last columns in Table 5.2 for the output variables. The displacements of the remaining nodes $(u_1, u_2, \cdots u_{28}, v_1, v_2, \cdots v_{28})$ are added for the first 56 columns in Table 5.2. The input variables in 57^{th} and 58^{th} columns are calculated by using Eq. (5.21).

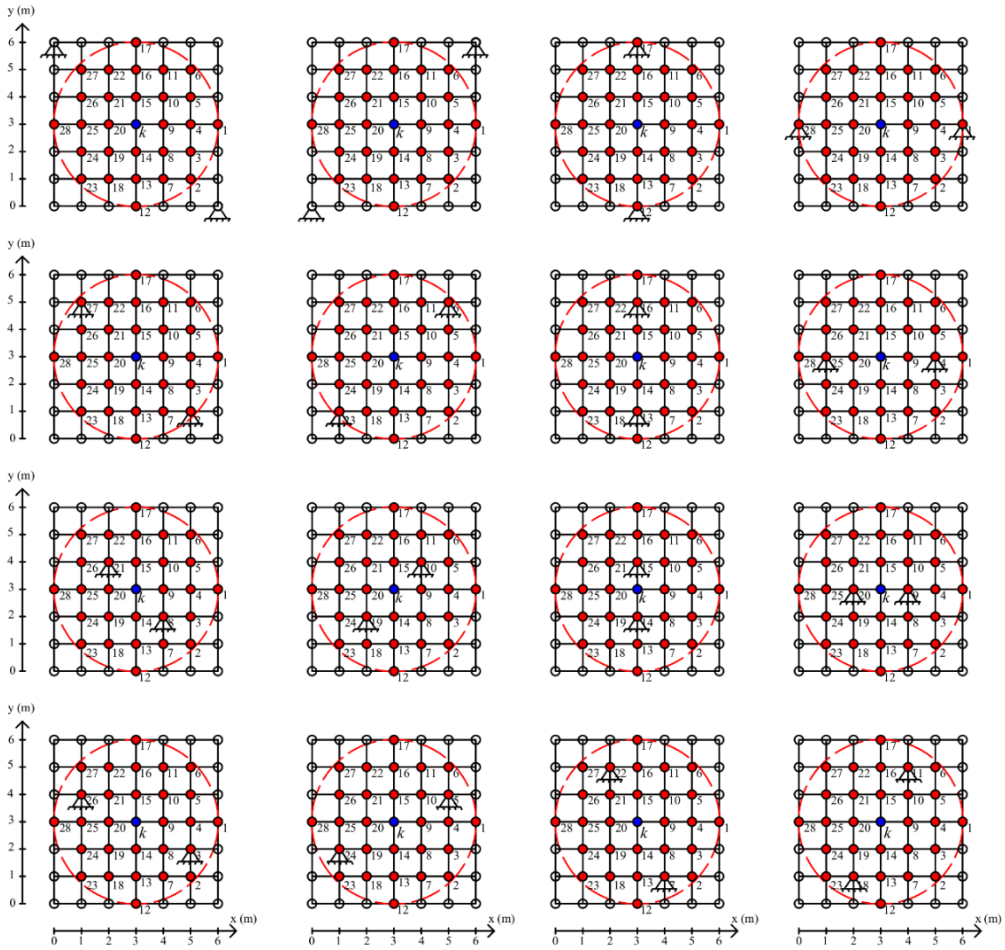

Fig. 5.4. Boundary conditions in modal analyses for the training model for 2D structures

Table 5.2. Arrangement for the dataset for 2D machine learning model

Dataset	Input variables								Output variables	
	u_1	$\cdots$	u_{28}	v_1	$\cdots$	v_{28}	$\frac{2(1+\nu)}{Eh}F_{x(k)}$	$\frac{2(1+\nu)}{Eh}F_{y(k)}$	$u_{(k)}$	$v_{(k)}$
1	-0.0014	.	-0.0014	0.0012	.	0.0012	-3.4E-05	3.4E-05	-0.0015	0.0015
2	0.0014	.	0.0014	0.0012	.	0.0012	3.4E-05	3.4E-05	0.0015	0.0015
.	.	.	.	.	.	.	.	.	.	.
.	.	.	.	.	.	.	.	.	.	.
319	-0.0023	.	0.0023	0.0011	.	-0.0011	0	0	0	0
320	-0.0024	.	-0.0024	0.0004	.	0.0004	-0.0006	-0.0008	-0.0005	-0.0007

Finding the coefficients for the ML model

To obtain the coefficients for the ML model, the obtained data set is split into two parts in which the 310 deformation states are used for training purposes and the remainders are used for testing the accuracy of the ML model. By using the training data, the coefficients of the linear relation given in Eq. (5.19) are obtained by using linear regression as

$$\begin{aligned}\mathbf{a}_j &= [a_1, a_2, \cdots, a_{28}] \\ &= \big[2.44126487\times10^{-2},\ 1.72599524\times10^{-2},\ 5.08783725\times10^{-2},\ 7.11047181\times10^{-2},\\ &\quad 5.08783714\times10^{-2},\ 1.72599441\times10^{-2},\ 1.27196452\times10^{-2},\ 5.02786632\times10^{-2},\\ &\quad 1.42209416\times10^{-1},\ 5.02786703\times10^{-2},\ 1.27196600\times10^{-2},\ -1.46844059\times10^{-8},\\ &\quad -4.0248502\times10^{-8},\ 3.72502411\times10^{-10},\ -3.46583395\times10^{-9},\ -4.29021655\times10^{-8},\\ &\quad -1.4904684\times10^{-8},\ 1.27196564\times10^{-2},\ 5.02786706\times10^{-2},\ 1.42209409\times10^{-1},\\ &\quad 5.02786670\times10^{-2},\ 1.27196465\times10^{-2},\ 1.72599458\times10^{-2},\ 5.08783714\times10^{-2},\\ &\quad 7.11047206\times10^{-2},\ 5.08783737\times10^{-2},\ 1.72599507\times10^{-2},\ 2.44126477\times10^{-2}\big]\end{aligned} \tag{5.22a}$$

$$\begin{aligned}\mathbf{b}_j &= [b_1, b_2, \cdots, b_{28}] \\ &= \big[-5.00827301\times10^{-9},\ -1.72599315\times10^{-2},\ -2.54392470\times10^{-2},\ 8.08215284\times10^{-9},\\ &\quad 2.54392437\times10^{-2},\ 1.72599372\times10^{-2},\ -2.54391797\times10^{-2},\ -5.02786804\times10^{-2},\\ &\quad -9.15180233\times10^{-9},\ 5.02786809\times10^{-2},\ 2.54391712\times10^{-2},\ 7.52227191\times10^{-9},\\ &\quad 1.07005713\times10^{-10},\ 3.63822413\times10^{-9},\ 4.78426226\times10^{-9},\ -1.99145690\times10^{-9},\\ &\quad 9.09132078\times10^{-9},\ 2.54391711\times10^{-2},\ 5.02786812\times10^{-2},\ -1.08530537\times10^{-8},\\ &\quad -5.02786775\times10^{-2},\ -2.54391817\times10^{-2},\ 1.72599362\times10^{-2},\ 2.54392469\times10^{-2},\\ &\quad 5.87137186\times10^{-9},\ -2.54392448\times10^{-2},\ -1.72599313\times10^{-2},\ -6.71179578\times10^{-9}\big]\end{aligned} \tag{5.22b}$$

$$[c \quad d] = \big[4.42141045\times10^{-1},\ 3.40539888\times10^{-9}\big] \tag{5.22c}$$

$$\begin{aligned}\mathbf{m}_j &= [m_1, m_2, \cdots, m_{28}] \\ &= \big[-1.01969796\times10^{-9},\ -1.72599441\times10^{-2},\ -2.54391664\times10^{-2},\ -3.12205277\times10^{-8},\\ &\quad 2.54391866\times10^{-2},\ 1.72599234\times10^{-2},\ -2.54392424\times10^{-2},\ -5.02786808\times10^{-2},\\ &\quad 3.25989664\times10^{-8},\ 5.02786841\times10^{-2},\ 2.54392514\times10^{-2},\ -5.28682972\times10^{-10},\\ &\quad -4.53987184\times10^{-9},\ -9.22966016\times10^{-9},\ -1.53501892\times10^{-8},\ -8.77134865\times10^{-9},\\ &\quad -8.79935283\times10^{-10},\ 2.54392457\times10^{-2},\ 5.02786845\times10^{-2},\ 2.19821744\times10^{-8},\\ &\quad -5.02786748\times10^{-2},\ -2.54392403\times10^{-2},\ 1.72599262\times10^{-2},\ 2.54391866\times10^{-2},\\ &\quad -2.71851724\times10^{-8},\ -2.54391645\times10^{-2},\ -1.72599468\times10^{-2},\ -2.58653592\times10^{-9}\big]\end{aligned} \tag{5.22d}$$

$$\begin{aligned}\mathbf{n}_j &= [n_1, n_2, \cdots, n_{28}] \\ &= \big[-1.14255206\times10^{-8},\ 1.72599501\times10^{-2},\ 1.27196621\times10^{-2},\ -2.96128749\times10^{-8},\\ &\quad 1.27196573\times10^{-2},\ 1.72599359\times10^{-2},\ 5.08783489\times10^{-2},\ 5.02787379\times10^{-2},\\ &\quad -1.67365554\times10^{-7},\ 5.02787515\times10^{-2},\ 5.08783560\times10^{-2},\ 2.44126537\times10^{-2},\\ &\quad 7.11046716\times10^{-2},\ 1.42209499\times10^{-1},\ 1.42209501\times10^{-1},\ 7.11046683\times10^{-2},\\ &\quad 2.44126562\times10^{-2},\ 5.08783559\times10^{-2},\ 5.02787519\times10^{-2},\ -1.70078338\times10^{-7},\\ &\quad 5.02787426\times10^{-2},\ 5.08783456\times10^{-2},\ 1.72599343\times10^{-2},\ 1.27196623\times10^{-2},\\ &\quad -3.31381429\times10^{-8},\ 1.27196654\times10^{-2},\ 1.72599505\times10^{-2},\ -1.41419238\times10^{-8}\big]\end{aligned} \tag{5.22e}$$

$$[p \quad q] = \big[-2.54221850\times10^{-8},\ 4.42141016\times10^{-1}\big] \tag{5.22f}$$

Similar to the 1D model, by using the testing data, the mean squared error between the predicted values and the original values from testing data is 6.42×10^{-23}.

Extending the PD based ML model for dynamic problems

As given in Eq. (5.22), the coefficients d and p are very small which can be ignored as

$$d \approx 0 \; ; \; p \approx 0 \tag{5.23}$$

Therefore, Eq. (5.19) can be rewritten as

$$u_{(k)} = \mathbf{a}_j \cdot \mathbf{u}_j + \mathbf{b}_j \cdot \mathbf{v}_j + c\left(\frac{2(1+\nu)}{Eh} F_{x(k)} \right) \tag{5.24a}$$

$$v_{(k)} = \mathbf{m}_j \cdot \mathbf{u}_j + \mathbf{n}_j \cdot \mathbf{v}_j + q\left(\frac{2(1+\nu)}{Eh} F_{y(k)} \right) \tag{5.24b}$$

or

$$\frac{1}{c}\left[\mathbf{a}_j \cdot \mathbf{u}_j + \mathbf{b}_j \cdot \mathbf{v}_j - u_{(k)} \right] + \bar{b}_{x(k)} \frac{2(1+\nu)}{Eh} \Delta x^2 = 0 \tag{5.24c}$$

$$\frac{1}{q}\left[\mathbf{m}_j \cdot \mathbf{u}_j + \mathbf{n}_j \cdot \mathbf{v}_j - v_{(k)} \right] + \bar{b}_{y(k)} \frac{2(1+\nu)}{Eh} \Delta x^2 = 0 \tag{5.24d}$$

or

$$\frac{Eh}{2(1+\nu)\Delta x^2} \frac{1}{c}\left[\mathbf{a}_j \cdot \mathbf{u}_j + \mathbf{b}_j \cdot \mathbf{v}_j - u_{(k)} \right] + \bar{b}_{x(k)} = 0 \tag{5.24e}$$

$$\frac{Eh}{2(1+\nu)\Delta x^2} \frac{1}{q}\left[\mathbf{m}_j \cdot \mathbf{u}_j + \mathbf{n}_j \cdot \mathbf{v}_j - v_{(k)} \right] + \bar{b}_{y(k)} = 0 \tag{5.24f}$$

Therefore, by reintroducing the inertia forces on the left-hand side of Eqs. (5.24e-f), the machine learning model can be extended for dynamic problems as

$$\rho h \ddot{u}_{(k)} = \frac{Eh}{2(1+\nu)\Delta x^2} \frac{1}{c}\left[\mathbf{a}_j \cdot \mathbf{u}_j + \mathbf{b}_j \cdot \mathbf{v}_j - u_{(k)} \right] + \bar{b}_{x(k)} \tag{5.25a}$$

$$\rho h \ddot{v}_{(k)} = \frac{Eh}{2(1+\nu)\Delta x^2} \frac{1}{q}\left[\mathbf{m}_j \cdot \mathbf{u}_j + \mathbf{n}_j \cdot \mathbf{v}_j - v_{(k)} \right] + \bar{b}_{y(k)} \tag{5.25b}$$

5.5. Numerical implementation

As given in Section 5.4, the PD based ML models for 1D and 2D structures are obtained for material points with full interactions with their family members. Specifically, the 1D ML model is applicable for material points with 6 interactions and the 2D ML model is applicable for material points with 28 interactions. However, for material points that have some missing family members or broken interactions such as material points near boundary surfaces or near crack surfaces, the developed ML models can produce significant errors. Moreover, generating training data for all of these special cases can be very time-consuming. Therefore, a hybrid approach that couples the ML model with the PD model is used. The behaviours of the material points with full interactions are predicted by using the ML model. Meanwhile, all other material points are predicted using the PD model.

Similar to the conventional PD solution, the deformations of structures can be obtained by using a meshless scheme. The domain is divided into a uniform mesh. In this study, for static and quasi-static loading conditions, the adaptive dynamic relaxation (ADR) method [76, 77] is used (Appendix A1). For dynamic problems, the explicit time integration scheme [44] is used.

For 1D problems, the PD region is defined by material points with less than 6 interactions (near boundary regions). Meanwhile, the ML region is defined by material points with 6 interactions (regions that are far from boundaries). For 1D static problems, the displacements of PD material points are obtained by solving the PD equations of motion given in Eq. (5.9). Then based on the displacements of PD material points, the displacements of ML points are obtained by using Eq. (5.13). For 1D dynamic problems, the force densities for all material points, including PD and ML regions, are calculated. If a material point belongs to the PD regions, the PD force densities for that material point are obtained by using Eq. (5.9). Meanwhile, the force densities of material points belong to ML regions are calculated by using Eq. (5.18). After that, the equations of motion are solved by using the time explicit integration scheme.

For 2D problems, the PD region is defined by material points with less than 28 intact interactions (near boundaries and crack surfaces). Meanwhile, the ML region is defined by material points with 28 intact interactions (regions that are far from boundaries and crack surfaces). For 2D static problems, the displacements of material points in PD regions are obtained by solving the PD equations of motion given in Eq. (5.11) and the displacements of material points in ML regions are obtained by using the linear relations given in Eq. (5.19). For 2D dynamic problems, the force densities for all material points, including PD and ML regions, are calculated according to Eq. (5.11) or Eq. (5.25). After that, the equations of motion are solved by using the time explicit integration scheme.

5.6. Numerical results

In this section, first, the PD based machine learning models are verified by considering various examples of 1D, 2D structures. As presented in Section 5.5, a hybrid approach for coupling the machine learning models and bond-based PD models are used. The results obtained by the coupled approach is compared to PD and finite element analysis (FEA) solutions. The FEA solutions are conducted by using ANSYS commercial software with the LINK180 element for the 1D bar and PLANE182 element for the 2D plate. To further verify the capabilities of the coupled approach, damage predictions on a plate with pre-existing crack subjected to tension, on a 2D representation of a three-point bending test, and a plate subjected to dynamic loading is performed.

5.6.1. Verification for 1D model

In this section, a 1D structure subjected to different loading conditions is investigated. The displacements of 4 material points on the left end and 4 material points on the right end of the bar are obtained by solving the PD equation of motion. On the other hand, the displacements of the remaining material points are obtained by using the machine learning model.

Bar subjected to simple axial loading

A bar with a cross-sectional area $A = 0.2 \times 0.2\ \mathrm{m}^2$ and a length of $L = 1\ \mathrm{m}$ is investigated as shown in Fig. 5.5. The bar has an elastic modulus of $E = 69 \times 10^9\ \mathrm{N/m}^2$. The bar is fixed on the left end and it is subjected to two different

loading conditions which are the tensile load of $F_x = 5 \times 10^7$ N and the compressive load of $F_x = -5 \times 10^7$ N.

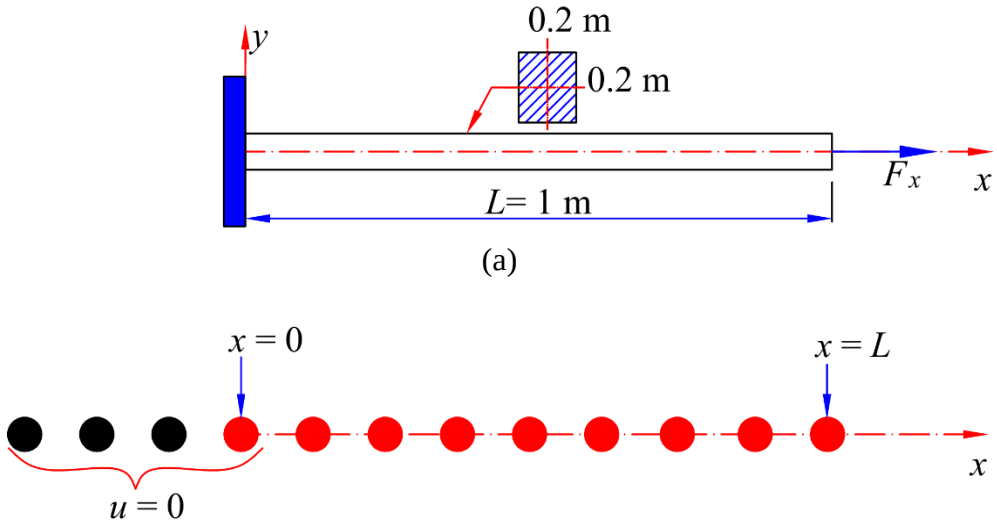

(a)

(b)

Fig. 5.5. Bar subjected to axial loading (a): geometry, (b): model discretization

The bar is discretized with uniform 100 integration points. To implement the boundary condition, three fictitious points [26, 95] are added on the left end of the bar as shown in Fig. 5.5(b). Displacements of three fictitious points as well as the displacement of the material point located at $x = 0$ are set equal to zero. Therefore, as shown in Fig. 5.5(b), the first four material points on the left end of the bar are subjected to the zero displacement condition. In Fig. 5.5(b), the red points represent the material points in the real region, and black points represent the material points in the fictitious region. In the FEA model, the bar is discretized with 100 elements by using the link180 element.

Fig. 5.6 shows the displacement variations along the bar for two loading conditions. As can be seen from the figures, the results captured by the coupled machine learning and PD models match very well with the results from FEA.

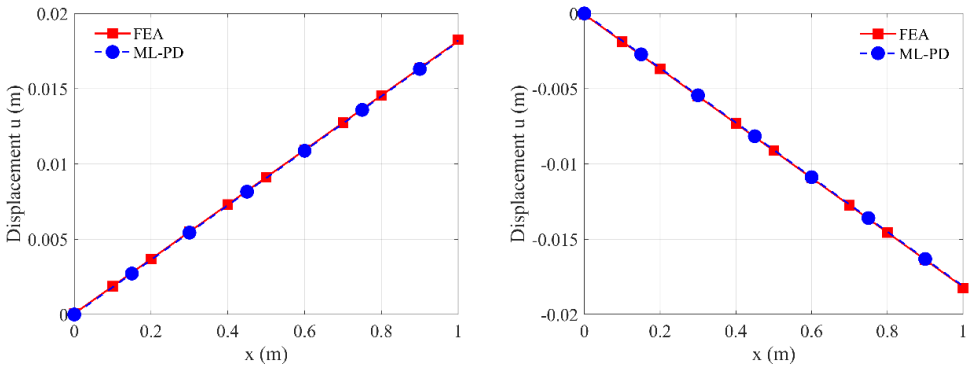

(a) (b)

Fig. 5.6. Displacement variation along the bar subjected to an axial force (a): $F_x = 5 \times 10^7$ N, (b): $F_x = -5 \times 10^7$ N

Bar subjected multiple axial loading

For further verification, another bar with different geometrical and material properties is investigated as shown in Fig. 5.7. The bar has a cross-sectional area of $A = 0.02\ \text{m}^2$ and length of $L = 2$ m and the elastic modulus of $E = 3.8 \times 10^9\ \text{N/m}^2$. The bar is subjected to forces $F_3 = 5 \times 10^6$ N at the right end, $F_1 = 0.4F_3$ at $x_1 = 0.6$ m and $F_2 = 0.5F_3$ at $x_2 = 1.4$ m.

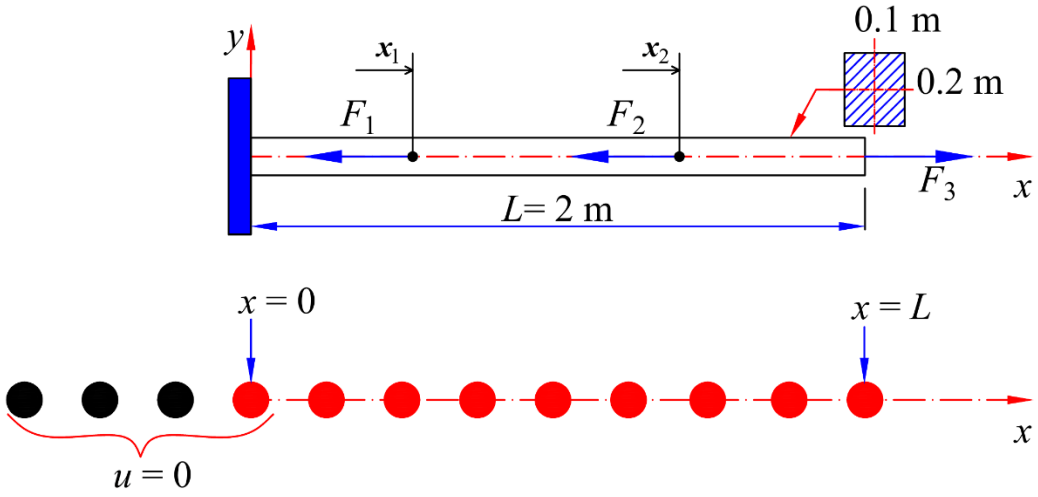

Fig. 5.7. Bar subjected to multiple axial loading

The bar is discretized with uniform 200 integration points. Fig. 5.8 shows the displacement variation along the bar. As can be seen from the figure, the results captured by the coupled model match very well with the FEA results.

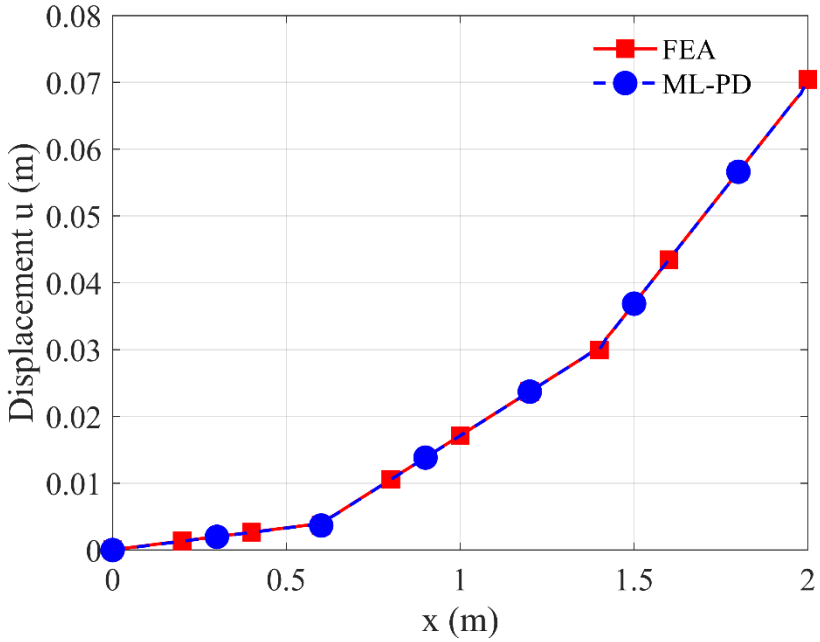

Fig. 5.8. Displacement variation along the bar length

Bar vibration

In this example, the vibration of a bar with a length of $L = 1$ m, a cross-sectional area of $A = 0.05\ \mathrm{m}^2$ is investigated. The bar has an elastic modulus of $E = 2 \times 10^{11}\ \mathrm{N/m}^2$ and it is discretized with a mesh size of $\Delta x = 0.005$ m. Initially, the bar is subjected to a displacement gradient of $\partial u/\partial x = 0.1$. Later, the bar is left to freely vibrate meanwhile the left end is fixed [44].

Fig. 5.9 shows the displacement variation of a material point located at $x = L/2$. As can be seen from the figure, the results captured by the coupled model match very well with the results in both PD and FEA. Therefore, the accuracy of the coupled ML and PD models is verified.

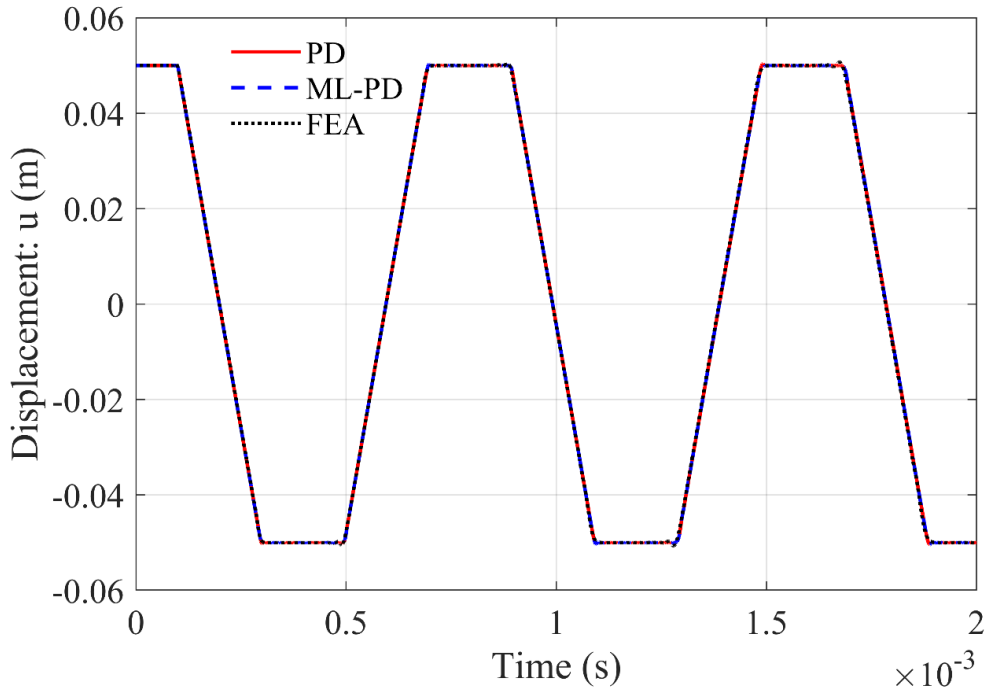

Fig. 5.9. Variation of displacement u (m) of the material located at $x = L/2$

5.6.2. Verification for 2D model

In this section, the coupled 2D model is verified by considering various examples of 2D structures with different geometrical and material properties.

Plate subjected to tension

A square plate with dimensions of $L = W = 1$ m and thickness of $h = 0.01$ m is investigated as shown in Fig. 5.10(a). The plate has an elastic modulus of $E = 69 \times 10^9$ N/m^2 and Poisson's ratio of $\nu = 1/3$ and it is subjected to tensional force per unit length of $f_x = 2 \times 10^8$ N/m.

The plate is discretized uniformly with a mesh size of $\Delta x = L/100$. Similar to 1D problems, the plate is discretized with two regions as shown in Fig. 5.10(b). The PD regions, shown in red, include 3 layers of material points on 4 edges of the plate. The displacements of these points are obtained by solving the PD equations of motion. Since the effects of near-surface boundaries are significant in the PD models, the surface correction [44] is adopted for the PD regions. The remaining material points, shown in blue, belong to the ML region. The displacements of these material points are obtained by using the machine learning model.

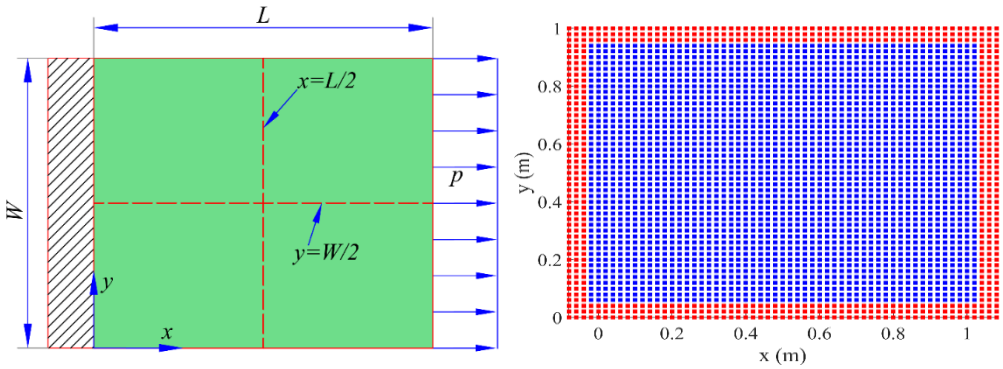

(a) (b)

Fig. 5.10. Plate subjected to axial loading (a): geometry, (b) Model discretization (PD regions are shown in red, ML regions are shown in blue)

Fig. 5.11 and Fig. 5.12 present the variations of displacement components of the plate. Fig. 5.13 shows variations of displacement components along two centrelines $x = L/2$ and $y = W/2$. As can be seen from the figures, the results captured by the coupled model match very well with FEA results.

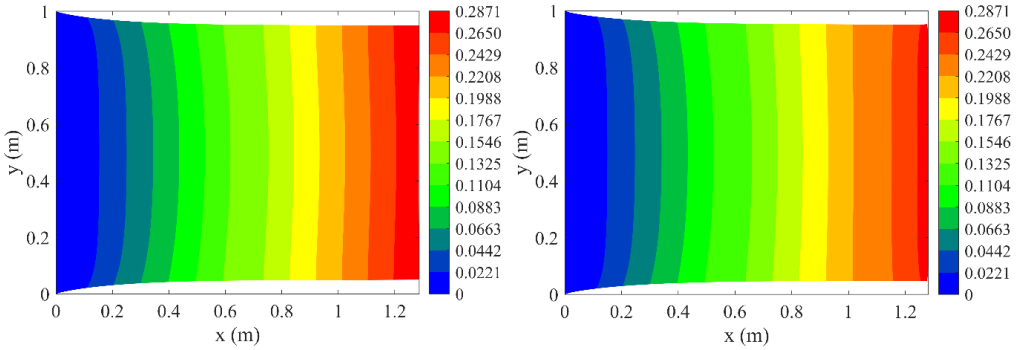

(a) (b)

Fig. 5.11. Variation of displacement $u\ (m)$ on the plate captured by (a): FEA, (b): coupled ML and PD models

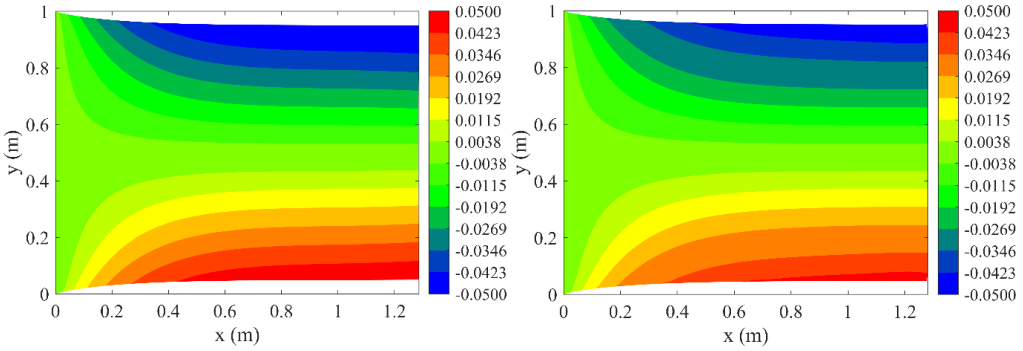

(a) (b)

Fig. 5.12. Variation of displacement $v\ (m)$ on the plate captured by (a): FEA, (b): coupled ML and PD models

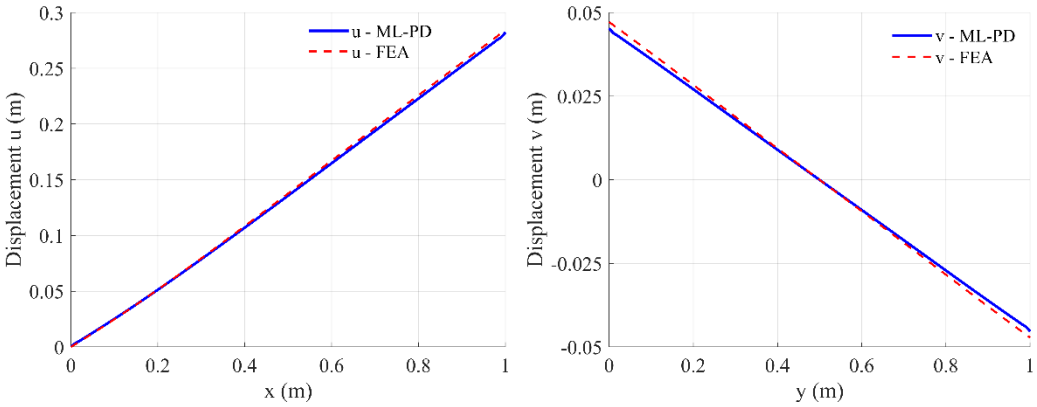

(a) (b)

Fig. 5.13. Variations of displacements (a) u along $y = W/2$; (b) v along $x = L/2$ (ML-PD: coupled ML and PD models)

Fig. 5.14 shows the comparison of the computational time for the bond-based PD model and the coupled approach. The relationships between run-time per time step and the total number of material points in the discretized models are considered. In the PD solution, the adaptive dynamic relaxation (ADR) method presented in Appendix A1 is used [76, 77]. In the coupled solution, the ADR method is also used for the PD region. As can be seen from the figure, the solution by using coupled ML and PD models requires less computational time for each time step than the conventional PD solution. Therefore, by using the coupled ML and PD models, the computational cost can be reduced.

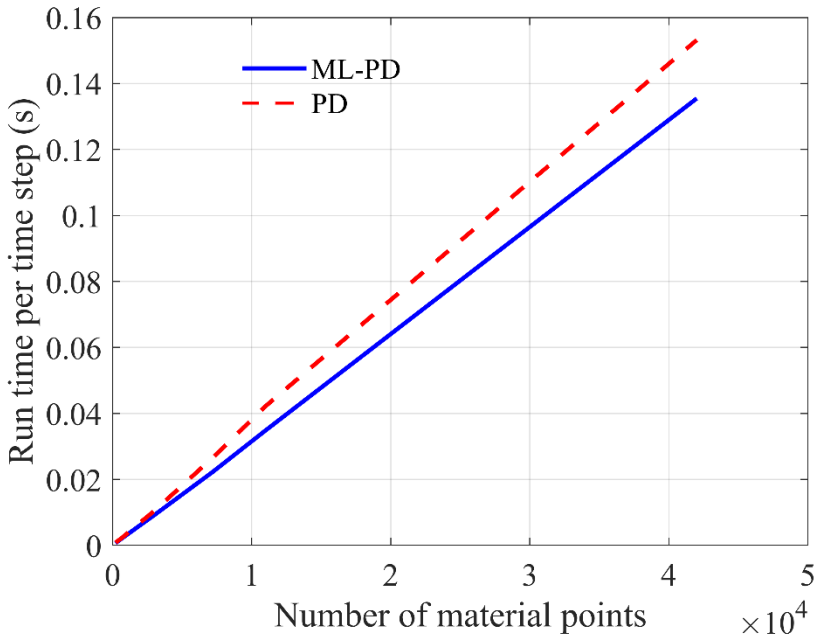

Fig. 5.14. Run time (s) per time step vs. the number of material points

Plate with square cut-out subjected to tension

In this section, a square plate with dimensions of $L = W = 0.05$ m and thickness of $h = 0.0005$ m is investigated as shown in Fig. 5.15(a). The plate has a

0.01×0.01 m^2 square cut-out in the middle and it is subjected to loading condition of $u_0 = \pm 0.005$ m at two ends. The plate has an elastic modulus of $E = 192 \times 10^9$ N/m^2 and Poisson's ratio of $\nu = 1/3$. The plate is discretized uniformly with a mesh size of $\Delta x = L/100$. As shown in Fig. 5.15(b), the PD regions are shown in red and the ML regions are shown in blue. Similar to the previous example, the surface correction [44] is adopted for the PD regions.

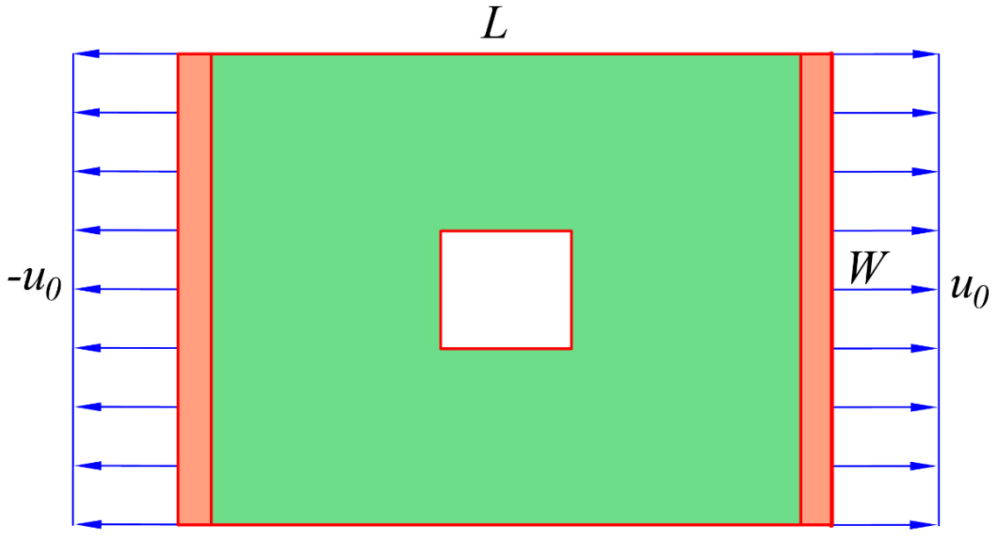

(a)

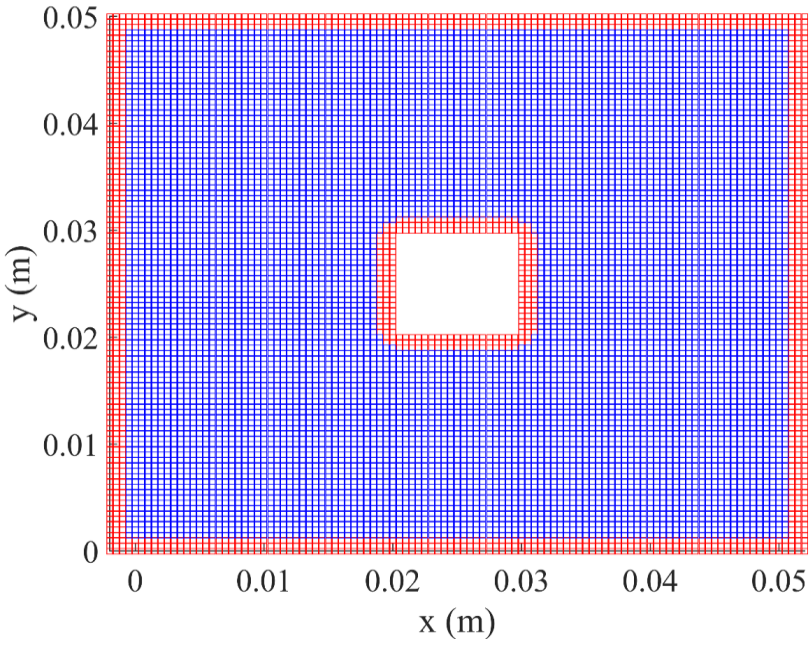

(b)

Fig. 5.15. Plate with square cutout subjected to axial loading (a): geometry, (b): model discretization (PD regions are shown in red, ML regions are shown in blue)

Fig. 5.16 and Fig. 5.17 show the displacement fields on the plate. Fig. 5.18 shows variations of displacement components along two centrelines $x = L/2$ and $y = W/2$. As can be seen from the figures, the results captured by using coupled ML and PD models and the FEA have a good agreement which shows the accuracy of the coupled model for 2D.

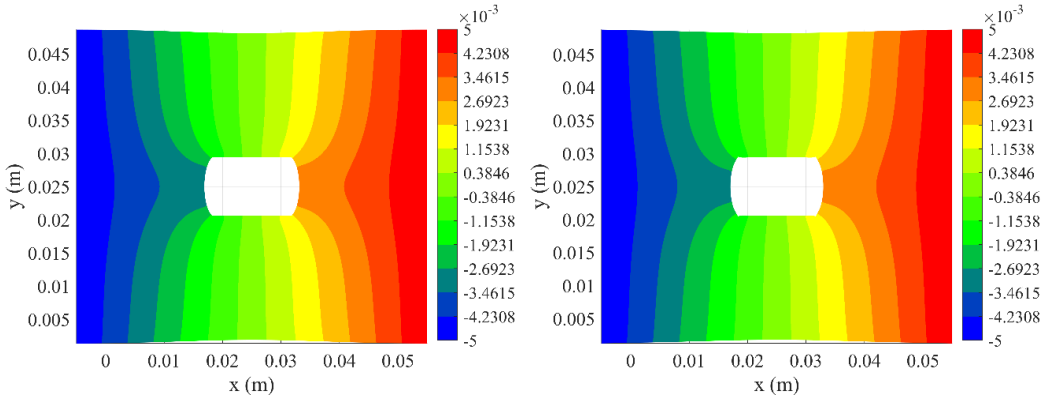

(a) (b)

Fig. 5.16. Variation of displacement $u\ (m)$ on the plate captured by (a): FEA, (b): coupled ML and PD models

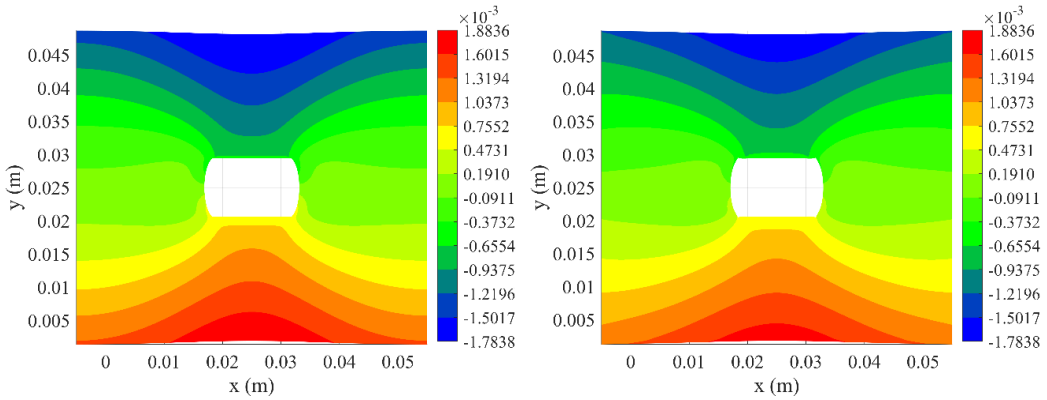

(a) (b)

Fig. 5.17. Variation of displacement $v\ (m)$ on the plate captured by (a): FEA, (b): coupled ML and PD models

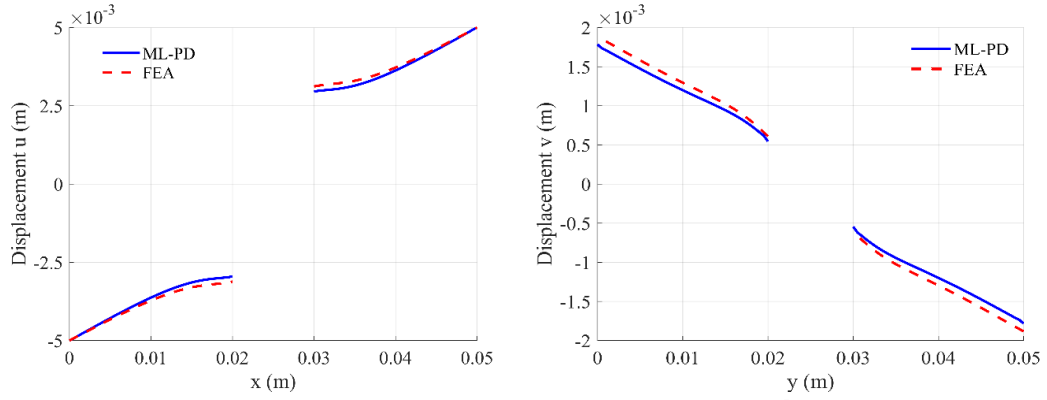

(a) (b)

Fig. 5.18. Variations of displacements (a) u along $y = W/2$; (b) v along $x = L/2$ (ML-PD: coupled ML and PD models)

5.6.3. Damage predictions

After verifying the accuracy of the hybrid approach by coupling of ML and PD models, in this section, damage predictions for 2D plates are presented. To properly capture the behaviours of the structures with progressive damages, the PD regions and ML regions are updated adaptively. At each time step, material points with 28 intact interactions are updated and the behaviours of these material points are obtained by using the 2D ML model. On the other hand, the behaviours of material points with less than 28 intact interactions, which are either near boundary surfaces or near crack surfaces, are obtained by using PD solution. Similar to the previous examples, the surface correction [44] is adopted for the PD regions near boundary surfaces.

5.6.3.1. Plate with pre-existing crack subjected to tension

In this example, a plate with dimensions of $L \times W = 0.5 \times 0.806$ m^2 and thickness of $h = 0.01$ m is investigated as shown in Fig. 5.19 [156]. The plate has a pre-existing crack with a length of $2a = 0.1$ m in the middle. The material properties are represented by the elastic modulus of $E = 2.16 \times 10^{11}$ N/m^2, Poisson's ratio of $\nu = 1/3$, fracture toughness $K_{Ic} = 70 \times 10^6$ Nm$^{-3/2}$[91]. For simplification, the critical energy release rate of the material is calculated as $G_c = G_{\mathrm{Ic}} = K_{Ic}^2/E = 21233$ J/m^2. The critical stretch can be calculated by using the relation given in Eq. (1.7b) as $s_c = 0.0021$.

The plate is subjected to incremental displacements on top and bottom by $|\Delta v| = 10^{-8}$ m per each time step as shown in Fig. 5.19. In the numerical model, the plate is discretized with a mesh size of $\Delta x = L/150$. As shown in Fig. 5.19(b), to apply loading conditions, three layers of material points, shown in red, are added on top and bottom of the plate and incremental displacements are applied to these material points as

$$ {}^{n}v_{(\mathrm{top})} = {}^{n-1}v_{(\mathrm{top})} + 10^{-8}\,dt \ (\mathrm{m}) \tag{5.33a} $$

$$ {}^{n}v_{(\mathrm{bot})} = {}^{n-1}v_{(\mathrm{bot})} - 10^{-8}\,dt \ (\mathrm{m}) \tag{5.33b} $$

$$ {}^{0}v_{(\mathrm{bot})} = {}^{0}v_{(\mathrm{top})} = 0 \tag{5.33c} $$

where ${}^{n}v_{(\mathrm{top})}$ and ${}^{n}v_{(\mathrm{bot})}$ represent displacements at the current time step of material points on the top and bottom boundaries, respectively. The terms ${}^{n-1}v_{(\mathrm{top})}$ and ${}^{n-1}v_{(\mathrm{bot})}$ represent displacements at the previous time step of material points on the top and bottom boundaries, respectively. The time step size is chosen as $dt = 1s$.

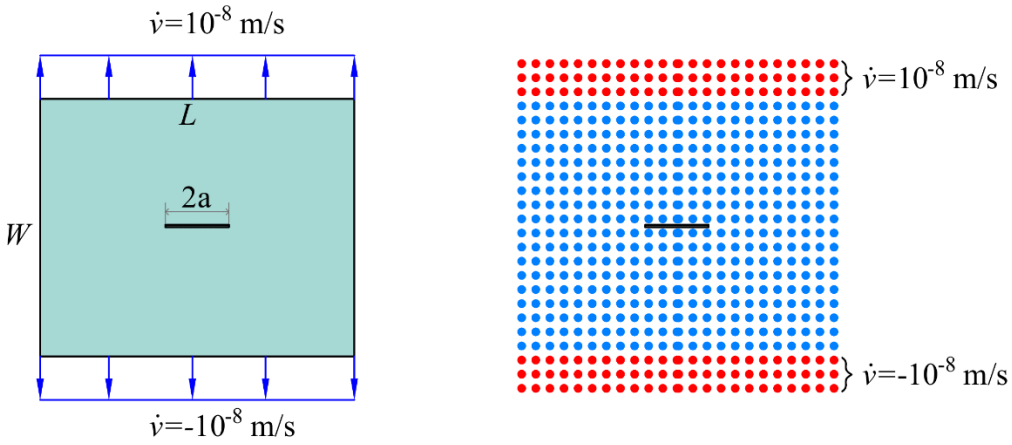

Fig. 5.19. Plate with pre-existing crack subjected to tensional loading

Fig. 5.20 shows the damage evolution on the plate. As shown in Fig. 5.20(a), the crack starts propagating when the applied displacements equal to 3.5×10^{-4} m. As the applied displacements increase, the crack propagates horizontally as expected and it nearly reaches two sides of the plate when applied displacements are 5.3×10^{-4} m. This observation has good agreement with the experimental results captured by Simonsen and Törnqvist [156].

Fig. 5.21 shows the machine learning and PD regions at different load steps. As can be seen from the figure, the PD and ML regions are adaptively updated as damage progresses. All material points with less than 28 intact interactions are determined at each load step and they are defined as PD region. The remaining material points, shown in blue, are defined as the ML region. As shown in Fig. 5.21, there are a small number of material points, shown in red, that need to use PD solution. As shown in Fig. 5.21(d), when the applied displacement equals to 5.3×10^{-4} m, the PD region includes 1602 material points, meanwhile, the total number of material points is 37750. Therefore, the computational cost for the simulation can be reduced by using this coupled approach.

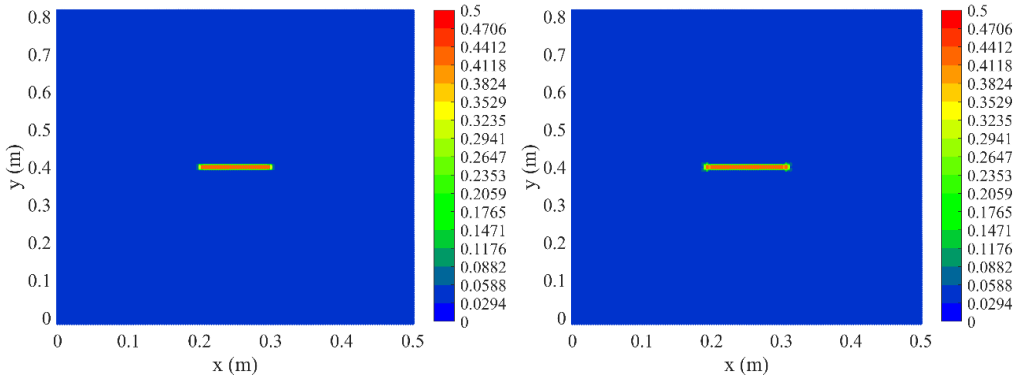

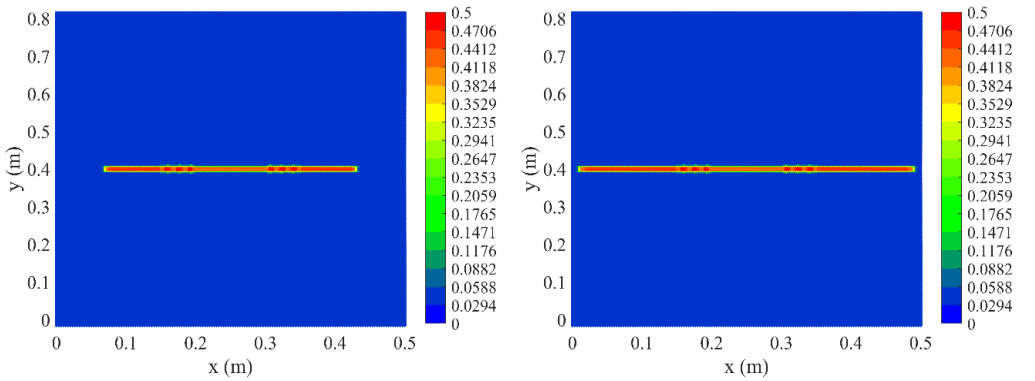

(c) (d)

Fig. 5.20. Damage evolution on the plate when the applied displacement equals to (a): 3.5×10^{-4} m, (b): 4.5×10^{-4} m, (c): 5×10^{-4} m, (d): 5.3×10^{-4} m

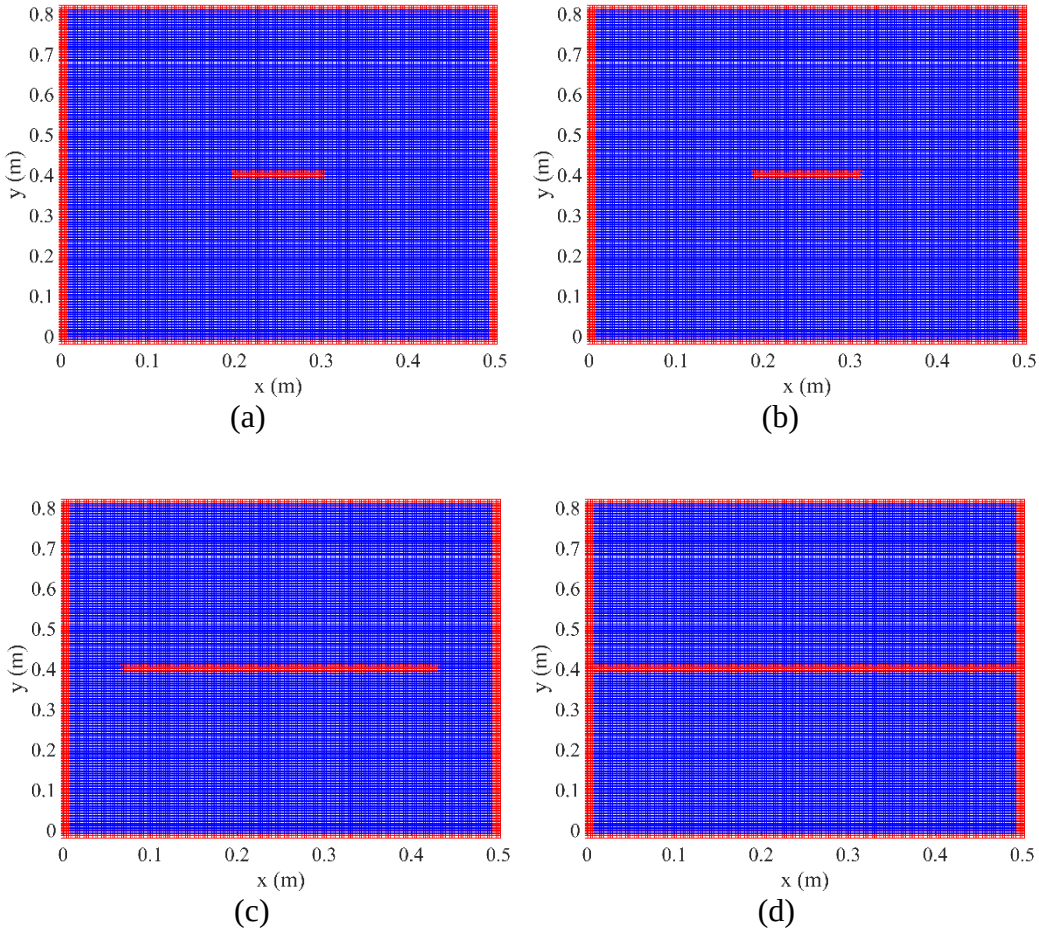

(a) (b)

(c) (d)

Fig. 5.21. Adaptive machine learning and PD regions when the applied displacement equals to (a): 3.5×10^{-4} m, (b): 4.5×10^{-4} m, (c): 5×10^{-4} m, (d): 5.3×10^{-4} m (PD regions are shown in red and ML regions are shown in blue)

5.6.3.2. Three-point-bending test

In this example, a 2D representation of a three-point-bending test for a concrete beam conducted by Jenq and Shah [93] is investigated as shown in Fig. 5.22. The

dimensions of the plate are defined by $S = 0.3048$ mand $H = 0.0702$ m. The plate has an initial crack located at $X = 0.25S$ with a crack length of $a = 0.5H$. The material properties are represented by the elastic modulus of $E = 30 \times 10^9$ N/m^2, Poisson's ratio of $\nu = 1/4$. For simplification, the critical energy release rate of the material is chosen as $G_c = G_{Ic} = 20.7368$ J/m^2[93]. The critical stretch can be calculated by using the relation given in Eq. (1.7b) as $s_c = 4.4376 \times 10^{-4}$.

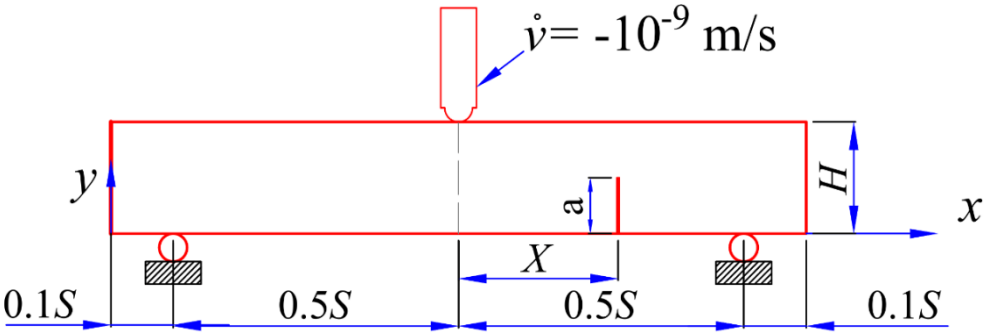

Fig. 5.22. Three-point bending problem

The plate is discretized with uniform 301×58 material points. The quasi-static loading is applied by increasing the displacement by $\Delta w = -10^{-9}$ at $x = 0.6S, y = H$ for each load step. A zero vertical displacement $v = 0$ is applied at $x = 0.1S$, $y = 0$ and $x = 1.1S$, $y = 0$.

Fig. 5.23 shows the damage evolution on the plate. As expected, the crack propagates towards the middle position of the specimen. As shown in Fig. 5.23(b), the angle between the crack path and vertical axis is approximate 35^0 which shows good agreement with the experimental result [93]. Fig. 5.24 shows the adaptive PD and ML regions at different load steps. Similar to the previous example, the PD and ML regions are automatically updated based on the progressive damages in the structure. As shown in Fig. 5.24(c), when the applied displacement equals to 14×10^{-5} m, the number of material points in the PD region is 2523, which is 14.5% of the total number of material points in the discretized model, 17458.

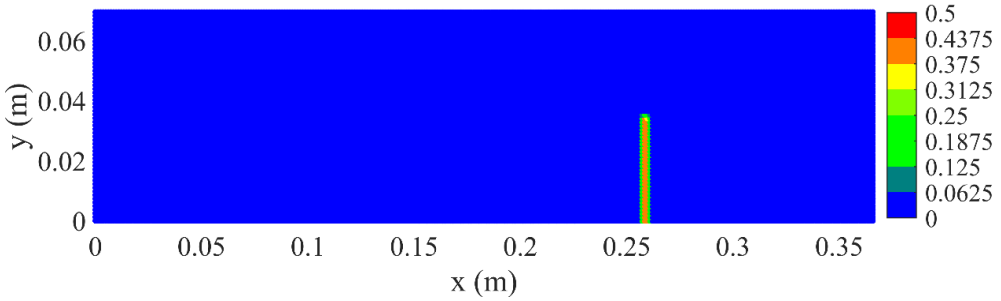

(a)

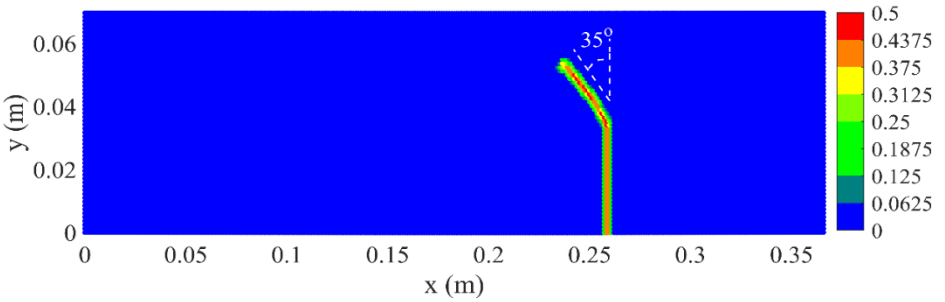

(b)

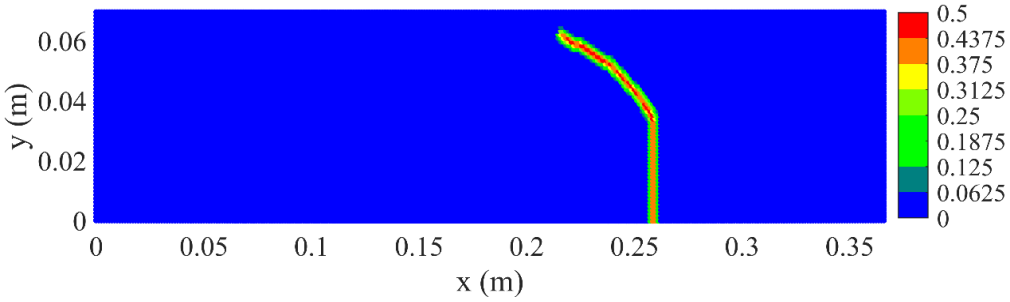

(c)

Fig. 5.23. Damage evolution on the beam when the applied displacement equals to (a): 8×10^{-5} m, (b): 11×10^{-5} m, (c): 14×10^{-5} m

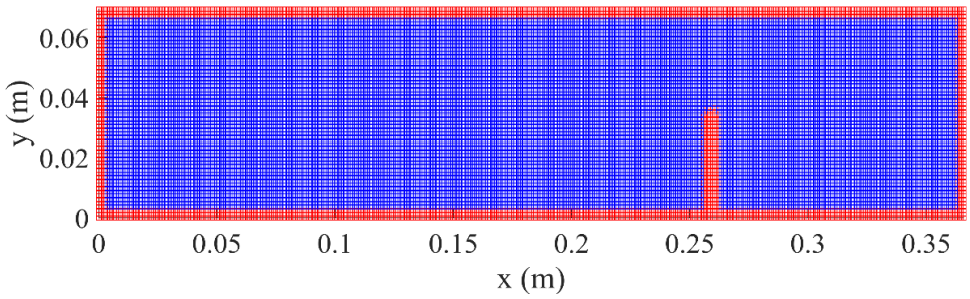

(a)

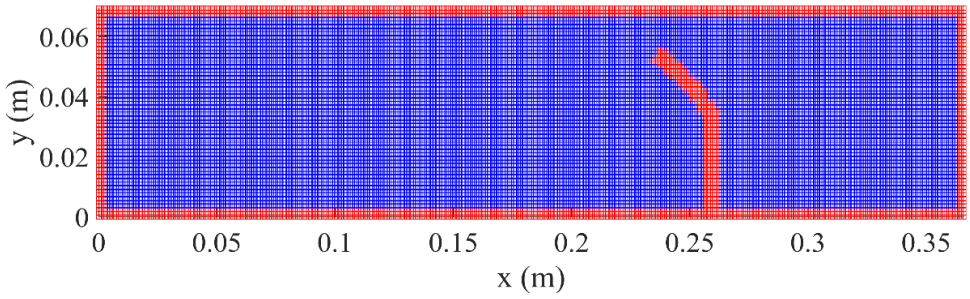

(b)

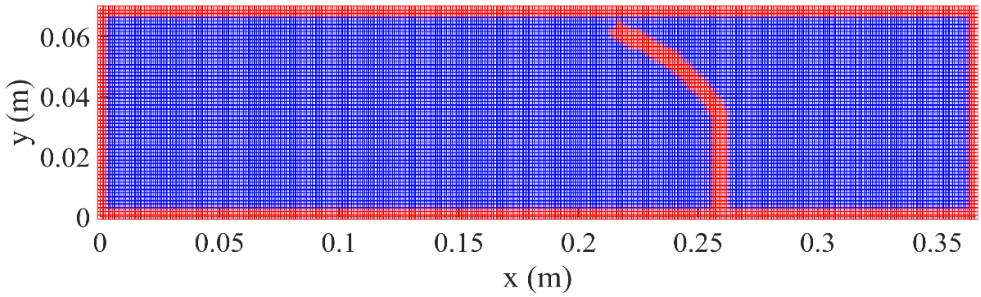

(c)

Fig. 5.24. Adaptive machine learning and PD regions when the applied displacement equals to (a): 8×10^{-5} m, (b): 11×10^{-5} m, (c): 14×10^{-5} m (PD regions are shown in red and ML regions are shown in blue)

5.6.3.3. Kalthoff experiment

In this section, the experiment presented by Kalthoff and Winkler [92], Kalthoff [87, 91] for a pre-notched plate subjected to dynamic load is simulated by using the coupled ML and PD models. Since the problem is symmetric, only the upper half plate with dimensions of $L = W = 0.1$ m and thickness of $h = 0.009$ m is modeled as shown in Fig. 5.25. The plate is made of steel with the elastic modulus of $E = 2 \times 10^{11}\text{N/m}^2$, Poisson's ratio of $\nu = 1/3$. The fracture toughness of steel is $K_{Ic} = 70 \times 10^6\ \text{Nm}^{-3/2}$[87]. For simplification, the critical energy release rate of the material is calculated as $G_c = G_{\text{Ic}} = K_{Ic}^2/E = 22714\ \text{J/m}^2$. The critical stretch can be calculated by using the relation given in Eq. (1.7b) as $s_c = 0.0089$. The left edge which is under the crack surface is subjected to velocity conditions as [96]

$$|\mathbf{v}| = \begin{cases} \dfrac{t}{t_0} v_0 & \text{for } t \le t_0 \\ v_0 & \text{for } t > t_0 \end{cases} \tag{5.34}$$

with $v_0 = 16.5\text{m/s}$, $t_0 = 1\mu s$.

The plate is discretized into 150×150 material points and the solution results are obtained by using a dynamic explicit time integration scheme with a time step of $0.01\mu s$ and the total simulation time of $80\mu s$. Similar to the previous examples, the solution results are obtained by solving Eq. (5.11) for the PD region and by using Eq. (5.25) for the ML region.

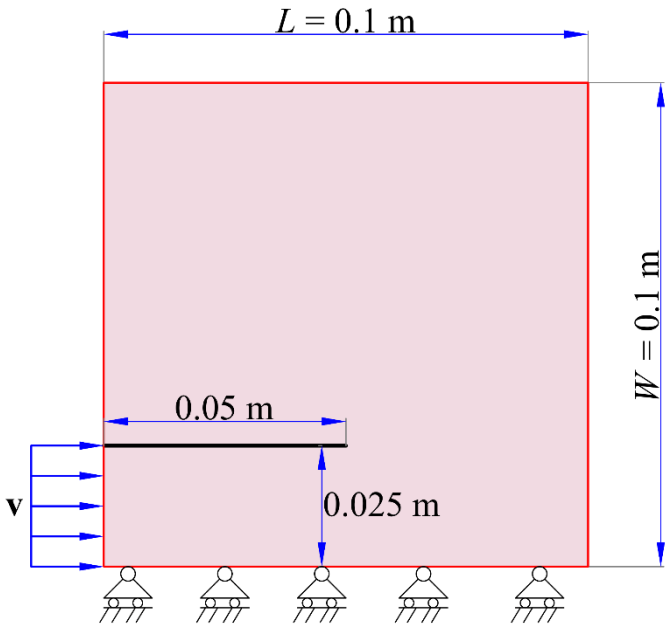

Fig. 5.25. The geometry and symmetrical boundary conditions for the Kalthoff experiment

Fig. 5.26 presents the damage evolution on the plate. As can be seen from the figure, under dynamic loading conditions, the crack propagates up 67.3^0 orientation with respect to the horizontal axis. After $80\mu s$, the crack propagates nearly to the top edge of the plate as shown in Fig. 5.26(d). As can be seen from the figure, the crack paths captured by coupled ML and PD models match very well with the experimental results in [87, 91, 92]. Fig. 5.27 shows the PD and ML regions at different time steps. As shown in Fig. 5.27(d) for the coupling model at $80\mu s$, 12.68% of the total number of material points (2909 per 22950 material points) belong to the PD region.

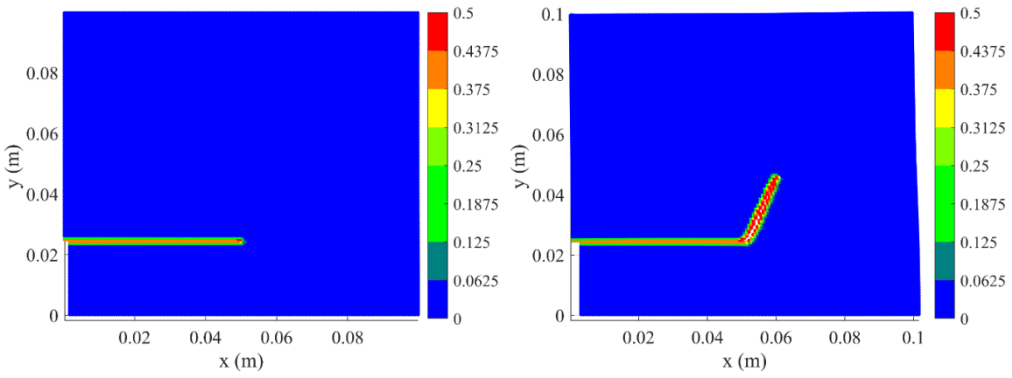

(a) (b)

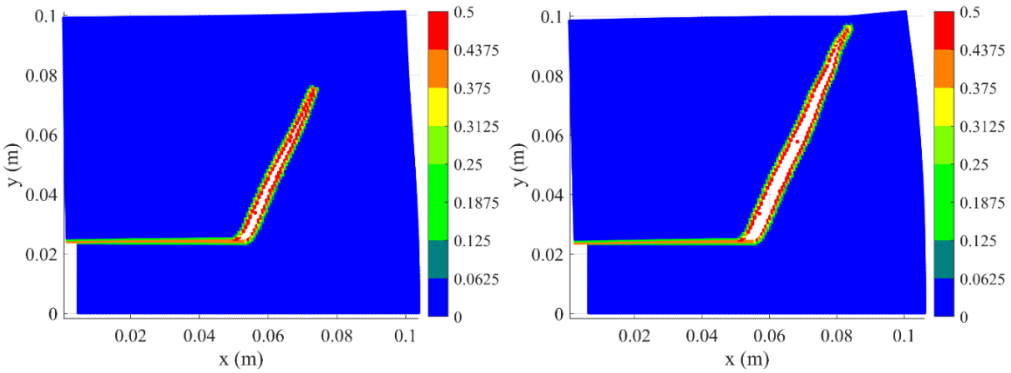

(c) (d)

Fig. 5.26. Damage evolution on the plate at (a): $20\mu s$, (b): $40\mu s$, (c): $60\mu s$, (d): $80\mu s$ (displacements are magnified by 5 times for deformed configurations)

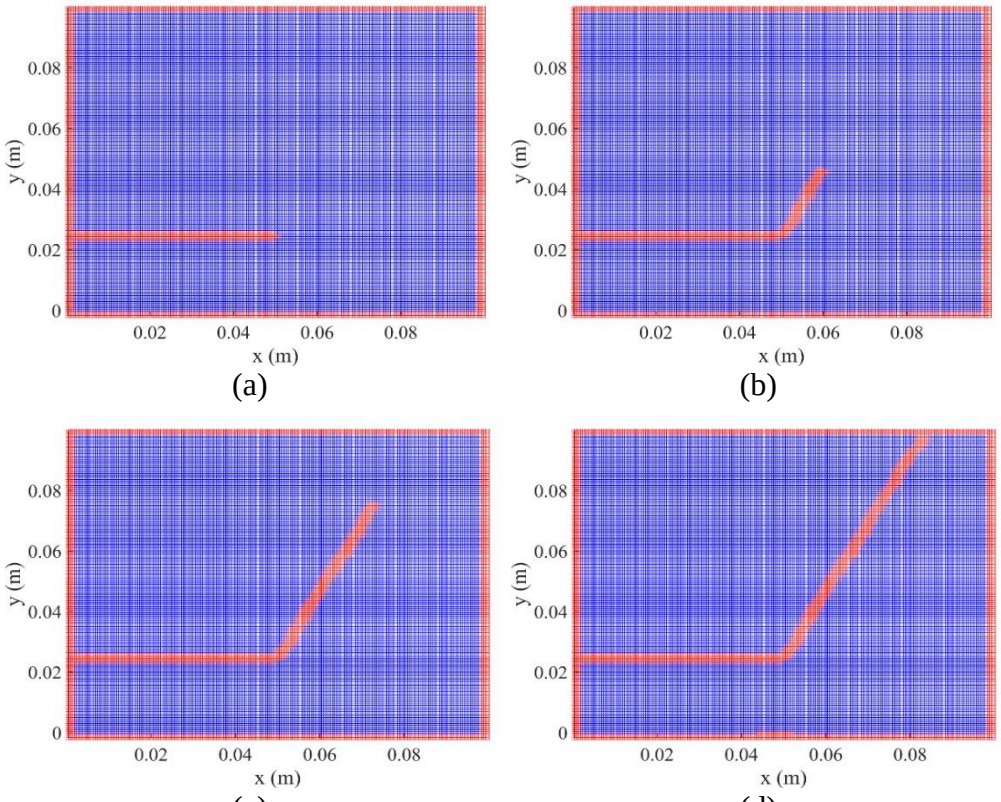

(a) (b)

(c) (d)

Fig. 5.27. Adaptive machine learning and PD regions at (a): $20\mu s$, (b): $40\mu s$, (c): $60\mu s$, (d): $80\mu s$ (PD regions are shown in red and ML regions are shown in blue in the undeformed configuration)

5.7. Concluding remarks

In this chapter, the PD based machine learning models for 1D and 2D structures are presented and verified by conducting various problems. The main conclusions arising from the present study are listed below:

(1) The PD based machine learning models are obtained for linear elastic material for the first time in the PD literature by using linear regression. The

linear relationships between displacements of a material point with displacements of its family members and its applied forces are presented in the analytical form which can be used straightforward.

(2) The machine learning models for both 1D and 2D structures can be coupled with the traditional PD solutions. The results captured by the coupling models show good agreements with both PD and FEA results.

(3) The capability of the coupled model is also further verified by considering various fracture problems. The results captured by the coupled model have very good agreement with the experimental results.

(4) The PD and ML regions can be updated adaptively at each time step. Therefore, the coupled ML and PD model can use the advantage of the PD model in terms of capturing complex fracture problems, and the advantages of the machine learning model in terms of saving computational cost.

(5) The hybrid approach proposed in this study can be further applied in the PD literature for other types of structures.

6. DISCUSSION

6.1. Novelty of the research

The biggest novelty of the research in this thesis lies in successfully applying a new method "Peridynamics" to predict progressive damages in ship and offshore structures. Unlike other methods, peridynamics can predict complex fracture phenomena in ship and offshore structures without any special treatment. Therefore, the structural behaviours during the damage process can be fully understood.

To apply peridynamics for damage prediction in ship and offshore structures, a crucially important task is the development of PD models that can analyse complex beam and shell structures. This work is done by the research presented in Chapter 2. Specifically, novel PD models for predicting damages in 3D complex beams, 3D shells, and complex stiffened structures were developed. These PD beam and shell models were the first studies that extended the applications of PD for ship and offshore structures. These PD beam and shell models can also be used for any type of beam and shell structures to predict possible damages that may occur during the operation process.

Moreover, to improve the capability of the developed PD models in Chapter 2 for large deformation problems, novel PD models for geometrically nonlinear analyses of 1D, 2D, and 3D structures, 3D beams, and plates were developed in Chapter 3. Therefore, PD can be further used to predict damages in ship and offshore structures for large deformation problems.

As also discussed in Chapter 1, due to the repetition of the sea loads, fatigue damages are very common problems for ship and offshore structures. Therefore, in Chapter 4, a novel energy-based PD fatigue model, which is more suitable for complex shell structures such as ship and offshore units, was developed.

Finally, due to nonlocal interactions, the PD simulations are often more expensive than FEA. Moreover, a relatively fine mesh is often used in PD simulations to ensure well-predicted crack paths. As a result, PD simulations are often expensive. On the other hand, data-driven models are becoming an alternative solution for many physics-based models in engineering and solid mechanics. Therefore, to reduce the computational cost for the simulations, this thesis proposed a novel idea to couple PD with machine learning for damage prediction. The rightness of the proposed idea is proven by the successful development of a novel PD-based machine learning model for fracture prediction was developed. The PD-based machine learning model can be adaptively coupled with the traditional PD model to predict complex fracture problems. By coupling PD-based machine learning and the traditional PD models, the hybrid models can take advantage of both data-driven and physics-based models. The data-driven models can help to reduce the computational cost. Meanwhile, the physics-based model can help to maintain the accuracy of the predictions for highly complex phenomena.

6.2. Contributions of the research findings

6.2.1. Contributions to the peridynamic literature

The biggest contribution of this research to the PD literature lies in expanding the applications of peridynamics to ship and offshore structures as well as any other types of beams and shell structures in the industry. To the best of the author's knowledge, this is the first time in the PD literature that the progressive damages of ships and offshore structures can be predicted by using Peridynamics.

Throughout the thesis, various novel PD models were developed with verified accuracy and proven capabilities. In summary, there are four main contributions to the peridynamic literature achieved in this thesis as follows

- Developed linear and nonlinear PD models for linear and geometrically nonlinear analyses of complex 3D beam and shell structures. These works expanded applications of the PD theory to slender, thin-wall, and stiffened structures which are the majority of offshore and onshore units in many industries.

- Developed nonlinear PD models for geometrically nonlinear analysis of 1D, 2D, and 3D structures. As discussed in Chapter 1, within the elasticity, the simplified 2D and 1D PD models in the PD literature are based on small deformations assumption which can be applicable only for linear elastic deformations. Therefore, by developing PD models for geometrically nonlinear analyses of 1D, 2D, and 3D structures, PD theory now becomes fully applicable for linear elastic, geometrically nonlinear, and material nonlinear problems.

- Developed a novel energy-based PD fatigue model that is suitable for shell and stiffened structures.

- Proposed and proved a novel approach to reduce the computational cost for PD simulations by coupling the traditional PD model with a PD-based machine learning model. This work can also open a new research direction for the PD community since the idea can apply to many PD models in many fields.

6.2.2. Contributions to the industry

This thesis proposed and successfully applied a new method, namely "Peridynamics", for damage prediction in ship and offshore structures. The developed PD models in this thesis can be used to predict brittle damages in ships and offshore structures which may be due to high cycle fatigue loading, low-temperature conditions, high-loading rate, multi-axial stress constraint, or low weldability of steel etc. As a mesh-free method based on the nonlocal theory, peridynamics can predict complex fracture problems without any special treatment. This method overcomes the limitations of the traditional FEA and modified versions of FEA that are currently used in the marine industry for structural design and assessment. Therefore, peridynamics can be a new powerful method for structural design and damage prediction in the shipbuilding and offshore industry.

By using such a new method, the behaviours of ship and offshore structures with progressive damages can be clearly understood and further actions can be announced to enhance the safety of the structures.

6.3. Recommendations for the industry

As demonstrated in this thesis, PD is suitable for damage prediction and it is also applicable for complex ship and offshore structures. Therefore, the following future applications of PD are recommended:

- The use of peridynamics for design stages

In the design stages, to ensure the safety of ship and offshore structures, many structural assessment processes including structural analysis for critical loading conditions as well as fatigue design assessments are conducted. For this purpose, PD can be a powerful tool that can predict possible damages on the structures as well as help to clearly understanding structural responses during the damage process. Peridynamic models can be coupled with FEM models for dealing with large complex structures. Specifically, FEM models can be used for global analyses to determine hotspot locations. Meanwhile, PD models can be used for local analyses for hotspot locations to answer whether there are possible damages or not. If there are some possible damages, the PD analyses can answer important questions such as where the exact locations are, when the damages happen, and how the damages will propagate. As the result, further action can be made to strengthen the structures to avoid the damages.

- The use of peridynamics for structural assessments

During the operational process, structures can subject to some unexpected critical conditions or they can have some small damages due to corrosion, fatigue, or collision. In these cases, the couple PD and FEM models can be used to investigate the structural safety. FEM model can be used for global analysis meanwhile PD model can be used for local analysis and damage prediction. Fundamental questions such as are there any new damages, how (how big, how fast, which direction) the damage will develop, what is the structural remaining strength, can be answered. As the result, the safety of structures can be carefully estimated, and further actions can be made if it is necessary.

6.4. Limitations

In Chapters 2-3, the novel PD models for linear and geometrically nonlinear analyses of 1D, 2D, 3D structures, 3D beams, and shell structures were developed. However, the developed PD formulations for beams and shells are based on a *small strain* assumption. For large strain problems, the change of the beam's cross-sectional area and the change of the shell's thickness need to be considered. Moreover, the material nonlinearity was not included in the formulations of the developed PD models. Therefore, the currently developed PD models are only applicable for brittle materials. For ductile materials, further studies that include material nonlinearity are needed.

In Chapter 4, a novel energy-based PD fatigue model was developed. The PD fatigue model is presented for 2D formulations. Also, both the energy-based PD fatigue model developed in this thesis and the original PD fatigue model in [60] were developed for elastic deformations which are mainly used for high cycle fatigue problems. For low cycle fatigue problems, in which the plastic deformations of the region surrounding the crack tip may become important, new PD fatigue models need to be proposed.

In Chapter 5, a PD-based machine learning model was developed. The bond-based PD formulations for 1D and 2D structures were considered. Therefore, the proposed idea in Chapter 5 can be further extended to 3D structures, beams, and shells, as well as other state-based PD models.

6.5. Future study

As a future study, first, the current nonlinear PD models for beams and shells presented in chapter 3 will be further developed by considering material nonlinearity. Second, the energy-based PD fatigue model presented in chapter 4 will be further developed for 3D structures, shells, and composite structures. Moreover, both the energy-based PD fatigue model developed in this thesis and the original PD fatigue model in [60] can be further extended for low cycle fatigue problems by considering plastic deformations. Finally, the idea of the PD-based machine learning model will be further extended to state-based PD models, 3D structures, beams, and shell structures.

7. CONCLUSION

Based on the research work discussed in this thesis, the following conclusions can be drawn:

1) The prediction of progressive damages in ship and offshore structures is very important but challenging work. Many approaches including FEA and modified versions of FEA have been proposed still face difficulties in terms of predicting complex fracture problems such as crack branching and multiple crack paths. By contrast, peridynamics is very suitable for damage prediction even for complex fracture phenomena. However, since the peridynamics is still in development, the applications of PD for ship and offshore structures are very limited. Therefore, the study in this thesis to make PD becomes applicable to ship and offshore structures are crucially important. This will help to propose a new method for structural analysis of ship and offshore structures which can improve structural safety.

2) In the literature, the PD formulations for beams and shells are still incomplete. Therefore, a crucially important task to apply peridynamics for damage prediction in ship and offshore structures is the development of linear and nonlinear PD models for complex beam and shell structures. This work is done in this thesis with the development of novel PD models for linear and geometrically nonlinear analyses of 1D, 2D, and 3D structures, 3D beams, and plates and shells.

3) Fatigue design assessment is also one of the design drivers for ship and offshore structures. Therefore, the development of a PD fatigue model that can apply for beam and shell structures is important. This work is done in this thesis by developing a novel energy-based PD fatigue model to predict fatigue crack initiation and propagation.

4) Another important task to make peridynamics becomes applicable to damage prediction in ship and offshore structures is reducing the computational cost for PD simulations. As point out in this thesis, due to nonlocal interactions, the PD simulations are often more expensive than FEA. Besides existing approaches such as coupling with FEA, using CPU and GPU techniques, this thesis proposed a novel method for computational cost reduction. That is coupling the traditional PD model with the PD-based machine learning model. The PD-based machine learning model help to speed up the simulations while the traditional PD model help to maintain the accuracy of the predictions for complex parts such as near boundary surfaces or near crack surfaces.

5) Through this research project, a new powerful method for damage prediction in ship and offshore structures, “peridynamics”, was successfully developed. Although there are still some limitations that require some future works, this thesis demonstrated the potential development of a powerful tool for structural analysis and damage prediction which can help to improve and ensure the safety of ship and offshore and marine structures.

Appendix A. Adaptive Dynamic Relaxation for static and quasi-static linear and nonlinear analyses

In this section, the adaptive dynamic relaxation method used for static and quasi-static problems in PD is presented. The procedure for using the explicit time integration scheme in the ADR method is described by Madenci and Oterkus [44], Kilic and Madenci [76]. In the ADR method, the calculation of the mass stable matrix $\mathbf{M}_{(k)}$ decides the stability and speed of the simulation. Too small values of $\mathbf{M}_{(k)}$ will cause the diverged simulations. Meanwhile, too big value of $\mathbf{M}_{(k)}$ will cause slowly convergent simulations which increases the simulation time. Therefore, this section focuses on the calculation of the mass stable matrix $\mathbf{M}_{(k)}$. First, the calculation of the mass stable matrices for 1D, 2D, 3D PD models are presented in Appendix A.1. Next, the calculation of the mass stable matrices for PD beam models are presented in Appendix A.2. Finally, the calculation of the mass stable matrices for PD models for plates and shells are presented in Appendix A.3

A1. ADR method used in PD simulations for 1D, 2D, 3D structures

According to Kilic and Madenci [76], Underwood [77], by using the adaptive dynamic relaxation, the equation of motion in Eq. (1.4) can be rewritten as

$$\mathbf{M}_{(k)}\ddot{\mathbf{u}}_{(k)} + \mathbf{C}_{(k)}\dot{\mathbf{u}}_{(k)} = \sum_{j=1}^{N} \psi_{(k)(j)} \left(\mathbf{t}_{(k)(j)} - \mathbf{t}_{(j)(k)}\right) V_{(j)} + \mathbf{b}_{(k)} \tag{A.1}$$

Similarly, the nonlinear PD equation of motion in Eq. (3.1a) can be rewritten as

$$\mathbf{M}_{(k)}\,{}^{t}\ddot{\mathbf{u}}_{(k)} + \mathbf{C}_{(k)}\,{}^{t}\dot{\mathbf{u}}_{(k)} = \sum_{j=1}^{N} \left({}^{t}_{0}\mathbf{t}_{(k)(j)} - {}^{t}_{0}\mathbf{t}_{(j)(k)}\right) {}^{0}V_{(j)} + {}^{t}\mathbf{b}_{(k)} \tag{A.2}$$

where $\mathbf{M}_{(k)}$ represents the mass stable matrix, $\mathbf{C}_{(k)}$ represents the damping matrix [77].

For one-dimensional PD model (either linear or nonlinear models), the mass stable matrix can be calculated as [44, 75]

$$M_{(k)} \geq \frac{1}{4}\frac{dt^2 A C_{ax} \delta}{\Delta x} \tag{A.3}$$

where $dt = 1$ represents the time step for a quasi-static solution [77], A is the beam cross-section area, δ is the horizon size, Δx is the mesh size used in the PD discretized model. The term C_{ax} represents the PD bond constant for 1D structures. This bond constant is given in Eq. (2.14), Eq. (5.9c) as

$$C_{ax} = \frac{2E}{A\delta^2} \tag{A.4}$$

For 2D PD models (either linear or nonlinear models), the mass stable matrix can be calculated as [44, 75]

$$\mathbf{M}_{(k)} = \begin{bmatrix} M^{u}_{(k)} & 0 \\ 0 & M^{v}_{(k)} \end{bmatrix} \tag{A.5a}$$

with

$$M^{u}_{(k)} = M^{v}_{(k)} \geq \frac{1}{4} dt^2 \frac{C\pi h \delta^2}{\Delta x} \tag{A.5b}$$

where C is the bond constant for the 2D bond-based PD model which is given in

Eq. (5.11e). This constant can also be calculated as

$$C = 4b \tag{A.6}$$

where b is PD constant for 2D nonlinear PD model which is given in Eq. (3.14).

For 3D PD models, the mass stable matrix can be calculated as [44, 75]

$$\mathbf{M}_{(k)} = \begin{bmatrix} M_{(k)}^{u} & 0 & 0 \\ 0 & M_{(k)}^{v} & 0 \\ 0 & 0 & M_{(k)}^{w} \end{bmatrix} \tag{A.7a}$$

with

$$M_{(k)}^{u} = M_{(k)}^{v} = M_{(k)}^{w} \geq \frac{1}{4} dt^2 \frac{(4b)}{\Delta x} \left(\frac{4}{3} \pi \delta^3 \right) \tag{A.7b}$$

where b is PD constant for 3D nonlinear PD model which is given in Eq. (3.12).

A2. ADR method used in PD simulations for beams

For the linear PD beam model in Chapter 2, to use the ADR method, the PD equation of motion given in Eq. (2.42) can be rewritten as

$$\mathbf{M}_{(k)} \ddot{\mathbf{u}}_{(k)}^{G} + \mathbf{C}_{(k)} \dot{\mathbf{u}}_{(k)}^{G} = \sum_{j=1} \mu_{(k)(j)} \mathbf{f}_{(k)(j)}^{G} V_{(j)} + \mathbf{b}_{(k)}^{G} \tag{A.8}$$

Similarly, the equation of motion for the nonlinear PD beam model given in Eq. (3.71b) can be rewritten as

$$\mathbf{M}_{(k)} {}^{t}\ddot{\mathbf{u}}_{(k)}^{G} + \mathbf{C}_{(k)} {}^{t}\dot{\mathbf{u}}_{(k)}^{G} = \sum_{j=1} \psi_{(k)(j)} {}_{0}^{t}\mathbf{f}_{(k)(j)}^{G} {}^{0}V_{(j)} + {}^{t}\mathbf{b}_{(k)}^{G} \tag{A.9}$$

According to Underwood [77], the right-hand side of Eq. (A.8-9) should be real physical values, but the left-hand side of Eq. (A.8-9), which includes mass stable vector and the damping matrix which can be chosen arbitrarily to get a converged solution. However, the matrix $\mathbf{M}_{(k)}$ is required to be a diagonal matrix. A simple way for determination of mass stable vectors in global coordinates is described as follows

$$\mathbf{M}_{(k)} = \begin{bmatrix} M_{(k)}^{u_1} & 0 & 0 & 0 & 0 & 0 \\ 0 & M_{(k)}^{u_2} & 0 & 0 & 0 & 0 \\ 0 & 0 & M_{(k)}^{u_3} & 0 & 0 & 0 \\ 0 & 0 & 0 & M_{(k)}^{\theta_1} & 0 & 0 \\ 0 & 0 & 0 & 0 & M_{(k)}^{\theta_2} & 0 \\ 0 & 0 & 0 & 0 & 0 & M_{(k)}^{\theta_3} \end{bmatrix} \tag{A.10a}$$

with

$$M_{(k)}^{u_1} = M_{(k)}^{u_2} = M_{(k)}^{u_3} = \max\left(M_{(k)}^{u}, M_{(k)}^{v}, M_{(k)}^{w} \right) \tag{A.10b}$$

$$M_{(k)}^{\theta_1} = M_{(k)}^{\theta_2} = M_{(k)}^{\theta_3} = \max\left(M_{(k)}^{\theta_x}, M_{(k)}^{\theta_y}, M_{(k)}^{\theta_z} \right) \tag{A.10c}$$

where $M_{(k)}^{u_1}$, $M_{(k)}^{u_2}$, $M_{(k)}^{u_3}$, $M_{(k)}^{\theta_1}$, $M_{(k)}^{\theta_2}$, $M_{(k)}^{\theta_3}$ represent the components mass stable vector corresponding to translational and rotational DOFs in the global coordinates. Meanwhile, $M_{(k)}^{u}$,$M_{(k)}^{v}$, $M_{(k)}^{w}$, $M_{(k)}^{\theta_x}$, $M_{(k)}^{\theta_y}$, $M_{(k)}^{\theta_z}$ represent the components of a mass stable vector in the local coordinates. The components of the mass stable vector in the local coordinates can be calculated based on PD bond constants as

$$M_{(k)}^{u} \geq \frac{1}{4}\frac{dt^2 AC_{ax}\delta}{dx} \tag{A.11a}$$

$$M_{(k)}^{v} = M_{(k)}^{w} \geq \frac{1}{4}\frac{dt^2 AC_{s}\delta}{dx} \tag{A.11b}$$

$$M_{(k)}^{\theta_x} \geq \frac{1}{4}\frac{dt^2 AC_{t}\delta}{dx} \tag{A.11c}$$

$$M_{(k)}^{\theta_y} \geq \frac{1}{4}\frac{dt^2 AC_{by}\delta}{dx} \tag{A.11d}$$

$$M_{(k)}^{\theta_z} \geq \frac{1}{4}\frac{dt^2 AC_{bz}\delta}{dx} \tag{A.11e}$$

where C_{ax}, C_s, C_{by}, C_{bz}, and C_t are PD bond constants that are given in Eq. (2.14), Eq. (2.24), Eq. (2.20), and Eq. (2.25) Chapter 2 or Eq. (3.51), Eq. (3.55), Eq. (3.53), and Eq. (3.57) in Chapter 3.

A3. ADR method used in PD simulations for plates and shells

For the linear PD shell model presented in Chapter 2, to use the ADR method, the PD equations of motion given in Eq. (2.88) can be rewritten as

$$\mathbf{M}_{(k)}\ddot{\mathbf{u}}_{(k)}^{G} + \mathbf{C}_{(k)}\dot{\mathbf{u}}_{(k)}^{G} = \sum_{j=1} \psi_{(k)(j)}\mathbf{f}_{(k)(j)}^{G} V_{(j)} + \mathbf{b}_{(k)}^{G} \tag{A.12}$$

For the nonlinear PD model for plates presented in Chapter 3, to use the ADR method, the PD equations of motion given in Eq. (3.114) can be rewritten as

$$\mathbf{M}_{(k)}\,{}^{t}\ddot{\mathbf{u}}_{(k)} + \mathbf{C}_{(k)}\,{}^{t}\dot{\mathbf{u}}_{(k)} = \sum_{j=1}^{N} \psi_{(k)(j)}\,{}_{0}^{t}\overline{\mathbf{f}}_{(k)(j)}\,{}^{0}V_{(j)} + {}^{t}\overline{\mathbf{b}}_{(k)} \tag{A.13}$$

where the mass stable matrix $\boldsymbol{M}_{(k)}$ can be calculated by using the same formulations given in Eq. (A.10). The components of the mass stable vector in the local coordinates can be calculated based on PD bond constants as

$$M_{(k)}^{u} = M_{(k)}^{v} \geq \frac{1}{4} dt^2 \frac{4b_{ip}\pi h\delta^2}{\Delta x} \tag{A.14}$$

$$M_{(k)}^{w} \geq \frac{1}{4} dt^2 \frac{C_s \pi h\delta^2}{\Delta x} \tag{A.15}$$

$$M_{(k)}^{\theta_x} = M_{(k)}^{\theta_y} \geq \frac{1}{4} dt^2 \frac{4b_b \pi h\delta^2}{\Delta x} \tag{A.16}$$

$$M_{(k)}^{\theta_z} \geq \frac{1}{4} dt^2 \frac{C_t \pi h\delta^2}{\Delta x}\frac{1}{(\Delta x)^2} \tag{A.17}$$

where b_{ip}, C_s, b_b represent PD constants for in-plane, shear, bending deformations which are given in Eq. (2.62d), Eq. (2.70), Eq. (2.67b) in Chapter 2 or Eq. (3.105c), Eq. (3.107), Eq. (3.109c) in Chapter 3. The term C_t represents PD constant for torsional deformations which is given in Eq. (2.73) in Chapter 2.

Appendix B. Peridynamics constants for linear PD shell model

B1. PD constants for in-plane deformations

B1.1. PD dilatation constant, d_{ip}

By using Taylor's series expansion and by ignoring the higher-order terms, the displacements and rotations of material point *j* can be expressed as

$$u_{(j)} = u_{(k)} + u_{,x(k)}\left(x_{(j)} - x_{(k)}\right) + u_{,y(k)}\left(y_{(j)} - y_{(k)}\right) \tag{B.1a}$$

$$v_{(j)} = v_{(k)} + v_{,x(k)}\left(x_{(j)} - x_{(k)}\right) + v_{,y(k)}\left(y_{(j)} - y_{(k)}\right) \tag{B.1b}$$

$$w_{(j)} = w_{(k)} + w_{,x(k)}\left(x_{(j)} - x_{(k)}\right) + w_{,y(k)}\left(y_{(j)} - y_{(k)}\right) \tag{B.1c}$$

$$\theta_{x(j)} = \theta_{x(k)} + \theta_{x,x(k)}\left(x_{(j)} - x_{(k)}\right) + \theta_{x,y(k)}\left(y_{(j)} - y_{(k)}\right) \tag{B.1d}$$

$$\theta_{y(j)} = \theta_{y(k)} + \theta_{y,x(k)}\left(x_{(j)} - x_{(k)}\right) + \theta_{y,y(k)}\left(y_{(j)} - y_{(k)}\right) \tag{B.1e}$$

The relations in Eq. (B.1) can be rewritten as

$$\frac{u_{(j)} - u_{(k)}}{\xi} = u_{,x(k)}\cos\varphi + u_{,y(k)}\sin\varphi \tag{B.2a}$$

$$\frac{v_{(j)} - v_{(k)}}{\xi} = v_{,x(k)}\cos\varphi + v_{,y(k)}\sin\varphi \tag{B.2b}$$

$$\frac{w_{(j)} - w_{(k)}}{\xi} = w_{,x(k)}\cos\varphi + w_{,y(k)}\sin\varphi \tag{B.2c}$$

$$\frac{\theta_{x(j)} - \theta_{x(k)}}{\xi} = \theta_{x,x(k)}\cos\varphi + \theta_{x,y(k)}\sin\varphi \tag{B.2d}$$

$$\frac{\theta_{y(j)} - \theta_{y(k)}}{\xi} = \theta_{y,x(k)}\cos\varphi + \theta_{y,y(k)}\sin\varphi \tag{B.2e}$$

Therefore, by using Eq. (B.2a) and (B.2b), the bond stretch for in-plane deformations given in Eq. (2.65) can be rewritten as

$$s_{ip(k)(j)} = u_{,x(k)}\cos^2\varphi + u_{,y(k)}\sin\varphi\cos\varphi + v_{,x(k)}\sin\varphi\cos\varphi + v_{,y(k)}\sin^2\varphi \tag{B.3}$$

Therefore, the dilatation for in-plane deformations given in Eq. (2.63) can be rewritten in an integral form as

$$\vartheta_{(k)} = d_{ip}h\int_0^{\delta}\int_0^{2\pi}\begin{pmatrix} u_{,x(k)}\cos^2\varphi + u_{,y(k)}\sin\varphi\cos\varphi \\ +v_{,x(k)}\sin\varphi\cos\varphi + v_{,y(k)}\sin^2\varphi - \alpha\,\Delta T_{(k)}\end{pmatrix}\xi\, d\xi\, d\varphi + 2\alpha\,\Delta T_{(k)} \tag{B.4}$$

By performing integrations given in Eq. (B.4), the dilatation for in-plane deformations can be calculated as

$$\vartheta_{(k)} = d_{ip}\frac{\pi h\delta^2}{2}\left(u_{,x(k)} + v_{,y(k)}\right) + \alpha\,\Delta T_{(k)}\left(2 - d_{ip}\pi h\delta^2\right) \tag{B.5}$$

Meanwhile, the classical form of dilatation can be described as

$$\vartheta_{(k)}^{CCM} = u_{,x(k)} + v_{,y(k)} \tag{B.6}$$

By comparing Eq. (B.5) and (B.6), the PD dilatation constant d_{ip} can be defined as

$$d_{ip} = \frac{2}{\pi h\delta^2} \tag{B.7}$$

B1.2. PD material constants, a_{ip1}, a_{ip2}, a_{ip3} and b_{ip}

By using the stretch definition in Eq. (B.3) and dilatation term in Eq. (B.6), the strain energy per unit area for in-plane deformations given in Eq. (2.61) can be rewritten in an integral form as

$$\begin{aligned}\bar{W}^{PD}_{inplane(k)} &= a_{ip1}\left(u_{,x(k)}+v_{,y(k)}\right)^2 - a_{ip2}\left(u_{,x(k)}+v_{,y(k)}\right)\Delta T_{(k)} + a_{ip3}\Delta T^2_{(k)} \\ &+ b_{ip}h\int_0^{\delta}\int_0^{2\pi}\left(\begin{matrix}u_{,x(k)}\cos^2\varphi + u_{,y(k)}\sin\varphi\cos\varphi \\ +v_{,x(k)}\sin\varphi\cos\varphi + v_{,y(k)}\sin^2\varphi - \alpha\Delta T_{(k)}\end{matrix}\right)^2 \xi^2 d\xi d\varphi\end{aligned} \tag{B.8}$$

After performing integrations given in Eq. (B.8), the strain energy per unit area for the in-plane deformations can be evaluated as

$$\begin{aligned}\bar{W}^{PD}_{inplane(k)} &= a_{ip1}\left(u_{,x(k)}+v_{,y(k)}\right)^2 - a_{ip2}\left(u_{,x(k)}+v_{,y(k)}\right)\Delta T_{(k)} + a_{ip3}\Delta T^2_{(k)} \\ &+ b_{ip}\frac{\pi h\delta^3}{12}\left(3u^2_{,x(k)} + 3v^2_{,y(k)} + u^2_{,y(k)} + v^2_{,x(k)} + 2u_{,x(k)}v_{,y(k)} + 2u_{,y(k)}v_{,x(k)}\right) \\ &+ b_{ip}\frac{2\pi h\delta^3}{3}\left[-\alpha\,\Delta T_{(k)}\left(u_{,x(k)}+v_{,y(k)}\right) + \alpha^2\Delta T^2_{(k)}\right]\end{aligned} \tag{B.9}$$

or

$$\begin{aligned}\bar{W}^{PD}_{inplane(k)} &= a_{ip1}\left(u_{,x(k)}+v_{,y(k)}\right)^2 \\ &+ b_{ip}\frac{\pi h\delta^3}{12}\left[3\left(u_{,x(k)}+v_{,y(k)}\right)^2 - 4u_{,x(k)}v_{,y(k)} + \left(u_{,y(k)}+v_{,x(k)}\right)^2\right] \\ &- \left(a_{ip2} + b_{ip}\frac{2\pi h\delta^3}{3}\alpha\right)\left(u_{,x(k)}+v_{,y(k)}\right)\Delta T_{(k)} \\ &+ \left(a_{ip3} + b_{ip}\frac{2\pi h\delta^3}{3}\alpha^2\right)\Delta T^2_{(k)}\end{aligned} \tag{B.10}$$

By comparing Eq. (B.10) and Eq. (2.58b) following relations can be obtained

$$b_{ip}\frac{\pi h\delta^3}{12} = \frac{Eh}{4(1+\nu)} \tag{B.11a}$$

$$a_{ip1} + b_{ip}\frac{\pi h\delta^3}{4} = \frac{Eh}{2(1-\nu^2)} \tag{B.11b}$$

$$a_{ip2} + b_{ip}\frac{2\pi h\delta^3}{3}\alpha = \frac{Eh}{1-\nu}\alpha \tag{B.11c}$$

$$a_{ip3} + b_{ip}\frac{2\pi h\delta^3}{3}\alpha^2 = \frac{Eh}{1-\nu}\alpha^2 \tag{B.11d}$$

Therefore, the PD constants for in-plane deformations can be defined as

$$b_{ip} = \frac{3E}{\pi\delta^3(1+\nu)} \tag{B.12a}$$

$$a_{ip1} = \frac{Eh(3\nu-1)}{4(1-\nu^2)} \tag{B.12b}$$

$$a_{ip2} = \frac{Eh\alpha}{1-\nu^2}(3\nu-1) \tag{B.12c}$$

$$a_{ip3} = \frac{Eh}{1-\nu^2}(3\nu - 1)\alpha^2 \tag{B.12d}$$

B2. PD constants for bending deformations

B2.1. PD constant, d_b

By using Eq. (B.2d-e), the term $s_{b(k)(j)}$ in Eq. (2.68b) can be rewritten as

$$s_{b(k)(j)} = -\theta_{y,x(k)}\cos^2\varphi - \theta_{y,y(k)}\sin\varphi\cos\varphi + \theta_{x,x(k)}\sin\varphi\cos\varphi + \theta_{x,y(k)}\sin^2\varphi \tag{B.13}$$

Therefore, the term $\vartheta_{b(k)}$ in Eq. (2.68a) can be rewritten in an integral form as

$$\vartheta_{b(k)} = d_b h\int_0^{\delta}\int_0^{2\pi}\begin{pmatrix} -\theta_{y,x(k)}\cos^2\varphi - \theta_{y,y(k)}\sin\varphi\cos\varphi \\ +\theta_{x,x(k)}\sin\varphi\cos\varphi + \theta_{x,y(k)}\sin^2\varphi \end{pmatrix}\xi\, d\xi\, d\varphi \tag{B.14}$$

By performing integrations in Eq. (B.14), the term $\vartheta_{b(k)}$ can be written as

$$\vartheta_{b(k)} = d_b\frac{\pi h\delta^2}{2}\left(-\theta_{y,x(k)} + \theta_{x,y(k)}\right) \tag{B.15}$$

On the other hand, the corresponding term in classical form can be described as

$$\vartheta_{b(k)}^{CCM} = -\theta_{y,x(k)} + \theta_{x,y(k)} \tag{B.16}$$

By comparing Eq. (B.15) and (B.16), the PD constant, d_b, can be defined as

$$d_b = \frac{2}{\pi h\delta^2} \tag{B.17}$$

B2.2. PD material constants, a_b and b_b

By using Eq. (B.13) and (B.16), the strain energy per unit area for bending deformations in Eq. (2.66) can be rewritten in an integral form as

$$\begin{aligned} \bar{W}_{bending(k)}^{PD} &= a_b\left(-\theta_{y,x(k)} + \theta_{x,y(k)}\right)^2 \\ &+ b_b h\int_0^{\delta}\int_0^{2\pi}\begin{pmatrix} -\theta_{y,x(k)}\cos^2\varphi - \theta_{y,y(k)}\sin\varphi\cos\varphi \\ +\theta_{x,x(k)}\sin\varphi\cos\varphi + \theta_{x,y(k)}\sin^2\varphi \end{pmatrix}^2\xi^2\, d\xi\, d\varphi \end{aligned} \tag{B.18}$$

After performing integrations given in Eq. (B.18), the strain energy per unit area for bending deformations can be written as

$$\begin{aligned} \bar{W}_{bending(k)}^{PD} &= a_b\left(\theta_{x,y(k)} - \theta_{y,x(k)}\right)^2 \\ &+ b_b\frac{\pi h\delta^3}{12}\left[3\left(\theta_{x,y(k)} - \theta_{y,x(k)}\right)^2 + 4\theta_{y,x(k)}\theta_{x,y(k)} + \left(\theta_{x,x(k)} - \theta_{y,y(k)}\right)^2\right] \end{aligned} \tag{B.19}$$

By comparing Eq. (B.19) and (2.58c), PD constants for bending deformations can be defined as

$$b_b = \frac{Eh^2}{4\pi\delta^3(1+\nu)},\ a_b = \frac{Eh^3(3\nu-1)}{48(1-\nu^2)} \tag{B.20}$$

B3. PD constant for shear deformations

By assuming material points k and j are very closed to each other, the approximation $\bar{\theta}_{(k)} \approx \bar{\theta}_{(j)}$ is assumed for small deformations. Therefore, the strain energy per unit area for shear deformations given in Eq. (2.69) becomes

$$\bar{W}^{PD}_{shear(k)} = \frac{1}{4}\sum_{j=1}^{N} C_s \left(\frac{w_{(j)} - w_{(k)}}{\xi} - \bar{\theta}_{(k)} \right)^2 \xi V_{(j)} \tag{B.21}$$

By using the relations in Eq. (B.2c) and (2.71a), the strain energy per unit area for shear deformations given in Eq. (B.21) can be rewritten in an integral form as

$$\bar{W}^{PD}_{shear(k)} = \frac{1}{4} C_s h \int_0^{\delta} \int_0^{2\pi} \begin{bmatrix} \left(w_{,x(k)} + \theta_{y(k)} \right) \cos\varphi \\ + \left(w_{,y(k)} - \theta_{x(k)} \right) \sin\varphi \end{bmatrix}^2 \xi^2 d\xi d\varphi \tag{B.22}$$

By performing integrations given in Eq. (B.22), the strain energy per unit area for shear deformations can be written as

$$\bar{W}^{PD}_{shear(k)} = \frac{1}{12} C_s \pi h \delta^3 \left[\left(w_{,x(k)} + \theta_{y(k)} \right)^2 + \left(w_{,y(k)} - \theta_{x(k)} \right)^2 \right] \tag{B.23}$$

By comparing Eq. (B.23) and (2.58d), the PD constants for shear deformations can be defined as

$$C_s = \frac{3k_s}{\pi\delta^3} \frac{E}{(1+\nu)} \tag{B.24}$$

B4. PD constant for torsional deformations

By using strain energy per unit area given in Eq. (2.59b), the potential energy corresponding to drilling rotation, θ_z, can be defined as

$$U_{torsional} = \int_A W_{torsional} dA = \int_A k_T \frac{Eh}{2(1+\nu)} \left[\theta_z - \frac{1}{2}\left(v_{,x} - u_{,y} \right) \right]^2 dA \tag{B.25}$$

The kinetic energy corresponding to drilling rotation can be defined as

$$T_{\theta_z} = \frac{1}{2} \rho h I_{zz} \dot{\theta}_z^{\,2} \tag{B.26}$$

By using Eq. (B.25) and (B.26), the Lagrangian corresponding to drilling rotation can be obtained as

$$L_{\theta_z} = T_{\theta_z} - U_{\theta_z} = \frac{1}{2} \rho h I_{zz} \dot{\theta}_z^{\,2} - \int_A k_T \frac{Eh}{2(1+\nu)} \left[\theta_z - \frac{1}{2}\left(v_{,x} - u_{,y} \right) \right]^2 dA \tag{B.27}$$

As mentioned in section 3.3, since the torsional strain energy is fictitious, the contribution of drilling rotation into the equation of motion other degrees of freedom can be neglected [71]. Therefore, the equation of motion for drilling rotation in classical continuum mechanics can be derived by using the Euler-Lagrange equation given in Eq. (2.26) in Chapter 2 as

$$\frac{\rho h I_{zz}}{A} \ddot{\theta}_z = k_T \frac{Eh}{1+\nu} \left[\theta_z - \frac{1}{2}\left(v_{,x} - u_{,y} \right) \right] \tag{B.28}$$

Meanwhile, by using relations given in Eq. (B.2a-b), the PD equation of motion for drilling rotation given in Eq. (2.77f) can be written in an integral form as

$$\frac{\rho h I_{zz(k)}}{A_{(k)}}\ddot{\theta}_{z(k)} = C_t h \int_0^{\delta}\int_0^{2\pi}\left[\frac{\theta_{z(k)}+\theta_{z(j)}}{2} - \begin{pmatrix} v_{,x(k)}\cos^2\varphi + v_{,y(k)}\sin\varphi\cos\varphi \\ -u_{,x(k)}\sin\varphi\cos\varphi - u_{,y(k)}\sin^2\varphi \end{pmatrix}\right]\xi^2 d\xi d\varphi \quad \text{(B.29)}$$

By assuming material points k and j are very closed to each other, the approximation $\theta_{z(j)} \approx \theta_{z(k)}$ is assumed for small deformations. Therefore, Eq. (B.29) can be rewritten as

$$\frac{\rho h I_{zz(k)}}{A_{(k)}}\ddot{\theta}_{z(k)} = C_t h \int_0^{\delta}\int_0^{2\pi}\left[\theta_{z(k)} - \begin{pmatrix} v_{,x(k)}\cos^2\varphi + v_{,y(k)}\sin\varphi\cos\varphi \\ -u_{,x(k)}\sin\varphi\cos\varphi - u_{,y(k)}\sin^2\varphi \end{pmatrix}\right]\xi^2 d\xi d\varphi \quad \text{(B.30)}$$

By performing integrations given in Eq. (B.30), the equation of motion for drilling rotation can be written as

$$\frac{\rho h I_{zz(k)}}{A_{(k)}}\ddot{\theta}_{z(k)} = C_t \frac{2\pi h\delta^3}{3}\left[\theta_{z(k)} - \frac{1}{2}\left(v_{,x(k)} - u_{,y(k)}\right)\right] \quad \text{(B.31)}$$

By comparing Eq. (B.28) and (B.31), the PD constant for drilling rotation can be defined as

$$C_t = k_T \frac{3}{2\pi\delta^3}\frac{E}{1+\nu} \quad \text{(B.32)}$$

Appendix C. Total Lagrangian Formulations For Nonlinear Analysis

In this section, classical formulations for deformation gradient, Green-Lagrange strain, Second Piola-Kirchhoff stress tensors, and the principle of virtual displacement are presented. The motions of a structure at different times in the Cartesian coordinate system are shown in Fig. C1. As shown in Fig. C1, P is a material point on the structure, and its coordinates at time $t = 0$ are denoted by $({}^0x,\ {}^0y,\ {}^0z)$. Meanwhile, the coordinates of this point at time t and $t + \Delta t$ are denoted by $({}^tx,\ {}^ty,\ {}^tz)$ and $({}^{t+\Delta t}x,\ {}^{t+\Delta t}y,\ {}^{t+\Delta t}z)$, respectively. The relationships between these coordinates can be represented as

$${}^t\mathbf{x} = {}^0\mathbf{x} + {}^t\hat{\mathbf{u}} \tag{C1a}$$

$${}^{t+\Delta t}\mathbf{x} = {}^0\mathbf{x} + {}^{t+\Delta t}\hat{\mathbf{u}} \tag{C1b}$$

with

$${}^0\mathbf{x} = \begin{bmatrix} {}^0x & {}^0y & {}^0z \end{bmatrix}^T \tag{C1c}$$

$${}^t\mathbf{x} = \begin{bmatrix} {}^tx & {}^ty & {}^tz \end{bmatrix}^T \tag{C1d}$$

$${}^{t+\Delta t}\mathbf{x} = \begin{bmatrix} {}^{t+\Delta t}x & {}^{t+\Delta t}y & {}^{t+\Delta t}z \end{bmatrix}^T \tag{C1e}$$

$${}^t\hat{\mathbf{u}} = \begin{bmatrix} {}^t\hat{u} & {}^t\hat{v} & {}^t\hat{w} \end{bmatrix}^T \tag{C1f}$$

$${}^{t+\Delta t}\hat{\mathbf{u}} = \begin{bmatrix} {}^{t+\Delta t}\hat{u} & {}^{t+\Delta t}\hat{v} & {}^{t+\Delta t}\hat{w} \end{bmatrix}^T \tag{C1g}$$

where ${}^t\hat{\mathbf{u}}$ and ${}^{t+\Delta t}\hat{\mathbf{u}}$ represent the displacement vectors for a material point which is initially located at $({}^0x,\ {}^0y,\ {}^0z)$ as shown in Fig. C1 at time t and $t + \Delta t$, respectively. The relationship between these vectors of displacements can be represented as

$${}^{t+\Delta t}\hat{\mathbf{u}} = {}^t\hat{\mathbf{u}} + \underline{\hat{\mathbf{u}}} \tag{C2a}$$

with

$$\underline{\hat{\mathbf{u}}} = \begin{bmatrix} \underline{\hat{u}} & \underline{\hat{v}} & \underline{\hat{w}} \end{bmatrix} \tag{C2b}$$

where $\underline{\hat{\mathbf{u}}}$ represents the vector of the incremental displacements from time t to $t + \Delta t$ of a material point which is initially located at $({}^0x,\ {}^0y,\ {}^0z)$.

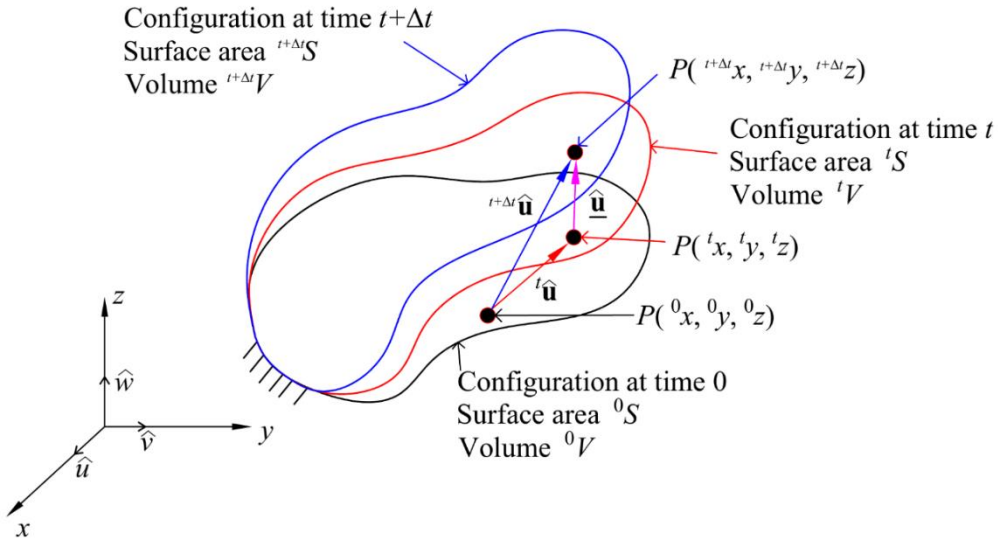

Fig. C1. Motions of a structure in the Cartesian coordinate frame

C1. Deformation gradient

The deformation gradient can be defined as [70]

$$ {}^{t}_{0}\mathbf{X} = \begin{bmatrix} \frac{\partial {}^{t}x}{\partial {}^{0}x} & \frac{\partial {}^{t}x}{\partial {}^{0}y} & \frac{\partial {}^{t}x}{\partial {}^{0}z} \\ \frac{\partial {}^{t}y}{\partial {}^{0}x} & \frac{\partial {}^{t}y}{\partial {}^{0}y} & \frac{\partial {}^{t}y}{\partial {}^{0}z} \\ \frac{\partial {}^{t}z}{\partial {}^{0}x} & \frac{\partial {}^{t}z}{\partial {}^{0}y} & \frac{\partial {}^{t}z}{\partial {}^{0}z} \end{bmatrix} \tag{C3a} $$

or

$$ {}^{t}_{0}\mathbf{X} = \left({}_{0}\nabla \left({}^{t}\mathbf{x}^{T} \right) \right)^{T} \tag{C3b} $$

with

$$ {}_{0}\nabla = \begin{bmatrix} \frac{\partial}{\partial {}^{0}x} & \frac{\partial}{\partial {}^{0}y} & \frac{\partial}{\partial {}^{0}z} \end{bmatrix}^{T} \tag{C3c} $$

where ${}_{0}\nabla$ represents the gradient operator with respect to the initial configuration and ${}^{t}\mathbf{x}^{T}$ represents the transposed vector of ${}^{t}\mathbf{x}$.

C2. Green-Lagrange strain

By using the deformation gradient given in Eq. (C3), the Green-Lagrange strain at time t can be defined as [70]

$$ {}^{t}_{0}\hat{\boldsymbol{\varepsilon}} = \frac{1}{2}\left({}^{t}_{0}\mathbf{X}^{T} \, {}^{t}_{0}\mathbf{X} - \mathbf{I} \right) \tag{C4a} $$

which can be explicitly rewritten as [70]

$$ {}_0^t\hat{\varepsilon}_{ij} = \frac{1}{2}\left({}_0^t\hat{u}_{i,j} + {}_0^t\hat{u}_{j,i} + {}_0^t\hat{u}_{k,i}\,{}_0^t\hat{u}_{k,j} \right) \tag{C4b} $$

or

$$ {}_0^t\hat{\varepsilon}_{xx} = {}_0^t\hat{u}_{,x} + \frac{1}{2}\left[\left({}_0^t\hat{u}_{,x} \right)^2 + \left({}_0^t\hat{v}_{,x} \right)^2 + \left({}_0^t\hat{w}_{,x} \right)^2 \right] \tag{C4c} $$

$$ {}_0^t\hat{\varepsilon}_{yy} = {}_0^t\hat{v}_{,y} + \frac{1}{2}\left[\left({}_0^t\hat{u}_{,y} \right)^2 + \left({}_0^t\hat{v}_{,y} \right)^2 + \left({}_0^t\hat{w}_{,y} \right)^2 \right] \tag{C4d} $$

$$ {}_0^t\hat{\varepsilon}_{zz} = {}_0^t\hat{w}_{,z} + \frac{1}{2}\left[\left({}_0^t\hat{u}_{,z} \right)^2 + \left({}_0^t\hat{v}_{,z} \right)^2 + \left({}_0^t\hat{w}_{,z} \right)^2 \right] \tag{C4e} $$

$$ {}_0^t\hat{\varepsilon}_{xy} = \frac{1}{2}\left[{}_0^t\hat{u}_{,y} + {}_0^t\hat{v}_{,x} \right] + \frac{1}{2}\left[\left({}_0^t\hat{u}_{,x} \right)\left({}_0^t\hat{u}_{,y} \right) + \left({}_0^t\hat{v}_{,x} \right)\left({}_0^t\hat{v}_{,y} \right) + \left({}_0^t\hat{w}_{,x} \right)\left({}_0^t\hat{w}_{,y} \right) \right] \tag{C4f} $$

$$ {}_0^t\hat{\varepsilon}_{xz} = \frac{1}{2}\left[{}_0^t\hat{u}_{,z} + {}_0^t\hat{w}_{,x} \right] + \frac{1}{2}\left[\left({}_0^t\hat{u}_{,x} \right)\left({}_0^t\hat{u}_{,z} \right) + \left({}_0^t\hat{v}_{,x} \right)\left({}_0^t\hat{v}_{,z} \right) + \left({}_0^t\hat{w}_{,x} \right)\left({}_0^t\hat{w}_{,z} \right) \right] \tag{C4g} $$

$$ {}_0^t\hat{\varepsilon}_{yz} = \frac{1}{2}\left[{}_0^t\hat{v}_{,z} + {}_0^t\hat{w}_{,y} \right] + \frac{1}{2}\left[\left({}_0^t\hat{u}_{,y} \right)\left({}_0^t\hat{u}_{,z} \right) + \left({}_0^t\hat{v}_{,y} \right)\left({}_0^t\hat{v}_{,z} \right) + \left({}_0^t\hat{w}_{,y} \right)\left({}_0^t\hat{w}_{,z} \right) \right] \tag{C4h} $$

where $\mathbf{I}$ represents the identity matrix. The term ${}_0^t\hat{u}_{k,j}$ represents the derivative of the displacement ${}^t\hat{u}_k$ (at time t) with respect to the initial configuration, ${}^0x_j$. The derivative ${}_0^t\hat{u}_{k,j}$ can be represented as

$$ {}_0^t\hat{u}_{k,j} = \frac{\partial\left({}^t\hat{u}_k \right)}{\partial\left({}^0x_j \right)} \tag{C5} $$

where ${}^t\hat{u}_k$ represents the displacement at time t and ${}^0x_j$ represents the initial (reference) configuration.

The Green-Lagrange strain at time $t + \Delta t$ can be calculated as [70, 108]

$$ {}_0^{t+\Delta t}\hat{\boldsymbol{\varepsilon}} = {}_0^t\hat{\boldsymbol{\varepsilon}} + {}_0\underline{\hat{\boldsymbol{\varepsilon}}} \tag{C6a} $$

or

$$ {}_0^{t+\Delta t}\hat{\varepsilon}_{ij} = {}_0^t\hat{\varepsilon}_{ij} + {}_0\underline{\hat{\varepsilon}}_{ij} \tag{C6b} $$

where ${}_0^{t+\Delta t}\hat{\boldsymbol{\varepsilon}}$ (or ${}_0^{t+\Delta t}\hat{\varepsilon}_{ij}$) represents the Green-Lagrange strain tensor (or components) at time $t + \Delta t$ as provided in Eq. (C4) and ${}_0\underline{\hat{\boldsymbol{\varepsilon}}}$ (or ${}_0\underline{\hat{\varepsilon}}_{ij}$) represents the incremental Green-Lagrange strain tensor (or components) from time t to time $t + \Delta t$. The incremental strain, ${}_0\underline{\hat{\varepsilon}}_{ij}$, can be decomposed as [70]

$$ {}_0\underline{\hat{\varepsilon}}_{ij} = {}_0\underline{\hat{e}}_{ij} + {}_0\underline{\hat{\eta}}_{ij} \tag{C7a} $$

with

$$ {}_0\hat{\underline{e}}_{ij} = \frac{1}{2}\left[{}_0\hat{\underline{u}}_{i,j} + {}_0\hat{\underline{u}}_{j,i} + {}_0^t\hat{u}_{k,i}\, {}_0\hat{\underline{u}}_{k,j} + {}_0^t\hat{u}_{k,j}\, {}_0\hat{\underline{u}}_{k,i} \right] \tag{C7b} $$

$$ {}_0\hat{\underline{\eta}}_{ij} = \frac{1}{2}\, {}_0\hat{\underline{u}}_{k,i}\, {}_0\hat{\underline{u}}_{k,j} \tag{C7c} $$

where ${}_0\hat{\underline{e}}_{ij}$ and ${}_0\hat{\underline{\eta}}_{ij}$ represent the linear and nonlinear components of the incremental Green-Lagrange strain, respectively. The term ${}_0\hat{\underline{u}}_{k,j}$ represents the derivative of the incremental displacement $\hat{\underline{u}}_k$ as provided in Eq. (C2b), with respect to the initial coordinate, ${}^0x_j$ which can be defined as [70]

$$ {}_0\hat{\underline{u}}_{k,j} = \frac{\partial \hat{\underline{u}}_k}{\partial\left({}^0x_j\right)} \tag{C8} $$

On the left-hand side of Eq. (C8), the subscript "0" in ${}_0\hat{\underline{u}}_{k,j}$ refers to the reference configuration at time $t = 0$.

Note that, the derivative ${}_0^t\hat{u}_{k,j}$ on the left-hand side of Eq. (C5) has the superscript "t" because ${}_0^t\hat{u}_{k,j}$ represents the derivative of the displacement at time t. On the other hand, the term ${}_0\hat{\underline{u}}_{k,j}$ in Eq. (C8) does not have any left superscript since it represents the derivative of the incremental displacement $\hat{\underline{u}}_k$.

The linear and nonlinear components of the incremental Green-Lagrange strain given in Eqs. (C7b-c) can also be written as [70]

$$ {}_0\hat{\underline{e}}_{xx} = {}_0\hat{\underline{u}}_{,x} + {}_0^t\hat{u}_{,x}\, {}_0\hat{\underline{u}}_{,x} + {}_0^t\hat{v}_{,x}\, {}_0\hat{\underline{v}}_{,x} + {}_0^t\hat{w}_{,x}\, {}_0\hat{\underline{w}}_{,x} \tag{C9a} $$

$$ {}_0\hat{\underline{e}}_{yy} = {}_0\hat{\underline{v}}_{,y} + {}_0^t\hat{v}_{,y}\, {}_0\hat{\underline{v}}_{,y} + {}_0^t\hat{u}_{,y}\, {}_0\hat{\underline{u}}_{,y} + {}_0^t\hat{w}_{,y}\, {}_0\hat{\underline{w}}_{,y} \tag{C9b} $$

$$ {}_0\hat{\underline{e}}_{zz} = {}_0\hat{\underline{w}}_{,z} + {}_0^t\hat{u}_{,z}\, {}_0\hat{\underline{u}}_{,z} + {}_0^t\hat{v}_{,z}\, {}_0\hat{\underline{v}}_{,z} + {}_0^t\hat{w}_{,z}\, {}_0\hat{\underline{w}}_{,z} \tag{C9c} $$

$$ {}_0\hat{\underline{e}}_{xy} = \frac{1}{2}\left({}_0\hat{\underline{u}}_{,y} + {}_0\hat{\underline{v}}_{,x} \right) + \frac{1}{2}\left(\begin{array}{l} {}_0^t\hat{u}_{,x}\, {}_0\hat{\underline{u}}_{,y} + {}_0^t\hat{u}_{,y}\, {}_0\hat{\underline{u}}_{,x} + {}_0^t\hat{v}_{,x}\, {}_0\hat{\underline{v}}_{,y} + {}_0^t\hat{v}_{,y}\, {}_0\hat{\underline{v}}_{,x} \\ + {}_0^t\hat{w}_{,x}\, {}_0\hat{\underline{w}}_{,y} + {}_0^t\hat{w}_{,y}\, {}_0\hat{\underline{w}}_{,x} \end{array} \right) \tag{C9d} $$

$$ {}_0\hat{\underline{e}}_{yz} = \frac{1}{2}\left({}_0\hat{\underline{v}}_{,z} + {}_0\hat{\underline{w}}_{,y} \right) + \frac{1}{2}\left(\begin{array}{l} {}_0^t\hat{u}_{,z}\, {}_0\hat{\underline{u}}_{,y} + {}_0^t\hat{u}_{,y}\, {}_0\hat{\underline{u}}_{,z} + {}_0^t\hat{v}_{,z}\, {}_0\hat{\underline{v}}_{,y} + {}_0^t\hat{v}_{,y}\, {}_0\hat{\underline{v}}_{,z} \\ + {}_0^t\hat{w}_{,y}\, {}_0\hat{\underline{w}}_{,z} + {}_0^t\hat{w}_{,z}\, {}_0\hat{\underline{w}}_{,y} \end{array} \right) \tag{C9e} $$

$$ {}_0\hat{\underline{e}}_{xz} = \frac{1}{2}\left({}_0\hat{\underline{u}}_{,z} + {}_0\hat{\underline{w}}_{,x} \right) + \frac{1}{2}\left(\begin{array}{l} {}_0^t\hat{u}_{,x}\, {}_0\hat{\underline{u}}_{,z} + {}_0^t\hat{u}_{,z}\, {}_0\hat{\underline{u}}_{,x} + {}_0^t\hat{v}_{,x}\, {}_0\hat{\underline{v}}_{,z} + {}_0^t\hat{v}_{,z}\, {}_0\hat{\underline{v}}_{,x} \\ + {}_0^t\hat{w}_{,x}\, {}_0\hat{\underline{w}}_{,z} + {}_0^t\hat{w}_{,z}\, {}_0\hat{\underline{w}}_{,x} \end{array} \right) \tag{C9f} $$

and

$$ {}_0\hat{\underline{\eta}}_{xx} = \frac{1}{2}\left(\left({}_0\hat{\underline{u}}_{,x} \right)^2 + \left({}_0\hat{\underline{v}}_{,x} \right)^2 + \left({}_0\hat{\underline{w}}_{,x} \right)^2 \right) \tag{C10a} $$

$$ {}_0\hat{\underline{\eta}}_{yy} = \frac{1}{2}\left(\left({}_0\hat{\underline{u}}_{,y} \right)^2 + \left({}_0\hat{\underline{v}}_{,y} \right)^2 + \left({}_0\hat{\underline{w}}_{,y} \right)^2 \right) \tag{C10b} $$

$$ {}_0\underline{\hat{\eta}}_{zz} = \frac{1}{2}\left(\left({}_0\underline{\hat{u}}_{,z} \right)^2 + \left({}_0\underline{\hat{v}}_{,z} \right)^2 + \left({}_0\underline{\hat{w}}_{,z} \right)^2 \right) \tag{C10c} $$

$$ {}_0\underline{\hat{\eta}}_{xy} = \frac{1}{2}\left({}_0\underline{\hat{u}}_{,x}\, {}_0\underline{\hat{u}}_{,y} + {}_0\underline{\hat{v}}_{,x}\, {}_0\underline{\hat{v}}_{,y} + {}_0\underline{\hat{w}}_{,x}\, {}_0\underline{\hat{w}}_{,y} \right) \tag{C10d} $$

$$ {}_0\underline{\hat{\eta}}_{xz} = \frac{1}{2}\left({}_0\underline{\hat{u}}_{,x}\, {}_0\underline{\hat{u}}_{,z} + {}_0\underline{\hat{v}}_{,x}\, {}_0\underline{\hat{v}}_{,z} + {}_0\underline{\hat{w}}_{,x}\, {}_0\underline{\hat{w}}_{,z} \right) \tag{C10e} $$

$$ {}_0\underline{\hat{\eta}}_{yz} = \frac{1}{2}\left({}_0\underline{\hat{u}}_{,y}\, {}_0\underline{\hat{u}}_{,z} + {}_0\underline{\hat{v}}_{,y}\, {}_0\underline{\hat{v}}_{,z} + {}_0\underline{\hat{w}}_{,y}\, {}_0\underline{\hat{w}}_{,z} \right) \tag{C10f} $$

C3. Second Piola-Kirchhoff stress

In nonlinear analyses, the second Piola-Kirchhoff stress (SPK) tensor, ${}_0^t\hat{\mathbf{S}}$, is always work-conjugate with the Green-Lagrange tensor, ${}_0^t\hat{\boldsymbol{\varepsilon}}$, since they are often used as a pair [70].

❖ SPK stress for 3D structures

For a generally 3D structure, the SPK stress tensor, ${}_0^t\hat{\mathbf{S}}$, can be calculated by using the following procedure [70]:

Step 1: Calculate the deformation gradient, ${}_0^t\mathbf{X}$ by using Eq. (C3).

Step 2: Using the relation ${}_0^t\mathbf{X} = {}_0^t\mathbf{R}\,{}_0^t\mathbf{U}$, find the rotational matrix, ${}_0^t\mathbf{R}$ and right stretch tensor, ${}_0^t\mathbf{U}$ by using polar decomposition [70]

2.1. Find the right Cauchy-Green deformation tensor, ${}_0^t\mathbf{C}$

$$ {}_0^t\mathbf{C} = {}_0^t\mathbf{X}^T\, {}_0^t\mathbf{X} \tag{C11} $$

2.2. Find eigenvalues, ${}_0^t\boldsymbol{\lambda}$ and eigenvectors, $\mathbf{P}$ of ${}_0^t\mathbf{C}$ by solving the following equation

$$ {}_0^t\mathbf{C}\mathbf{P} = \mathbf{P}\,{}_0^t\boldsymbol{\lambda} \tag{C12} $$

2.3. Find rotational matrix, ${}_0^t\mathbf{R}$, and right stretch tensor, ${}_0^t\mathbf{U}$

- Find the deformation gradient in the principal coordinates, ${}_0^t\mathbf{X}'$

$$ {}_0^t\mathbf{X}' = \mathbf{P}^T\, {}_0^t\mathbf{X}\, \mathbf{P} \tag{C13} $$

- Find rotational matrix and right stretch tensor

$$ {}_0^t\mathbf{R} = \mathbf{P}\,\mathbf{R}'\,\mathbf{P}^T \tag{C14a} $$

$$ {}_0^t\mathbf{U} = \mathbf{P}\,\boldsymbol{\Lambda}\,\mathbf{P}^T \tag{C14b} $$

with

$$\mathbf{\Lambda} = \left({}^{t}_{0}\boldsymbol{\lambda}\right)^{1/2} \tag{C14c}$$

$$\mathbf{R}' = {}^{t}_{0}\mathbf{X}'\left({}^{t}_{0}\boldsymbol{\lambda}\right)^{-1/2} \tag{C14d}$$

Step 3: Find the Hencky strain tensor, ${}^{t}_{0}\hat{\mathbf{E}}^{H}$ [70]

$${}^{t}_{0}\hat{\mathbf{E}}^{H} = \mathbf{P}\left(\ln\left(\mathbf{\Lambda}\right)\right)\mathbf{P}^{T} \tag{C15a}$$

Mean strain:

$${}^{t}_{0}\hat{E}^{H}_{m} = \frac{1}{3}tr\left({}^{t}_{0}\hat{\mathbf{E}}^{H}\right) \tag{C15b}$$

Deviatoric strain:

$${}^{t}_{0}\hat{\mathbf{E}}^{H}_{d} = {}^{t}_{0}\hat{\mathbf{E}}^{H} - {}^{t}_{0}\hat{E}^{H}_{m}\mathbf{I} \tag{C15c}$$

where $\mathbf{I}$ represents the identity matrix.

Step 4: Calculate Cauchy stress, ${}^{t}\hat{\boldsymbol{\sigma}}$ [70]

- Calculate stress measure, $\bar{\boldsymbol{\sigma}}$

$$\bar{\boldsymbol{\sigma}} = \bar{\boldsymbol{\sigma}}_{d} + \bar{\sigma}_{m}\mathbf{I} \tag{C16a}$$

with

$$\bar{\boldsymbol{\sigma}}_{d} = 2\mu\left({}^{t}_{0}\hat{\mathbf{E}}^{H}_{d}\right) \tag{C16b}$$

$$\bar{\sigma}_{m} = 3\kappa\left({}^{t}_{0}\hat{E}^{H}_{m}\right) \tag{C16c}$$

where κ represents the Bulk modulus of the material, μ represents the Lame's constant as given in Eq. (3.13).

- Calculate Cauchy stress, ${}^{t}\hat{\boldsymbol{\sigma}}$

$${}^{t}\hat{\boldsymbol{\sigma}} = \frac{1}{\det {}^{t}_{0}\mathbf{X}}\left({}^{t}_{0}\mathbf{R}\right)\bar{\boldsymbol{\sigma}}\left({}^{t}_{0}\mathbf{R}^{T}\right) \tag{C17}$$

Step 5: Calculate SPK stress [70]

$${}^{t}_{0}\hat{\mathbf{S}} = \left(\det {}^{t}_{0}\mathbf{X}\right)\left({}^{t}_{0}\mathbf{X}^{-1}\right)\left({}^{t}\hat{\boldsymbol{\sigma}}\right)\left({}^{t}_{0}\mathbf{X}^{-T}\right) \tag{C18}$$

❖ SPK stress for beams and shells

For beam and shell structures subjected to large deformations, large rotations, but small strains, the SPK stress tensor can be simply estimated as [70]

$${}^{t}_{0}\hat{\mathbf{S}} = {}^{t}_{0}\mathbf{C}\,{}^{t}_{0}\hat{\boldsymbol{\varepsilon}} \tag{C19}$$

where ${}^{t}_{0}\mathbf{C}$ represents the elasticity tensor.

For plates and shells, the SPK stress, ${}_0^t\hat{\mathbf{S}}$, the Green-Lagrange strain, ${}_0^t\hat{\boldsymbol{\varepsilon}}$, and the elasticity tensor, ${}_0^t\mathbf{C}$, can be represented as [70]

$${}_0^t\hat{\mathbf{S}} = \begin{bmatrix} {}_0^t\hat{S}_{xx} & {}_0^t\hat{S}_{yy} & {}_0^t\hat{S}_{xy} & {}_0^t\hat{S}_{yz} & {}_0^t\hat{S}_{xz} \end{bmatrix}^T \tag{C20a}$$

$${}_0^t\hat{\boldsymbol{\varepsilon}} = \begin{bmatrix} {}_0^t\hat{\varepsilon}_{xx} & {}_0^t\hat{\varepsilon}_{yy} & {}_0^t\hat{\varepsilon}_{xy} & {}_0^t\hat{\varepsilon}_{yz} & {}_0^t\hat{\varepsilon}_{xz} \end{bmatrix}^T \tag{C20b}$$

$${}_0^t\mathbf{C} = \frac{E}{1-\nu^2}\begin{bmatrix} 1 & \nu & 0 & 0 & 0 \\ \nu & 1 & 0 & 0 & 0 \\ 0 & 0 & (1-\nu) & 0 & 0 \\ 0 & 0 & 0 & k_s(1-\nu) & 0 \\ 0 & 0 & 0 & 0 & k_s(1-\nu) \end{bmatrix} \tag{C20c}$$

with

$$k_s = 5/6 \tag{C20d}$$

where E and ν represent the elastic modulus and Poisson's ratio of the material, k_s represents shear correction factor [70].

For beam structures, the SPK stress, ${}_0^t\hat{\mathbf{S}}$, the Green-Lagrange strain, ${}_0^t\hat{\boldsymbol{\varepsilon}}$, and the elasticity tensor, ${}_0^t\mathbf{C}$, can be represented as [70]

$${}_0^t\hat{\mathbf{S}} = \begin{bmatrix} {}_0^t\hat{S}_{xx} \\ {}_0^t\hat{S}_{xy} \\ {}_0^t\hat{S}_{xz} \end{bmatrix};\ {}_0^t\hat{\boldsymbol{\varepsilon}} = \begin{bmatrix} {}_0^t\hat{\varepsilon}_{xx} \\ {}_0^t\hat{\varepsilon}_{xy} \\ {}_0^t\hat{\varepsilon}_{xz} \end{bmatrix};\ {}_0^t\mathbf{C} = \begin{bmatrix} E & 0 & 0 \\ 0 & 2k_sG & 0 \\ 0 & 0 & 2k_sG \end{bmatrix} \tag{C21}$$

where k_s represents the shear correction factor for the beam cross-section [70], G represents the elastic modulus and shear modulus of the material.

The SPK stress tensor at time $t+\Delta t$ can be represented as [70, 108]

$${}_0^{t+\Delta t}\hat{\mathbf{S}} = {}_0^t\hat{\mathbf{S}} + {}_0\underline{\hat{\mathbf{S}}} \tag{C22a}$$

or

$${}_0^{t+\Delta t}\hat{S}_{ij} = {}_0^t\hat{S}_{ij} + {}_0\underline{\hat{S}}_{ij} \tag{C22b}$$

where ${}_0\underline{\hat{\mathbf{S}}}$ represents the incremental SPK stress tensor from time t to time $t+\Delta t$.

C4. Principle of virtual displacement

In this section, the principle of virtual displacement based on Total Lagrange formulation is presented. In the Total Lagrange formulation, the equation of motion for a structure is written with respect to the initial configuration as [70]

$$\int_{{}_0V}\left({}_0^{t+\Delta t}\hat{S}_{ij}\right)\delta\left({}_0^{t+\Delta t}\hat{\varepsilon}_{ij}\right)d\left({}^0V\right) = {}^{t+\Delta t}\Re \tag{C23}$$

where ${}^{t+\Delta t}_{0}\hat{S}_{ij}$ and ${}^{t+\Delta t}_{0}\hat{\varepsilon}_{ij}$ represent components of SPK stress tensor and Green Lagrange strain at time $t+\Delta t$ as given in Eq. (C22) and Eq. (C6), respectively. The term $\delta\left({}^{t+\Delta t}_{0}\hat{\varepsilon}_{ij}\right)$ represents the virtual value of ${}^{t+\Delta t}_{0}\hat{\varepsilon}_{ij}$, ${}^{0}V$ represents the volume in the undeformed configuration, ${}^{t+\Delta t}\Re$ represents the external virtual work which can be calculated as

$${}^{t+\Delta t}\Re = \int_{{}^{t+\Delta t}V}\left({}^{t+\Delta t}\mathbf{f}^{B}\right)\left(\delta\hat{\mathbf{u}}\right)d\left({}^{t+\Delta t}V\right)+\int_{{}^{t+\Delta t}S}\left({}^{t+\Delta t}\mathbf{f}^{S}\right)\left(\delta\hat{\mathbf{u}}^{s}\right)d\left({}^{t+\Delta t}S\right) \tag{C24}$$

where ${}^{t+\Delta t}\mathbf{f}^{B}$ and ${}^{t+\Delta t}\mathbf{f}^{S}$ represent external force per unit volume and external force per unit surface area at time $t+\Delta t$, respectively. ${}^{t+\Delta t}S$ represents surface at time $t+\Delta t$ on which the external force per unit surface area is applied, $\delta\hat{\mathbf{u}}^{s}$ represents virtual displacement evaluated on the surface ${}^{t+\Delta t}S$.

By using the relations given in Eq. (C6) and Eq. (C22), the principle of virtual displacements given in Eq. (C23) can be rewritten as

$$\int_{{}_{0}V}\left({}_{0}\underline{\hat{S}}_{ij}\right)\delta\left({}_{0}\underline{\hat{\varepsilon}}_{ij}\right)d\,{}^{0}V+\int_{{}_{0}V}\left({}^{t}_{0}\hat{S}_{ij}\right)\delta\left({}_{0}\underline{\hat{\eta}}_{ij}\right)d\,{}^{0}V={}^{t+\Delta t}\Re-\int_{{}_{0}V}\left({}^{t}_{0}\hat{S}_{ij}\right)\delta\left({}_{0}\underline{\hat{e}}_{ij}\right)d\,{}^{0}V \tag{C25}$$

For dynamic problems, the work caused by the inertia forces can be added on the left-hand side of Eq. (C25) as [70]

$$\begin{aligned}\int_{{}_{0}V}\delta\left(\underline{\hat{\mathbf{u}}}^{T}\right)\hat{\mathbf{m}}\left({}^{t+\Delta t}\ddot{\underline{\hat{\mathbf{u}}}}\right)d\,{}^{0}V+\int_{{}_{0}V}\left({}_{0}\underline{\hat{S}}_{ij}\right)\delta\left({}_{0}\underline{\hat{\varepsilon}}_{ij}\right)d\,{}^{0}V\\ +\int_{{}_{0}V}\left({}^{t}_{0}\hat{S}_{ij}\right)\delta\left({}_{0}\underline{\hat{\eta}}_{ij}\right)d\,{}^{0}V={}^{t+\Delta t}\Re-\int_{{}_{0}V}\left({}^{t}_{0}\hat{S}_{ij}\right)\delta\left({}_{0}\underline{\hat{e}}_{ij}\right)d\,{}^{0}V\end{aligned} \tag{C26}$$

where the first term on the left-hand side of Eq. (C26) represents the virtual work of the inertia forces, $\hat{\mathbf{m}}$ represents the time-independent mass matrix, ${}^{t+\Delta t}\ddot{\underline{\hat{\mathbf{u}}}}$ represents the acceleration vector at time $t+\Delta t$ of the material point located at $({}^{0}x,\,{}^{0}y,\,{}^{0}z)$, $\underline{\hat{\mathbf{u}}}$ represents the incremental displacement vector of the material point located at $({}^{0}x,\,{}^{0}y,\,{}^{0}z)$ as given in Eq. (C2b), $\underline{\hat{\mathbf{u}}}^{T}$ represents the transpose of the incremental displacement vector, $\underline{\hat{\mathbf{u}}}$.

According to Bathe [70], the equation of motion given in Eq. (C26) is written for dynamic problems for the implicit time integration scheme. If the explicit time integration scheme is used, Eq. (C26) can be simplified as [70]

$$\int_{{}_{0}V}\delta\left(\underline{\hat{\mathbf{u}}}^{T}\right)\hat{\mathbf{m}}\left({}^{t}\ddot{\underline{\hat{\mathbf{u}}}}\right)d\,{}^{0}V={}^{t}\Re-\int_{{}_{0}V}\left({}^{t}_{0}\hat{S}_{ij}\right)\delta\left({}_{0}\underline{\hat{e}}_{ij}\right)d\,{}^{0}V \tag{C27}$$

The second term on the right-hand side of Eq. (C27) is the virtual work which is associated with the element stress at time t. The corresponding strain energy density (SED) for this virtual work can be written for a 3D structure as [102]

$$W^{NL}=\sum_{i=1}^{3}\sum_{j=1}^{3}\left({}^{t}_{0}\hat{S}_{ij}\right)\left({}_{0}\underline{\hat{e}}_{ij}\right) \tag{C28a}$$

or

$$W^{NL}={}^{t}_{0}\hat{S}_{xx}\,{}_{0}\underline{\hat{e}}_{xx}+{}^{t}_{0}\hat{S}_{yy}\,{}_{0}\underline{\hat{e}}_{yy}+{}^{t}_{0}\hat{S}_{zz}\,{}_{0}\underline{\hat{e}}_{zz}+2\,{}^{t}_{0}\hat{S}_{xy}\,{}_{0}\underline{\hat{e}}_{xy}+2\,{}^{t}_{0}\hat{S}_{yz}\,{}_{0}\underline{\hat{e}}_{yz}+2\,{}^{t}_{0}\hat{S}_{xz}\,{}_{0}\underline{\hat{e}}_{xz} \tag{C28b}$$

For 1D and 2D structures, the nonlinear SED in Eq. (C28b) can be simplified as

$$W^{NL} = {}_0^t\hat{S}_{xx}\,{}_0\underline{\hat{e}}_{xx} \text{ for 1D} \tag{C29a}$$

$$W^{NL} = {}_0^t\hat{S}_{xx}\,{}_0\underline{\hat{e}}_{xx} + {}_0^t\hat{S}_{yy}\,{}_0\underline{\hat{e}}_{yy} + 2\,{}_0^t\hat{S}_{xy}\,{}_0\underline{\hat{e}}_{xy} \text{ for 2D} \tag{C29b}$$

For plates and shells, the nonlinear SED in Eq. (C28b) can be simplified as

$$W^{NL} = {}_0^t\hat{S}_{xx}\,{}_0\underline{\hat{e}}_{xx} + {}_0^t\hat{S}_{yy}\,{}_0\underline{\hat{e}}_{yy} + 2\,{}_0^t\hat{S}_{xy}\,{}_0\underline{\hat{e}}_{xy} + 2\,{}_0^t\hat{S}_{yz}\,{}_0\underline{\hat{e}}_{yz} + 2\,{}_0^t\hat{S}_{xz}\,{}_0\underline{\hat{e}}_{xz} \tag{C30}$$

For beam structures, the nonlinear SED in Eq. (C28b) can be simplified as

$$W^{NL} = {}_0^t\hat{S}_{xx}\,{}_0\underline{\hat{e}}_{xx} + 2\,{}_0^t\hat{S}_{xy}\,{}_0\underline{\hat{e}}_{xy} + 2\,{}_0^t\hat{S}_{xz}\,{}_0\underline{\hat{e}}_{xz} \tag{C31}$$

By considering the beams with symmetrical cross-sections, the SED for the beam can be averaged through the cross-section as

$$\bar{W}^{NL} = \frac{\int_{{}^0A} W^{NL} d\left({}^0A\right)}{{}^0A} = \frac{\int_{{}^0A} \left({}_0^t\hat{S}_{xx}\,{}_0\underline{\hat{e}}_{xx} + 2\,{}_0^t\hat{S}_{xy}\,{}_0\underline{\hat{e}}_{xy} + 2\,{}_0^t\hat{S}_{xz}\,{}_0\underline{\hat{e}}_{xz} \right) d\left({}^0A\right)}{{}^0A} \tag{C32}$$

Appendix D. PD constants for nonlinear 1D, 2D, and 3D PD models

D1. PD constants for 3D structures

To determine PD constants, two different loading cases resulting in isotropic expansion and simple shear can be considered [44] by comparing the virtual values of strain energy density in classical continuum mechanics and their PD representations. The procedure for PD bond constants for 3D structures can be summarised as follows:

The virtual values of SED and volumetric strain in classical continuum mechanics for isotropic expansion is calculated in Section D1.1.1. The PD representation of SED and volumetric strain for isotropic expansion is represented in Section D1.1.2. By comparing the PD and the classical continuum mechanics representations, the relations for PD constants and material constants are provided in Section D1.1.3.

Similarly, the virtual values of SED in classical continuum mechanics and PD for simple shear loading are presented in Sections D1.2.1 and D1.2.2, respectively. By comparing the PD and the classical continuum mechanics representations, the relations for PD constants and material constants are provided in Section D1.2.3.

In this section, to simplify the notations, we write the displacements at time t ${}^t\hat{u}, {}^t\hat{v}, {}^t\hat{w}$ as ${}^t u, {}^t v, {}^t w$, and incremental displacements $\underline{\hat{u}}, \underline{\hat{v}}, \underline{\hat{w}}$ as $\underline{u}, \underline{v}, \underline{w}$.

D1.1. Loading 1: Isotropic expansion

D1.1.1. Strain Energy Density and volumetric strain definitions in classical continuum mechanics

A loading case of isotropic expansion can be obtained by applying the following conditions

$$ {}^t_0\underline{u}_{,x} = {}^t_0\underline{v}_{,y} = {}^t_0\underline{w}_{,z} = \zeta \; ; \;\; {}^t_0\underline{u}_{,y} = {}^t_0\underline{u}_{,z} = {}^t_0\underline{v}_{,x} = {}^t_0\underline{v}_{,z} = {}^t_0\underline{w}_{,x} = {}^t_0\underline{w}_{,y} = 0 \tag{D1}$$

The corresponding deformation gradient tensor can be calculated as

$$ {}^t_0\mathbf{X} = \begin{bmatrix} 1+\zeta & 0 & 0 \\ 0 & 1+\zeta & 0 \\ 0 & 0 & 1+\zeta \end{bmatrix} \tag{D2}$$

By using the procedure in Appendix C3 for the calculation of SPK stress, the right stretch tensor and rotational tensor can be represented as

$$ {}^t_0\mathbf{U} = {}^t_0\mathbf{X} \text{ and } {}^t_0\mathbf{R} = \mathbf{I} \tag{D3}$$

Therefore, the Hencky strain tensor and the SPK stress tensor can be obtained as

$$ {}^t_0\hat{\mathbf{E}}^H = \begin{bmatrix} \ln(1+\zeta) & 0 & 0 \\ 0 & \ln(1+\zeta) & 0 \\ 0 & 0 & \ln(1+\zeta) \end{bmatrix} \tag{D4}$$

$$ {}_0^t\hat{\mathbf{S}} = \frac{(3\lambda+2\mu)}{(1+\zeta)^2}\begin{bmatrix} \ln(1+\zeta) & 0 & 0 \\ 0 & \ln(1+\zeta) & 0 \\ 0 & 0 & \ln(1+\zeta) \end{bmatrix} \tag{D5} $$

For the loading case provided in Eq. (D1), virtual strain values can be represented by using Eq. (C9) as

$$ \begin{aligned} \delta\left({}_0\underline{\hat{e}}_{xx}\right) &= \delta\left({}_0\underline{u}_{,x}\right) + \left({}_0^t u_{,x}\right)\delta\left({}_0\underline{u}_{,x}\right) + \left({}_0^t v_{,x}\right)\delta\left({}_0\underline{v}_{,x}\right) \\ &\quad + \left({}_0^t w_{,x}\right)\delta\left({}_0\underline{w}_{,x}\right) = (1+\zeta)\delta\zeta \end{aligned} \tag{D6a} $$

$$ \begin{aligned} \delta\left({}_0\underline{\hat{e}}_{yy}\right) &= \delta\left({}_0\underline{v}_{,y}\right) + \left({}_0^t v_{,y}\right)\delta\left({}_0\underline{v}_{,y}\right) + \left({}_0^t u_{,y}\right)\delta\left({}_0\underline{u}_{,y}\right) \\ &\quad + \left({}_0^t w_{,y}\right)\delta\left({}_0\underline{w}_{,y}\right) = (1+\zeta)\delta\zeta \end{aligned} \tag{D6b} $$

$$ \begin{aligned} \delta\left({}_0\underline{\hat{e}}_{zz}\right) &= \delta\left({}_0\underline{w}_{,z}\right) + \left({}_0^t u_{,z}\right)\delta\left({}_0\underline{u}_{,z}\right) + \left({}_0^t v_{,z}\right)\delta\left({}_0\underline{v}_{,z}\right) \\ &\quad + \left({}_0^t w_{,z}\right)\delta\left({}_0\underline{w}_{,z}\right) = (1+\zeta)\delta\zeta \end{aligned} \tag{D6c} $$

$$ \delta\left({}_0\underline{\hat{e}}_{xy}\right) = \delta\left({}_0\underline{\hat{e}}_{yz}\right) = \delta\left({}_0\underline{\hat{e}}_{xz}\right) = 0 \tag{D6d} $$

with

$$ \delta\left({}_0\underline{u}_{,x}\right) = \delta\left({}_0\underline{v}_{,y}\right) = \delta\left({}_0\underline{w}_{,z}\right) = \delta\zeta \tag{D6e} $$

$$ \delta\left({}_0\underline{u}_{,y}\right) = \delta\left({}_0\underline{u}_{,z}\right) = \delta\left({}_0\underline{v}_{,x}\right) = \delta\left({}_0\underline{v}_{,z}\right) = \delta\left({}_0\underline{w}_{,x}\right) = \delta\left({}_0\underline{w}_{,y}\right) = 0 \tag{D6f} $$

By substituting the SPK stress tensor given in Eq. (D5) and strain components in Eq. (D6) into Eq. (C28b), the virtual value of SED in classical continuum mechanics can be calculated as

$$ \delta W^{CCM} = 3(3\lambda+2\mu)\frac{\delta\zeta}{(1+\zeta)}\ln(1+\zeta) \tag{D7} $$

The volumetric strain in classical continuum mechanics for isotropic expansion can be calculated by using the Hencky strain tensor given in Eq. (D4) as

$$ {}_0^t\vartheta^{CCM} = {}_0^t E_{xx}^H + {}_0^t E_{yy}^H + {}_0^t E_{zz}^H = 3\ln(1+\zeta) \tag{D8} $$

D1.1.2. Strain Energy Density and volumetric strain definitions in Peridynamic form

The displacement components of material point $\boldsymbol{j}$ can be expressed in terms of displacements of material point $\boldsymbol{k}$ by using Taylor's series expansion by ignoring the higher-order terms as

$$ \begin{aligned} {}^t u_{(j)} &= {}^t u_{(k)} + \left({}_0^t u_{(k),x}\right)\left({}^0 x_{(j)} - {}^0 x_{(k)}\right) \\ &\quad + \left({}_0^t u_{(k),y}\right)\left({}^0 y_{(j)} - {}^0 y_{(k)}\right) + \left({}_0^t u_{(k),z}\right)\left({}^0 z_{(j)} - {}^0 z_{(k)}\right) \end{aligned} \tag{D9a} $$

$$
\begin{aligned}
{}^{t}v_{(j)} = {}^{t}v_{(k)} &+ {}^{t}_{0}v_{(k),x}\left({}^{0}x_{(j)} - {}^{0}x_{(k)}\right) \\
&+ {}^{t}_{0}v_{(k),y}\left({}^{0}y_{(j)} - {}^{0}y_{(k)}\right) + {}^{t}_{0}v_{(k),z}\left({}^{0}z_{(j)} - {}^{0}z_{(k)}\right)
\end{aligned}
\tag{D9b}
$$

$$
\begin{aligned}
{}^{t}w_{(j)} = {}^{t}w_{(k)} &+ {}^{t}_{0}w_{(k),x}\left({}^{0}x_{(j)} - {}^{0}x_{(k)}\right) \\
&+ {}^{t}_{0}w_{(k),y}\left({}^{0}y_{(j)} - {}^{0}y_{(k)}\right) + {}^{t}_{0}w_{(k),z}\left({}^{0}z_{(j)} - {}^{0}z_{(k)}\right)
\end{aligned}
\tag{D9c}
$$

or

$$
\frac{{}^{t}u_{(j)} - {}^{t}u_{(k)}}{{}^{0}\xi} = {}^{t}_{0}u_{(k),x}c_x + {}^{t}_{0}u_{(k),y}c_y + {}^{t}_{0}u_{(k),z}c_z \tag{D9d}
$$

$$
\frac{{}^{t}v_{(j)} - {}^{t}v_{(k)}}{{}^{0}\xi} = {}^{t}_{0}v_{(k),x}c_x + {}^{t}_{0}v_{(k),y}c_y + {}^{t}_{0}v_{(k),z}c_z \tag{D9e}
$$

$$
\frac{{}^{t}w_{(j)} - {}^{t}w_{(k)}}{{}^{0}\xi} = {}^{t}_{0}w_{(k),x}c_x + {}^{t}_{0}w_{(k),y}c_y + {}^{t}_{0}w_{(k),z}c_z \tag{D9f}
$$

with

$$
c_x = \frac{{}^{0}x_{(j)} - {}^{0}x_{(k)}}{{}^{0}\xi} = \sin\phi\cos\theta \tag{D9g}
$$

$$
c_y = \frac{{}^{0}y_{(j)} - {}^{0}y_{(k)}}{{}^{0}\xi} = \sin\phi\sin\theta \tag{D9h}
$$

$$
c_z = \frac{{}^{0}z_{(j)} - {}^{0}z_{(k)}}{{}^{0}\xi} = \cos\phi \tag{D9i}
$$

where (ξ,θ,ϕ) serve as spherical coordinates [44].

Meanwhile, the linear bond stretch, ${}^{t}_{0}s$ given in Eq. (3.5) can be rewritten as

$$
{}^{t}_{0}s = \frac{{}^{t}\xi}{{}^{0}\xi} - 1 = \frac{\sqrt{\left({}^{t}x_{(j)} - {}^{t}x_{(k)}\right)^2 + \left({}^{t}y_{(j)} - {}^{t}y_{(k)}\right)^2 + \left({}^{t}z_{(j)} - {}^{t}z_{(k)}\right)^2}}{{}^{0}\xi} - 1 \tag{D10a}
$$

or

$$
{}^{t}_{0}s = \sqrt{\begin{aligned}
&\left(\frac{\left({}^{0}x_{(j)} - {}^{0}x_{(k)}\right) + \left({}^{t}u_{(j)} - {}^{t}u_{(k)}\right)}{{}^{0}\xi}\right)^2 + \left(\frac{\left({}^{0}y_{(j)} - {}^{0}y_{(k)}\right) + \left({}^{t}v_{(j)} - {}^{t}v_{(k)}\right)}{{}^{0}\xi}\right)^2 \\
&+ \left(\frac{\left({}^{0}z_{(j)} - {}^{0}z_{(k)}\right) + \left({}^{t}w_{(j)} - {}^{t}w_{(k)}\right)}{{}^{0}\xi}\right)^2
\end{aligned}} - 1 \tag{D10b}
$$

By using the relations in Eq. (D9), the linear bond stretch, ${}^{t}_{0}s$ given in Eq. (D10b) can be rewritten as

$$
{}_0^t s = \sqrt{\begin{aligned}&\left(c_x + {}_0^t u_{(k),x} c_x + {}_0^t u_{(k),y} c_y + {}_0^t u_{(k),z} c_z\right)^2 \\ &+\left(c_y + {}_0^t v_{(k),x} c_x + {}_0^t v_{(k),y} c_y + {}_0^t v_{(k),z} c_z\right)^2 \\ &+\left(c_z + {}_0^t w_{(k),x} c_x + {}_0^t w_{(k),y} c_y + {}_0^t w_{(k),z} c_z\right)^2\end{aligned}} - 1 \tag{D11}
$$

By substituting the conditions given in Eq. (D1) into Eq. (D11), the linear PD bond stretch can be calculated as

$$
{}_0^t s = \zeta \tag{D12}
$$

Therefore, the logarithmic bond stretch can be calculated by using Eq. (3.4a) as

$$
{}_0^t s_H = \ln\left(1+\zeta\right) \tag{D13}
$$

By using the logarithmic bond stretch given in Eq. (D13), the volumetric strain in PD given in Eq. (3.7) can be rewritten as

$$
{}_0^t \vartheta_{(k)} = d\sum_{j=1}^{N} \ln\left(1+\zeta\right) {}^0V_{(j)} \tag{D14}
$$

By disregarding the PD interactions beyond the horizon of material point k, the expression for ${}_0^t\vartheta_{(k)}$ in Eq. (D14) can be recast as

$$
{}_0^t \vartheta_{(k)} = d\int_0^{\delta}\int_0^{2\pi}\int_0^{\pi} \ln\left(1+\zeta\right) {}^0\xi^2 \sin\phi d\phi d\theta d\,{}^0\xi = d\,\frac{4\pi\delta^3}{3}\ln\left(1+\zeta\right) \tag{D15}
$$

where δ represents the horizon size on the initial configuration.

Similarly, by substituting the logarithmic stretch given in Eq. (D13) and volumetric strain in Eq. (D8) into Eq. (3.3a), the strain energy density in PD for isotropic expansion can be defined as

$$
W_{(k)}^{NLPD} = 9a\ln^2\left(1+\zeta\right) + b\sum_{j=1}^{N} \ln^2\left(1+\zeta\right) {}^0\xi\, {}^0V_{(j)} \tag{D16}
$$

By disregarding the PD interactions beyond the horizon of material point k, the expression for $W_{(k)}^{NLPD}$ can be rewritten in the integral form as

$$
W_{(k)}^{NLPD} = 9a\ln^2\left(1+\zeta\right) + b\int_0^{\delta}\int_0^{2\pi}\int_0^{\pi} \ln^2\left(1+\zeta\right) {}^0\xi^3 \sin\phi d\phi d\theta d\,{}^0\xi \tag{D17}
$$

By performing the integrations in Eq. (D17), the SED in PD for isotropic expansion state can be defined as

$$
W_{(k)}^{NLPD} = 9a\ln^2\left(1+\zeta\right) + b\pi\delta^4 \ln^2\left(1+\zeta\right) \tag{D18}
$$

Therefore, the virtual value of strain energy density in PD can be calculated as

$$
\delta W_{(k)}^{NLPD} = 18a\,\frac{\delta\zeta}{1+\zeta}\ln\left(1+\zeta\right) + 2b\pi\delta^4\,\frac{\delta\zeta}{1+\zeta}\ln\left(1+\zeta\right) \tag{D19}
$$

D1.1.3. PD constants

By comparing volumetric strain given in Eq. (D8) and Eq. (D15), the PD constant, d , can be determined as

$$d = \frac{9}{4\pi\delta^3} \tag{D20}$$

By comparing the virtual value of strain energy density definitions in Eq. (D7) and Eq. (D19), the relationships between PD constants and engineering material constants can be obtained as

$$18a + 2b\pi\delta^4 = 3\left(3\lambda + 2\mu\right) \tag{D21}$$

D1.2. Loading 2: Simple shear

D1.2.1. Strain Energy Density and volumetric strain definitions in classical continuum mechanics

The simple shear can be obtained by assuming the following conditions

$${}^{t}_{0}u_{,x} = {}^{t}_{0}u_{,z} = {}^{t}_{0}v_{,x} = {}^{t}_{0}v_{,y} = {}^{t}_{0}v_{,z} = {}^{t}_{0}w_{,x} = {}^{t}_{0}w_{,y} = {}^{t}_{0}w_{,z} = 0\,;\;\; {}^{t}_{0}u_{,y} = \zeta \tag{D22}$$

Therefore, the deformation gradient tensor can be defined as

$${}^{t}_{0}\mathbf{X} = \begin{bmatrix} 1 & \zeta & 0 \\ 0 & 1 & 0 \\ 0 & 0 & 1 \end{bmatrix} \tag{D23}$$

By using the procedure in Appendix C3 for the calculation of SPK stress, the Hencky strain tensor and Second Piola-Kirchhoff stress tensor can be obtained as

$${}^{t}_{0}\hat{\mathbf{E}}^{H} = \frac{\hat{E}_1^H}{\sqrt{\zeta^2+4}} \begin{bmatrix} -\zeta & 2 & 0 \\ 2 & \zeta & 0 \\ 0 & 0 & 0 \end{bmatrix} \tag{D24a}$$

$${}^{t}_{0}\hat{\mathbf{S}} = 2\mu \frac{\hat{E}_1^H}{\sqrt{\zeta^2+4}} \begin{bmatrix} -\zeta\left(\zeta^2+3\right) & \zeta^2+2 & 0 \\ \zeta^2+2 & -\zeta & 0 \\ 0 & 0 & 0 \end{bmatrix} \tag{D24b}$$

with

$$\hat{E}_1^H = \frac{1}{2}\ln\left(\frac{\zeta^2+2}{2} + \frac{\zeta\sqrt{\zeta^2+4}}{2}\right) \tag{D24c}$$

For the loading conditions provided in Eq. (D22), the strain components corresponding to virtual displacements given in Eq. (C9) can be calculated as

$$\delta\left({}_0\underline{\hat{e}}_{xx}\right) = \delta\left({}_0\underline{\hat{e}}_{zz}\right) = \delta\left({}_0\underline{\hat{e}}_{xz}\right) = \delta\left({}_0\underline{\hat{e}}_{yz}\right) = 0 \tag{D25a}$$

$$\delta\left({}_0\underline{\hat{e}}_{yy}\right)=\delta\left({}_0\underline{v}_{,y}\right)+{}_0^t v_{,y}\,\delta\left({}_0\underline{v}_{,y}\right)+{}_0^t u_{,y}\,\delta\left({}_0\underline{u}_{,y}\right)+{}_0^t w_{,y}\,\delta\left({}_0\underline{w}_{,y}\right)=\zeta\delta\zeta \tag{D25b}$$

$$\begin{aligned}\delta\left({}_0\underline{\hat{e}}_{xy}\right)=&\frac{1}{2}\left(\delta\left({}_0\underline{u}_{,y}\right)+\delta\left({}_0\underline{v}_{,x}\right)\right)\\&+\frac{1}{2}\left({}_0^t u_{,x}\,\delta\left({}_0\underline{u}_{,y}\right)+{}_0^t v_{,x}\,\delta\left({}_0\underline{v}_{,y}\right)+{}_0^t u_{,y}\,\delta\left({}_0\underline{u}_{,x}\right)\right)\\&+\frac{1}{2}\left({}_0^t v_{,y}\,\delta\left({}_0\underline{v}_{,x}\right)+{}_0^t w_{,x}\,\delta\left({}_0\underline{w}_{,y}\right)+{}_0^t w_{,y}\,\delta\left({}_0\underline{w}_{,x}\right)\right)=\frac{1}{2}\delta\zeta\end{aligned} \tag{D25c}$$

with

$$\delta\left({}_0\underline{u}_{,x}\right)=\delta\left({}_0\underline{u}_{,z}\right)=\delta\left({}_0\underline{v}_{,x}\right)=\delta\left({}_0\underline{v}_{,y}\right)=0 \tag{D25d}$$

$$\delta\left({}_0\underline{v}_{,z}\right)=\delta\left({}_0\underline{w}_{,x}\right)=\delta\left({}_0\underline{w}_{,y}\right)=\delta\left({}_0\underline{w}_{,z}\right)=0 \tag{D25e}$$

$$\delta\left({}_0\underline{u}_{,y}\right)=\delta\zeta \tag{D25f}$$

By using the SPK stress tensor given in Eq. (D24b) and the strain components in Eq. (D25), the virtual value of strain energy density in classical continuum mechanics given in Eq. (C28b) can be calculated as

$$\delta W^{CCM}=2\mu\frac{1}{\sqrt{\zeta^2+4}}\ln\left(1+\frac{\zeta^2+\zeta\sqrt{\zeta^2+4}}{2}\right)\delta\zeta \tag{D26}$$

By assuming small shear strain condition, $\zeta\ll 1$, the virtual value of strain energy density in classical continuum mechanics given in Eq. (D26) can be simplified as

$$\delta W^{CCM}\approx\mu\left(\zeta-\frac{1}{6}\zeta^3-\frac{1}{6}\zeta^5-\frac{1}{3}\zeta^6-\frac{1}{4}\zeta^7-\frac{1}{8}\zeta^8\right)\delta\zeta\approx\mu\zeta\delta\zeta+O^3(\zeta) \tag{D27}$$

where $O^3(\zeta)$ represents third and higher-order terms which can be neglected.

The volumetric strain in classical continuum mechanics for simple shear can be calculated by using the Hencky strain tensor given in Eq. (D24a) as

$$\vartheta^{CCM}={}_0^t\hat{E}^H_{xx}+{}_0^t\hat{E}^H_{yy}+{}_0^t\hat{E}^H_{zz}=0 \tag{D28}$$

D1.2.2. Strain Energy Density strain definition in PD form

By using the relations given in Eq. (D22), the linear bond stretch in Eq. (D11) can be calculated as

$${}_0^t s=\sqrt{1+2\zeta\sin^2\phi\sin\theta\cos\theta+\zeta^2\sin^2\phi\sin^2\theta}-1 \tag{D29}$$

By assuming small shear strain, $\zeta\ll 1$, Eq. (D29) can be simplified as

$${}_0^t s\approx\zeta\sin^2\phi\sin\theta\cos\theta \tag{D30}$$

Therefore, the logarithmic bond stretch can be calculated as

$$
\begin{aligned}
{}_0^t s_H &\approx \ln\left(1+\zeta \sin^2\phi \sin\theta\cos\theta\right) \\
&\approx \zeta \sin^2\phi \sin\theta\cos\theta - \frac{1}{2}\left(\zeta \sin^2\phi \sin\theta\cos\theta\right)^2 + \cdots
\end{aligned}
\tag{D31}
$$

By using the stretch definition given in Eq. (D31) and volumetric strain in Eq. (D28), the strain energy density in PD given in Eq. (3.3a) can be calculated as

$$
W_{(k)}^{NLPD} \approx b\sum_{j=1}^{N}\left[\zeta \sin^2\phi \sin\theta\cos\theta - \frac{1}{2}\left(\zeta \sin^2\phi \sin\theta\cos\theta\right)^2\right]^2 {}^0\xi\, {}^0V_{(j)} \tag{D32}
$$

By disregarding the PD interactions beyond the horizon of material point k, the strain energy density in Eq. (D32) can be recast as

$$
W_{(k)}^{NLPD} \approx b\int_0^{\delta}\int_0^{2\pi}\int_0^{\pi}\left[\begin{array}{l}\zeta \sin^2\phi \sin\theta\cos\theta \\ -\frac{1}{2}\left(\zeta \sin^2\phi \sin\theta\cos\theta\right)^2\end{array}\right]^2 {}^0\xi^3 \sin\phi d\phi d\theta d\, {}^0\xi \tag{D33a}
$$

or

$$
W_{(k)}^{NLPD} \approx b\int_0^{\delta}\int_0^{2\pi}\int_0^{\pi}\zeta^2 \sin^5\phi \sin^2\theta\cos^2\theta\, {}^0\xi^3 d\phi d\theta d\, {}^0\xi + O(\zeta^3) \tag{D33b}
$$

By performing integrations given in Eq. (D33b), the strain energy density in PD for the simple shear state can be calculated as

$$
W_{(k)}^{NLPD} \approx b\pi\delta^4 \frac{1}{15}\zeta^2 + O^3(\zeta) \tag{D34}
$$

Therefore, the virtual value of the strain energy density in PD can be calculated as

$$
\delta W_{(k)}^{NLPD} \approx b\pi\delta^4 \frac{2}{15}\zeta\delta\zeta + O^3(\zeta) \tag{D35}
$$

D1.2.3. PD constants

By comparing Eq. (D27) and Eq. (D35) and by neglecting third and higher-order terms, the following relations are obtained

$$
b\frac{2}{15}\pi\delta^4\zeta\delta\zeta = \mu\zeta\delta\zeta \tag{D36a}
$$

or

$$
b = \frac{15}{2}\frac{\mu}{\pi\delta^4} \tag{D36b}
$$

Substituting PD constant, b given in Eq. (D36b) into Eq. (D21), the PD constant, a can be determined as

$$
a = \frac{\lambda-\mu}{2} \tag{D37}
$$

D2. PD constants for 2D structures

Similar to 3D formulations, the PD constants for the 2D case can also be obtained by comparing the virtual values of strain energy density in classical continuum mechanics and peridynamics in two basic loading conditions: isotropic expansion and simple shear. The procedure for PD bond constants for 2D structures can be summarised as follows:

The virtual values of SED and volumetric strain in classical continuum mechanics for isotropic expansion is calculated in Section D2.1.1. The PD representation of SED and volumetric strain for isotropic expansion is represented in Section D2.1.2. By comparing the PD and the classical continuum mechanics representations, the relations for PD constants and material constants are provided in Section D2.1.3.

Similarly, the virtual values of SED in classical continuum mechanics and PD for simple shear loading are presented in Sections D2.2.1 and D2.2.2, respectively. By comparing the PD and the classical continuum mechanics representations, the relations for PD constants and material constants are provided in Section D2.2.3.

D2.1. Loading 1: Isotropic expansion

D2.1.1. Strain Energy Density and volumetric strain definitions in classical continuum mechanics

The isotropic expansion can be obtained by assuming the following conditions

$$ {}^{t}_{0}u_{,x} = {}^{t}_{0}v_{,y} = \zeta \; ; \;\; {}^{t}_{0}u_{,y} = {}^{t}_{0}v_{,x} = 0 \tag{D38} $$

Therefore, the deformation gradient tensor in 2D form can be defined as

$$ {}^{t}_{0}\mathbf{X} = \begin{bmatrix} 1+\zeta & 0 \\ 0 & 1+\zeta \end{bmatrix} \tag{D39} $$

By using the procedure in Appendix C3 for the calculation of SPK stress, the Hencky strain tensor can be obtained as

$$ {}^{t}_{0}\hat{\mathbf{E}}^{H} = \begin{bmatrix} {}^{t}_{0}\hat{E}^{H}_{xx} & 0 & 0 \\ 0 & {}^{t}_{0}\hat{E}^{H}_{yy} & 0 \\ 0 & 0 & {}^{t}_{0}\hat{E}^{H}_{zz} \end{bmatrix} = \begin{bmatrix} \ln(1+\zeta) & 0 & 0 \\ 0 & \ln(1+\zeta) & 0 \\ 0 & 0 & 2(\alpha-1)\ln(1+\zeta) \end{bmatrix} \tag{D40} $$

where α is defined in Eq. (3.15).

Similarly, by using the procedure given in Appendix C3, the SPK stress tensor can be obtained as

$$
{}_0^t\hat{\mathbf{S}} = \begin{bmatrix} \dfrac{2(\lambda\alpha+\mu)\ln(1+\zeta)}{(1+\zeta)^2} & 0 & 0 \\ 0 & \dfrac{2(\lambda\alpha+\mu)\ln(1+\zeta)}{(1+\zeta)^2} & 0 \\ 0 & 0 & \dfrac{2(\lambda\alpha+2\mu(\alpha-1))\ln(1+\zeta)}{(1+\zeta)^{4(\alpha-1)}} \end{bmatrix} \tag{D41}
$$

For the loading conditions provided in Eq. (D38), the strain components corresponding to virtual displacements given in Eq. (C9) can be calculated as

$$
\delta\left({}_0\hat{\underline{e}}_{xx}\right) = \delta\left({}_0\underline{u}_{,x}\right) + {}_0^t u_{,x}\,\delta\left({}_0\underline{u}_{,x}\right) + {}_0^t v_{,x}\,\delta\left({}_0\underline{u}_{,x}\right) = (1+\zeta)\delta\zeta \tag{D42a}
$$

$$
\delta\left({}_0\hat{\underline{e}}_{yy}\right) = \delta\left({}_0\underline{v}_{,y}\right) + {}_0^t v_{,y}\,\delta\left({}_0\underline{v}_{,y}\right) + {}_0^t u_{,y}\,\delta\left({}_0\underline{u}_{,y}\right) = (1+\zeta)\delta\zeta \tag{D42b}
$$

$$
\delta\left({}_0\hat{\underline{e}}_{xy}\right) = 0 \tag{D42c}
$$

with

$$
\delta\left({}_0\underline{u}_{,x}\right) = \delta\left({}_0\underline{v}_{,y}\right) = \delta\zeta\,,\ \ \delta\left({}_0\underline{u}_{,y}\right) = \delta\left({}_0\underline{v}_{,x}\right) = 0 \tag{D42d}
$$

Since ${}_0^t\hat{S}_{zz}\delta\left({}_0\hat{\underline{e}}_{zz}\right) = 0$ for both plane strain and plane stress conditions, the virtual value of SED in classical continuum mechanics can be calculated as

$$
\delta W^{CCM} = {}_0^t\hat{S}_{xx}\delta\left({}_0\hat{\underline{e}}_{xx}\right) + {}_0^t\hat{S}_{yy}\delta\left({}_0\hat{\underline{e}}_{yy}\right) + 2\,{}_0^t\hat{S}_{xy}\delta\left({}_0\hat{\underline{e}}_{xy}\right) \tag{D43}
$$

By substituting the SPK stress tensor given in Eq. (D41) and strain components in Eq. (D42) into Eq. (D43), the virtual value of SED can be calculated as

$$
\delta W^{CCM} = 4(\lambda\alpha+\mu)\frac{\delta\zeta}{(1+\zeta)}\ln(1+\zeta) \tag{D44}
$$

The 2D volumetric strain in classical continuum mechanics can be calculated from Eq. (D40) as

$$
\vartheta^{CCM} = {}_0^t E_{xx}^H + {}_0^t E_{yy}^H = 2\ln(1+\zeta) \tag{D45}
$$

D2.1.2. Strain Energy Density and volumetric strain definitions in PD form

The displacement components of material point j can be expressed in terms of displacements of material point k by using Taylor's series expansion by ignoring the higher-order terms as

$$
{}^t u_{(j)} = {}^t u_{(k)} + {}_0^t u_{(k),x}\left({}^0 x_{(j)} - {}^0 x_{(k)}\right) + {}_0^t u_{(k),y}\left({}^0 y_{(j)} - {}^0 y_{(k)}\right) \tag{D46a}
$$

$$
{}^t v_{(j)} = {}^t v_{(k)} + {}_0^t v_{(k),x}\left({}^0 x_{(j)} - {}^0 x_{(k)}\right) + {}_0^t v_{(k),y}\left({}^0 y_{(j)} - {}^0 y_{(k)}\right) \tag{D46b}
$$

or

$$\frac{{}^{t}u_{(j)} - {}^{t}u_{(k)}}{{}^{0}\xi} = {}^{t}_{0}u_{(k),x}\cos\varphi + {}^{t}_{0}u_{(k),y}\sin\varphi \tag{D46c}$$

$$\frac{{}^{t}v_{(j)} - {}^{t}v_{(k)}}{{}^{0}\xi} = {}^{t}_{0}v_{(k),x}\cos\varphi + {}^{t}_{0}v_{(k),y}\sin\varphi \tag{D46d}$$

with

$$\cos\varphi = \frac{{}^{0}x_{(j)} - {}^{0}x_{(k)}}{{}^{0}\xi} \tag{D46e}$$

$$\sin\varphi = \frac{{}^{0}v_{(j)} - {}^{0}v_{(k)}}{{}^{0}\xi} \tag{D46f}$$

Meanwhile, the linear bond stretch, ${}^{t}_{0}s$ given in Eq. (3.5) can be rewritten as

$${}^{t}_{0}s = \sqrt{\left(\frac{{}^{t}x_{(j)} - {}^{t}x_{(k)}}{{}^{0}\xi}\right)^{2} + \left(\frac{{}^{t}y_{(j)} - {}^{t}y_{(k)}}{{}^{0}\xi}\right)^{2}} - 1 \tag{D47a}$$

or

$${}^{t}_{0}s = \sqrt{\left(\frac{\left({}^{0}x_{(j)} - {}^{0}x_{(k)}\right) + \left({}^{t}u_{(j)} - {}^{t}u_{(k)}\right)}{{}^{0}\xi}\right)^{2} + \left(\frac{\left({}^{0}y_{(j)} - {}^{0}y_{(k)}\right) + \left({}^{t}v_{(j)} - {}^{t}v_{(k)}\right)}{{}^{0}\xi}\right)^{2}} - 1 \tag{D47b}$$

By using the relations in Eqs. (D46c-f), the linear bond stretch, ${}^{t}_{0}s$ given in Eq. (D47b) can be rewritten as

$${}^{t}_{0}s = \sqrt{\begin{array}{l}\left(\cos\varphi + {}^{t}_{0}u_{(k),x}\cos\varphi + {}^{t}_{0}u_{(k),y}\sin\varphi\right)^{2} \\ + \left(\sin\varphi + {}^{t}_{0}v_{(k),x}\cos\varphi + {}^{t}_{0}v_{(k),y}\sin\varphi\right)^{2}\end{array}} - 1 \tag{D48}$$

By substituting conditions given in Eq. (D38) into Eq. (D48), the PD linear bond stretch can be calculated as

$${}^{t}_{0}s = \zeta \tag{D49}$$

Therefore, the logarithmic bond stretch can be calculated as

$${}^{t}_{0}s_{H} = \ln\left(1+\zeta\right) \tag{D50}$$

By using the logarithmic bond stretch given in Eq. (D50), the PD volumetric strain given in Eq. (3.7) can be rewritten as

$$\vartheta_{(k)} = d\sum_{j=1}^{N}\ln\left(1+\zeta\right){}^{0}V_{(j)} \tag{D51}$$

By disregarding the PD interactions beyond the horizon of material point k, the expression for $\vartheta_{(k)}$ in Eq. (D51) can be recast as

$$\vartheta_{(k)} = dh\int_0^{\delta}\int_0^{2\pi} \ln\left(1+\zeta\right) {}^0\xi d\,{}^0\xi d\varphi = d\pi h\delta^2 \ln\left(1+\zeta\right) \tag{D52}$$

where h represents the plate thickness on the initial configuration.

Similarly, by substituting the logarithmic bond stretch given in Eq. (D50) and volumetric strain in Eq. (D45) into Eq. (3.3a), the strain energy density in PD in the isotropic expansion state can also be defined as

$$W_{(k)}^{NLPD} = 4a\ln^2\left(1+\zeta\right) + b\sum_{j=1}^{N} \ln^2\left(1+\zeta\right) {}^0\xi\, {}^0V_{(j)} \tag{D53}$$

By disregarding the PD interactions beyond the horizon of material point k, the expression for $W_{(k)}^{NLPD}$ can be recast in the integral form as

$$W_{(k)}^{NLPD} = 4a\ln^2\left(1+\zeta\right) + bh\int_0^{\delta}\int_0^{2\pi} \ln^2\left(1+\zeta\right) {}^0\xi^2 d\varphi d\,{}^0\xi \tag{D54a}$$

or

$$W_{(k)}^{NLPD} = 4a\ln^2\left(1+\zeta\right) + b\frac{2\pi h\delta^3}{3}\ln^2\left(1+\zeta\right) \tag{D54b}$$

Therefore, the virtual value of strain energy density in PD can be calculated as

$$\delta W_{(k)}^{NLPD} = 8a\frac{\delta\zeta}{1+\zeta}\ln\left(1+\zeta\right) + b\frac{4\pi h\delta^3}{3}\frac{\delta\zeta}{1+\zeta}\ln\left(1+\zeta\right) \tag{D55}$$

D2.1.3. PD constants

By comparing Eq. (D45) and Eq. (D52), the PD constant, d can be determined as

$$d = \frac{2}{\pi h\delta^2} \tag{D56}$$

By comparing Eq. (D44) and Eq. (D55), the relationships between PD constants and engineering material constants can be obtained as

$$2a + b\frac{\pi h\delta^3}{3} = \lambda\alpha + \mu \tag{D57}$$

D2.2. Loading 2: Simple shear

D2.2.1. Strain Energy Density definition in classical continuum mechanics
The simple shear in 2D structures can be obtained by assuming the following conditions

$$ {}^{t}_{0}u_{,x} = {}^{t}_{0}v_{,x} = {}^{t}_{0}v_{,y} = 0\,; \quad {}^{t}_{0}u_{,y} = \zeta \tag{D58} $$

Therefore, the deformation gradient tensor can be defined as

$$ {}^{t}_{0}\mathbf{X} = \begin{bmatrix} 1 & \zeta \\ 0 & 1 \end{bmatrix} \tag{D59} $$

By using the procedure in Appendix C3 for the calculation of SPK stress, the Hencky strain tensor and the SPK stress tensor can be obtained as

$$ {}^{t}_{0}\hat{\mathbf{E}}^{H} = \frac{\hat{E}_1^H}{\sqrt{\zeta^2+4}} \begin{bmatrix} -\zeta & 2 & 0 \\ 2 & \zeta & 0 \\ 0 & 0 & 0 \end{bmatrix} \tag{D60a} $$

$$ {}^{t}_{0}\hat{\mathbf{S}} = 2\mu \frac{\hat{E}_1^H}{\sqrt{\zeta^2+4}} \begin{bmatrix} -\zeta\left(\zeta^2+3\right) & \zeta^2+2 & 0 \\ \zeta^2+2 & -\zeta & 0 \\ 0 & 0 & 0 \end{bmatrix} \tag{D60b} $$

where

$$ \hat{E}_1^H = \frac{1}{2}\ln\left(\frac{\zeta^2+2}{2} + \frac{\zeta\sqrt{\zeta^2+4}}{2} \right) \tag{D60c} $$

Note that in simple shear loading condition, the component ${}^{t}_{0}\hat{E}^{H}_{zz} = 0$ and ${}^{t}_{0}\hat{S}_{zz}\delta\left({}_{0}\underline{\hat{e}}_{zz}\right) = 0$ in both plane stress and plane strain conditions.

For the loading case provided in Eq. (D58), the strain components corresponding to virtual displacements can be defined as

$$ \delta\left({}_{0}\underline{\hat{e}}_{xx}\right) = \delta\left({}_{0}\underline{u}_{,x}\right) + {}^{t}_{0}u_{,x}\,\delta\left({}_{0}\underline{u}_{,x}\right) + {}^{t}_{0}v_{,x}\,\delta\left({}_{0}\underline{v}_{,x}\right) = 0 \tag{D61a} $$

$$ \delta\left({}_{0}\underline{\hat{e}}_{yy}\right) = \delta\left({}_{0}\underline{v}_{,y}\right) + {}^{t}_{0}v_{,y}\,\delta\left({}_{0}\underline{v}_{,y}\right) + {}^{t}_{0}u_{,y}\,\delta\left({}_{0}\underline{u}_{,y}\right) = \zeta\delta\zeta \tag{D61b} $$

$$ \begin{aligned} \delta\left({}_{0}\underline{\hat{e}}_{xy}\right) &= \frac{1}{2}\left(\delta\left({}_{0}\underline{u}_{,y}\right) + \delta\left({}_{0}\underline{v}_{,x}\right)\right) \\ &+ \frac{1}{2}\left({}^{t}_{0}u_{,x}\,\delta\left({}_{0}\underline{u}_{,y}\right) + {}^{t}_{0}v_{,x}\,\delta\left({}_{0}\underline{v}_{,y}\right) + {}^{t}_{0}u_{,y}\,\delta\left({}_{0}\underline{u}_{,x}\right) + {}^{t}_{0}v_{,y}\,\delta\left({}_{0}\underline{v}_{,x}\right)\right) = \frac{\delta\zeta}{2} \end{aligned} \tag{D61c} $$

with

$$ \delta\left({}_{0}\underline{u}_{,x}\right) = \delta\left({}_{0}\underline{v}_{,x}\right) = \delta\left({}_{0}\underline{v}_{,y}\right) = 0 \tag{D61d} $$

$$ \delta\left({}_{0}\underline{u}_{,y}\right) = \zeta \tag{D61e} $$

By substituting the SPK stress tensor given in Eq. (D60b) and the strain components given in Eq. (D61) into Eq. (D43), the virtual value of strain energy density in classical continuum mechanics can be calculated as

$$\delta W^{CCM} = 2\mu \frac{1}{\sqrt{\zeta^2+4}} \ln\left(1+\frac{\zeta^2+\zeta\sqrt{\zeta^2+4}}{2}\right)\delta\zeta \tag{D62}$$

Similar to 3D structures, by assuming that $\zeta \ll 1$, the virtual value of strain energy density in classical continuum mechanics given in Eq. (D62) can be simplified as

$$\delta W^{CCM} \approx \mu\left(\zeta - \frac{1}{6}\zeta^3 - \frac{1}{6}\zeta^5 - \frac{1}{3}\zeta^6 - \frac{1}{4}\zeta^7 - \frac{1}{8}\zeta^8\right)\delta\zeta \approx \mu\zeta\delta\zeta + O^3(\zeta) \tag{D63}$$

The volumetric strain in classical continuum mechanics for simple shear can be calculated by using the Hencky strain tensor given in Eq. (D60a) as

$$\vartheta^{CCM} = {}_0^t\hat{E}^H_{xx} + {}_0^t\hat{E}^H_{yy} + {}_0^t\hat{E}^H_{zz} = 0 \tag{D64}$$

D2.2.2. Strain Energy Density strain definition in PD form

In peridynamics, by using conditions given in Eq. (D58), the linear stretch given in Eq. (D48) can be calculated for $\zeta \ll 1$ as

$${}_0^t s = \sqrt{1+2\zeta\sin\varphi\cos\varphi+\zeta^2\sin^2\varphi}-1 \approx \zeta\sin\varphi\cos\varphi \tag{D65}$$

Therefore, the logarithmic stretch given in Eq. (3.4a) can be calculated as

$${}_0^t s_H \approx \ln\left(1+\zeta\sin\varphi\cos\varphi\right) \approx \zeta\sin\varphi\cos\varphi - \frac{1}{2}\left(\zeta\sin\varphi\cos\varphi\right)^2 \tag{D66}$$

By using the logarithmic bond stretch given in Eq. (D66) and the volumetric strain in Eq. (D64), the strain energy density in PD given in Eq. (3.3a) can be calculated as

$$W_{(k)}^{NLPD} \approx b\sum_{j=1}^{N}\zeta^2\sin^2\varphi\cos^2\varphi\,{}^0\xi\,{}^0V_{(j)} + O^3(\zeta) \tag{D67}$$

The strain energy density given in Eq. (D67) can be recast as

$$W_{(k)}^{NLPD} = bh\int_0^{\delta}\int_0^{2\pi}\zeta^2\sin^2\varphi\cos^2\varphi\,{}^0\xi^2 d\,{}^0\xi d\varphi + O^3(\zeta) \tag{D68}$$

By performing integrations given in Eq. (D68), the strain energy density in PD for the simple shear state can be calculated as

$$W_{(k)}^{NLPD} \approx \frac{1}{12}b\pi h\delta^3\zeta^2 + O^3(\zeta) \tag{D69}$$

Therefore, the virtual value of the strain energy density in PD can be calculated as

$$\delta W_{(k)}^{NLPD} \approx \frac{1}{6}b\pi h\delta^3\zeta\delta\zeta + O^3(\zeta) \tag{D70}$$

D2.2.3. PD constants

By comparing Eq. (D63) and Eq. (D70), the following relations are obtained

$$\frac{1}{6} b\pi h\delta^3 \zeta\delta\zeta = \mu\zeta\delta\zeta \tag{D71a}$$

or

$$b = \frac{6\mu}{\pi h\delta^3} \tag{D71b}$$

Substituting PD constant, b given in Eq. (D71b) into Eq. (D57), the PD constant, a can be determined as

$$a = \frac{\lambda\alpha - \mu}{2} \tag{D72}$$

D3. PD constants for 1D structures

The procedure for PD bond constants for 1D structures can be summarised as follows:

The virtual values of SED in classical continuum mechanics for uniform stretch is calculated in Section D3.1. The PD representation of SED and volumetric strain for uniform stretch is represented in Section D3.2. By comparing the PD and the classical continuum mechanics representations, the relations for PD constants and material constants are provided in Section. D3.3.

D3.1. Strain Energy Density definitions in classical continuum mechanics

To determine the PD constant, a bar can be assumed to be subjected to a uniform stretch of

$${}^t_0 u_{,x} = \zeta \tag{D73}$$

which results in the deformation gradient as

$${}^t_0 \mathbf{X} = 1 + \zeta \tag{D74}$$

By using the procedure as given in Appendix C3, the Hencky strain tensor and the SPK stress tensor can be

$${}^t_0 \hat{\mathbf{E}}^H = \ln(1+\zeta) \tag{D75a}$$

$${}^t_0 \hat{\mathbf{S}} = E \frac{1}{(1+\zeta)^2} \ln(1+\zeta) \tag{D75b}$$

For the loading case provided in Eq. (D73), virtual strain values can be represented by using Eq. (C9) as

$$\delta\left({}_0\underline{\hat{e}}_{xx}\right) = \delta\left({}_0\underline{u}_{,x}\right) + {}^t_0 u_{,x}\,\delta\left({}_0\underline{u}_{,x}\right) = \delta\zeta + \zeta\delta\zeta = (1+\zeta)\delta\zeta \tag{D76a}$$

with

$$\delta\left({}_0\underline{u}_{,x}\right)=\delta\zeta \tag{D76b}$$

Therefore, the virtual value of strain energy density in classical continuum mechanics can be calculated as

$$\delta W^{CCM}={}_0^t\hat{S}_{xx}\delta\left({}_0\underline{\hat{e}}_{xx}\right)=E\frac{\delta\zeta}{1+\zeta}\ln\left(1+\zeta\right) \tag{D77}$$

D3.2. Strain Energy Density in Peridynamic form

The relation between the relative coordinate of two material points in the initial and deformed configurations can be assumed as

$$\left({}^0x_{(j)}-{}^0x_{(k)}\right)\left({}^tx_{(j)}-{}^tx_{(k)}\right)>0\quad\forall k\neq j \tag{D78a}$$

or

$$\frac{{}^0x_{(j)}-{}^0x_{(k)}}{{}^0\xi}=\frac{{}^tx_{(j)}-{}^tx_{(k)}}{{}^t\xi}\quad\forall k\neq j \tag{D78b}$$

Moreover, the linear bond stretch given in Eq. (3.5) can be rewritten for 1D structure as

$${}_0^ts=\frac{\left|{}^tx_{(j)}-{}^tx_{(k)}\right|}{{}^0\xi}-1=\frac{{}^tx_{(j)}-{}^tx_{(k)}}{{}^0\xi}\frac{{}^tx_{(j)}-{}^tx_{(k)}}{{}^t\xi}-1 \tag{D79}$$

Therefore, by using the relation given in Eq. (D78b), the linear bond stretch given in Eq. (D79) can be rewritten as

$${}_0^ts=\frac{{}^0x_{(j)}-{}^0x_{(k)}+{}^tu_{(j)}-{}^tu_{(k)}}{{}^0\xi}\frac{{}^0x_{(j)}-{}^0x_{(k)}}{{}^0\xi}-1=\frac{{}^tu_{(j)}-{}^tu_{(k)}}{{}^0\xi}\frac{{}^0x_{(j)}-{}^0x_{(k)}}{{}^0\xi} \tag{D80}$$

Meanwhile, the displacement components of material point j can be expressed in terms of displacements of material point k by using Taylor's series expansion by ignoring the higher-order terms as

$${}^tu_{(j)}={}^tu_{(k)}+{}_0^tu_{,x(k)}\left({}^0x_{(j)}-{}^0x_{(k)}\right)+\cdots \tag{D81a}$$

or

$$\frac{{}^tu_{(j)}-{}^tu_{(k)}}{{}^0\xi}={}_0^tu_{,x(k)}\frac{\left({}^0x_{(j)}-{}^0x_{(k)}\right)}{{}^0\xi}+\cdots \tag{D81b}$$

Therefore, by utilizing the relation given in Eq. (D81b), the linear bond stretch given in Eq. (D80) can be rewritten as

$${}_0^ts={}_0^tu_{,x(k)}\left(\frac{{}^0x_{(j)}-{}^0x_{(k)}}{{}^0\xi}\right)^2={}_0^tu_{,x(k)} \tag{D82}$$

By substituting the relation given in Eq. (D73) into Eq. (D82), the linear PD bond stretch can be obtained as

$$ {}_{0}^{t}s = \zeta \tag{D83} $$

Therefore, the logarithmic bond stretch can be obtained as

$$ {}_{0}^{t}s_{H} = \ln\left(1+\zeta\right) \tag{D84} $$

By utilizing the logarithmic bond stretch given in Eq. (D84), the strain energy density given in Eq. (3.3b) can be written as

$$ W_{(k)}^{NLPD} = b\sum_{j=1}^{N} \ln^{2}\left(1+\zeta\right) {}^{0}\xi\, {}^{0}V_{(j)} \tag{D85} $$

The SED given in Eq. (D85) can be rewritten in an integral form with respected to the initial configuration as

$$ W_{(k)}^{NLPD} = 2b\left({}^{0}A\right)\int_{0}^{\delta} \ln^{2}\left(1+\zeta\right) {}^{0}\xi\, d\, {}^{0}\xi \tag{D86} $$

where ${}^{0}A$ represents the cross-section area on the initial configuration.

By performing integration given in Eq. (D86), the SED for the bar can be calculated as

$$ W_{(k)}^{NLPD} = b\left({}^{0}A\right)\delta^{2} \ln^{2}\left(1+\zeta\right) \tag{D87} $$

Therefore, the virtual value of strain energy density in PD can be calculated as

$$ \delta W_{(k)}^{NLPD} = 2b\left({}^{0}A\right)\delta^{2} \frac{\delta\zeta}{1+\zeta} \ln\left(1+\zeta\right) \tag{D88} $$

D3.3. PD constant

By comparing Eq. (D77) and Eq. (D88), the PD bond constant can be defined as

$$ b = \frac{E}{2\left({}^{0}A\right)\delta^{2}} \tag{D89} $$

Appendix E. PD constants for nonlinear PD beam model

In this section, the derivations to obtain the PD constants are presented. First, let k and j be two material points in a beam structure. By using Taylor's series expansion, a variable $f\left({}^0x_{(j)}\right)$ at material point j can be expressed in term of the variable $f\left({}^0x_{(k)}\right)$ at material point k as

$$f\left({}^0x_{(j)}\right)=f\left({}^0x_{(k)}\right)+\left({}^0x_{(j)}-{}^0x_{(k)}\right)\frac{\partial}{\partial {}^0x}f\left({}^0x_{(k)}\right)+\cdots \tag{E1a}$$

or

$$f\left({}^0x_{(j)}\right)=f\left({}^0x_{(k)}\right)+{}_0f_{,x(k)}\left({}^0x_{(j)}-{}^0x_{(k)}\right)+\cdots \tag{E1b}$$

with

$${}_0f_{,x(k)}=\frac{\partial}{\partial {}^0x}f\left({}^0x_{(k)}\right) \tag{E1c}$$

In Eq. (E1), the parameter f can be any variable. For instance, f can be the displacements and rotations of material points, $\left(u,v,w,\theta_x,\theta_y,\theta_z\right)$.

If k and j are two different material points ($k\neq j$), the distance between them in the undeformed configuration is nonzero (${}^0\xi_{(k)(j)}\neq 0$). Therefore, Eq. (E1b) can be rewritten as

$$\frac{f\left({}^0x_{(j)}\right)-f\left({}^0x_{(k)}\right)}{{}^0\xi_{(k)(j)}}={}_0f_{,x(k)}\frac{{}^0x_{(j)}-{}^0x_{(k)}}{{}^0\xi_{(k)(j)}}+\cdots \tag{E2}$$

By using the relations given in Eq. (3.50h), Eq. (E2) can be rewritten as

$$\frac{f\left({}^0x_{(j)}\right)-f\left({}^0x_{(k)}\right)}{{}^0\xi_{(k)(j)}}={}_0f_{,x(k)}\,{}^0\beta_{(k)(j)}+\cdots \tag{E3}$$

Replacing f variable in Eq. (E3) by displacements, rotations, and director vectors at time t of material points k and j results in the following relations

$$\frac{{}^tu_{(j)}-{}^tu_{(k)}}{{}^0\xi_{(k)(j)}}={}_0^tu_{,x(k)}\,{}^0\beta_{(k)(j)}+\cdots \tag{E4a}$$

$$\frac{{}^tv_{(j)}-{}^tv_{(k)}}{{}^0\xi_{(k)(j)}}={}_0^tv_{,x(k)}\,{}^0\beta_{(k)(j)}+\cdots \tag{E4b}$$

$$\frac{{}^tw_{(j)}-{}^tw_{(k)}}{{}^0\xi_{(k)(j)}}={}_0^tw_{,x(k)}\,{}^0\beta_{(k)(j)}+\cdots \tag{E4c}$$

$$\frac{{}^t\theta_{x(j)}-{}^t\theta_{x(k)}}{{}^0\xi_{(k)(j)}}={}_0^t\theta_{x,x(k)}\,{}^0\beta_{(k)(j)}+\cdots \tag{E4d}$$

$$\frac{{}^{t}\theta_{y(j)} - {}^{t}\theta_{y(k)}}{{}^{0}\xi_{(k)(j)}} = {}_{0}{}^{t}\theta_{y,x(k)}\,{}^{0}\beta_{(k)(j)} + \cdots \tag{E4e}$$

$$\frac{{}^{t}\theta_{z(j)} - {}^{t}\theta_{z(k)}}{{}^{0}\xi_{(k)(j)}} = {}_{0}{}^{t}\theta_{z,x(k)}\,{}^{0}\beta_{(k)(j)} + \cdots \tag{E4f}$$

$$\frac{{}^{t}V_{sx(j)} - {}^{t}V_{sx(k)}}{{}^{0}\xi_{(k)(j)}} = {}_{0}{}^{t}V_{sx,x(k)}\,{}^{0}\beta_{(k)(j)} + \cdots \tag{E4g}$$

$$\frac{{}^{t}V_{sy(j)} - {}^{t}V_{sy(k)}}{{}^{0}\xi_{(k)(j)}} = {}_{0}{}^{t}V_{sy,x(k)}\,{}^{0}\beta_{(k)(j)} + \cdots \tag{E4h}$$

$$\frac{{}^{t}V_{sz(j)} - {}^{t}V_{sz(k)}}{{}^{0}\xi_{(k)(j)}} = {}_{0}{}^{t}V_{sz,x(k)}\,{}^{0}\beta_{(k)(j)} + \cdots \tag{E4i}$$

$$\frac{{}^{t}V_{tx(j)} - {}^{t}V_{tx(k)}}{{}^{0}\xi_{(k)(j)}} = {}_{0}{}^{t}V_{tx,x(k)}\,{}^{0}\beta_{(k)(j)} + \cdots \tag{E4j}$$

$$\frac{{}^{t}V_{ty(j)} - {}^{t}V_{ty(k)}}{{}^{0}\xi_{(k)(j)}} = {}_{0}{}^{t}V_{ty,x(k)}\,{}^{0}\beta_{(k)(j)} + \cdots \tag{E4k}$$

$$\frac{{}^{t}V_{tz(j)} - {}^{t}V_{tz(k)}}{{}^{0}\xi_{(k)(j)}} = {}_{0}{}^{t}V_{tz,x(k)}\,{}^{0}\beta_{(k)(j)} + \cdots \tag{E4l}$$

Similarly, replacing f in Eq. (E3) by incremental displacements and incremental rotations (from time t to time $t+\Delta t$) of material points k and j results in the following relations

$$\frac{\underline{u}_{(j)} - \underline{u}_{(k)}}{{}^{0}\xi_{(k)(j)}} = {}_{0}\underline{u}_{,x(k)}\,{}^{0}\beta_{(k)(j)} + \cdots \tag{E5a}$$

$$\frac{\underline{v}_{(j)} - \underline{v}_{(k)}}{{}^{0}\xi_{(k)(j)}} = {}_{0}\underline{v}_{,x(k)}\,{}^{0}\beta_{(k)(j)} + \cdots \tag{E5b}$$

$$\frac{\underline{w}_{(j)} - \underline{w}_{(k)}}{{}^{0}\xi_{(k)(j)}} = {}_{0}\underline{w}_{,x(k)}\,{}^{0}\beta_{(k)(j)} + \cdots \tag{E5c}$$

$$\frac{\underline{\theta}_{x(j)} - \underline{\theta}_{x(k)}}{{}^{0}\xi_{(k)(j)}} = {}_{0}\underline{\theta}_{x,x(k)}\,{}^{0}\beta_{(k)(j)} + \cdots \tag{E5d}$$

$$\frac{\underline{\theta}_{y(j)} - \underline{\theta}_{y(k)}}{{}^{0}\xi_{(k)(j)}} = {}_{0}\underline{\theta}_{y,x(k)}\,{}^{0}\beta_{(k)(j)} + \cdots \tag{E5e}$$

$$\frac{\underline{\theta}_{z(j)} - \underline{\theta}_{z(k)}}{{}^{0}\xi_{(k)(j)}} = {}_{0}\underline{\theta}_{z,x(k)}\,{}^{0}\beta_{(k)(j)} + \cdots \tag{E5f}$$

Therefore, by using the relation given in Eq. (E4) and Eq. (E5), the terms, ${}_0^t a_1^{PD}$, ${}_0^t a_2^{PD}$, ${}_0^t a_3^{PD}$ given in Eq. (3.50d-f) can be rewritten as

$${}_0^t a_1^{PD} = {}_0^t u_{,x(k)} \left({}^0\beta_{(k)(j)} \right)^2 = {}_0^t u_{,x(k)} \tag{E6a}$$

$${}_0^t a_2^{PD} = {}_0^t v_{,x(k)} \left({}^0\beta_{(k)(j)} \right)^2 = {}_0^t v_{,x(k)} \tag{E6b}$$

$${}_0^t a_3^{PD} = {}_0^t w_{,x(k)} \left({}^0\beta_{(k)(j)} \right)^2 = {}_0^t w_{,x(k)} \tag{E6c}$$

with

$$\left({}^0\beta_{(k)(j)} \right)^2 = \left(\frac{{}^0x_{(j)} - {}^0x_{(k)}}{{}^0\xi_{(k)(j)}} \right)^2 = 1 \tag{E6d}$$

Similarly, by using the relation given in Eq. (E4) and Eq. (E5), the terms, ${}_0^t a_4^{PD}$, ${}_0^t a_5^{PD}$, ${}_0^t a_6^{PD}$, ${}_0^t a_7^{PD}$, ${}_0^t a_8^{PD}$, ${}_0^t a_9^{PD}$ given in Eq. (3.52f-k) can be rewritten as

$${}_0^t a_4^{PD} = {}_0^t V_{sx,x(k)}; \quad {}_0^t a_5^{PD} = {}_0^t V_{sy,x(k)}; \quad {}_0^t a_6^{PD} = {}_0^t V_{sz,x(k)} \tag{E7a}$$

$${}_0^t a_7^{PD} = {}_0^t V_{tx,x(k)}; \quad {}_0^t a_8^{PD} = {}_0^t V_{ty,x(k)}; \quad {}_0^t a_9^{PD} = {}_0^t V_{tz,x(k)} \tag{E7b}$$

Therefore, the terms, ${}_0^t a_{10}^{PD}$, ${}_0^t a_{11}^{PD}$, ${}_0^t a_{12}^{PD}$ given in Eq. (3.50b) and Eq. (3.52b-c) can be obtained as

$${}_0^t a_{10}^{PD} = {}_0^t a_1^{PD} + \frac{1}{2}\left(\left({}_0^t a_1^{PD} \right)^2 + \left({}_0^t a_2^{PD} \right)^2 + \left({}_0^t a_3^{PD} \right)^2 \right) \tag{E8a}$$

$${}_0^t a_{11}^{PD} = {}_0^t a_4^{PD} \left(1 + {}_0^t a_1^{PD} \right) + \left({}_0^t a_2^{PD} \right)\left({}_0^t a_5^{PD} \right) + \left({}_0^t a_3^{PD} \right)\left({}_0^t a_6^{PD} \right) \tag{E8b}$$

$${}_0^t a_{12}^{PD} = \left({}_0^t a_7^{PD} \right)\left(1 + {}_0^t a_1^{PD} \right) + \left({}_0^t a_2^{PD} \right)\left({}_0^t a_8^{PD} \right) + \left({}_0^t a_3^{PD} \right)\left({}_0^t a_9^{PD} \right) \tag{E8c}$$

Moreover, by assuming that the beam is discretized with fine mesh, material points k and j are very close to each other within the horizon size. Therefore, the following approximation can be assumed

$$\frac{{}^t V_{sx(j)} + {}^t V_{sx(k)}}{2} \approx {}^t V_{sx(k)}; \quad \frac{{}^t V_{sy(j)} + {}^t V_{sy(k)}}{2} \approx {}^t V_{sy(k)}; \quad \frac{{}^t V_{sz(j)} + {}^t V_{sz(k)}}{2} \approx {}^t V_{sz(k)} \tag{E9a}$$

$$\frac{{}^t V_{tx(j)} + {}^t V_{tx(k)}}{2} \approx {}^t V_{tx(k)}; \quad \frac{{}^t V_{ty(j)} + {}^t V_{ty(k)}}{2} \approx {}^t V_{ty(k)}; \quad \frac{{}^t V_{tz(j)} + {}^t V_{tz(k)}}{2} \approx {}^t V_{tz(k)} \tag{E9b}$$

Therefore, by using the relations given in Eq. (E9), the terms, ${}_0^t a_{13}^{PD}$, ${}_0^t a_{14}^{PD}$ and ${}_0^t a_{15}^{PD}$ given in Eq. (3.54b-c) and Eq. (3.56b) can be approximated as

$${}_0^t a_{13}^{PD} = \left(1 + {}_0^t a_1^{PD} \right) {}^t V_{sx(k)} + \left({}_0^t a_2^{PD} \right) {}^t V_{sy(k)} + \left({}_0^t a_3^{PD} \right) {}^t V_{sz(k)} \tag{E10a}$$

$$ {}_0^t a_{14}^{PD} = \left(1+ {}_0^t a_1^{PD}\right) {}^t V_{tx(k)} + \left({}_0^t a_2^{PD}\right) {}^t V_{ty(k)} + \left({}_0^t a_3^{PD}\right) {}^t V_{tz(k)} \tag{E10b} $$

$$ {}_0^t a_{15}^{PD} = \left({}_0^t a_8^{PD}\right) {}^t V_{sy(k)} + \left({}_0^t a_7^{PD}\right) {}^t V_{sx(k)} + \left({}_0^t a_9^{PD}\right) {}^t V_{sz(k)} \tag{E10c} $$

By comparing Eq. (E6-8), Eq. (E10) to Eq. (3.44e-m), it can be observed that the terms, ${}_0^t a_1^{PD}$,..., ${}_0^t a_{15}^{PD}$ in PD and the terms ${}_0^t a_1$,..., ${}_0^t a_{15}$ in classical continuum mechanics are equal to each other.

Similarly, by using the relations given in Eq. (E4-5), the terms ${}_0\underline{a}_{10}^{PD}$, ${}_0\underline{a}_{11}^{PD}$, ${}_0\underline{a}_{12}^{PD}$ given in Eq. (3.50c) and Eq. (3.52d-e) can be rewritten as

$$ {}_0\underline{a}_{10}^{PD} = \left({}_0\underline{u}_{,x(k)}\right)\left(1+ {}_0^t a_1^{PD}\right) + {}_0^t a_2^{PD}\left({}_0\underline{v}_{,x(k)}\right) + {}_0^t a_3^{PD}\left({}_0\underline{w}_{,x(k)}\right) \tag{E11a} $$

$$ {}_0\underline{a}_{11}^{PD} = \begin{pmatrix} \left({}_0^t a_4^{PD}\right)\left({}_0\underline{u}_{,x(k)}\right) + \left({}_0^t a_5^{PD}\right)\left({}_0\underline{v}_{,x(k)}\right) + \left({}_0^t a_6^{PD}\right)\left({}_0\underline{w}_{,x(k)}\right) \\ + \left(1+ {}_0^t a_1^{PD}\right)\dfrac{\partial}{\partial {}^0x}\left(\underline{\theta}_{y(k)} {}^t V_{sz(k)} - \underline{\theta}_{z(k)} {}^t V_{sy(k)}\right) \\ + \left({}_0^t a_2^{PD}\right)\dfrac{\partial}{\partial {}^0x}\left(\underline{\theta}_{z(k)} {}^t V_{sx(k)} - \underline{\theta}_{x(k)} {}^t V_{sz(k)}\right) \\ + \left({}_0^t a_3^{PD}\right)\dfrac{\partial}{\partial {}^0x}\left(\underline{\theta}_{x(k)} {}^t V_{sy(k)} - \underline{\theta}_{y(k)} {}^t V_{sx(k)}\right) \end{pmatrix} \tag{E11b} $$

$$ {}_0\underline{a}_{12}^{PD} = \begin{pmatrix} \left({}_0^t a_7^{PD}\right)\left({}_0\underline{u}_{,x(k)}\right) + \left({}_0^t a_8^{PD}\right)\left({}_0\underline{v}_{,x(k)}\right) + \left({}_0^t a_9^{PD}\right)\left({}_0\underline{w}_{,x(k)}\right) \\ + \left(1+ {}_0^t a_1^{PD}\right)\dfrac{\partial}{\partial {}^0x}\left(\underline{\theta}_{y(k)} {}^t V_{tz(k)} - \underline{\theta}_{z(k)} {}^t V_{ty(k)}\right) \\ + \left({}_0^t a_2^{PD}\right)\dfrac{\partial}{\partial {}^0x}\left(\underline{\theta}_{z(k)} {}^t V_{tx(k)} - \underline{\theta}_{x(k)} {}^t V_{tz(k)}\right) \\ + \left({}_0^t a_3^{PD}\right)\dfrac{\partial}{\partial {}^0x}\left(\underline{\theta}_{x(k)} {}^t V_{ty(k)} - \underline{\theta}_{y(k)} {}^t V_{tx(k)}\right) \end{pmatrix} \tag{E11c} $$

By using the relations given in Eq. (E4-5) and Eq. (E9), the terms ${}_0\underline{a}_{13}^{PD}$, ${}_0\underline{a}_{14}^{PD}$ and ${}_0\underline{a}_{15}^{PD}$ given in Eq. (3.54d-e) and Eq. (3.56c) can be rewritten as

$$ {}_0\underline{a}_{13}^{PD} = \begin{pmatrix} {}^t V_{sx(k)}\left({}_0\underline{u}_{,x(k)}\right) + {}^t V_{sy(k)}\left({}_0\underline{v}_{,x(k)}\right) + {}^t V_{sz(k)}\left({}_0\underline{w}_{,x(k)}\right) \\ + \left(1+ {}_0^t a_1^{PD}\right)\left(\underline{\theta}_{y(k)} {}^t V_{sz(k)} - \underline{\theta}_{z(k)} {}^t V_{sy(k)}\right) \\ + \left({}_0^t a_2^{PD}\right)\left(\underline{\theta}_{z(k)} {}^t V_{sx(k)} - \underline{\theta}_{x(k)} {}^t V_{sz(k)}\right) \\ + \left({}_0^t a_3^{PD}\right)\left(\underline{\theta}_{x(k)} {}^t V_{sy(k)} - \underline{\theta}_{y(k)} {}^t V_{sx(k)}\right) \end{pmatrix} \tag{E12a} $$

$$ {}_0\underline{a}_{14}^{PD} = \begin{pmatrix} {}^t V_{tx(k)}\left({}_0\underline{u}_{,x(k)}\right) + {}^t V_{ty(k)}\left({}_0\underline{v}_{,x(k)}\right) + {}^t V_{tz(k)}\left({}_0\underline{w}_{,x(k)}\right) \\ + \left(1+ {}_0^t a_1^{PD}\right)\left(\underline{\theta}_{y(k)} {}^t V_{tz(k)} - \underline{\theta}_{z(k)} {}^t V_{ty(k)}\right) \\ + \left({}_0^t a_2^{PD}\right)\left(\underline{\theta}_{z(k)} {}^t V_{tx(k)} - \underline{\theta}_{x(k)} {}^t V_{tz(k)}\right) \\ + \left({}_0^t a_3^{PD}\right)\left(\underline{\theta}_{x(k)} {}^t V_{ty(k)} - \underline{\theta}_{y(k)} {}^t V_{tx(k)}\right) \end{pmatrix} \tag{E12b} $$

$$
{}_0\underline{a}_{15}^{PD} = \begin{pmatrix} \left({}^tV_{ty(k)}\,{}^tV_{sz(k)} - {}^tV_{tz(k)}\,{}^tV_{sy(k)}\right)\left({}_0\underline{\theta}_{x,x(k)}\right) \\ +\left({}^tV_{tz(k)}\,{}^tV_{sx(k)} - {}^tV_{tx(k)}\,{}^tV_{sz(k)}\right)\left({}_0\underline{\theta}_{y,x(k)}\right) \\ +\left({}^tV_{tx(k)}\,{}^tV_{sy(k)} - {}^tV_{ty(k)}\,{}^tV_{sx(k)}\right)\left({}_0\underline{\theta}_{z,x(k)}\right) \end{pmatrix} \tag{E12c}
$$

By comparing Eq. (E11-E12) with Eq. (3.44n-s), it can be observed that the terms, ${}_0\underline{a}_{10}^{PD}, {}_0\underline{a}_{11}^{PD}, ..., {}_0\underline{a}_{15}^{PD}$ in PD and the terms ${}_0\underline{a}_{10}, {}_0\underline{a}_{11}, ..., {}_0\underline{a}_{15}$ in classical continuum mechanics are equal to each other.

E1. PD constant for axial deformations

By disregarding the PD interactions beyond the horizon, the PD strain energy density for axial deformations given in Eq. (3.50a) can be rewritten in integral form as

$$
\bar{W}_{axial}^{NLPD} = \left({}^0A\right)\int_0^{\delta} C_{ax}\left({}_0^t a_{10}^{PD}\right)\left({}_0\underline{a}_{10}^{PD}\right)\left({}^0\xi_{(k)(j)}\right)d\left({}^0\xi_{(k)(j)}\right) \tag{E13}
$$

By performing the integrations in Eq. (E13), the nonlinear PD strain energy density for axial deformations can be rewritten as

$$
\bar{W}_{axial}^{NLPD} = \frac{1}{2}\left({}^0A\right)\delta^2 C_{ax}\left({}_0^t a_{10}^{PD}\right)\left({}_0\underline{a}_{10}^{PD}\right) \tag{E14}
$$

As proved in the previous section, the terms ${}_0^t a_{10}^{PD}$, ${}_0\underline{a}_{10}^{PD}$ in PD and ${}_0^t a_{10}$, ${}_0\underline{a}_{10}$ in classical continuum mechanics are equal to each other. Therefore, by comparing Eq. (3.50a) and Eq. (E14), the PD bond constant for axial deformations, C_{ax} can be obtained as

$$
C_{ax} = \frac{2E}{\left({}^0A\right)\delta^2} \tag{E15}
$$

E2. PD constants for bending deformations

By disregarding interactions beyond the horizon of material point k, the PD strain energy density for bending deformations given in Eq. (3.52a) can be rewritten as

$$
\begin{aligned}
\bar{W}_{bending}^{NLPD} &= C_{bz}\left({}^0A\right)\int_0^{\delta}\left({}_0^t a_{11}^{PD}\right)\left({}_0\underline{a}_{11}^{PD}\right)\left({}^0\xi_{(k)(j)}\right)d\left({}^0\xi_{(k)(j)}\right) \\
&\quad + C_{by}\left({}^0A\right)\int_0^{\delta}\left({}_0^t a_{12}^{PD}\right)\left({}_0\underline{a}_{12}^{PD}\right)\left({}^0\xi_{(k)(j)}\right)d\left({}^0\xi_{(k)(j)}\right)
\end{aligned} \tag{E16}
$$

By performing the integrations in Eq. (E16), the SED for bending deformations can be rewritten as

$$
\bar{W}_{bending}^{NLPD} = \frac{1}{2}C_{bz}\left({}^0A\right)\delta^2\left({}_0^t a_{11}^{PD}\right)\left({}_0\underline{a}_{11}^{PD}\right) + \frac{1}{2}C_{by}\left({}^0A\right)\delta^2\left({}_0^t a_{12}^{PD}\right)\left({}_0\underline{a}_{12}^{PD}\right) \tag{E17}
$$

As proved in the previous section, the terms ${}_0^t a_{11}^{PD}$, ${}_0\underline{a}_{11}^{PD}$, ${}_0^t a_{12}^{PD}$, ${}_0\underline{a}_{12}^{PD}$ in PD and ${}_0^t a_{11}$, ${}_0\underline{a}_{11}$, ${}_0^t a_{12}$, ${}_0\underline{a}_{12}$ in classical continuum mechanics are equal to each other. Therefore, by comparing Eq. (3.44b) and Eq. (E17), the PD bond constants for bending deformations, C_{by} and C_{bz}, can be represented as

$$C_{by} = \frac{2EI_{yy}}{\left({}^0A\right)^2 \delta^2} \tag{E18a}$$

$$C_{bz} = \frac{2EI_{zz}}{\left({}^0A\right)^2 \delta^2} \tag{E18b}$$

E3. PD constants for shear deformations

By disregarding interactions beyond the horizon of material point k, the PD strain energy density for bending deformations given in Eq. (3.54a) can be rewritten as

$$\bar{W}_{shear}^{NLPD} = C_s\left({}^0A\right)\int_0^{\delta}\left[\left({}_0^t a_{13}^{PD}\right)\left({}_0\underline{a}_{13}^{PD}\right)+\left({}_0^t a_{14}^{PD}\right)\left({}_0\underline{a}_{14}^{PD}\right)\right]\left({}^0\xi_{(k)(j)}\right)d\left({}^0\xi_{(k)(j)}\right) \tag{E19}$$

By performing the integrations in Eq. (E19), the SED for shear deformations can be rewritten as

$$\bar{W}_{shear}^{NLPD} = \frac{1}{2}C_s\left({}^0A\right)\delta^2\left[\left({}_0^t a_{13}^{PD}\right)\left({}_0\underline{a}_{13}^{PD}\right)+\left({}_0^t a_{14}^{PD}\right)\left({}_0\underline{a}_{14}^{PD}\right)\right] \tag{E20}$$

As proved in the previous section, the terms ${}_0^t a_{13}^{PD}$, ${}_0\underline{a}_{13}^{PD}$, ${}_0^t a_{14}^{PD}$, ${}_0\underline{a}_{14}^{PD}$ in PD and ${}_0^t a_{13}$, ${}_0\underline{a}_{13}$, ${}_0^t a_{14}$, ${}_0\underline{a}_{14}$ in classical continuum mechanics are equal to each other. Therefore, by comparing Eq. (3.44c) and Eq. (E20), the PD bond constants for shear deformations, C_{sh}, can be represented as

$$C_s = \frac{2k_s G}{\left({}^0A\right)\delta^2} \tag{E21}$$

E4. PD constants for torsional deformations

By disregarding interactions beyond the horizon of material point k, the PD strain energy density for bending deformations given in Eq. (3.56a) can be rewritten as

$$\bar{W}_{torsion}^{NLPD} = C_t\left({}^0A\right)\int_0^{\delta}\left({}_0^t a_{15}^{PD}\right)\left({}_0\underline{a}_{15}^{PD}\right)\left({}^0\xi_{(k)(j)}\right)d\left({}^0\xi_{(k)(j)}\right) \tag{E22}$$

By performing the integrations in Eq. (E22), the nonlinear PD strain energy density for torsional deformations can be rewritten as

$$\bar{W}_{torsion}^{NLPD} = \frac{1}{2}C_t\left({}^0A\right)\delta^2\left({}_0^t a_{15}^{PD}\right)\left({}_0\underline{a}_{15}^{PD}\right) \tag{E23}$$

As proved in the previous section, the terms ${}_0^t a_{15}^{PD}$, ${}_0\underline{a}_{15}^{PD}$ in PD and ${}_0^t a_{15}$, ${}_0\underline{a}_{15}$ in classical continuum mechanics are equal to each other. Therefore, by comparing Eq. (3.44d) and Eq. (E23), the PD bond constants for torsional deformations, C_t can be obtained as

$$C_t = \frac{2k_t G}{\left({}^0A\right)^2 \delta^2} \tag{E24}$$

Appendix F. PD constants for nonlinear PD model for plates

F1. PD constants for in-plane deformations

In this section, the derivations to obtain the PD constants for in-plane deformations are presented. First, let k and j be two material points in a two-dimensional structure. By using Taylor's series expansion, a variable $f\left({}^0x_{(j)}, {}^0y_{(j)}\right)$ at material point j can be expressed in term of the variable $f\left({}^0x_{(k)}, {}^0y_{(k)}\right)$ at material point k as

$$\begin{aligned} f\left({}^0x_{(j)}, {}^0y_{(j)}\right) = f\left({}^0x_{(k)}, {}^0y_{(k)}\right) + \left[{}^0x_{(j)} - {}^0x_{(k)}\right] \frac{\partial}{\partial {}^0x}\left(f({}^0x_{(k)}, {}^0y_{(k)})\right) \\ + \left[{}^0y_{(j)} - {}^0y_{(k)}\right] \frac{\partial}{\partial {}^0y}\left(f({}^0x_{(k)}, {}^0y_{(k)})\right) + \cdots \end{aligned} \tag{F1a}$$

or

$$\begin{aligned} f\left({}^0x_{(j)}, {}^0y_{(j)}\right) = f\left({}^0x_{(k)}, {}^0y_{(k)}\right) + {}_0f_{,x(k)}\left[{}^0x_{(j)} - {}^0x_{(k)}\right] \\ + {}_0f_{,y(k)}\left[{}^0y_{(j)} - {}^0y_{(k)}\right] + \cdots \end{aligned} \tag{F1b}$$

with

$${}_0f_{,x(k)} = \frac{\partial}{\partial {}^0x}\left(f({}^0x_{(k)}, {}^0y_{(k)})\right) \tag{F1c}$$

and

$${}_0f_{,y(k)} = \frac{\partial}{\partial {}^0y}\left(f({}^0x_{(k)}, {}^0y_{(k)})\right) \tag{F1d}$$

In Eq. (F1), the parameter f can be any variable. For instance, f can be the displacements and rotations of material points.

If k and j are two different material points ($k \neq j$), the distance between them in the undeformed configuration is nonzero (${}^0\xi \neq 0$). Therefore, Eq. (F1b) can be rewritten as

$$\frac{f\left({}^0x_{(j)}, {}^0y_{(j)}\right) - f\left({}^0x_{(k)}, {}^0y_{(k)}\right)}{{}^0\xi} = {}_0f_{,x(k)}\frac{{}^0x_{(j)} - {}^0x_{(k)}}{{}^0\xi} + {}_0f_{,y(k)}\frac{{}^0y_{(j)} - {}^0y_{(k)}}{{}^0\xi} + \cdots \tag{F2}$$

By using the relations given in Eq. (3.104), Eq. (F2) can be rewritten as

$$\frac{f\left({}^0x_{(j)}, {}^0y_{(j)}\right) - f\left({}^0x_{(k)}, {}^0y_{(k)}\right)}{{}^0\xi} = {}_0f_{,x(k)}\cos\varphi + {}_0f_{,y(k)}\sin\varphi + \cdots \tag{F3}$$

where the angle φ represents the angle between the ${}^0x$ axis in the undeformed configuration and the line connecting material points k and j.

Replacing f variable in Eq. (F3) by displacements and rotations at time t of material points k and j results in the following relations

$$\frac{{}^{t}u_{(j)} - {}^{t}u_{(k)}}{{}^{0}\xi} = {}^{t}_{0}u_{,x(k)}\cos\varphi + {}^{t}_{0}u_{,y(k)}\sin\varphi + \cdots \tag{F4a}$$

$$\frac{{}^{t}v_{(j)} - {}^{t}v_{(k)}}{{}^{0}\xi} = {}^{t}_{0}v_{,x(k)}\cos\varphi + {}^{t}_{0}v_{,y(k)}\sin\varphi + \cdots \tag{F4b}$$

$$\frac{{}^{t}w_{(j)} - {}^{t}w_{(k)}}{{}^{0}\xi} = {}^{t}_{0}w_{,x(k)}\cos\varphi + {}^{t}_{0}w_{,y(k)}\sin\varphi + \cdots \tag{F4c}$$

$$\frac{{}^{t}\theta_{x(j)} - {}^{t}\theta_{x(k)}}{{}^{0}\xi} = {}^{t}_{0}\theta_{x,x(k)}\cos\varphi + {}^{t}_{0}\theta_{x,y(k)}\sin\varphi + \cdots \tag{F4d}$$

$$\frac{{}^{t}\theta_{y(j)} - {}^{t}\theta_{y(k)}}{{}^{0}\xi} = {}^{t}_{0}\theta_{y,x(k)}\cos\varphi + {}^{t}_{0}\theta_{y,y(k)}\sin\varphi + \cdots \tag{F4e}$$

Similarly, replacing f in Eq. (F3) by incremental displacements and incremental rotations (from time t to time $t+\Delta t$) of material points k and j results in the following relations

$$\frac{\underline{u}_{(j)} - \underline{u}_{(k)}}{{}^{0}\xi} = {}_{0}\underline{u}_{,x(k)}\cos\varphi + {}_{0}\underline{u}_{,y(k)}\sin\varphi + \cdots \tag{F5a}$$

$$\frac{\underline{v}_{(j)} - \underline{v}_{(k)}}{{}^{0}\xi} = {}_{0}\underline{v}_{,x(k)}\cos\varphi + {}_{0}\underline{v}_{,y(k)}\sin\varphi + \cdots \tag{F5b}$$

$$\frac{\underline{w}_{(j)} - \underline{w}_{(k)}}{{}^{0}\xi} = {}_{0}\underline{w}_{,x(k)}\cos\varphi + {}_{0}\underline{w}_{,y(k)}\sin\varphi + \cdots \tag{F5c}$$

$$\frac{\underline{\theta}_{x(j)} - \underline{\theta}_{x(k)}}{{}^{0}\xi} = {}_{0}\underline{\theta}_{x,x(k)}\cos\varphi + {}_{0}\underline{\theta}_{x,y(k)}\sin\varphi + \cdots \tag{F5d}$$

$$\frac{\underline{\theta}_{y(j)} - \underline{\theta}_{y(k)}}{{}^{0}\xi} = {}_{0}\underline{\theta}_{y,x(k)}\cos\varphi + {}_{0}\underline{\theta}_{y,y(k)}\sin\varphi + \cdots \tag{F5e}$$

Therefore, by using the relations given in Eqs. (F4-5), the bond stretches given in Eqs. (3.102b-c) can be rewritten as

$$\begin{aligned} {}^{t}_{0}s_{ip(k)(j)} = {}&{}^{t}_{0}u_{,x(k)}\cos^2\varphi + {}^{t}_{0}u_{,y(k)}\sin\varphi\cos\varphi + {}^{t}_{0}v_{,x(k)}\sin\varphi\cos\varphi + {}^{t}_{0}v_{,y(k)}\sin^2\varphi \\ &+ \frac{1}{2}\left[\begin{array}{l}\left({}^{t}_{0}u_{,x(k)}\cos\varphi + {}^{t}_{0}u_{,y(k)}\sin\varphi\right)^2 + \left({}^{t}_{0}v_{,x(k)}\cos\varphi + {}^{t}_{0}v_{,y(k)}\sin\varphi\right)^2 \\ + \left({}^{t}_{0}w_{,x(k)}\cos\varphi + {}^{t}_{0}w_{,y(k)}\sin\varphi\right)^2 \end{array}\right] \end{aligned} \tag{F6a}$$

$$
\begin{aligned}
{}_0\underline{s}_{ip(k)(j)} = {}&{}_0\underline{u}_{,x(k)}\cos^2\varphi + {}_0\underline{u}_{,y(k)}\sin\varphi\cos\varphi + {}_0\underline{v}_{,x(k)}\sin\varphi\cos\varphi + {}_0\underline{v}_{,y(k)}\sin^2\varphi \\
&+\left[\begin{array}{l}
\left({}^t_0u_{,x(k)}\cos\varphi + {}^t_0u_{,y(k)}\sin\varphi\right)\left({}_0\underline{u}_{,x(k)}\cos\varphi + {}_0\underline{u}_{,y(k)}\sin\varphi\right) \\
+\left({}^t_0v_{,x(k)}\cos\varphi + {}^t_0v_{,y(k)}\sin\varphi\right)\left({}_0\underline{v}_{,x(k)}\cos\varphi + {}_0\underline{v}_{,y(k)}\sin\varphi\right) \\
+\left({}^t_0w_{,x(k)}\cos\varphi + {}^t_0w_{,y(k)}\sin\varphi\right)\left({}_0\underline{w}_{,x(k)}\cos\varphi + {}_0\underline{w}_{,y(k)}\sin\varphi\right)
\end{array}\right]
\end{aligned}
\tag{F6b}
$$

Therefore, by using the bond stretches given in Eq. (F6) and by disregarding the interactions beyond the horizon size of a material point, the dilatations given in Eqs. (3.102d-e) can be rewritten as

$$
{}^t_0\vartheta_{(k)} = d_{ip}h\int_0^{2\pi}\int_0^{\delta}\left[\begin{array}{l}
{}^t_0u_{,x(k)}\cos^2\varphi + {}^t_0u_{,y(k)}\sin\varphi\cos\varphi \\
+{}^t_0v_{,x(k)}\sin\varphi\cos\varphi + {}^t_0v_{,y(k)}\sin^2\varphi \\
+\frac{1}{2}\left({}^t_0u_{,x(k)}\cos\varphi + {}^t_0u_{,y(k)}\sin\varphi\right)^2 \\
+\frac{1}{2}\left({}^t_0v_{,x(k)}\cos\varphi + {}^t_0v_{,y(k)}\sin\varphi\right)^2 \\
+\frac{1}{2}\left({}^t_0w_{,x(k)}\cos\varphi + {}^t_0w_{,y(k)}\sin\varphi\right)^2
\end{array}\right]{}^0\xi d\,{}^0\xi d\varphi
\tag{F7a}
$$

$$
{}_0\underline{\vartheta}_{(k)} = d_{ip}h\int_0^{2\pi}\int_0^{\delta}\left[\begin{array}{l}
{}_0\underline{u}_{,x(k)}\cos^2\varphi + {}_0\underline{u}_{,y(k)}\sin\varphi\cos\varphi \\
+{}_0\underline{v}_{,x(k)}\sin\varphi\cos\varphi + {}_0\underline{v}_{,y(k)}\sin^2\varphi \\
+\left({}^t_0u_{,x(k)}\cos\varphi + {}^t_0u_{,y(k)}\sin\varphi\right)\left({}_0\underline{u}_{,x(k)}\cos\varphi + {}_0\underline{u}_{,y(k)}\sin\varphi\right) \\
+\left({}^t_0v_{,x(k)}\cos\varphi + {}^t_0v_{,y(k)}\sin\varphi\right)\left({}_0\underline{v}_{,x(k)}\cos\varphi + {}_0\underline{v}_{,y(k)}\sin\varphi\right) \\
+\left({}^t_0w_{,x(k)}\cos\varphi + {}^t_0w_{,y(k)}\sin\varphi\right)\left({}_0\underline{w}_{,x(k)}\cos\varphi + {}_0\underline{w}_{,y(k)}\sin\varphi\right)
\end{array}\right]{}^0\xi d\,{}^0\xi d\varphi
\tag{F7b}
$$

By performing the integrations in Eq. (F7), the dilatations can be calculated as

$$
{}^t_0\vartheta_{(k)} = d_{ip}\frac{\pi h\delta^2}{2}\left[\left({}^t_0u_{,x(k)} + {}^t_0v_{,y(k)}\right) + \frac{1}{2}\left(\begin{array}{l}
{}^t_0u^2_{,x(k)} + {}^t_0u^2_{,y(k)} + {}^t_0v^2_{,x(k)} \\
+{}^t_0v^2_{,y(k)} + {}^t_0w^2_{,x(k)} + {}^t_0w^2_{,y(k)}
\end{array}\right)\right]
\tag{F8a}
$$

$$
{}_0\underline{\vartheta}_{(k)} = d_{ip}\frac{\pi h\delta^2}{2}\left[\begin{array}{l}
{}_0\underline{u}_{,x(k)} + {}_0\underline{v}_{,y(k)} + {}_0\underline{u}_{,x(k)}\,{}^t_0u_{,x(k)} + {}_0\underline{u}_{,y(k)}\,{}^t_0u_{,y(k)} \\
+{}_0\underline{v}_{,x(k)}\,{}^t_0v_{,x(k)} + {}_0\underline{v}_{,y(k)}\,{}^t_0v_{,y(k)} \\
+{}_0\underline{w}_{,x(k)}\,{}^t_0w_{,x(k)} + {}_0\underline{w}_{,y(k)}\,{}^t_0w_{,y(k)}
\end{array}\right]
\tag{F8b}
$$

By comparing Eq. (F8) with Eqs. (3.95d-e), the PD constant for dilatations can be obtained as

$$
d_{ip} = \frac{2}{\pi h\delta^2}
\tag{F9}
$$

Similarly, by disregarding the interactions beyond the horizon size of material point k, the nonlinear strain energy per unit area for the in-plane deformations given in Eq. (3.102a) can be rewritten in the integral form as

$$\bar{W}_{ip(k)}^{NLPD} = 2a_{ip}\left({}_0^t\vartheta_{(k)}\right)\left({}_0\underline{\vartheta}_{(k)}\right) + 2b_{ip}h\int_0^{2\pi}\int_0^{\delta}\left({}_0^t s_{ip(k)(j)}\right)\left({}_0\underline{s}_{ip(k)(j)}\right){}^0\xi^2 d\,{}^0\xi d\varphi \qquad \text{(F10)}$$

By utilizing the bond stretches in Eq. (F6) and by performing the integrations given in Eq. (F10), the nonlinear strain energy per unit area for the in-plane deformations can be calculated as

$$\bar{W}_{ip(k)}^{NLPD} = 2a_{ip}\,{}_0^t\vartheta_{(k)}\,{}_0\underline{\vartheta}_{(k)}$$

$$+b_{ip}\frac{\pi h\delta^3}{6}\left[\begin{array}{l} +3\,{}_0^t\vartheta_{(k)}\,{}_0\underline{\vartheta}_{(k)} + \left(\begin{array}{l} {}_0^t u_{,y(k)} + {}_0^t v_{,x(k)} \\ +{}_0^t u_{,x(k)}\,{}_0^t u_{,y(k)} \\ +{}_0^t v_{,x(k)}\,{}_0^t v_{,y(k)} \\ +{}_0^t w_{,x(k)}\,{}_0^t w_{,y(k)} \end{array}\right)\left(\begin{array}{l} {}_0\underline{u}_{,y(k)} + {}_0\underline{v}_{,x(k)} + {}_0\underline{u}_{,x(k)}\,{}_0^t u_{,y(k)} \\ +{}_0\underline{u}_{,y(k)}\,{}_0^t u_{,x(k)} + {}_0\underline{v}_{,x(k)}\,{}_0^t v_{,y(k)} \\ +{}_0\underline{v}_{,y(k)}\,{}_0^t v_{,x(k)} \\ +{}_0\underline{w}_{,x(k)}\,{}_0^t w_{,y(k)} + {}_0\underline{w}_{,y(k)}\,{}_0^t w_{,x(k)} \end{array}\right) \\ -2\left[\begin{array}{l} \left(\begin{array}{l} {}_0^t v_{,y(k)} + \frac{1}{2}\left(\begin{array}{l} {}_0^t u_{,y(k)}^2 + {}_0^t v_{,y(k)}^2 \\ +{}_0^t w_{,y(k)}^2 \end{array}\right) \end{array}\right)\left(\begin{array}{l} {}_0\underline{u}_{,x(k)} + {}_0\underline{u}_{,x(k)}\,{}_0^t u_{,x(k)} \\ +{}_0\underline{v}_{,x(k)}\,{}_0^t v_{,x(k)} + {}_0\underline{w}_{,x(k)}\,{}_0^t w_{,x(k)} \end{array}\right) \\ +\left(\begin{array}{l} {}_0^t u_{,x(k)} + \frac{1}{2}\left(\begin{array}{l} {}_0^t u_{,x(k)}^2 + {}_0^t v_{,x(k)}^2 \\ +{}_0^t w_{,x(k)}^2 \end{array}\right) \end{array}\right)\left(\begin{array}{l} {}_0\underline{v}_{,y(k)} + {}_0\underline{u}_{,y(k)}\,{}_0^t u_{,y(k)} \\ +{}_0\underline{v}_{,y(k)}\,{}_0^t v_{,y(k)} + {}_0\underline{w}_{,y(k)}\,{}_0^t w_{,y(k)} \end{array}\right) \end{array}\right] \end{array}\right] \qquad \text{(F11a)}$$

or

$$\bar{W}_{ip(k)}^{NLPD} = \left(2a_{ip} + b_{ip}\frac{\pi h\delta^3}{2}\right){}_0^t\vartheta_{(k)}\,{}_0\underline{\vartheta}_{(k)}$$

$$+b_{ip}\frac{\pi h\delta^3}{6}\left[\begin{array}{l} \left(\begin{array}{l} {}_0^t u_{,y(k)} + {}_0^t v_{,x(k)} \\ +{}_0^t u_{,x(k)}\,{}_0^t u_{,y(k)} \\ +{}_0^t v_{,x(k)}\,{}_0^t v_{,y(k)} \\ +{}_0^t w_{,x(k)}\,{}_0^t w_{,y(k)} \end{array}\right)\left(\begin{array}{l} {}_0\underline{u}_{,y(k)} + {}_0\underline{v}_{,x(k)} + {}_0\underline{u}_{,x(k)}\,{}_0^t u_{,y(k)} \\ +{}_0\underline{u}_{,y(k)}\,{}_0^t u_{,x(k)} + {}_0\underline{v}_{,x(k)}\,{}_0^t v_{,y(k)} \\ +{}_0\underline{v}_{,y(k)}\,{}_0^t v_{,x(k)} \\ +{}_0\underline{w}_{,x(k)}\,{}_0^t w_{,y(k)} + {}_0\underline{w}_{,y(k)}\,{}_0^t w_{,x(k)} \end{array}\right) \\ -2\left[\begin{array}{l} {}_0^t\bar{\varepsilon}_{yy(k)}\left(\begin{array}{l} {}_0\underline{u}_{,x(k)} + {}_0\underline{u}_{,x(k)}\,{}_0^t u_{,x(k)} \\ +{}_0\underline{v}_{,x(k)}\,{}_0^t v_{,x(k)} + {}_0\underline{w}_{,x(k)}\,{}_0^t w_{,x(k)} \end{array}\right) \\ +{}_0^t\bar{\varepsilon}_{xx(k)}\left(\begin{array}{l} {}_0\underline{v}_{,y(k)} + {}_0\underline{u}_{,y(k)}\,{}_0^t u_{,y(k)} \\ +{}_0\underline{v}_{,y(k)}\,{}_0^t v_{,y(k)} + {}_0\underline{w}_{,y(k)}\,{}_0^t w_{,y(k)} \end{array}\right) \end{array}\right] \end{array}\right] \qquad \text{(F11b)}$$

where ${}_0^t\varepsilon_{xx}$ and ${}_0^t\varepsilon_{yy}$ are defined in Eqs. (3.95b-c).

By comparing Eq. (F11b) with Eq. (3.96b), the following relations are obtained

$$b_{ip}\frac{\pi h\delta^3}{6} = \frac{Eh}{2(1+\nu)} \qquad \text{(F12a)}$$

$$a_{ip} + b_{ip}\frac{\pi h\delta^3}{2} = \frac{Eh}{1-\nu^2} \qquad \text{(F12b)}$$

Therefore, the PD constants for in-plane deformations can be obtained as

$$b_{ip} = \frac{3E}{(1+\nu)\pi\delta^3} \tag{F13a}$$

$$a_{ip} = \frac{Eh}{4(1-\nu^2)}(3\nu-1) \tag{F13b}$$

F2. PD constant for shear deformations

In this section, the determination of the PD constant, C_{sh}, for shear deformations is presented. As shown in Fig. 6.3, ${}^t\hat{\theta}_{(k)}$, ${}^t\hat{\theta}_{(j)}$ and $\underline{\hat{\theta}}_{(k)}$, $\underline{\hat{\theta}}_{(j)}$ are rotations and incremental rotations around the line of interaction between material points k and j. The relative values of these rotations and incremental rotations represent the torsional angles (twisting angles) of the bond between material points k and j. Therefore, by assuming the PD model is discretized with a fine mesh and the torsional deformations of the bond between material points k and j are insignificant, the approximation ${}^t\hat{\theta}_{(k)} \approx {}^t\hat{\theta}_{(j)}$ and $\underline{\hat{\theta}}_{(k)} \approx \underline{\hat{\theta}}_{(j)}$ can be assumed [61]. Thus, the nonlinear PD strain energy per unit area for the shear deformations given in Eq. (3.106a) can be rewritten as

$$\bar{W}_{sh(k)}^{NLPD} = \frac{1}{2}C_s \sum_{j=1}^{N} \left(\frac{{}^t w_{(j)} - {}^t w_{(k)}}{{}^0\xi} - {}^t\hat{\theta}_{(k)} \right) \left(\frac{\underline{w}_{(j)} - \underline{w}_{(k)}}{{}^0\xi} - \underline{\hat{\theta}}_{(k)} \right) {}^0\xi \, {}^0V_{(j)} \tag{F14}$$

By using Eqs. (3.106b-c), the nonlinear PD strain energy per unit area for the shear deformations given in Eq. (F14) can be rewritten as

$$\bar{W}_{sh(k)}^{NLPD} = \frac{1}{2}C_s \sum_{j=1}^{N} \begin{pmatrix} \frac{{}^t w_{(j)} - {}^t w_{(k)}}{{}^0\xi_{(k)(j)}} + \\ +\left(\sin {}^t\theta_{y(k)}\right)\cos\varphi \\ -\left(\sin {}^t\theta_{x(k)}\right)\sin\varphi \end{pmatrix} \begin{pmatrix} \frac{\underline{w}_{(j)} - \underline{w}_{(k)}}{{}^0\xi_{(k)(j)}} + \\ +\theta_{y(k)}\cos\left({}^t\theta_{y(k)}\right)\cos\varphi \\ -\theta_{x(k)}\cos\left({}^t\theta_{x(k)}\right)\sin\varphi \end{pmatrix} {}^0\xi_{(k)(j)} \, {}^0V_{(j)} \tag{F15}$$

By using the relation given in Eq. (F4c) and Eq. (F5c), and by disregarding the interactions beyond the horizon size of material point k, Eq. (F15) can be rewritten as

$$\bar{W}_{sh(k)}^{NLPD} = \frac{1}{2}C_s h \int_0^{2\pi}\int_0^{\delta} \begin{pmatrix} \left({}^t_0 w_{,x(k)} + \sin {}^t\theta_{y(k)}\right)\cos\varphi \\ +\left({}^t_0 w_{,y(k)} - \sin {}^t\theta_{x(k)}\right)\sin\varphi \end{pmatrix} \begin{pmatrix} \left({}_0\underline{w}_{,x(k)} + \underline{\theta}_{y(k)}\cos {}^t\theta_{y(k)}\right)\cos\varphi \\ +\left({}_0\underline{w}_{,y(k)} - \underline{\theta}_{x(k)}\cos {}^t\theta_{x(k)}\right)\sin\varphi \end{pmatrix} {}^0\xi^2 d\, {}^0\xi d\varphi \tag{F16}$$

By performing the integrations in Eq. (F16), the nonlinear PD strain energy per unit area for the shear deformations can be obtained as

$$\bar{W}_{sh(k)}^{NLPD} = \frac{1}{2}C_s \frac{\pi h \delta^3}{3} \begin{bmatrix} \left({}^t_0 w_{,x(k)} + \sin {}^t\theta_{y(k)}\right)\left({}_0\underline{w}_{,x(k)} + \underline{\theta}_{y(k)}\cos\left({}^t\theta_{y(k)}\right)\right) \\ +\left({}^t_0 w_{,y(k)} - \sin {}^t\theta_{x(k)}\right)\left({}_0\underline{w}_{,y(k)} - \underline{\theta}_{x(k)}\cos\left({}^t\theta_{x(k)}\right)\right) \end{bmatrix} \tag{F17}$$

By comparing Eq. (F17) with Eq. (3.96c), the PD constant for shear deformations can be obtained as

$$C_s = \frac{3k_s E}{(1+\nu)\pi\delta^3} \tag{F18}$$

F3. PD constants for bending deformations

By using the relations given in Eqs. (F4d-e) and Eqs. (F5d-e), the bond stretches for bending deformations given in Eqs. (3.108d-e) can be rewritten as

$$\begin{aligned} {}^{t}_{0}s_{b(k)(j)} = &-{}^{t}_{0}\theta_{y,x(k)}\cos^2\varphi - {}^{t}_{0}\theta_{y,y(k)}\sin\varphi\cos\varphi \\ &+ {}^{t}_{0}\theta_{x,x(k)}\sin\varphi\cos\varphi + {}^{t}_{0}\theta_{x,y(k)}\sin^2\varphi \end{aligned} \tag{F19a}$$

$$\begin{aligned} {}_{0}\underline{s}_{b(k)(j)} = &-{}_{0}\underline{\theta}_{y,x(k)}\cos^2\varphi - {}_{0}\underline{\theta}_{y,y(k)}\sin\varphi\cos\varphi \\ &+ {}_{0}\underline{\theta}_{x,x(k)}\sin\varphi\cos\varphi + {}_{0}\underline{\theta}_{x,y(k)}\sin^2\varphi \end{aligned} \tag{F19b}$$

By using Eq. (F19) and disregarding the interactions beyond the horizon of material point k, the terms given in Eqs. (3.108b-c) can be expressed as

$${}^{t}_{0}\vartheta_{b(k)} = d_b h \int_0^{2\pi}\int_0^{\delta} \begin{pmatrix} -{}^{t}_{0}\theta_{y,x(k)}\cos^2\varphi - {}^{t}_{0}\theta_{y,y(k)}\sin\varphi\cos\varphi \\ +{}^{t}_{0}\theta_{x,x(k)}\sin\varphi\cos\varphi + {}^{t}_{0}\theta_{x,y(k)}\sin^2\varphi \end{pmatrix} {}^{0}\xi d\,{}^{0}\xi d\varphi \tag{F20a}$$

$${}_{0}\underline{\vartheta}_{b(k)} = d_b h \int_0^{2\pi}\int_0^{\delta} \begin{pmatrix} -{}_{0}\underline{\theta}_{y,x(k)}\cos^2\varphi - {}_{0}\underline{\theta}_{y,y(k)}\sin\varphi\cos\varphi \\ +{}_{0}\underline{\theta}_{x,x(k)}\sin\varphi\cos\varphi + {}_{0}\underline{\theta}_{x,y(k)}\sin^2\varphi \end{pmatrix} {}^{0}\xi d\,{}^{0}\xi d\varphi \tag{F20b}$$

Performing the integrations given in Eq. (F20) results in

$${}^{t}_{0}\vartheta_{b(k)} = d_b \frac{\pi h\delta^2}{2}\left(-{}^{t}_{0}\theta_{y,x(k)} + {}^{t}_{0}\theta_{x,y(k)}\right) \tag{F21a}$$

$${}_{0}\underline{\vartheta}_{b(k)} = d_b \frac{\pi h\delta^2}{2}\left(-{}_{0}\underline{\theta}_{y,x(k)} + {}_{0}\underline{\theta}_{x,y(k)}\right) \tag{F21b}$$

By comparing Eq. (F21) with Eqs. (3.97c-d), the PD constant d_b can be obtained as

$$d_b = \frac{2}{\pi h\delta^2} \tag{F22}$$

Similarly, by using Eq. (F19) and by disregarding the interactions beyond the horizon of material point k, the nonlinear PD strain energy per unit area for bending formulations given in Eq. (3.108a) can be expressed as

$$\bar{W}^{NLPD}_{b(k)} = 2a_b\left({}^{t}_{0}\vartheta_{b(k)}\right)\left({}_{0}\underline{\vartheta}_{b(k)}\right) + 2b_b h\int_0^{2\pi}\int_0^{\delta} AB\,{}^{0}\xi^2 d\,{}^{0}\xi d\varphi \tag{F23a}$$

with

$$A=\begin{pmatrix} -{}_0^t\theta_{y,x(k)}\cos^2\varphi-{}_0^t\theta_{y,y(k)}\sin\varphi\cos\varphi \\ +{}_0^t\theta_{x,x(k)}\sin\varphi\cos\varphi+{}_0^t\theta_{x,y(k)}\sin^2\varphi \end{pmatrix} \tag{F23b}$$

and

$$B=\begin{pmatrix} -{}_0\underline{\theta}_{y,x(k)}\cos^2\varphi-{}_0\underline{\theta}_{y,y(k)}\sin\varphi\cos\varphi \\ +{}_0\underline{\theta}_{x,x(k)}\sin\varphi\cos\varphi+{}_0\underline{\theta}_{x,y(k)}\sin^2\varphi \end{pmatrix} \tag{F23c}$$

By performing the integration in Eq. (F23a), the nonlinear PD strain energy per unit area for bending formulations can be obtained as

$$\begin{aligned} \bar{W}_{b(k)}^{NLPD} &= 2a_b\left({}_0^t\vartheta_{b(k)}\right)\left({}_0\underline{\vartheta}_{b(k)}\right) \\ &+b_b\frac{\pi h\delta^3}{6}\begin{bmatrix} 3\left({}_0^t\theta_{y,x(k)}-{}_0^t\theta_{x,y(k)}\right)\left({}_0\underline{\theta}_{y,x(k)}-{}_0\underline{\theta}_{x,y(k)}\right) \\ +\left({}_0^t\theta_{x,x(k)}-{}_0^t\theta_{y,y(k)}\right)\left({}_0\underline{\theta}_{x,x(k)}-{}_0\underline{\theta}_{y,y(k)}\right) \\ +2\,{}_0^t\theta_{x,y(k)}\,{}_0\underline{\theta}_{y,x(k)}+2\,{}_0^t\theta_{y,x(k)}\,{}_0\underline{\theta}_{x,y(k)} \end{bmatrix} \end{aligned} \tag{F24a}$$

or

$$\begin{aligned} \bar{W}_{b(k)}^{NLPD} &= 2a_b\left({}_0^t\vartheta_{b(k)}\right)\left({}_0\underline{\vartheta}_{b(k)}\right) \\ &+b_b\frac{\pi h\delta^3}{6}\begin{bmatrix} 3\left({}_0^t\vartheta_{b(k)}\right)\left({}_0\underline{\vartheta}_{b(k)}\right) \\ +\left({}_0^t\theta_{x,x(k)}-{}_0^t\theta_{y,y(k)}\right)\left({}_0\underline{\theta}_{x,x(k)}-{}_0\underline{\theta}_{y,y(k)}\right) \\ +2\,{}_0^t\theta_{x,y(k)}\,{}_0\underline{\theta}_{y,x(k)}+2\,{}_0^t\theta_{y,x(k)}\,{}_0\underline{\theta}_{x,y(k)} \end{bmatrix} \end{aligned} \tag{F24b}$$

Therefore, by comparing Eq. (F24b) with Eq. (3.97b), the following relations between PD constants for bending deformations and material constants can be obtained as

$$b_b\frac{\pi h\delta^3}{6}=\frac{Eh^3}{24(1+\nu)} \tag{F25a}$$

$$2a_b+b_b\frac{\pi h\delta^3}{2}=\frac{Eh^3}{12(1-\nu^2)} \tag{F25a}$$

Therefore, the PD constants for bending deformations can be obtained as

$$a_b=\frac{Eh^3(3\nu-1)}{48(1-\nu^2)} \tag{F26a}$$

$$b_b=\frac{Eh^2}{4(1+\nu)\pi\delta^3} \tag{F26b}$$

Appendix G. Calibration for the parameter A_2 in the PD fatigue model and implicit solution for fatigue simulations

G1. Calibration for parameter A_2

In this section, details of the calibration for the parameter A_2 used in Section 7.5.1 are presented. The calibration for the parameter A_2 is conducted by the following steps;

Step 1: Assume a trial value for A_2 as: $A_{2(\text{trial})} = 1174$

Step 2: Conduct a PD fatigue simulation with the trial value $A_{2(\text{trial})} = 1174$ and calculate $\left(dq/dN\right)_{(\text{trial})}$ and $\Delta K_{(\text{trial})}$.

Step 2.1. Calculate $\left(dq/dN\right)_{(\text{trial})}$

First, by using the PD results for $A_{2(\text{trial})} = 1174$, the crack length, $q_{(\text{trial})}$ versus load cycle, $N_{(\text{trial})}$ is obtained as shown in red in Fig. G1. Later, a smoothed curve for the PD results is obtained as shown in blue in Fig. G1. Finally, $\left(dq/dN\right)_{(\text{trial})}$ is numerically obtained from the smoothed curve as

$$\left(dq/dN\right)_{(\text{trial})} = \frac{\Delta q_{(\text{trial})}}{\Delta N_{(\text{trial})}} \tag{G1}$$

Step 2.2. Calculate $\Delta K_{(\text{trial})}$

By using the data of the crack length, $q_{(\text{trial})}$ obtained from the trial PD fatigue simulation and by assuming that the material is linear-elastic, the stress intensity factor (SIF) range, $\Delta K_{(\text{trial})}$ can be calculated as [157]

$$\Delta K_{(\text{trial})} = \frac{\Delta P}{h\sqrt{W}} \frac{2+\bar{q}}{\left(1-\bar{q}\right)^{3/2}} \left(0.886 + 4.64\bar{q} - 13.32\bar{q}^2 + 14.72\bar{q}^3 - 5.6\bar{q}^4\right) \tag{G2a}$$

with

$$\bar{q} = \frac{q_{(\text{trial})}}{W} \tag{G2b}$$

$$\Delta P = P_{\max}(1-R) \tag{G2b}$$

Step 3: Plot the scatter data of $\left(dq/dN\right)_{(\text{trial})}$ versus $\Delta K_{(\text{trial})}$ in the logarithmic scale and find the best fit Paris law equation for the scatter data: $\left(dq/dN\right)_{(\text{trial})} = C_{(\text{trial})}\Delta K^M$

First, by using the $\left(dq/dN\right)_{(\text{trial})}$ and $\Delta K_{(\text{trial})}$ calculated in Eq. (G1) and Eq. (G2a), respectively; the scatter data $\left(dq/dN\right)_{(\text{trial})}$ versus $\left(\Delta K\right)_{(\text{trial})}$, shown in blue in Fig.

G2, is plotted in the logarithmic scale. From this scatter data, the best fit curve, shown in black in Fig. G2, is obtained as

$$\left(dq/dN\right)_{(\text{trial})} = 4.8295\times10^{-7}\,\Delta K^{2.6183} \tag{G3}$$

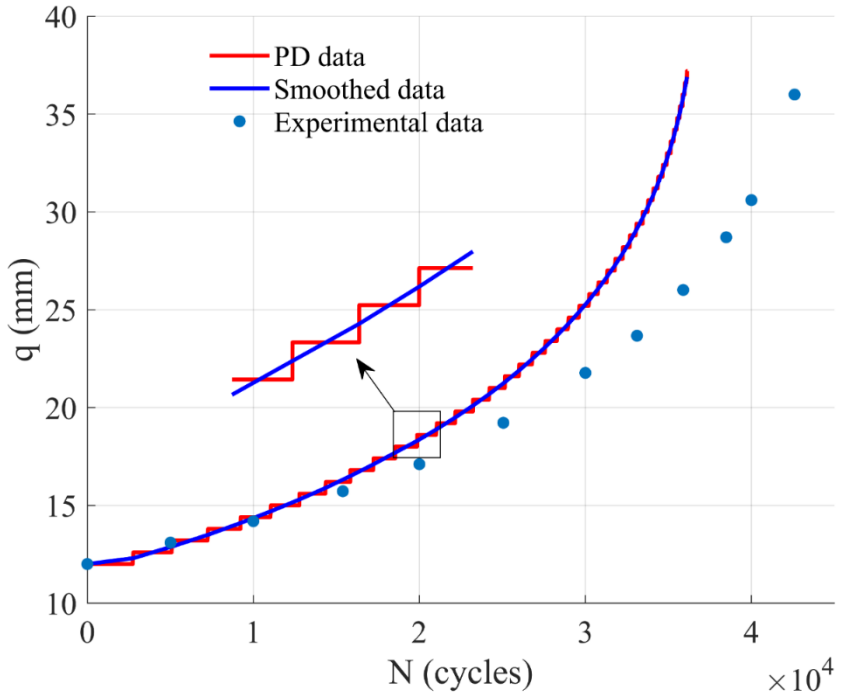

Fig. G1. Fatigue crack length, $q_{(\text{trial})}$ versus load cycle, $N_{(\text{trial})}$ (the experimental data is obtained from [136])

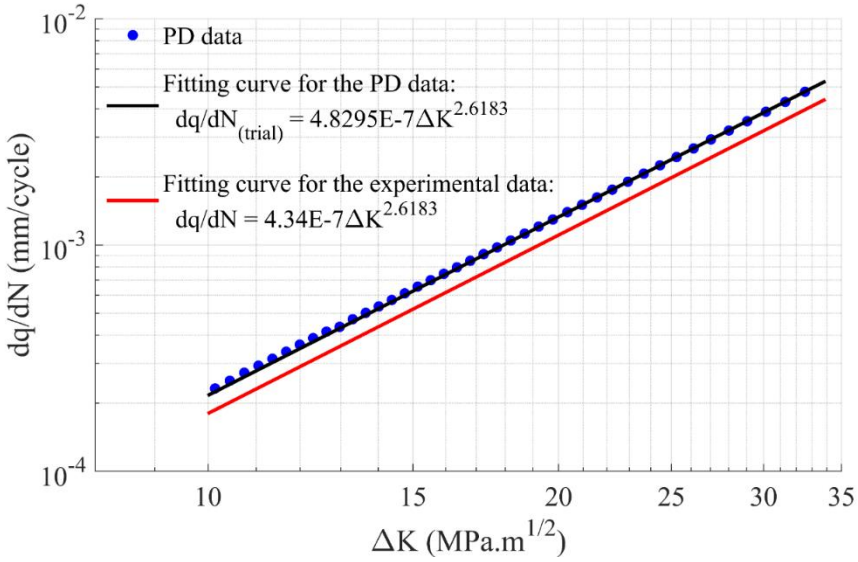

Fig. G2. Fatigue crack growth curve for $\left(dq/dN\right)_{(\text{trial})}$ versus $\left(\Delta K\right)_{(\text{trial})}$ with $A_{2(\text{trial})} = 1174$ (the experimental data is obtained from [136])

Step 4: Calibrate the value for A_2

As can be found in [136], the best fit Paris law equation for the experimental results is written as

$$\left(dq/dN\right)_{\text{(experiment)}} = 4.34\times10^{-7}\,\Delta K^{2.6183} \tag{G4}$$

Therefore, the value of the parameter A_2 can be estimated as

$$A_2 = A_{2\text{(trial)}}\frac{4.34\times10^{-7}\,\Delta K^{2.6183}}{4.8295\times10^{-7}\,\Delta K^{2.6183}} = 1174\frac{4.34\times10^{-7}}{4.8295\times10^{-7}} = 1055 \tag{G5}$$

G2. Implicit solver for static conditions in ordinary state-based peridynamics

In this section, the implicit solver for ordinary state-based peridynamics for static conditions is presented. First, the PD equations of motion for static conditions given in Eq. (4.17) can be rewritten as

$$-\sum_{j=1}^{N}\psi_{(k)(j)}\left[2ad\frac{1}{\xi}\left(\vartheta_{(k)}+\vartheta_{(j)}\right)+4bs_{(k)(j)}\right]\cos\varphi V_{(j)} = \bar{b}_{x(k)} \tag{G6a}$$

$$-\sum_{j=1}^{N}\psi_{(k)(j)}\left[2ad\frac{1}{\xi}\left(\vartheta_{(k)}+\vartheta_{(j)}\right)+4bs_{(k)(j)}\right]\sin\varphi V_{(j)} = \bar{b}_{y(k)} \tag{G6b}$$

By using the dilatation given in Eq. (2.63) without consideration of temperature effects and the bond stretch given in Eq. (2.65), the equations of motion given in Eq. (G6) can be rewritten in a matrix form as

$$\sum_{j=1}^{N}\mathbf{k}^{dila}_{(k)(j)}\begin{bmatrix}\vartheta_{(k)}\\ \vartheta_{(j)}\end{bmatrix}+\sum_{j=1}^{N}\mathbf{k}^{BB}_{(k)(j)}\begin{bmatrix}u_{(k)}\\ u_{(j)}\\ v_{(k)}\\ v_{(j)}\end{bmatrix}=\begin{bmatrix}\bar{b}_{x(k)}\\ \bar{b}_{y(k)}\end{bmatrix} \tag{G7a}$$

with

$$\mathbf{k}^{BB}_{(k)(j)} = \psi_{(k)(j)}\frac{4bV_{(j)}}{\xi}\begin{bmatrix}\cos^2\varphi & -\cos^2\varphi & \sin\varphi\cos\varphi & -\sin\varphi\cos\varphi\\ \sin\varphi\cos\varphi & -\sin\varphi\cos\varphi & \sin^2\varphi & -\sin^2\varphi\end{bmatrix} \tag{G7b}$$

and

$$\mathbf{k}^{dila}_{(k)(j)} = \psi_{(k)(j)}\frac{2ad}{\xi}V_{(j)}\begin{bmatrix}-\cos\varphi & -\cos\varphi\\ -\sin\varphi & -\sin\varphi\end{bmatrix} \tag{G7c}$$

Note that, Eq. (G7) is the equation of motion for material point k. Assuming that the PD discretized model has m material points. Therefore, the equation of motion for all material points in the PD model can be written as

$$\left(\mathbf{K}^{dila}\right)\boldsymbol{\theta}+\left(\mathbf{K}^{BB}\right)\mathbf{U}=\bar{\mathbf{B}} \tag{G8a}$$

with

$$\mathbf{U}=\begin{bmatrix}u_{(1)} & u_{(2)} & \dots & u_{(m)} & v_{(1)} & v_{(2)} & \dots & v_{(m)}\end{bmatrix}^T \tag{G8b}$$

$$\boldsymbol{\theta}=\begin{bmatrix}\vartheta_{(1)} & \vartheta_{(2)} & \dots & \vartheta_{(m-1)} & \vartheta_{(m)}\end{bmatrix}^T \tag{G8c}$$

$$\bar{\mathbf{B}}=\begin{bmatrix}\bar{b}_{x(1)} & \bar{b}_{x(2)} & \dots & \bar{b}_{x(m)} & \bar{b}_{y(1)} & \bar{b}_{y(2)} & \dots & \bar{b}_{y(m)}\end{bmatrix}^T \tag{G8d}$$

$$\mathbf{K}^{BB}=\begin{bmatrix} k_{1,1}^{BB} & k_{1,2}^{BB} & \dots & k_{1,2m}^{BB} \\ k_{2,1}^{BB} & k_{2,2}^{BB} & \dots & k_{2,2m}^{BB} \\ \dots & \dots & \dots & \dots \\ k_{2m,1}^{BB} & k_{2m,2}^{BB} & \dots & k_{2m,2m}^{BB} \end{bmatrix} \tag{G8e}$$

$$\mathbf{K}^{dila}=\begin{bmatrix} k_{1,1}^{dila} & k_{1,2}^{dila} & \dots & k_{1,m}^{dila} \\ k_{2,1}^{dila} & k_{2,2}^{dila} & \dots & k_{2,m}^{dila} \\ \dots & \dots & \dots & \dots \\ k_{2m,1}^{dila} & k_{2m,2}^{dila} & \dots & k_{2m,m}^{dila} \end{bmatrix} \tag{G8f}$$

where $\bar{\mathbf{B}}$ and $\mathbf{U}$ represent the vector of applied forces per unit area and the vector of displacements of the PD discretized model. The term $\mathbf{K}^{BB}$ represents the global stiffness matrix corresponding to the local stiffness $\mathbf{k}_{(k)(j)}^{BB}$, $\mathbf{K}^{dila}$ represents the global stiffness matrix corresponding to the local stiffness $\mathbf{k}_{(k)(j)}^{dila}$. Note that, the matrix $\mathbf{K}^{BB}$ in Eq. (G8e) has a size of $\left(2m\times 2m\right)$. Meanwhile, $\mathbf{K}^{dila}$ given in Eq. (G8f) has a size of $\left(2m\times m\right)$.

On the other hand, by excluding the effect of temperature, the dilatation given in Eq. (2.63) can be rewritten as

$$\vartheta_{(k)}=d\sum_{j=1}^{N}\psi_{(k)(j)}\frac{\left(u_{(j)}-u_{(k)}\right)\cos\varphi+\left(v_{(j)}-v_{(k)}\right)\sin\varphi}{\xi}V_{(j)} \tag{G9a}$$

or

$$\vartheta_{(k)}=\sum_{j=1}^{N}\psi_{(k)(j)}\frac{d}{\xi}\begin{bmatrix}-\cos\varphi & \cos\varphi & -\sin\varphi & \sin\varphi\end{bmatrix}\begin{bmatrix}u_{(k)}\\ u_{(j)}\\ v_{(k)}\\ v_{(j)}\end{bmatrix}V_{(j)} \tag{G9b}$$

or

$$\vartheta_{(k)}=\sum_{j=1}^{N}\mathbf{k}_{(k)(j)}^{\vartheta}\begin{bmatrix}u_{(k)}\\ u_{(j)}\\ v_{(k)}\\ v_{(j)}\end{bmatrix} \tag{G9c}$$

with

$$\mathbf{k}_{(k)(j)}^{\vartheta}=\psi_{(k)(j)}\frac{d}{\xi}V_{(j)}\begin{bmatrix}-\cos\varphi & \cos\varphi & -\sin\varphi & \sin\varphi\end{bmatrix} \tag{G9d}$$

Note that Eq. (G9c) is the dilatation for material point k. By assuming the PD discretized model has m material points, the global dilatation vector of all material points in the PD model can be calculated as

$$\boldsymbol{\theta}=\left(\mathbf{K}^{\vartheta}\right)\mathbf{U} \tag{G10a}$$

with

$$\mathbf{K}^{\vartheta}=\begin{bmatrix} k_{1,1}^{\vartheta} & k_{1,2}^{\vartheta} & \dots & k_{1,2m}^{\vartheta} \\ k_{2,1}^{\vartheta} & k_{2,2}^{\vartheta} & \dots & k_{2,2m}^{\vartheta} \\ \dots & \dots & \dots & \dots \\ k_{m,1}^{\vartheta} & k_{m,2}^{\vartheta} & \dots & k_{m,2m}^{\vartheta} \end{bmatrix} \tag{G10b}$$

Note that, the matrix $\mathbf{K}^{\vartheta}$ in Eq. (G10b) has a size of $(m\times 2m)$.

Therefore, by substituting Eq. (G10a) into Eq. (G8a), the PD equation of motion for static loading conditions can be written as

$$\left(\left(\mathbf{K}^{dila}\right)\left(\mathbf{K}^{\vartheta}\right)+\left(\mathbf{K}^{BB}\right)\right)\mathbf{U}=\bar{\mathbf{B}} \tag{G11a}$$

or

$$\mathbf{K}\mathbf{U}=\bar{\mathbf{B}} \tag{G11b}$$

with

$$\mathbf{K}=\left(\mathbf{K}^{dila}\right)\left(\mathbf{K}^{\vartheta}\right)+\left(\mathbf{K}^{BB}\right) \tag{G11c}$$

where $\mathbf{K}$ represent the total stiffness matrix of the PD model.
By solving Eq. (G11b), the displacement field of the PD model is obtained. In this chapter, the PD simulation is implemented in MATLAB and the displacement field is obtained by using the backslash (\) operator.

PUBLICATIONS

The following papers have been either published or submitted for consideration for publication, in scientific journals and conferences. All of the papers listed below have been drawn from this thesis.

Journal papers:

- **Refereed journal articles**

(1) **Nguyen, C.T**., Oterkus, S. and Oterkus, E., 2020. A physics-guided machine learning model for two-dimensional structures based on ordinary state-based peridynamics. Theoretical and Applied Fracture Mechanics, p.102872.

(2) **Tien Nguyen, C**. and Oterkus, S., 2020. Ordinary state-based peridynamics for geometrically nonlinear analysis of plates. Theoretical and Applied Fracture Mechanics.

(3) **Nguyen, C.T.**, Oterkus, S. and Oterkus, E., 2020. An energy-based peridynamic model for fatigue cracking. Engineering Fracture Mechanics, 241, p.107373.

(4) **Nguyen, C.T**. and Oterkus, S., 2020. Ordinary state-based peridynamic model for geometrically nonlinear analysis. Engineering Fracture Mechanics, 224, p.106750.

(5) **Nguyen, C.T**. and Oterkus, S., 2020. Investigating the effect of brittle crack propagation on the strength of ship structures by using peridynamics. Ocean Engineering, 209, p.107472.

(6) **Nguyen, C.T**., Oterkus, S. and Oterkus, E., 2020. A peridynamic-based machine learning model for one-dimensional and two-dimensional structures. Continuum Mechanics and Thermodynamics, pp.1-33.

(7) **Nguyen, C.T**. and Oterkus, S., 2020. Brittle damage prediction for corroded stiffened structures by using peridynamics, (Accepted/In press) In : Ships and Offshore Structures.

(8) **Nguyen, C.T**. and Oterkus, S., 2019. Peridynamics formulation for beam structures to predict damage in offshore structures. Ocean Engineering, 173, pp.244-267.

(9) **Nguyen, C.T**. and Oterkus, S., 2019. Peridynamics for the thermomechanical behavior of shell structures. Engineering Fracture Mechanics, 219, p.106623.

(10) Yang, Z., Oterkus, E., **Nguyen, C.T**. and Oterkus, S., 2019. Implementation of peridynamic beam and plate formulations in finite element framework. Continuum Mechanics and Thermodynamics, 31(1), pp.301-315.

- **Journal articles under review**

(11) **Nguyen, C. T**., Oterkus, S., Peridynamics for geometrically nonlinear analysis of three-dimensional beam structures, under review

Book chapter:

(1) **C.T. Nguyen**, S. Oterkus, E. Oterkus, Application of Artificial Intelligence & Machine Learning in Peridynamics, in: Peridynamic Modeling, Numerical Techniques, and Applications, Elsevier.

Conference papers:

(1) **Nguyen, C.T**. and Oterkus, S., 2020. Damage prediction on stiffened structures by using peridynamics, Damaged Ship V, The Royal Institution of Naval Architects, March 11, London, UK.

(2) **Nguyen, C.T**. and Oterkus, S., 2020. Brittle damage prediction for corroded stiffened structures by using peridynamics, Manuscript accepted for publication.

Abstracts and Conference presentations:

(1) Nguyen, C.T. and Oterkus, S., 2020. Brittle damage prediction for corroded stiffened structures by using peridynamics, International Conference on Ships and Offshore Structures, 1– 4 Sep 2020, Glasgow, UK

(2) Nguyen, C.T. and Oterkus, S., 2020. Damage prediction on stiffened structures by using peridynamics, Damaged Ship V, The Royal Institution of Naval Architects, March 11, London, UK

(3) Nguyen, C.T. and Oterkus, S., 2020. Progressive damage prediction in offshore structures by using peridynamics, Workshop on Ships and Offshore Structures 2020, February 5-8, Glasgow, UK

(4) Nguyen, C.T. and Oterkus, S., 2019, Peridynamic Formulation for Beam Structures with an Application to Predict Damages in Offshore Structures, 15th US National Congress on Computational Mechanics, July 28-August 1, Texas, USA

(5) Nguyen, C.T. and Oterkus, S., 2019, Peridynamic formulation for predicting damages in jacket platform, International Conference on Nonlinear Solid Mechanics, June 16-19, ROMA, Italy

(6) Nguyen, C.T. and Oterkus, S., 2019, Damage prediction for ship and offshore structures, NAOME Postgraduate Conference, June 18, Glasgow, UK

(7) Nguyen, C.T. and Oterkus, S., 2018, Damage prediction in lattice structures by using peridynamics, 28th International Workshop on Computational Mechanics of Materials, September 10-12, Glasgow, UK.

(8) Nguyen, C.T. and Oterkus, S., 2018, Damage prediction for ship and offshore structures, NAOME Postgraduate Conference, June 18, Glasgow, UK

REFERENCES

1. SE, A.G.C.a.S., *Safety and Shipping Review 2019*, in *An annual review of trends and developments in shipping losses and safety*. 2019, Allianz Global Corporate & Specialty SE: Munich, Germany. p. 52.
2. Sutar, S.S., G.S. Kale, and S.H. Merad, *Analysis of ductile-to-brittle transition temperature of mild steel.* Int. J. Innov. Eng. Res. Technol., 2014. **1**: p. 1-10.
3. Benac, D.J., N. Cherolis, and D. Wood, *Managing cold temperature and brittle fracture hazards in pressure vessels.* Journal of Failure Analysis and Prevention, 2016. **16**(1): p. 55-66.
4. Kobayashi, H. and H. Onoue, *Brittle fracture of liberty ships.* Failure Knowledge Database, 1943. **100**: p. 67.
5. Kim, K.J., J.H. Lee, D.K. Park, B.G. Jung, X. Han, and J.K. Paik, *An experimental and numerical study on nonlinear impact responses of steel-plated structures in an Arctic environment.* International Journal of Impact Engineering, 2016. **93**: p. 99-115.
6. Drouin, P., *Brittle fracture in ships–a lingering problem.* Ships and Offshore Structures, 2006. **1**(3): p. 229-233.
7. Moës, N., J. Dolbow, and T. Belytschko, *A finite element method for crack growth without remeshing.* International journal for numerical methods in engineering, 1999. **46**(1): p. 131-150.
8. Moës, N. and T. Belytschko, *Extended finite element method for cohesive crack growth.* Engineering fracture mechanics, 2002. **69**(7): p. 813-833.
9. Sukumar, N., N. Moës, B. Moran, and T. Belytschko, *Extended finite element method for three-dimensional crack modelling.* International journal for numerical methods in engineering, 2000. **48**(11): p. 1549-1570.
10. Laborde, P., J. Pommier, Y. Renard, and M. Salaün, *High-order extended finite element method for cracked domains.* International Journal for Numerical Methods in Engineering, 2005. **64**(3): p. 354-381.
11. Pook, L.P., *Linear elastic fracture mechanics for engineers: theory and applications*. 2000: WIT press.
12. Banks-Sills, L., *Application of the finite element method to linear elastic fracture mechanics.* 1991.
13. Elices, M., G. Guinea, J. Gomez, and J. Planas, *The cohesive zone model: advantages, limitations and challenges.* Engineering fracture mechanics, 2002. **69**(2): p. 137-163.
14. Barenblatt, G.I., *The mathematical theory of equilibrium cracks in brittle fracture.* Advances in applied mechanics, 1962. **7**(1): p. 55-129.
15. Falk, M.L., A. Needleman, and J.R. Rice, *A critical evaluation of cohesive zone models of dynamic fracture.* Le Journal de Physique IV, 2001. **11**(PR5): p. Pr5-43-Pr5-50.
16. Chandra, N., H. Li, C. Shet, and H. Ghonem, *Some issues in the application of cohesive zone models for metal–ceramic interfaces.* International Journal of Solids and Structures, 2002. **39**(10): p. 2827-2855.
17. Park, K., G.H. Paulino, and J.R. Roesler, *A unified potential-based cohesive model of mixed-mode fracture.* Journal of the Mechanics and Physics of Solids, 2009. **57**(6): p. 891-908.
18. Park, K. and G.H. Paulino, *Cohesive zone models: a critical review of traction-separation relationships across fracture surfaces.* Applied Mechanics Reviews, 2011. **64**(6).

19. Needleman, A., *Some issues in cohesive surface modeling.* Procedia IUTAM, 2014. **10**: p. 221-246.
20. Silling, S.A., *Reformulation of elasticity theory for discontinuities and long-range forces.* Journal of the Mechanics and Physics of Solids, 2000. **48**(1): p. 175-209.
21. Silling, S.A. and E. Askari, *A meshfree method based on the peridynamic model of solid mechanics.* Computers & structures, 2005. **83**(17-18): p. 1526-1535.
22. Foster, J.T., S.A. Silling, and W.W. Chen, *Viscoplasticity using peridynamics.* International journal for numerical methods in engineering, 2010. **81**(10): p. 1242-1258.
23. Mitchell, J.A., *A non-local, ordinary-state-based viscoelasticity model for peridynamics.* Sandia National Lab Report, 2011. **8064**: p. 1-28.
24. Mitchell, J.A., *A Nonlocal Ordinary State-Based Plasticity Model for Peridynamics*. 2011, Sandia National Lab.(SNL-NM), Albuquerque, NM (United States).
25. Madenci, E. and S. Oterkus, *Ordinary state-based peridynamics for plastic deformation according to von Mises yield criteria with isotropic hardening.* Journal of the Mechanics Physics of Solids, 2016. **86**: p. 192-219.
26. Madenci, E. and S. Oterkus, *Ordinary state-based peridynamics for thermoviscoelastic deformation.* Engineering Fracture Mechanics, 2017. **175**: p. 31-45.
27. Oterkus, E., *Peridynamic theory for modeling three-dimensional damage growth in metallic and composite structures*. 2010, The University of Arizona: The University of Arizona.
28. Oterkus, E. and E. Madenci. *Peridynamic theory for damage initiation and growth in composite laminate*. in *Key Engineering Materials*. 2012. Trans Tech Publ.
29. Oterkus, E., E. Madenci, O. Weckner, S. Silling, P. Bogert, and A. Tessler, *Combined finite element and peridynamic analyses for predicting failure in a stiffened composite curved panel with a central slot.* Composite Structures, 2012. **94**(3): p. 839-850.
30. De Meo, D., N. Zhu, and E. Oterkus, *Peridynamic modeling of granular fracture in polycrystalline materials.* Journal of Engineering Materials Technology, 2016. **138**(4): p. 041008.
31. Hu, W., Y.D. Ha, and F. Bobaru, *Peridynamic model for dynamic fracture in unidirectional fiber-reinforced composites.* Computer Methods in Applied Mechanics Engineering, 2012. **217**: p. 247-261.
32. Alpay, S. and E. Madenci. *Crack growth prediction in fully-coupled thermal and deformation fields using peridynamic theory*. in *54th AIAA/ASME/ASCE/AHS/ASC structures, structural dynamics, and materials conference*. 2013.
33. Oterkus, S., *Peridynamics for the solution of multiphysics problems*, in *Aerospace and Mechanical Engineering Faculty*. 2015, The University of Arizona.
34. Madenci, E. and S. Oterkus, *Peridynamics for coupled field equations.* Handbook of Peridynamic Modeling, 2016: p. 489-531.
35. Askari, E., F. Bobaru, R. Lehoucq, M. Parks, S. Silling, and O. Weckner. *Peridynamics for multiscale materials modeling*. in *Journal of Physics: Conference Series*. 2008. IOP Publishing.

36. Bobaru, F. and Y.D. Ha, *Adaptive refinement and multiscale modeling in 2D peridynamics.* Journal for Multiscale Computational Engineering, 2011: p. 635–659.
37. Kilic, B. and E. Madenci, *Coupling of peridynamic theory and the finite element method.* Journal of mechanics of materials structures, 2010. **5**(5): p. 707-733.
38. Liu, W. and J.-W. Hong, *A coupling approach of discretized peridynamics with finite element method.* Computer methods in applied mechanics engineering, 2012. **245**: p. 163-175.
39. Bie, Y., X. Cui, and Z. Li, *A coupling approach of state-based peridynamics with node-based smoothed finite element method.* Computer Methods in Applied Mechanics Engineering, 2018. **331**: p. 675-700.
40. Macek, R.W. and S.A. Silling, *Peridynamics via finite element analysis.* Finite Elements in Analysis Design, 2007. **43**(15): p. 1169-1178.
41. Han, S., C. Diyaroglu, S. Oterkus, E. Madenci, E. Oterkus, Y. Hwang, and H. Seol. *Peridynamic direct concentration approach by using ANSYS*. in *2016 IEEE 66th Electronic Components and Technology Conference (ECTC)*. 2016. IEEE.
42. Diyaroglu, C., S. Oterkus, E. Oterkus, and E. Madenci, *Peridynamic modeling of diffusion by using finite-element analysis.* IEEE Transactions on Components, Packaging Manufacturing Technology, 2017. **7**(11): p. 1823-1831.
43. Silling, S.A. and R. Lehoucq, *Peridynamic theory of solid mechanics*, in *Advances in applied mechanics*. 2010, Elsevier. p. 73-168.
44. Madenci, E. and E. Oterkus, *Peridynamic Theory and Its Applications*. Peridynamic Theory and Its Applications. 2014: Springer.
45. Javili, A., R. Morasata, E. Oterkus, and S. Oterkus, *Peridynamics review.* Mathematics Mechanics of Solids, 2018: p. 1081286518803411.
46. Silling, S.A., M. Epton, O. Weckner, J. Xu, and E. Askari, *Peridynamic states and constitutive modeling.* Journal of Elasticity, 2007. **88**(2): p. 151-184.
47. Foster, J.T., S.A. Silling, and W. Chen, *An energy based failure criterion for use with peridynamic states.* International Journal for Multiscale Computational Engineering, 2011. **9**(6).
48. Silling, S.A., M. Zimmermann, and R. Abeyaratne, *Deformation of a peridynamic bar*. Journal of Elasticity, 2003. **73**(1-3): p. 173-190.
49. O'Grady, J. and J. Foster, *Peridynamic beams: a non-ordinary, state-based model.* International Journal of Solids Structures, 2014. **51**(18): p. 3177-3183.
50. Diyaroglu, C., E. Oterkus, S. Oterkus, and E. Madenci, *Peridynamics for bending of beams and plates with transverse shear deformation.* International Journal of Solids Structures, 2015. **69**: p. 152-168.
51. Silling, S.A. and F. Bobaru, *Peridynamic modeling of membranes and fibers.* International Journal of Non-Linear Mechanics, 2005. **40**(2-3): p. 395-409.
52. O'Grady, J. and J. Foster, *Peridynamic plates and flat shells: A non-ordinary, state-based model.* International Journal of Solids Structures, 2014. **51**(25-26): p. 4572-4579.
53. Rahaman, M.M., P. Roy, D. Roy, and J. Reddy, *A peridynamic model for plasticity: Micro-inertia based flow rule, entropy equivalence and*

localization residuals. Computer Methods in Applied Mechanics and Engineering, 2017. **327**: p. 369-391.
54. Amani, J., E. Oterkus, P. Areias, G. Zi, T. Nguyen-Thoi, and T. Rabczuk, *A non-ordinary state-based peridynamics formulation for thermoplastic fracture.* International Journal of Impact Engineering, 2016. **87**: p. 83-94.
55. Sun, S. and V. Sundararaghavan, *A peridynamic implementation of crystal plasticity.* International Journal of Solids and Structures, 2014. **51**(19-20): p. 3350-3360.
56. LADANYI, G. and I. JENEI. *Investigation of peridynamic plastic material model*. in *Proceedings of the 4th IASME/WSEAS International Conference on Continuum Mechanics (CM'09)*. 2009.
57. Sarego, G., Q.V. Le, F. Bobaru, M. Zaccariotto, and U. Galvanetto, *Linearized state-based peridynamics for 2-D problems.* International Journal for Numerical Methods in Engineering, 2016. **108**(10): p. 1174-1197.
58. Diyaroglu, C., E. Oterkus, and S. Oterkus, *An Euler–Bernoulli beam formulation in an ordinary state-based peridynamic framework.* Mathematics Mechanics of Solids, 2019. **24**(2): p. 361-376.
59. Chowdhury, S.R., P. Roy, D. Roy, and J. Reddy, *A peridynamic theory for linear elastic shells.* International Journal of Solids and Structures, 2016. **84**: p. 110-132.
60. Silling, S.A. and A. Askari, *Peridynamic model for fatigue cracking.* SAND-18590. Albuquerque: Sandia National Laboratories, 2014.
61. Nguyen, C.T. and S. Oterkus, *Peridynamics for the thermomechanical behavior of shell structures.* Engineering Fracture Mechanics, 2019: p. 106623.
62. Nguyen, C.T. and S. Oterkus, *Peridynamics formulation for beam structures to predict damage in offshore structures.* Ocean Engineering, 2019. **173**: p. 244-267.
63. Nguyen, C.T. and S. Oterkus, *Brittle damage prediction for corroded stiffened structures by using peridynamics.* Manuscript submitted for publication.
64. Nguyen, C.T. and S. Oterkus, *Investigating the effect of brittle crack propagation on the strength of ship structures by using peridynamics.* Ocean Engineering, 2020. **209**: p. 107472.
65. Nguyen, C.T. and S. Oterkus, *Ordinary state-based peridynamic model for geometrically nonlinear analysis.* Engineering Fracture Mechanics, 2020. **224**: p. 106750.
66. Tien Nguyen, C. and S. Oterkus, *Ordinary state-based peridynamics for geometrically nonlinear analysis of plates.* Theoretical and Applied Fracture Mechanics, 2020.
67. Nguyen, C.T. and S. Oterkus, *Peridynamics for geometrically nonlinear analysis of three-dimensional beam structures.* Manuscript submitted for publication.
68. Nguyen, C.T. and S. Oterkus, *An energy-based peridynamic model for fatigue cracking.* Manuscript submitted for publication.
69. Nguyen, C.T., S. Oterkus, and E. Oterkus, *A peridynamic-based machine learning model for one-dimensional and two-dimensional structures.* Continuum Mechanics and Thermodynamics, 2020: p. 1-33.
70. Bathe, K.-J., *Finite element procedures*. 2006: Klaus-Jurgen Bathe.

71. Kanok-nukulchai, W., *A simple and efficient finite element for general shell analysis.* International Journal for Numerical Methods in Engineering, 1979. **14**(2): p. 179-200.
72. Timoshenko, S.P. and J.N. Goodier, *Theory of Elasticity*. 1970, McGraw Hill: London: McGraw-Hill, New York. p. 403-408.
73. Stephen, N., *Considerations on second order beam theories.* International Journal of Solids and Structures, 1981. **17**(3): p. 325-333.
74. Boresi, A.P., R.J. Schmidt, and O.M. Sidebottom, *Advanced mechanics of materials*. Vol. 6. 1985: Wiley New York et al.
75. Diyaroglu, C., *Peridynamics and its applications in marine structures*. 2016, University of Strathclyde.
76. Kilic, B. and E. Madenci, *An adaptive dynamic relaxation method for quasi-static simulations using the peridynamic theory*. Theoretical Applied Fracture Mechanics, 2010. **53**(3): p. 194-204.
77. Underwood, P., *Dynamic relaxation.* Computational method for transient analysis, 1986. **1**: p. 245-263.
78. Mindlin, R.D., *Influence of rotatory inertia and shear on flexural motions of isotropic, elastic plates.* J. appl. Mech., 1951. **18**: p. 31-38.
79. Reissner, E., *The effect of transverse shear deformation on the bending of elastic plates.* J. appl. Mech., 1945: p. A69-A77.
80. Reissner, E., *On the theory of transverse bending of elastic plates.* International Journal of Solids and Structures, 1976. **12**(8): p. 545-554.
81. Wisniewski, K., *"Finite rotation shells", Basic equations finite elements for Reissner kinematics*. 2010: CIMNE-Springer.
82. Hetnarski, R.B., M.R. Eslami, and G. Gladwell, *Thermal stresses: advanced theory and applications*. Vol. 158. 2009: Springer.
83. Ugural, A.C. and S.K. Fenster, *Advanced strength and applied elasticity*. 2003: Pearson education.
84. Bhatti, M.A., *Advanced topics in finite element analysis of structures: with Mathematica and MATLAB computations*. 2006: John Wiley & Sons, Inc.
85. Yuan, H., F. Wang, Y. Liu, H. Bian, W. Chen, and Y. Wang, *Time-dependent behavior of subcritical crack growth for rock plate: Experimental and numerical study.* International Journal of Distributed Sensor Networks, 2018. **14**(11): p. 1550147718812019.
86. Atkinson, B. *Fracture toughness of Tennessee sandstone and Carrara marble using the double torsion testing method*. in *International journal of rock mechanics and mining sciences & geomechanics abstracts*. 1979. Elsevier.
87. Kalthoff, J.F., *Shadow optical analysis of dynamic shear fracture.* Optical Engineering, 1988. **27**(10): p. 271035.
88. Nishihara, S., *Ultimate longitudinal strength of midship cross-section.* Naval architecture and ocean engineering, 1984. **22**: p. 200-214.
89. Matthews, W.T., *Plane strain fracture toughness (KIC) data handbook for metals*. 1973, ARMY MATERIALS AND MECHANICS RESEARCH CENTER WATERTOWN MA.
90. Ambati, M. and L. De Lorenzis, *Phase-field modeling of brittle and ductile fracture in shells with isogeometric NURBS-based solid-shell elements.* Computer Methods in Applied Mechanics and Engineering, 2016. **312**: p. 351-373.
91. Kalthoff, J.F., *Modes of dynamic shear failure in solids.* International Journal of Fracture, 2000. **101**(1-2): p. 1-31.

92. Kalthoff, J. and S. Winkler, *Failure mode transition at high rates of shear loading.* DGM Informationsgesellschaft mbH, Impact Loading Dynamic Behavior of Materials, 1988. **1**: p. 185-195.
93. Jenq, Y. and S.P. Shah, *Mixed-mode fracture of concrete.* International Journal of Fracture, 1988. **38**(2): p. 123-142.
94. Anand, L., *On H. Hencky's approximate strain-energy function for moderate deformations.* Journal of Applied Mechanics, 1979. **46**(1): p. 78-82.
95. Oterkus, S. and E. Madenci, *Peridynamics for antiplane shear and torsional deformations.* Journal of Mechanics of Materials Structures, 2015. **10**(2): p. 167-193.
96. Borden, M.J., C.V. Verhoosel, M.A. Scott, T.J. Hughes, and C.M. Landis, *A phase-field description of dynamic brittle fracture.* Computer Methods in Applied Mechanics Engineering, 2012. **217**: p. 77-95.
97. Gao, Y. and S. Oterkus, *Peridynamic analysis of marine composites under shock loads by considering thermomechanical coupling effects.* Journal of Marine Science Engineering, 2018. **6**(2): p. 38.
98. Le, Q. and F. Bobaru, *Surface corrections for peridynamic models in elasticity and fracture.* Computational Mechanics, 2018. **61**(4): p. 499-518.
99. Butt, S.N., J.J. Timothy, and G. Meschke, *Wave dispersion and propagation in state-based peridynamics.* Computational Mechanics, 2017. **60**(5): p. 725-738.
100. Dipasquale, D., M. Zaccariotto, and U. Galvanetto, *Crack propagation with adaptive grid refinement in 2D peridynamics.* International Journal for Numerical Methods in Engineering, 2014. **190**(1-2): p. 1-22.
101. Hesch, C., A. Gil, R. Ortigosa, M. Dittmann, C. Bilgen, P. Betsch, M. Franke, A. Janz, and K. Weinberg, *A framework for polyconvex large strain phase-field methods to fracture.* Computer Methods in Applied Mechanics Engineering, 2017. **317**: p. 649-683.
102. Nguyen, C.T. and S. Oterkus, *Ordinary state-based peridynamic model for geometrically nonlinear analysis.* Engineering Fracture Mechanics, 2019.
103. Pai, P. and A. Palazotto, *Large-deformation analysis of flexible beams.* International Journal of Solids and Structures, 1996. **33**(9): p. 1335-1353.
104. Bathe, K.J. and S. Bolourchi, *Large displacement analysis of three-dimensional beam structures.* International journal for numerical methods in engineering, 1979. **14**(7): p. 961-986.
105. Heisser, R.H., V.P. Patil, N. Stoop, E. Villermaux, and J. Dunkel, *Controlling fracture cascades through twisting and quenching.* Proceedings of the National Academy of Sciences, 2018. **115**(35): p. 8665-8670.
106. Guinea, G., F. Rojo, and M. Elices, *Brittle failure of dry spaghetti.* Engineering Failure Analysis, 2004. **11**(5): p. 705-714.
107. Barut, A., *Nonlinear thermo-mechanical analysis of stiffened composite laminates by a new finite element*, in *Aerospace and Mechanical Engineering Faculty*. 1998, The University of Arizona.
108. Bathe, K.-j. and S. Bolourchi, *A geometric and material nonlinear plate and shell element.* Computers & Structures, 1980. **11**(1-2): p. 23-48.
109. Muscat-Fenech, C. and A. Atkins, *Out-of-plane stretching and tearing fracture in ductile sheet materials.* International Journal of Fracture, 1997. **84**(4): p. 297-306.

110. Areias, P., T. Rabczuk, and M. Msekh, *Phase-field analysis of finite-strain plates and shells including element subdivision.* Computer Methods in Applied Mechanics and Engineering, 2016. **312**: p. 322-350.
111. Areias, P. and T. Rabczuk, *Finite strain fracture of plates and shells with configurational forces and edge rotations.* International Journal for Numerical Methods in Engineering, 2013. **94**(12): p. 1099-1122.
112. Mai, Y.-W., H. He, R. Leung, and R.S. Seth, *In-plane fracture toughness measurement of paper*, in *Fracture Mechanics: 26th Volume*. 1995, ASTM International.
113. Zavattieri, P.D., *Modeling of crack propagation in thin-walled structures using a cohesive model for shell elements.* Journal of Applied Mechanics, 2006.
114. LR, *ShipRight Design and Construction: Fatigue Design Assessment – Application and Notations (Notice 1 and Notice 2)*. 2016, Lloyd's Register Group Limited: London, UK.
115. LR, *ShipRight Design and Construction: Fatigue Design Assessment – Level 3 Procedure Guidance on Direct Calculations (Notice 1)*. 2016, Lloyd's Register Group Limited: London, UK.
116. Glenn, I., R. Paterson, L. Luznik, A. Dinovitzer, and C. Bayley, *Fatigue resistant detail design guide for ship structures*. 1999, Ship Structure Committee.
117. DNV.GL, *Fatigue assessment of ship structures*, in *DNVGL-CG-0129*. 2015, DNV GL.
118. ClassNK, *Guidelines for Direct Load Analysis and Strength Assessment*. 2018, Development Operations Headquarters, Hull Rules Development Department, ClassNK: Tokyo, Japan.
119. Veritas, B., *Guidelines for Fatigue Assessment of Steel Ships and Offshore Units: Guidance Note NI 6114 DT R00 E*. 2016, Neuilly sur Seine Cedex, France: Bureau Veritas, Marine & Offshore Division.
120. ABS, *Guide for Fatigue Assessment of Offshore Structures*. 2003, American Bureau of Shipping: Houston, TX 77060 USA.
121. Thompson, I., *Fatigue damage variation within a class of naval ships.* Ocean Engineering, 2018. **165**: p. 123-130.
122. De Gracia, L., H. Wang, W. Mao, N. Osawa, I. Rychlik, and G. Storhaug, *Comparison of two statistical wave models for fatigue and fracture analysis of ship structures.* Ocean Engineering, 2019. **187**: p. 106161.
123. Yan, X., X. Huang, Y. Huang, and W. Cui, *Prediction of fatigue crack growth in a ship detail under wave-induced loading.* Ocean Engineering, 2016. **113**: p. 246-254.
124. Li, Z., W. Mao, J.W. Ringsberg, E. Johnson, and G. Storhaug, *A comparative study of fatigue assessments of container ship structures using various direct calculation approaches.* Ocean engineering, 2014. **82**: p. 65-74.
125. Kim, M.H., S.M. Kim, Y.N. Kim, S.G. Kim, K.E. Lee, and G.R. Kim, *A comparative study for the fatigue assessment of a ship structure by use of hot spot stress and structural stress approaches.* Ocean Engineering, 2009. **36**(14): p. 1067-1072.
126. Branco, R., F. Antunes, and J. Costa, *A review on 3D-FE adaptive remeshing techniques for crack growth modelling.* Engineering Fracture Mechanics, 2015. **141**: p. 170-195.

127. Loghin, A., U. Ozkan, A. Kaya, J. LeMonds, R. McClain, D. Decesare, S. Akkaram, and J. Laflen, *3DFAS: framework for conducting 3D crack growth simulation.* Propulsion-Safety Affordable Readiness, 2012.
128. Pathak, H., A. Singh, and I.V. Singh, *Fatigue crack growth simulations of 3-D problems using XFEM.* International Journal of Mechanical Sciences, 2013. **76**: p. 112-131.
129. Bhattacharya, S., I. Singh, B. Mishra, and T. Bui, *Fatigue crack growth simulations of interfacial cracks in bi-layered FGMs using XFEM.* Computational Mechanics, 2013. **52**(4): p. 799-814.
130. Erdogan, F. and G. Sih, *On the crack extension in plates under plane loading and transverse shear.* ASME. J. Basic Eng, 1963. **85(4)** p. 519–525.
131. Hussain, M., S. Pu, and J. Underwood. *Strain energy release rate for a crack under combined mode I and mode II*. in *Fracture analysis: Proceedings of the 1973 national symposium on fracture mechanics, part II*. 1974. ASTM International.
132. Maiti, S.K. and R. Smith, *Comparison of the criteria for mixed mode brittle fracture based on the preinstability stress-strain field.* International Journal of Fracture, 1984. **24**(1): p. 5-22.
133. Eshelby, J.D., *The force on an elastic singularity.* Philosophical Transactions of the Royal Society of London. Series A, Mathematical Physical Sciences, 1951. **244**(877): p. 87-112.
134. Zhang, G., Q. Le, A. Loghin, A. Subramaniyan, and F. Bobaru, *Validation of a peridynamic model for fatigue cracking.* Engineering Fracture Mechanics, 2016. **162**: p. 76-94.
135. Jung, J. and J. Seok, *Mixed-mode fatigue crack growth analysis using peridynamic approach.* International Journal of Fatigue, 2017. **103**: p. 591-603.
136. Sajith, S., K. Murthy, and P. Robi, *Experimental and numerical investigation of mixed mode fatigue crack growth models in aluminum 6061-T6.* International Journal of Fatigue, 2020. **130**: p. 105285.
137. MacMaster, F., K. Chan, S. Bergsma, and M. Kassner, *Aluminum alloy 6069 part II: fracture toughness of 6061-T6 and 6069-T6.* Materials Science Engineering: A, 2000. **289**(1-2): p. 54-59.
138. McCullough, R., J. Jordon, P. Allison, T. Rushing, and L. Garcia, *Fatigue crack nucleation and small crack growth in an extruded 6061 aluminum alloy.* International Journal of Fatigue, 2019. **119**: p. 52-61.
139. Chung, K.H. and W.H. Yang, *Mixed mode fatigue crack growth in aluminum plates with composite patches.* International journal of fatigue, 2003. **25**(4): p. 325-333.
140. Borrego, L., F. Antunes, J. Costa, and J. Ferreira, *Mixed-mode fatigue crack growth behaviour in aluminium alloy.* International Journal of Fatigue, 2006. **28**(5-6): p. 618-626.
141. Krizhevsky, A., I. Sutskever, and G.E. Hinton. *Imagenet classification with deep convolutional neural networks*. in *Advances in neural information processing systems*. 2012.
142. LeCun, Y., Y. Bengio, and G.J.n. Hinton, *Deep learning.* 2015. **521**(7553): p. 436-444.
143. Lake, B.M., R. Salakhutdinov, and J.B. Tenenbaum, *Human-level concept learning through probabilistic program induction.* Science, 2015. **350**(6266): p. 1332-1338.

144. Alipanahi, B., A. Delong, M.T. Weirauch, and B.J. Frey, *Predicting the sequence specificities of DNA-and RNA-binding proteins by deep learning.* Nature biotechnology, 2015. **33**(8): p. 831.
145. Lukka, T.J., T. Tossavainen, J.V. Kujala, and T. Raiko. *ZenRobotics Recycler–Robotic sorting using machine learning*. in *Proceedings of the International Conference on Sensor-Based Sorting (SBS)*. 2014.
146. Kutz, J.N., *Deep learning in fluid dynamics.* Journal of Fluid Mechanics, 2017. **814**: p. 1-4.
147. Tesche, C., C.N. De Cecco, S. Baumann, M. Renker, T.W. McLaurin, T.M. Duguay, R.R. Bayer 2nd, D.H. Steinberg, K.L. Grant, and C. Canstein, *Coronary CT angiography–derived fractional flow reserve: machine learning algorithm versus computational fluid dynamics modeling.* Radiology, 2018. **288**(1): p. 64-72.
148. Farrar, C.R. and K. Worden, *Structural Health Monitoring.: A Machine Learning Perspective*. 2012: John Wiley & Sons.
149. Söderberg, R., K. Wärmefjord, J.S. Carlson, and L. Lindkvist, *Toward a Digital Twin for real-time geometry assurance in individualized production.* CIRP Annals, 2017. **66**(1): p. 137-140.
150. Do, D.T., J. Lee, and H. Nguyen-Xuan, *Fast evaluation of crack growth path using time series forecasting.* Engineering Fracture Mechanics, 2019. **218**: p. 106567.
151. Unger, J.F. and C. Könke, *Neural networks as material models within a multiscale approach.* Computers & Structures, 2009. **87**(19-20): p. 1177-1186.
152. Kim, M., N. Winovich, G. Lin, and W. Jeong, *Peri-Net: Analysis of Crack Patterns Using Deep Neural Networks.* Journal of Peridynamics and Nonlocal Modeling, 2019. **1**(2): p. 131-142.
153. Raissi, M., P. Perdikaris, and G.E. Karniadakis, *Physics informed deep learning (part i): Data-driven solutions of nonlinear partial differential equations*. 2017: arXiv preprint arXiv:.10561.
154. Montgomery, D.C., E.A. Peck, and G.G. Vining, *Introduction to linear regression analysis*. Vol. 821. 2012: John Wiley & Sons.
155. Alpaydin, E., *Introduction to machine learning*. 2014: MIT press.
156. Simonsen, B.C. and R. Törnqvist, *Experimental and numerical modelling of ductile crack propagation in large-scale shell structures.* Marine Structures, 2004. **17**(1): p. 1-27.
157. Standard, A.S.T.M., *E647-15: Standard Test Method for Measurement of Fatigue Crack Growth Rates*. 2015, ASTM International West Conshohocken.